

Studies concerning the electronic structure and the electron transfer in electron poor intermetallics

Dissertation

zur Erlangung des Grades
des Doktors der Naturwissenschaften
der Naturwissenschaftlich-Technischen Fakultät
der Universität des Saarlandes

von

Stefan Engel

Saarbrücken
2025

Tag des Kolloquiums:	30.04.2025
Dekan:	Prof. Dr.-Ing. Dirk Bähre
Berichterstatter:	Priv.-Doz. Dr. Oliver Janka Prof. Dr. Holger Kohlmann
Akad. Mitglied:	Dr. Andreas Rammo
Vorsitz:	Prof. Dr.-Ing. Frank Mücklich

The experimental part of this work was performed from August 2021 to July 2024 at the department for inorganic solid state chemistry at Saarland University under the supervision of Mr. PD Dr. Oliver Janka.

Der experimentelle Teil dieser Dissertation wurde zwischen dem August 2021 und Juli 2024 an der Naturwissenschaftlichen-Technischen Fakultät der Universität des Saarlandes im Fachbereich der Chemie in der Anorganischen Festkörperchemie unter der Aufsicht von Herrn PD Dr. Oliver Janka durchgeführt.

I thank my mentor PD Dr. Oliver Janka for the interesting and challenging topic, the everlasting interest, the exceptional scientific guidance and all the valuable suggestions during the execution of this work.

Acknowledgments

I want to thank the following people for the support during my work:

- Mr. PD Dr. Oliver Janka for the topic, the trust, the discussions and the overall exceptional guidance.
- Mr. Prof. Dr. Guido Kickelbick for letting us use the laboratories.
- Mrs. Susanne Limbach for the support with the organization and the procurement of the chemicals.
- Mr. Dr. Bernd Morgenstern, Mrs. Dipl.-Ing. Jutta Kösters and Mr. PD Dr. Oliver Janka for the single crystal diffraction analysis and the help with arising crystallographic questions.
- Mr. M.Sc. Elias C.J. Gießelmann for the solid state NMR measurements and analysis, as well as the synthetic support.
- Mr. Dr. Frank Stegemann and Mr. Matthis Radzieowski for the treasures left in the drawer.
- Mr. Dr. Maximilian K. Reimann, Mr. M.Sc. Japer Baldauf and Mr. M.Sc. Lars Schumacher for the magnetic measurements.
- Mrs. M.Sc. Aylin Koldemir for the ^{151}Eu -Mößbauer spectroscopic measurements.
- Mr. Prof. Dr. Rainer Pöttgen for the cooperation working on the reviews, physical properties measurements as well as on the resulting manuscripts.
- Mr. Dipl.-Ing. Jörg Schmauch and Mr. Dr. Marcus Koch for the supervision and support at the SEM and measurements with the eSEM.
- Mr. Assoc. Prof. Dr. Gunter Heymann for the high-pressure synthesis of the $AEAl_2$ phases.

- Mr. M.Sc. Johannes G. Volpini and Mr. Prof. Dr. Hubert Huppertz for support on the Oxidation of the CaAl_2 phase.
- Mr. PD Dr. Frank Müller for the XPS measurements.
- Mrs. Dr. Petra Herbeck-Engel for the Raman microscope measurements.
- Mr. Dr. Rachid S. Touzani, Mr. Prof. Dr. V. Pavlyuk, Prof. Dr. Host P. Beck, Dr. Yuemei Zhang, Mr. Prof. Dr. Samir F. Matar, Mr. Dr. Peter C. Müller, Mr. Prof. Dr. Richard Dronskowski and Mr. PD Dr. Oliver Janka for the quantum chemical calculations and bonding analysis.
- Mrs. Dr. Kristina Brix and apl. Prof. Dr. Ralf Kautenburger for the ICP-MS measurements and analysis.
- Mrs. Dr. Eteri Svanidze, Mr. Dr. Mitja Krnel, Mr. Dr. Nazar Zaremba and Mr. Dr. Markus König for the electrical resistivity measurements on the SrAl_8Rh_2 single crystals.
- Cooperation partners and colleagues for the synthetic and analytical support.

Abstract

This doctoral thesis contains results in the field of new ternary intermetallic aluminum compounds with the general composition $M_xAl_yT_z$ with $M = \text{Ca-Ba, Y, La-Nd, Sm-Lu}$ and T being a transition metal of group nine and ten (Co-Pt). The goal was to synthesize new compounds and investigate their chemical bonding situation, charge transfer and influence of spectroscopic measurements. The first part shows results of the binary compounds $AEAl_2$ and $AEAl_4$ with $AE = \text{Ca, Sr, Ba}$ and the influence of the AE element on the chemical shift in ^{27}Al MAS NMR, supported by quantum chemical calculations. The second part contains new ternary aluminum compounds with a divalent cationic element M , which include Ca, Sr and Eu. Besides structure and ^{27}Al MAS NMR investigations, quantum calculations were performed giving insight into the chemical bonding situation as well as the charge transfer occurring in the compounds. In addition to the analytic methods mentioned above, electrical resistance measurements of the new compound SrAl_8Rh_2 and magnetic susceptibility data of the solid solution $\text{Eu}_2\text{Al}_{15}\text{Pt}_{6-x}\text{T}_x$ with $T = \text{Pd, Ir and Au}$ were recorded, showing the electronic behavior and the influence of the substitution on the magnetic behavior respectively.

The third part contains compounds with formally the trivalent cationic species. The series from the ternary compounds MAl_5Pt_3 and $M_2Al_{16}Pt_9$ could be extended by Y, La-Nd, Sm, Gd-Er or La-Nd, Sm and Gd, respectively. Magnetic measurements were conducted for the MAl_5Pt_3 series with $M = \text{Y, Ce-Nd, Gd-Ho}$ showing Pauli-paramagnetism for YAl_5Pt_3 whereas the compounds with Nd, Gd, Tb, Dy and Ho exhibit an antiferromagnetic ordering at low temperatures. Additionally, quantum chemical calculations, XPS and ^{27}Al MAS NMR measurements of YAl_5Pt_3 have been carried out.

In the fourth chapter, preliminary results of new ternary phases, namely CaAl_5Ni_2 , $\text{Eu}_5\text{Al}_{0.70(1)}\text{Pd}_{2.30(1)}$ and an extension of the $\text{RE}_4\text{Al}_{13}\text{Pt}_9$ series with $\text{RE} = \text{La-Nd}$ are summarized.

Zusammenfassung

Diese Dissertationsschrift beinhaltet Ergebnisse aus dem Gebiet neuer intermetallischer Aluminiumverbindungen mit der allgemeinen Zusammensetzung $M_xAl_yT_z$, wobei $M = \text{Ca-Ba, Y, La-Nd, Sm-Lu}$ und T ein Element der Gruppen neun oder zehn (Co-Pt) enthalten. Neben der Synthese neuer Verbindungen wird außerdem über Untersuchungen der chemischen Bindung und des Ladungsübertrags sowie der Einfluss auf spektroskopische Analysen berichtet.

Im ersten Teil dieser Arbeit werden neue Ergebnisse im binären System $AEAl_2$ und $AEAl_4$ über den Einfluss der Erdalkalimetalle Ca, Sr und Ba auf die chemische Verschiebung des ^{27}Al MAS NMR Signals gezeigt, die Untersuchungen wurden dabei mit Hilfe von quantenchemischen Rechnungen unterstützt.

Der zweite Teil der Arbeit berichtet über neue ternäre Aluminiumverbindungen, indem das Metall M als divalentes Kation in der Struktur vorzufinden ist, diese inkludieren Ca, Sr and Eu. Dabei wurden neben der Strukturanalyse und ^{27}Al MAS NMR Untersuchungen, quantenchemische Rechnungen durchgeführt, um die Bindungssituation und den Ladungsübertrag zu untersuchen. Zusätzlich wurden elektrische Widerstandsmessungen bei SrAl_8Rh_2 und Untersuchungen der magnetischen Eigenschaften an $\text{Eu}_2\text{Al}_{15}\text{Pt}_{6-x}\text{T}_x$ mit $T = \text{Pd, Ir und Au}$ aufgenommen, welche den Einfluss der Substitution auf das magnetische Verhalten aufweisen.

Der dritte Teil umfasst die Verbindungen in dem das Metall M den trivalenten Zustand annimmt. Dies sind die Reihen basierend auf divalenten Verbindungen MAl_5Pt_3 und $M_2Al_{16}Pt_9$, welche mit Y, La-Nd, Sm, Gd-Er beziehungsweise La-Nd, Sm und Gd erweitert werden konnten. Von den Verbindungen der MAl_5Pt_3 Serie mit $M = \text{Y, Ce-Nd, Gd-Ho}$ wurden die magnetischen Eigenschaften vermessen, wobei YAl_5Pt_3 Pauli-paramagnetisch ist, die Phasen mit Nd, Gd, Tb, Dy und Ho hingegen einen antiferromagnetischen Übergang bei niedrigen Temperaturen aufweisen. Zusätzlich wurden quantenchemische Rechnungen, XPS und ^{27}Al MAS NMR Messungen an YAl_5Pt_3 durchgeführt.

Im vierten Kapitel der Thesis werden erste Ergebnisse neu gefundener Phasen vorgestellt, diese enthalten Erkenntnisse zu CaAl_5Ni_2 , $\text{Eu}_5\text{Al}_{0.70(1)}\text{Pd}_{2.30(1)}$ und eine Erweiterung der $\text{RE}_4\text{Al}_{13}\text{Pt}_9$ Serie mit den $\text{RE} = \text{La-Nd}$.

1. Introduction.....	1
a. General introduction.....	1
b. Alkaline earth metal containing compounds.....	5
c. Europium containing compounds.....	20
d. Goals of this thesis	26
2. Experimental	27
a. Solid State Synthesis	27
I. Used Reactants	27
II. Arc Furnace	28
III. Induction Furnace.....	29
IV. Fused Silica Ampule.....	30
V. Alumina-Crucible.....	31
VI. Conventional Resistance Heating Muffle Furnace.....	31
b. Diffraction Techniques	33
I. Powder X-Ray Diffraction – PXRD.....	33
II. Single Crystal X-Ray Diffraction – SCXRD	34
c. Physical Properties – Magnetism	37
I. Ferro-/Antiferromagnetism	37
II. RKKY Interactions.....	39
III. Kondo-Effect.....	39
IV. Determination of Magnetic Properties via PPMS Measurements.....	40
d. Spectroscopy	43
I. Nuclear Magnetic Resonance – NMR.....	43
II. Scanning Electron Microscopy/Energy Dispersive X-Ray Spectroscopy – SEM/EDX	45
III. Raman Spectroscopy	46
IV. Inductive Coupled Plasma Mass Spectroscopy – ICP-MS	47
V. X-Ray Photoelectron Spectroscopy – XPS	48
VI. Mößbauer Spectroscopic Investigations.....	49
e. Quantum Chemical Calculations.....	51
3. Results.....	55
a. Results from Own Work (published).....	55

I.	Important Structure Types	55
II.	Investigations of Binary Intermetallic Compounds M_xAl_y containing Divalent Species with $M = \text{Ca-Ba}$	82
	1. Introduction	82
	2. Theoretical and ^{27}Al NMR Spectroscopic Investigations of Binary Intermetallic Alkaline Earth Aluminides	83
III.	Investigations of New Ternary Intermetallic Compounds $M_xAl_zT_y$ containing Divalent Species with $M = \text{Ca \& Sr}$	99
	1. Introduction / Motivation	99
	2. New compounds in the system Ca-Al-Pt and Sr-Al-T with $T = \text{Rh, Pt}$; MA_5Pt_3 , $M_2Al_{16}Pt_9$, $CaAl_2Pt_2$, Ca_2Al_3Pt , $SrRh_2Al_8$	103
IV.	Investigations of New Ternary Intermetallic Compounds $M_xAl_zT_y$ containing Divalent Species with $M = \text{Eu}$	157
	1. Introduction	157
	2. $\text{Eu}_4\text{Al}_{13}\text{Pt}_9$ – a coloring variant of the $\text{Ho}_4\text{Ir}_{13}\text{Ge}_9$ type structure.....	159
	3. Modifying the valence phase transition in $\text{Eu}_2\text{Al}_{15}\text{Pt}_6$ via the solid solutions $\text{Eu}_2\text{Al}_{15}(\text{Pt}_{1-x}\text{T}_x)_6$ ($T = \text{Pd, Ir, Au}$; $x = 1/6$)	173
V.	New Intermetallic Aluminum Compounds with a Trivalent Cationic Species	185
	1. Introduction	185
	2. Trivalent Compounds in the MA_5Pt_3 Series	186
	3. Trivalent members of the $RE_2Al_{16}Pt_9$ series adopting the $\text{Ce}_2\text{Al}_{16}\text{Pt}_9$ type structure 203	
b.	Unpublished Results from Own Work	217
	1. Introduction	217
	2. On the Existence of CaAl_5Ni_2	219
	3. The First Europium Rich Aluminum Palladinide Eu_5AlPd_2	225
	4. New Representatives with the $M_4Al_{13}Pt_9$ Structure	235
	5. ^{27}Al NMR Investigations in the System Yb-Al-T	245
c.	Cooperation Work	249
I.	Intermetallic Compounds	249
	1. MA_4Ir_2 ($M = \text{Ca, Sr, Eu}$): Superstructures of the KAu_4In_2 Type.....	249
	2. Raman and NMR Spectroscopic and Theoretical Investigations of the Cubic Laves-Phases $REAl_2$ ($RE = \text{Sc, Y, La, Yb, Lu}$)	252
	3. On the RE_2TiAl_3 ($RE = \text{Y, Gd-Tm, Lu}$) Series – the First Aluminum Representatives of the Rhombohedral $\text{Mg}_2\text{Ni}_3\text{Si}$ Type Structure.....	253

4.	Searching for Laves Phase Superstructures: Structural and ^{27}Al NMR Spectroscopic Investigations in the Hf–V–Al System	255
5.	Systematic Investigations of the Solid Solution $\text{Zr}(\text{V}_{1-x}\text{Al}_x)_2$ Adopting the Laves Phase Structures	257
6.	Structure, Physical and ^{27}Al NMR Spectroscopic Properties of the Missing Members of the Equiatomic REAlRh ($\text{RE} = \text{Sm}, \text{Tb}, \text{Dy}, \text{Er}, \text{and Lu}$) Series.....	259
7.	Working Title: NMR Spectroscopic Properties of the RE_2AlE_2 Series ($\text{RE} = \text{Sc}, \text{Y}, \text{Lu}; \text{E} = \text{Si}, \text{Ni}$).....	260
II.	Oxidation of Intermetallic Compounds.....	263
1.	Mechanistic Studies on the Formation of Ternary Oxides by Thermal Oxidation of the Cubic Laves Phase CaAl_2	263
2.	Rapid Synthesis of a Green Emitting Phosphor by Sulfidation of Intermetallic EuAl_2 and Its Use in a Hybrid Material	267
d.	Review Articles and Book Chapters.....	271
1.	Review: On the Ytterbium Valence and the Physical Properties in Selected Intermetallic Phases.....	271
2.	Review: Trivalent Europium – A Scarce Case in Intermetallics	271
3.	Book Chapter: “Bulk Metallic Glasses” in Applied Inorganic Chemistry	272
4.	Book Chapter: “Shape Memory Alloys” in Applied Inorganic Chemistry	272
4.	Conclusion	273
	Bibliography	277
	Cooperation Partners	287
	Publication List.....	289

1. Introduction

a. General introduction

The use of metals, alloys and intermetallic compounds plays a crucial role in the daily life of every person. Due to the versatility and the plethora of metals in the periodic table, a wide range of applications, for example in the field of transportation, is resulting. The element iron is the most used metal in cast iron steel, stainless steel or for more sophisticated applications such as magnets. Steel plays an important role in the construction industry, used as rebar rods in concrete or purely in T- or I-bars, but also as material for construction tools and in the transportation industry for shipping containers, railroad tracks and as crucial components in vehicles.¹ The second most used metal is aluminum, used due to its food safety, comparable low hardness (Mohs hardness of 2.75) and low density of 2.70 g cm^{-3} . The resulting light weight material is used as packaging material in soda cans and food containers, as vehicle parts and in the aerospace section.²⁻⁴

Another widely used metal is copper used as tubing for freshwater and gases, also it is the main applicant for electrical conducting wires due to the exceptionally high electrical conductivity compared to the material and manufacturing price.⁵

Besides iron the group 8 to 10 elements have a plethora of applications, Pd, Pt and the rest of the platin group elements are widely used in catalysis, where the specific element is precipitated in the surface of the bulk material, e.g. platinum on carbon or metal oxides like alumina, ceria or magnesia.⁶ The most commonly used catalyst is found in cars converting the exhaust gases (NO_x , C_xH_y and CO) to less environmentally harmful substances (N_2 , H_2O and CO_2). Elemental platinum was used in Döbereiner's lamp to catalytic react hydrogen with oxygen. The hydrogen was produced by the reaction of zinc metal with diluted sulfuric acid.⁷

Also, platinum metals are used in the dental industry, in jewelry, in photovoltaics and in fuel cells. Going to the elements in group 11, whereas copper is widely used in electrical wiring due to the good electrical conductivity, also intermetallic compounds with copper, e.g. brass and bronzes possess a wide range of applications. Silver and gold applications are primarily in the field of fashion and jewelry, also gold is used as electrical contacts ($\sim 0.034 \text{ g}$ in a cell phone) and as an investment option, whereas Ag on $\alpha\text{-Al}_2\text{O}_3$ was used as catalyst for the direct oxidation of ethene with oxygen to ethylene oxide.⁶

Another element which possesses a plethora of applications is nickel, but these applications are using intermetallic compounds containing nickel. For example, a material class known as shape

memory alloys, which exhibit the shape memory effect. Material with the shape memory effect can be deformed by an external force, stay in the deformed state until a stimulus in form of e.g. temperature or a magnetic field is applied. With the stimulus active the material will return to its original shape. When a stimulus is applied a crystal structure change occurs leading to a significant force during the self-reshaping. One of the most widely known shape memory alloy is the compound NiTi, better known as NiTiNOL, which was discovered at the Naval Ordnance Laboratory in White Oak, Maryland, USA.⁸ NiTi exhibits two crystal structures, first the austenite and secondly the martensite structure type. Even though the HT-phase of NiTi is called austenitic, the compounds crystallize with space group $Pm\bar{3}m$ and is not related to the austenitic steel phase which has space group $Fm\bar{3}m$. The martensitic structure on the other hand crystallizes with space group $P12_1/m1$ and corresponds to the RT-phase of the NiTi.^{9, 10} The transition between the HT and RT-phase takes place via a tetragonal or rhombohedral phase with the rhombohedral phase being either $P\bar{3}$, $P3$, $R3$ or $P31m$, as stated by the corresponding works.¹¹⁻¹⁵ With this effect, a material can use this property to store or generate force and/or motion, which leads to a plethora of researched applications in many different fields. Shape memory alloys are used exemplarily as springs for valves, fixators^{16, 17} or couplings in the transportation sector,¹⁸ these materials can also be used as rotor blades in helicopters¹⁹ or washers to reduce vibration,²⁰ as well as other applications.²¹⁻³⁹

As in the case of stainless steel, other elements like chromium or nickel and others are added to improve various mechanical or chemical properties like hardness and corrosion resistance,⁴⁰ analogue to that daily used aluminum foil also is alloyed with iron, copper, magnesium, zinc to improve the tensile strength to resist tears during use.⁴¹ Due to the versatility of aluminum, a plethora of interesting intermetallics containing said metal are known, even superconductivity with a critical transition temperature of 17.5 K was reported in Nb_3Al ,⁴² but it is outclassed by the widely used Nb_3Sn , which is used as superconducting coils in NMR devices.⁴³ By combining nickel with aluminum, $AlNi$ and $AlNi_3$ can be produced, these compounds are used as a high temperature material in e.g. turbines in airplanes.⁴⁴ During the high temperatures while using the turbines in an airplane, the Al atoms in the $AlNi$ get oxidized resulting in the formation of an alumina protective layer, preventing corrosion of bulk material and the slightly Ni enriched layer lying underneath.⁴⁵ Another used compound is Ti_3Al as high temperature material,⁴⁶ in analogy to $AlNi_3$ which belongs to the super alloys due to their superior chemical resistivity. Besides the aforementioned materials, many more compounds have been reported with highly interesting properties and applications, $Nd_2Fe_{14}B$ is widely used as hard magnets,⁴⁷

CeCu₂Si₂ exhibits superconductivity⁴⁸ and Mg₃Bi₂ functions as intermetallic thermoelectric material.⁴⁹

Before aluminum can be used as a reactant for the application either in materials or for researching new compounds, it has to be produced with high purity. For the production of aluminum, two ways are possible, first from mining the Al containing ore bauxite and subsequent refining, the so-called primary Al or by recycling already refined Al, the secondary aluminum.

The production of primary Al starts from mining bauxite in e.g. Australia, which is then transformed to pure alumina via the Bayer process. In the Bayer process crushed bauxite is placed in a pressure vessel alongside a sodium hydroxide solution at 433 to 543 K to dissolve the aluminum from the minerals found in bauxite like gibbsite (γ -Al(OH)₃), boehmite (AlO(OH) and γ -AlO(OH)) and diaspore (α -AlO(OH)) to receive sodium aluminate. The residual unsolved minerals contain TiO₂, SiO₂ and Fe₂O₃ and are called red mud. The sodium aluminate solution along the red mud is then diluted with water and transferred into a thickener and filtered. The thickened red mud gets transferred into a vacuum drum filter and is washed until no more alkaline solution is emitted and then gets removed, whereas the solution is cooled to around 333 K and an Al(OH)₃ crystallization seed is added to precipitate the dissolved aluminum hydroxide. The hydroxide is separated from the solution via the vacuum drum filter and the solid material is transferred into a furnace. Wherein a calcination process is started at temperatures of 1473 to 1573 K converting the Al(OH)₃ to nearly pure Al₂O₃ with 0.01-0.02% residual Fe₂O₃, SiO₂ and 0.5% Na₂O. The separated solution is reduced and recycled as the starting alkaline solution.⁵⁰

In the next step, the alumina is electrolytic reduced to aluminum using an electrolysis based on the Hall-Héroult process. The process was independently developed by the French scientist Paul L.-T. Héroult and the American chemist Charles M. Hall at the same time, thus leading to the name Hall-Héroult process. Although there have been many improvements in the process of the electrolytic reduction of alumina to aluminum, the process remains the same. The electrolysis uses graphite electrodes as anodes and cathodes, cryolite, a sodium hexafluoroaluminate (Na₃AlF₆), which in its liquid state can dissolve alumina. The electrolytic solution possesses five percent of dissolved alumina at a temperature of 1223 to 1253 K, cutting the melting point of alumina of 2327 K³ below half. At the cathode the aluminum ions are reduced to elemental liquid aluminum which get drained, but at the anode side, the oxygen anions react with the carbon to carbon dioxide, consuming the carbon anode slabs, also as soon as the melt is

depleting of oxide anions, a voltage rise is occurring enabling the reaction of the fluoride anions with the carbon to CF_4 and C_2F_6 . The resulting aluminum has a purity of 99.8 to 99.9%.^{3, 50, 51} Due to the environmental impact of the bauxite mining and refining to primary aluminum, the recycling of aluminum products is preferred due to the significant reduction in energy consumption to secondary Al by 95%. The secondary aluminum is extracted from scrap metal from leftovers or used materials. For used materials like soda cans and other painted junk the organic materials must be reduced first using ovens. Likewise alloyed metals have to be removed before the Al can be used again, in which the scrap metal gets shredded, passed through a magnetic remover and a flotation system to remove dust, iron, steels, Zn and Cu from the recycled aluminum.⁵⁰

Governmental report mineral commodity summaries 2024 gives insight into the production quantity in every country, showing that Australia mined the most bauxite with 102 million tons with Guinea on second place with 100 million tons followed by China with 90 million tons, which is nearly three quarters of the world mining of 400 million tons in 2022. When looking at the estimated bauxite resources Guinea leads with 7400 million tons and nearly half of the resources are found in Australia with 3500 million tons, followed by Canada with 2700 million tons and Jamaica with 2000 million tons, the overall bauxite resources stand around 30 billion tons. In the case of the actual alumina and aluminum productions, China stands at the top with 81.9 and 40.2 million tons in 2022.⁵² The advantage of mining and refining aluminum from bauxite is that Ga is produced as side product, which is also contained in the bauxite mineral.⁵²

The periodic table of the elements possesses to date 118 elements of which 92 are metals and 9 metalloids, with this overwhelming majority of elements an even larger number of possible combinations of the elements in form of intermetallic compounds can occur. This leads to a plethora of possible structure types, alongside individual properties, leading to extended possibilities to study structure-property relationships.

Our group primarily focuses on aluminum containing intermetallics, so the research topic in this work covers ternary intermetallic compounds which contain aluminum, a less electron negative element like the alkaline earth elements Ca-Ba or the rare earth elements Y, La-Sm, Gd-Lu, as well as an element with a higher electronegativity than aluminum. Here the transition metals cobalt, nickel, rhodium, palladium, iridium and platinum were used, to investigate the electron transfer in electron poor ternary intermetallic compounds. Since the electron transfer in binary compounds is significantly easier to understand and thus predictable by simply looking at the electronegativity of the corresponding elements of the compounds, two cases can

be described for the literature known binary compounds in which one element is always Al. Firstly the case Al–*T* compounds, in which Al has a lower electronegativity as *T* and donates electrons to the transition metal. The second case is *AE*–Al, here the electronegativity of Al is higher and receives electrons from the less electronegative alkaline earth element.

b. Alkaline earth metal containing compounds

As for the ternary compounds containing *AE*–Al–*T* the bonding situation cannot be predicted as easily as for the binary compounds, especially when Al–Al or *T*–*T* interactions are present. These systems contain not only ionic, covalent or metallic bonding behavior but rather a mixture of all three, with a varying degree.

In the Pearson's Crystal Database (version 2023/2024), 3884 entries are stated of known ternary aluminum intermetallic compounds. If the number of elements is limited to aluminum, the alkaline earth elements Ca, Sr and Ba as well as the rare earth elements Y, La-Nd, Sm-Lu and transition metals of group nine and ten (Co-Pt) the number shrinks to 1429 entries, of which the majority are rare earth compounds (1393 entries) compared to the alkaline earth representatives with 36 entries.⁵³ In **Figure 1.1** all known compounds in the system *AE*–Al–*T* (*T* being elements of group nine) with a total of seven phases, of which four contain Co, one Rh and two Ir are shown. Interestingly the cobalt containing phases are the only compounds which exhibit structures with all three alkaline earth metals and is also the only phase with barium with a transition metal of group 9. Besides the *AEAl₉Co₂* phases existing with all three alkaline earth elements, whereas the *AE₂Al₉Rh₃* can also be synthesized with Ca and Sr. Furthermore, by looking into the Gibbs triangle, the literature known phases are all in the Al rich corner, without any *T* or *AE* rich compounds found.

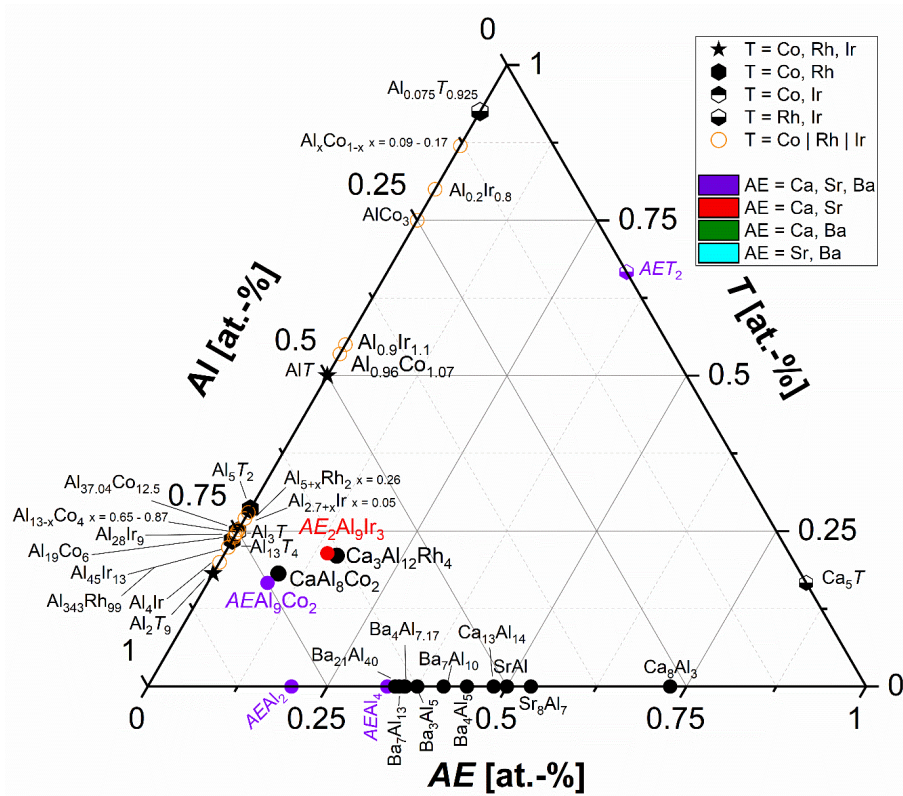


Figure 1.1: The Gibbs triangle of the ternary system AE - Al - T ($T = Co, Rh, Ir$). The data for the depicted compounds has been taken from the Pearson's crystal database or the papers cited in the introduction.

In comparison, **Figure 1.2** shows all compounds with the transition metals of group 10, here besides the Al rich phases, also phases with a significantly lower Al content could be characterized. In addition to the higher variety of the compositions, the number of compounds found is significantly higher with 25 phases. Like in the previous Gibbs triangle only one composition exists with the three alkaline earth elements Ca, Sr and Ba, but this time it is not the $AEAl_9T_2$ phase but the $AEAl_2Pt$ compounds. The composition $AEAl_9T_2$ also exists with Ni but only with Sr and Ba. Another composition with multiple element combinations is the AE_2AlT_2 phase, which exists with Ca and Sr with Pd and additionally with Ca and Pt. Besides related compounds in the transition metal groups alone, there are analogue phases between the group 9 and 10 transition metals, like $CaAl_8T_2$ with T being Ni, Co and $CaAlT$ with $T = Pd, Pt$. All the other known phases are singular, meaning that only this one phase exists with the corresponding alkaline earth and transition metal.

In the following a short overview of the literature known phases will be given alongside performed analytical methods.

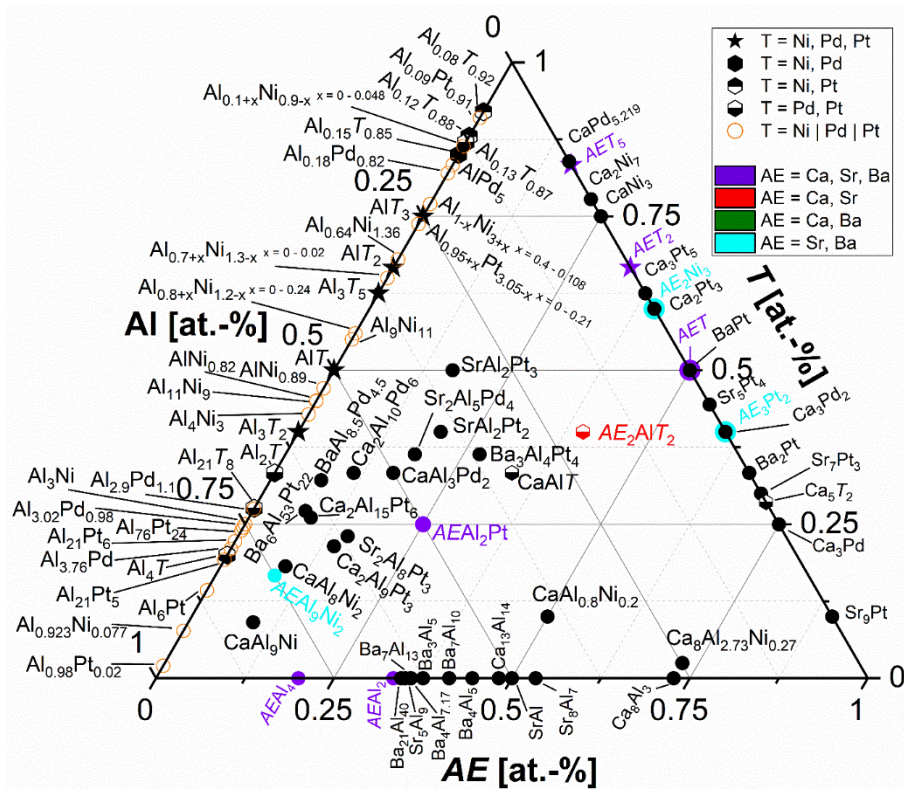


Figure 1.2: The Gibbs triangle of the ternary system AE - Al - T ($T = Ni, Pd, Pt$). The data for the depicted compounds has been taken from the Pearson's crystal database or the papers cited in the introduction.

In 1975 Turban and Schäfer reported about new structures with the $BaAl_9Fe_2$ type structure where they synthesized $SrAl_9Co_2$, $BaAl_9Co_2$, $SrAl_9Ni_2$ and $BaAl_9Ni_2$,⁵⁴ followed by the discovery of $CaAl_9Ni_2$ in 1988 by Zarechnyuk et al.⁵⁵ All compounds crystallize isostructural in the hexagonal crystal system with space group $P6/mmm$, containing one crystallographic independent position for the alkaline earth element ($1a, 0,0,0$), one for the transition metal ($2c, 1/3,2/3,0$) and two Al positions ($3f, 1/2,0,0$ and $6m, x,2x,1/2$). The AE atoms reside in an $AE@Al_{12}Al_6AE_2$ hexagonal prism capped on all six sides with additional Ba Al atoms and also on top and bottom with the next AE atoms, resulting in a coordination number of $12 + 6 + 2 = 20$. The transition metal atoms are surrounded in a trifold capped Al_6 trigonal prism with an overall coordination number of nine. The Al atoms on the $3f$ Wyckoff position exhibit a coordination number of $8 + 2 + 2 = 12$, consisting of a distorted Al_8 cuboid capped with opposing two T atoms and two AE atoms. The Al atoms on $6m$ are surrounded by eight aluminum atoms forming a highly distorted Al_8 cube capped on four sides with two neighboring AE and two T atoms, resulting in a coordination number of 12. In 2020 Ryzynska et al. grew single crystal of $SrAl_9Co_2$ and $BaAl_9Co_2$ and measured the physical properties and calculated the density of states of these compounds. The physical properties show no phase transition down to 1.8 K, but metallic behavior, which is in line with the calculated DOS. The d states of the transition metal

are completely filled, whereas the DOS at the Fermi level are contributed by the Al atoms. The *AE* contribution is above the Fermi level indicating the electron transfer from the *AE* to the Al_9Co_2 network.⁵⁶ Beside CaAl_9Co_2 another phase is known in the ternary system Ca–Al–Co, CaAl_8Co_2 , crystallizing like the nickel variant CaAl_8Ni_2 in the CeAl_8Fe_2 type structure in the orthorhombic crystal system with space group *Pbam*.^{55, 57, 58} The crystal structure will be discussed later in detail in **Chapter 3.II.4** for the SrAl_8Rh_2 compound.

In the work of Janka et al., quantum chemical calculations regarding the bonding interactions were conducted. The calculated Bader charges show a positive charge on the Ca atoms of +1.20, but also of the Al atoms between +0.25 to +1.29, the Ni atoms exhibit negative charges of –3.06 to –3.46. Despite the high charges, the DOSs shows states across the Fermi level indicating metallic behavior. The ICOHP values reveal covalent interactions of Al–Al and Al–Ni seemingly form a polyanionic $[\text{Al}_8\text{Ni}_2]^{\delta-}$ network with $\text{Ca}^{\delta+}$ occupying half of the formed pentagonal cavities.

In the system Ca–Al–Ni three more phases are known: CaAl_9Ni (own type), $\text{CaAl}_{0.8}\text{Ni}_{0.2}$ (MgCu₂ type) and the only compound with a high *AE* content $\text{Ca}_8\text{Al}_{2.73}\text{Ni}_{0.27}$ (own type). CaAl_9Ni was discovered by Manyako et al. in 1987, which crystallizes in the hexagonal crystal system with space group *P6₃/mmc* and four crystallographic independent atom positions one each for Ca (*2b*, 0,0,1/4) and Ni (*2c*, 1/3,2/3,1/4) and two for Al (*6h*, *x*,2*x*,1/4; *12k*, *x*,2*x*,*z*). The coordination number of the Ca atoms is 23 by 18 Al, two Ca and three Ni atoms forming a pseudo Frank-Kasper polyhedron, the Al atoms are surrounded each by eight Al and one Ni in a distorted capped square prism and Ni has a coordination environment of an Al capped Al_8 square antiprism.⁵⁵ The last two phases in the Ca–Al–Ni system were discovered in 2004 and 2005 by Zhang et al., they reported on the existence of the intermetallic compounds $\text{Ca}_8\text{Al}_{2.73}\text{Ni}_{0.7}$ ⁵⁹ and $\text{CaAl}_{1.8}\text{Ni}_{0.2}$,⁶⁰ which are results from substitution experiments of the Ca_8Al_3 and CaAl_2 compounds with Ni. In the case of the $\text{CaAl}_{1.8}\text{Ni}_{0.2}$ the compound crystallizes in the cubic crystal system with space group *Fd $\bar{3}m$* and exhibits two crystallographic independent atom positions, one for the Ca (*8b*, 3/8,3/8,3/8) and one for the mixed occupied Al/Ni position (*16c*, 0,0,0). The Ni substituted Ca_8Al_3 compound crystallizes like the unsubstituted phase in the triclinic crystal system with space group *P $\bar{1}$* . The structure features eight Ca positions ($8 \times 2i$, *x*,*y*,*z*), two mixed occupied positions for Al/Ni (*1c*, 0,1/2,0; *1f*, 1/2,0,1/2) and additional two positions for each Al and Ni ($2 \times 2 \times 2i$, *x*,*y*,*z*). No physical properties or quantum chemical calculations were done for the last three compounds, which is not the case of the following compounds, when descending from cobalt to the heavier homologues (Rh and Ir) only three compounds are known, $\text{Ca}_3\text{Al}_{12}\text{Rh}_4$, $\text{Ca}_2\text{Al}_9\text{Ir}_3$ and $\text{Sr}_2\text{Al}_9\text{Ir}_3$.

In the system Sr–Al–Rh as well as Ba–Al–Rh no phases were known to literature before this thesis (see **Chapter 3.II.4**), the same is true for the Ba–Al–Ir system. $\text{Ca}_3\text{Al}_{12}\text{Rh}_4$ crystallizes in the hexagonal $\text{Gd}_3\text{Al}_{12}\text{Ru}_4$ type structure with space group $P6_3/mmc$, featuring one Ca ($6h, x, 2x, 1/4$), two Rh ($6g, 1/2, 0, 0$; $2a, 0, 0, 0$) and four crystallographic independent Al atom positions ($12k, x, 2x, z$; $6h, x, y, 1/4$; $4f, 1/3, 2/3, z$; $2b, 0, 0, 1/4$). The two independent Rh sites are both surrounded by eight Al atoms in a distorted cube, which are connected over common corners and edges building strands along $[001]$. The Ca site has a coordination number of 19, consisting of two Ca, six Rh and eleven Al atoms. Beside the reported crystal structure, quantum chemical calculations were performed, showing negative Bader charges of -3.54 to -3.98 for the Rh atoms and positive Bader charges for Ca ($+1.24$) and Al ($+0.64$ to $+1.04$), which indicate alongside the interatomic distances to the formation of a $[\text{Al}_{12}\text{Rh}_4]^{\delta-}$ polyanionic network. Also, SEM/EDX measurements were performed, the results show good agreement with the theoretical composition values.⁶¹

Within the same publication of $\text{Ca}_3\text{Al}_{12}\text{Rh}_4$ also $\text{Ca}_2\text{Al}_9\text{Ir}_3$, $\text{Sr}_2\text{Al}_9\text{Ir}_3$ and $\text{Ca}_2\text{Al}_9\text{Pt}_3$ were reported. Single crystal studies were performed for the Ca containing compounds as well as the quantum chemical calculations. The three $AE_2\text{Al}_9T_3$ compounds all crystallize in the orthorhombic crystal system in the $\text{Y}_2\text{Ga}_9\text{Co}_3$ type structure with space group $Cmcm$ featuring one crystallographically independent site for the AE ($8g, x, y, 1/4$), two for T ($8e, x, 0, 0$; $4a, 0, 0, 0$) and four for the Al atoms ($16h, x, y, z$; $8g, x, y, 1/4$; $8f, 0, y, z$; $4c, 0, y, 1/4$). The Rh atoms are the same as in the $\text{Ca}_3\text{Al}_{12}\text{Rh}_4$ compound coordinated by eight Al atoms in a distorted cube. The coordination environment of the AE consists of six T atoms and eleven Al atoms in two corrugated hexagons of three Al and three T atoms which are connected to each other using three Al atoms as Al–Ni connections. The hexagons are capped on top with additional Al atoms, resulting in a coordination number of 17. The Al atoms form a Al_{11} supertetrahedron from face-capped trigonal bipyramids. The Bader charges of the Ca atoms were calculated to $+1.25/+1.22$, $+0.79$ to $+1.44$ and $+0.79$ to $+1.26$ for the Al atoms and -4.41 to -4.42 and -4.06 to -4.09 for the T atoms for $\text{Ca}_2\text{Al}_9\text{Ir}_3$ and $\text{Ca}_2\text{Al}_9\text{Pt}_3$ respectively, indicate analog to the $\text{Ca}_3\text{Al}_{12}\text{Rh}_4$ phase the formation of a polyanionic network consisting of the Al and T atoms.⁶¹

The Rh and Ir system exhibit only three compounds with alkaline earth elements, which is not the case for the Pd and Pt phases, seven Pd compounds and eleven Pt compounds in the system $AE\text{--Al--}T$ are known. As already mentioned before, another structure family exist with all three alkaline earth elements, the $AE\text{Al}_2\text{Pt}$ compounds. These crystallize in the MgAl_2Cu type structure with the orthorhombic space group $Cmcm$. The MgAl_2Cu structure is described in **Chapter 3.a.I** and features one crystallographically independent atomic position for each

element *AE*, Pt (both $4c, 0,y,1/4$) and Al ($8f, 0,y,z$). To understand the bonding situation and electron transfer of the *AEAl₂Pt* compounds, XPS, ²⁷Al as well as ¹⁹⁵Pt NMR investigations and quantum chemical calculations were performed. The XPS spectra of the *AE* compounds show decreasing Pt 4f binding energies when decreasing the electronegativity from Ca to Ba with Pt 4f binding energies of 70.7/74.0 (Ca), 70.6/73.9 (Sr), 70.5/74.3 eV (Ba). The Al 2s spectra show two signals, of which one originates from alumina on the surface and the second signal from the bulk material with lower binding energies, due to reduced formal valence of the Al atoms with binding energies of 117.5 (Ca and Sr) and 117.4 eV (Ba). When looking at the X-ray photoelectron spectra of the alkaline earth elements Ca 2p, Sr 3d and Ba 3d, the binding energy of the Sr and Ba electrons are between the ones of the pure element and of their corresponding oxides SrO and BaO with values of 133.5, 135.4 eV for SrAl₂Pt and 779.7 and 795.1 eV for BaAl₂Pt. In the case for the Ca compound the bonding energies of 347.4 and 351.0 eV is slightly larger than found in CaO.

The ²⁷Al NMR measurements revealed the expected one signal for the Ca and Ba compound, in the Sr phase an oxidic impurity is present, resulting in two signals, also the Ca and Sr compounds show spinning sidebands whereas the Ba compound only exhibits a single signal originating from the one crystallographically independent Al position, due to the large broadening. The isotropic Knight shifts of CaAl₂Pt, SrAl₂Pt and BaAl₂Pt are 711(2), 750(2) and 767(2) ppm. Also, when looking at the NMR spectrum of BaAl₂Pt, a broadening is observable, originating by a wide distribution of the Knight shifts, as results from structural distortions in the structure, which is also observable in ¹⁹⁵Pt spectra. The strongly distorted local environments can also be shown by the large quadrupolar coupling constants of $C_Q = 9.6(2)$ (Ca), 11.7(2) (Sr), 11.0(2) MHz (Ba). The ¹⁹⁵Pt NMR spectra of BaAl₂Pt shows isotropic magnetic shielding, but significant line broadening, due to the distribution of the isotropic shift. The isotropic Knight shift of the Ba compound is $\delta_{\text{iso}}^{\text{ms}} = 316(5)$ ppm. The Ca and Sr compounds do not show a single signal but the main signal with spinning sidebands, due to anisotropic magnetic shielding with Knight shifts of $\delta_{\text{iso}}^{\text{ms}} = 302(5)$ and 302(5) ppm as well as the axial magnetic shielding component $\delta_{\text{ax}} = -870(50)$ and 1090(50) ppm for CaAl₂Pt and SrAl₂Pt, respectively.

ICOHP values were calculated, showing that the Al–Pt interactions have the strongest covalent bonding interaction forming a covalent $[\text{Al}_2\text{Pt}]^{\delta-}$ network, which is additionally strengthened by Al–Al interactions. The Al–Al bonds also function as connection points for the polyanionic layers. *AE*–Al and *AE*–Pt have weak covalent interactions. Bader charges were calculated showing positive charges for the *AE* elements and Al, whereas Pt is negatively charged, which

is in line with the electronegativity. An additional observation is that the charge of the *AE* elements is not fully +2, but +1.31 (Ca), +1.27 (Sr), +1.11 (Ba) as well as Al is not +3 but exhibits a charge of +1.11 (Ca), +1.12 (Sr) and +1.16 (Ba), indicating not only ionic interactions, but also covalent interactions, especially of the Al with the Pt atoms. Lastly electron localization functions were calculated and plotted showing again strong Al–Al covalent bonding interactions, which become weaker when descending from Ca over Sr to Ba.

The magnetic properties of the *AEAl*₂Pt compounds were reported, showing nearly temperature independent susceptibilities with an upturn at lower temperatures, due to trace amounts of paramagnetic magnetic impurities. The intrinsic diamagnetism of the Ca and Sr compounds are overcompensated by the Pauli contribution of the conduction electrons, which is not the case for the Ba compound, where the diamagnetic behavior is observable.^{62, 63}

Next are compositions, which are present in more than one ternary system, starting with the Ca₂AlPd₂ which also exists with Pt and Sr, although the Sr compound crystallizes in another structure type. The compounds Ca₂AlPd₂ and Ca₂AlPt₂ were discovered by Miller et al. in 2015, they crystallize in the monoclinic crystal system with space group *C2/c* in the Ca₂SiIr₂ type structure featuring one crystallographically independent position for each element, Al (*4e*, 0,*y*,1/4), Pd/Pt and Ca (all on *8f*, *x,y,z*). A description of the Ca₂SiIr₂ type structure is given in **Chapter 3.a.I**. The structure features linear chains of the transition metals, which are aligned parallel in the *ab* plane and stacked along the *c*-axis, but the orientation of two adjacent slabs are nearly perpendicular to each other. Additionally, the interatomic distances of the transition metal are distorted leading to short and long distances of 283, 273 and 295, 295 pm for the Pd and Pt compounds, respectively, which lead to vastly different covalent bonding interactions as shown in the calculated ICOHP. The ICOHP values also indicate that the long *T–T* interactions have higher bonding interaction than the Ca–Al and Ca–*T* interactions. The highest values appear in the postulated polyanionic network between the Al and transition metal atoms followed by homoatomic *T* atom interactions. Additionally Bader charges were calculated, showing the expected positive charges on the Ca (+1.04 (Pd), +1.10 (Pt)) and Al (+0.31 (Pd), +0.62 (Pt)) atoms as well as the negative charge on the transition metal atoms (–1.19 (Pd), –1.42 (Pt)), again indicating the non-purely ionic interactions, but also covalent interactions of the Al atoms with the noble metal atoms. The calculated DOS of these compounds show that the Fermi level is close to a pseudo gap and also in combination with the COHP calculations, that the bonding is not optimized, resulting in slightly open shell structures with stabilizing through localized two center - two electron (2c-2e) and three center - two electron (3c-2e) multicenter bonding.⁶⁴

When substituting Ca for Sr, Sr₂AlPd₂ emerges, which crystallizes in the orthorhombic crystal system with space group *Fdd2*, isostructural to the Ca₂GePd₂ type structure. The reported structure features one crystallographic independent atomic position for each Sr, Pd (both $16b$, x,y,z) and Al ($8a$, $0,0,z$). Similar to the Ca compounds before, the structure exhibits parallel Pd chains in the *ac* plane, but these are equidistant with 301 pm and the stacking of the chain slabs is in an ABA'B' pattern, where the A and A' as well the B and B' are offset by $1/4 z$. The Al atoms together with the Pd atoms form zigzag chains, due to the position of the Al atoms alternatingly up and down along the Pd chains. The dihedral angle between the planes is 60.3° with the Sr atoms residing between the chains in puckered hexagonal layers. These corrugated honeycomb layers are stacked in an ABCD pattern along the *b*-axis. As an alternative description of the structure the tetrahedral Al@Pd₄ units can be used, which are connected over common corners forming the polyanionic network. The density-of-states were calculated and show that states at the Fermi level are present, indicating metallic characteristic of the phase, but lies near a local maximum of states, indicating electronic instability. By looking into the bonding states between the elements, it was shown that this structure is not a very stable polymorph, which leads to the calculation of the monoclinic variant analog to the Ca compounds resulting in a more stable structure by 8 meV per f.u., but due to the lower volume the orthorhombic structure, it becomes the more stable one. The low ICOHP values of the Sr–Pd and Sr–Al in combination with the Bader charges indicate more ionic than covalent interactions and an electron transfer from the Sr to the Pd atoms or the resulting polyanionic network. The high covalency of the Al–Pd bonds along the low positive Bader charge of the Al atoms result in the formation of the anionic network. Besides Sr₂AlPd₂ reactions with Pt instead of Pd resulted in the formation of SrAl₂Pt₃, which crystallizes in the CaCu₅ related CeCo₃B₂ type structure in the hexagonal crystal system with space group *P6/mmm*. The structure exhibits one crystallographic position for Sr ($1a$, $0,0,0$), Al ($2c$, $2/3,1/3,0$) and Pt ($3g$, $1/2,0,1/2$). The compound exhibits $(3.6)^2$ Kagomé nets of the Pt atoms in the *ab* plane, with Al atoms as interconnection points above and below the triangular meshes, resulting in a stacking along the *c*-axis. The Al atoms are coordinated by Al@Pt₆ trigonal prisms. The Sr atoms reside in the hexagonal prisms of twelve Pt atoms, which are additionally capped by six Al atoms, resulting in a coordination number of 18 for Sr@Pt₁₂Al₆. To understand the electron transfer and bonding situation ICOHP values, Bader charges and DOS calculations were performed. The ICOHP values in combination with the Bader charges also here indicate the formation of a polar covalent polyanionic [Al₂Pt₃]^{δ-} network, due to the strong ICOHP interaction of the Pt and Al, as well as the Pt and Pt atoms paired with the Bader charge of the Al being far away from +3.

Furthermore, the weak covalent interactions of Sr with the Al and Pt atoms and Bader charge of less than +2 of the Sr atoms, indicate a more ionic bonding behavior than covalent, resulting in the charge transfer from the Sr to Pt atoms. Due to the presents of states at the Fermi level, a metallic character of the compound can be associated, also the Fermi level resides in a small pseudo gap, which indicates good electronic stability.⁶⁵

Advancing from a composition which existed with both Ca and Sr together with Pt and Pd, to a composition that only exists with calcium, CaAlPd and CaAlPt. CaAlPd crystallizes in the orthorhombic crystal system with space group *Pbcm* and exhibits its own type. The structure has one crystallographically independent position for each Al ($4c, x, 1/4, 0$), Pd and Ca ($4d, x, y, 1/4$). CaAlPd consists of Ca atoms, which form double layers, whereas Al and Pd atoms form edge sharing square pyramids with four Al atoms as base and one Pd atom as top of the pyramid, the top is alternatingly above and below the Al pyramid base.⁶⁶ In contrast to CaAlPd, the platinum variant as well crystallizes in the orthorhombic crystal system, but in the TiNiSi type structure with space group *Pnma*, as reported by Hullinger et al. in 1993. The structure exhibits, similar to the Pd compound, one crystallographically independent position for each element Ca, Al and Pt (all $4c, x, 1/4, z$). With regards to the coordination environment, the Al atoms are surrounded by four Pt and four Ca atoms in form of two interpenetrating Al@Pt₄ and Al@Ca₄ tetrahedra and two additional Al atoms. The Ca atoms exhibit a coordination environment of five Pt and two Al atoms in form of a twofold Al capped tetragonal Pt₅ pyramid and the Pt atoms are placed in a trigonal prism consisting of four Ca and two Al atoms, which is additionally tricapped by two Al and one Ca atom. In 2011 Ponou et al. confirmed the crystal structure of CaAlPt with single crystal X-ray diffraction measurements.^{67, 68}

Three more compounds in the Ca–Al–*T* system with *T* being a transition metal of group 10 are known, of which two are formed with palladium, Ca₂Al₁₀Pd₆ and CaAl₃Pd₂, the final phase containing calcium and platinum is the modulated structure of Ca₂Al₁₅Pt₆. Ca₂Al₁₀Pd₆ crystallizes in a CaCu₅ related own structure type in the hexagonal crystal system with space group *P6/mmm* and exhibits one crystallographically independent position for Ca ($2c, 1/3, 2/3, 0$), one mixed occupied position Al1/Pd1 ($0.12/0.88, 1b, 0, 0, 1/2$), two for Al (Al2: $3g, 1/2, 0, 1/2$; Al3: $6j, x, 0, 0$) and one for the Pd atoms ($6m, x, y, 1/2$). The structure can, like CaCu₅, be described by Kagomé layers with identical stacking perpendicular to the *c*-axis consisting of the Al2 and Pd atoms, in the middle of one third of the resulting hexagons are the Al1/Pd1 mixed occupied atoms placed, in the remaining two thirds of the hexagonal prisms the Ca atoms, whereas the Al3 atoms are placed in the trigonal prisms of formed by the Kagomé layers. The following coordination environments result: the Al1/Pd1 atoms are surrounded by twelve

Al₃ atoms forming hexagonal prisms capped by three Al₂ and three Pd₂, resulting in a coordination number of 18, the Ca atoms reside in 2/3 of hexagonal prisms of twelve Al₂/Pd₂ atoms, which are capped by six Al₃ atoms on the sides and two Ca atoms on the basis of the hexagonal prism, resulting in a CN of 18+2. The Pd₂ atoms are coordinated by four Al₃ and two Ca atoms in form of trigonal prisms and additional two Al₂ and one Al₁/Pd₁ one sides as well as two Pd₂ atoms, adding up to a coordination number of eleven, the Al₃ atoms reside in trigonal prism consisting of four Pd₂ and two Al₂ atoms, two sides of the prisms are capped by Ca atoms and two edges by Al₃ atoms with additionally two Al₁/Pd₁ atoms over the edges of the triangular faces, the resulting coordination number is ten plus two, whereas the Al₂ atoms exhibit a coordination of 12 atoms, in form of a distorted icosahedron of four Al₃, four Pd₂ and four Ca atoms.⁶⁹

The compound CaAl₃Pd₂ crystallizes in the YAl₃Ni₂ type structure with space group *P6/mmm* and exhibits, like most of the aforementioned compounds, a polyanionic [Al₃Pd₂]^{δ-} framework with two crystallographically independent Ca atoms residing in hexagonal cavities of sixfold Pd₆ capped Al₁₂ and sixfold Al₆ capped Al₆Pd₆ hexagonal prisms. The X-ray photoelectron spectra of the Pd 3d_{5/2} and 3d_{3/2} lines show a shift to higher binding energies compared to elemental Pd, that is due to the formation of the polyanion and therefore additional formed bonds in the [Al₃Pd₂]^{δ-} network, but the measured electron density is still close to the one of elemental Pd with a small negative charge. The Ca lines are in range of formal divalent Ca atoms e.g. the ionic compounds CaO or CaCO₃. As for the magnetic properties, CaAl₃Pt₂ shows diamagnetism.⁷⁰

Janka et al. reported on the existence of Ca₂Al₁₅Pt₆ in 2017. The compound crystallizes in a modulated superstructure of the RE_{0.67}Al₅Pt₂ type structure (*RE* = Y, Ce, Gd-Tm, *P6₃/mmc*), which can be described using (3+2)D (*P6₃/m(α,β,0)00(ᾱ-β,α,0)00*) or (3+1)D (using the super space group *Cmcm(α,0,0)0s0*) interpretation and has an average structure with space group *P6₃/mmc*. The average structure is described in **Chapter 3.a.I**. Magnetic measurements of the compounds were performed showing that Ca₂Al₁₅Pt₆ exhibits diamagnetism at 300 K but below upturn of susceptibility is visible due to paramagnetic impurities. A better description is that the material is a Pauli-paramagnetic material, in which the diamagnetism is overcompensated with the paramagnetism from the conduction electrons.⁷¹

After showcasing all the calcium compounds, the remaining literature known Sr compounds should be addressed. Here, three additional structures are known: Sr₂Al₅Pd₄, Sr₂Al₈Pt₃ and the modulated structure SrAl₂Pt₂. Starting with the only palladium containing compound,

$\text{Sr}_2\text{Al}_5\text{Pd}_4$ crystallizes in the orthorhombic crystal system with space group $Pnma$ in its own structure type. The structure contains two crystallographically independent Sr, five Al and four Pd positions all on the Wyckoff site $4c (x, 1/4, z)$. The Al and Pd atoms form a network, which has two independent sixfold-capped pentagonal cavities in which the Sr atoms reside. These prismatic cavities are condensed via the pentagonal faces along the b -axis building strands and are shifted by $1/2$ to each other in the along b -axis. The capping atoms of one pentagonal prism form the cornerstones of the neighboring pentagonal prisms. These double strands are placed in a herringbone sequence, resulting in small cavities between the strands. The single crystal from the SCXRD measurements was used for semiquantitative measurements using SEM/EDX analysis showing a good agreement of the composition values with the theoretical ones. Besides the semiquantitative analysis, also quantum chemical calculations were performed. The density-of-states shows, that the compound has a metallic character, due to the existence of state at the Fermi level. In combination with the calculated Bader charges of Sr with +1.30 to +1.31, Al +0.91 to +1.25 and Pd -1.66 to -2.20 , it was shown that the Sr–Al as well as the Sr–Pd interactions are rather ionic due to the Bader charge and the small ICOHP value than covalent. In contrast to that, the Al–Pd exhibit high covalence that leads paired with the low Bader charge of +0.91 to +1.25 to a more covalent bonding, forming the postulated polyanionic $[\text{Al}_5\text{Pd}_4]^{5-}$ network, which is strengthened by covalent Al–Al bonding, with Sr being the cationic element transferring its electrons to the polyanion.⁷²

In 2021 the group of Janka reported on the existence of $\text{Sr}_2\text{Al}_8\text{Pt}_3$, which crystallizes in the tetragonal crystal system with space group $P4_2/nmc$ in the $\text{Eu}_2\text{Ni}_8\text{Si}_3$ type structure, exhibiting one crystallographically independent position for Sr ($8g, 1/4, y, z$), three for Al (Al1 and Al3: $8g, 1/4, y, z$, Al2: $16h, x, y, z$) and two for Pt (Pt1: $4d, 1/4, 1/4, z$; Pt2: $8f, x, -x, 1/4$). The structure can be described by a supertetrahedral arrangement of five Al_4 tetrahedra, the central Al_4 tetrahedron is connected to four other tetrahedra over common corners in a distorted bcc arrangement. The supertetrahedra form cavities in which distorted Sr_4 tetrahedra and Pt atoms reside in. The Pt atom arrangement of the structure is similar to the structure motive of CuAl_2 .⁷³ The coordination environment of the Sr atoms consists of eleven Al, five Pt and two additional Sr atoms, resulting in a coordination number of $16+2$. In the case for the two Pt sites, a coordination number of 18 for Pt1 consisting of 16 Al from the supertetrahedra and two Sr atoms and a CN of 22 for Pt2 from four Sr atoms and the remaining 18 Al atoms from the supertetrahedra. The Al1 and Al2 sites have three Sr atoms in their coordination environment, whereas Al3 is surrounded by two Sr atoms. Additionally exhibits Al1 six Al and four Pt atoms resulting in a CN of 13, Al2 has additionally five Al and three Pt atoms (CN = 11) and Al3 six

Al and two Pt added to the two Sr atoms in its environment (CN = 10). The structure exhibits three crystallographically independent Al positions, which are all observable in the measured ^{27}Al NMR spectra with a isotropic shift of $\delta_{\text{ms}}^{\text{iso}} = 505, 595$ and 543 ppm for Al1, Al2 and Al3, respectively, along an intensity ratio of 1:2:1, as well as significant line broadening at the magnetic field strength of $B_0 = 5.64$ T, due to strong nuclear electric quadrupole interactions. The signal broadening was reduced by measurement at a higher magnetic field of 14.1 T. Due to the metallic character of the compound, the magnetic shielding interaction is primarily influenced by the Knight shift. The reported experimental quadrupole parameters from the measurements of 5.3 (Al1), 7.6 (Al2), 6.6 MHz (Al3) are in good agreement with the theoretical values from the quantum chemical calculations of $+5.589, -6.344$ and $+6.027$ MHz. Besides the ^{27}Al NMR also ^{195}Pt NMR measurements were performed, showing a signal ration of 1:2, the Knight shift exhibit a large difference in the magnitude of the Pt signals as well as a large anisotropy in the magnetic shielding of -1500 ± 1000 ppm, resulting in a more negative magnetic shift of Pt2 than Pt1. The Pt1 site exhibits a higher symmetric environment resulting in a significant smaller magnetic shielding anisotropy of -800 ± 1000 ppm. Not only theoretical NMR values were calculated but also a bonding analysis was performed by calculating ICOHP values and Bader charges. The results show again a strong covalently bound polyanionic $[\text{Al}_8\text{Pt}_3]^{\delta-}$ network with Sr as cationic species, transferring its electrons to the polyanion. The Bader charges were calculated for Sr with $+1.21$, Al $+0.67$ to $+1.62$ and Pt -3.86 to -3.91 . Besides the NMR and quantum chemical analysis, the magnetic properties were investigated. Magnetic measurements resulted in nearly temperature independent susceptibility until 75 K, below that temperature an upturn is observable due to paramagnetic impurities.⁷⁴

Finally, SrAl_2Pt_2 crystallizes in an CaBe_2Ge_2 type structure related incommensurately modulated (3+2)D structure, which exhibits, due to the modulation, short to long Pt–Pt distances in the ab plane. During the temperature dependent X-ray studies, second order satellite reflections appeared, leading to the orthorhombic description of the crystal structure with the super space group $Pm\bar{m}n(\alpha,0,0)0s0(0,\beta,0)$ with $\alpha = 0.222(1) a^*$ and $\beta = 0.224(1) b^*$. The group-subgroup relations were formulated in the work of Janka et al. starting from the CaBe_2Ge_2 type structure ($P4/nmm$) a translationengleiche transition of index 2 lead to space group $Pm\bar{m}n$. For the (3+2)D structure the q -vectors have to get multiplied with the denominators, resulting in enlarged unit cell vectors a, b and c . By further transitions the (3+2)D super space group $Pm\bar{m}n(\alpha,0,0)0s0(0,\beta,0)s00$ can be transformed into the space groups $P2_12_12$, $Pba2$ or $P112/n$.⁷⁵

Lastly three Ba compounds are known. One compound, BaAl_{8.5}Pd_{4.5}, in the ternary Ba–Al–Pd system and two compounds with Pt, the Ba₃Al₄Pt₄ and Ba₆Al₅₃Pt₂₂ phases.

BaAl_{8.5}Pd_{4.5} crystallizes in the tetragonal LaFe₉Si₄ type structure with space group *I4/mcm* and features one crystallographically independent Ba (*4a*, 0,0,0), one Pd (*16l*, *x,y,z*), two Al (Al1: *16l*, *x,y,z*; Al2: *4d*, 0,1/2,0) as well as one mixed occupied Al/Pd position (0.13/0.87; *16k*, *x,y*,0). The Ba atoms are coordinated in pseudo-Frank-Kasper polyhedra of Ba@Al₁₆Pd₈, whereas the Pd atoms are inside an icosahedra of Pd@Ba₂Al₉Pd. The Al2 atoms are surrounded by four Pd and eight Al atoms also in form of an icosahedron (Al2@Pd₄Al₈), Al1 in pseudo-Frank-Kasper polyhedron of Al1@Ba₂Al₇Pd₄ and lastly the Al/Pd atoms on the mixed occupied position are surrounded by two Ba, seven Al and four Pd atoms resulting in a pseudo-Frank-Kasper polyhedron of Al/Pd@Ba₂Al₇Pd₄.⁷⁶

In 2015 Janka et al. reported on Ba₃Al₄Pt₄ compound, which is isopointal to the A₂Zn₅As₄ type structure (*A* = K, Rb), crystallizing in the orthorhombic crystal system with space group *Cmcm*, featuring two crystallographically independent positions for each Ba (Ba1: *8e*, *x*,0,0; Ba2: *4c*, 0,*y*,1/4), Al (Al1: *8g*, *x,y*,1/4; Al2: *8f*, 0,*y,z*) and Pt (Pt1: *8g*, *x,y*,1/4; Pt2: *8f*, 0,*y,z*). The structure can be described by a framework of distorted Al–Pt cubes, in which cavities the Ba atoms reside in. The heterocuban-like Al₄Pt₄ arrangements form strands along the *b*-axis by connection over common Al2/Pt2 edges. The strands are connected to each other via Pt1/Al1 atoms forming a hexagonal packing. In the cavities the Ba atoms are located. When looking along [010], the Ba2 atoms are placed between two distorted cubes, whereas the Ba1 atoms reside in channels formed by the framework. The Ba1 atoms are surrounded by four Al and four Pt atoms forming a half-sphere with additionally two Ba2 and two Pt atoms on the second half-sphere, resulting in a coordination number of twelve. Ba2 is coordinated by also four Al and four Pt atoms in the form of a distorted octagon with four Ba1, two Pt2 and two Al2 atoms above and below the octagon plane resulting in a coordination number of 16. The compound was semiquantitatively analyzed via SEM/EDX measurements. Additionally, the magnetic properties of Ba₃Al₄Pt₄ were investigated, showing intrinsic diamagnetism at 300 K, but at lower temperatures an increase of the susceptibility due to trace amounts of paramagnetic impurities. Besides the magnetic properties, also the electronic states of the compound were investigated via XPS, ²⁷Al NMR and quantum chemical calculations. The XPS measurements revealed that the Pt signal in the 4f_{7/2} spectrum is shifted to lower binding energies (70.9(2) eV) compared to elemental platinum, due to a higher electron density at the Pt atoms. The signal values of the Ba 4d_{5/2} and 4d_{3/2} are reported as 89.9(2) and 92.5(2) eV, respectively. The ²⁷Al NMR spectrum shows two

signals corresponding to the two crystallographically independent Al sites with a ratio of 1:1. The NMR signal at 1031 ppm ($Q_C = 3100$ kHz) exhibits a stronger quadrupolar interaction than the signal at 762 ppm ($Q_C = 2550$ kHz) due to the higher distortion of the local environment of the corresponding Al atom. In this case, both Al sites are coordinated tetrahedrally by two Pt1 and two Pt2 atoms. By using geometrical considerations, it could be shown that the tetrahedron surrounding of Al2 is more distorted than the one around Al1, leading to the signal at 762 ppm being that of Al1 and the signal at 1031 ppm originating from Al2. The bonding analysis via quantum chemical calculations using calculations of the density-of-states, ICOHP values and Bader charges showed the present of states at the Fermi level, suggesting metallic behavior. ICOHP values indicating in covalent bonding interactions between Al and Pt. The calculated Bader charges show positive values for the Ba and Al atoms whereas the charges of the Pt atoms are negative as expected with regard to the electronegativity. The bonding analysis suggests, due to the present of strong covalent Al–Pt bonding interaction as well as the relatively low charge on the Al atoms, a formation of a polyanionic $[Al_4Pt_4]^{\delta-}$ network, in which the barium atoms function as cationic species transferring their electrons to the network.⁷⁷

The last remaining literature known alkaline earth compound is nominal $Ba_6Al_{53}Pt_{22}$, which crystallizes in the hexagonal crystal system with space group $P6_3/mmc$ in its own structure type. The structure exhibits one crystallographically independent position for Ba ($12k, x, 0, z$), nine for Al (Al1 and Al2: $2 \times 24l, x, y, z$; Al7 and Al8: $2 \times 6g, x, 0, 1/4$; Al3: $12k, x, 0, z$; Al4: $12j, x, y, 1/4$; Al5: $12i, x, 2x, 0$; Al6: $8h, 1/3, 2/3, z$; Al9: $2b, 0, 0, 0$) and five for Pt (Pt1: $12k, x, 0, z$; Pt2: $12j, x, y, 1/4$; Pt3: $12i, x, 2x, 0$; Pt4: $4e, 0, 0, z$; Pt5: $4c, 1/3, 2/3, 1/4$), of which the Pt4 site is not fully occupied (at 285 K 96.1(4)% and at 90 K 98.2(6)%) resulting in phase compositions of $Ba_6Al_{22}Pt_{21.92(1)}$ and $Ba_6Al_{53}Pt_{21.96(1)}$. The structure can be described based on the coordination environments of the different crystallographic sites. Pt3 exhibits a coordination number of eight formed by a distorted $Pt3@Al_8$ cube. The Pt1 site is additionally capped by one Al atoms, resulting in a coordination number of nine. The $Pt3@Al_8$ cubes form threefold clusters by condensing over common faces in a hexagonal pattern in the ab plane at height $z = 0$, which is defined as layer A. The Pt2 atoms are surrounded by nine Al and the Pt5 atoms by eleven Al atoms. These irregular polyhedral are placed in a honeycomb-like arrangement (layer C) on the heights $z = 1/4$ and $3/4$, the resulting voids are filled above and below with the polyhedra of $Pt1@Al_9$ and $Pt4@Al_7$, which function as layer B, resulting in a stacking sequence of ABCB along the c -axis. One consequence of this stacking is the formation of Pt dumbbells along $[001]$. Between the BAB layers cavities remain, which are filled by Ba atoms, having a large

coordination number of 20+2 from $\text{Al}_{14}\text{Pt}_6+\text{Ba}_2$. SEM/EDX analysis showed good agreement of the measured composition with the stoichiometric values. Density-of-states were calculated for the structure, revealing that the most states are caused by the Pt and Al atoms. The number of Ba states is so low, that compared to the Al and Pt states no real contribution is observable in the DOS, also the shape of the Al and Pt states are similar, indicating covalent bonding interactions. The Fermi level resides in a pseudo gap, indicating a stable structure. To investigate the bonding situation ICOHPs were calculated, showing no significant covalent bonding interactions between Ba and Al or Pt, whereas the Al–Pt bonds exhibit a significant higher value per bond, suggesting strong covalent bonds. In the case of the Pt–Pt and Al–Al interactions, low bonding character was deduced. The calculated Mulliken charges of Ba atoms are +0.71, Al +0.14 to +0.60 and Pt –0.89 to –1.12. The Ba and Al atoms show positive values, whereas Pt atoms exhibit negative charges, as expected regarding the electronegativities. Overall suggest the low charges on the Al atoms as well the high ICOHP values a strong covalent bonding, which leads to the formation of the polyanionic $[\text{Al}_{53}\text{Pt}_{22}]^{\delta-}$ network, in which the Ba remains as cationic species, forming a polar intermetallic compound. In addition to the bonding analysis, heat capacity measurements were conducted to investigate a possible phase transition. The temperature dependence of the heat capacity at normal pressure from 100 to 2 K were recorded, but no signal in the specific heat capacity was reported, due to the presence of side product Al_2Pt with 33 wt.-%. The heat capacity exhibits a broad signal at 95 K, but no additional heat tone, suggesting no phase transition.⁷⁸

c. Europium containing compounds

The above summarized literature known phases show that the alkaline earth element acts as counter cations residing in various cavities in the polyanionic networks formed by the Al and T elements. With this knowledge, the sizes of the alkaline earth elements can be assumed to be that of the divalent ions with the corresponding ionic radii. This is useful in the investigation of isotypic structures, especially with e.g. europium having an ionic radius of 125 pm in case of the divalent cation, whereas strontium exhibits 126 pm.⁷⁹ With a difference of one picometer, analogous structures should be able to exist. In the field of intermetallic europium compounds, europium is commonly found in the divalent state inside the structure, with a few and rare exceptions like $\text{Eu}_2\text{Al}_9\text{Ir}_3$, which is then isotypic to the calcium compound. Other examples of intermetallic trivalent Eu compounds can be found in the review article.⁸⁰ When investigating europium compounds, in contrast to alkaline earth compounds, interesting physical properties emerge, due to the magnetic moment of the Eu ions and two possible oxidation states giving rise to a plethora of physical properties. Along with the valence of the europium inside the structure, the magnetic and electric properties can change significantly, whereas purely divalent Eu atoms exhibit a susceptibility near that of free Eu^{2+} ions $\mu_{\text{eff}} = 7.94 \mu_{\text{B}}$, Eu^{3+} ions do not exhibit a magnetic moment in theory due to spin-orbit coupling. However, at elevated temperatures, the first excited state is accessible leading to an effective magnetic moment of $\sim 3.5 \mu_{\text{B}}$ and van Vleck paramagnetism.^{81, 82} The divalent Eu compounds can exhibit a ferromagnetic or antiferromagnetic ordering at low temperatures, in which the magnetic moments of the Eu atoms arrange parallel or antiparallel. If the antiparallel ordering can be changed by applying an external magnetic field, the compound exhibits meta magnetism or spin reorientation. Besides a magnetic ordering, also the Eu valence can change depending on the temperature or pressure. These changes between the divalent and trivalent Eu atoms, result in valence fluctuations or valence changes. But not only purely divalent and purely trivalent Eu species can be found in intermetallic compounds, also phases, in which both Eu^{2+} and Eu^{3+} are simultaneously present can occur by changing the temperature, resulting in lower effective magnetic moments in these compounds. Besides the magnetic properties, the electrical resistivity is directly influenced by valence changes or magnetic ordering phenomena. Sharp drops of the electrical resistivity can occur at the respective transition temperatures. Pöttgen and Johrendt reported an overview of the equiatomic $\text{Eu}XT$ with $X = \text{Al, Ga, In, Si, Ge, Sn, Pb, P, As, Sb, Bi}$ and $T = \text{transition metals}$ alongside their physical properties.⁸³ Therefore, in the next part, all literature known Eu–Al– T compounds with $T = \text{Co–Pt}$ will be summarized along

with the performed analyses. **Figure 1.3** shows all existing compounds in the aforementioned element system, with twelve known phases. Starting in similar fashion with the Co to Ir phases, followed by the Ni to Pt compounds.

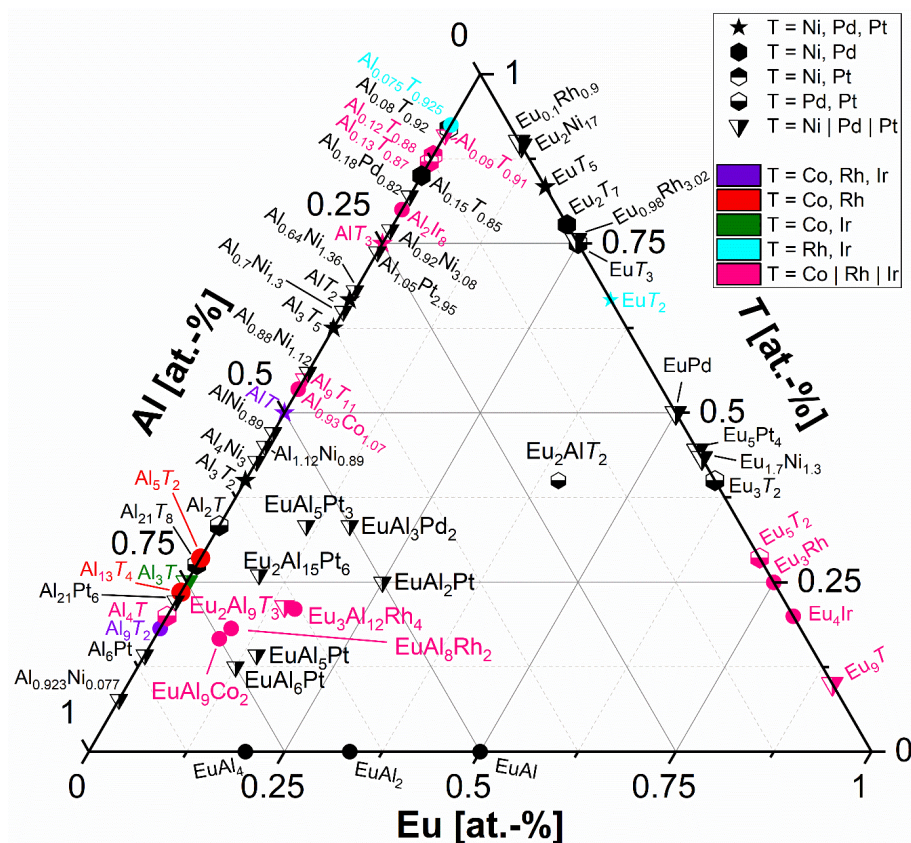


Figure 1.3: The Gibbs triangle of the ternary system Eu–Al–*T* (*T* = Ni–Pt). The data for the depicted compounds have been taken from the Pearson crystal database or the papers cited in the introduction.

The only cobalt containing compound is EuAl_9Co_2 and crystallizes isotypic to the alkaline earth variants in the BaAl_9Fe_2 type structure with space group $P6/mmm$. The structure was already described before in **Chapter 1.b**.⁸⁴

Two rhodium containing compounds are known with europium and aluminum, the EuAl_8Rh_2 and the $\text{Eu}_3\text{Al}_{12}\text{Rh}_4$ phases. $\text{Eu}_3\text{Al}_{12}\text{Rh}_4$ crystallizes isotypic to the analog to Ca compound (see **Chapter 1.b**),⁶¹ while the EuAl_8Rh_2 does not possess a literature known Sr variant, but it is isotypic to CaAl_8Co_2 , crystallizing in the CeAl_8Fe_2 type structure. Here the magnetic properties have been investigated. The Eu atoms in the structure form a Shastry-Sutherland lattice of triangles and squares along the *c*-axis. The performed physical measurements, resulted in a $T_{N1} = 12.5$ K, originating from magnetic coupling along the *c*-axis (Eu–Eu distance of 411 pm) and a $T_{N2} = 8.2$ K, due to in-plane antiferromagnetic coupling (Eu–Eu distances of 663 and 771 pm). Above 20 K the susceptibility becomes Curie-Weiss like paramagnetic with an effective

magnetic moment of $\mu_{\text{eff}} = 8.02$ and $7.91 \mu_{\text{B}}/\text{Eu}$ as well as Weiss temperatures of $\theta_{\text{P}} = -17.2$ and -15.5 K for $H||ab$ - and $H||c$ -axis, respectively. It was shown that with higher applied magnetic fields the Néel-temperatures T_{N1} and T_{N2} shift to lower temperatures and above a magnetic field of 6 T the T_{N2} vanishes. Also, with an external field above 6 T the in-plane (ab plane) configuration is tunable, resulting in a spin-flop process at 1/3 of full magnetization below 5 K. The specific heat measurements showed two sharp λ -like increases at 12.2 and 8.2 K due to the antiferromagnetic ordering and a large Sommerfeld coefficient of $\gamma = 393 \text{ mJ mol}^{-1} \text{ K}^{-2}$ could be calculated, which are larger than normal metal but comparable to other heavy-fermion compounds. The electrical resistivity shows metallic character with large residual resistivity ratio and a T^2 -dependence below T_{N2} and a robust linear T -dependence above T_{N1} , which describes a transition from Fermi-liquid-like behavior to strange-metal-like behavior.⁸⁵

In analogy to the calcium compounds, $\text{Eu}_2\text{Al}_9\text{Ir}_3$ and $\text{Eu}_2\text{Al}_9\text{Pt}_3$ are isotypic with each other and the Ca and Sr phases, crystallizing in the $\text{Y}_2\text{Ga}_9\text{Co}_3$ type structure with space group $Cmcm$.^{61, 86} The magnetic properties of $\text{Eu}_2\text{Al}_9\text{Ir}_3$ were investigated, showing van Vleck paramagnetic behavior, as a result of the trivalent Eu atoms, with trace amounts of paramagnetic impurities (3(1)% Eu^{2+}), due to an upturn below 25 K. When the trace amounts of Eu^{2+} are neglected, a coupling constant of $\lambda = 380(10)$ K was calculated, which is near the value of a free Eu^{3+} ion (480 K), with an effective magnetic moment of $\mu_{\text{eff}} = 4.56(1) \mu_{\text{B}}$ at 300 K. Also, Mößbauer spectroscopic investigations were performed to investigate the valence of the Eu atoms, resulting in isomer indicating purely trivalent Eu atoms in the bulk material.^{61, 86}

As no nickel containing compound is known, next the phases contain palladium and later platinum are discussed. EuAl_3Pd_2 was reported to be isotypic to CaAl_3Pd_2 , crystallizing in the YAl_3Ni_2 type structure with space group $P6/mmm$. Two crystallographically independent positions for each Eu (Eu1: $2d, 1/3, 2/3, 1/2$; Eu2: $1a, 0, 0, 0$) and Al (Al1: $6k, x, 0, 1/2$; Al2: $3f, 1/2, 0, 0$) as well as one Pd ($6l, x, 2x, 0$) site are present in the structure. A Kagomé lattice perpendicular to $[001]$ is formed consisting of three fourths of Pd and one fourths of Al atoms by the Al2 and Pd atoms with identically stacked on top of each other. The resulting trigonal and hexagonal prisms are filled with Al1 in the trigonal and Eu1 atoms in 2/3 of the hexagonal prisms, the Eu2 atoms reside in the plane of the hexagonal rings.⁸⁷

For the compound EuAl_5Pd no structure or structural data was reported only the synthesis from aluminum flux and magnetic measurements, which show an antiferromagnetic transition at T_{N2} 17.4 K and T_{N1} 15.8 K.⁸⁸

The EuAl_6Pd structure crystallizes with space group $Cmmm$ and exhibits one crystallographically independent site for each Eu ($2b, 1/2, 0, 0$) and Pd ($2d, 0, 0, 1/2$) as well as

two sites for the Al atoms (Al1: $4j, 0/2, y, 1/2$; Al2: $8n, 0, y, z$). The structure was described by Eu atoms forming a trigonal mesh on the ab plane, which is elongated along the b -axis. Additionally, physical properties were recorded, the magnetic measurements show an antiferromagnetic transition at $T_N = 17.5$ K. Below the Néel-temperature M/H decreases along the a - and b -axes but becomes constant along the c -axis with a small bend at 8 K, due to spin orientation. Above the Néel-temperature M/H follows the Curie-Weiss law with an effective magnetic moment μ_{eff} and a Curie-Weiss-temperature of θ_P of 7.87, 7.81, 7.84 μ_B/Eu and 7.91, 6.78 and 3.78 K with $H||a$, $H||b$ and $H||c$ -axis, respectively. The antiferromagnetic ordering is present on the easy c -axis near zero magnetic field. The structure possesses a saturation magnetization around 7 μ_B . When the magnetic field is perpendicular to the c -axis, metamagnetic steps around 22 and 25 kOe occur along the a and b -axes, respectively. The electrical resistivity measurements show a linear decrease with decreasing temperature, whereas the decrease of the electrical resistivity is reduced below 100 K and bends at the T_N . Below the T_N the resistivity decreases again. A residual resistance of 20 $\mu\Omega\text{cm}$ was calculated.⁸⁹ The EuAl_2Pt phase crystallizes isotypic to the AE compounds in the MgAl_2Cu type structure. Besides structural investigations also the physical properties were measured. The magnetic measurements reveal an effective magnetic moment of $\mu_{\text{eff}} = 7.97(1) \mu_B$ per Eu, which is a good fit for free Eu^{2+} with 7.94 μ_B per Eu. A Weiss constant of 52.7(1) K was determined, indicating dominant ferromagnetic interactions in the paramagnetic temperature range with a Curie-temperature of $T_C = 54.0(5)$ K. The saturation magnetization of 6.53(1) μ_B/Eu at 3 K and 80 kOe was reported. In the case of the heat capacity, the temperature dependent heat capacity measurements exhibit a λ -shaped increase at 50.9(2) K, indicating a second order transition. The electrical resistivity is decreasing linearly with decreasing temperature until the transition temperature, indicated by a bump at 53.2(2) K. After the transition a slope is present, due to spin order scattering reduction. The residual resistivity ratio of $\text{RRR} = 3.3$ indicates a bad metallic character of the compound. Mößbauer spectra show an isomer shift of $\delta = -9.94(1) \text{ mm s}^{-1}$ at 78 K, whereas at 4 K two isomer shift appear at $-9.45(2)$ and $+1.9(4) \text{ mm s}^{-1}$, which originate from 1.4(1)% Eu^{3+} impurity. X-ray photoelectron spectra of EuAl_2Pt were recorded for the Pt 4f, Eu 3d and Al 2s binding energies. The Pt 4f binding energy is equal to elemental Pt, suggesting no significant electron transfer to Pt. The Al 2s spectra show two peaks, one originating from oxidic layer on surface and one from bulk material at lower binding energies. The recorded Eu 3d spectra feature four signals, two for each di- and trivalent Eu atoms, the trivalent europium peaks have higher intensity, which emerged possibly from hydrolysis or decomposition on the surface. The bonding interactions were investigated via

ICOHP and DOS calculations. The ICOHP show, that structure exhibits strong covalent Pt–Al interaction as well as weak Eu–Al covalent bonding, leading to the several times mentioned description of a covalent $[\text{Al}_2\text{Pt}]^{\delta-}$ network with weakly interactions with the Eu atoms. The Density-of-states shows no gap at the Fermi level and the majority of the Eu 4f spin states are occupied, whereas minority spin states are unoccupied resulting in high spin (divalent) Eu. Bader charges were calculated showing positive values for Eu and Al atoms, Pt atoms exhibits negative charges, the Eu charge between +1 and +2 indicating divalent Eu atoms in the structure and also weak covalent interactions with the Al atom, similar to the *AE* variants the Al atoms have a charge close to +1 indicating rather covalent bonding in the Al–Pt network, the ELF calculations reveal covalent Al–Al bonding, which is weaker in the Eu compound than with the *AE* phases.⁶³

Eu_2AlPt_2 crystallizes in the aforementioned Ca_2SiIr_2 type structure with space group *C2/c* (see **Chapter 1.b**). The Pd variant Eu_2AlPd_2 in contrast crystallizes in the orthorhombic crystal system with space group *Fdd2* in the Ca_2GePd_2 type structure.⁹⁰

In 2022 the group of Ōnuki et al. reported on the existence of EuAl_5Pt_3 , crystallizing isotypic to the cerium compound in the YNi_5Si_3 type structure with space group *Pnma*. A detailed description of the structure can be found below in **chapter 3.a.I**. In the publication, physical properties were investigated, the magnetic measurements show an antiferromagnetic transition at $T_N = 12.4$ K with an easy *c*-axis. The electrical resistivity is highly anisotropic, whereas the measured resistivity along the *b*-axis is smaller than along the other axes. The Pt and Al atoms mainly contribute to conduction electrons. The resistivity decreases nearly linearly below Néel-temperature in all three directions. In addition, specific heat measurements were conducted, showing a second-order transition (antiferromagnetic transition) in form of a sharp λ -type anomaly at 12.4 K. Above 100 K, Curie-Weiss law behavior for all three axes is present. Below the Néel temperature, the susceptibility decreases for the $H||c$ -axis, but is unchanged for the other two axes, indicating an antiferromagnetic easy *c*-axis. The saturation magnetic field along the *c*-axis is approximately 9 T. The group of Ōnuki showed, that the Néel temperature T_N is tunable by increasing the pressure, as observable in the pressure-dependent resistivity measurements. The results led to a higher T_N up to 18 K at an applied pressure of 8 GPa. T_N is 14.7 K at 8.5 GPa and a vanishing of the antiferromagnetic transition above 9.5 GPa is observed, due to valence transformation of Eu^{2+} to a valence fluctuating state.⁹¹

The last literature known Eu containing compound is $\text{Eu}_2\text{Al}_{15}\text{Pt}_6$. It is isostructurally to $\text{Sc}_2\text{Al}_{15}\text{Pt}_6$, crystallizing in a commensurately modulated superstructure of the hexagonal $\text{RE}_{0.67}\text{Al}_5\text{Pt}_2$ compounds (*P6₃/mmc*, *RE* = Y, Ce, Gd-Tm, $\text{Sc}_{0.6}\text{Fe}_2\text{Si}_{4.9}$ type).⁷¹ The average

structure is described in **Chapter 3.a.I**. Temperature dependent powder X-ray diffraction measurements were conducted, showing a decrease of the lattice parameter c of -18 pm (-1.1%) below 60 K, whereas the a -axis decreased by -1 pm (-0.2%). Magnetic property investigations resulted in a rise of the susceptibility by decreasing temperature until the anomaly at $T = 50.7(1)$ K, below anomaly susceptibility rises slowly. No antiferromagnetic ordering was observable, the derivative reveals anomalies at $41.7(1)$ and $47.8(1)$ K and a paramagnetic Curie temperature of $-39.9(1)$ K. The effective magnetic susceptibility was calculated to be $\mu_{\text{eff}} = 7.90(1) \mu_{\text{B}}$, indicating divalent Eu atoms, but below 50 K the magnetic moment decreases to $\mu_{\text{eff}} = 1.67(1) \mu_{\text{B}}$, which indicates a trivalent Eu species with van Vleck paramagnetism. The heat capacity measurements show λ -shaped anomalies at $40.7(1)$ and $47.9(1)$ K, indicating a transition in two steps. When looking at the electrical resistivity, it decreases linearly with decreasing temperature until $51(1)$ K, where a small bump exists, below the bump the slope abruptly changes, indicating a drastic change in the band structure, which is caused due to valence change from Eu^{2+} to Eu^{3+} by delocalization of an electron, which is supported by the Mößbauer spectroscopic investigations. ^{151}Eu Mößbauer spectra were taken between 6 and 78 K, exhibiting one signal of trivalent Eu, that upon heating splits into two signals while above 55 K only one signal for divalent Eu is present. Lastly quantum chemical calculations were performed using DFT, indicating that the compound exhibits a metallic character and should possess an antiferromagnetic ground state with C -type antiferromagnetism, in which the spins couple antiparallel within layer and parallel between layers. The Density-of-states show that the Al states similar to aluminum metal and spread over whole energy range, with also the Pt states being broad and contribute equally to Fermi energy. The Eu $4f$ α -spin peak at Fermi level, indicates coupling of the Eu atoms with conduction electrons, whereas the remaining Eu states are located above Fermi level, also does the DOS indicate a possible variation of the occupation of the Eu $4f$ states.⁹²

d. Goals of this thesis

Main research focus of this work is the explorative and systematic preparative investigation of new intermetallic aluminum compounds to study their electronic structure and the electron transfer. The chemical bonding situation is highly complicated due to the presence of ionic and covalent bonding paired with conduction electrons. With these different parameters for the bonding situation, every compound is unique and has to be investigated in detail to understand the bonding. In this thesis the investigations of the electron transfer with electron poor compounds $M\text{-Al-}T$, with M being alkaline earth metals (Ca, Sr, Ba), europium and ytterbium and the transition metals T being elements from the Co and Ni group, are conducted, which also were investigated to a lesser degree so far according to literature. The influence on the covalent bonding characteristic found in these compounds is investigated using theoretical calculations on the DFT level and different spectroscopic measurements, for example ^{27}Al solid state NMR (indirectly probe the electronic structure at the Al nucleus) and X-ray photoelectron spectroscopy (shift of the signal depending on the electron count). Due to the different sizes of the alkaline earth elements, structural distortions occur when the same structure type is formed with different alkaline earth metals. This distortion can also be investigated by the ^{27}Al NMR studies, due to the change of the local environment surrounding the Al atoms inside the structures.

To receive insight into the bonding situation and electron transfer the experiments are placed on three pillars, (1) synthesis and crystallographic investigation of the intermetallic aluminum compounds, (2) the investigation of the bonding situation using DFT based methods including ELF, ICOHP, LOBSTER, ICOBI, Bader and Löwdin charges and (3) the extension and support of the theoretical findings with spectroscopic (XPS, NMR, Mößbauer) as well as physical measurements (magnetism, electrical resistivity).

With the results of these three pillars combined, an overall picture of the bonding situation and electron transfer can be obtained. As side product of the investigation of the bonding situations and electron transfer, also new ternary compounds are found, filling the gapps within the Gibbs triangles (**Figure 1.1-1.3**).

2. Experimental

a. Solid State Synthesis

I. Used Reactants

In this work all synthesized substances or intermetallic precursors were prepared by using their respective pure elements within the necessary stoichiometric ratio. All used elements are listed in **Table 2.1** according to their atomic number alongside their form, supplier and purity.

Due to the high reactivity with water and air the alkaline earth (*AE*) and early rare earth (*RE*) elements were stored in an argon (Air Liquide, 99.999%) filled dry box. Prior to use, the surface impurities on the *AE* and *RE* were removed mechanically using a sharpened spatula and metal brush. After the removal of the surface impurities, the elements were cut and weighed to the according calculated masses with a maximum deviation of 0.2 mg.

Table 2.1: Listing of the elements used with their atomic number, their supplier, form, and purity.

Element	Producer	Form	Purity (%)
Al #13	Koch chemicals	pellets	99.99
	Alujet	foil	99.5
S #16	ChemPUR	powder	99.95
Ca #20	ChemPUR	pieces	99.5
Fe #26	Carl Roth	powder	99.5
Co #27	Onyxmet	pellets	99.99
Ni #28	ChemPUR	wire	99.98
Cu #29	Riedel-de Haën AG	pieces	99
Ga #31	Onyxmet	button	99.99
Sr #38	Sigma Aldrich	rod	99
Y #39	Onyxmet	chunks	99.99
Ru #44	Onyxmet	pieces	99.9
Pd #46	ChemPUR	sponge	99.9+
Ag #47	Onyxmet	pellets	99.99
In #49	Fluka AG	pieces	99.5
Ba #56	Onyxmet	chunk	99.95
La #57	Onyxmet	chunks	99.6
Ce #58	Onyxmet	chips	99.9
Pr #59	Onyxmet	chips	99.9
Nd #60	Onyxmet	chips	99.9
Sm #62	Onyxmet	ingot	99.9
Eu #63	Onyxmet	ingot	99.9
Gd #64	smart elements	pieces	99.99
Tb #65	smart elements	chunks	99.95
Dy #66	smart elements	chunks	99.95
Ho #67	Onyxmet	dendritic	99.99
Er #68	Onyxmet	dendritic	99.99
Tm #69	smart elements	dendritic	99.95
Yb #70	Onyxmet	chunks	99.95

Lu #71	Onyxmet	chunks	99.95
Ir #77	ChemPUR	granules	99.9
Pt #78	Agosi AG	pieces	99.95
Au #79	abcr	shots	99.95

II. Arc Furnace

The arc furnace was built after the blueprint of Pöttgen et al.⁹³ consisting of a two-piece fused silica sample chamber, connected to a vacuum and Ar line, a water-cooled copper hearth with a recess for a copper or brass crucible, being the counter-electrode and a CeO₂ doped tungsten electrode. To produce the necessary electric current, a high frequency transformer (Lorch, HandyTIG 180 DC) is used with a foot pedal, to regulate the power output. The arc furnace can generate temperatures over 3000 K locally. The schematic structure alongside photographs is shown in **Figure 2.1**.

Many of the experiments were carried out in the arc furnace, either direct synthesis of the elements in a copper crucible or to close non-reactive metallic containers made of the refractory metals Nb or Ta (WHS Sondermetalle), in which the reactions were performed subsequently. Due to the presence of at least one low boiling element in the reaction, aluminum foil was used to wrap the reactants and prevent loss of the volatile element during the direct synthesis in the arc furnace. Prior to the reaction, the arc furnace was evacuated at least four times ($<15 \times 10^{-3}$ mbar) and refilled with argon. The argon was purified using titanium sponge at 873 K, molecular sieve, activated carbon and silica gel prior to the use. The reactions were performed under 800 mbar Ar and the resulting melting bead was turned over two to three times using the electrode as a handle and again melted to increase homogeneity.

If reactions were performed in the induction system, ampoules made of Nb and Ta were used due to the high melting points of Nb (2741 K) and the additional inertness of Ta (3269 K).⁴ To produce the metal ampoules, Nb/Ta tubes were cut to approximately 3 cm length. For the base and lid, sheets of the same material were punched to the according size and formed. The tubes and lids were subsequently washed with hexane to remove oily and metallic residues. The cleaned tube was inserted into the brass crucible and topped with a lid and arc-welded on one side. Subsequently, it was filled with the reactants and closed in the arc furnace with a second lid.

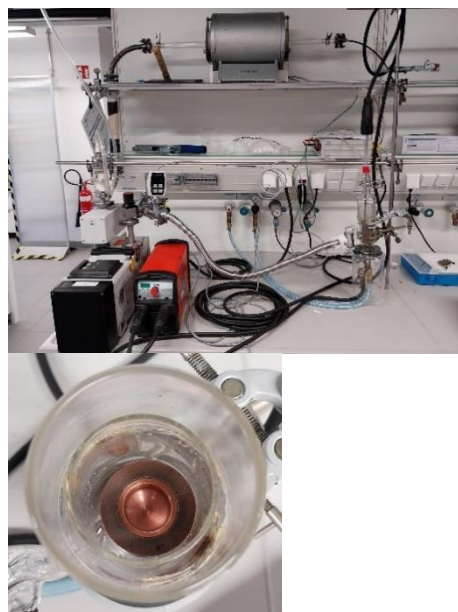
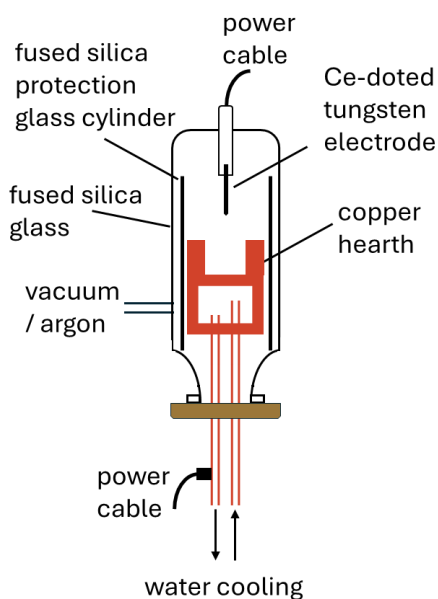


Figure 2.1: Schematic structure of the arc furnace and picture of the one used for the experiments in this thesis.⁹³

III. Induction Furnace

The induction furnace consists of an external oscillating circuit coupled to the midfrequency transformer (Trumpf Hüttinger, Truheat HF5010) providing the power output, the copper induction coil, and a water-cooled sample chamber. The schematic structure is shown in **Figure 2.2**. The transformer generates an alternating electrical field in the copper coil, which subsequently produces a fluctuating magnetic field. If a sample or the used container material is placed in the field, an Eddy-current will be induced, leading to the heating of the sample up to 2500 K due to its intrinsic electrical resistance.

The induction furnace was mainly used for direct syntheses in Ta or Nb ampoules and for heat treatments after reactions in alumina crucibles or directly in the metal ampoule. In either case the sample chamber was evacuated at least three times and filled with purified argon, which was reduced to around 800 mbar Ar pressure at the start of the heating process. A power output of around 0.7 kW was sufficient to heat most samples to over 1200 K. These temperatures were held for 10 min and subsequently cooled to RT or 1073 K for an additional heat treatment and holding for a prolonged time. Due to the possible step sizes of 0.01 kW, a lower cooling rate compared to the arc furnace was achievable.

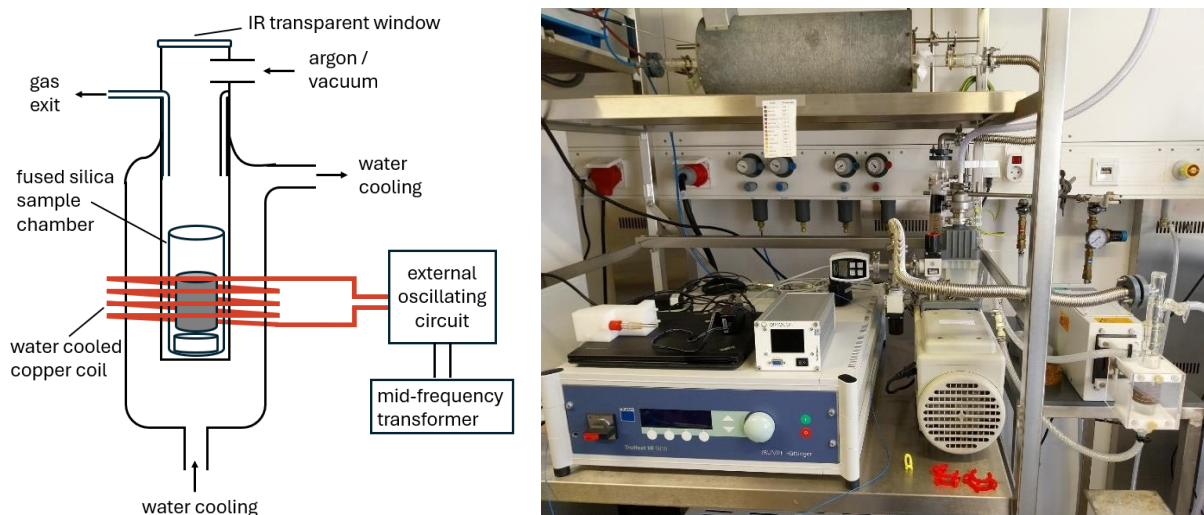


Figure 2.2: Schematic structure of the induction furnace and the photograph of the used induction furnace.⁹⁴

IV. Fused Silica Ampoule

Fused silica ampoules were prepared from silica tubes by cutting them to approximately 30 cm pieces and subsequently separated in the middle using a hydrogen/oxygen burner. These ampoules were filled with samples for heat treatment or for direct synthesis. For the direct synthesis without Ta/Nb ampoules, the fused silica ampoules had to additionally be coated with carbon, preventing the metals to react with the glass, by pyrolyzing acetone under anaerobe conditions at high temperatures.

The filled ampoules were evacuated ten times and filled with argon, which subsequently were sealed by melting using the hydrogen/oxygen burner and afterwards placed in the muffle furnace for heating. Examples are shown in **Figure 2.3**.



Figure 2.3: Filled fused silica ampoules, (top) with Ta ampoules and (bottom) with melting bead.

V. Alumina-Crucible

Due to the inert nature and high melting point (2345 K) of alumina (Al_2O_3), alumina crucibles were used as containers in annealing steps in the induction furnace and for direct syntheses using the aluminum flux method by stacking two crucibles on top of one another with the open side facing each other. The top was filled with fiberglass. When the reaction using a flux is finished, the temperature is still above the melting point of aluminum at around 973 K, subsequently the ampoule with the stacked alumina crucibles gets turned by 180° so that the crucible with the flux alongside the crystals is upside down. The still liquid aluminum then flows through the fiberglass, whereas the crystals are too big to go through, being retained at the fiberglass. After cooling, the fused silica ampoule is opened, and the two crucibles are separated with one holding the residue Al flux at the bottom and the upper one having the grown crystals on top of the fiberglass.

VI. Conventional Resistance Heating Muffle Furnace

Commercially available muffle furnaces (Nabertherm, N 11/HR) were used either for direct syntheses in fused silica ampoules with or without metal containers, or for subsequent heat treatment. Due to the conventional resistance heating of two opposing ceramic plates (**Fig. 2.4**, left) and a NiCr/Cr-thermal element coupled to the control unit (Nabertherm, C290, C30, P300), a defined temperature program was usable with cooling rates down to 2 K h^{-1} . In contrast to the arc furnace and induction furnace, only temperatures of 1553 K could be used in the muffle furnace.

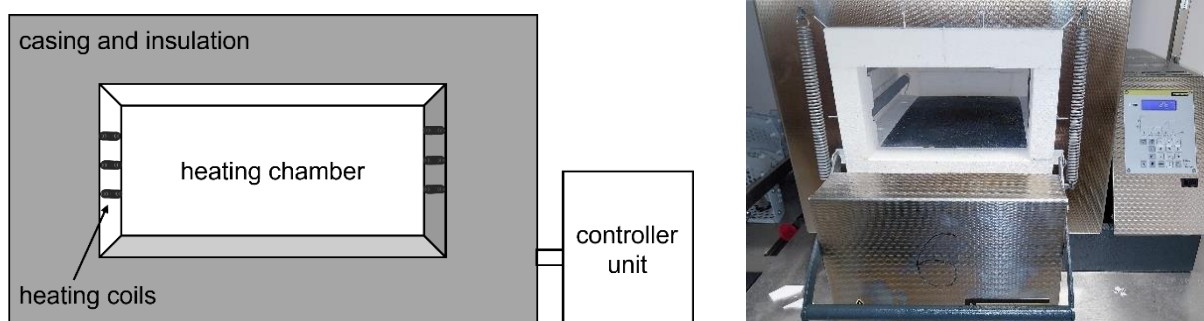


Figure 2.4: Schematic structure of a muffle furnace and picture of a Nabertherm N 11/HR including a P300 controlling unit.

b. Diffraction Techniques

I. Powder X-Ray Diffraction – PXRD

The first characterization technique after the reaction is powder X-ray diffraction, to analyze if the target phase has formed during the reaction and if a phase pure product or a mixture of two or more phases is obtained. For the preparation, the melting bead resulting from the arc furnace was first broken into smaller pieces in a steel mortar. A few big pieces were stored for later use, the remaining pieces were transferred to an agate mortar, covered in *n*-pentane and ground to a fine grayish powder. For the measurement, two sample holder types were used, firstly for high volume samples a steel sample holder with different cutout depths for the powder to fill up. Secondly, for low volume samples silicon zero-background sample holders were used, mainly due to the necessary sample sizes being only ~100 mg. If the powder was sensitive to air and the sample had to be stored in the glovebox, a Si zero-background holder with a thread alongside the dome counterpart was used to prevent the decomposition of the sample.

The measurements were performed on a Bruker D8-A25-Advance diffractometer with Bragg Brentano θ - θ geometry (goniometer radius of 280 mm) in a 2θ range of 6 to 130° with a step size of 0.013° equipped with a copper X-ray tube ($\lambda_1 = 154.0596$ and $\lambda_2 = 154.4426$ pm). A 12 μm Ni foil was used as a Cu K_β filter, additionally a variable divergence slit was installed on the primary beam site. On the secondary beam side, a LYNXEYE detector with 192 channels was installed.

The recorded diffraction data was evaluated with the Bruker TOPAS 5.0 software⁹⁵ using the instruments fundamental parameters. CIF-files taken from single crystal measurements or from Pearson's Crystal Data⁵³ were used for comparison. If no phase could be identified in comparison with the literature, at least one new compound formed. If the PXRD pattern fits to literature known phases, then the structures were loaded and the lattice parameters were refined first, followed by the crystal size, atomic parameters and lastly, if necessary, the preferred orientation.

II. Single Crystal X-Ray Diffraction – SCXRD

The SCXRD measurements and data integration were conducted by Dr. Bernd Morgenstern and PD Dr. Oliver Janka, both Saarland University.

Single crystal X-ray diffraction measurements were used, when an unknown phase was present in the PXRD pattern. For this a bigger piece of the melting bead was saved. This piece was crushed into small crystallites in a steel mortar and then transferred into a petri dish and placed under a Carl Zeiss Stemi 305 light microscope. Crystals with distinct crystal surfaces and no visible surface contaminations were isolated and fixed to a glass fiber using beeswax or nail polish. Subsequently the pin holding the single crystal was placed into the goniometer of either a Bruker X8 APEX2 or a Bruker D8 Venture diffractometer. The crystals were positioned centered in the X-ray beam using a high precision camera. Both diffractometers are equipped with CCD detectors and are using graphite monochromated Mo $K_{\alpha 1}$ radiation with a wavelength of $\lambda_1 = 71.073$ pm.

Before all reflection intensities were recorded, the unit cell was determined by taking either three sets of twelve frames (Bruker X8 APEX2) or 180 frames in a phi scan (Bruker D8 Venture) and indexing the reflections, suggesting a preliminary Bravais lattice and unit cell parameters. These parameters were compared to existing structures in the PCD⁵³ as indication whether it is a new structure or a crystal of a known side phase from the sample. If it seemed to be an unknown structure, the measurement method was set up by adjusting the area of the diffraction angle and exposure time. Intensity data sets with diffraction angles of up to $2\theta = 90^\circ$ were recorded and exposure times of 10-30 s were used depending on the crystallite size and instrument.

The multi-scan absorption correction was performed after the measurement, using the Bruker SadABS data package.⁹⁶ The generated .p4p and .hkl files were loaded into JANA2006^{97, 98} to solve and refine the structure. The algorithm SUPERFLIP,⁹⁹ implemented in JANA2006, was used for the structure solution. The data was subsequently refined using a full matrix refinement using the least square method on F^2 . The structure refinements were optimized by reduction of the residual factors $R1$ and $wR2$ as well as the goodness of fit GoF . $R1$ and $wR2$ are calculated as followed¹⁰⁰:

$$R1 = \frac{\sum_{hkl} ||F_{obs}| - |F_{calc}||}{\sum_{hkl} |F_{obs}|}$$

$$wR2 = \sqrt{\frac{\sum_{hkl} w (|F_{obs}^2 - F_{calc}^2|)^2}{\sum_{hkl} w (F_{obs}^2)}}$$

with F_{obs} as observed and F_{calc} as calculated structure factors. The weight parameter w is defined as:

$$w = \frac{1}{\sigma^2(F_{obs}^2) + (aP)^2 + (bP)}$$

with $P = \frac{1}{3} \max(0, F_{obs}^2) + \frac{2}{3} F_{calc}^2$.

The parameters a and b are optimized in a way that an equal distribution of the variances over the whole diffraction angle and intensity is present.

The *GoF* or Goodness of Fit is defined as:

$$GoF = \sqrt{\frac{\sum_{hkl} w (|F_{obs}^2 - F_{calc}^2|)^2}{m+n}}$$

with m representing the number of collected reflections and n as the number of parameters. A good structure refinement should lead to a *GoF* around 1.

Structural drawings were generated with Diamond 4¹⁰¹ and edited with Adobe Illustrator CS6.

c. Physical Properties – Magnetism

I. Ferro-/Antiferromagnetism

Ferromagnetism is a magnetic phenomenon, in which the magnetic moments align themselves spontaneously parallel below the so-called Curie-temperature T_C . If the material is heated above the Curie-temperature, the spin alignment and thus the magnetic properties will be lost, as shown in **Figure 2.5**. Every ferromagnetic material possesses domains, where the magnetic moments are aligned, these are called Weiss domains, named after Pierre-Ernest Weiss, but every domain possesses a different orientation. If a magnetic field is applied, the Weiss domains start to align in the direction of the magnetic field until every domain is aligned, leading to the magnetic saturation and thus the highest magnetic strength. In the field of ferromagnetic and also ferrimagnetic materials there are two different kinds of magnetic materials, namely soft and hard magnets. The difference in these two kinds is the magnetization strength, for soft magnets the magnetization hysteresis exhibits a slender hysteresis with small values of coercivity and remanence after the external magnetic field is removed. These materials are commonly used in transformer cores. Hard magnets on the other hand have a broad hysteresis with an ideal hard magnet having a square shape. Alongside the broad hysteresis, also large coercivity and remanence after the external magnetic field is removed are observed, also the magnetization changes after passing the coercivity value. Hard magnets are commonly used in magnetic memory and permanent magnets.⁸²

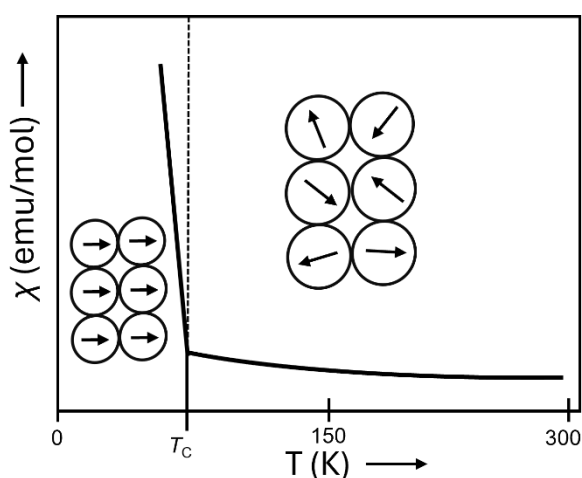


Figure 2.5: Ferromagnetic alignment of magnetic moment and temperature dependent susceptibility.

Antiferromagnetism is like two layers of ferromagnetic materials, which are antiparallel to each other. This results in a decrease and subsequent vanishing of the magnetic susceptibility below the Néel-temperature T_N . Above T_N the paramagnetic behavior is dominant leading to a slight increase of the susceptibility. There are different kinds of antiferromagnetic ordering, which can occur. The two most common kinds are firstly in-plane ordering, in which the magnetic moments of the atoms in a plane are alternatingly oriented and the secondly the layer-like antiferromagnetic ordering, which has parallel magnetic moments in-plane and an antiparallel ordering alternating between layer. The in-plane antiferromagnetic ordering originates from direct interactions (super exchange) from the magnetic moments, occurring when the distance of the magnetic moments of the atoms is under 300 pm, and results in an expected negative Weiss constant. In metallic compounds also RKKY interactions (see following chapter) are possible and are prominent in metallic samples, when the interaction distance is over 300 pm. The layer-like antiferromagnetism originates from indirect interactions resulting from coupling of the magnetic elements over a non-magnetic element, e.g. in Fe_3O_4 in which the magnetic moment of the iron atoms are coupled over the oxygen atoms resulting in the antiparallel ordering of the magnetic moments. The layer-like antiferromagnetic ordering results not in a negative Weiss constant but either 0 or slightly positive values.¹⁰²

Antiferromagnetism commonly originates in body-centered cubic or tetragonal structures, in these the magnetic moments of the atoms on the corners of the unit cell and the body centered atoms form substructures with antiparallel ordering, inside the substructure all moments are aligned parallel below the Néel-temperature. Below the Néel-temperature the magnetic moments couple inside the substructure resulting in a net zero magnetization due to the same strength of the magnetic moments of the substructures, as shown in **Figure 2.6**.⁸²

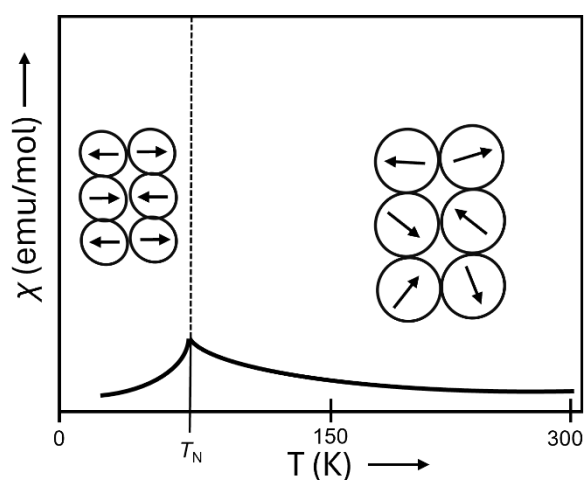


Figure 2.6: Antiferromagnetic alignment of electron spins and temperature dependent susceptibility.

A rather rare phenomenon is the so-called ferrimagnetism in which the magnetic moments are antiparallel but do not have the same strength, leading to an overall seemingly weak ferromagnetic behavior.

II. RKKY Interactions

The RKKY exchange interactions, firstly described by the name giving scientists Ruderman and Kittel (RK) in 1954, Kasuya (K) 1956 and Yosida (Y) in 1957, describes the interactions of the magnetic moments of the localized f-electrons in rare earth elements via conducting electrons over a large distance. A conduction electron interacts with the effective magnetic moment of the f-element atom in the crystal structure, so that the electron becomes spin polarized and carries the polarization to the next atomic site of the f-block element, where a relaxation of the magnetic moment occurs and causes a change in the spin polarization of the electron in the crystallographic site.¹⁰³⁻¹⁰⁵

III. Kondo-Effect

When the electrical resistivity of a metallic material is measured in dependency of the temperature, the resistance should decrease with lower temperature, as stated in the Matthiessen equation.

However, during the temperature dependent resistance measurements of a magnetic impure metallic sample having low amounts of impurities, Jun Kondo observed that the resistance showed a minimum at low temperatures and when cooled further the resistance would rise again. Jun Kondo explained this occurrence by using the fermi-level of the bulk material, also called fermi-sea. If this level is higher than that of the impurity, then the impurity is surrounded by potential walls. The electron of the impurity inside the potential walls can then tunnel through the wall as long as the temperature is low enough to a hole residing in the bulk material. When that happens an electron from the bulk material takes the place in the impurity, regardless of the spin orientation.¹⁰⁶

IV. Determination of Magnetic Properties via PPMS Measurements

PPMS measurements were performed by Lars Schumacher, M.Sc., Joshua Wiethölter, M.Sc., Jasper Arne Baldauf, M.Sc. and Dr. Maximilian K. Reimann from the group of Prof. Dr. Rainer Pöttgen (Institut für Anorganische und Analytische Chemie, University of Münster) and interpreted with the help of PD Dr. Oliver Janka.

The PPMS, short for Physical Property Measurement Systems, is an instrument, which is able to measure mechanical, thermal, electrical and magnetic properties between 1.9 and 395 K with the possibility to apply an external magnetic field up to 90 kOe. The measurements were performed on either the Quantum Design Physical Property Measurement System (PPMS2) or the Quantum Design PPMS DynaCool. These devices use a super conducting Nb_3Sn coil to generate the magnetic field and liquid He to achieve the cooling to the single digit Kelvin temperature region. For the preparation, two options are available, firstly using powdered samples e.g. after PXRD analysis or secondly using crystalline pieces directly. Subsequently, the samples were attached to the sample holder rod of the Vibrating Sample Magnetometer (VSM) by using PE (polyethylene) capsules for powdered samples or Kapton-foil for pieces to measure the magnetization $M(H,T)$. The schematic structure of the VSM is shown in **Figure 2.7**. The sample holder is placed into the PPMS, in which the sample is oscillating with a frequency of 40 Hz through the ring-shaped superconducting Josephson-contact to 2 mm above and below, inducing an electrical current. With this method a change in the magnetization of up to 10^{-6} emu can be detected.

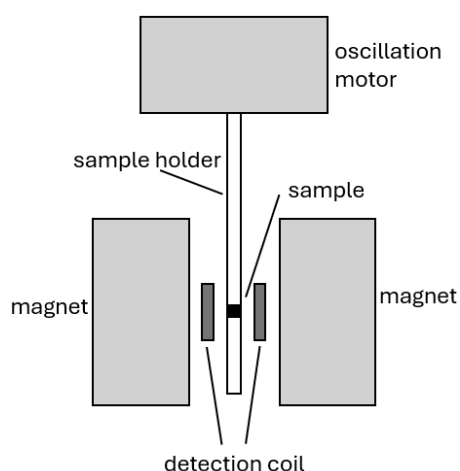


Figure 2.7: Schematic sketch of the VSM principle.¹⁰⁷

For the measurements of the magnetic properties, three experimental settings were used. First the zero-field-cooled (ZFC) measurement, in which the sample is cooled to the starting temperature of usually 3 K, at this point the external, high magnetic field of 10 kOe is applied. Heating of the sample and simultaneous measuring of the magnetization, leads to the possibility to calculate the magnetic susceptibility $\chi(T)$ and to subsequently extract the effective magnetic moment μ_{eff} .

The magnetic susceptibility can be fitted by using the modified Curie-Weiss law in the temperature range, where a linear increase of the curve is present and approximately 50 K apart from non-linear features:

$$\chi(T) = \frac{C}{T - \Theta} + \chi_0$$

With χ_0 as temperature independent term, in which e.g. the Pauli-paramagnetic value from the conducting electrons is included, C as Curie constant, T temperature and Θ as Weiss constant. The Weiss constant is above the magnetic ordering temperature either positive for ferromagnetic compounds or negative for antiferromagnetic materials.

The effective magnetic moment μ_{eff} is calculated by:

$$\mu_{\text{eff}} = \sqrt{8C}$$

with C being Curie constant.

The second setting is the zero-field-cooled / field-cooled (ZFC/FC) measurement at lower magnetic field (100 Oe). In this experiment the sample is cooled one time without and subsequently one time with the external magnetic field applied, giving insights into the magnetic ground state of the material.

Lastly, the third experiment is the measurement of the magnetization isotherms, in which the sample is cooled to and held at a specific temperature, then the applied magnetic field changes and the magnetization of the sample is measured. With this method the saturation magnetization can be determined and underlying magnetic phenomena verified.

For an in depth and more detailed insight in the theory of the magnetic measurement and magnetochemistry, the following literature is recommended.^{82, 108, 81}

d. Spectroscopy

I. Nuclear Magnetic Resonance – NMR

All NMR studies, both measurements and data analysis, were performed by Elias C.J. Gießelmann, M.Sc. Saarland University. Additional ^{27}Al MAS NMR measurements of CaAl_2S_4 and SrAl_2S_4 were performed in cooperation with Lukas P. Rütting, M.Sc. and Prof. Dr. Jörn Schmedt auf der Günne (Department of Chemistry and Biology, Faculty IV: School of Science and Technology, Inorganic Materials Chemistry and Center of Micro- and Nanochemistry and Engineering (Cm), University of Siegen).

Solid state NMR can be used to determine the number of different crystallographic positions of Al in a crystalline or amorphous solid. The number of signals observed in the spectrum correlates with the number of similar chemical environments. Depending on the first and second coordination sphere of the Al sites, and more precisely on the s-electron density at the Al nuclei, the observed NMR shift can differ significantly. Typical ranges for the ^{27}Al signals in intermetallic compounds are from 200 to 1200 ppm.¹⁰⁹ If the coordination environment of the Al position inside the crystal structure is not symmetrical or is distorted during the sample preparation, the measured peak form in the spectrum possesses an broadened and asymmetric peak form.

The intern *Hamilton* operator, which describes the resonance shift occurring during the resonance absorption and subsequent relaxation of electromagnetic with the *Lamour*-frequency inside an applied magnetic field, is a sum of different interactions found inside the measured sample. The intern *Hamilton* operator can be described as:

$$\hat{H}_{int} = \hat{H}_Z + \hat{H}_{RF} + \hat{H}_D + \hat{H}_{CS} + \hat{H}_J + \hat{H}_P + \hat{H}_K + \hat{H}_Q$$

The interactions are summarized in **Table 2.2** alongside the magnitude of influence.

Table 2.2: interaction of the nuclear spin and order of magnitude.¹¹⁰

Interaction	Magnitude (Hz)	Description
\hat{H}_Z	10^7 - 10^9	<i>Zeeman</i> -interaction
\hat{H}_{RF}	10^3 - 10^5	Interaction with the radiofrequency field
\hat{H}_D	10^3 - 10^4	Direct dipole-dipole interaction between nuclear spins
\hat{H}_{CS}	10^2 - 10^5	Magnetic shielding of the nucleus from the electron hull also called chemical shift
\hat{H}_J	10^0 - 10^3	Indirect dipole-dipole interaction via bonding electrons
\hat{H}_P	10^2 - 10^5	Interactions with unpaired electrons
\hat{H}_K	10^2 - 10^5	Interactions with conducting electrons, also known as <i>Knight</i> shift
\hat{H}_Q	10^3 - 10^7	Interactions of the nuclear quadrupole moment with the electric field gradient (EFG)

The ^{27}Al NMR spectroscopy is used in this work to validate the crystal structures, by the number of the Al position as well as the local environment of the Al positions. The interaction of the magnetic shielding of the nuclei with the electron hull shows the bonding situation and the local symmetry of the nuclei, whereas the interaction of the conducting electrons with the nuclei and the quadrupole interaction of the quadrupole moment of the nuclei with the electrical field gradient presents the information about the local environment of the Al positions. These interactions can shift the NMR signal to a few thousand ppm compared to the reference material AlCl_3 .

For a detailed insight about the theory of solid state NMR spectroscopy, please refer to the literature.^{109,111-115}

The samples were ground to a powder and mixed with dried sodium chloride in a ratio of 1:9 to reduce the density and the electrical conductivity. Subsequently the mixed sample were transferred into the 4 mm outer diameter cylindrical ZrO_2 rotor. The rotor was introduced into the Bruker Avance III 400 WB spectrometer, spun at the magic angle with 13 kHz using an air stream and the measurements were taken a resonant frequency of 104 MHz and a single pulse of 0.83 μs with a relaxation delay of 1 s. As reference to the measured resonance shifts, an aqueous 1 molar AlCl_3 solution was used.

The measurements of CaAl_2S_4 and SrAl_2S_4 were performed in cooperation with the group of Prof. Dr. Jörn Schmedt auf der Günne using a Bruker Avance Neo 600WB spectrometer with a magnetic field of 14.1 T. The two samples were measured without prior dilution and with a resonance frequency of 156.38 MHz.

The NMR spectra were recorded using Bruker Topspin software¹¹⁶ and subsequently analyzed using DMFit.¹¹⁷

II. Scanning Electron Microscopy/Energy Dispersive X-Ray Spectroscopy – SEM/EDX

SEM/EDX measurements were performed with supervision of Mr. Dipl.-Ing. Jörg Schmauch (Institut für Experimentalphysik) at Saarland University and ESEM analysis of the single crystals were done by Dr. Marcus Koch at the Institut für Neue Materialien (INM) in Saarbrücken.

Scanning electron microscopy is a method to analyze the morphology of samples and in combination with an energy dispersive X-ray spectroscopy detector, to qualitative and semi-quantitative element analysis. The interactions of free electrons with localized electrons are significantly higher than X-ray radiation or neutron interactions, so only a small sample size is necessary to analyze the compounds. The energy dispersive X-ray spectroscopy measures the characteristic X-ray radiation of the respective elements, which originates from the transition of an electron of an outer shell into a core near electron hole, whereas the core near electron holes are generated by the accelerated electron beam. This analysis method is dependent on the electron count of the elements, resulting in a lower detection limit of Na. Also, the EDX measurements are highly dependent on the surface of the sample, ideally the sample should be perfectly perpendicular to the electron beam as well as sanded and polished to receive a flat surface, to prevent absorption or scattering of the X-ray radiation by the own sample.

The SEM provides the focused electron beam via a thermionic cathode with a small emission energy, typical LaB₆ or W is used as cathode material. The emitted electrons are accelerated by using a high voltage on the anode side and are focused by different magnetic coils built in the electron microscope. The scanning electron microscope is equipped with two detectors, the secondary electron (SE) detector and the back scattering electron (BSE) detector. With the SE detector the topology of the sample can be visualized and using the BSE detector results in different brightness arises if an inhomogeneous sample is measured, due to the different averaged electron / element number in the respective phases of the sample.

For the analysis, powdered bulk samples were sprinkled on an aluminum sample holder covered by a sticky electrical conducting carbon tape. The excess material was removed by tapping the sample holder. Subsequently up to 7 samples were transferred into the sample holder, on which

the samples could be additionally sputtered with gold or carbon to make them electrically conducting. The samples were subsequently introduced in the JEOL 7000F scanning electron microscope, equipped with an EDAX Genesis 2000 EDX detector . Due to the preparation method (sprinkling of the sample on the sticky tape), the EDX results have a higher standard deviation with around 2 at.-%.

To investigate selected single crystals ESEM measurements were conducted on a Zeiss Evo MA10 scanning electron microscope, equipped with an Oxford Instrument EDX detector and using the variable pressure mode with under 60 Pa N₂ atmosphere. The internal standards *REF*₃, TiO₂, and Al₂O₃ were used for the calibration of the EDX measurements.

III. Raman Spectroscopy

The Raman measurements were performed by Dr. Petra Herbeck-Engel at the Institut für Neue Materialien (INM) in Saarbrücken.

The Raman spectroscopy is an analytical method to measure the vibrational energy modes of samples by using scattered light. During the light exposure of the sample, atoms with Raman-active modes get excited and one out of three events occur, the majority of scattering is the elastic scattering, also called Rayleigh scattering, in which the same wavelength of the incident photon and the scattered photon is present. The other two cases are the Raman scattering events with inelastic scattering leading to a higher or lower wavelength of the scattered photon.

In the case for the measured *MA*₂ compounds, crystallizing in the MgCu₂ Laves phase type structure, one Raman-active mode, which is the *8b* site of the *M* atom and being the T_{2g} mode is present.¹¹⁸ To prepare the measurement, powdered and crystalline samples were placed on the LabRAM HR Evolution HORIBA Jobin Yvon A Raman microscope, which is equipped with a 532 nm and a 633 nm Lasers. Additionally, an 1800 lines mm⁻¹ grating and a 100er LWD objective was used for the acquisition of the spectra.

IV. Inductive Coupled Plasma Mass Spectroscopy – ICP-MS

ICP-MS analysis was performed by Dr. Kristina Brix of the group of apl. Prof. Dr. Ralf Kautenburger at Saarland University.

ICP-MS is the abbreviation for inductive coupled plasma mass spectrometry and is a highly sensitive element analytical method for measuring element concentrations or the element ratio in compounds. The inductive coupled plasma consists of high heated and ionized argon by streaming it through a fused silica glass tube (torch) in an induction coil with a high frequency, the coil is generating a microwave field to which the Ar couples and is heated to 6800 to 10000 K.¹¹⁹

For the measurements, 1 to 7 mg of the sample were taken, dissolved in ultrapure hydrochloric acid and subsequently diluted with ultra-pure water to get a concentration of 5 to 100 $\mu\text{g L}^{-1}$. 10 $\mu\text{g L}^{-1}$ ^{165}Ho solution were added as internal standard as well as 69% ultra-pure HNO_3 to reach an acid concentration of 3-5%. External standards for the calibration of the measurements were Ca^{2+} , Al^{3+} , Ba^{2+} and Sr^{2+} with a concentration of 1 g L^{-1} . The solution were introduced in the Ar plasma by using a nebulizer, in which the elements become ionized and transferred into the Agilent 8900 Triple Quad and SPS 4 autosampler MS system. The mass spectrometer is equipped with three quadrupoles, the first quadrupole functions as a mass filter to prevent non-analytical compounds from being measured and interfering with the results. Subsequently the ions pass through the collision and reaction cell (CRC), where the measured isotopes ^{44}Ca and ^{137}Ba collide with He as the collision gas and ^{88}Sr and ^{27}Al collide with O_2 as the reaction gas to prevent signal overlap due to similar m/z . After the CRC follows a second quadrupole, which rejects off-mass ions so only the target ions are detected.

V. X-Ray Photoelectron Spectroscopy – XPS

The XPS measurements were performed and partially interpreted by PD Dr. Frank Müller (Institut für Experimentalphysik) at Saarland University.

X-ray photoelectron spectroscopy is based on the photoelectron effect, which is the emission of core near electrons using radiation and used to get an insight of the oxidation state of the elements in the sample. To detect the emitted electrons, an ultra-high vacuum is necessary. The technique is highly surface sensitive, due to the short mean free path length of the photoelectron of 0.5 to 3 nm. The kinetic energy of the emitted electron E_{kin} is calculated by:

$$E_{\text{kin}} = h\nu - \phi_{\text{S}} - E_{\text{B}}$$

With $h\nu$ as energy of the X-ray photon, ϕ_{S} as emission energy of the spectrometer and E_{B} as binding energy of the electron.^{120, 121} The ϕ_{S} is a sample specific and not a device parameter, which can be influenced by the conductivity of the material.

The samples of Al_3Pt_2 and YAl_5Pt_3 were ground to a fine powder, pressed to pellets with a diameter of ~ 4 mm and subsequently glued onto a conductive carbon tape Al sample holder. The Al sample holder had a smaller diameter than the pellet to prevent spectral features from the carbon tape and the Al holder. The sample was introduced into the ESCALab Mk II spectrometer, equipped with a Vacuum Generators and a 180° -type PreVac EA 15 analyzer with a multichannel plate detector. An ultra-high vacuum of approximately 1×10^{-8} bar was applied. To reduce the oxidic layer on the surface of the elemental references for the Pt 4f and Al 2s spectra, Pt foil was cleaned by Ar ion etching as well as the oxide layer of an Al sheet was partially removed by etching. The spectra were taken with a monochromatic Al K_{α} radiation ($\lambda = 1486.6$ eV) in normal emission mode (polar angle $\vartheta = 0^\circ$) with an energy pass of 50 eV, additional of 20 eV and step widths of 1 eV and 100 meV for survey and detailed spectra respectively. The binding energy was calibrated by the C 1s peak of the samples.

VI. Mößbauer Spectroscopic Investigations

The ^{151}Eu Mößbauer spectroscopic measurements were conducted in cooperation with Aylin Koldemir, M.Sc. from the group of Prof. Dr. Rainer Pöttgen, Institut für Anorganische und Analytische Chemie at the University of Münster.

Mößbauer spectroscopy is a method to analyze the electronic and magnetic hyperfine interactions and the oxidation state of elements e. g. ^{151}Eu in samples, by determination of the so-called isomer shift δ , which is the energy difference of the radiation source and the sample. The analytical method is based on the Mößbauer effect and describes the recoil free nuclear resonance absorption of gamma radiation in solid state matter. It is named after Rudolf L. Mößbauer.¹²² When an atom absorbs or emits a γ -photon, a recoil occurs. If this happens in a crystalline material, the whole structure will divide the recoil energy, resulting in a significantly reduced recoil of the single atom. For gases and liquids, the division of the recoil energy is not possible. Also, the loss of energy of the γ -ray is bigger than the width of the emission and absorption lines, so no overlap of both lines is happening.

For a detailed insight about the theory of the Mößbauer spectroscopy, please refer to the literature.¹²³⁻¹²⁶

The used radiation source for the measurement of ^{151}Eu is $^{151}_{62}\text{SmF}_3$. The $^{151}_{62}\text{Sm}$ isotope possesses a half-life of 90 years and is decaying in a β^- -process into $^{151}_{63}\text{Eu}$, which is to 99% a direct and radiation free transition into the 5/2 ground state of the Eu, but 1% of the Sm decays into Eu with the excited ground state of 7/2.¹²⁷ This excited state then relaxes by emitting a γ -photon with the energy of 21.53 keV with a half-life of 9.7 ns. These photons are used for the spectroscopic investigations. 1% of the total activity of the $^{151}\text{Sm}:\text{EuF}_3$ source (65 MBq) was used for the measurement in the transmission geometry. The frequency of the emitted γ -radiation has to be varied using the doppler effect, by movement of the source dependent on the sample, due to the difference of the nucleus environment of the source and the sample. The sample was filled into an enclosed PMMA container with the required mass calculated from the work Long et al.¹²⁸ Whereas EuAl_2S_4 was measured in pure form, EuAl_2 had to be diluted with SiO_2 . For the measurement, the source was kept at room temperature, whereas the sample was cooled to 6 / 78 K using a continuous flow He (Janis Research Co LLC) or a liquid nitrogen bath cryostat system with a resistance thermometer as temperature controller. The γ -radiation was detected with a NaI(Tl) scintillation crystal, measurements were fitted using the WinNormos for Igor6 program package.¹²⁹

e. Quantum Chemical Calculations

Quantum chemical calculations were performed and interpreted by Dr. Rachid S. Touzani (Otto von Guericke Universität Magdeburg), Prof. Dr. Horst P. Beck (Universität des Saarlandes), Prof. Dr. Volodymyr Pavlyuk (Ivan Franko National University of Lviv, Ukraine, department of inorganic chemistry), Prof. Dr. Yuemei Zhang (Warren Wilson College, Swannanoa, NC, USA) and PD Dr. Oliver Janka. Dr. Peter C. Müller and Prof. Dr. Richard Dronskowski (Institute of Inorganic Chemistry, Solid State and Quantum Chemistry, RWTH Aachen) provided support and an in-depth introduction in the LOBSTER program package.

Due to the different quantum chemical calculations methods a brief overview of the calculations will be given in the following.

The quantum chemical calculations for SrAl_5Pt_3 , $\text{Sr}_2\text{Al}_{16}\text{Pt}_9$ and $\text{Eu}_4\text{Al}_{13}\text{Pt}_9$ were made with Quantum ESPRESSO,^{130, 131} the PAW pseudopotentials¹³² from the PSLibrary version 1.0.0¹³³ for Al, Pt, Sr were used, in the case of Eu only a non-magnetic model was available, so a ferromagnetic model was created by the Wentzcovitch method¹³⁴ to use in the structural relaxation. 100 Ry and 400 Ry were chosen as the kinetic energy cut-off for the plane waves and cut-off for the charge density and potential respectively. The relaxation of the structure was stopped, as soon as either a total energy convergence of 10^{-6} Ry or a force convergence of 10^{-5} Ry/ a_0 was reached. The Brillouin-zone integration was calculated by the Marzari-Vanderbilt cold smearing,¹³⁵ additionally a Gaussian spreading of 0.01 Ry were applied. By using the Monkhorst-Pack algorithm¹³⁶ the k -meshes were divided into $2 \times 14 \times 8$ for SrAl_5Pt_3 , $14 \times 6 \times 4$ for $\text{Sr}_2\text{Al}_{16}\text{Pt}_9$ and $14 \times 4 \times 2$ for $\text{Eu}_2\text{Al}_{13}\text{Pt}_9$. The generalized gradient approximation (GGA) functional, parameterized by Perdew, Bruke and Ernzerhof (PBE-GGA)¹³⁷ was used to treat the exchange and correlation in the density functional theory (DFT) calculation. The Bader charges were calculated using the methods by Henkelman et al.¹³⁸⁻¹⁴⁰ and Yu and Trinkle¹⁴¹ with the critic2 program^{142, 143} by firstly generating all-electron and valence electron densities. Subsequently, the chemical bonding analyses were performed by using the TB-LMTO 4.7 program¹⁴⁴ and the implemented tight-binding, linear muffin-tin orbitals with the atomic spheres approximation (TB-LMTO-ASA).^{145, 146} This program calculated a new k -mesh with the exchange and correlation treated with the GGA functional, parameterized by Perdew et al.¹⁴⁷, with $4 \times 22 \times 12$ for SrAl_5Pt_3 , $22 \times 22 \times 22$ for $\text{Sr}_2\text{Al}_{16}\text{Pt}_9$ and $22 \times 8 \times 4$ for $\text{Eu}_4\text{Al}_{13}\text{Pt}_9$, leading to 252 k -points, 1530 k -points and 180 k -points in the irreducible Brillouin zone (IBZ)

respectively. The radii of the automatically generated Wigner–Seitz cells for Sr, Pt and Al were 2.32 Å, 1.48–1.53 Å and 1.39–1.56 Å in SrAl₅Pt₃, 2.37 Å, 1.50–1.53 Å and 1.42–1.54 Å in Sr₂Al₁₆Pt₉ and in Eu₄Al₁₃Pt₉ the radii for Eu, Pt, Al were 2.07–2.15 Å, 1.47–1.55 Å and 1.40–1.47 Å respectively. Empty spheres were included in the calculation of the LMTO for Sr₂Al₁₆Pt₉ and Eu₄Al₁₃Pt₉, whereas no empty spheres were needed for SrAl₅Pt₃. The bonding analyses were done by the calculation of the Density-of-states (DOS) and the crystal orbital Hamilton population (COHP)¹⁴⁸ alongside their integrals (ICOHP). Negative –COHP show antibonding states, whereas positive states are bonding and non-bonding states have –COHP values of zero. The Fermi level was set to 0 eV as reference.

The density functional theory (DFT) calculations of the *AEAl_x* (*AE* = Ca–Ba, *x* = 2, 4) series, *REAl₂* (*RE* = Sc, Y, La, Yb, Lu), the oxidation products of CaAl₂, *REAlRh* series, YAl₅Pt₃, Ca₂AlPt₂, CaAl₂Pt₂ and Ca₂Al₃Pt were conducted by using the Vienna *ab initio* simulation package (VASP),^{149, 150} in which the projector augmented wave method (PAW) of Blöchl^{132, 151} was implemented. The generalized gradient approximation (GGA) with exchange and correlation treated by Perdew–Burke–Enzerhof (PBE)¹³⁷ was used in all calculations, but did not lead to changes compared to using the PAW_PBE potentials. For the specific potential, please visit the corresponding paper.

The cut-off energy for the plane wave calculations was set to 500 eV for the *REAl₂* and YAl₅Pt₃ compounds, whereas a cut-off energy of 550 eV and 800 eV were chosen for *AEAl_x* and oxidation products of CaAl₂, the *REAlRh* compounds as well as for Ca₂AlPt₂, CaAl₂Pt₂ and Ca₂Al₃Pt respectively. For the *AEAl_x* the Brillouin zone integration was done by an automated Γ -centered 20-fold *k*-point mesh, in which a *k*-point mesh with a spacing of ≈ 0.02 for all compounds were used in the oxidation products of CaAl₂ as well as the intermetallic compounds Ca₂AlPt₂, *REAlRh*, Ca₂AlPt₂, CaAl₂Pt₂ and Ca₂Al₃Pt. In the case of the *REAl₂* and YAl₅Pt₃ a *k*-mesh of 9 × 9 × 9 and 3 × 15 × 9 was used for the Brillouin zone integration respectively. High precision integrations of the Brillouin zone were done for the *REAlRh* compounds with a *k*-mesh of 9 × 11 × 9 and for Ca₂AlPt₂ of 9 × 15 × 11; CaAl₂Pt₂: 15 × 15 × 9 and Ca₂Al₃Pt of 13 × 13 × 9. Additionally, Bader charges were calculated from the VASP outputs using the Bader program by Henkelman et al.¹³⁸⁻¹⁴⁰ for the *AEAl_x*, *REAl₂* and YAl₅Pt₃. For the *REAlRh* and the CaAlPt compounds Bader charges were calculated based on the charge density from calculations by the AIM (atoms in molecules theory) approach¹⁵² developed by Bader. The NMR parameters of *AEAl_x* and YAl₅Pt₃ could be evaluated through the field gradient tensor calculations in VASP using the nuclear quadrupole moment of 146.6 mb for ²⁷Al and –220 mb for ⁴⁵Sc. For the *REAl₂* the chemical bonding analysis was performed by calculating

the Electron Localization Functions (ELF)^{153, 154} from the VASP calculations. The tight-binding, linear muffin-tin orbitals with the atomic spheres approximation (TB-LMTO-ASA) method, implemented in the TB-LMTO 4.7 program,¹⁴⁴ were used to calculate the crystal orbital Hamiltonian population (COHP).

As for the MA_4Ir_2 ($M = Ca, Sr, Eu$) compounds the calculations were done with the TB-LMTO-ASA,^{146, 155, 156} in which the exchange and correlation effects were considered by the LDA.¹⁵⁷ The chemical bonding analysis were performed by using the DOS and iCOHP¹⁴⁸ values, additionally the ELF map were calculated as described in literature¹⁵⁸ and were visualized with the program wxDragon.¹⁵⁹

In the past, COHP calculations were only possible using the TB-LMTO or SIESTA methods, but not by DFT calculations due to the use of plane waves, which are delocalized. With more recently developed tools by Dronskowski et al. namely the Local-Orbital Basis Suite Towards Electronic-Structure Reconstruction (short LOBSTER),^{160, 161} a reconstruction and projection of the COHP from the plane wave data is possible, resulting in projected COHP or pCOHP. A very recent implementation is the concept of Crystal Orbital Bond Indices (COBI), which can be calculated from the projected crystal orbital overlap population (pCOOP) and the projected crystal orbital Hamilton population (pCOHP) resulting from the LOBSTER calculations. When integrating the COBI to ICOBI, it gives insight into the chemical bond order. High values indicating a high covalent bonding, low values indicate a weak covalent bonding or a higher ionicity, whereas a value of zero indicate no bonding between the addressed atoms.^{162, 163}

LOBSTER calculations were performed on $SrAl_8Rh_2$, the elements Ca, Al and Pt, as well as all known binary and ternary compounds in the system Ca-Al-Pt. Using DFT calculations in VASP with the PAW method of Blöchl was already done with the structures mentioned above, a structure relaxation was performed firstly, then the plane wave calculations were done with a cutoff energy of 800 eV, the Brillouin zone integration used a k-point mesh with a spacing of ≈ 0.2 for all compounds. With this data the COBI values were calculated using the LOBSTER program package.

3. Results

a. Results from Own Work (published)

I. Important Structure Types

In the following, results from binary and ternary compounds will be discussed, which are already published in different scientific papers (see publication list).

Binary Structure Types

Firstly, a description of the used crystal structures will be given, starting with the widely and well known Laves phases MgZn_2 ¹⁶⁴ and MgCu_2 ,¹⁶⁵ also known as C14 and C15 phases respectively. Both structure types can be described in two ways: first the description using the atom packing and second the one using coordination polyhedral.

The description of crystal structure of MgCu_2 is in two ways possible, firstly by looking at the atom packing. The Cu atoms form closed packed atomic layers, in which 1/4 of the atoms were removed resulting in hexagonal cavities (Schläfli symbol 3.6.3.6. or 3^6 Kagomé layer), surrounded by Cu triangles along [111] as shown in **Figure 3.2**. The cavities of the Kagomé layer are topped with different atoms, on top of the hexagonal cavities the Mg atoms reside, whereas above the triangles of the Kagomé layers alternating Mg and Cu atoms can be found. The Cu atoms in the Kagomé layer and on top of the triangles form empty Cu_4 tetrahedra. Topped is the structure with a second Kagomé layer, which is slipped, so that the Mg atoms on the trigonal places of the first Kagomé layer reside in the hexagonal cavities of the second layer. The resulting coordination number for the Cu atoms are 12 atoms consisting of six Mg atoms and two times three Cu atoms, forming a distorted icosahedron, shown in **Figure 3.2**. The Mg atoms possess a coordination number of 16 consisting of six plus three plus three Cu atoms and four Mg atoms, resulting in a capped tetrahedron or Frank-Casper polyhedron. The Mg atoms arrange in the same way as the carbon atoms in the cubic diamond structure. With this the structure can be viewed as Kagomé layer sequence of ABCABC. The alternative description is using the polyhedra. The Frank-Casper polyhedra are face-shared to each other forming cavities which are occupied by the Cu_4 tetrahedra.

The hexagonal MgZn_2 structure type ($P6_3/mmc$) is shown in **Figure 3.1** alongside the coordination environment for the Mg as well as both Zn positions. The structure of MgZn_2 (C14 type) can be described with the following motifs: the Mg atoms form a lonsdaleite structure whereas the Zn1 atoms form the so-called 3^6 Kagomé lattice, e.g. hexagons which are made out of six corner-shared triangles of Zn1 on the ab plane with $z = 1/4$. These triangles are connected via the Zn2 atom forming corner-shared trigonal bipyramids along the c -axis, to another 3^6 Kagomé lattice. The second Kagomé layer is shifted slightly, so that one of the Zn1 triangles occupies the position of the middle of the hexagon $z = 3/4$. In the hexagonal cavity reside two Mg atoms. The two Kagomé layers are alternating along $[001]$ in a sequence of ABABAB. The coordination number of the Mg atoms is 16 consisting of four Mg atoms forming a distorted tetrahedron, six Zn1 from the hexagon of the first Kagomé lattice, three Zn1 from the triangles of the second Kagomé lattice and three Zn2, forming a fourfold capped tetrahedron. The coordination number of the Zn1 and Zn2 atoms are both 12, consisting of six Mg and six Zn atoms, whereas for the Zn1 the Mg atoms are in a boat conformation and in a chair conformation for the Zn2 position, both coordination spheres result in distorted icosahedra.

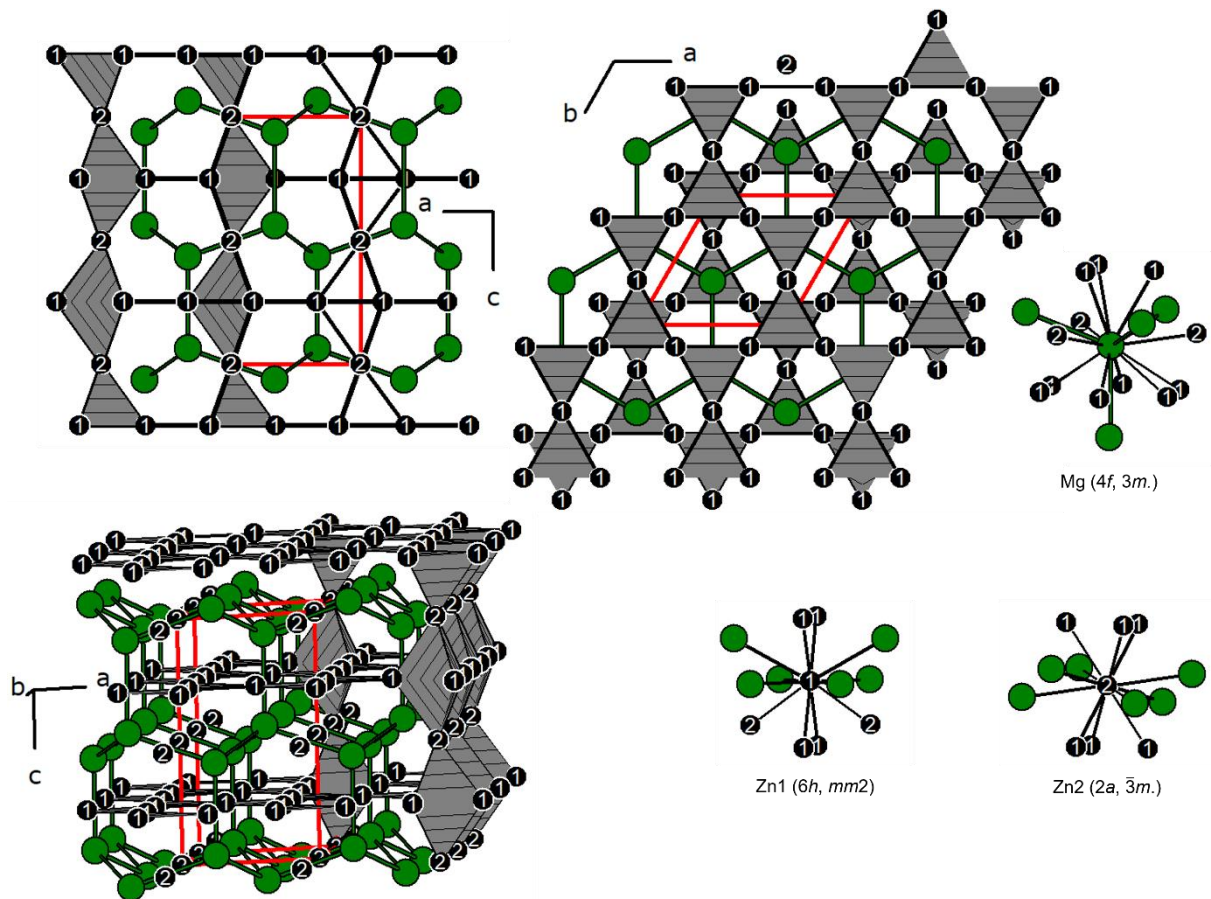


Figure 3.1: Unit cell (bottom left) along the *b*-axis (top left), *c* (top middle) and coordination environments surrounding the Mg (top right side), Zn1 (bottom mid) and Zn2 (bottom right) of MgZn₂. Mg and Zn atoms are shown in green and black circles, respectively. Wyckoff positions and site symmetries are given.

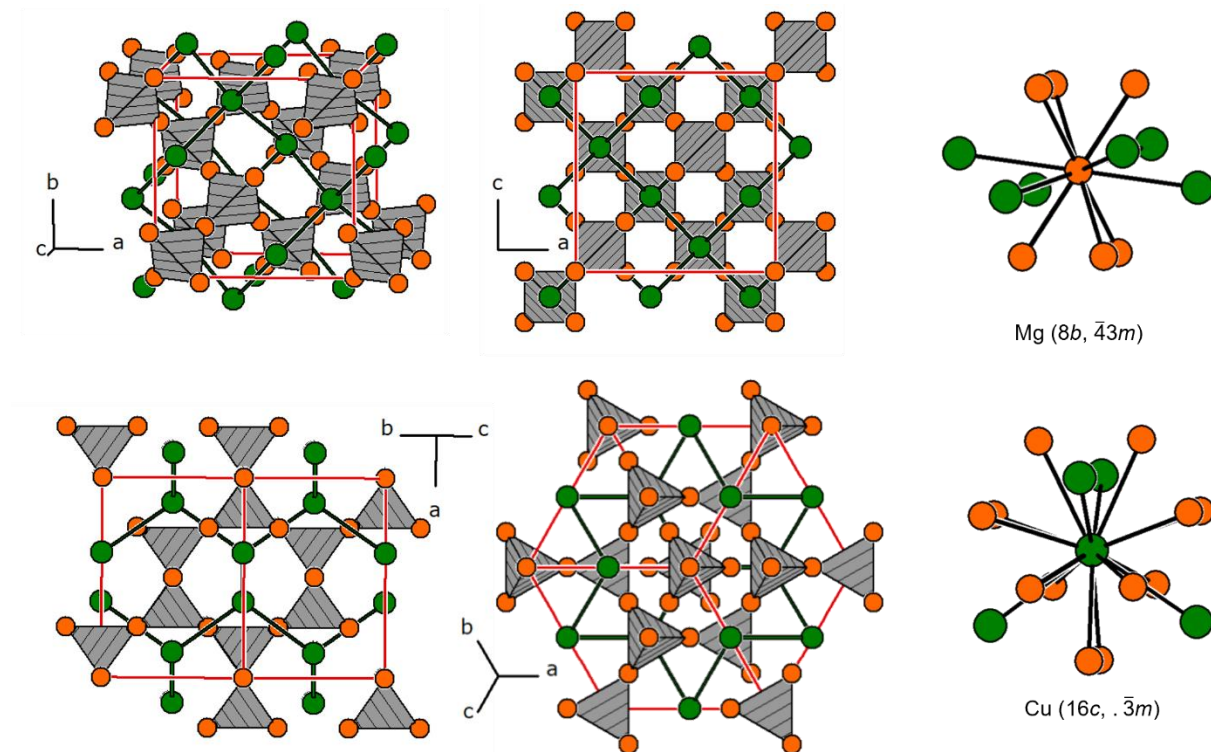


Figure 3.2: Unit cell (top left) along [010] (top middle), [011] (bottom left), [111] (bottom middle) and coordination environments surrounding the Mg (top right side) and Cu (bottom right) of $MgCu_2$. Mg and Cu atoms are shown in green and orange circles, respectively. Wyckoff positions and site symmetries are given.

By stacking the 3^6 Kagomé lattice on top of each other, the $CaCu_5^{166}$ structure originates. This structure crystallizes with space group $P6/mmm$ with one calcium atom position and two copper positions, the Cu2 atoms form the 3^6 Kagomé lattice on the ab plane and trigonal bipyramid with the Cu1 atoms above and below the trigonal base. The resulting hexagonal prismatic cavities are occupied with the Ca atoms. **Figure 3.3** shows the unit cell as well as the atomic coordination environments. Ca is surrounded by twelve Cu2 forming the hexagonal prism, which is capped on all sides with six Cu1 atoms. The Cu1 and Cu2 positions have a coordination number of twelve, which consists of six Cu2 plus three Cu1 forming the trigonal bipyramids capped by three Ca and four Cu1 plus four Cu2 forming the bipyramids with four Ca in the resulting cavities.

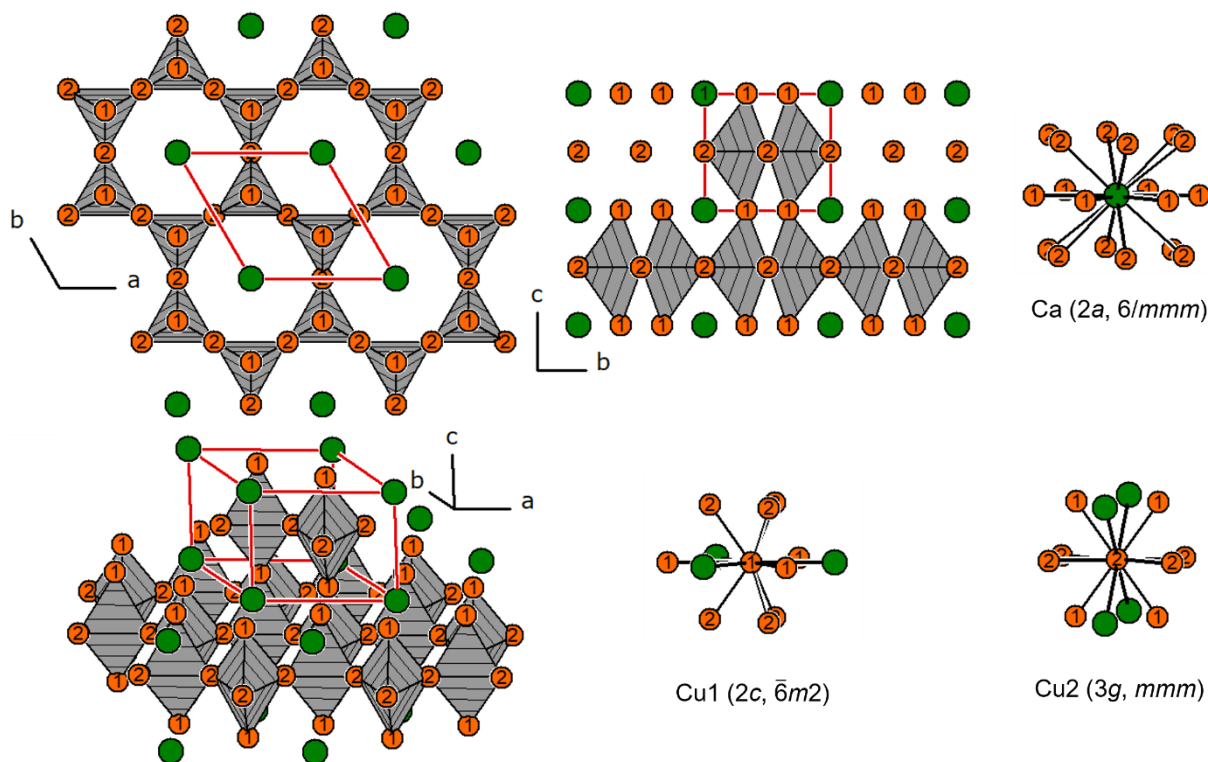


Figure 3.3: Unit cell (bottom left) along $[001]$ (top left), a (top middle) and coordination environments surrounding the Ca (top right side), Cu1 (bottom mid) and Cu2 (bottom right) of CaCu_5 . Ca and Cu atoms are shown in green and orange circles, respectively. Wyckoff positions and site symmetries are given.

SrAl_2 crystallizes under normal pressure in the KHg_2 type structure¹⁶⁷ with space group $Imma$, the structure alongside the atomic positions are shown in **Figure 3.4**. In this structure the Hg atoms form a network with hexagonal/octagonal cavities in which the K atoms reside. The coordination number of the K atoms is 16 consisting of two times six Hg atoms forming six-membered rings and four K atoms forming a superimposed tetrahedron. As for Hg atoms, the coordination numbers are two times three K atoms forming a distorted trigonal prism with four sides capped by Hg atoms.

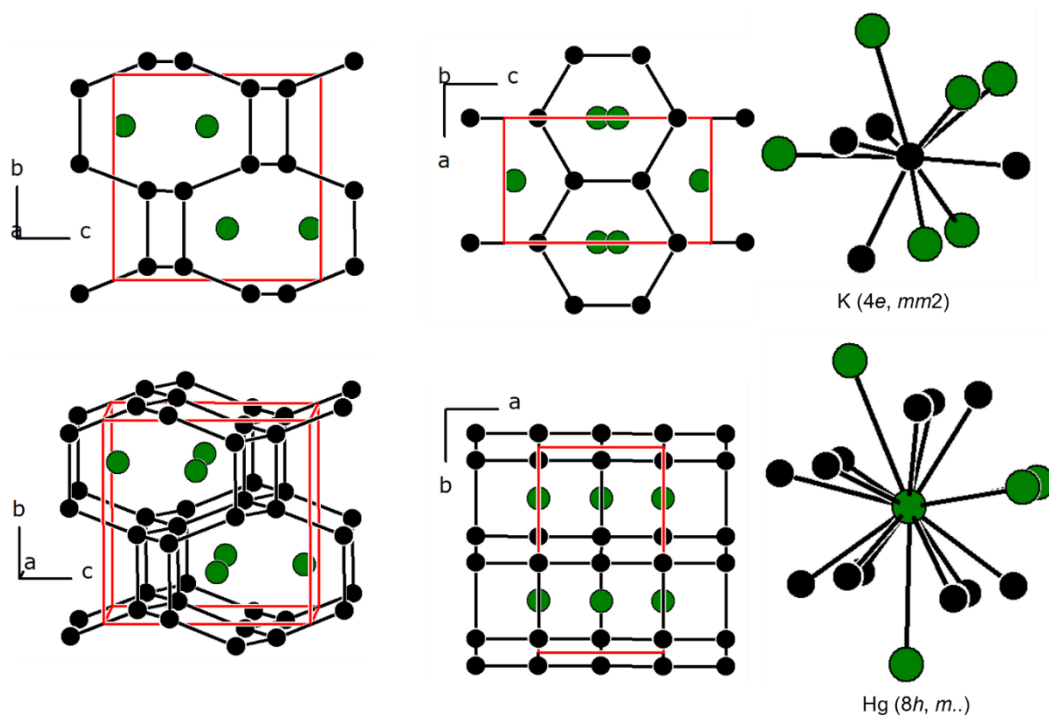


Figure 3.4: Unit cell (bottom left) along the a -axis (top left), b (top middle), c (bottom middle) and coordination environments surrounding the K (top right side) and Hg (bottom right) of KHg_2 . K and Hg atoms are shown in green and black circles, respectively. Wyckoff positions and site symmetries are given.

The BaAl_4 type structure crystallizes in the tetragonal crystal system with space group $I4/mmm$ and two independent aluminum positions as well as one barium position (**Fig. 3.5**).¹⁶⁸ The aluminum atoms form a network with hexagonal cavities in which the Ba atoms reside, resulting in a coordination number of 18 for the barium atom in a fourfold capped hexagonal prism consisting of eight A11 and eight A12. The coordination numbers of A11 and A12 are nine and twelve respectively. A11 resides in a square antiprism of one square of A12 and the opposite of Ba atoms, the Ba side is additionally capped with an A11 atom. As for the A12 position, four A12 reside in the same plane and a double tetrahedra coordination of four A11 and four Ba atoms. Besides the barium compound, also the calcium (high-temperature phase) and strontium compounds crystallize in this structure type.

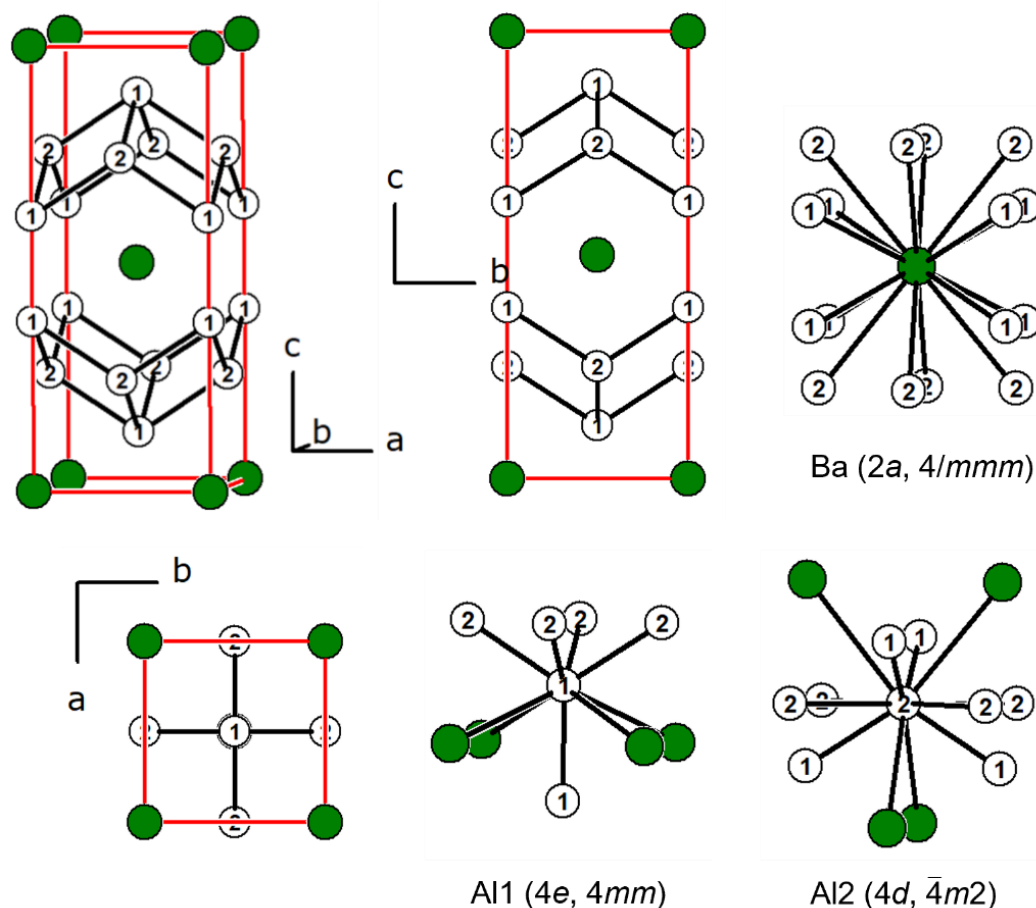


Figure 3.5: Unit cell (top left) along $[100]$ (top middle), c (bottom left) and coordination environments surrounding the Ba (top right side), Al1 (bottom middle) and Al2 site (bottom right) of $BaAl_4$. Ba and Al atoms are shown in green and white circles, respectively. Wyckoff positions and site symmetries are given.

$CaAl_4$ not only crystallizes in the $BaAl_4$ type, but also exhibits a low temperature modification in the monoclinic $CaGa_4$ type structure¹⁶⁹ with space group $C2/m$,¹⁷⁰ as shown in **Figure 3.6** alongside the independent atomic positions. This structure type possesses, like the $BaAl_4$ type, two positions for the more electron negative element Ga as well as one Ca position, in which the Ga atoms form distorted square layers of Ga2 atoms, these are connected via Ga1-Ga1 interactions sitting alternately above and below the square layers. In the resulting cavities reside the Ca atoms. The coordination number of the Ca atoms are 16 Ga atoms which form distorted double square prisms around the Ca atoms. The Ga1 exhibits a coordination number of nine, consisting of four Ga2, one Ga1 and four Ca atoms. The Ga2 and Ca atoms form a square antiprism which is capped on the Ca side with the Ga1. The Ga2 are like the Al2 in the $BaAl_4$ type, surrounded by four Ga2 in plain and a distorted double tetrahedron of four Al1 and Ca atoms.

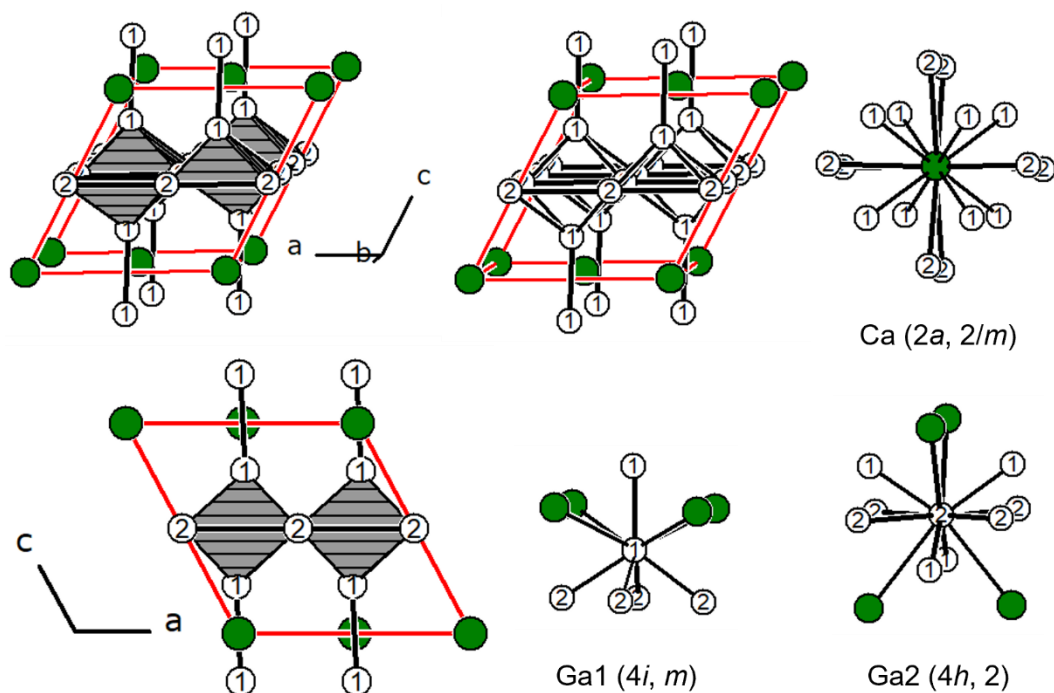


Figure 3.6: Unit cell with (top left) and without (top middle) square pyramidal polyhedra drawn, along the *b*-axis (bottom left) and coordination environments surrounding the Ca (top right side), Ga1 (bottom middle) and Ga2 site (bottom right) of CaGa₄. Ca and Ga atoms are shown in green and white circles, respectively. Wyckoff positions and site symmetries are given.

In the following part, ternary structure types will be discussed, which are ordered based on the structural motifs observed. Firstly, the structures featuring a polyanionic network of $[X_xT_y]^{\delta-}$ are shown, which form cavities in which the $M^{\delta+}$ cation resides. Subsequent structures with a layer-like character will be shown, in which distinct layers of $[X_xT_y]$ and M/MX are present.

Structures featuring a polyanionic network:

The compounds with the composition of MX_5T_3 with $M = \text{Ca, Sr, Y, Ba, La-Nd, Sm-Lu}$; $X = \text{Al, Ga, Si, Ge}$; $T = \text{Ni, Pd, Pt}$ crystallize with the orthorhombic space group $Pnma$ in the YNi_5Si_3 type structure. The YNi_5Si_3 type is however is not isotype to the MX_5T_3 but rather the antitype structure, leading to an isopointal relationship of YNi_5Si_3 with the MX_5T_3 compounds.¹⁷¹

Figures 3.7 and 3.8 show the unit cell alongside the coordination sphere of the atoms of the representative LaAl_5Pt_3 .¹⁷² The structure exhibits one La, three Pt and five Al positions, the latter form a polyanion of $[\text{Al}_5\text{Pt}_3]^{\delta-}$ is formed. Three crystallographically independent Pt and three Al positions form the hexagonal prismatic cavity in which the La atoms reside, leading to a coordination number of twelve. Three additional contacts are observed capping the hexagonal prism. In the case of the Pt positions, all Pt atoms are surrounded by seven Al atoms, two La

atoms and an additional one Pt atom for Pt1 and Pt2, resulting in highly asymmetrical coordination spheres. The Al positions exhibit also a highly asymmetrical coordination environment, with Al1 surrounded by three La, four Pt forming a tetrahedron and five additional Al atoms. The coordination sphere of Al2 consists of again four Pt atoms forming a tetrahedron, seven Al and one La atoms. Al3 has also four Pt in the coordination sphere as well as five Al and two La atoms. Al4 on the other hand does not possess a Pt₄ tetrahedron, but a distorted Pt₅ bipyramid alongside a distorted square antiprism formed by eight Al atoms. It is furthermore capped at one side with the remaining La atom. Al5 exhibits again the Pt tetrahedron and an additional five Al and two La atoms.

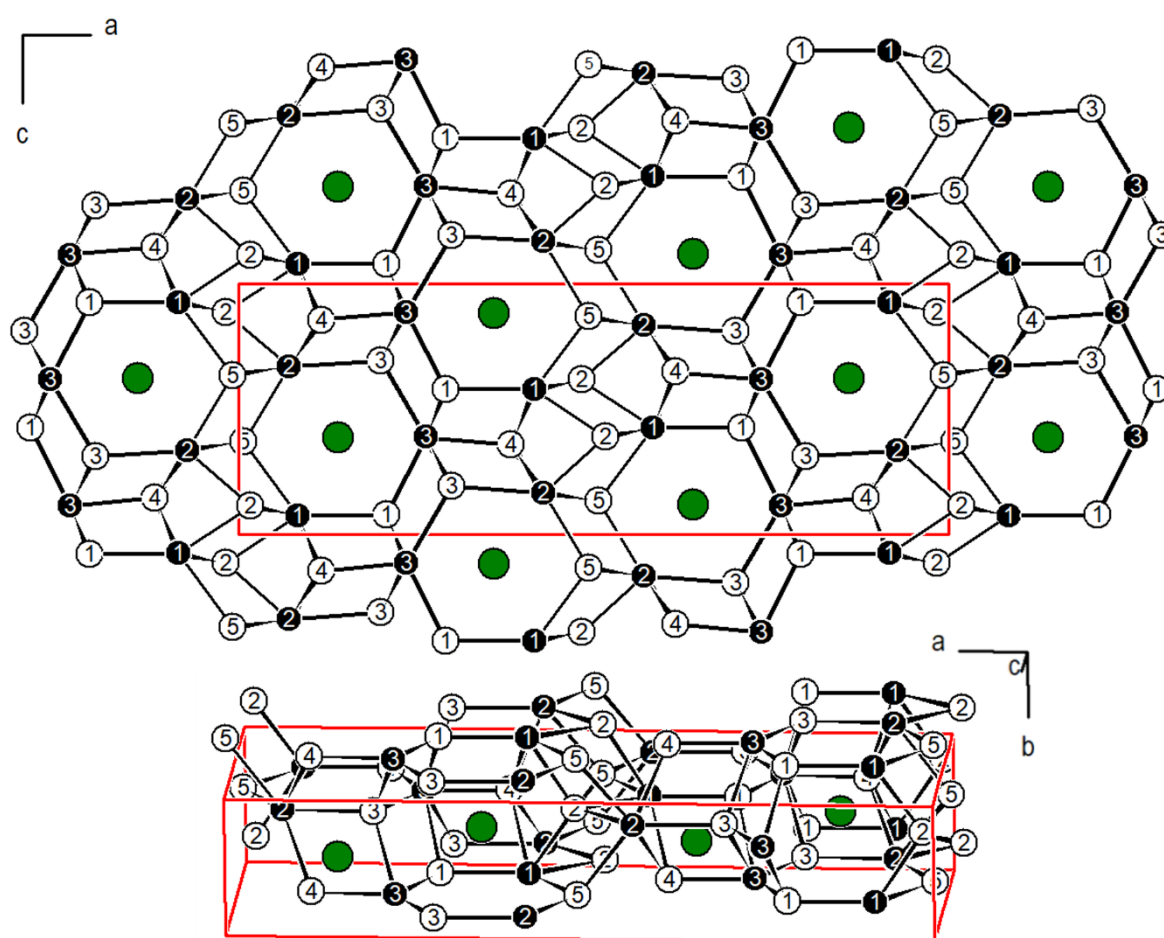


Figure 3.7: Unit cell (bottom) along [010] (top) of LaAl₅Pt₃, Al–Pt interactions drawn to show the [Al₅Pt₃]^{δ-} polyanionic network. La, Al and Pt atoms are shown in green, white and black circles, respectively.

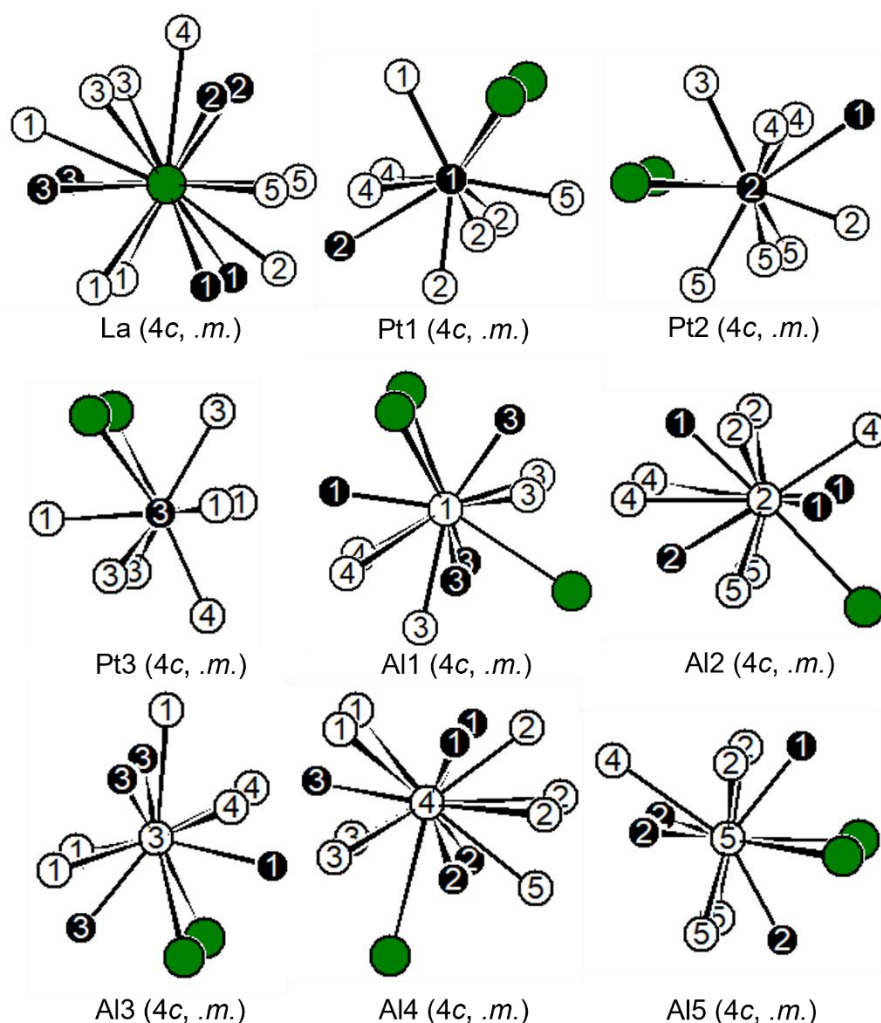


Figure 3.8: Coordination environments surrounding the La, Al and Pt atoms in LaAl_5Pt_3 . La, Al and Pt atoms are shown in green, white and black circles, respectively. Wyckoff positions and site symmetries are given.

Another structure series beside the MX_5T_3 compounds are the $\text{M}_2\text{Al}_{16}\text{Pt}_9$ compounds, crystallizing with the orthorhombic space group Immm in the $\text{Ce}_2\text{Al}_{16}\text{Pt}_9$ type¹⁷³ structure.¹⁷⁴ The only literature known structure with this type is the cerium compound, which was extended to Ca, Sr, La-Nd and Sm-Gd. As representative the structure of $\text{Sr}_2\text{Al}_{16}\text{Pt}_9$ is shown in **Figure 3.9** alongside the atomic coordination spheres in **Figure 3.10**.¹⁷⁵ Like the MAl_5Pt_3 structures the $\text{M}_2\text{Al}_{16}\text{Pt}_9$ also forms a polyanionic network consisting of the Al and Pt atoms $[\text{Al}_{16}\text{Pt}_9]^{\delta-}$ and forming hexagonal prismatic cavities in which the $\text{Sr}^{\delta+}$ cation resides. The hexagonal prism consists of six Pt and six Al atoms and is additionally capped on four sides with four Al atoms, leading to a coordination number of 16 for the Sr atoms. The Pt atoms exhibit four independent positions with the Pt1 and Pt2 having two Sr atoms in the coordination sphere alongside one Pt and seven Al atoms for Pt1 and eight Al atoms for Pt2. The Al2 atoms form a distorted square prism, which can also be found in Pt4, Pt3 also has eight Al atoms surrounding it, but these form a square antiprism with additional two Pt atoms capping the edge of the bottom square.

Besides the four Pt positions and the one Sr position, the structure exhibits five crystallographically independent Al positions. The positions Al1, Al3-Al5 possess Pt₄ tetrahedra, additionally Al1, Al3 and Al5 has one and two Sr atoms in the coordination environment respectively. Al1 exhibits beside the Pt₄ tetrahedron a distorted quadratic Al₅ pyramid in the coordination sphere. Al2 is surrounded by a distorted quadratic pyramid of Pt atoms and a one-sided Al capped Al₄ tetrahedron. The Al3 coordination environment consists of a highly distorted square Al₅ pyramid intertwined with a Pt₄ tetrahedron additionally to the two Sr atoms. Al4 is surrounded by a planar Al₄ square and a by two Sr atoms capped Pt₄ tetrahedron. The coordination sphere of Al5 consists of an Pt₄ tetrahedron intertwined with a distorted Al₆ trigonal prism capped with an additional Al.

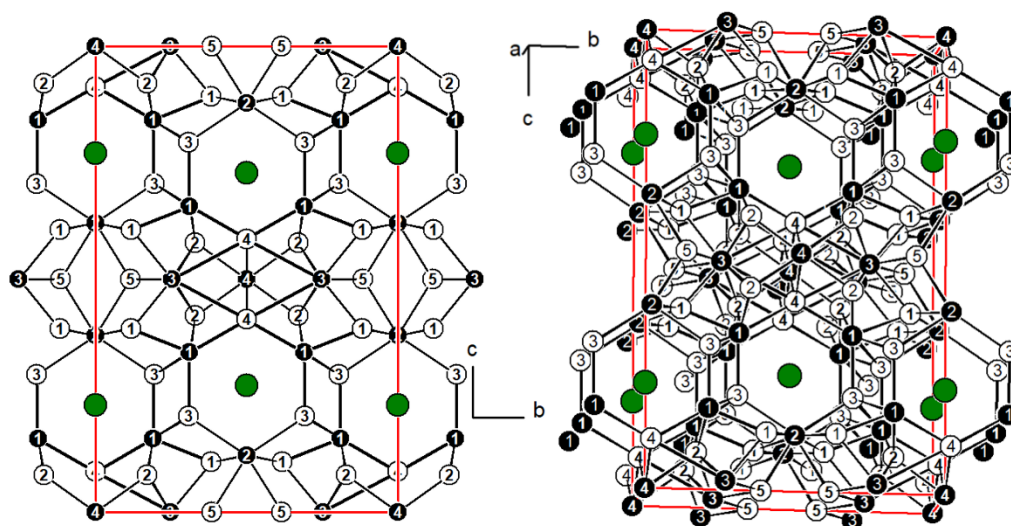


Figure 3.9: Unit cell (right) along the *b*-axis (left) of Sr₂Al₁₆Pt₉, Al–Pt interactions are drawn to show the [Al₁₆Pt₉]^{δ-} polyanionic network. Sr, Al and Pt atoms are shown in green, white and black circles, respectively.

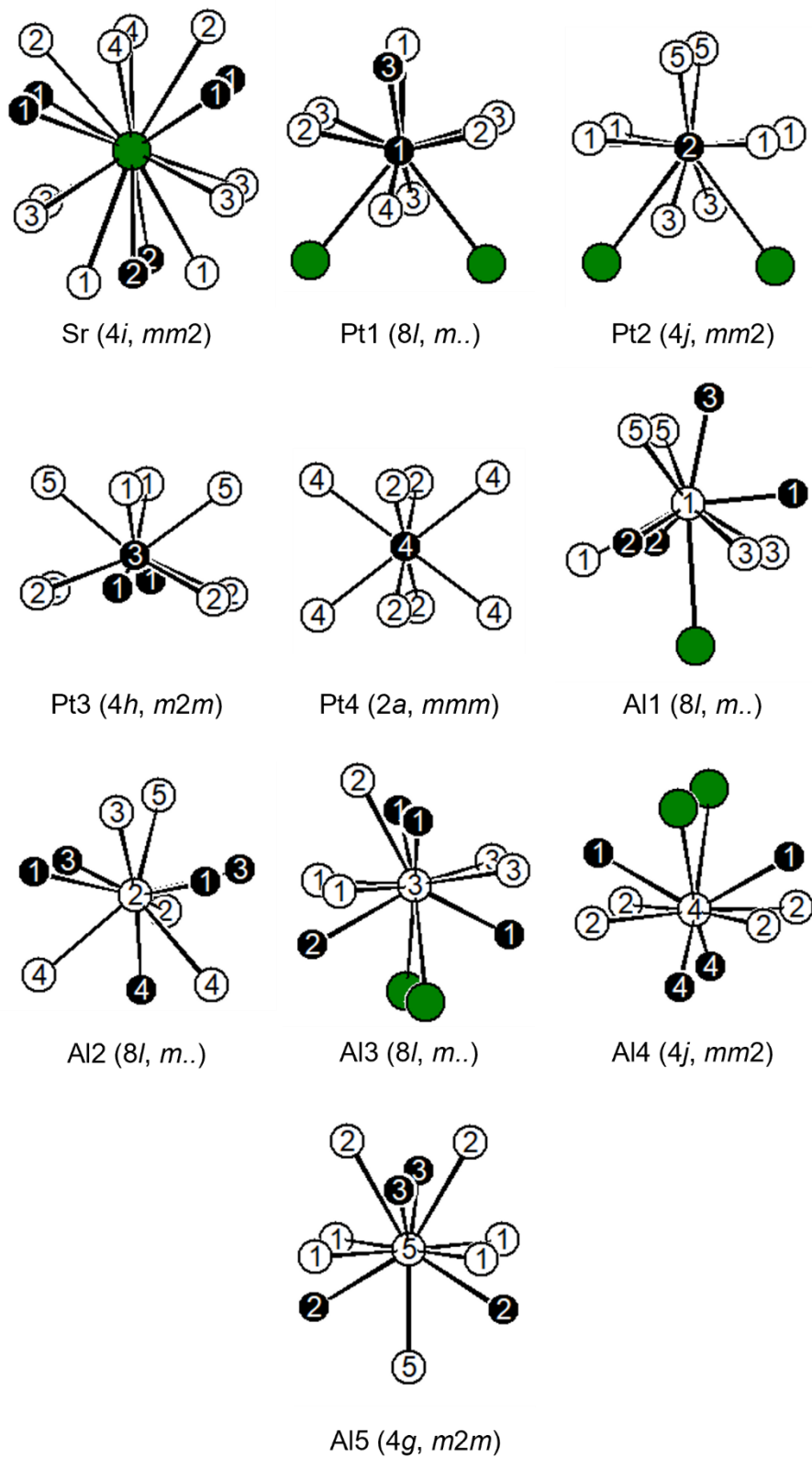


Figure 3.10: Coordination environments surrounding the Sr, Al and Pt atoms in $Sr_2Al_{16}Pt_9$. Sr, Al and Pt atoms are shown in green, white and black circles, respectively. Wyckoff positions and site symmetries are given.

The next series exhibit not only one M position observed in the MA_3Pt_3 and $M_2Al_{16}Pt_9$ series but three independent M positions with an overall composition of $RE_4Al_{13}Pt_9$ ($RE = La, Ce, Pr$,

Nd, Sm, Eu, Gd).¹⁷⁶ The prototype crystallizes with the orthorhombic space group *Pmmn* in the $\text{Ho}_4\text{Ge}_9\text{Ir}_{13}$ type structure.¹⁷⁷ As representative $\text{Nd}_4\text{Al}_{13}\text{Pt}_9$ is shown in **Figures 3.11** and **3.12**. Like the $M\text{Al}_5\text{Pt}_3$ and $M_2\text{Al}_{16}\text{Pt}_9$ compounds the $M_4\text{Al}_{13}\text{Pt}_9$ series also forms a polyanionic network $[\text{Al}_{13}\text{Pt}_9]^{\delta-}$ of the Al and Pt atoms but in comparison to the other two series in which the hexagonal prisms are separated from each other by the polyanion, here three hexagonal prisms form clusters with an additional hexagonal prism being separated from the other ones. By looking at the structure, features like Al triangles and Al–Pt squares can be seen within the *bc* plane. The Nd atoms reside in the hexagonal prisms consisting of six Pt and six Al atoms. To complete the coordination sphere of the *RE* atoms three sides of the prism are capped with two Al atoms for Nd1 and Nd3 and four Al atoms for Nd2. The Pt coordination spheres are the same for Pt3 and Pt4 with six Al forming a distorted trigonal prism alongside a superimposed tetrahedron of two Pt and two Nd atoms. Pt1, Pt2, Pt5 and Pt6 on the other hand are surrounded by five Al and four Nd (Pt1, Pt5) and two Nd and seven Al atoms (Pt2, Pt6) subsequently. The four neodymium and four aluminum atoms form a distorted square antiprism with the Nd side capped with the fifth Al. Six out of the seven Al atoms around Pt2 and Pt6 form a distorted trigonal prism, which is capped on the three sides with two Nd and one Al atom.

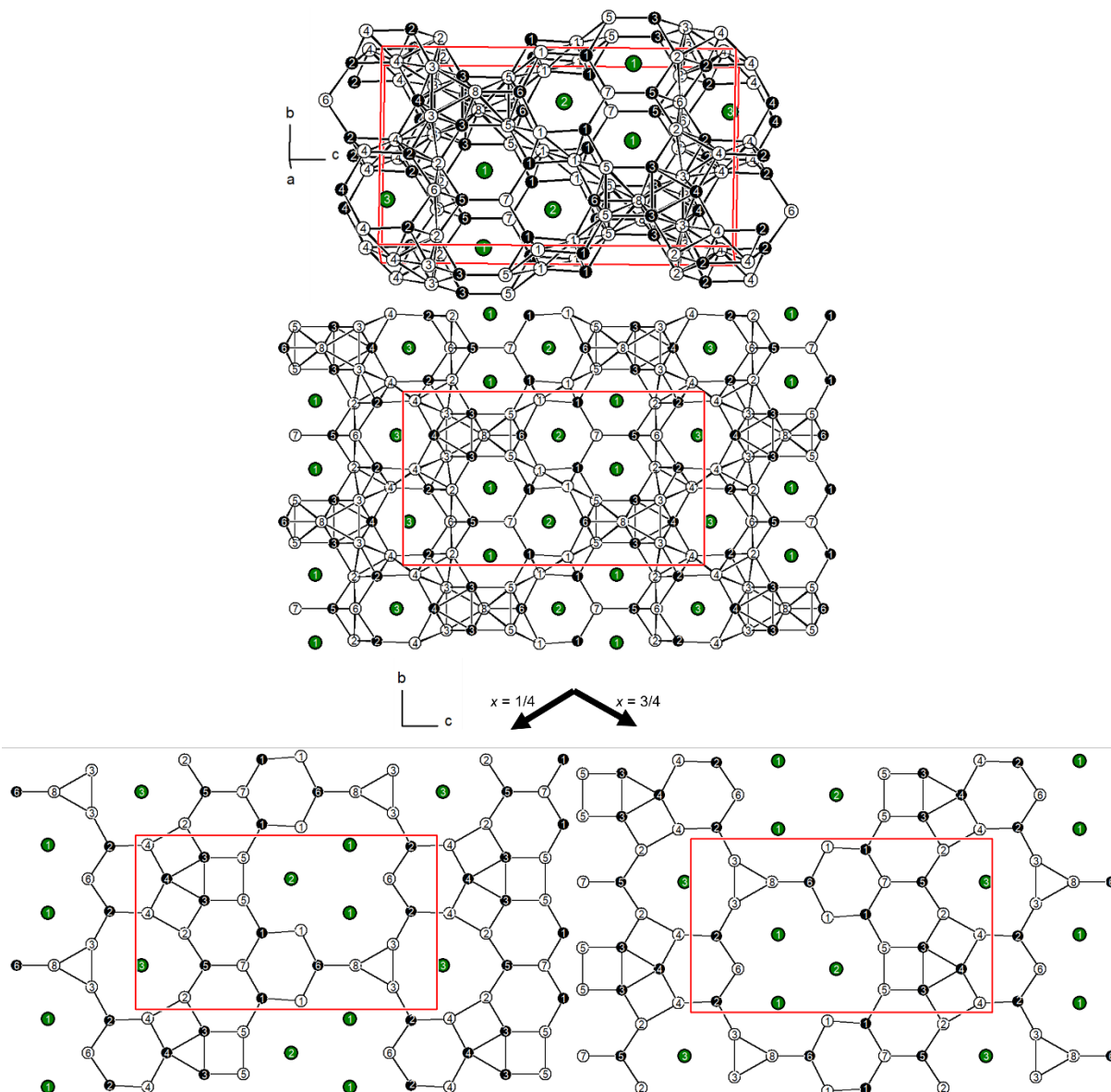


Figure 3.11: Unit cell (top) of $\text{Nd}_4\text{Al}_{13}\text{Pt}_9$ along $[100]$ (middle), alongside both layers separately, Al–Pt interactions drawn to show $[\text{Al}_{13}\text{Pt}_9]^{6-}$ polyanionic network. Nd, Al and Pt atoms are shown in green, white and black circles, respectively.

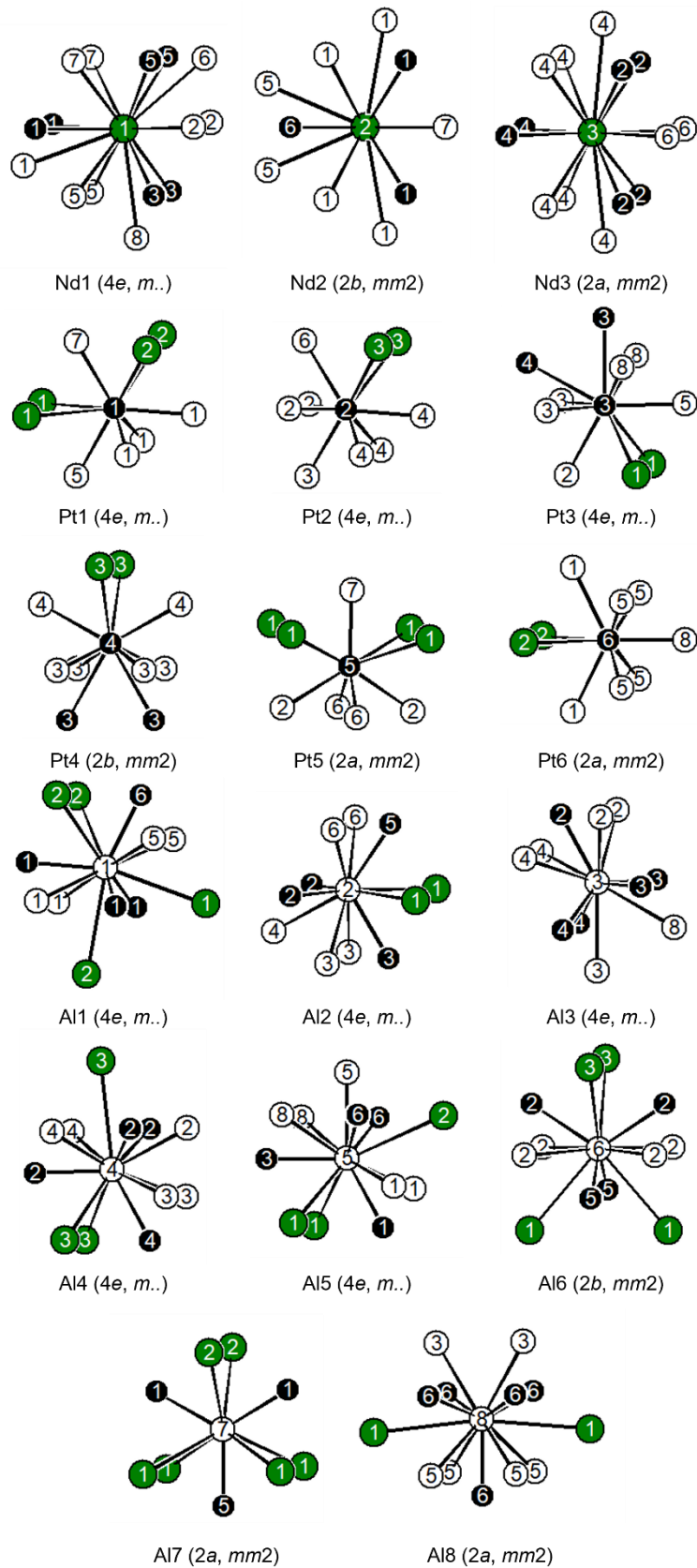


Figure 3.12: Coordination environments surrounding the Nd, Al and Pt atoms of $Nd_4Al_{13}Pt_9$. Nd, Al and Pt atoms are shown in green, white and black circles, respectively. Wyckoff positions and site symmetries are given.

Another network structure that exhibits a polyanion is the Ca_2SiIr_2 type structure. It crystallizes with the monoclinic space group $C2/c$ and exhibits one Ca, one Ir and one Si position.¹⁷⁸ Interestingly beside the $[\text{SiIr}_2]^{2-}$ anionic network, the calcium cations seem to also form a network with hexagonal cavities in which the columns of Si and Ir atoms reside in. The two later atoms on the other hand form the Si–Ir pillars of the network with rhombohedral cavities in which the Ca atoms reside, as seen in **Figure 3.13**. The pillars are connected to each other via Ir–Ir interactions, which are alternating long and short depending if the interaction is in the column or between the pillars. The Si atoms then connect the Ir chains along c -axis. **Figure 3.14** shows the coordination environments of the three atomic positions. The Ca and Si positions are highly asymmetrically coordinated with seven Ca, six Ir, two Si and six Ca, four Ir atoms respectively. The Ir atoms are surrounded by six Ca, two Ir and two Si atoms, the Ca and Si atoms form a distorted square antiprism which is capped on the top and bottom side with the remaining Ir atoms forming the chain with alternating long and short distances.

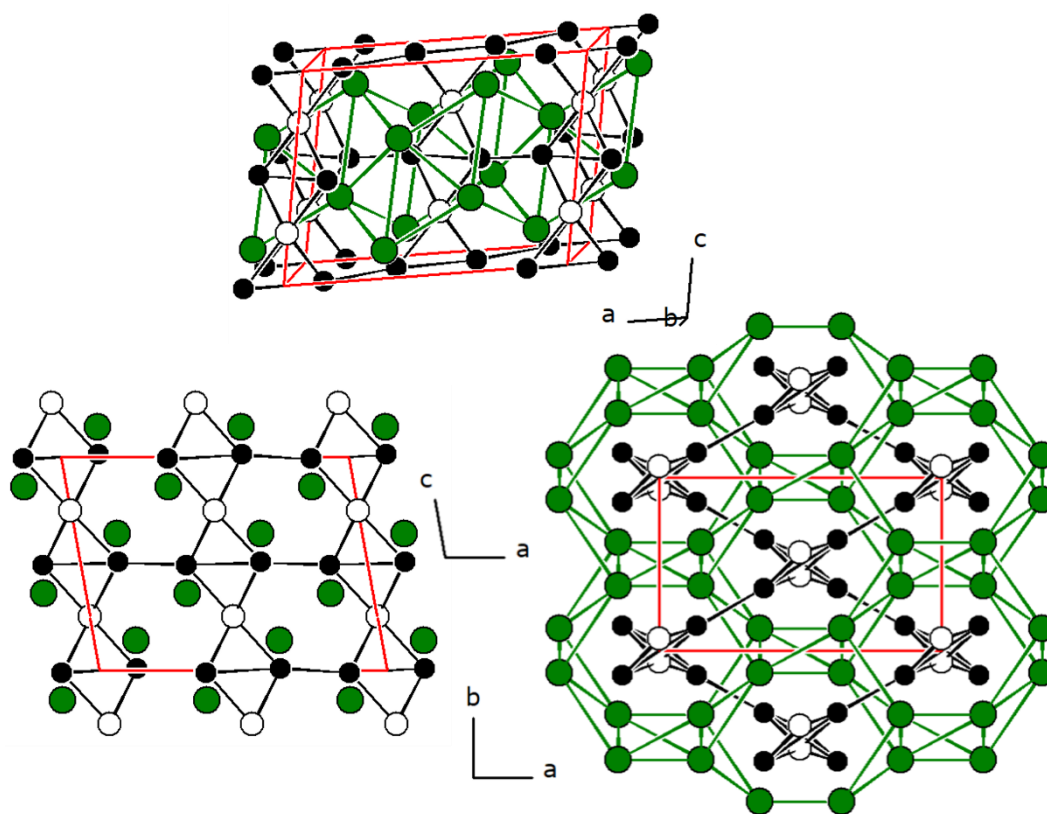


Figure 3.13: Unit cell (top) of Ca_2SiIr_2 along $[010]$ (bottom left) and c (bottom right), Ca–Ca, Si–Ir and Ir–Ir interactions are drawn to show $[\text{SiIr}_2]^{2-}$ polyanionic network and the hexagonal prisms. Ca, Si and Ir atoms are shown in green, white and black circles, respectively.

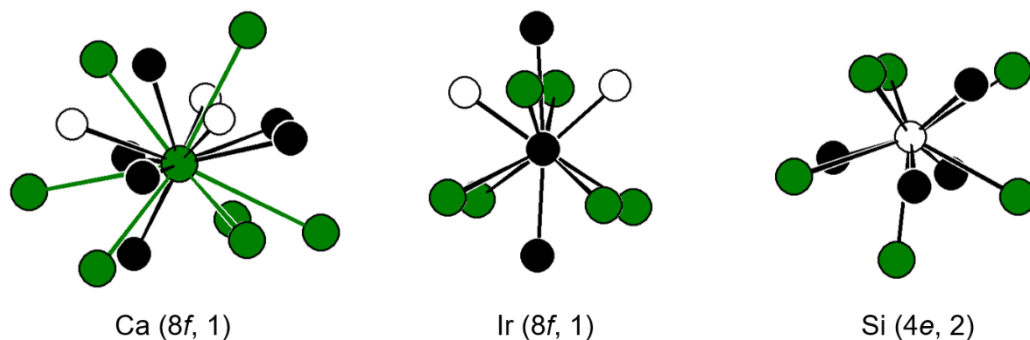


Figure 3.14: Coordination environments surrounding the Ca, Si and Ir atoms of Ca_2SiIr_2 . Ca, Si and Ir atoms are shown in green, white and black circles, respectively. Wyckoff positions and site symmetries are given.

The binary structure type of BaAl_4 can be transformed into the ternary CaBe_2Ge_2 type structure by alternating the Al1 and Al2 layers with other atoms, so the Al2–Al1–Al2–Al2–Al1–Al2–Al2–Al1–Al2 layers become Be2–Ge1–Be2–Ge2–Be1–Ge2–Be2–Ge1–Be2 layers in the CaBe_2Ge_2 compound and is a coloring variant of the BaAl_4 type, as shown in **Figure 3.15**.¹⁷⁹ Due to the different coloring space group changes from $I4/mmm$ in BaAl_4 to $P4/nmm$ in CaBe_2Ge_2 , the structure relationship can be visualized using the group-subgroup relation as showed in the work of the R. Pöttgen in 2014.¹⁸⁰

Like the binary version, the ternary structure exhibits a polyanionic network with hexagonal prismatic cavities in which the Ca resides. The square pyramids are also heteroatomic with Be being the tip and Ge the base and in the following layer, the Be is the base with Ge being the tip. The structure possesses five crystallographic independent positions, one for Ca, two for Be and two for Ge (**Fig. 3.16**). The Ca atoms are surrounded square planar by four Ca atoms, and two square prisms with one prism consisting of four Be1 and four Ge1 and the other prism of four Be2 and four Ge2 atoms. The coordination sphere of Be1 consists of four Be1 square planar, and two tetrahedra one consisting of Ge2₄ and one of Ca₄. The environment of Ge1 is the same for Be1 just with exchanged Be with Ge atoms and vice versa. The coordination environment of Be2 and Ge2 are analogous to each other with only the corresponding elements exchanged. The Be2 atoms exhibit a coordination environment of a Ge2 capped square antiprism consisting of four Ca and four Ge1. The Ge2 atoms on the other hand has a coordination sphere of a Be2 capped square antiprism containing four Be1 and four Ca atoms.

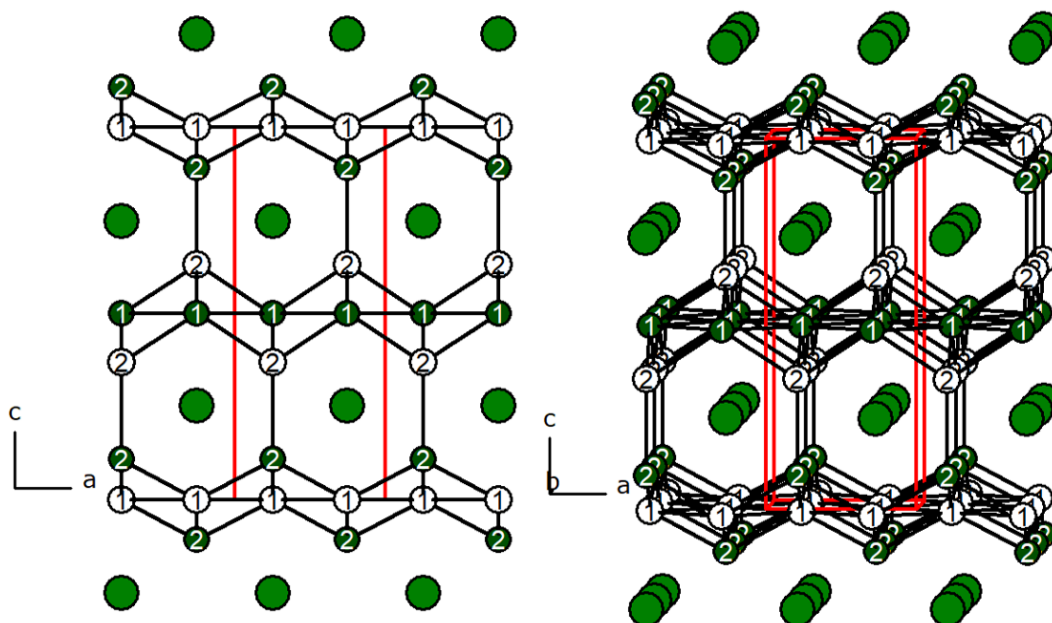


Figure 3.15: Unit cell (top) of CaBe_2Ge_2 (right) and along the b -axis (left), Be–Ge interactions are drawn to show the $[\text{BeGe}]^{6-}$ polyanionic network and the hexagonal prisms. Ca, Be and Ge atoms are shown in green, dark green and white circles, respectively.

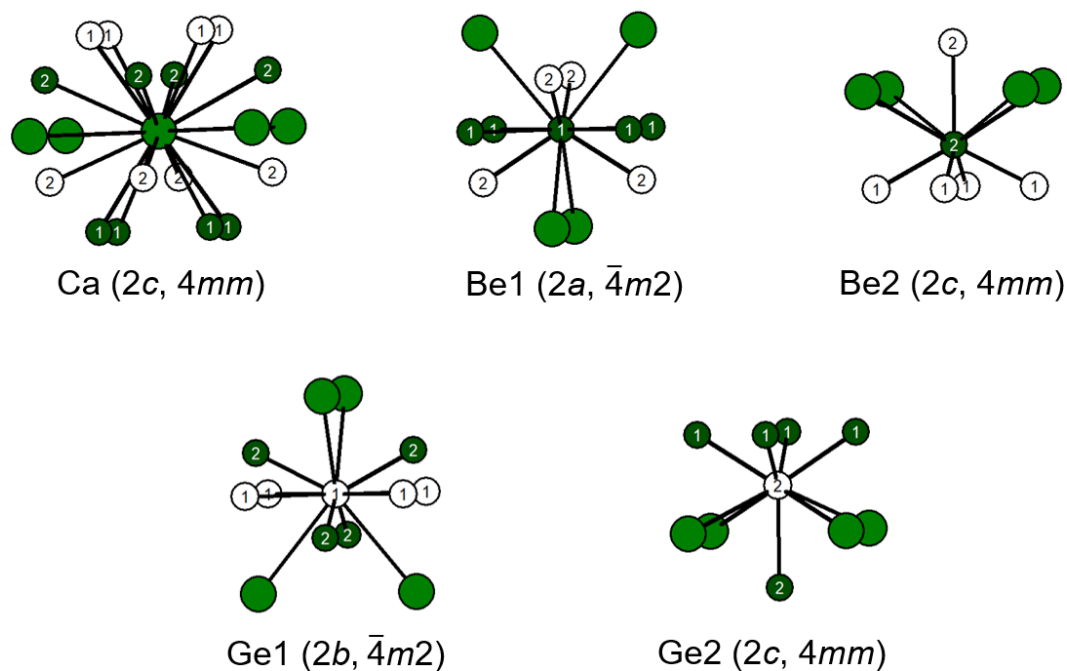


Figure 3.16: Coordination environments surrounding the Ca, Be and Ge atoms of CaBe_2Ge_2 . Ca, Be and Ge atoms are shown in green, dark green and white circles, respectively. Wyckoff positions and site symmetries are given.

A coloring variant of the MgZn_2 type structure can as well be observed by completely replacing the connecting Zn atoms in the tetrahedra along c -axis with Si atoms, the Zn atoms on the Kagomé lattice become Cu atoms and the $\text{Mg}_2\text{Cu}_3\text{Si}$ type structure is made.¹⁸¹ With the

differentiation of the atoms, the Mg_2Cu_3Si structure exhibits three atomic positions, one for each element, displayed in **Figure 3.17**.

Si is surrounded by six Mg and six Cu atoms forming a distorted icosahedra whereas the Mg atoms are surrounded by four Mg atoms forming a tetrahedron, which is capped additionally on three sides with Si atoms. The Cu atoms form the Kagomé lattice and possess a coordination environment of four Cu atoms placed square planar around the Cu with two Cu on one side forming a trigonal bipyramid with the Si atoms above and below the Kagomé lattice.

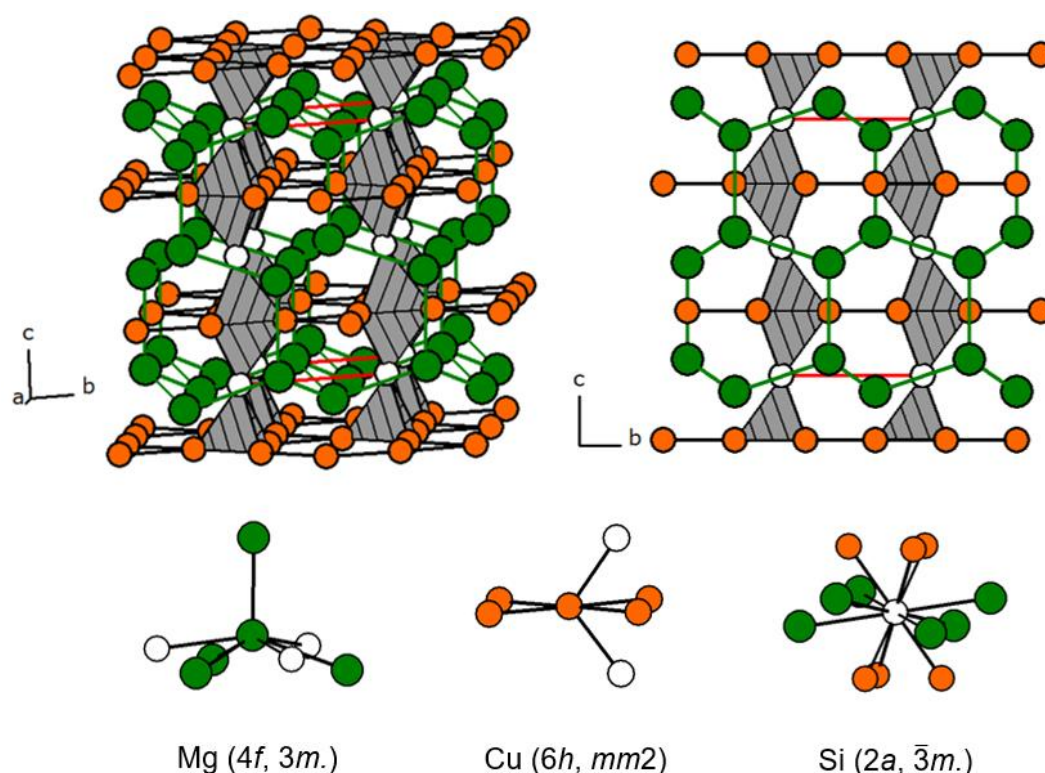


Figure 3.17: Unit cell of the Mg_2Cu_3Si type structure (top left) and along the a -axis (top right), as well as the coordination spheres of the Mg, Cu and Si atoms (bottom). Mg–Mg, Cu–Cu and Cu–Si interactions are drawn to show the $[Cu_3Si]^{6-}$ polyanionic network and the diamond substructure of the Ca atoms. Mg, Cu and Si atoms are shown in green, orange and white circles, respectively. Wyckoff positions and site symmetries are given.

The $CeAl_8Fe_2$ type structure¹⁸² crystallizes with space group $Pbam$ and forms like the MA_5Pt_3 and $RE_2Al_6Pt_9$ series a polyanionic network with separated cavities, but in case of the $CeAl_8Fe_2$ the cavities are not hexagonal but pentagonal and formed only from Al atoms, as seen in **Figure 3.18**. The Ce atoms reside in the cavities surrounded by a threefold Al capped Al_{10} pentagonal prism. The two Fe positions reside in threefold capped distorted trigonal prisms of Al atoms, additionally the capped prism has another Fe1 in its coordination environment according to $Fe1@Al_6Al_3Fe1$. In addition to the one Ce and two Fe positions the structure exhibits nine crystallographically independent Al positions.

Al1 and Al7 exhibit the same coordination environment consisting of two Ce, two Fe and eight Al atoms, which form a fourfold capped distorted cube. Al2 is surrounded by eight Al atoms forming a distorted square prism capped on four sides with Fe atoms. Al6 possesses a coordination number of thirteen, consisting of ten Al forming a pentagonal prism which is threefold capped with iron atoms. Al3-A15, Al7 and Al8 all have a coordination number of twelve and a coordination environment of two Fe, two Ce and eight Al forming highly distorted cuboctahedra. All independent atomic positions are depicted in **Figure 3.19**.

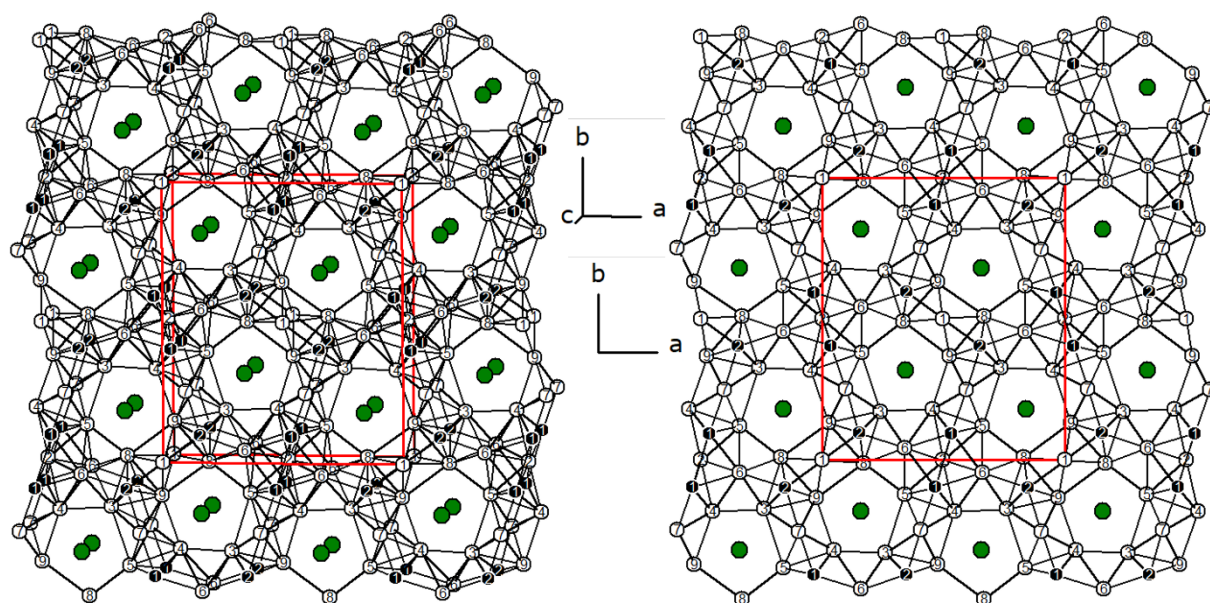


Figure 3.18: Unit cell of CeAl_8Fe_2 (left) and along $[001]$ (right), Fe–Al interactions are drawn to show the $[\text{Al}_8\text{Fe}_2]^\delta$ polyanionic network and the hexagonal prisms. Ce, Al and Fe atoms are shown in green, white and black circles, respectively.

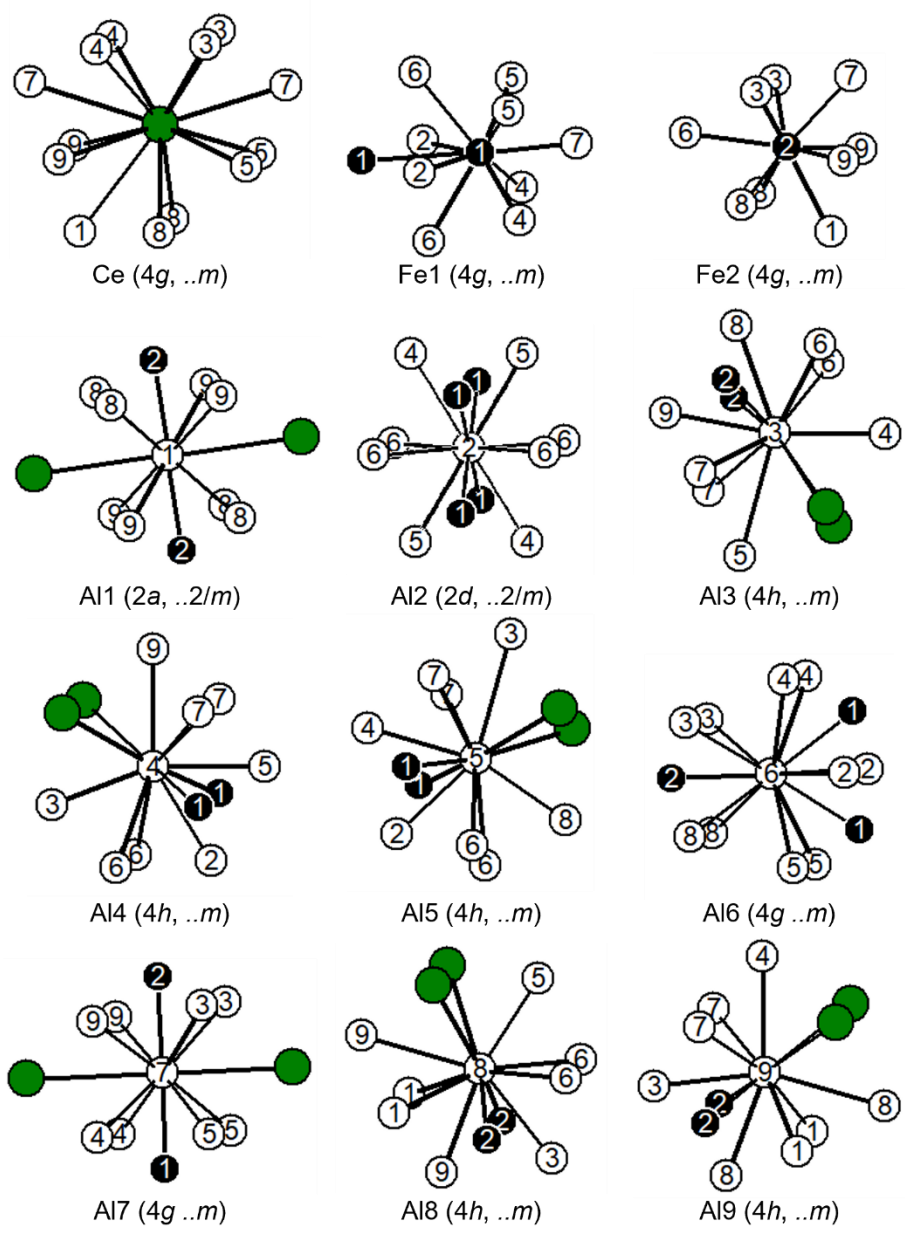


Figure 3.19: Coordination environments surrounding the Ce, Al and Fe atoms of CeAl_8Fe_2 . Ce, Al and Fe atoms are shown in green, white and black circles, respectively. Wyckoff positions and site symmetries are given.

Structures featuring layer-like arrangements:

In contrast to the structures forming polyanionic networks, the following compounds exhibit layer-like features with one layer in which the T and X atoms reside and the other layer with the less electronegative atoms along with additional X atoms. The X atoms in the cationic layer then form separated triangles, which are placed in the cavities of the honeycomb-like positions of the cationic atoms. One of the structures is the $\text{Sc}_2\text{Al}_{15}\text{Pt}_6$, this structure was formerly described using the $\text{Sc}_{0.6}\text{Fe}_2\text{Si}_{4.9}$ type structure,¹⁸³ but newer research could show, that the structure exhibit a modulation in the structure.⁷¹ The basic structure crystalizes with the hexagonal space group $P6_3/mmc$ and as the term basic structure implies possesses the $\text{Sc}_2\text{Al}_{15}\text{Pt}_9$ a superstructure due

to modulation of the structure. The superstructure crystallizes with the monoclinic space group $P2_1/m$.⁷¹ For the description of the structure only the hexagonal average structure will be used. The structure exhibits two different layers. The A layer contains slabs of $[Al_4Pt_2]^{6-}$, which form double layers of corrugated condensed six-membered rings of three Al and three Pt atoms. The six-membered rings are additionally connected to the other six-membered rings in the slab via Al–Pt bonds along the *b*-axis. Between the slabs are the second type of layer (B) consisting of Sc atoms arranged in a honeycomb pattern with the hexagonal cavities filled with Al_3 triangles. The triangles from layer B are rotated at 180° to layer B' resulting in a shift of the B' layer and the A' layer, so that a stacking of ABA'B' emerges, as seen in **Figure 3.20**.

Sc1 and Sc2 exhibit a coordination number of 17, consisting of six Pt, eleven Al, the six Pt along with six Al form a hexagonal prism, which is capped by five Al atoms. All independent Pt positions have a coordination number of ten with eight Al forming a distorted cube, capped by two Sc atoms. The coordination numbers of Al1–Al3 are 10 forming a highly distorted bicapped square prism of four Al, two Sc and two Pt atoms with one Al and one Pt being the capping atoms. A coordination number of eleven is found by the Al4 and Al5 consisting of four Pt atoms forming a tetrahedron, six Al forming a square bipyramid and one Sc capping the bipyramid on one side. Al6 is the only independent atomic position, which does not have a scandium in its coordination environment with consists of four Pt and six Al atoms forming again a Pt_4 tetrahedron and Al_6 square bipyramid as seen with Al4 and Al5. A7–A19 possess a coordination number of 10, consisting of six Al, two Sc and two Pt atoms. The Al and Sc form a square prism, which is capped by the remaining two Pt atoms. All independent atomic positions are depicted in **Figure 3.21**.

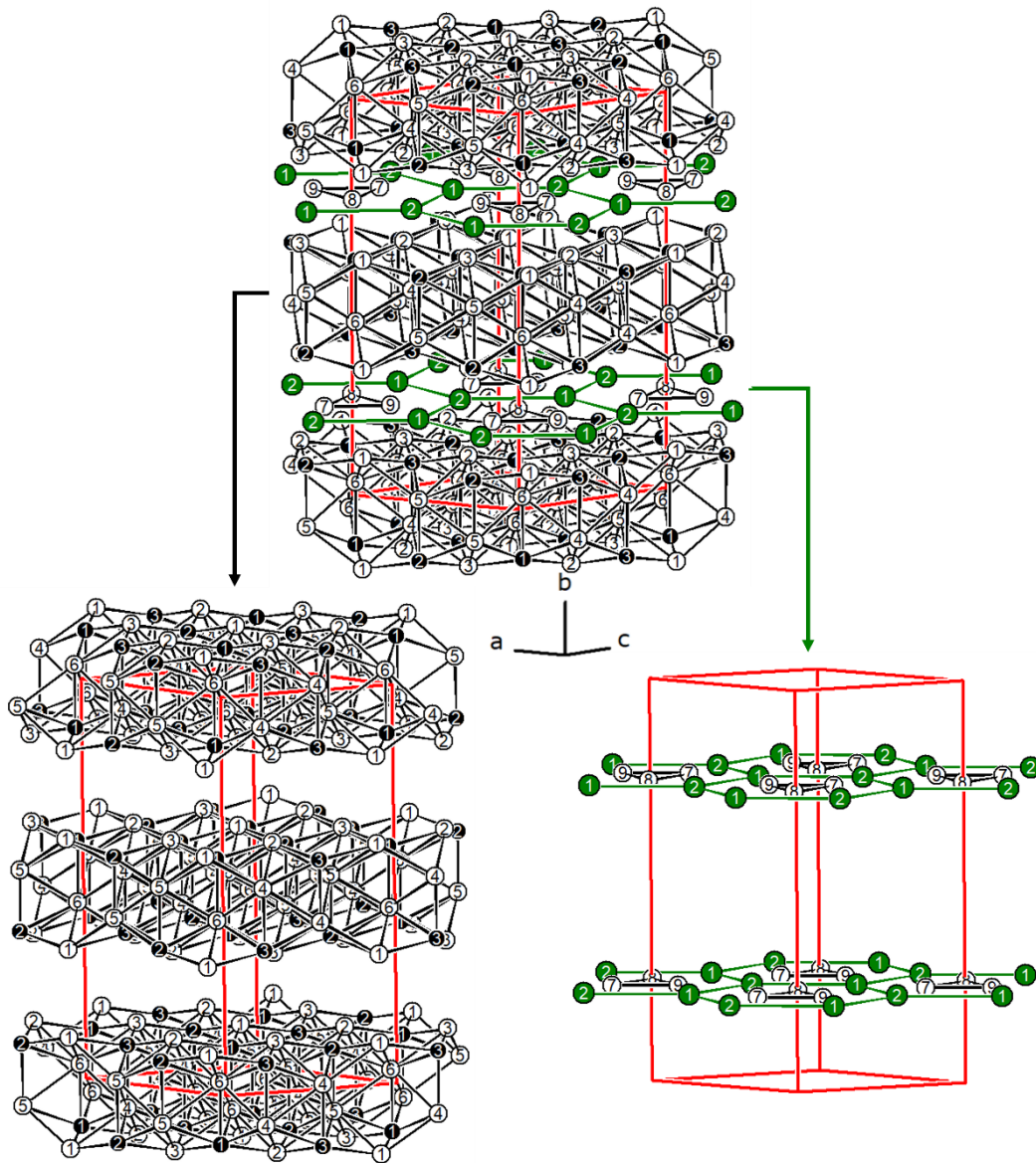


Figure 3.20: Unit cell of $\text{Sc}_2\text{Al}_{15}\text{Pt}_6$ (top) along the ScAl (bottom right) and the AlPt layers (bottom left), Ca–Ca, Al–Al and Al–Pt interactions are drawn to show motifs found in the layers. Sc, Al and Pt atoms are shown in green, white and black circles, respectively.

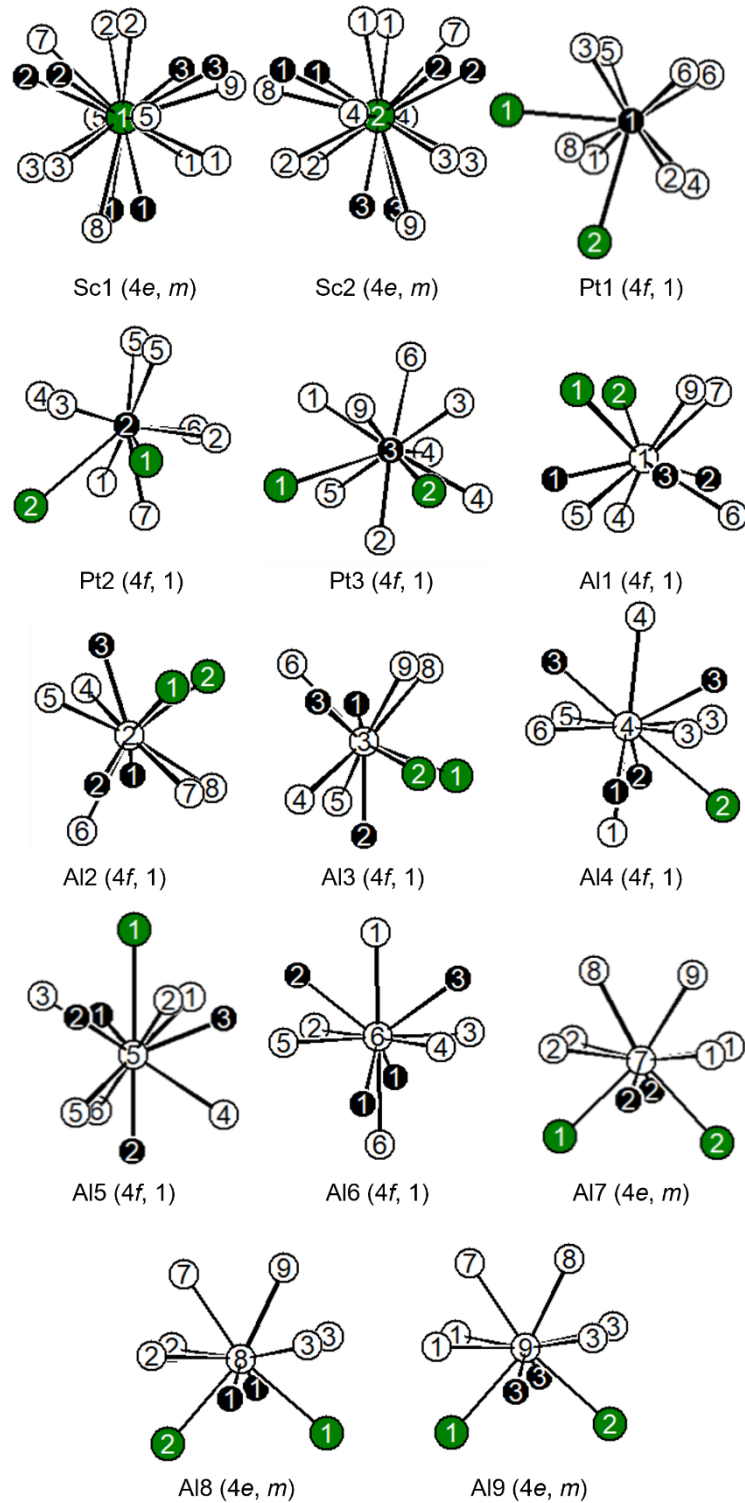


Figure 3.21: Coordination environments surrounding the Sc, Al and Pt atoms of $\text{Sc}_2\text{Al}_{15}\text{Pt}_6$. Sc, Al and Pt atoms are shown in green, white and black circles, respectively. Wyckoff positions and site symmetries are given.

Another layer-like building structure is the $\text{Y}_2\text{Ga}_9\text{Co}_3$ type structure crystallizing in the orthorhombic crystal system with space group $Cmcm$.¹⁸⁴ As representative the compound $\text{Ca}_2\text{Al}_9\text{Pt}_3$ is shown.⁶¹ The structure exhibits one Ca, two Pt and four independent Al positions. As in the $M_2\text{Al}_{15}\text{Pt}_6$ structure the Al and Pt atoms form a $[\text{Al}_6\text{Pt}_3]^{\delta-}$ polyanionic slabs (layer A),

which are connected via the Al triangles in layer B to the slab in layer A'. Layer B and B' are slightly shifted due to the rotation of the Al triangles of 180°. The Ca atoms again form a honeycomb-like pattern in which the Al triangles reside. As found in the $\text{Sc}_2\text{Al}_{15}\text{Pt}_6$ structure, the $\text{Ca}_2\text{Al}_9\text{Pt}_3$ structure exhibits an ABA'B' layer stacking, shown in **Figure 3.22**. Calcium exhibits a coordination number of seventeen with six Pt and eleven Al atoms forming a fivefold capped hexagonal prism. Pt1 and Pt2 are surrounded by eight Al and four Ca atoms forming a fourfold by Ca atoms capped distorted Al cube. Al2 and Al4 exhibit a coordination number of twelve in the form of a fourfold capped distorted cube of six Al and two Pt capped by two Al and two Ca atoms. Three Ca, three Pt and six Al are in the coordination environment of Al1 forming a fourfold capped distorted cube by two Pt, four Al and two Ca atoms. Al3 exhibits a coordination number of 13, consisting of three Pt, two Ca and eight Al atoms. The two Ca, three Pt and four Al atoms form a half of a cuboctahedron, which is capped on four sides with the remaining Al atoms. All independent atomic positions are depicted in **Figure 3.23**.

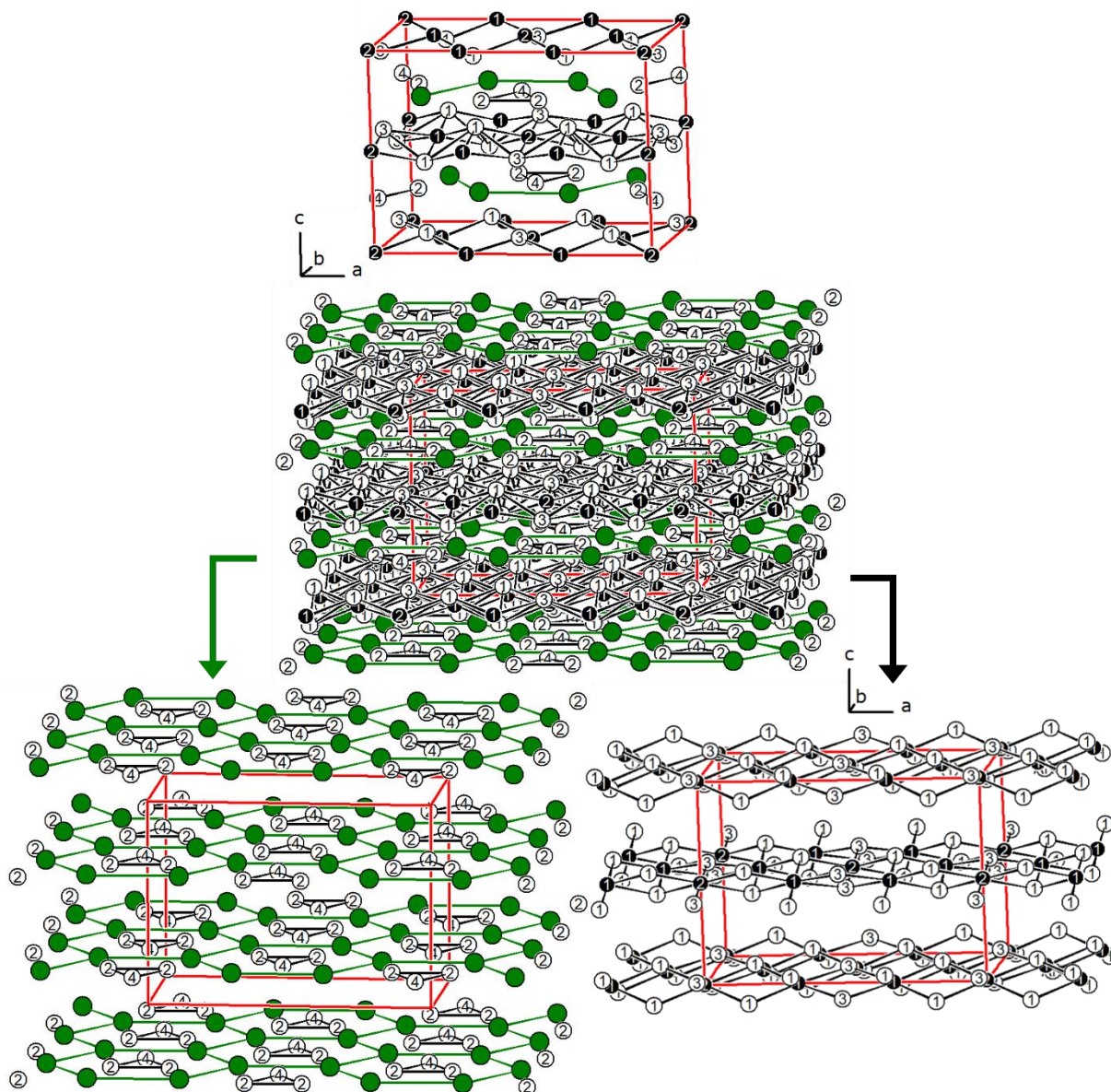


Figure 3.22: Unit cell (top) of $\text{Ca}_2\text{Al}_9\text{Pt}_3$ (top) along the layer like motive (middle and bottom) with the CaAl (bottom left) and AlPt substructures (bottom right), Ca-Ca , Al-Al and Al-Pt interactions drawn to show motifs found in the layers. Ca , Al and Pt atoms are shown in green, white and black circles, respectively.

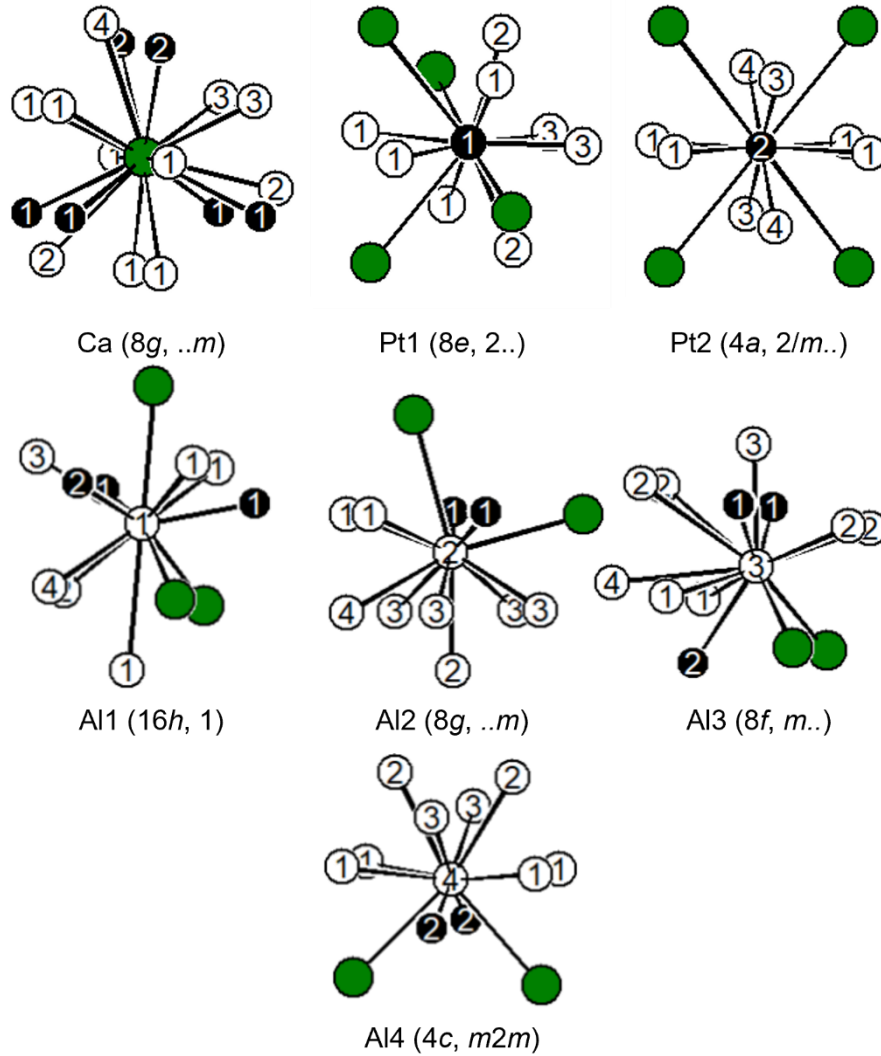


Figure 3.23: Coordination environments surrounding the Ca, Al and Pt atoms of $\text{Ca}_2\text{Al}_9\text{Pt}_3$. Ca, Al and Pt atoms are shown in green, white and black circles, respectively. Wyckoff positions, site symmetries are given.

II. Investigations of Binary Intermetallic Compounds M_xAl_y containing Divalent Species with $M = \text{Ca-Ba}$

1. Introduction

In the next part of the work, new results of the literature known binary compounds $AEAl_2$ and $AEAl_4$ with $AE = \text{Ca, Sr and Ba}$ in relation to their electronic states in combination with ^{27}Al NMR spectroscopic measurements will be given. Although the existence of these compounds is already known for multiple decades, for example CaAl_2 was first discovered in 1940, no comparing characterization of these phases was conducted until now.

The CaAl_2 compound crystallizes in the cubic Laves phase type structure,¹⁸⁵ whereas SrAl_2 adopts the orthorhombic KHg_2 type structure,¹⁸⁶ both exhibit one Al site. Also, the existence of BaAl_2 was initially reported, which was later corrected by single crystal studies, indicating that the correct composition is $\text{Ba}_7\text{Al}_{13}$ under normal pressure.¹⁸⁷ Under high pressure and at high temperatures, BaAl_2 was reported to exist and SrAl_2 can be transformed to the cubic Laves phase.¹⁸⁸⁻¹⁹⁰ As for the $AEAl_4$ compounds, SrAl_4 ,¹⁹¹ BaAl_4 ¹⁶⁸ and the high temperature modification of CaAl_4 all crystallize in the BaAl_4 type structure,¹⁸⁵ featuring two Al sites, which also the low temperature modification of CaAl_4 in the CaGa_4 type structure exhibits.¹⁹² With one and two Al sites, ^{27}Al NMR studies can be performed, allowing to indirectly investigate the electron transfer, which is occurring at the Al atoms. In combination with quantum chemical calculations, this can give insight into the electronic structure of these compounds.

The investigations could show that CaAl_2 , SrAl_2 (NP and HP modification) and the $AEAl_4$ phases could be synthesized, but not BaAl_2 . The powder X-ray diffraction studies resulted in X-ray pure samples, except for the CaAl_4 , which contained both the high and low temperature phase as well as CaAl_2 and Al. This cannot be avoided, as shown in the quantum chemical calculations of the formation energies per atom. Quantitative analysis was performed via ICP-MS showing no contamination of the samples. The NMR studies showed similar chemical shifts for the cubic $AEAl_2$ compounds, whereas the SrAl_2 differs, due to the different coordination environment of the Al site. Similar results were taken from the $AEAl_4$ spectra, in which the two different Al sites could be assigned to the two signals. Also, a group-subgroup relation of the two CaAl_4 modifications could be formulated. Lastly, the quantum chemical analysis via Bader charges indicated that the electron transfer is happening from the Sr to the Al atoms, making these compounds aluminides.

2. Theoretical and ^{27}Al NMR Spectroscopic Investigations of Binary Intermetallic Alkaline Earth Aluminides

Collaborations to disclose: For this work, ^{27}Al MAS NMR spectra of the alkaline earth aluminides were recorded and interpreted by Elias C.J. Gießelmann, who also optimized the synthesis of NP-SrAl₂ together with Lukas E. Schank. Gunter Heymann prepared the HP/HT phase of SrAl₂ via a multianvil press. For the quantitative analysis, ICP-MS was performed by Kristina Brix and Ralf Kautenburger and the quantum chemical calculations were done by Horst P. Beck.

The results are published in: *Inorg. Chem.* **2023**, 62, 4260-4271.¹⁹³

During the attempts to synthesize CaAl₅Ni₂ (PrAl₅Ni₂ type, *Immm*), CaAl₂ (MgCu₂ type, *Fd $\bar{3}m$*)¹⁸⁵ always formed as majority phase, which subsequently sparked the interest why this phase is so dominant, which in turn led to the investigations of the formation energy of the AE_xAl_y phases alongside calculations of the Bader charges and determination of the ^{27}Al NMR shifts of both the $AEAl_2$ and $AEAl_4$ phases. These phases are by no means new, their structure types and the specific chemical compositions are well known and have been analyzed rigorously. For this work, the existing binary compounds $AEAl_2$ and $AEAl_4$ with $AE = \text{Ca-Ba}$ were synthesized from the elements, which resulted in crystallographic phase pure samples for normal pressure (NP) SrAl₂, SrAl₄ and BaAl₄, whereas CaAl₂ had CaAl₄ and CaAl₄ traces CaAl₂ and additional Al as side phases. Exemplarily the Rietveld refinement of CaAl₂ is shown in **Figure 3.24**. The synthesis of CaAl₄ resulted in the formation of the low temperature modification crystallizing in the monoclinic CaGa₄ type with space group *C2/m*, which is the only AE out of the three (Ca, Sr, Ba) which is polymorphic. The high temperature phase of CaAl₄, SrAl₄ and BaAl₄ crystallize in the tetragonal BaAl₄ type structure with space group *I4/mmm*. The BaAl₄ type structure is related to the CaGa₄ type structure. The group-subgroup relation of the high and low temperature structure of CaAl₄ is shown in **Figure 3.25**. The BaAl₄ type structure undergoes two *translationsgleiche* transitions of index 2 to become the CaGa₄ type structure. In the case of the CaAl₂ and SrAl₂, the calcium compound exists only in the cubic MgCu₂ type Laves phase, whereas the SrAl₂ crystallizes under normal conditions in the KHg₂ type structure (*Imma*), but with an applied pressure the MgCu₂ type structure of SrAl₂ can be obtained, which exhibits compared to the CaAl₄ modifications no structural relationship between both modifications but is rather a complete rearrangement of the Al polyanion inside the structure. The structures and atomic positions of the MgCu₂, KHg₂, BaAl₄ and CaGa₄ type

are shown above in **Figures 3.2, 3.4-3.6** alongside the description of the corresponding structure. Due to the presence of only one crystallographic Al site for the $AEAl_2$ and two Al positions for the $AEAl_4$ compounds, ^{27}Al MAS-NMR spectra were recorded, showing the expected one respective two signals corresponding to the number of independent Al positions in the structure. Additionally, the side phases present in the CaAl_2 , CaAl_4 and in HP/HT- SrAl_2 resulting in additional signals. The quantitative analysis via ICP-MS showed a smaller amount of Al found in all compounds, which can be explained by the formation of Al_2O_3 , which is not dissolved in the used HCl for the analysis.

The Convex-hull diagram is shown in **Figure 3.26** for the Ca–Al, Sr–Al and Ba–Al systems, with the formation energies per atom received from the structural DFT calculations at 0 K. When comparing the different systems, the same trend is observable with all compounds sitting under the marked straight line, indicating that all compounds should be obtainable by using the elements, caused by the higher formation energy per atom compared to the elements. CaAl_2 is compared to CaAl_4 further away from the dashed line indicating a more stable compounds, as seen during the synthesis, where CaAl_2 and Al are forming as side products in the attempt to synthesize CaAl_4 .

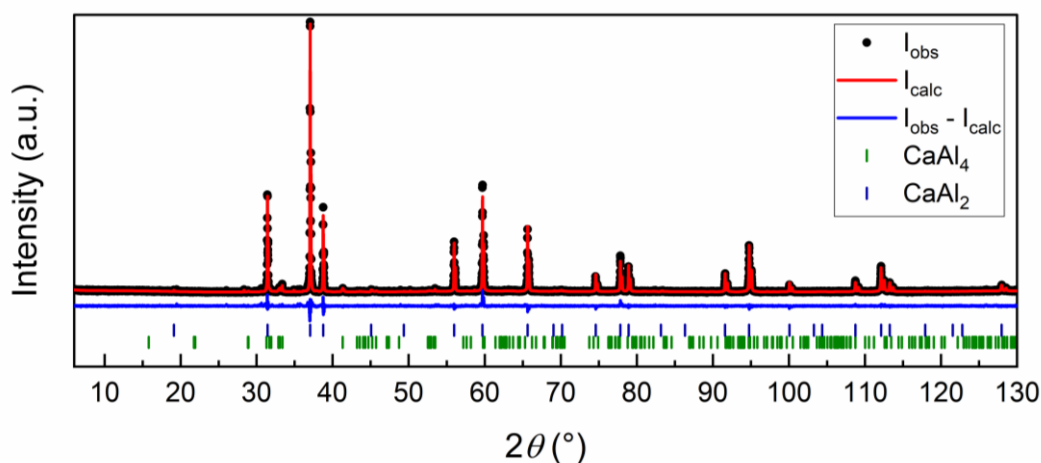


Figure 3.24: Rietveld refinement of the powder X-ray diffraction pattern of CaAl_2 . Collected data is shown in black dots, the refinement as red and the difference as blue line. Royal blue ticks indicate the Bragg positions CaAl_2 (MgCu_2 type, $Fd\bar{3}m$), olive ticks of CaAl_4 (CaGa_4 type, $C2/m$) respectively.

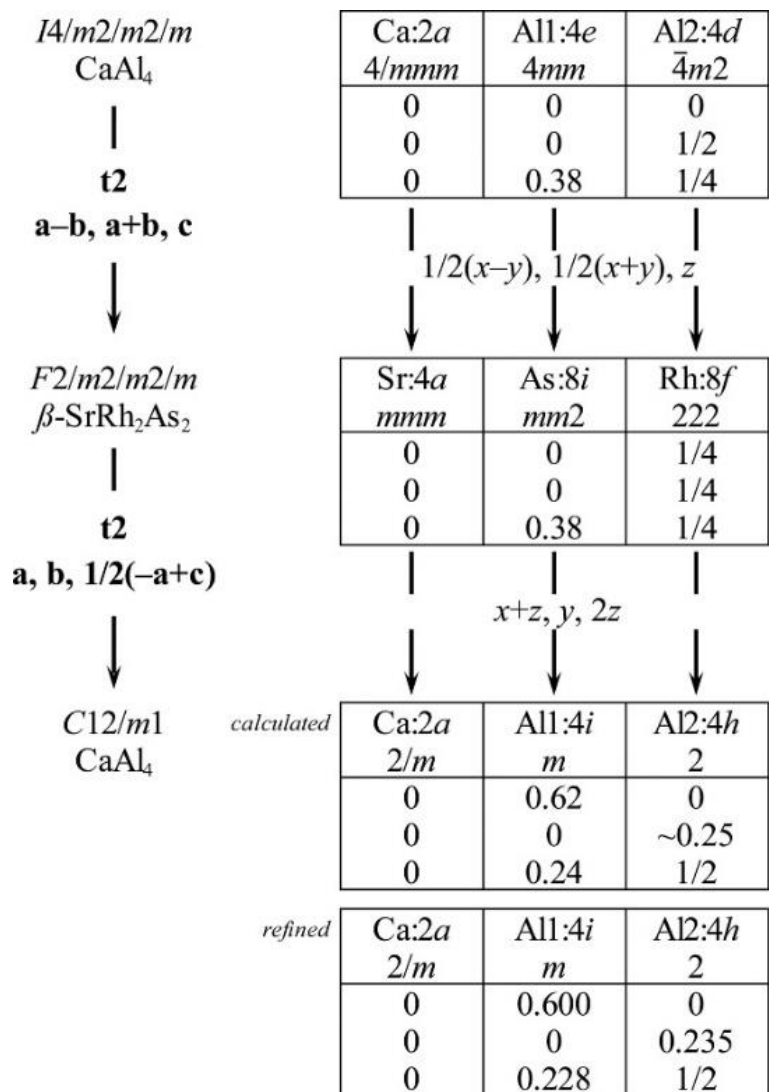


Figure 3.25: Group-subgroup scheme in the Bärnighausen formalism for the BaAl_4 type and CaGa_4 type for CaAl_4 .

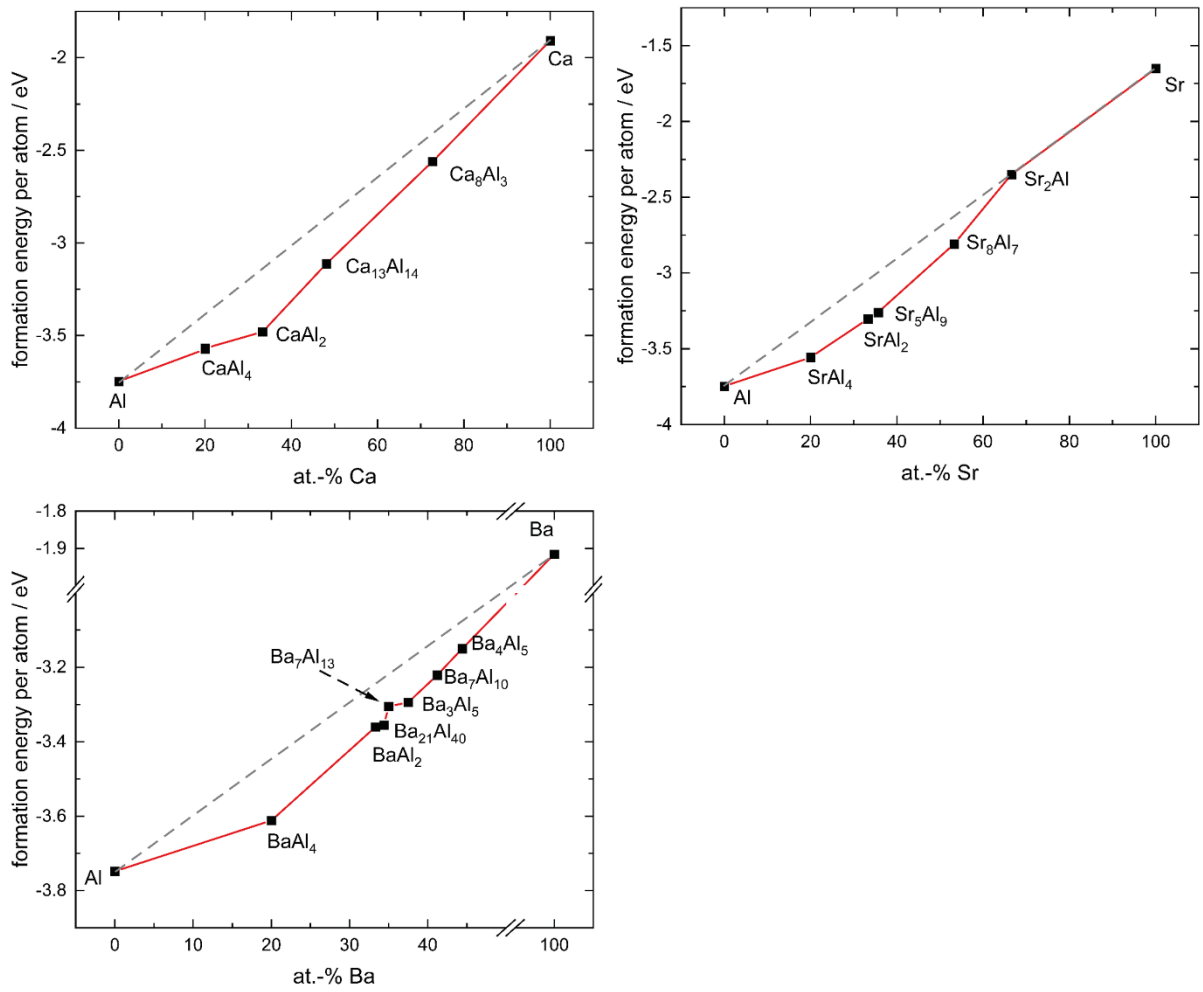


Figure 3.26: Convex-hull diagrams for Ca_xAl_y , Sr_xAl_y and Ba_xAl_y structures.

Theoretical and ^{27}Al NMR Spectroscopic Investigations of Binary Intermetallic Alkaline-Earth Aluminides

Stefan Engel, Elias C. J. Giebelmann, Lukas E. Schank, Gunter Heymann, Kristina Brix, Ralf Kautenburger, Horst Philipp Beck, and Oliver Janka*

Cite This: *Inorg. Chem.* 2023, 62, 4260–4271

Read Online

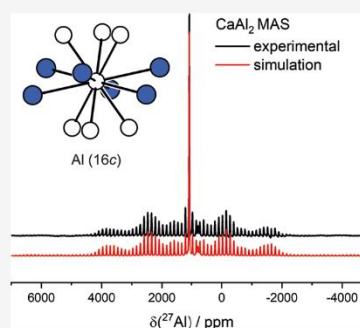
ACCESS |

Metrics & More

Article Recommendations

Supporting Information

ABSTRACT: The binary alkaline-earth aluminides AEAl_2 ($\text{AE} = \text{Ca}$ and Sr) and AEAl_4 ($\text{AE} = \text{Ca}$ – Ba) have been synthesized from the elements and investigated via powder X-ray diffraction experiments. CaAl_2 adopts the cubic MgCu_2 -type structure ($Fd\bar{3}m$), while SrAl_2 crystallizes in the orthorhombic KHg_2 -type ($Imma$). LT- CaAl_4 crystallizes with the monoclinic CaGa_4 -type ($C2/m$), while HT- CaAl_4 , SrAl_4 , and BaAl_4 adopt the tetragonal BaAl_4 -type structure ($I4/mmm$). The close structural relation of the two CaAl_4 polymorphs was established using a group–subgroup relation in the Bärnighausen formalism. In addition to the room-temperature and normal pressure phase of SrAl_2 , a high-pressure/high-temperature phase has been prepared using multianvil techniques, and its structural and spectroscopic parameters were determined. Elemental analysis by inductively coupled plasma mass spectrometry showed that no significant impurities with other elements besides the weighed ones are present and the chemical compositions match the synthesized ones. The title compounds have been furthermore investigated by ^{27}Al solid-state magic angle spinning NMR experiments to validate the crystal structure and to gain information about the influence of the composition on the electron transfer and the NMR characteristics. This has also been investigated from a quantum chemical point of view using Bader charges, while the stabilities of the binary compounds in the three phase diagrams (Ca – Al , Sr – Al and Ba – Al) have been studied by calculations of formation energies per atom.



INTRODUCTION

Intermetallics are a diverse class of compounds with a rich plethora regarding their crystal chemistry and numerous important technical applications, for example, as the superconducting material for NMR and MRT machines or high-field accelerator magnets (Nb_3Sn),^{1,2} as a high-temperature (HT) structural material ($\gamma\text{-TiAl}$ or Ti_3Al),^{3,4} or as precipitates in lightweight alloys (CuAl_2 and MgCuAl_2).^{5–13} Aluminum-based intermetallics are historically often called aluminides, which suggests an electron transfer from the participating elements onto the aluminum atoms. When looking at the electronegativity scale (EN), aluminum exhibits a value of $\chi = 1.61$ according to Pauling.¹⁴ Therefore, the denomination “aluminide” is only correct for compounds in which the other constituent elements exhibit electronegativities smaller than that of Al. In the case of binary compounds, this is only so for the alkali-, the alkaline-earth, the rare-earth, and some transition metals. In these compounds, the aluminum atoms often form a network which, due to the electron transfer, is often referred to as a polyanion. Intermetallic aluminum compounds with the late transition metals, however, should not be termed aluminides. Here, the transition metal exhibits an electronegativity larger than that of aluminum, rendering these compounds rather metallides.

In ternary intermetallics, we often find polyanionic networks formed by two of the three elements with the atoms of the third one usually located in their cavities. For these, the term “polar intermetallics” was coined as in these compounds a significant ΔEN is also observed within the polyanion. This electron transfer can be visualized by quantum chemical calculations using Bader charges but also spectroscopically, for example, via X-ray photoelectron spectroscopy (XPS) studies. Also, again, NMR studies are useful to investigate and understand this charge transfer.¹⁵ We have addressed this phenomenon for several ternary intermetallic aluminum-based metallides over the last years. All of them contained an electron-rich transition metal (e.g., Pd, Pt, and Au) besides aluminum and a main group metal with a low electronegativity. Exemplarily, $\text{Na}_2\text{Au}_3\text{Al}$,¹⁶ the AEAuX ($\text{AE} = \text{Ca}$ – Ba , $\text{X} = \text{Al}$ – In) series,¹⁷ $\text{Ba}_3\text{Pt}_4\text{Al}_4$,¹⁸ and the MPtAl_2 ($M = \text{Ca}$ – Ba , Eu) series¹⁹ should be named. In all these studies, we used a

Received: December 15, 2022

Published: February 27, 2023



combination of NMR, XPS, and theory to probe the bonding situation.

For the present study, the binary alkaline-earth (AE) metal aluminides of composition $AEAl_2$ and $AEAl_4$ with $AE = Ca, Sr,$ and Ba were chosen. While $CaAl_2$ crystallizes in the cubic $MgCu_2$ -type structure (cubic Laves phase, $Fd\bar{3}m$),²⁰ $SrAl_2$ adopts the orthorhombic KHg_2 -type structure ($Imma$).²¹ Initially, $BaAl_2$ was reported to crystallize in the trigonal crystal system;²² however, subsequent single-crystal studies revealed the correct composition to be Ba_7Al_{13} ($P\bar{3}m1$).²³ Later on, it was reported that both $SrAl_2$ and $BaAl_2$ can be obtained under high-pressure/high-temperature (HP/HT) conditions^{24–26} in the cubic $MgCu_2$ -type structure. In all cases, the $AEAl_2$ compounds exhibit a single Al site. HT- $CaAl_4$,²⁷ $SrAl_4$,²⁸ and $BaAl_4$ ²⁹ adopt the tetragonal $BaAl_4$ -type structure ($I4/mmm$), while LT- $CaAl_4$ crystallizes with the monoclinic $CaGa_4$ -type structure ($C2/m$).³⁰ Both structure types exhibit two crystallographic Al sites.

Therefore, $AEAl_2$ and $AEAl_4$ compounds are good candidates for ^{27}Al solid-state NMR investigations, allowing us to probe the influence of the electronic situation onto the ^{27}Al NMR resonance¹⁵ with one or two distinct crystallographic Al sites. The prepared compounds were investigated via powder X-ray diffraction and elemental analyses via inductively coupled plasma mass spectrometry (ICP-MS) measurements to show the actual sample composition and that these samples contain no other elements. For $AEAl_2$, one signal in the ^{27}Al solid-state magic angle spinning (MAS) NMR data is expected, while the $AEAl_4$ compounds should show two resonances. Changes of the alkaline-earth elements result in changes of the unit cell dimensions and differences in the interatomic distances even in the case of isotopic structures. These changes affect the bonding situation and the electronic structure, which in turn leads to changes in the NMR experiments. Besides the NMR spectroscopic investigations, quantum chemical calculations were used to obtain NMR parameters (quadrupolar interactions) and Bader charges of the constituent elements to understand the NMR results. Formation energies were used to analyze the respective stabilities of the compounds in the binary system $Ca-Al$, $Sr-Al$, and $Ba-Al$. Finally, the structural relationship between the two modifications of $CaAl_4$ has been elucidated by a group–subgroup scheme.

EXPERIMENTAL SECTION

Synthesis. The alkaline-earth aluminides were synthesized by arc-melting the elements using Ca, Sr, or Ba ingots (Sigma-Aldrich, Smart Elements) and aluminum pieces (Onyxmet) all with purities of 99.9% or higher. The starting materials were weighed in an argon-filled dry box (M. Braun, Garching, Germany) in the ideal stoichiometric ratios of 1:2 or 1:4 (AE/Al). For $SrAl_2$, a slight surplus of Sr (1.02:2) was weighed. The alkaline-earth pieces were either placed into the copper crucible, while the Al pieces were piled on top or the alkaline-earth pieces along with the aluminum pieces wrapped in aluminum foil (Alujet, 99.5%). In both cases, the crucibles were transported to the arc-furnace in a sealed argon-filled jar. The reactants were arc-melted under an argon atmosphere of about 800 mbar.²⁷ The obtained buttons were remelted several times to increase the homogeneity and directly used after arc-melting. The $SrAl_2$ and $BaAl_4$ beads were transferred to an Al_2O_3 crucible; an additional thermal treatment far below the melting point (~ 950 K) over a 2 h period in an induction furnace (Trumpf Hüttinger, TruHeat 5010) was performed. All obtained samples show metallic luster, while ground powders are gray. They are stable under ambient conditions over months.

X-ray Diffraction. Powder X-ray diffraction patterns of the pulverized samples were recorded at room temperature on a D8-A25-Advance diffractometer (Bruker, Karlsruhe, Germany) in Bragg-Brentano θ - θ -geometry (goniometer radius 280 mm) with $Cu K\alpha$ radiation ($\lambda = 154.0596$ pm). A 12 μm Ni foil working as the $K\beta$ filter and a variable divergence slit were mounted at the primary beam side. A LYNXEYE detector with 192 channels was used at the secondary beam side. Experiments were carried out in a 2θ range of 6 – 130° with a step size of 0.013° and a total scan time of 1 h. The recorded data was evaluated using the Bruker TOPAS 5.0 software package,³¹ with the observed reflections being treated via single-line fits. Lattice parameters and structural models for the data analysis were taken from the Pearson database.³²

Inductively Coupled Plasma Mass Spectrometry. The elemental quantification was conducted with a commercial ICP-MS system (8900 Triple Quad and SPS4 autosampler, Agilent, Santa Clara, USA). Single-element ICP-MS standards of Ho^{3+} , Ca^{2+} , and Al^{3+} (all Merck Millipore, Darmstadt, Germany) as well as Ba^{2+} and Sr^{2+} (both Sigma-Aldrich, St. Louis, USA) with a concentration of 1 g/L each were used. The detector dwell time was 100 μs , the repetition was three times, and the measured isotopes were ^{44}Ca and ^{137}Ba using He as the collision gas as well as ^{88}Sr and ^{27}Al using O_2 as the reaction gas. ^{165}Ho was used as the internal standard in the He mode and via mass pair (Q_1, Q_2) = (165, 181) in the O_2 mode.

Between 1 and 7 mg of the samples were weighed in 15 mL polypropylene tubes where the samples were dissolved using ultrapure hydrochloric acid (Merck Millipore, Darmstadt, Germany). Samples were diluted with ultrapure water (PURELAB Chorus 1, ELGA Veolia Water Technologies Deutschland GmbH, Celle, Germany) to reach concentrations of the analyte between 5 and 100 $\mu g L^{-1}$. Additionally, 10 $\mu g L^{-1}$ internal standard (^{165}Ho) and HNO_3 (69%, ultra-pure, Carl Roth GmbH & Co. KG, Karlsruhe, Germany) were added to reach an acid concentration of 3–5% for the measurement.

HP/HT Syntheses. The HP/HT treatment was carried out via a multianvil press, equipped with a Walker-type module (Max Vöggenreiter GmbH, Mainleus, Germany). Details about the technique and the construction of the different assemblies can be found in numerous references.^{33–35} Carefully milled powder of NP- $SrAl_2$ was loaded into an 18/11-assembly crucible made of hexagonal boron nitride and compressed to a pressure of 7 GPa within 180 min. Subsequent heating to 1340 K within 15 min was followed by a period of 20 min at constant temperature, ending with quenching of the sample. After a decompression time of 540 min, the sample was carefully separated from the surrounding assembly parts by mechanical fragmentation. The polycrystalline sample appeared silvery with metallic luster. A powdered sample of HP/HT- $SrAl_2$ is gray and stable in air. Attempts to synthesize $BaAl_2$ using Ba_7Al_{13} as the starting material and similar experimental conditions, however, were unsuccessful.

Solid-State NMR Spectroscopy. ^{27}Al solid-state NMR spectra of all obtained compounds were recorded with a Bruker Avance III 400 WB at 104.31 MHz using magic-angle spinning techniques. To reduce the electrical conductivity and density, the finely powdered samples were mixed in approximate mass ratios of 1:9 with dry sodium chloride and filled into a conventional ZrO_2 -MAS rotor with 4 mm diameter. The spectra were recorded using one-pulse experiments with a typical pulse length of 0.83 μs , a relaxation delay of $d_1 = 1$ s, and a MAS spinning frequency of 13 kHz. The shifts reported are referenced to a 1 molar aqueous solution of aluminum chloride. The spectra were recorded with the help of the Bruker Topspin software³⁶ and analyzed with the Dmfit software package.³⁷

Quantum Chemical Calculations. Electronic structure calculations of the AE_xAl_y compounds were performed using the projector-augmented wave (PAW) method of Blöchl^{38,39} coded in the Vienna ab initio simulation package (VASP).^{40,41} VASP calculations employed the potentials PAW_PBE Ca 06Sep2000, PAW_PBE Sr_sv 07Sep2000, PAW_PBE Ba_sv 06Sep2000, and PAW_PBE Al 04Jan2000. Runs using the generalized gradient approximation with exchange and correlation treated by Perdew–Burke–Erzerhof (PBE)⁴² for comparison did not result in significant changes. The

Table 1. Lattice Parameters of the Binary Alkaline-Earth Aluminum Intermetallics Refined from Powder X-ray Diffraction Data

compound	structure type	<i>a</i> (pm)	<i>b</i> (pm)	<i>c</i> (pm)	β (°)	<i>V</i> (nm ³)	literature
CaAl ₂	MgCu ₂	804.02(1)				0.5198	^a
		802.2				0.5162	20
SrAl ₂	KHg ₂	479.62(1)	789.30(1)	795.51(1)		0.3011	^a
		484	792	799		0.3063	21
HP/HT-SrAl ₂	MgCu ₂	829.35(1)				0.5704	^a
		832.5				0.5770	24
HP/HT-BaAl ₂	MgCu ₂	870.2				0.6590	25
LT-CaAl ₄	CaGa ₄	616.91(1)	618.50(1)	634.34(1)	118.03(1)	0.2136	^a
		615.3	617.3	632.9	118.03	0.212	30
HT-CaAl ₄	BaAl ₄	453.3		1107		0.2098	20
SrAl ₄	BaAl ₄	446.41(1)		1121.18(1)		0.2234	^a
		446.3		1120.3		0.2232	46
BaAl ₄	BaAl ₄	456.72(1)		1128.63(2)		0.2354	^a
		456.6		1125		0.2345	47

^aThis work.

cutoff energy for the plane wave calculations was set to 550 eV, and the Brillouin zone integration was carried out using an automated Γ -centered 20-fold *k*-point mesh. The Bader charge analysis was based on VASP outputs with subsequent calculations with the Bader program developed by the Henkelman group.^{43–45}

RESULTS AND DISCUSSION

X-ray Diffraction. All samples were investigated by powder X-ray diffraction experiments to check their phase purity. As structural models for the Rietveld refinements, the data from the references given in Table 1 have been used. Some of the compounds could not be obtained as X-ray pure materials (vide infra); the respective phase contributions of the impurities are given in Table S1. The refined lattice and atomic parameters are listed in Tables 1 and 2. The interatomic distances are listed in Tables 3 and 4. The

Table 2. Positional Parameters of the Binary Alkaline-Earth Aluminum Intermetallics Refined from Powder X-ray Diffraction Data

atom	Wyckoff site	<i>x</i>	<i>y</i>	<i>z</i>
CaAl ₂ (MgCu ₂ -type, <i>Fd</i> $\bar{3}m$)				
Ca	8 <i>b</i>	3/8	3/8	3/8
Al	16 <i>c</i>	0	0	0
SrAl ₂ (KHg ₂ -type, <i>Imma</i>)				
Sr	4 <i>e</i>	0	1/4	0.5503(2)
Al	8 <i>h</i>	0	0.0676(3)	0.1624(1)
HP/HT-SrAl ₂ (MgCu ₂ -type, <i>Fd</i> $\bar{3}m$)				
Sr	8 <i>b</i>	3/8	3/8	3/8
Al	16 <i>c</i>	0	0	0
LT-CaAl ₄ (CaGa ₄ -type, <i>C2/m</i>)				
Ca	2 <i>a</i>	0	0	0
Al1	4 <i>i</i>	0.6006(3)	0	0.2287(2)
Al2	4 <i>h</i>	0	0.2362(3)	1/2
SrAl ₄ (BaAl ₄ -type, <i>I4/mmm</i>)				
Sr	2 <i>a</i>	0	0	0
Al1	4 <i>e</i>	0	0	0.3816(2)
Al2	4 <i>d</i>	0	1/2	1/4
BaAl ₄ (BaAl ₄ -type, <i>I4/mmm</i>)				
Ba	2 <i>a</i>	0	0	0
Al1	4 <i>e</i>	0	0	0.3810(2)
Al2	4 <i>d</i>	0	1/2	1/4

Table 3. Interatomic Distances (pm) for CaAl₂ (MgCu₂-Type), SrAl₂ (KHg₂-Type), HP/HT-SrAl₂ (MgCu₂-Type), and HP/HT-BaAl₂ (MgCu₂-Type) Determined from Powder X-ray Diffraction Experiments^a

		CaAl ₂		HP/HT-SrAl ₂			
Ca	12	Al	333.3	Sr	12	Al	343.8
	4	Ca	348.2		4	Sr	359.1
Al	6	Al	284.3	Al	6	Al	293.2
	6	Ca	333.3		6	Sr	343.8
SrAl ₂							
Sr	4	Al	327.5	Al	2	Al	277.3
	2	Al	338.2		1	Al	278.5
	2	Al	341.2		1	Al	290.8
	4	Al	357.1		2	Sr	327.5
	2	Sr	398.1		1	Sr	338.2
	2	Sr	402.7		1	Sr	341.2
2	Sr	357.1					

^aAll distances of the first coordination spheres are listed. All standard uncertainties were less than 0.1 pm.

diffraction pattern along with the Rietveld refinement of SrAl₄ is exemplarily shown in Figure 1; all other diffraction patterns are depicted as Figures S1–S6 in the Supporting Information.

HP Experiments. NP-SrAl₂ and Ba₇Al₁₃ were reported to transform into their respective cubic HP/HT phases when treated via HP/HT conditions.^{24–26} While the synthetic attempts for BaAl₂ were unsuccessful, Figure 2 shows the comparison of the obtained powder X-ray patterns of NP-SrAl₂ and HP/HT-SrAl₂. As can be seen, they significantly differ due to the different structures they adopt. HP/HT-SrAl₂ could be obtained as an almost X-ray pure sample (trace impurities of SrO) which was subsequently used for further investigations.

Inductively Coupled Plasma Mass Spectrometry. ICP-MS was used to determine potential contaminations from other elements in CaAl₂, NP-SrAl₂, CaAl₄, SrAl₄, and BaAl₄. Screening over all masses clearly showed that the strongest impurities are present in concentrations well below 0.1 mass %. Analyses of the chemical compositions indicate that a certain Al shortage was detected in all investigated samples (Table 5). However, when looking at the detected concentrations of AE and Al, in all cases, only a maximum of ~92% of the weighed solid could be found in all cases [*c*(AE) + *c*(Al)]/initial

Table 4. Interatomic Distances (pm) for LT-CaAl₄ (CaGa₄-Type), SrAl₄ (BaAl₄-Type), and BaAl₄ (Own Type) Determined from Powder X-ray Diffraction Experiments^a

LT-CaAl ₄				SrAl ₄					
Ca	2	Al1	328.3	Sr	8	Al1	342.4		
	4	Al1	334.8		8	Al2	358.3		
	2	Al1	339.6		Al1	1	Al1	265.5	
	4	Al2	349.2		4	Al2	267.6		
Al1	4	Al2	361.1	Sr	4	Sr	342.4		
	1	Al1	256.4		Al2	4	Al1	267.6	
	2	Al2	264.8		4	Al2	315.7		
	2	Al2	268.0		4	Sr	358.3		
Al2	1	Ca	328.3	BaAl ₄	Ba	8	Al1	349.8	
	2	Ca	334.8			8	Al2	363.0	
	1	Ca	339.6			Al1	1	Al1	268.6
	2	Al1	264.8			4	Al2	272.0	
Al2	2	Al1	268.0	Al2	4	Ba	349.8		
	1	Al2	292.2		4	Al1	272.0		
	2	Al2	308.9		4	Al2	322.9		
	1	Al2	326.3		4	Ba	363.0		
	2	Ca	349.2		4	Al2	322.9		
	2	Ca	361.1		4	Ba	363.0		

^aAll distances of the first coordination spheres are listed. All standard uncertainties were less than 0.1 pm.

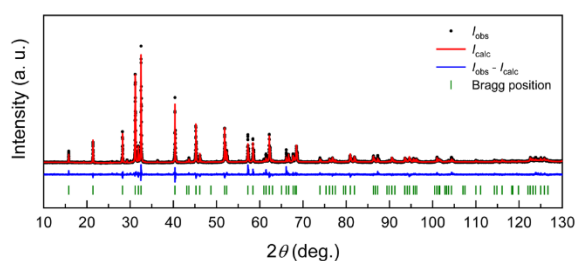


Figure 1. Powder X-ray diffraction data and Rietveld refinement of SrAl₄. The black dots represent the experimental data, the red line represents the respective fit, while the blue line indicates the difference between experimental and theoretical data. The green bars show the Bragg positions of tetragonal SrAl₄ (BaAl₄-type).

concentration]. In the cases of SrAl₄ and BaAl₄, traces of undissolved solid were visually observed. Since Al₂O₃ is the only possible impurities that would not readily dissolve in hydrochloric acid, the discrepancies in the determined AE to Al ratios can most likely be attributed to this side product.

Group–Subgroup Relations. Two modifications have been reported for both SrAl₂ and CaAl₄. While orthorhombic RT/NP-SrAl₂ (KHg₂ type) can only be transformed into the cubic phase using HP/HT conditions (vide supra), tetragonal CaAl₄ can be obtained from the monoclinic phase via quenching and can therefore be considered as the HT phase. When looking at the structures, it becomes evident that for the transformation from RT/NP-SrAl₂ to the HP/HT modification (cubic MgCu₂ type), a rearrangement of the Al polyanion has to take place with a severe movement of the atoms, that is, a reconstructive phase transition. Tetragonal (BaAl₄ type) and monoclinic CaAl₄ (CaGa₄ type) in contrast shows a structural relationship that had already been established based on their space group relations⁴⁸ that was later updated by Kneidinger et al.⁴⁹ Therefore, this is only a displacive phase transition rather than a reconstructive one. The corresponding Bärnighausen

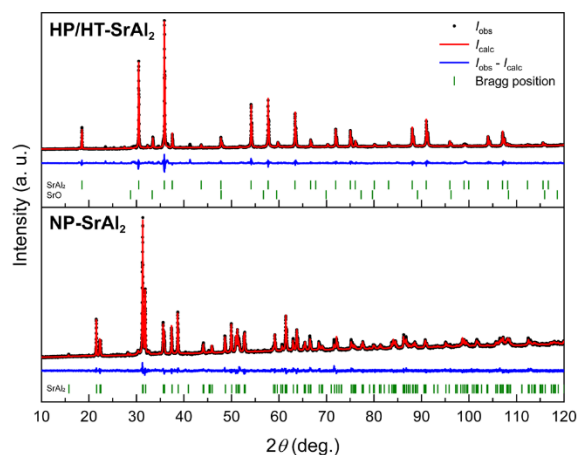


Figure 2. Comparison of the powder X-ray diffraction data and Rietveld refinement of HP/HT-SrAl₂ (top) and NP-SrAl₂ (bottom). The black dots represent the experimental data; the red line indicates the respective fit, while the blue line indicates the difference between experimental and theoretical data. The Bragg positions indicate the HP/HT-SrAl₂ (top) and SrO (bottom) positions (top panel) and NP-SrAl₂ of the precursor (bottom panel).

formalism^{50–53} also containing the relations of the atomic positions is shown in Figure 3 for the first time. The first step of the symmetry reduction is a *translationengleiche* transition of index 2 to space group *Fmmm*. In this step, a symmetry reduction along with a cell transformation takes place, but no additional degrees of freedom are introduced for the respective occupied sites. However, the variable *z* parameter of the Al1 site as well as the decoupling of the lattice parameters allows for an orthorhombic distortion that is realized in β-SrRh₂As₂ showing just this symmetry and general topology.⁵⁴ In the second step, again a *translationengleiche* transition of index 2 along with a cell transformation into the monoclinic crystal system and to space group *C12/m1* takes place. No splitting of the Wyckoff positions is observed; however, additional translatory degrees of freedom are introduced for both the Al1 and Al2 sites. The refined positional parameters (powder X-ray data) are also given in Figure 3.

Crystal Chemistry. The alkaline-earth aluminum phase diagrams contain several binary compounds;^{32,46,55–59} however, of all these, only the AEAl₂ and AEAl₄ representatives exhibit one respectively two crystallographic Al sites, enabling useful ²⁷Al solid-state NMR investigations at this stage.

CaAl₂ (Figure 4, top) crystallizes in the cubic MgCu₂-type structure (*Fd3m*), also known as cubic Laves phase. In this structure, the Al atoms form empty Al₄ tetrahedra that are connected over all corners to form a network. The coordination number of the Al atoms is 12 (Al@Al₆Ca₆) with a distorted icosahedral coordination environment. The Ca atoms reside in the cavities of the framework and exhibit a coordination number of 16 (Ca@Al₁₂Ca₄), forming a Frank–Kasper polyhedron. NP-SrAl₂ (Figure 4, bottom) in contrast crystallizes in the orthorhombic KHg₂-type structure (*Imma*). Again, the Al atoms form a network with the Sr atoms residing in cavities. The coordination number of the Sr atoms is also 16 (Sr@Al₁₂Sr₄) and the coordination number of the Al atoms is 12 (Al@Al₆Ca₆), but the coordination polyhedra differ significantly. BaAl₂ was proposed to exist; more detailed

Table 5. ICP-MS Data for the Alkaline-Earth Aluminides $AEAl_2$ ($AE = Ca$ and Sr) and $AEAl_4$ ($AE = Ca-Ba$)

compound	initial con. (mg L ⁻¹)	dilution	c(AE) (mg L ⁻¹)	c(Al) (mg L ⁻¹)	c(AE) (mmol L ⁻¹)	c(Al) (mmol L ⁻¹)	AE/Al
CaAl ₂	250	2000	84	111	2.1	4.1	1:2.0
SrAl ₂	420	2000	248	140	2.8	5.2	1:1.8
CaAl ₄	260	2000	63	159	1.6	5.9	1:3.8
SrAl ₄ ^a	120	1000	45	50	0.5	1.8	1:3.6
BaAl ₄ ^a	110	1000	32	24	0.24	0.8	1:3.7

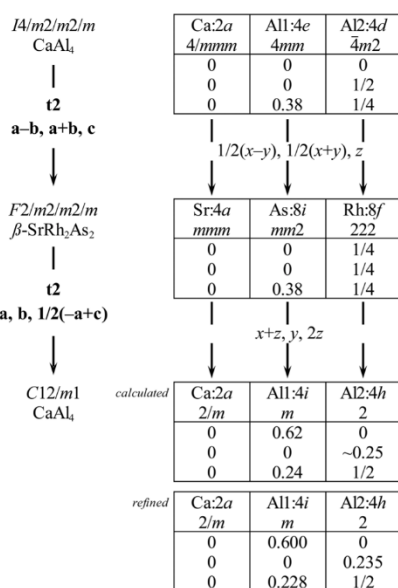
^aInsoluble components.

Figure 3. Group-subgroup scheme in the Bärnighausen formalism^{50–53} for the structures of tetragonal (BaAl₄-type) and monoclinic CaAl₄ (CaGa₄-type). The indices for the *translationengleiche* (*t*) symmetry reductions, the unit cell transformations, and the evolution of the atomic parameters are given.

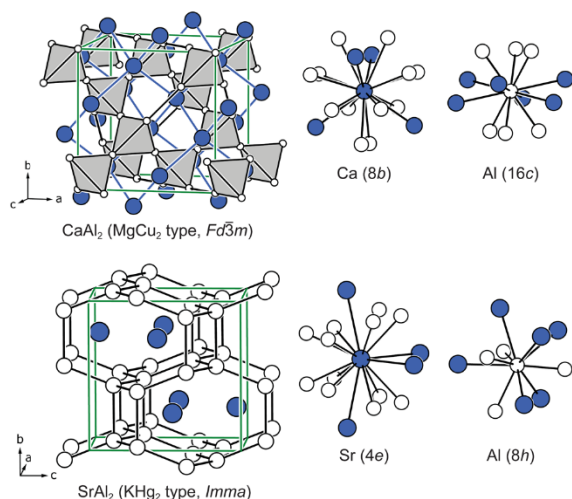


Figure 4. Unit cells and coordination polyhedra of (top) cubic CaAl₂ (MgCu₂-type) and (bottom) orthorhombic SrAl₂ (KHg₂-type). AE atoms are depicted in blue and Al atoms as white circles.

investigations, however, revealed that the correct composition is Ba₇Al₁₃ ($P\bar{3}m1$).²³ Both, SrAl₂ and BaAl₂, exist in the cubic MgCu₂-type structure when prepared via an HP/HT synthesis. While HP/HT-SrAl₂ can be obtained as a phase-pure sample starting from orthorhombic SrAl₂,²⁴ HP/HT-BaAl₂ was obtained using Ba₇Al₁₃ as an educt with byproducts according to the literature.²⁵ More recent HP investigations showed that Ba₂₁Al₄₀ is a more suitable precursor that yields phase-pure samples.²⁶ The HP/HT attempts presented in this work underline the observation regarding MgCu₂-type SrAl₂; however, BaAl₂ could not be prepared (*vide supra*).

For the AEAl₄ compounds, SrAl₄ and BaAl₄ (Figure 5, top) crystallize in the well-known tetragonal BaAl₄-type structure ($I4/mmm$) and HT-CaAl₄ was also reported to adopt this structure type. In the BaAl₄-type structure, two independent aluminum positions can be observed again forming a network in which the AE atoms are located. These exhibit a coordination number of 18 ($AE@Al_{18}$) with a fourfold capped hexagonal prismatic coordination environment. Of the two Al sites, Al1 is surrounded by five Al atoms as a square pyramid along with four AE atoms (giving in total a monocapped square antiprism), while Al2 exhibits a double-tetrahedral coordination by four Al1 and four AE atoms as well as four Al2 atoms within the same plane resulting in a CN = 12 ($Al2@Al_4Al_2_4AE_4$). Finally, the LT phase of CaAl₄ (Figure 5, bottom) crystallizes in the monoclinic crystal system ($C2/m$) with the CaGa₄-type structure. Here, again one Ca and two Al sites are observed with CN(Ca) = 16 ($Ca@Al_{16}$), CN(Al1) = 9 ($Al1@Al_1Al_2_4Ca_4$), and CN(Al2) = 12 ($Al2@Al_1_4Al_2_4AE_4$). The Al2 atoms form slightly distorted square layers with the Al1 atoms alternatingly located above and below the Al2 layer. These slabs are connected over Al1–Al1 interactions with the Ca atoms residing inside the cavities.

Quantum Chemical-Based Stability Analysis. When discussing issues with the phase-pure synthesis of the mentioned intermetallic phases, a closer look at quantum chemical calculations can be helpful. Structure-based DFT calculations of the formation energy per atom in the binary systems AE_xAl_y ($AE = Ca-Ba$) resulted in the convex-hull diagrams given in Figure 6. In these diagrams, the stability of the respective intermetallic compounds relative to the energy of the elements in appropriate composition is shown (Tables 6 and S2). It becomes clear that at 0 K, which is the only temperature considered in these calculations, almost every binary phase of the AE_xAl_y ($AE = Ca-Ba$) compounds should be obtainable by reacting the two constituent elements. Their formation energy per atom is larger (more negative) than the energy determined when considering a direct average of energy per atom between the two elements.

When looking at the intermetallics discussed in this article, the formation energy analysis can be used to explain problems occurring in the preparation of, for example, CaAl₄. At 0 K, this compound should decompose into CaAl₂ and Al since its

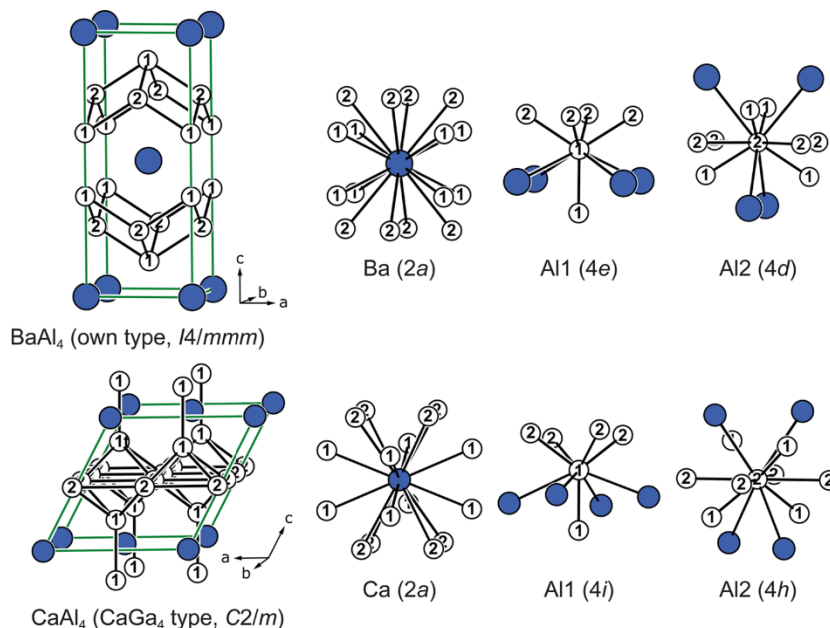


Figure 5. Unit cells and coordination polyhedra of (top) tetragonal BaAl_4 (own type) and (bottom) monoclinic CaAl_4 (CaGa_4 -type). AE atoms are depicted in blue and Al atoms as white circles.

formation energy per atom is smaller than the weighted average of the energies of Al and CaAl_2 . Therefore, it is evidently an entropically stabilized compound. CaAl_2 should by far be the most stable compound given the energy difference between the dashed line and its calculated formation energy per atom. When looking at the respective plots for Sr and Ba, the opposite is the case. Here, the 1:4 compounds are more stable, which is also found in all synthetic attempts of the respective compounds.

However, the data cannot explain the differences in low- and high-temperature/-pressure phases of, for example, SrAl_2 and CaAl_4 . The differences of the energies per atom are too small to be taken into consideration, and such 0 K calculations rarely depict the energetics in an HT or HP situation.

Figures 7 and 8 summarize the ^{27}Al MAS-NMR spectroscopic results. Consistent with the crystal structures, the spectra of the AEAl_2 ($\text{AE} = \text{Ca}$ and Sr) compounds confirm the presence of solely one crystallographically independent Al site. In contrast, the spectra of the AEAl_4 ($\text{AE} = \text{Ca}$ – Ba) compounds show two strong signals originating from two independent Al sites in the crystal structure. The individual spectra are shown in Figures S7–S12 in the Supporting Information.

The intense central line originating from the $|+1/2\rangle \leftrightarrow |-1/2\rangle$ transition can be modeled with a Gauss–Lorentz fit, which is a first hint that the electric quadrupolar couplings C_Q are rather small (in a range <5 MHz) and second-order quadrupole effects (SOQEs) are not dominant (vide infra). The spectra are characterized by substantial line broadening effects arising from the structural distortions from the asymmetric local environments of the ^{27}Al nuclei caused by the crystal structure itself and by extrinsic effects such as grinding of the sample. This results in strong nuclear electric quadrupolar interactions, which can in parts be described by the second-order perturbation theory. The position of the

central transition, referenced to an aqueous solution of Al^{3+} (AlCl_3), is significantly shifted, however, in line with the reported shifts for intermetallic aluminum. This shift, typically in the range of 200–1200 ppm,¹⁵ is dominated by the *Knight* shift contribution. The drastic shift range is caused by the s -electron spin density at the Fermi level as probed by the ^{27}Al nuclei.¹⁵ Under magic angle spinning conditions, one observes a wide spinning sideband pattern in all recorded spectra. This originates from the outer satellite transitions, $|\pm 1/2\rangle \leftrightarrow |\pm 3/2\rangle$ and $|\pm 3/2\rangle \leftrightarrow |\pm 5/2\rangle$. For electric quadrupolar couplings <3 MHz, C_Q parameters can be extracted by simulation and fitting from the intensity profile of the spinning sideband pattern or are taken from electronic DFT calculations without further refinement.

To shed light on the effects of the SOQE on the position of the respective NMR signals, the magnetic shielding δ_{ms} can be calculated using the experimental resonance shifts δ along with the C_Q values obtained from DFT calculations. The magnetic shielding δ_{ms} has the following contributions

$$\delta_{\text{ms}} = \delta_{\text{dia}} + \delta_{\text{orb}} + \delta_{\text{Curie}} + \delta_{\text{K}} \quad (1)$$

with δ_{dia} being the diamagnetic and δ_{orb} being the orbital angular momentum contribution. δ_{Curie} arises from the interactions with unpaired localized electrons, while finally δ_{K} is the so-called *Knight* shift originating from the interaction with the conduction electrons in metallic materials. Since the title compounds are intermetallics with only closed-shell atoms, the contributions of δ_{dia} , δ_{orb} , and δ_{Curie} can be neglected. Therefore, the magnetic shielding is dominated by the *Knight* shift contribution. If SOQE is present, the magnetic shielding δ_{ms} is influenced, leading to changes in the observed resonance shifts described by the following equation

$$\delta = \delta_{\text{ms}} - (\text{SOQE})^2 \frac{N}{(\nu_L)} \quad (2)$$

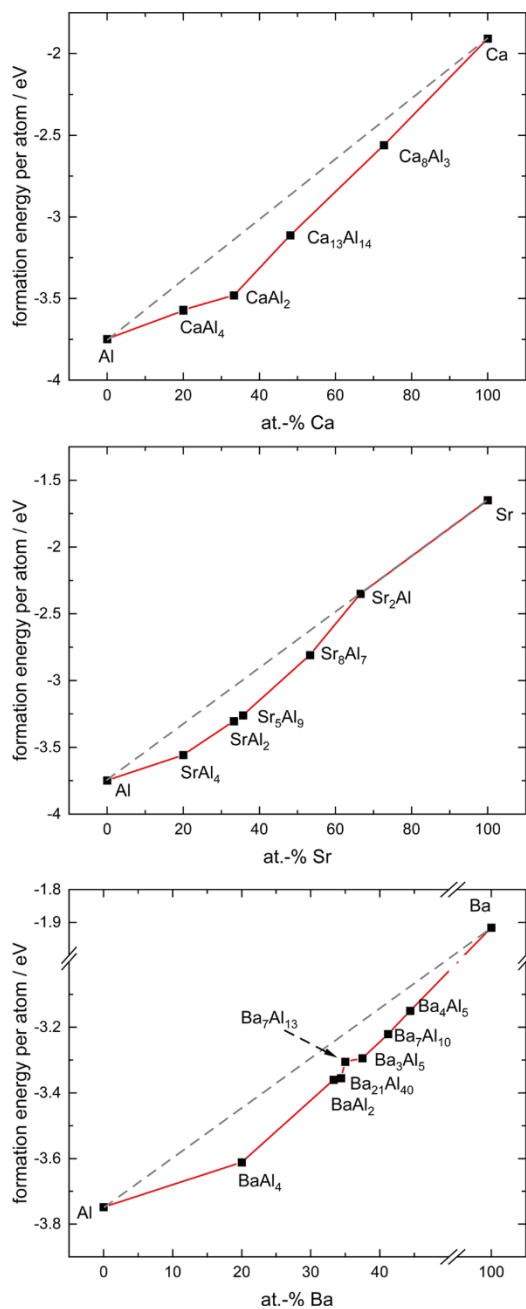


Figure 6. Convex-hull diagrams (formation energy per atom vs chemical composition) for the binary systems AE_xAl_y , with $AE = \text{Ca}$ (top), Sr (middle), and Ba (bottom). The formation energy per atom is obtained from DFT calculations.

with

$$\text{SOQE} = C_Q \sqrt{1 + \frac{\eta_Q^2}{3}} \quad (3)$$

Here, C_Q represents again the electric quadrupolar coupling, while N is an element-specific value ($N = 6000$ for ^{27}Al), ν_L represents the Larmor frequency of the respective nuclei ($\nu_L =$

Table 6. Formation Energy per Atom (in Electron Volt) for the $AEAl_2$ ($AE = \text{Ca}$ and Sr) and $AEAl_4$ ($AE = \text{Ca}$ – Ba) Compounds Discussed in This Work^a

element	formation energy per atom / eV	compound	formation energy per atom / eV
Al	−3.748		
Ca	−1.908	CaAl_2	−3.480
		LT- CaAl_4	−3.568
		HT- CaAl_4	−3.573
Sr	−1.650	NP- SrAl_2	−3.305
		HP/HP- SrAl_2	−3.302
		SrAl_4	−3.556
Ba	−1.916	HP/HT- BaAl_2	−3.360
		BaAl_4	−3.612

^a ^{27}Al solid-state NMR spectroscopy.

104.3 MHz for ^{27}Al) and η_Q is the asymmetry parameter.¹⁵ In most of the present cases, η_Q is 0 (Table 7); therefore, for these compounds, SOQE equals C_Q . Due to the experimentally determined values of δ and the quantum-chemically calculated values for C_Q and η_Q it is possible to yield information about the influence of the SOQE and this allows the subsequent calculation of $\delta_{\text{ms}} = \delta_K$ using eqs 2 and 3 given above.⁶⁰ The calculated Knight shifts δ_K are listed in Table 7.

Figure 7 (left) shows the spectra for the $AEAl_2$ ($AE = \text{Ca}$ and Sr) compounds, as well as a zoomed region (right) of the central transition. In Table 7, the extracted values for the experimental C_Q parameter obtained from DMFit software as well as the calculated ones are given. Based on DFT calculations and structural features of the Al sites, the asymmetry parameter η_Q was set to 0 except for orthorhombic NP- SrAl_2 (KHg₂ type).

While the observed resonances show the typical shifts of intermetallic materials, one can clearly see that KHg₂-type SrAl_2 (Figure 7, middle) shows a significantly lower shift along with a signal typical for an asymmetric coordination environment. The latter can be explained by the distorted coordination environment (Figure 4, bottom right) leading to an asymmetry parameter $\eta_Q = 0.86$. In contrast, HP/HT- SrAl_2 has a similar shift to CaAl_2 , which is somehow expected, since both adopt the MgCu₂-type structure and therefore most likely exhibit similar electronic structures.

Spectra of the $AEAl_4$ ($AE = \text{Ca}$ – Ba) compounds depicted in Figure 8 are in line with the crystallographic observation of two independent Al sites. In addition, the spectrum of CaAl_4 also shows the characteristic signals of the 1:2 compound CaAl_2 (1091 ppm) and elemental aluminum (1639 ppm). The reason for the formation of these two side products has been given above (vide supra).

As explained before, the exact determination of C_Q based on the intensity profile of the spinning sideband pattern can hardly be done for $C_Q > 3$ –5 MHz which is the case at least for one Al site in the systems. Here, a refinement of the quadrupole parameters has been carried out only in parts. For the simulation of the spectra in Figure 8, the results from DFT calculations have partially been used without further refinement. Assignment of the Al sites to the signals has been done based on the C_Q parameters, the literature,⁶¹ and the observation that the signal at higher-resonance shifts is anisotropically broadened and does not show a Gauss–Lorentz line shape anymore. Here, SOQEs come into play. The coordination environments of the two distinct Al sites (Figure 5, right) clearly show that the one of the Al atoms is

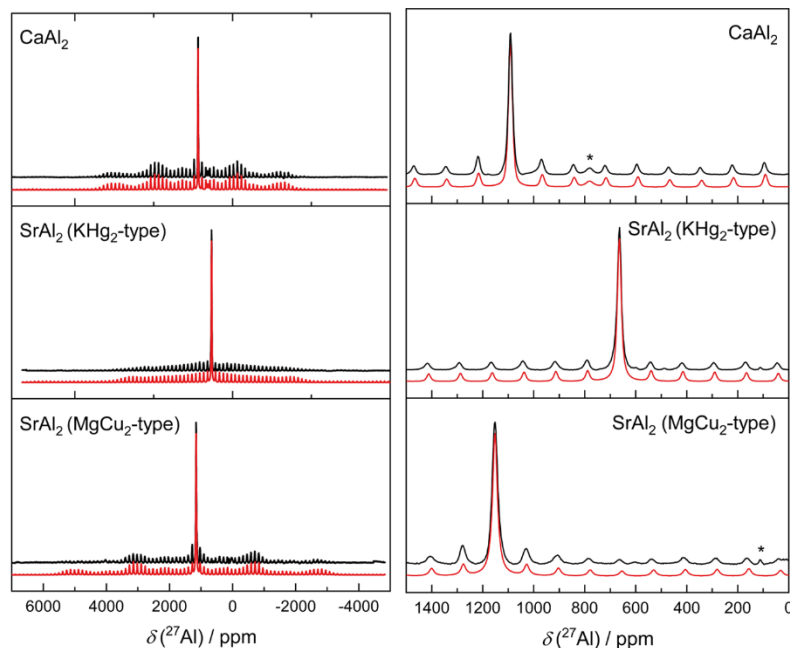


Figure 7. ^{27}Al MAS-NMR spectra (left) of CaAl_2 (MgCu_2 -type, top), NP-SrAl_2 (KHg_2 -type, middle), and HP/HT-SrAl_2 (MgCu_2 -type, bottom). Zoomed view of the region around the central $|+1/2\rangle \leftrightarrow |-1/2\rangle$ transition is shown on the right. The observed impurities are marked with an asterisk.

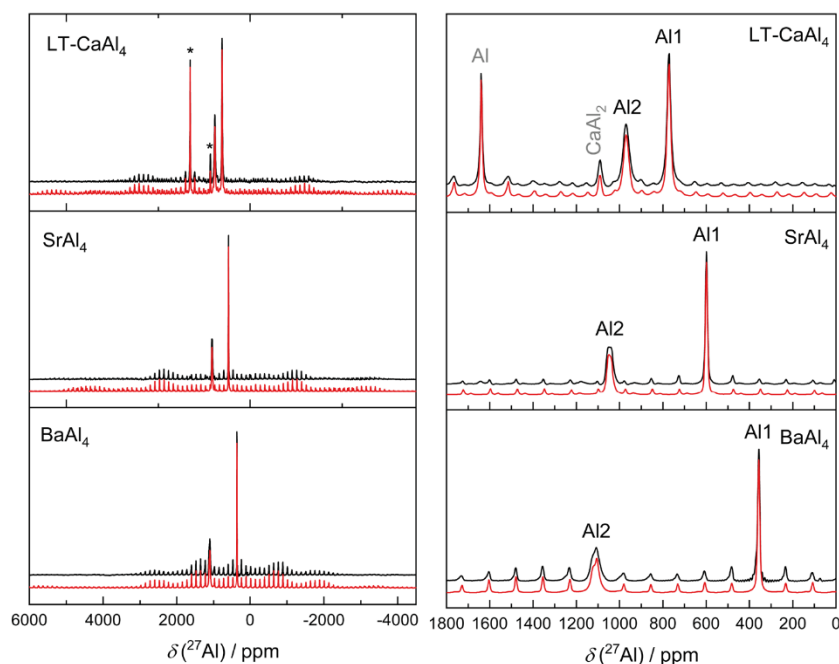


Figure 8. ^{27}Al MAS-NMR spectra (left) of CaAl_4 (CaGa_4 -type, top), SrAl_4 (BaAl_4 -type, middle), and BaAl_4 (BaAl_4 -type, bottom). Zoomed view of the region around the central $|+1/2\rangle \leftrightarrow |-1/2\rangle$ transition is shown on the right. The site assignment is given. The observed impurities are marked with asterisk (left) and labeled (right).

more asymmetric compared to the one of Al2; therefore, one would expect the broadened signal at higher shifts to be the one of the Al1 sites, while the sharper signal originates from the Al2 site. However, Pecher et al. already mentioned that the

V_{zz} component of the electric field gradient (EFG) in SrAl_4 and BaAl_4 is significantly larger for Al2 with respect to Al1 (see Table S3 in the Supporting Information).⁶¹ Therefore, the Al1 site, although being the less symmetric one, exhibits the smaller

Table 7. Summary of NMR Observables of the $AEAl_2$ and $AEAl_4$ Series ($AE = Ca, Sr, \text{ and } Ba$) Extracted from the DMFit Simulation of the ^{27}Al MAS-NMR Spectra with δ Being the Resonance and δ_K Being the Knight Shift (in Parts per Million), C_Q the Quadrupolar Parameter (in kHz), η_Q the Asymmetry Parameter, G/L the Gaussian to Lorentz Ratio, and dCs the Chemical Shift Anisotropy Parameter (in Parts per Million)^a

site	δ	δ_K	$C_{Q,theo}$	$C_{Q,exp}$	η_{theo}	η_{exp}	G/L	dCs	literature	
CaAl ₂										
Al	(16c)	1091	1094	228	2085	0	0	0.47	−82	^b
	<i>i</i> [CaAl ₄]	781				0		0		^b
Al	(16c)	1050			2190					62
NP-SrAl ₂										
Al	(8h)	664	669	−1757	2180	0.92	0.86	0.14	+2	^b
HP/HT-SrAl ₂										
Al	(16c)	1152	1154	1807	2955	0		0	−76	^b
HP/HT-BaAl ₂										
Al	(16c)			2773		0				^b
LT-CaAl ₄										
Al1	(4i)	772	779	−3634	4163	0.20		0.28		^b
Al2	(4h)	970	984	−5009		0.01		0.40		^b
	<i>i</i> [CaAl ₂]	1091		2085					1.00	^b
	<i>i</i> [Al]	1639		92					0	^b
HT-CaAl ₄										
Al1	(4e)		−3469			0				^b
Al2	(4d)		−4588			0				^b
SrAl ₄										
Al1	(4e)	599	605	−3316	2865	0		0.52		^b
Al2	(4d)	1062	1079	−5483		0				^b
Al1	(4e)	564		−2410	2836	0			100	61
Al2	(4d)	1030		−6557	6167	0			0	61
BaAl ₄										
Al1	(4e)	357	360	−2185	1758	0		0.39		^b
Al2	(4d)	1136	1161	−6706		0				^b
Al1	(4e)	347		−1134	1808	0			106	61
Al2	(4d)	1128		−7904	7302	0			−54	61

^aTheoretically calculated values from DFT are given in a separate column. Impurity signals are given as *i*[]. ^bThis work.

quadrupolar coupling constant C_Q . The Al2 site has the higher point symmetry, but the EFG is more elongated (larger V_{zz}) and leads to an overall larger C_Q value. It is interesting to note that the Al1 signal shifts to lower-resonance frequencies, while the Al2 signal shifts to higher-resonance frequencies. At the same time, the Bader charges (vide infra) of the Al2 sites increase slightly, while the ones of the Al1 site decrease rather significantly. These changes in the Bader charges most likely influence the s-electron density at the respective Al nuclei and hence their behavior in the ^{27}Al NMR experiments.

Quantum Chemical Bader Charge Analysis. The Bader charges extracted from DFT calculations for the investigated $AEAl_2$ and $AEAl_4$ compounds are summarized in Table 8. Calculated values are also given for Ca_8Al_3 , which has not been characterized by NMR spectroscopy yet due to the large number of crystallographically independent aluminum sites.

The analysis shows that for the Ca atoms, the Bader charges are positive; subsequently, the Al atoms exhibit negative charges rendering these compounds as aluminides. The Bader charges on the Al atoms show a significantly broader range due to the different Al content and the different binding topology in the investigated Ca compounds (Table 8).

When reviewing the Bader charges in these different compounds, an interesting correlation emerges. The tendency to form polar intermetallics results from the electronegativity difference. However, this “ionicity” is quite different in these compounds. It can be seen very nicely that the relative Ca/Al

amounts of the two atomic species have a great influence. In Ca-poor phases, the Bader charge of Ca is higher because there is a certain “electron suction” by the large Al matrix. The Al atoms, for their part and high in number, achieve only relatively small negative charges. In Ca-rich phases in turn, the more electropositive element drives up the negative charges of the anion lattice. LT-CaAl₄ (CaGa₄ type, $C2/m$) shows Bader charges for Ca of +1.29, Al1 of −0.01, and Al2 of −0.63. The opposite behavior regarding the anion charges is Ca₈Al₃ (Ca₈In₃ type, $P\bar{1}$). Here, anionic (Bader) charges of more than −3 occur. The high concentration of the weakly electronegative element Ca forces a stronger electron transfer and thus a significantly higher ionicity. The resulting higher Madelung energy for the stabilization of the crystal structure is obviously also the reason why this compound appears dystematically in the phase diagram.

However, it is interesting to note that also within a single compound, the Bader charges may vary considerably, for example, in the $AEAl_4$ ($AE = LT-Ca, HT-Ca, Sr, \text{ and } Ba$) compounds. Here, the Al2 sites exhibit Bader charge close to 0, while the Al1 site carries the majority of the negative charge. When looking back at the coordination environments (Figure 5, right), it becomes clear that the Al2 atoms are tetrahedrally surrounded by four Al1 atoms and four AE atoms; however, four additional Al2 contacts are observed. Therefore, a higher number of aluminum atoms can be found in the coordination sphere making this situation “less polarized”, while the Al1

Table 8. Bader Charges Calculated for the Different AE_xAl_y ($AE = Ca-Ba$) Compounds Discussed Herein^a

compound	atom/site	Bader charge/ e^-
CaAl ₂	Ca (8b)	+1.19
	Al (16c)	-0.60
NP-SrAl ₂	Sr (4e)	+1.19
	Al (8h)	-0.59
HP/HT-SrAl ₂	Sr (8b)	+1.13
	Al (16c)	-0.56
HP/HT-BaAl ₂	Ba (8b)	+0.91
	Al (16c)	-0.45
LT-CaAl ₄	Ca (2a)	+1.28
	Al1 (4i)	-0.63
	Al2 (4h)	-0.01
HT-CaAl ₄	Ca (2a)	+1.29
	Al1 (4e)	-0.59
	Al2 (4d)	-0.06
SrAl ₄	Sr (2a)	+1.26
	Al1 (4e)	-0.55
	Al2 (4d)	-0.08
BaAl ₄	Ba (2a)	+1.07
	Al1 (4e)	-0.41
	Al2 (4d)	-0.13
Ca ₈ Al ₃	Ca1-Ca8	+1.05 to +1.13
	Al1-Al4	-2.88 to -3.08

^aFor Ca₈Al₃, only a range is given due to the many atoms in different sites.

atoms are surrounded by five Al atoms (1× Al1 and 4× Al2) as well as four AE atoms rendering this coordination mode “more polarized”. Within the series Ca → Sr → Ba, the charge on the Al2 site increases successively (−0.06 to −0.13), while at the same time, the charge of the Al1 site decreases (−0.59 to −0.41). Overall, the Bader charge on the alkaline-earth atoms is reduced from Ca → Ba, counterintuitive with respect to the EN. However, the AE-Al distances increase significantly; therefore, the electron transfer from AE to Al is reduced overall. Comparing the different AE-Al distances, the AE-Al1 contacts increase stronger compared to the AE-Al2 ones. Therefore, the electron density on the Al1 atoms is reduced and shifted to the Al2 atoms. This, in turn, must lead to changes in the s-electron density at the respective Al nuclei resulting in shifts of the NMR resonances. A similar behavior regarding the amount of electron transfer can be observed in the isostructural compounds of the MgCu₂-type AEAl₂ series. Here, the Bader charge on the AE atoms is reduced in this series, while at the same time, the AE-Al distances increase. The same trend can be seen, for example, in the AEPtAl₂ series (AE = Ca–Ba) where the [PtAl₂]^{δ−} polyanion distorts drastically from 3D to a 2D situation, and at the same time, the Bader charge on the AE atoms is reduced when going from CaPtAl₂ over SrPtAl₂ to BaPtAl₂.¹⁹

This argumentation can be furthermore underlined by the fact that both polymorphs of SrAl₂ have almost the same Bader charges, despite the significantly different structures (Figure 4). However, the average distances $d_{av}(Sr-Al)$ are 341 pm for the KHg₂ type compound, while the MgCu₂ type polymorph shows $d(Sr-Al) = 344$ pm.

Figure 9 finally depicts a correlation that emerges from the calculated NMR Knight shifts δ_K in comparison with the Bader charges. It is evident that δ_K evolves differently for the Al1 and Al2 sites within the AEAl₄ series (AE = Ca–Ba). As stated

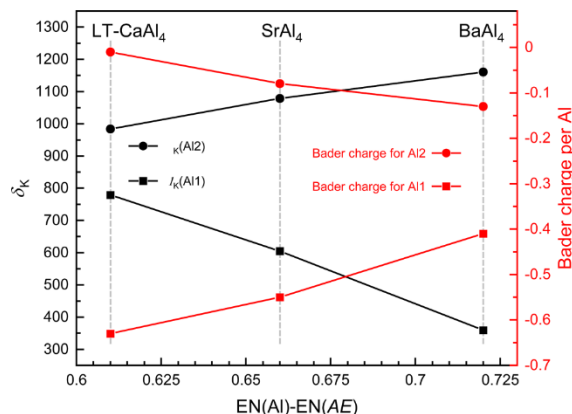


Figure 9. ²⁷Al Knight shift δ_K (black) and Bader charges (red) of the two crystallographically independent Al positions in LT-CaAl₄, SrAl₄, and BaAl₄ plotted vs the electronegativity difference ΔEN ($EN(Al) - EN(AE)$).

before, the sum of the Bader charges on the Al1 and Al2 sites decreases in the series Ca → Sr → Ba; however, the charge on the Al2 site increases while the one of the Al1 site decreases. An inverse trend is observed for the Knight shift contributions δ_K . When the absolute values of the Bader charges are compared with δ_K , no clear trend is visible. A formal reduction of the Al1 atoms (Bader charge changes from −0.06 to −0.13) causes the NMR signal to shift from 984 to 1161 ppm. At the same time, the Al2 atoms get oxidized (Bader charge changes from −0.59 to −0.41), which shift the NMR signal from $\delta_K = 779$ to 360 ppm—showing exactly the opposite trend that is also visible in Figure 9. These observations clearly show that the bonding situation and subsequently the actual electron configuration at the respective Al site cannot be effectively described when only using Bader charges.

CONCLUSIONS

CaAl₂, NP-SrAl₂, as well as CaAl₄, SrAl₄, and BaAl₄ have been successfully synthesized from the elements. HP/HT-SrAl₂ was prepared using HP/HT conditions in a multianvil cell. While in most cases X-ray pure samples could be obtained, the samples of CaAl₄ show both the high- and the low-temperature phases along with CaAl₂ and elemental Al as impurities. The formation of these impurities is hard to avoid as shown by the calculations of the formation energies per atom. ICP-MS measurements clearly show that no significant contaminations from other elements are present. ²⁷Al solid-state MAS NMR spectroscopic investigations proved that the respective compounds contain one (AEAl₂) or two (AEAl₄) crystallographically independent Al sites. The resonances for the cubic AEAl₂ (AE = Ca, Sr) compounds exhibit symmetric signals with similar shifts, while the one for orthorhombic SrAl₂ varies due to the significantly different crystal structure. For the AEAl₄ compounds, a group–subgroup relation has been established for HT- and LT-CaAl₄ and a site assignment in the ²⁷Al NMR spectra for all three compounds was possible for the two Al sites due to their different coordination environments. Finally, quantum chemical calculations of the quadrupolar coupling constants were conducted as well as Bader charge analyses, proving that these binary intermetallics can indeed be considered as aluminides.

■ ASSOCIATED CONTENT**SI Supporting Information**

The Supporting Information is available free of charge at <https://pubs.acs.org/doi/10.1021/acs.inorgchem.2c04391>.

Additional powder X-ray data, individual ^{27}Al NMR spectra, and additional quantum chemical data (PDF)

■ AUTHOR INFORMATION**Corresponding Author**

Oliver Janka – *Anorganische Festkörperchemie, Universität des Saarlandes, D-66123 Saarbrücken, Germany*; orcid.org/0000-0002-9480-3888; Phone: +49(0)681-302-70665; Email: oliver.janka@uni-saarland.de

Authors

Stefan Engel – *Anorganische Festkörperchemie, Universität des Saarlandes, D-66123 Saarbrücken, Germany*; orcid.org/0000-0002-6813-8490

Elias C. J. Giebelmann – *Anorganische Festkörperchemie, Universität des Saarlandes, D-66123 Saarbrücken, Germany*; orcid.org/0000-0001-6137-9729

Lukas E. Schank – *Anorganische Festkörperchemie, Universität des Saarlandes, D-66123 Saarbrücken, Germany*

Gunter Heymann – *Institut für Allgemeine, Anorganische und Theoretische Chemie, Universität Innsbruck, A-6020 Innsbruck, Austria*; orcid.org/0000-0001-8500-9159

Kristina Brix – *Anorganische Festkörperchemie, Universität des Saarlandes, D-66123 Saarbrücken, Germany*

Ralf Kautenburger – *Anorganische Festkörperchemie, Universität des Saarlandes, D-66123 Saarbrücken, Germany*

Horst Philipp Beck – *Anorganische Festkörperchemie, Universität des Saarlandes, D-66123 Saarbrücken, Germany*; orcid.org/0000-0002-9986-1454

Complete contact information is available at:

<https://pubs.acs.org/doi/10.1021/acs.inorgchem.2c04391>

Author Contributions

All authors have accepted responsibility for the entire content of this submitted manuscript and approved the submission.

Notes

The authors declare no competing financial interest.

■ ACKNOWLEDGMENTS

Instrumentation and technical assistance for this work were provided by the Service Center X-ray Diffraction, with financial support from Saarland University and German Science Foundation (project number INST 256/349-1) and by the Service Center NMR with financial support from Saarland University and German Research Foundation DFG. Funding has been provided by the Deutsche Forschungsgemeinschaft DFG (JA 1891-10-1).

■ REFERENCES

(1) den Ouden, A.; Wessel, S.; Krooshoop, E.; ten Kate, H. Application of Nb_3Sn superconductors in high-field accelerator magnets. *IEEE Trans. Appl. Supercond.* **1997**, *7*, 733–738.
(2) Xu, X. A review and prospects for Nb_3Sn superconductor development. *Supercond. Sci. Technol.* **2017**, *30*, 093001.
(3) Peters, M.; Hempfenmacher, J.; Kumpfert, J.; Leyens, C. Structure and Properties of Titanium and Titanium Alloys. *Titanium and Titanium Alloys*; Wiley-VCH Verlag GmbH: Weinheim, 2003; pp 1–36.

(4) Sauthoff, G. Intermetallics. *Ullmann's Encyclopedia of Industrial Chemistry*; Wiley-VCH Verlag GmbH: Weinheim, 2012.

(5) Kilaas, R.; Radmilovic, V.; Dahmen, U. Structure refinement of S-phase precipitates in Al-Cu-Mg alloys by quantitative HRTEM. *Mater. Res. Soc. Symp. Proc.* **1999**, *589*, 273–278.

(6) Laves, F.; Witte, H. Untersuchungen im System Mg-Cu-Al, speziell auf dem Schnitt $\text{MgCu}_2\text{-MgAl}_2$. *Metallwirtsch* **1936**, *15*, 15–22.

(7) Mondolfo, L. F. Al-Cu-Mg Aluminum-Copper-Magnesium system. In *Aluminum Alloys: Structure and Properties*; Butterworths: London, Boston, 1976, pp 497–505.

(8) Cuisiat, F.; Duval, P.; Graf, R. Etude des premiers stades de décomposition d'un alliage Al-Cu-Mg. *Scripta Metall.* **1984**, *18*, 1051–1056.

(9) Yan, J.; Chunzhi, L.; Minggao, Y. On the crystal structure of S' phase in Al-Cu-Mg alloy. *J. Mater. Sci. Lett.* **1990**, *9*, 421–424.

(10) Heying, B.; Hoffmann, R.-D.; Pöttgen, R. Structure Refinement of the S-Phase Precipitate MgCuAl_2 . *Z. Naturforsch., B: J. Chem. Sci.* **2005**, *60*, 491–494.

(11) Friauf, J. B. The crystal structures of two intermetallic compounds. *J. Am. Chem. Soc.* **1927**, *49*, 3107–3114.

(12) Andersen, S. J.; Marioara, C. D.; Friis, J.; Wenner, S.; Holmestad, R. Precipitates in aluminium alloys. *Adv. Phys.: X* **2018**, *3*, 1479984.

(13) Meetsma, A.; De Boer, J. L.; Van Smaalen, S. Refinement of the crystal structure of tetragonal Al_3Cu . *J. Solid State Chem.* **1989**, *83*, 370–372.

(14) Emsley, J. *The Elements*; Clarendon Press, Oxford University Press: Oxford, New York, 1998.

(15) Benndorf, C.; Eckert, H.; Janka, O. Structural Characterization of Intermetallic Compounds by ^{27}Al Solid State NMR Spectroscopy. *Acc. Chem. Res.* **2017**, *50*, 1459–1467.

(16) Stegemann, F.; Benndorf, C.; Zhang, Y.; Bartsch, M.; Zacharias, H.; Fokwa, B. P. T.; Eckert, H.; Janka, O. Network Formation by Condensed Tetrahedral $[\text{Au}_3\text{Al}]$ Units in $\text{Na}_2\text{Au}_3\text{Al}$: Crystal and Electronic Structure, Spectroscopic Investigations, and Physical Properties of an Ordered Ternary Auride. *Inorg. Chem.* **2017**, *56*, 1919–1931.

(17) Benndorf, C.; Stegemann, F.; Seidel, S.; Schubert, L.; Bartsch, M.; Zacharias, H.; Mausolf, B.; Haarmann, F.; Eckert, H.; Pöttgen, R.; Janka, O. Equiatomic AEAuX (AE = Ca-Ba, X = Al-In) Intermetallics: A Systematic Study of their Electronic Structure and Spectroscopic Properties. *Chem.—Eur. J.* **2017**, *23*, 4187–4196.

(18) Stegemann, F.; Benndorf, C.; Bartsch, T.; Touzani, R. S.; Bartsch, M.; Zacharias, H.; Fokwa, B. P. T.; Eckert, H.; Janka, O. $\text{Ba}_3\text{Pt}_4\text{Al}_4$ - Structure, Properties, and Theoretical and NMR Spectroscopic Investigations of a Complex Platinide Featuring Heterocubane $[\text{Pt}_4\text{Al}_4]$ Units. *Inorg. Chem.* **2015**, *54*, 10785–10793.

(19) Stegemann, F.; Block, T.; Klenner, S.; Zhang, Y.; Fokwa, B. P. T.; Timmer, A.; Mönig, H.; Doerenkamp, C.; Eckert, H.; Janka, O. From 3D to 2D: Structural, Spectroscopic and Theoretical Investigations of the Dimensionality Reduction in the $[\text{PtAl}_2]^{6-}$ Polyanions of the Isotypic MPtAl_2 Series (M = Ca–Ba, Eu). *Chem.—Eur. J.* **2019**, *25*, 10735–10747.

(20) Nowotny, H.; Wormnes, E.; Mohrheim, A. Untersuchungen in den Systemen Aluminium-Kalzium, Magnesium-Kalzium und Magnesium-Zirkon. *Z. Metallkd.* **1940**, *32*, 39.

(21) Nagorsen, G.; Posch, H.; Schäfer, H.; Weiss, A. Die Kristallstruktur von SrAl_2 . *Z. Naturforsch., B: Anorg. Chem., Org. Chem., Biochem., Biophys., Biol.* **1969**, *24*, 1191.

(22) Iandelli, A. MX_2 -Verbindungen der Erdalkali- und Seltenen Erdmetalle mit Gallium, Indium und Thallium. *Z. Anorg. Allg. Chem.* **1964**, *330*, 221–232.

(23) Fornasini, M. L.; Bruzzone, G. The crystal structure of the Ba_3Al_3 phase. *J. Less Common. Met.* **1975**, *40*, 335–340.

(24) Cordier, G.; Czech, E.; Schäfer, H. Über eine Hochdruckmodifikation des SrAl_2 / On a High Pressure Modification of SrAl_2 . *Z. Naturforsch., B: Anorg. Chem., Org. Chem.* **1982**, *37*, 1442–1445.

- (25) Cordier, G.; Czech, E.; Schäfer, H. Zur Kenntnis der Hochdruckphase BaAl_2 / On BaAl_2 , a High Pressure Phase. *Z. Naturforsch., B: Anorg. Chem., Org. Chem.* **1984**, *39*, 421–423.
- (26) Kal, S.; Stoyanov, E.; Belieres, J.-P.; Groy, T. L.; Norrestam, R.; Häussermann, U. High-pressure modifications of CaZn_2 , SrZn_2 , SrAl_2 , and BaAl_2 : Implications for Laves phase structural trends. *J. Solid State Chem.* **2008**, *181*, 3016–3023.
- (27) Pöttgen, R.; Gulden, T.; Simon, A. Miniaturisierte Lichtbogenapparat für den Laborbedarf. *GIT Labor-Fachz.* **1999**, *43*, 133–136.
- (28) Nowotny, H.; Wesenberg, H. Untersuchungen im System Aluminium-Strontium. *Z. Metallkd.* **1939**, *31*, 363–364.
- (29) Andress, K. R.; Alberti, E. Röntgenographische Untersuchung der Legierungsreihe Aluminium-Barium. *Z. Metallkd.* **1935**, *27*, 126.
- (30) Miller, G. J.; Li, F.; Franzen, H. F. The structural phase transition in calcium-aluminum compound (CaAl_4): a concerted application of Landau theory and energy band theory. *J. Am. Chem. Soc.* **1993**, *115*, 3739–3745.
- (31) Bruker AXS Inc. *Topas*. Version 5: Karlsruhe (Germany), 2014.
- (32) Villars, P.; Cenzual, K. *Pearson's Crystal Data: Crystal Structure Database for Inorganic Compounds*. Release 2022/23; ASM International: Materials Park, Ohio (USA), 2023.
- (33) Rubie, D. C. Characterising the sample environment in multianvil high-pressure experiments. *Ph. Trans.* **2006**, *68*, 431–451.
- (34) Walker, D. Lubrication, gasketing, and precision in multianvil experiments. *Am. Mineral.* **1991**, *76*, 1092–1100.
- (35) Huppertz, H. Multianvil high-pressure / high-temperature synthesis in solid state chemistry. *Z. Kristallogr.* **2004**, *219*, 330–338.
- (36) Bruker Corp. *Topspin*. (Version 2.1): Karlsruhe, 2008.
- (37) Massiot, D.; Fayon, F.; Capron, M.; King, I.; Le Calvé, S.; Alonso, B.; Durand, J.-O.; Bujoli, B.; Gan, Z.; Hoatson, G. Modelling one- and two-dimensional solid-state NMR spectra. *Magn. Reson. Chem.* **2002**, *40*, 70–76.
- (38) Blöchl, P. E. Projector augmented-wave method. *Phys. Rev. B: Condens. Matter Mater. Phys.* **1994**, *50*, 17953–17979.
- (39) Kresse, G.; Joubert, D. From ultrasoft pseudopotentials to the projector augmented-wave method. *Phys. Rev. B: Condens. Matter Mater. Phys.* **1999**, *59*, 1758–1775.
- (40) Kresse, G.; Furthmüller, J. Efficient iterative schemes for ab initio total-energy calculations using a plane-wave basis set. *Phys. Rev. B: Condens. Matter Mater. Phys.* **1996**, *54*, 11169–11186.
- (41) Kresse, G.; Furthmüller, J. Efficiency of ab-initio total energy calculations for metals and semiconductors using a plane-wave basis set. *Comput. Mater. Sci.* **1996**, *6*, 15–50.
- (42) Perdew, J. P.; Burke, K.; Ernzerhof, M. Generalized Gradient Approximation Made Simple. *Phys. Rev. Lett.* **1996**, *77*, 3865–3868.
- (43) Sanville, E.; Kenny, S. D.; Smith, R.; Henkelman, G. Improved grid-based algorithm for Bader charge allocation. *J. Comput. Chem.* **2007**, *28*, 899–908.
- (44) Henkelman, G.; Arnaldsson, A.; Jónsson, H. A fast and robust algorithm for Bader decomposition of charge density. *Comput. Mater. Sci.* **2006**, *36*, 354–360.
- (45) Tang, W.; Sanville, E.; Henkelman, G. A grid-based Bader analysis algorithm without lattice bias. *J. Phys.: Condens. Matter* **2009**, *21*, 084204.
- (46) Bruzzone, G.; Merlo, F. The strontium-aluminium and barium-aluminium systems. *J. Less Common. Met.* **1975**, *39*, 1–6.
- (47) Das, D. K.; Pitman, D. T. Preparation and diffraction data of Ba-Al alloys. *JOM* **1957**, *9*, 1175.
- (48) Kußmann, D.; Pöttgen, R.; Rodewald, U. C.; Rosenhahn, C.; Mosel, B. D.; Kotzyba, G.; Künnen, B. Structure and Properties of the Stannide $\text{Eu}_2\text{Au}_2\text{Sn}_3$, and its Relationship with the Family of BaAl_4 -related Structures. *Z. Naturforsch., B: J. Chem. Sci.* **1999**, *54*, 1155–1164.
- (49) Kneidinger, F.; Salamakha, L.; Bauer, E.; Zeiringer, I.; Rogl, P.; Blaas-Schneider, C.; Reith, D.; Podloucky, R. Superconductivity in noncentrosymmetric BaAl_4 derived structures. *Phys. Rev. B: Condens. Matter Mater. Phys.* **2014**, *90*, 024504.
- (50) Bärnighausen, H. Group-Subgroup Relations between Space Groups: A Useful Tool in Crystal Chemistry. *MATCH, Commun. Math. Comput. Chem.* **1980**, *9*, 139–175.
- (51) Bärnighausen, H.; Müller, U. *Symmetriebeziehungen zwischen den Raumgruppen als Hilfsmittel zur straffen Darstellung von Strukturzusammenhängen in der Kristallchemie*; Universität Karlsruhe und Universität-Gh Kassel: Germany, 1996.
- (52) Müller, U. Kristallographische Gruppe-Untergruppe-Beziehungen und ihre Anwendung in der Kristallchemie. *Z. Anorg. Allg. Chem.* **2004**, *630*, 1519–1537.
- (53) Müller, U. *Symmetry Relationships between Crystal Structures*; Oxford University Press, 2013.
- (54) Hellmann, A.; Löhken, A.; Wurth, A.; Mewis, A. Neue Arsenide mit ThCr_2Si_2 - oder einer damit verwandten Struktur: Die Verbindungen ARh_2As_2 (A: Eu, Sr, Ba) und BaZn_2As_2 / New Arsenides with ThCr_2Si_2 -type or Related Structures: The Compounds ARh_2As_2 (A: Eu, Sr, Ba) and BaZn_2As_2 . *Z. Naturforsch., B: J. Chem. Sci.* **2007**, *62*, 155–161.
- (55) Kevorkov, D.; Schmid-Fetzer, R. The Al–Ca System, Part 1: Experimental Investigation of Phase Equilibria and Crystal Structures. *Int. J. Mater. Res.* **2002**, *92*, 946–952.
- (56) Islam, F.; Medraj, M. Thermodynamic Modelling of the Mg–Al–Ca System. *Can. Metall. Q.* **2005**, *44*, 523–536.
- (57) Okamoto, H. Al–Sr (Aluminum–Strontium). *J. Phase Equilibria Diffus.* **2005**, *26*, 394.
- (58) Srikanth, S.; Jacob, K. T. Thermodynamics of aluminum-barium alloys. *Metall. Trans. B* **1991**, *22*, 607–616.
- (59) Azza, H.; Selhaoui, N.; Achgar, K. Thermodynamic description of the aluminum-barium phase diagram. *Eur. Phys. J. Spec. Top.* **2017**, *226*, 1143–1150.
- (60) Benndorf, C.; Eckert, H.; Janka, O. Ternary rare-earth aluminium intermetallics $\text{RE}_{10}\text{TAl}_3$ (RE = Y, Ho, Tm, Lu; T = Fe, Co, Ni, Ru, Rh, Pd, Os, Ir, Pt) with an ordered anti- Co_2Al_3 structure. *Dalton Trans.* **2017**, *46*, 1083–1092.
- (61) Pecher, O.; Mausolf, B.; Peters, V.; Lamberts, K.; Korthaus, A.; Haarmann, F. Unravelling Local Atomic Order of the Anionic Sublattice in $\text{M}(\text{Al}_{1-x}\text{Ga}_x)_4$ with M=Sr and Ba by Using NMR Spectroscopy and Quantum Mechanical Modelling. *Chem.—Eur. J.* **2016**, *22*, 17833–17842.
- (62) Barnes, R. G.; Jones, W. H.; Graham, T. P. Large Anisotropic Knight Shifts in Intermetallic Compounds. *Phys. Rev. Lett.* **1961**, *6*, 221–223.

III. Investigations of New Ternary Intermetallic Compounds $M_xAl_zT_y$ containing Divalent Species with $M = Ca \& Sr$

1. Introduction / Motivation

The Gibbs triangles, shown in the beginning of the thesis (**Figs. 1.1** and **1.2**), gave an overview of all existing phases in the ternary systems and showed that the corresponding systems are not particularly well investigated, for example there are no compounds reported in the ternary systems Sr–Al–Rh and Ba–Al–Rh, also the most phases which were found reside in the Al rich corner, with only a few exceptions like the AE_2AlT_2 phases ($AE = Ca, Sr, T = Pd, Pt$). The **Figure 3.27** gives an overview of all the existing phases $AE_xAl_zT_y$ in regard to their compositions, as they were cited above in the **Chapter 1**.

$T \backslash AE$	Co	Rh	Ir	Ni	Pd	Pt
Ca	1-8-2, 1-9-2	3-12-4	2-9-3	1-9-1, 1-8-2, 1-0.8-0.2, 8-2.73-0.27	2-10-6, 1-3-2, 1-1-1, 2-1-2	1-1-1, 1-1-2, 2-2-1, 2-9-3, 2-16-5
Sr	1-9-2	-	2-9-3	1-9-2	2-5-4, 2-1-2	1-2-1, 1-2-3, 1-2-2, 2-8-3
Ba	1-9-2	-	-	1-9-2	1-8.5-4.5	1-2-1, 3-4-4, 6-53-22

Figure 3.27: Overview of all literature known ternary phase in the system $AE-Al-T$ with $AE = Ca, Sr, Ba$ and $T = Co-Pt$.

Whenever the literature investigated the bonding situation, the structures were described by the formation of a polyanionic network of the Al and T atoms, in which the alkaline earth element forms a cationic species and resides in cavities of said network. These building blocks were supported, due to the in most cases strongest bonding interaction determined from the ICOHP values as well the low positive charge of the Al atoms and the similar shape of the Al and T states in the DOS, indicating covalent interactions. The AE element on the other hand had weakly bonding interactions paired with a high Bader charge. This led to the bonding interaction being dominantly ionic with the polyanion. The electron transfer can additionally be directly investigated by XPS spectroscopy, showing the shift of the binding energy of the electrons to higher or lower values in the Al 2s spectra, indicating additional or less electron density at the Al atoms. The electron transfer can be investigated by ^{27}Al NMR spectroscopy, in which the chemical shift of the Al signal, is dependent on the electronic shielding.

Due to these insight of the similar bonding in these different compounds, the DFG project with the project number: 441210509 and title: “Studies concerning the electronic structure and the electron transfer in electron poor intermetallics” was granted to investigate the electronic transfer happening in such polar intermetallic phases.

The electron transfer of ternary compounds is more complex than in binary compounds, in which the less electronegative element provides the electrons to the more electronegative element. Exemplary, in CaAl_2 the calcium is less electronegative with an EN value of 1.00 eV (Pauling scale), providing the electrons, and aluminum exhibits an EN value of 1.61 eV (Pauling scale),⁴ receiving the electrons. The other case is, when a late transition metal e.g. $T = \text{Co-Pt}$ and Al react, the transition metal has a higher electronegativity than the Al, leading to the electron transfer from Al to the T element. But what is happening in ternary compounds, which contain an alkaline earth element, aluminum and a late transitions element (Co-Pt)? In these compounds Al has an electronegativity between the AE and T elements. There are a few possible scenarios: (I) the AE and Al give their valence electrons to the transition metal, (II) only the AE atoms provide the valence electrons to both Al and T without any interaction of Al and T , or (III) the AE atoms provides the valence electrons to both Al and T , with interact of these two elements each other (sharing the electrons transferred from the AE element). The latter leads to forming a polyanionic network with covalent bonding interactions inside the polyanion. The literature as well as the results of this thesis indicate that the third case is happening, if the aluminum and transition metal atoms are within range of being able to interact with each other, they will form a polyanion in form of a network or slabs.

The investigations in the ternary systems with an alkaline earth element, aluminum alongside a late transition metal alone led to five publications on “ SrAl_5Pt_3 and $\text{Sr}_2\text{Al}_{16}\text{Pt}_9$ – two new strontium aluminum platinides” (*Z. Naturforsch. B.* **2022**, 77b, 367),¹⁷⁵ “Nominal CaAl_2Pt_2 and $\text{Ca}_2\text{Al}_3\text{Pt}$ – two new intermetallic compounds in the ternary system Ca–Al–Pt” (*Z. Anorg. Allg. Chem.* **2024**, 650, e202400094),¹⁹⁴ “Synthesis, Magnetic and NMR spectroscopic properties of the $M\text{Al}_5\text{Pt}_3$ series ($M = \text{Ca, Y, La-Nd, Sm-Er}$)” (*Dalton Trans.* **2024**, 53, 12176),¹⁷² “New rare earth representatives adopting the $\text{Ce}_2\text{Al}_{16}\text{Pt}_9$ type structure” (*Z. Naturforsch.* **2024**, 79b, 595)¹⁷⁴ and “ SrAl_8Rh_2 – the first phase in the Sr/Al/Rh system and representative of the CeAl_8Fe_2 type structure” (*Z. Kristallogr.* **2024**, 240, 1-11)¹⁹⁵ of which the first Sr–Al–Rh compound, SrAl_8Rh_2 , was synthesized and investigated via single crystal X-ray diffraction as well as electrical resistivity measurements on single crystals on top of the bonding analysis via the LOBSTER program package.

This chapter will start with the two Sr containing compounds SrAl_5Pt_3 ¹⁷⁵ and $\text{Sr}_2\text{Al}_{16}\text{Pt}_9$,¹⁷⁵ which were found in the same sample of the nominal composition $\text{Sr}_4\text{Al}_{13}\text{Pt}_9$. Single crystal studies revealed that SrAl_5Pt_3 and $\text{Sr}_2\text{Al}_{16}\text{Pt}_9$ crystallize isotypic to the literature known cerium compounds in the isopointal YNi_5Si_3 type structure (*Pnma*)¹⁹⁶ and isotypic $\text{Ce}_2\text{Al}_{16}\text{Pt}_9$ type structure (*Immm*).¹⁷³ No phase pure samples could be obtained, due to the simultaneous formation of both new phases. Quantum chemical calculation showed strong Al–Pt interactions as well as weak Pt–Pt and Al–Al interactions. Due to the report on EuAl_5Pt_3 , subsequent investigations of the existence range of the $M\text{Al}_5\text{Pt}_3$ and $M_2\text{Al}_{16}\text{Pt}_9$ were sparked, resulting in the synthesis of the calcium and europium variant of both compositions. The obtained trivalent compounds adopting the same structure types will be discussed in **Chapter 3.III**. The Ca and Eu containing samples could not be synthesized X-ray pure, since binary Al_3Pt_2 or the corresponding other phase were present (for the synthesis of the $M\text{Al}_5\text{Pt}_3$ $M_2\text{Al}_{16}\text{Pt}_9$ appeared as side phase, whereas attempts to synthesize $M_2\text{Al}_{16}\text{Pt}_9$ resulted in $M\text{Al}_5\text{Pt}_3$ as side phase). Following the investigations on these series, the results in the system Ca–Al–Pt,¹⁹⁴ where the two new structures of CaAl_2Pt_2 and $\text{Ca}_2\text{Al}_3\text{Pt}$ crystallizing in the CaBe_2Ge_2 (*P4/nmm*) and $\text{Mg}_2\text{Cu}_3\text{Si}$ type structure (*P6₃/mmc*) will be discussed. Both phases exhibit Al/Pt mixing, resulting in refined compositions of $\text{CaAl}_{2.24(1)}\text{Pt}_{1.76(1)}$ and $\text{Ca}_2\text{Al}_{3.09(1)}\text{Pt}_{0.91(1)}$. Additionally, the literature known phase Ca_2AlPt_2 (Ca_2SiIr_2 type, *C2/c*) was found in the same sample, which does not exhibit mixed occupied atomic sites. No X-ray pure samples of the newly found compounds could be obtained. The bonding analysis shows that the charge transfer happens from the Ca atoms to the Pt atoms, which exhibit covalent bonding to the Al atoms forming like the $M\text{Al}_5\text{Pt}_3$ and $M_2\text{Al}_{16}\text{Pt}_9$ series polyanionic networks. Subsequent to the newly found compounds in the Ca–Al–Pt system, an extensive bonding analysis with the LOBSTER program package was started by calculating the Löwdin charges, ICOBI values and formal oxidation states of many literature known binary and all ternary compounds. The results show similarities to the ICOHP and Bader charge calculations performed on the SrAl_5Pt_3 and $\text{Sr}_2\text{Al}_{16}\text{Pt}_9$ compounds, in which the Ca atoms always have a positive charge, due to the transfer of the electrons to the polyanionic network of Al and Pt, but with the calculation of the Löwdin charges now, the Pt exhibits a positive charge and Al a negative charge, which is in contrast to the Bader charges and to the electronegativity. Therefore, the Dronskowski group in Aachen extended the LOBSTER code and introduced a feature that allows the calculation of formal oxidation states. However, this development was not final upon finishing this thesis. The ICOBI values also show significant covalent bonding interactions between the Al–Al and Al–Pt atoms, forming the postulated polyanionic network.

In the last part of this chapter the single compound SrAl_8Rh_2 will be discussed. It crystallizes in the CeAl_8Fe_2 type structure (space group $Pbam$) in large rod-shaped crystals. The electrical resistivity shows metallic behavior down to a minimum around 7.5 K, which rises below the minimum. Also, below 0.6 K a possible onset of a superconductivity transition can be observed. The bonding analysis showed strong interactions between the Al and Rh atoms and nearly no interactions of the Sr atoms with either the Al or Rh atoms, suggesting the formation of an $[\text{Al}_8\text{Rh}_2]^{\delta-}$ polyanionic network.

2. New compounds in the system Ca–Al–Pt and Sr–Al–T with $T = \text{Rh, Pt}$; MA_5Pt_3 , $\text{M}_2\text{Al}_{16}\text{Pt}_9$, CaAl_2Pt_2 , $\text{Ca}_2\text{Al}_3\text{Pt}$, SrRh_2Al_8

During this thesis, five papers were published containing the results on the newly found compounds in the $AE\text{--Al--}T$ system. The title of these papers are “ SrAl_5Pt_3 and $\text{Sr}_2\text{Al}_{16}\text{Pt}_9$ – two new strontium aluminum platinides” (*Z. Naturforsch. B.* **2022**, 77b, 367), “Nominal CaAl_2Pt_2 and $\text{Ca}_2\text{Al}_3\text{Pt}$ – two new intermetallic compounds in the ternary system Ca–Al–Pt” (*Z. Anorg. Allg. Chem.* **2024**, 650, e202400094), “Synthesis, Magnetic and NMR spectroscopic properties of the MA_5Pt_3 series ($M = \text{Ca, Y, La-Nd, Sm-Er}$)” (*Dalton Trans.* **2024**, 53, 12176), “New rare earth representatives adopting the $\text{Ce}_2\text{Al}_{16}\text{Pt}_9$ type structure” (*Z. Naturforsch.* **2024**, 79b, 595) and “ SrAl_8Rh_2 – the first phase in the Sr–Al–Rh system and representative of the CeAl_8Fe_2 type structure” (*Z. Kristallogr.* **2025**, 240, 1-11) as well as the publication in cooperation with the Dronskowski group in Aachen (P. C. Müller, L. Reitz, R. Dronskowski) entitled “Differences and similarities in the bonding situation of intermetallic phases in the Ca–Al–Pt system” (Manuscript). The results of these publications will be summarized in this chapter.

Collaborations to disclose: J. Bönnighausen (SrAl_5Pt_3), Dr. F. Stegemann (sample with the nominal composition of $\text{Sr}_4\text{Al}_{13}\text{Pt}_9$ from which the SrAl_5Pt_3 and $\text{Sr}_2\text{Al}_{16}\text{Pt}_9$ single crystals were extracted), Dr. M. K. Reimann (SrRh_2Al_8) provided bulk samples, E. C. J. Gießelmann performed the analysis of the YA_5Pt_3 via ^{27}Al NMR. Dr. F. Müller performed the XPS measurements, L. Schumacher made the magnetic property measurements and the eSEM measurements were done by Dr. M. Koch. The quantum chemical calculations were conducted by Dr. R. S. Touzani (SrAl_5Pt_3 & $\text{Sr}_2\text{Al}_{16}\text{Pt}_9$), Prof. Dr. Y. Zhang (YA_5Pt_3) and PD Dr. O. Janka (Ca–Al–Pt and SrAl_8Rh_2) along with Dr. P. C. Müller, L. Reitz and Prof. Dr. R. Dronskowski (LOBSTER calculations). PD Dr. O. Janka supervised the work, and all the aforementioned people contributed to the manuscript with their respective expertise.

Many phases in the $AE\text{--Al--}T$ system are singular, meaning that only one of the alkaline earth metals exist with the corresponding compound, e.g. CaAl_3Pd_2 (YA_3Ni_2 type, $P6/mmm$),⁷⁰ $\text{Sr}_2\text{Al}_5\text{Pd}_4$ (own type, $Pnma$),⁷² SrAl_8Pt_3 ($\text{Eu}_2\text{Ni}_8\text{Si}_3$ type, $P4_2/nmc$)⁷⁴ or $\text{Ba}_3\text{Al}_4\text{Pt}_4$ (own type, $Cmcm$)⁷⁷. To expand the compositional manifold in the $AE\text{--Al--}T$ systems the compositions of the singular phases were taken as starting points and attempts to synthesize the isotypic structures with different AE metals were pursued. This led to the attempt of creating $\text{Ca}_3\text{Al}_4\text{Pt}_4$ in analogy to $\text{Ba}_3\text{Al}_4\text{Pt}_4$ to the formation of the new compounds CaAl_2Pt_2 and $\text{Ca}_2\text{Al}_3\text{Pt}$

alongside the literature known phase Ca_2AlPt_2 . In analogy to changing the *AE* element, also the triel element can be changed from In or Ga to Al, which was the case in the attempt to synthesize $\text{Sr}_4\text{Al}_{13}\text{Pt}_9$ as an isotypic compound to the existing $\text{Sr}_4\text{In}_{13}\text{Pt}_9$ ($\text{Ho}_4\text{Ge}_9\text{Ir}_{13}$ type, *Pmmn*).¹⁹⁷ The reaction resulted in a mixture of different products of which two new Sr–Al–Pt phases emerged: SrAl_5Pt_3 (YNi_5Si_3 type, *Pnma*) and $\text{Sr}_2\text{Al}_{16}\text{Pt}_9$ ($\text{Ce}_2\text{Al}_{16}\text{Pt}_9$ type, *Immm*) (Single crystals shown in **Fig. 3.28**). Whereas SrAl_5Pt_3 forms needle shaped crystals, $\text{Sr}_2\text{Al}_{16}\text{Pt}_9$ on the other hand exhibits a block shaped habitus. Due to the two new Sr phases found and the reported existence of the EuAl_5Pt_3 (YNi_5Si_3 type, *Pnma*) compound in 2022 by Onuki et al.⁹¹ as well as the literature known cerium compounds CeAl_5Pt_3 (YNi_5Si_3 type, *Pnma*)¹⁹⁶ and $\text{Ce}_2\text{Al}_{16}\text{Pt}_9$ (own type, *Immm*)¹⁷³ an investigation was conducted how far the series of the two structures types reach and whether other *AE* containing compounds exist. The investigation resulted in the successful synthesis of CaAl_5Pt_3 , $\text{Ca}_2\text{Al}_{16}\text{Pt}_9$ and $\text{Eu}_2\text{Al}_{16}\text{Pt}_9$ with respect to the divalent phases, however no phase formation with barium was observed. The isostructural compounds containing trivalent rare earth elements will be discussed in a later chapter (**Chapter 3.a.III**). The Ca and Eu phases crystallize like the Sr compounds in the corresponding YNi_5Si_3 ¹⁹⁸ or $\text{Ce}_2\text{Al}_{16}\text{Pt}_9$ type structure. Bulk samples of the Sr and Eu compounds with a slight excess of the *AE/RE* element were prepared due to the evaporation of these elements in the arc furnace. The melting beads were crushed and analyzed via powder X-ray diffraction experiments. The Rietveld refinements are shown in **Figure 3.29** and **3.30** for SrAl_5Pt_3 , EuAl_5Pt_3 and $\text{Eu}_2\text{Al}_{16}\text{Pt}_9$ respectively. The Rietveld refinement of SrAl_5Pt_3 resulted in a mixture of the targeted compound and the $\text{Sr}_2\text{Al}_{16}\text{Pt}_9$, $\text{Sr}_2\text{Al}_8\text{Pt}_3$ and Al_3Pt_2 as side phases. The phase composition from the Rietveld refinement are summarized in **Table 3.1** for SrAl_5Pt_3 , EuAl_5Pt_3 and $\text{Eu}_2\text{Al}_{16}\text{Pt}_9$. An overall composition is summarized in **Table 3.2**.

Table 3.1: Phase composition of the SrAl_5Pt_3 , EuAl_5Pt_3 and $\text{Eu}_2\text{Al}_{16}\text{Pt}_9$ samples from the Rietveld refinement, alongside their structure type, space group and refined lattice parameters.

Sample	Phase (wt.-%)	Structure type (SG)	Lattice parameters (pm)
SrAl_5Pt_3	SrAl_5Pt_3 (46)	YNi_5Si_3 (<i>Pnma</i>)	$a = 2067.35(8)$, $b = 414.28(2)$, $c = 739.99(3)$
	$\text{Sr}_2\text{Al}_{16}\text{Pt}_9$ (47)	$\text{Ce}_2\text{Al}_{16}\text{Pt}_9$ (<i>Immm</i>)	$a = 417.03(2)$, $b = 1194.22(4)$, $c = 1833.16(7)$
	$\text{Sr}_2\text{Al}_8\text{Pt}_3$ ⁷⁴ (6)	$\text{Eu}_2\text{Ni}_8\text{Si}_3$	$a = 1085.0(2)$, $c = 823.3(2)$
	Al_3Pt_2 ¹⁹⁹ (1)	(<i>P4₂/nmc</i>)	$a = 414.93(7)$, $c = 502.61(9)$
		Al_3Ni_2 (<i>P$\bar{3}$m1</i>)	
EuAl_5Pt_3	EuAl_5Pt_3 ⁹¹ (89)	YNi_5Si_3 (<i>Pnma</i>)	$a = 2059.88(3)$, $b = 413.21(7)$, $c = 736.36(1)$
	EuAl_2Pt ⁶³ (2)	MgAl_2Cu (<i>Cmcm</i>)	$a = 420.5(2)$, $b = 1112.2(3)$, $c = 726.2(2)$
	Al_3Pt_2 ¹⁹⁹ (1)	Al_3Ni_2 (<i>P$\bar{3}$m1</i>)	$a = 421.8(1)$, $c = 516.6(1)$
	AlPt ²⁰⁰ (5)	FeSi (<i>P2₁3</i>)	$a = 486.00(4)$
	AlPt_2 ²⁰¹ (3)	GaPt_2 (<i>Pmma</i>)	$a = 1626.8(7)$, $b = 383.0(1)$, $c = 533.0(2)$

Eu ₂ Al ₁₆ Pt ₉	Eu ₂ Al ₁₆ Pt ₉ (86)	Ce ₂ Al ₁₆ Pt ₉ (<i>Immm</i>)	$a = 416.69(6), b = 1190.08(1), c = 1827.64(2)$
	EuAl ₅ Pt ₃ ⁹¹ (3)	YNi ₅ Si ₃ (<i>Pnma</i>)	$a = 2044.6(4), b = 417.3(1), c = 730.3(2)$
	Al ₃ Pt ₂ ¹⁹⁹ (10)	Al ₃ Ni ₂ (<i>P$\bar{3}$m1</i>)	$a = 420.74(1), c = 517.34(3)$
	AlPt ²⁰² (1)	AlPd (<i>R$\bar{3}$</i>)	$a = 1597.2(1), c = 518.62(8)$

The structures are already discussed in **Chapter 3.1** in **Figure 3.7** to **Figure 3.10**, showing five independent Al positions for the MA_5Pt_3 and $M_2Al_{16}Pt_9$ phases. With the number of side phases and thus large number of additional different Al positions in the powdered samples, no ²⁷Al NMR measurements could be conducted on these compounds. The lattice parameters of the divalent MA_5Pt_3 and $M_2Al_{16}Pt_9$ compounds are summarized in **Table 3.3**, showing similar unit cell parameters for the Sr compared to the Eu compounds, suggesting that the europium in this structure has a divalent nature. The lattice parameters of the calcium phases are, as expected, smaller when compared to the strontium containing ones due to the size of the alkaline earth metals ($r_{\text{ionic}}(\text{Ca}^{2+}) = 112$, $r_{\text{ionic}}(\text{Sr}^{2+}) = 126$ pm).⁷⁹ From the nominal Sr₄Al₁₃Pt₉ sample single crystals of the SrAl₅Pt₃ and Sr₂Al₁₆Pt₉ phases were isolated and single crystal studies were conducted, resulting in the two new phases and being isopointal/isotypic to the YNi₅Si₃ and Ce₂Al₁₆Pt₉ type respectively, which was also the case for Eu₂Al₁₆Pt₉, where the single crystal was isolated from the attempt to synthesize the bulk sample of this compound. The single crystal refinement parameters are listed in the corresponding papers. (*Z. Naturforsch. B.* **2022**, 77b, 367; *Z. Naturforsch.* **2024**, 79b, 595)

SrAl₅Pt₃ and Sr₂Al₁₆Pt₉ exhibit Sr–Al distances ranging from 322 to 342 pm and 332–341 pm, respectively, as well as Sr–Pt distances between 328–330 pm and 334–345 pm. These found distances are in line with the binary and ternary compounds SrAl₂ (KHg₂ type, *Imma*, $d(\text{Sr–Al}) = 327\text{--}360$ pm),¹⁸⁶ SrAl₄ (BaAl₄ type, *I4/mmm*, $d(\text{Sr–Al}) = 342$ pm),¹⁹¹ SrPt₂ (MgCu₂ type, $d(\text{Sr–Pt}) = 274$ pm),²⁰³ SrPt₅ (CaCu₅ type, $d(\text{Sr–Pt}) = 312\text{--}347$ pm),²⁰³ SrAl₂Pt ($d(\text{Sr–Al}) = 340\text{--}343$ pm, $d(\text{Sr–Pt}) = 308\text{--}336$ pm),⁶³ Sr₂Al₈Pt₃ ($d(\text{Sr–Al}) = 314\text{--}343$ pm, $d(\text{Sr–Pt}) = 335\text{--}352$ pm),⁷⁴ SrAl₂Pt₂ (CaBe₂Ge₂ related type, 3+2D modulated structure, $d(\text{Sr–Al}) = 335\text{--}338$ pm, $d(\text{Sr–Pt}) = 330\text{--}334$ pm)⁷⁵ and SrAl₂Pt₃ (CeCo₃B₂ type, *P6/mmm*, $d(\text{Sr–Al}) = 327$ pm, $d(\text{Sr–Pt}) = 344$ pm),⁶⁵ as well as the sum of the covalent radii (Sr + Al = 192 + 125 = 317 pm; Sr + Pt = 192 + 129 = 321 pm).⁴ Eu₂Al₁₆Pt₉ exhibits interatomic Eu–Al distances ranging from 330 to 332 pm and Eu–Pt distances of 332 and 342 pm. The distances are in line with the binary and ternary compounds EuAl₂ (MgCu₂ type, $d(\text{Eu–Al}) = 337$ pm)²⁰⁴ or EuAl₄ (BaAl₄ type, $d(\text{Eu–Al}) = 339\text{--}356$ pm),²⁰⁵ EuPt₂ (MgCu₂ type, $d(\text{Eu–Pt}) = 320$ pm),²⁰⁶ Eu₄Al₁₃Pt₉ (Ho₄Ge₉Ir₁₃ type, *Pmmn*, $d(\text{Eu–Al}) = 326\text{--}360$ pm, $d(\text{Eu–Pt}) = 322\text{--}332$ pm),¹⁷⁶ Eu₂Al₉Pt₃ ($d(\text{Eu–Al}) = 306\text{--}$

313 pm, $d(\text{Eu-Pt}) = 347\text{-}348$ pm),⁶¹ EuAl_2Pt (MgAl_2Cu type, $Cmcm$) ($d(\text{Eu-Al}) = 335\text{-}355$ pm, $d(\text{Eu-Pt}) = 302\text{-}330$ pm),⁶³ as well as the sum of the covalent radii of $\text{Eu} + \text{Al} = 185 + 125 = 310$ pm⁴ and $\text{Eu} + \text{Pt} = 185 + 129 = 314$ pm.⁴ Similar Al-Pt distances of 245-272 pm, 248-278 pm and 247-274 pm can be found in SrAl_5Pt_3 , $\text{Sr}_2\text{Al}_{16}\text{Pt}_9$ and $\text{Eu}_2\text{Al}_{16}\text{Pt}_9$ respectively, which are in line with the following binary and ternary compounds AlPt (FeSi type, $P2_13$) $d(\text{Al-Pt}) = 248\text{-}273$ pm,²⁰⁰ Al_2Pt (CaF_2 type, $Fm\bar{3}m$) $d(\text{Al-Pt}) = 256$ pm,²⁰⁷ SrAl_2Pt (MgAl_2Cu type, $Cmcm$) $d(\text{Al-Pt}) = 255\text{-}257$ pm,⁶³ $\text{Sr}_2\text{Al}_8\text{Pt}_3$ ($\text{Eu}_2\text{Ni}_8\text{Si}_3$ type, $P4_2/nmc$) $d(\text{Al-Pt}) = 252\text{-}279$ pm,⁷⁴ SrAl_2Pt_2 (CaBe_2Ge_2 related type, 3+2D modulated structure) $d(\text{Al-Pt}) = 249\text{-}255$ pm,⁷⁵ SrAl_2Pt_3 (CeCo_3B_2 type, $P6/mmm$) $d(\text{Al-Pt}) = 254$ pm,⁶⁵ $\text{Eu}_4\text{Al}_{13}\text{Pt}_9$ ($\text{Ho}_4\text{Ge}_9\text{Ir}_{13}$ type, $Pmmm$) $d(\text{Al-Pt}) = 247\text{-}265$ pm,¹⁷⁶ $\text{Eu}_2\text{Al}_9\text{Pt}_3$ ($\text{Y}_2\text{Ga}_9\text{Co}_3$ type, $Cmcm$) $d(\text{Al-Pt}) = 256\text{-}264$ pm,⁶¹ EuAl_2Pt (MgAl_2Cu type, $Cmcm$) $d(\text{Al-Pt}) = 254\text{-}258$ pm,⁶³ as well as the sum of the covalent radii ($\text{Pt} + \text{Al} = 129 + 125 = 254$ pm).⁴ In case of the homoatomic Al-Al distances also similar ranges of 276-347 pm, 276-317 pm and 275-297 pm can be found for the three compounds, although the europium containing structure does not exhibit Al-Al distances longer than 300 pm like the Sr compounds. The range of the Al-Al contacts are in line with the ones found in elemental Al (Cu type, $Fm\bar{3}m$) of 286 pm.²⁰⁸ When looking at the Pt-Pt distances, SrAl_5Pt_3 displays $d(\text{Pt-Pt})$ of 301 pm, $\text{Sr}_2\text{Al}_{16}\text{Pt}_9$ of 297 pm and $\text{Eu}_2\text{Al}_{16}\text{Pt}_9$ of 296 pm, the compounds show a high similarity of the Pt-Pt distances, but these are longer than the sum of the covalent radii $r_{\text{cov}} = 129 + 129 = 258$ pm⁴ as well as the distances in elemental Pt (Cu type, $Fm\bar{3}m$) with 277 pm.²⁰⁹ The similar distances of the three compounds led to the assumption that all three structures form a polyanionic network of Al and Pt with the Sr or Eu residing in the hexagonal cavities.

In addition to the single crystal XRD studies EDX measurements were conducted for the $\text{Eu}_2\text{Al}_{16}\text{Pt}_9$ sample, with 86 wt.-% of the phase being the main component. The measurement points as well as the mean element value are in good agreement with the ideal composition, the results of the EDX measurements are shown in **Table 3.4** alongside the SEM image of the measured area in **Figure 3.31**. Slight differences occur which are mostly caused by the roughness of the sample alongside the non-perpendicular alignment of the crystal to the electron beam.

To investigate the bonding character of the Sr compounds DFT calculations were performed, using the single crystal data as starting points. The structure relaxation resulted in optimized lattice parameters shown in **Table 3.3**, which are in good agreement with the experimental single crystal data. The DOS of SrAl_5Pt_3 show states at and near the Fermi-level indicating a

non-purely ionic character, this is also observed in $\text{Sr}_2\text{Al}_{16}\text{Pt}_9$ (**Figure 3.32** and **Figure 3.a.33**, left). Both compounds exhibit pseudogaps ranging from -2.5 to $+2.5$ eV and -3 to $+1.5$ for SrAl_5Pt_3 and $\text{Sr}_2\text{Al}_{16}\text{Pt}_9$, respectively. In the range between -11 to -6 eV in SrAl_5Pt_3 and -11 to -7 eV in $\text{Sr}_2\text{Al}_{16}\text{Pt}_9$ the Al contribution is dominant, whereas Pt possesses significant contributions to the DOS between -6 to -1 eV in SrAl_5Pt_3 and -7 to -0.5 eV in $\text{Sr}_2\text{Al}_{16}\text{Pt}_9$, indicating that Pt is involved in both ionic and covalent bonding. The Sr contribution is in both compounds low, so the Sr contribution is responsible for the metallic bonding character alongside Al. Due to the similar shape to the Pt states, Al exhibits strong covalent Al-Pt bonding, forming the polyanionic network. To get an even deeper insight into the bonding situation integrated crystal orbital Hamilton populations (ICOHP) were calculated. Plots for selected Al-Pt, Pt-Pt and Al-Al bonds are showed in **Figure 3.32** for SrAl_5Pt_3 and **Figure 3.33** for $\text{Sr}_2\text{Al}_{16}\text{Pt}_9$. The ICOHP values for the Sr-Al range between -0.20 and -0.29 eV and -0.17 to -0.31 eV for SrAl_5Pt_3 and $\text{Sr}_2\text{Al}_{16}\text{Pt}_9$ respectively. Slightly higher values can be found for Sr-Pt with -0.29 and -0.35 eV in SrAl_5Pt_3 and -0.30 to -0.32 eV in $\text{Sr}_2\text{Al}_{16}\text{Pt}_9$. The Pt-Al bonds show weak antibonding and strong bonding interactions below and non-bonding states near the Fermi-level, as observable in the $-\text{COHP}$ -plots. The ICOHP values of Al-Pt bonds for the compounds range from -1.60 to -2.28 eV and -1.23 to -2.27 eV. This indicates very stable covalent bonding between the Al and Pt atoms. In the case of the homoatomic atomic interactions, the Pt-Pt bonds are weaker with ICOHP values of -0.59 and -0.73 eV for SrAl_5Pt_3 and $\text{Sr}_2\text{Al}_{16}\text{Pt}_9$ respectively and when looked in the $-\text{COHP}$ show strong antibonding states below the Fermi-level. The ICOHP values of the existing Al-Al bonds are -0.25 to -1.05 and -0.11 to -0.96 eV for both phases respectively.

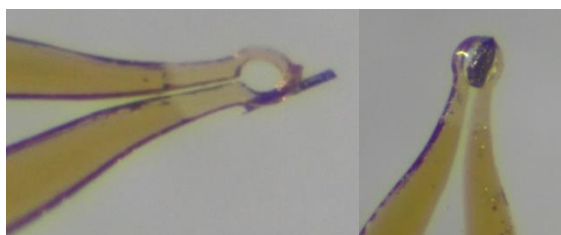


Figure 3.28: Single crystals of SrAl_5Pt_3 (left, needle shaped) and $\text{Sr}_2\text{Al}_{16}\text{Pt}_9$ (right, block shaped), placed on a lube.

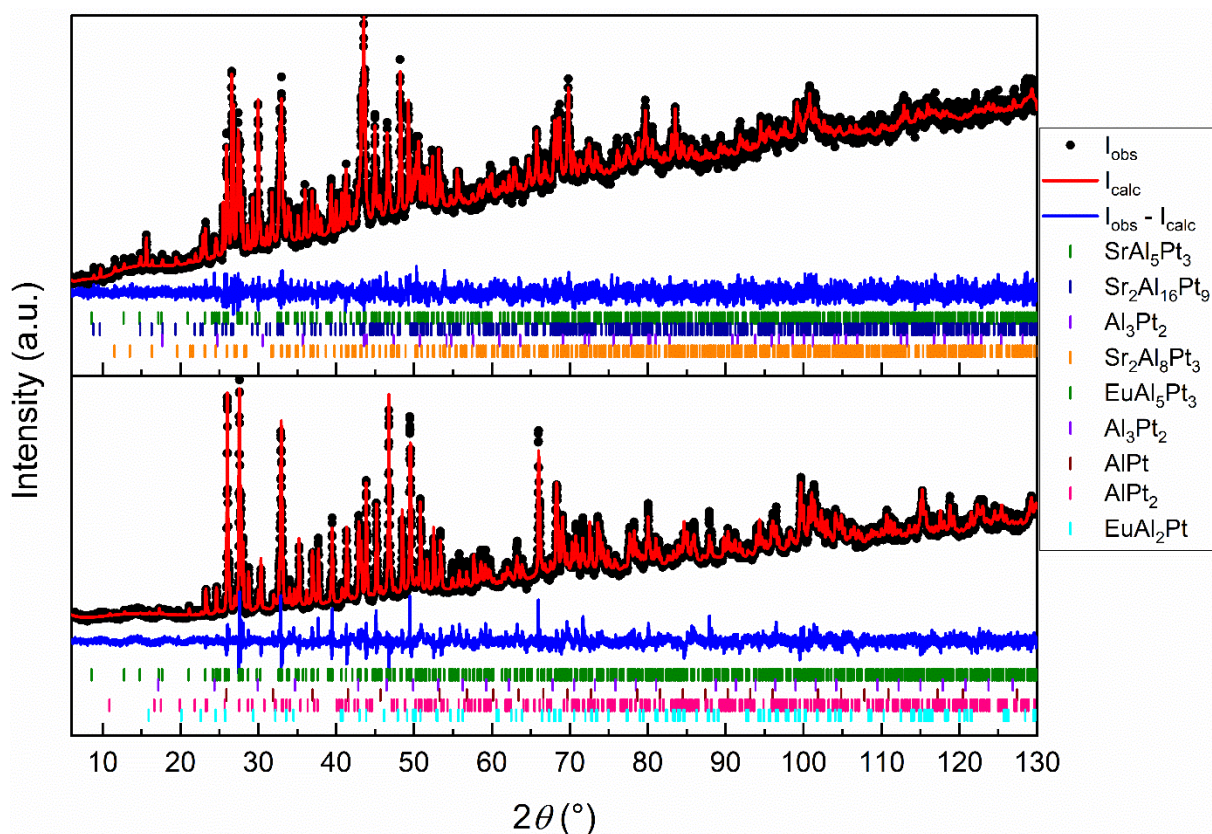


Figure 3.29: Rietveld refinement of the powder X-ray diffraction pattern of SrAl_5Pt_3 (top) and EuAl_5Pt_3 (bottom). Collected data are shown in black dots, the refinement as red and the difference as blue line. Olive ticks indicate the Bragg positions of the corresponding MA_5Pt_3 phase (YNi_5Si_3 type, $Pnma$), royal blue of $\text{Sr}_2\text{Al}_{16}\text{Pt}_9$ ($\text{Ce}_2\text{Al}_{16}\text{Pt}_9$ type, $Immm$), violet of Al_3Pt_2 (Al_3Ni_2 type, $P\bar{3}m1$), orange of $\text{Sr}_2\text{Al}_8\text{Pt}_3$ ($\text{Eu}_2\text{Ni}_8\text{Si}_3$, $P4_2/nmc$), wine-red of AlPt (FeSi type, $P2_13$), pink of AlPt_2 (GaPt_2 type, $Pnma$) and cyan ticks of EuAl_2Pt (MgAl_2Cu type, $Cmcm$).

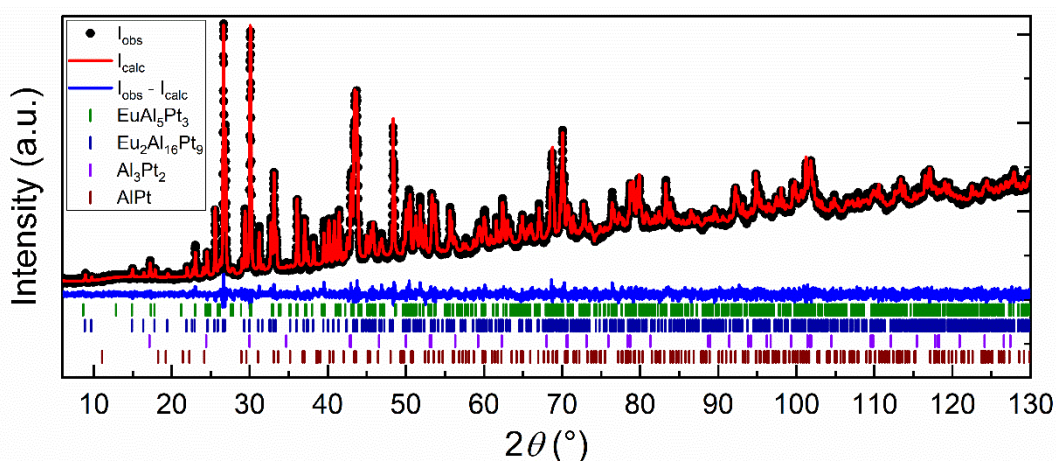


Figure 3.30: Rietveld refinement of the powder X-ray diffraction pattern of $\text{Eu}_2\text{Al}_{16}\text{Pt}_9$. Collected data are shown in black dots, the refinement as red and the difference as blue line. Olive ticks indicate the Bragg positions of EuAl_5Pt_3 (YNi_5Si_3 type, $Pnma$), royal blue of $\text{Eu}_2\text{Al}_{16}\text{Pt}_9$ ($\text{Ce}_2\text{Al}_{16}\text{Pt}_9$ type, $Immm$), violet of Al_3Pt_2 (Al_3Ni_2 type, $P\bar{3}m1$) and wine-red ticks of AlPt (AlPd type, $R\bar{3}$).

Table 3.2: Phase composition from the PXRD measurements of $RE_4Al_{13}Pt_9$ ($RE = La-Nd, Sm, Gd$), overall composition normalized on Pt_3 .

Sample	Main phase (wt.-%)	Side phase (wt.-%)	Over composition
CaAl ₅ Pt ₃	CaAl ₅ Pt ₃ (74)	Al ₃ Pt ₂ (14), Ca ₂ Al ₁₆ Pt ₉ (11)	Ca _{0.8(1)} Al _{5.0(1)} Pt ₃
SrAl ₅ Pt ₃	SrAl ₅ Pt ₃ (44)	Sr ₂ Al ₁₆ Pt ₉ (1), Al ₂ Pt (44), AlPt (11)	Sr _{0.4(1)} Al _{5.2(1)} Pt ₃
Sr ₂ Al ₁₆ Pt ₉	Sr ₂ Al ₁₆ Pt ₉ (51)	SrAl ₅ Pt ₃ (49)	Sr _{2.5(1)} Al _{15.5(1)} Pt ₃
EuAl ₅ Pt ₃	EuAl ₅ Pt ₃ (89)	EuAl ₂ Pt (2), Al ₃ Pt ₂ (1), AlPt (5), AlPt ₂ (3)	Eu _{0.9(1)} Al _{4.7(1)} Pt ₃
Eu ₂ Al ₁₆ Pt ₉	Eu ₂ Al ₁₆ Pt ₉ (86)	EuAl ₅ Pt ₃ (3), Al ₃ Pt ₂ (10), AlPt (1)	Eu _{1.8(1)} Al _{15.6(1)} Pt ₉

Table 3.3: Lattice parameters of CaAl₅Pt₃, Ca₂Al₁₆Pt₉, SrAl₅Pt₃, Sr₂Al₁₆Pt₉, EuAl₅Pt₃ and Eu₂Al₁₆Pt₉.

Compound	<i>a</i> (pm)	<i>b</i> (pm)	<i>c</i> (pm)	<i>V</i> (nm ³)
CaAl ₅ Pt ₃ ^{P*}	2050.3(1)	409.0(1)	736.4(1)	0.6175
SrAl ₅ Pt ₃ ^{P*}	2065.04(7)	413.74(1)	738.98(3)	0.6314
SrAl ₅ Pt ₃ ^{SC*}	2067.07(6)	414.16(2)	739.88(3)	0.6334
SrAl ₅ Pt ₃ ^{T,*}	2081.49	417.83	746.95	0.6496
EuAl ₅ Pt ₃ ^{P*}	2059.88(3)	413.19(1)	736.35(1)	0.6267
EuAl ₅ Pt ₃ ⁹¹	2066.2(3)	412.58(6)	738.16(11)	0.6293
Ca ₂ Al ₁₆ Pt ₉ ^{P*}	414.02(1)	1181.6(2)	1830.4(3)	0.8954
Sr ₂ Al ₁₆ Pt ₉ ^{P*}	416.69(2)	1193.53(6)	1832.38(9)	0.9113
Sr ₂ Al ₁₆ Pt ₉ ^{SC*}	417.08(1)	1194.25(5)	1833.08(8)	0.9131
Sr ₂ Al ₁₆ Pt ₉ ^{T,*}	418.57	1207.65	1854.44	0.9374
Eu ₂ Al ₁₆ Pt ₉ ^{P*}	416.67(1)	1189.76(1)	1827.87(2)	0.9061
Eu ₂ Al ₁₆ Pt ₉ ^{SC*}	416.08(2)	1187.98(5)	1823.92(8)	0.9016

^P powder, ^{SC} single crystal, ^T DFT, * own work

Table 3.4: Energy dispersive X-ray spectroscopy results of Eu₂Al₁₆Pt₉.

Compound	Ideal	P1	P2	P3	Mean
Eu ₂ Al ₁₆ Pt ₉	Eu: 7.4	7	7	8	7
	Al: 59.3	57	60	55	58
	Pt: 33.3	36	33	37	35

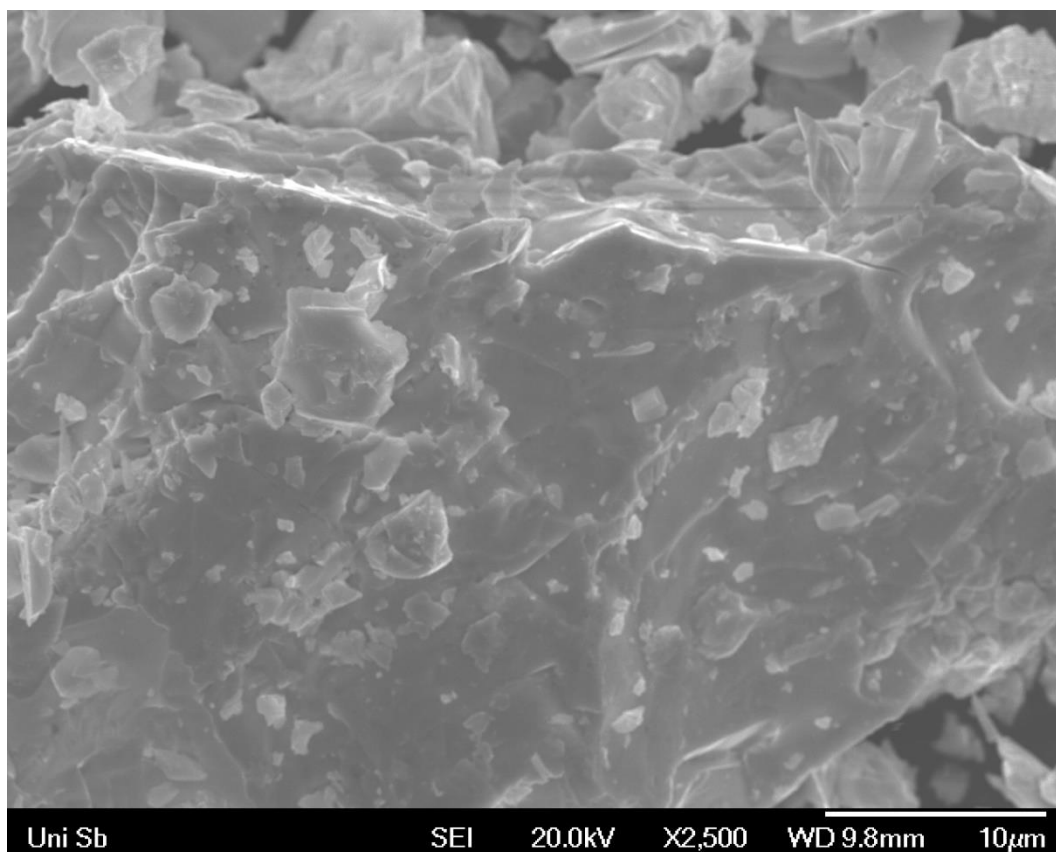


Figure 3.31: Scanning electron microscope image of $\text{Eu}_2\text{Al}_{16}\text{Pt}_9$.

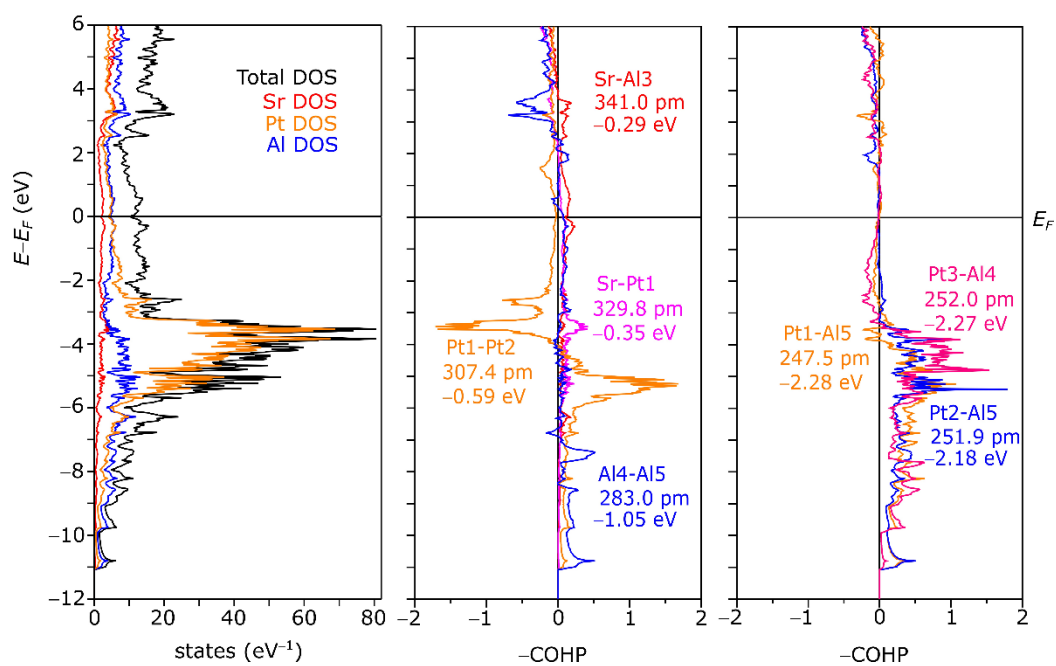


Figure 3.32: Density of states (DOS) of SrAl_5Pt_3 (left), for selected Sr-Pt, Sr-Al, Al-Al and Pt-Pt (middle), and Pt-Al bonds (right).

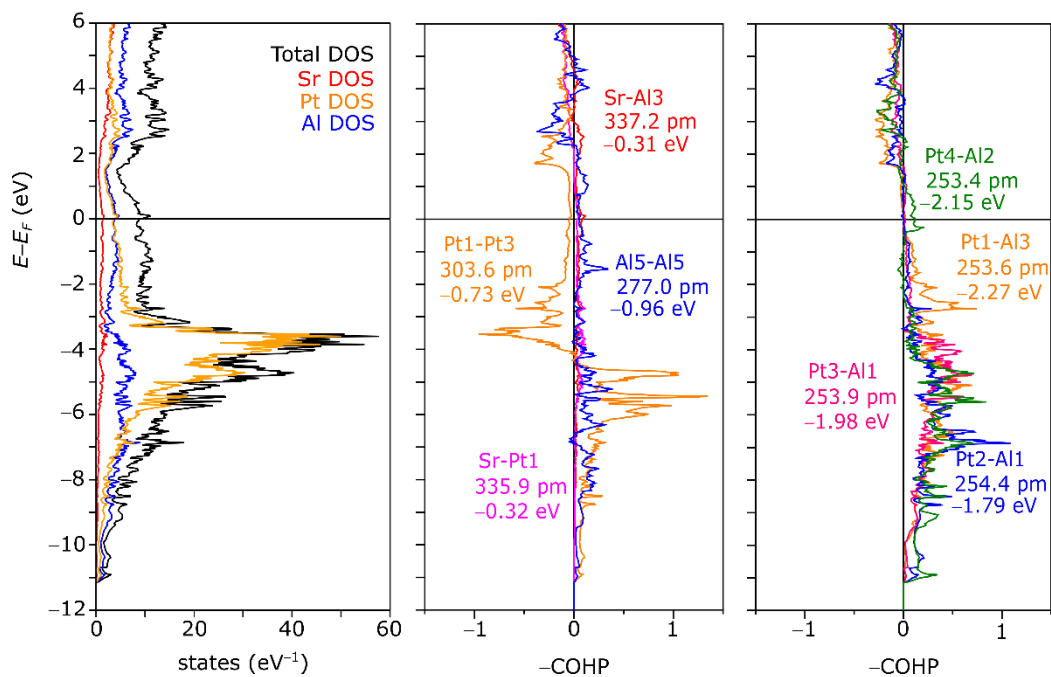


Figure 3.33: Density of states (DOS) of $\text{Sr}_2\text{Al}_{16}\text{Pt}_9$ (left), for selected Sr-Pt, Sr-Al, Al-Al and Pt-Pt (middle), and Pt-Al bonds (right).

As mentioned before, the attempt of synthesizing $\text{Ca}_3\text{Al}_4\text{Pt}_4$ resulted in a mixture of multiple phases, of which Ca_2AlPt_2 ($\text{Ca}_2\text{Ir}_2\text{Si}$ type, $C12/c1$) was already literature known,⁶⁴ the new phases with the nominal composition CaAl_2Pt_2 (CaBe_2Ge_2 type, $P4/nmm$) and $\text{Ca}_2\text{Al}_3\text{Pt}$ ($\text{Mg}_2\text{Cu}_3\text{Si}$ type, $P6_3/mmc$), were identified using SCXRD measurement of isolated crystals. The refinement parameters are shown in the corresponding paper (*Z. Anorg. Allg. Chem.* **2024**, 650, e202400094). The structures were already described in the chapter above and are shown in **Figure 3.13-3.17**. The lattice parameters of the single crystal studies as well as from the bulk powder samples and quantum chemical calculations are summarized in **Table 3.5**. The SCXRD analysis showed that Ca_2AlPt_2 exhibits no mixed occupancy of the Pt and Al positions, which is not the case in the two new phases with the nominal compositions CaAl_2Pt_2 and $\text{Ca}_2\text{Al}_3\text{Pt}$. During the single crystal refinement mixed occupancies of the Al and Pt positions leading to a refined composition of $\text{CaAl}_{2.2,4(1)}\text{Pt}_{1.76(1)}$ and $\text{Ca}_2\text{Al}_{3.09(1)}\text{Pt}_{0.91(1)}$ have been observed. Bulk samples of the nominal Ca–Al–Pt phases Ca_2AlPt_2 , $\text{Ca}_2\text{Al}_3\text{Pt}$ and additionally Ca_2AlPt_2 were prepared by encapsulating the elements inside arc-welded Ta ampoules. The ampoules were placed inside the induction furnace, heated to ~ 1500 K within 2 min, hold for 10 min at this temperature followed by a slow cooling to ~ 1000 K, dwelled for 4 h with subsequent cooling to room temperature by shutting off the induction furnace. The reactions resulted in a mixture of different phases, for example the powder diffraction pattern of the Ca_2AlPt_2 sample is shown in **Figure 3.34** alongside all formed phases. The sample consists of 98 wt.-% Ca_2AlPt_2 ($\text{Ca}_2\text{Ir}_2\text{Si}$

type, $C12/c1$, $a = 981.03(2)$, $b = 573.74(1)$, $c = 772.95(2)$ pm),⁶⁴ 1 wt.-% AlPt (FeSi type, $P2_13$, $a = 477.53(4)$ pm)²⁰⁰ and 1 wt.-% Al₂₁Pt₈ (own type, $I4_1/a$, $a = 1284.6(2)$, $c = 1041.7(2)$ pm).²¹⁰ With an overall composition of Ca_{1.97(1)}Al_{1.06(1)}Pt₂ in the reaction mixture it shows a loss of a small amount of calcium during the reaction as well as a small surplus of Al leading to the assumption that the Pt could have reacted with the Ta ampoule or coated the Ta ampoule wall and staying behind as unreacted species in the ampoule.

CaAl₂Pt₂ crystallizes in the tetragonal CaBe₂Ge₂ type structure, exhibiting five independent crystallographic atom positions one for Ca, two for Al and two for Pt, in which the Pt₁ position is mixed occupied with Al and the Pt₂ position is split into two sites due to an enlarged anisotropic displacement parameter, leading to the refined compositions of CaAl_{2.24(1)}Pt_{1.76(1)}. Interatomic distances of $d(\text{Ca-Pt}) = 322\text{-}331$ pm, $d(\text{Ca-Al}) = 329\text{-}351$ pm, $d(\text{Al-Pt}) = 240\text{-}268$ pm, $d(\text{Pt-Pt}) = 302$ pm and $d(\text{Al-Al}) = 302$ pm are observed. Nominal Ca₂Al₃Pt crystallizes in the hexagonal Mg₂Cu₃Si type structure and exhibits three independent crystallographic atom positions, one for each Ca, Al and Pt. Whereas the Pt position is filled with 10% Al, the Al position possesses a mixed occupancy with Pt of 0.4% due to additional residual electron density, resulting in a compositions of Ca₂Al_{3.09(1)}Pt_{0.91(1)}. The compound exhibits interatomic distances of $d(\text{Ca-Pt}) = 328$ pm, $d(\text{Ca-Al}) = 316\text{-}328$ pm, $d(\text{Al-Pt}) = 270$ pm and $d(\text{Al-Al}) = 274\text{-}287$ pm.

Ca₂AlPt₂ exhibits Pt atoms, which form chains with alternating distances $d(\text{Pt-Pt}) = 274$ and 295 pm along the ab plane at a high $z = 0$ and $1/2$ with an angle of 61° to each other. The chains are connected to each other via Al atoms forming cavities in which the Ca atoms reside in. The interatomic distances found in Ca₂AlPt₂ are $d(\text{Ca-Pt}) = 306\text{-}311$ pm, $d(\text{Ca-Al}) = 327\text{-}351$ pm, $d(\text{Al-Pt}) = 249\text{-}252$ pm, $d(\text{Pt-Pt}) = 274$ and 295 pm, also no Al-Al bonds were observable.

All observed atomic distances in the three compounds are in agreement with the binaries and ternary compounds CaAl₂ (MgCu₂ type, $Fd\bar{3}m$, $d(\text{Al-Al}) = 284$ pm, $d(\text{Ca-Al}) = 333$ pm),¹⁸⁵ CaPt₂ (MgCu₂ type, $Fd\bar{3}m$, $d(\text{Pt-Pt}) = 270$ pm, $d(\text{Ca-Pt}) = 316$ pm),²¹¹ Al₂Pt (CaF₂ type, $Fm\bar{3}m$, $d(\text{Al-Pt}) = 256$ pm, $d(\text{Al-Al}) = 296$ pm),²⁰⁷ CaAlPt (TiNiSi type, $Pnma$, $d(\text{Ca-Pt}) = 294\text{-}305$ pm, $d(\text{Ca-Al}) = 308\text{-}336$ pm, $d(\text{Al-Pt}) = 261\text{-}275$ pm, $d(\text{Al-Al}) = 311$ pm),⁶⁷ Ca₂Al₉Pt₃ (Y₂Ga₉Co₃ type, $Cmcm$, $d(\text{Ca-Pt}) = 343\text{-}347$ pm, $d(\text{Ca-Al}) = 303\text{-}318$ pm, $d(\text{Al-Pt}) = 257\text{-}264$ pm, $d(\text{Al-Al}) = 269\text{-}293$ pm),⁶¹ CaAl₂Pt (MgAl₂Cu type, $Cmcm$, $d(\text{Ca-Pt}) = 284\text{-}314$ pm, $d(\text{Ca-Al}) = 323\text{-}342$ pm, $d(\text{Al-Pt}) = 255\text{-}258$ pm, $d(\text{Al-Al}) = 276\text{-}290$ pm),⁶³ CaAl₅Pt₃ (YNi₅Si₃ type, $Pnma$, $d(\text{Ca-Al}) = 317\text{-}347$ pm, $d(\text{Ca-Pt}) = 322\text{-}329$ pm, $d(\text{Al-Al}) = 221\text{-}335$ pm, $d(\text{Al-Pt}) = 234\text{-}289$ pm, $d(\text{Pt-Pt}) = 304$ pm)¹⁷² and Ca₂Al₁₆Pt₉ (Ce₂Al₁₆Pt₉ type, $Immm$, $d(\text{Ca-Al}) = 323\text{-}334$ pm, $d(\text{Ca-Pt}) = 329\text{-}338$ pm, $d(\text{Al-Al}) = 241\text{-}338$ pm, $d(\text{Al-Pt}) =$

240–335 pm, $d(\text{Pt–Pt}) = 302$ pm).¹⁷⁴ The relatively short Al–Pt and Al–Al distances again point towards bonding interactions.

By using the single crystal data from the SCXRD measurements with the ideal occupancy as starting points DFT calculations were performed. The lattice parameter after the structure relaxations were in good agreement with the experimental ones for Ca_2AlPt_2 and $\text{Ca}_2\text{Al}_3\text{Pt}$ (Table 3.5). In the case of CaAl_2Pt_2 the theoretical lattice parameters exhibit a higher deviation from the experimental parameters due to the mixed occupancy of both Pt positions with Al, which were idealized for the quantum chemical calculations, resulting in the difference in the theoretical and experimental lattice parameters. After the structure relaxation Bader charges were calculated, showing positive values for Ca and Al as well as the expected negative charge for the Pt atoms, in regard to the electronegativities of the three elements ($\chi(\text{Ca}) = 1.00$; $\chi(\text{Al}) = 1.61$; $\chi(\text{Pt}) = 2.28$). The charge of the Pt atoms increases from -1.42 to -3.30 starting from Ca_2AlPt_2 to $\text{Ca}_2\text{Al}_3\text{Pt}$ with CaAl_2Pt_2 in the middle, which is explainable by looking at the Ca to Pt content inside the compounds progressing from 1:1 over 1:2 to 2:1. Therefore, the Pt content decreases with the Al content additionally increasing. Due to the charge transfer as well as the atomic distances the compounds can be viewed as polar intermetallics with a polyanion consisting of the Al and Pt atoms with Ca being the cationic species.

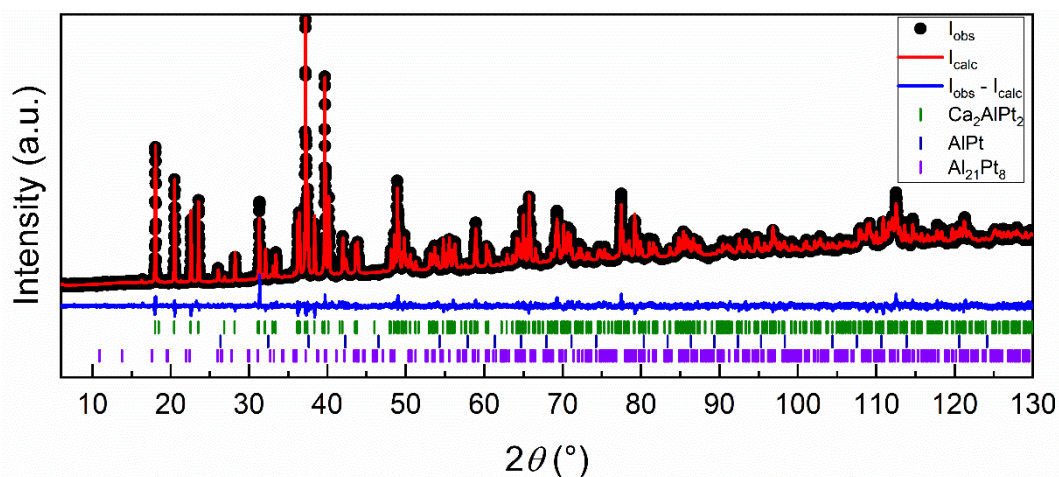


Figure 3.a.34: Rietveld refinement of the powder X-ray diffraction pattern of Ca_2AlPt_2 . Collected data is shown in black dots, the refinement as red and the difference as blue line. Olive ticks indicate the Bragg positions of Ca_2AlPt_2 ($\text{Ca}_2\text{Ir}_2\text{Si}$ type, $C2/c$), royal blue of AlPt (FeSi type, $P2_13$) and violet ticks of $\text{Al}_{21}\text{Pt}_8$ (own type, $I4_1/a$).

Table 3.5: Lattice parameters and unit cell volumes of Ca₂AlPt₂, CaAl₂Pt₂ and Ca₂Al₃Pt from PXRD, SCXRD and DFT calculations.

Compound	source	<i>a</i> (pm)	<i>b</i> (pm)	<i>c</i> (pm)	β (°)	<i>V</i> (nm ³)
Ca ₂ AlPt ₂	PXRD	981.03(2)	573.74(1)	772.95(2)	101.862(1)	0.4258
	SCXRD	981.0(1)	573.8(1)	772.9(1)	101.847(1)	0.4258
	DFT	977.9	568.7	770.2	102.11	0.4183
CaAl ₂ Pt ₂	PXRD	426.79(2)	<i>b</i>	988.79(6)	90	0.1801
	SCXRD	423.6(1)	<i>b</i>	963.5(1)	90	0.1729
	DFT	412.2	<i>b</i>	1074.3	90	0.1825
Ca ₂ Al ₃ Pt	PXRD	561.46(5)	<i>b</i>	876.94(8)	90	0.2394
	SCXRD	561.7(1)	<i>b</i>	876.8(1)	90	0.2396
	DFT	556.6	<i>b</i>	869.3	90	0.2332

In cooperation with Dr. P. C. Müller, L. Reitz and Prof. Dr. R. Dronskowski, research on the electronic transfer and bonding characterization were conducted within the binary Ca–Al, Ca–Pt and Al–Pt systems as well as the ternary Ca–Al–Pt system using the LOBSTER program package, leading to the preparation of a manuscript. An overview of the interatomic distances along the bonding interactions are summarized in **Table 3.6**. The preliminary results will be discussed in the following paragraph alongside a comparison with the quantum chemical calculations of the Sr–Al–Pt and Ca–Al–Pt compounds of the paragraph above. When looking at the binary compounds CaAl₂, CaAl₄, CaPt₂ and CaPt₅, Löwdin charges and ICOBIs are calculated, as it is expected, the Ca atoms have always a positive charge between +1.54, +1.66, +1.17 and +1.44, due to Ca being the less electronegative element and the corresponding Al or Pt atom exhibiting negative charges of –0.77, –0.60/–0.25, –0.58 and –0.38/–0.23 for CaAl₂, CaAl₄, CaPt₂ and CaPt₅, respectively. Also, the ICOBI values show that there are no or barely any covalent interactions between Ca and Al (0.05, 0.02-0.04) or Ca and Pt atoms (0.04, 0.02-0.05), but between Al and Al (0.43, 0.22-0.81) as well as Pt and Pt (0.11, 0.03-0.13) atoms weak covalent bonding can be observed. Going from the alkaline earth compounds to the binaries of the polyanion building elements Al and Pt for the ternary phases, the ICOBIs calculated for Al₃Pt₂, AlPt and Al₂Pt show, again, bonding interactions between Al–Al atoms (0.23-0.31, 0.18, 0.27) and as already discussed above in the ternary *AE*–Al–Pt compounds, interactions between Al and Pt atoms (0.15-0.30, 0.17-0.25, 0.26) are present, but no or barely any between the Pt atoms (0.04, 0.04, 0.02) themselves. These are in the expected range, but when looking at the Löwdin charges counterintuitive values are calculated, with Pt being positively charged, therefore give electrons and Al having negative charges (receiving electrons), even though Pt has a significant higher electron negativity than Al. This situation is currently addressed by the Dronskowski group and attempts have been made to establish the calculation of oxidation

states. Preliminary tests show, that these produce more reliable results compared to the Löwdin charges. A similar trend is observable in the ternary compounds (CaAlPt, CaAl₂Pt, CaAl₂Pt₂, CaAl₅Pt₃, Ca₂AlPt₂, Ca₂Al₃Pt, Ca₂Al₉Pt₃, Ca₂Al₁₅Pt₆, Ca₂Al₁₆Pt₉), the Ca exhibits always a positive Löwdin charge. The charge of the Al atoms is always negative and for Pt, the charge is positive for Al rich compounds (CaAl₂Pt (+0.20), CaAl₂Pt₂ (+0.06 to +0.20), CaAl₅Pt₃ (+0.26 to +0.28), Ca₂Al₃Pt (+0.23), Ca₂Al₉Pt₃ (+0.44 to +0.45), Ca₂Al₁₅Pt₆ (+0.38) and Ca₂Al₁₆Pt₉ (+0.28 to +0.39)) or negative for Al poor compounds (CaAlPt (−0.17) and Ca₂AlPt₂ (−0.45)). The ICOBI values for the Ca–Al and Ca–Pt are in all cases insignificantly small, indicating rather ionic interactions, which is also the case for nearly all Pt–Pt interactions, resulting in non-bonding interactions. In comparison to that, the ICOBI values of the Al–Al and Al–Pt are in the same range with high values, suggesting high covalency in the bonding interactions.

Table 3.6: Löwdin charges, ICOBI and interatomic distances of binary and ternary Ca–Al–Pt compounds.

compound	atom	Löwdin charge	atom pair	distance /pm	ICOBI(<i>M–M</i>)
CaAlPt	Ca	+1.26	Ca–Ca	347	0.01
			Ca–Al	314	0.04
			Ca–Pt	296	0.05
	Al	−1.08	Al–Al	311	0.26
			Al–Pt	257	0.29
			Al–Pt	260	0.33
			Al–Pt	266	0.43
	Pt	−0.17	Pt–Pt	410	0.02
CaAl ₂ Pt	Ca	+1.47	Ca–Ca	381	0.00
			Ca–Al	320	0.05
			Ca–Pt	287	0.04
	Al	−0.84	Al–Al	279	0.42
			Al–Al	292	0.34
			Al–Al	340	0.31
			Al–Pt	255	0.32
	Al	−0.84	Al–Pt	258	0.29
			Pt–Pt	>500	–
CaAl ₂ Pt ₂	Ca	+1.46	Ca–Ca	413	0.00
			Ca–Al ₂	316	0.03
			Ca–Al ₁	318	0.07
			Ca–Pt ₂	338	0.01
			Ca–Pt ₁	338	0.03
	Al ₁	−0.66	Al ₁ –Al ₁	292	0.30
			Al ₁ –Pt ₁	253	0.28
	Al ₂	−1.06	Al ₂ –Pt ₁	250	0.45
			Al ₂ –Pt ₂	250	0.34
	Pt ₁	+0.06	Pt ₁ –Pt ₁	413	0.01
	Pt ₂	+0.20	Pt ₂ –Pt ₂	292	0.08
	CaAl ₅ Pt ₃	Ca	+1.49	Ca–Ca	409
Ca–Al ₅				317	0.03
Ca–Pt ₃				320	0.03

compound	atom	Löwdin charge	atom pair	distance /pm	ICOBI(<i>M-M</i>)
	Al1	-0.43	Al1-Al1	281	0.35
			Al1-Al14	306	0.22
			Al1-Al15	278	0.32
			Al1-Pt1	253	0.37
			Al1-Pt2	261	0.32
	Al2	-0.56	Al1-Pt2	265	0.27
			Al1-Pt2	266	0.28
			Al2-Al3	283	0.31
			Al2-Al3	289	0.32
			Al2-Al4	293	0.28
			Al2-Pt1	261	0.32
			Al2-Pt3	256	0.31
	Al3	-0.55	Al2-Pt3	262	0.22
			Al3-Al4	286	0.27
			Al3-Pt2	254	0.19
			Al3-Pt3	250	0.32
	Al4	-0.38	Al3-Pt3	256	0.25
			Al4-Al5	282	0.34
			Al4-Pt1	264	0.23
			Al4-Pt2	272	0.18
	Al5	-0.40	Al4-Pt3	250	0.25
Al5-Al5			275	0.27	
Al5-Pt1			246	0.24	
Pt1	+0.28	Al5-Pt2	253	0.22	
		Pt1-Pt2	306	0.02	
		Pt2-Pt2	407	0.02	
Pt2	+0.28	Pt3-Pt3	409	0.02	
Ca ₂ AlPt ₂	Ca	+1.16	Pt3-Pt3	409	0.02
			Ca-Ca	357	0.01
			Ca-Al	326	0.07
	Al	-1.43	Ca-Pt	304	0.02
			Al-Pt	250	0.36
			Al-Pt	252	0.36
	Pt	-0.45	Pt-Pt	270	0.30
			Pt-Pt	304	0.03
Ca ₂ Al ₃ Pt	Ca	+1.44	Pt-Pt	304	0.03
			Ca-Ca	336	0.01
			Ca-Al	313	0.05
	Al	-1.03	Ca-Pt	325	0.03
			Al-Al	272	0.37
			Al-Al	285	0.52
			Al-Pt	268	0.28
Pt	+0.23	Pt-Al	434	0.04	
Ca ₂ Al ₉ Pt ₃	Ca	+1.62	Pt-Al	434	0.04
			Ca-Ca	427	0.01
			Ca-Al	303	0.03
	Al1	-0.59	Ca-Pt	343	0.02
			Al1-Al1	289	0.34
			Al1-Al1	292	0.32
			Al1-Al2	280	0.31
			Al1-Al3	280	0.33
			Al1-Al4	275	0.33
			Al2-Al2	269	0.37
	Al2	-0.40	Al2-Al3	284	0.33
			Al2-Al4	274	0.35

compound	atom	Löwdin charge	atom pair	distance /pm	ICOBI(<i>M-M</i>)
	Al3	-0.49	Al3-Al3	274	0.35
	Al4	-0.44	-	-	-
	Pt1	+0.45	Pt1-Al1	257	0.30
			Pt1-Al1	263	0.22
			Pt1-Al2	263	0.20
			Pt1-Al3	256	0.26
	Pt2	+0.44	Pt2-Al1	264	0.22
			Pt2-Al3	258	0.26
			Pt2-Al4	256	0.26
Ca ₂ Al ₁₅ Pt ₆	Ca1	+1.59	-	-	-
	Ca2	+1.59	-	-	-
	Al1	-0.45	Al1-Al4	289	0.30
			Al1-Al5	289	0.20
			Al1-Al6	281	0.30
			Al1-Al7	286	0.32
			Al1-Al9	286	0.32
			Al1-Pt1	250	0.26
			Al1-Pt2	250	0.26
			Al1-Pt3	251	0.26
	Al2	-0.45	Al2-Al4	289	0.30
			Al2-Al5	289	0.30
			Al2-Al6	289	0.30
			Al2-Al7	286	0.32
			Al2-Al8	286	0.33
			Al2-Pt1	250	0.26
			Al2-Pt2	251	0.26
			Al2-Pt3	250	0.33
	Al3	-0.45	Al3-Al4	281	0.30
			Al3-Al5	281	0.30
			Al3-Al6	281	0.31
			Al3-Al8	286	0.33
			Al3-Al9	286	0.32
			Al3-Pt1	250	0.26
			Al3-Pt2	251	0.33
			Al3-Pt3	251	0.26
	Al4	-0.23	Al4-Al4	289	0.30
			Al4-Al5	289	0.30
			Al4-Al6	290	0.30
			Al4-Pt1	265	0.22
			Al4-Pt2	264	0.22
			Al4-Pt3	255	0.26
	Al5	-0.23	Al5-Al5	289	0.30
			Al5-Al6	291	0.30
			Al5-Pt1	264	0.22
			Al5-Pt2	264	0.22
			Al5-Pt3	264	0.22
	Al6	-0.18	Al6-Al6	292	0.30
			Al6-Pt1	255	0.27
			Al6-Pt2	272	0.18
			Al6-Pt3	272	0.18
	Al7	-0.48	Al7-Al8	264	0.43
			Al7-Al9	264	0.43

compound	atom	Löwdin charge	atom pair	distance /pm	ICOBI(<i>M-M</i>)
			Al7–Pt2	257	0.26
	Al8	–0.49	Al8–Al9	264	0.43
			Al8–Pt1	258	0.25
	Al9	–0.48	Al9–Pt3	257	0.26
	Pt1	+0.38	–	–	–
	Pt2	+0.38	–	–	–
	Pt3	+0.38	–	–	–
<hr/>					
Ca ₂ Al ₁₆ Pt ₉	Ca	+1.55	Ca–Ca	413	0.00
			Ca–Al	330	0.04
			Ca–Pt	328	0.03
	Al1	–0.36	Al1–Al1	282	0.34
			Al1–Al2	329	0.13
			Al1–Al3	286	0.27
			Al1–Al5	274	0.36
			Al1–Pt1	248	0.43
			Al1–Pt2	252	0.26
			Al1–Pt3	253	0.27
	Al2	–0.35	Al2–Al2	294	0.24
			Al2–Al3	281	0.31
			Al2–Al4	289	0.31
			Al2–Al5	294	0.19
			Al2–Pt1	253	0.26
			Al2–Pt2	271	0.25
			Al2–Pt3	269	0.18
			Al2–Pt4	250	0.25
	Al3	–0.48	Al3–Al3	299	0.29
			Al3–Pt1	250	0.21
			Al3–Pt1	266	0.19
	Al4	–0.42	Al4–Al4	319	0.17
			Al4–Pt1	257	0.31
			Al4–Pt4	261	0.21
	Al5	–0.20	Al5–Al5	285	0.27
			Al5–Pt2	264	0.19
			Al5–Pt3	263	0.24
	Pt1	+0.28	Pt1–Pt3	300	0.03
	Pt2	+0.35	–	–	–
	Pt3	+0.39	–	–	–
	Pt4	+0.32	–	–	–

In **Figure 3.35** a plot of all bonding interactions sorted by the interatomic distance are plotted against the ICOBI value, showing that the Al–Pt have a narrow size distribution, but a relatively large distribution of the ICOBI values, which are besides the Al–Al the strongest. The Al–Al distances have a larger distance distribution along the largest range of ICOBI values, with short bonds being significantly more covalent bonding than larger interatomic distances. When taking a look at the Pt–Pt, Ca–Al and

Ca–Pt bonding interactions, most distances are larger than in Al–Al with ICOBIs extremely low or 0, resulting in non-covalent / ionic bonding interactions or no bonding at all. The distribution of the single bonds indicates a clear dependency of the strength of the bond with the distance between the atoms.

By comparing the ICOHP and Bader charges of the SrAl_5Pt_3 and $\text{Sr}_2\text{Al}_{16}\text{Pt}_9$ with the ICOBI values and Löwdin charges of the isotype Ca compounds, a similar trend is present, the atomic charges for the cationic element are +1.33, +1.32 and +1.49, +1.55 for SrAl_5Pt_3 , $\text{Sr}_2\text{Al}_{16}\text{Pt}_9$ and CaAl_5Pt_3 , $\text{Ca}_2\text{Al}_{16}\text{Pt}_9$, respectively. As already discussed, the Löwdin charges for Pt and Al are counterintuitive with values of Al: -0.38 to -0.56 , -0.20 to -0.48 e and Pt: $+0.26$ to $+0.28$, $+0.28$ to $+0.39$. The Bader charges of the two elements are -3.02 to -3.35 , -2.71 to -3.43 (Pt) and $+1.52$ to $+1.80$, $+1.53$ to $+1.82$ (Al) for the $M\text{Al}_5\text{Pt}_3$ and the $M_2\text{Al}_{16}\text{Pt}_9$ phases, respectively, showing the expected trend. The ICOHP values are calculated as Sr–Al = -0.20 to -0.29 and -0.17 to -0.31 eV, Sr–Pt = -0.29 to -0.35 and -0.30 to -0.32 eV, Al–Pt = -1.60 to -2.28 and -1.23 to -2.27 eV, Pt–Pt = -0.59 and -0.73 eV and Al–Al = -0.25 to -1.05 and -0.11 to -0.96 eV for SrAl_5Pt_3 and $\text{Sr}_2\text{Al}_{16}\text{Pt}_9$, respectively. The ICOBI values are Ca–Al: 0.03 and 0.04, Ca–Pt: 0.03 and 0.03, Al–Pt: 0.18 to 0.37 and 0.18 to 0.43, Pt–Pt: 0.02 and 0.03, Al–Al: 0.22 to 0.35 and 0.13 to 0.36 eV per bond. The ICOBI values are significantly lower than the ICOHP values but show the same trend of weak AE –Al and AE –Pt interactions and strong Al–Al and Al–Pt bonding interactions. The Pt–Pt interactions indicate a higher bonding character in the ICOHP calculations than suggested in the ICOBI calculations.

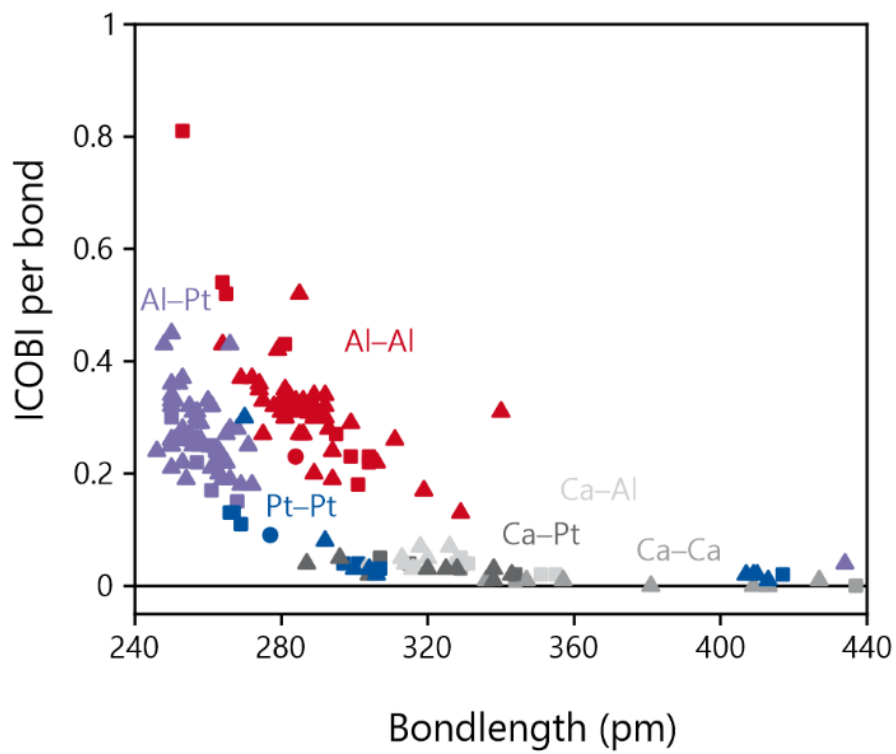


Figure 3.35: Bond length plotted versus the ICObI per bond of the compounds in the Ca–Al–Pt system.

SrAl₈Rh₂ – the First Phase in the Sr–Al–Rh System and New Representative of the CeAl₈Fe₂ Type Structure

Collaborations to disclose: In this part the work published in the *Zeitschrift für Kristallographie* (**2025**, 240, 1-11) under the title given above is summarized. Mrs. Dr. E. Svanidze along with Mr. Dr. Mitja Krnel, Mr. Dr. Nazar Zaremba and Mr. Dr. Markus König performed the temperature dependent electrical resistivity measurements on the SrAl₈Rh₂ single crystal and PD Dr. O. Janka along with the aforementioned worked on the manuscript.

During the attempt to synthesize SrAl₄Rh₂, in analogy to the existing Ir compounds SrAl₄Ir₂ and EuAl₄Ir₂,²¹² an unknown phase was found. Indexing of the powder diffraction pattern revealed an orthorhombic crystal system with space group *Pbam*, so single crystal X-ray diffraction experiments were carried out leading to the new CeAl₈Fe₂ type representative SrAl₈Rh₂. The refinement data along with the atomic parameters as well as the interatomic distances are summarized in the publication with the same name as the title above (*Z. Kristallogr.* **2025**, 240, 1-11; DOI: 10.1515/zkri-2024-0115). A picture of a single crystal is shown in **Figure 3.36**. The new compound was attempted to synthesize phase pure but resulted in a mixture of big lath shaped crystal of the SrAl₈Rh₂ phase (CeAl₈Fe₂ type, *Pbam*, $a = 1477.55(2)$, $b = 1270.92(2)$, $c = 412.959(7)$ pm, 75 wt.-%) along AlRh (CsCl type, *Pm $\bar{3}m$* , $a = 296.897(5)$ pm, 18 wt.-%),²¹³ SrAl₄ (BaAl₄ type, *I4/mmm*, $a = 443.08(6)$, $c = 1118.2(2)$ pm, 1 wt.-%),¹⁹¹ a structure derived from Mo₄Zn₈₉Au₁₀ (Cu_{12.3}(Cu_{0.26}Cr_{0.74})₄(Cu_{0.23}Al_{0.77})₂₂Cr₁₄Al₅₀ type, *F $\bar{4}3m$* , $a = 1864.0(2)$ pm)²¹⁴ in which the Mo were replaced by Sr, Zn by Al and Au by Rh atoms, Al₂₁Pt₈ (own type, *I4₁/a*, $a = 1295.1(2)$, $c = 1070.1(3)$ pm, 6 wt.-%)²¹⁰ and at least one unknown phase. The platinum inside the samples most likely originated from the recycled rhodium, which contains Pt as impurity, suggesting that the unknown phase could also contain Pt.

Some of the bigger crystals were sent to Mrs. Dr. Eteri Svanidze (MPI CPFS Dresden) for temperature-dependent electrical resistivity measurements. The results of the resistivity measurements are shown in **Figure 3.36** bottom left. Between 15 and 300 K the resistivity decreases linearly to the decreasing temperature, below 15 K an increase in the electrical resistivity is observable, hinting to a small amount of magnetic impurity. Additionally, a sharp drop below 0.8 K is visible, suggesting a superconducting state, which gets suppressed by applying an external magnetic field as seen with the red measurement with an applied magnetic field of 9 T.

Regarding the crystal chemistry, the interatomic distances found in SrAl₈Rh₂ are $d(\text{Sr}-\text{Al}) = 320\text{-}341$ pm, $d(\text{Al}-\text{Al}) = 270\text{-}329$ pm, $d(\text{Rh}-\text{Al}) = 238\text{-}266$ pm and $d(\text{Rh}-\text{Rh}) = 295$ pm, no Sr–Sr and Sr–Rh distances below 350 pm were observed. The Sr–Al distances are in line with the binary and ternary compounds SrAl₄ (BaAl₄ type, *I4/mmm*): $d(\text{Sr}-\text{Al}) = 341$ pm,¹⁹¹ Sr₅Al₉ (ow type, *R $\bar{3}m$*): $d(\text{Sr}-\text{Al}) = 330\text{-}346$ pm,²¹⁵ Sr₈Al₇ (Ba₈Ga₇ type, *P2₁3*): $d(\text{Sr}-\text{Al}) = 334\text{-}342$ pm,²¹⁶ Sr₂Al₅Pd₄ (own type, *Pnma*): $d(\text{Sr}-\text{Al}) = 337\text{-}347$ pm⁷² and slightly larger than the ones found in Sr₂Al₉Ir₃ (Y₂Ga₉Co₃ type, *Cmcm*): $d(\text{Sr}-\text{Al}) = 309\text{-}314$ pm⁶¹ and smaller than Sr₂AlPd₂ (Ca₂GePd₂ type, *Fdd2*): $d(\text{Sr}-\text{Al}) = 345\text{-}369$ pm.⁶⁵

The Al–Al distances ranges from 270–329 pm, similar distances can be found in SrAl₄ (BaAl₄ type, *I4/mmm*): $d(\text{Al}-\text{Al}) = 265\text{-}315$ pm,¹⁹¹ Sr₅Al₉ (ow type, *R $\bar{3}m$*): $d(\text{Al}-\text{Al}) = 271\text{-}346$ pm,²¹⁵ Sr₈Al₇ (Ba₈Ga₇ type, *P2₁3*): $d(\text{Al}-\text{Al}) = 263\text{-}270$ pm,²¹⁶ Al₉Rh₂ (Al₉Co₂ type, *P12₁/c1*): $d(\text{Al}-\text{Al}) = 273\text{-}347$ pm,²¹⁷ Al₁₃Rh₄ (Al₁₃Fe₄ type, *C12/m1*): $d(\text{Al}-\text{Al}) = 254\text{-}349$ pm,²¹⁸ Al₅Rh₂ (Al₅Co₂ type, *P6₃/mmc*): $d(\text{Al}-\text{Al}) = 272\text{-}325$ pm,²¹⁹ AlRh (CsCl type, *Pm $\bar{3}m$*): $d(\text{Al}-\text{Al}) = 299$ pm,²¹³ as well as in the following ternary compounds, Ca₃Al₁₂Rh₄ (Gd₃Al₁₂Ru₄ type, *P6₃/mmc*): $d(\text{Al}-\text{Al}) = 274\text{-}326$ pm,⁶¹ Eu₃Al₁₂Rh₄ (Gd₃Al₁₂Ru₄ type, *P6₃/mmc*): $d(\text{Al}-\text{Al}) = 275\text{-}331$ pm,⁶¹ Sr₂Al₉Ir₃ (Y₂Ga₉Co₃ type, *Cmcm*): $d(\text{Al}-\text{Al}) = 278\text{-}349$ pm,⁶¹ Sr₂Al₅Pd₄ (own type, *Pnma*): $d(\text{Al}-\text{Al}) = 270\text{-}311$ pm⁷² and SrAl₉Co₂ (BaAl₉Fe₂ type, *P6/mmm*): $d(\text{Al}-\text{Al}) = 285\text{-}290$ pm.⁵⁴ The Rh–Rh distances are smaller than found in Al₁₃Rh₄ (Al₁₃Fe₄ type, *C2/m*): $d(\text{Rh}-\text{Rh}) = 306\text{-}332$ pm,²²⁰ AlRh (CsCl type, *Pm $\bar{3}m$*): $d(\text{Rh}-\text{Rh}) = 299$ pm²¹³ and larger than in Al₅Rh₂ (Al₅Co₂ type, *P6₃/mmc*): $d(\text{Rh}-\text{Rh}) = 284$ pm.²¹⁹ The Al–Rh distances are all in line compared to the binary compounds Al₉Rh₂: $d(\text{Al}-\text{Rh}) = 245\text{-}260$ pm, Al₁₃Rh₄: $d(\text{Al}-\text{Rh}) = 253\text{-}335$ pm,²²⁰ Al₅Rh₂: $d(\text{Al}-\text{Rh}) = 239\text{-}277$ pm,²¹⁹ AlRh: $d(\text{Al}-\text{Rh}) = 259$ pm²¹³ and ternary compounds Ca₃Al₁₂Rh₄ (Gd₃Al₁₂Ru₄ type, *P6₃/mmc*): $d(\text{Al}-\text{Rh}) = 238\text{-}270$ pm,⁶¹ Eu₃Al₁₂Rh₄ (Gd₃Al₁₂Ru₄ type, *P6₃/mmc*): $d(\text{Al}-\text{Rh}) = 240\text{-}270$ pm.⁶¹ When compared to the isotypic EuAl₈Rh₂ (CeAl₈Fe₂ type, *Pbam*, $d(\text{Eu}-\text{Al}) = 317\text{-}339$ pm, $d(\text{Al}-\text{Al}) = 269\text{-}323$ pm, $d(\text{Al}-\text{Rh}) = 237\text{-}267$ pm, $d(\text{Rh}-\text{Rh}) = 294$ pm)⁸⁵ the distances are in a good agreement, suggesting that the Eu is divalent due to the same Eu–Al compared to the Sr–Al distances.

With the single crystal data as starting point, DFT and subsequent LOBSTER calculations were performed, the structure relaxation changes the unit cell parameters by less than one percent. Löwdin charges and bond orders were subsequently calculated using the LOBSTER program package, resulting in high Löwdin charges for the Sr atoms of +1.75 and high Löwdin charges for the Al atoms in the coordination environment of the Sr of –0.30 to –0.36, whereas the Rh and the Al with only Al and Rh in the coordination environment show nearly no charge. Löwdin charges of –0.13 and –0.14 are calculated for two Al positions in the fourfold capped distorted

cube, which possesses Sr atoms in their coordination environment, suggesting that the charge transfer in the structure happens solely from the Sr to the Al atoms in its coordination vicinity. To get insight into the bond order, ICOBIs were calculated and show values below 0.05, indicating ionic interactions between the Sr and Al atoms. In case of the Rh–Al and Al–Al bonding, ICOBI values of 0.20-0.35 and 0.23-0.57 are shown, indicating covalent bonding between the Al–Al and Al–Rh, leading to the polyanionic network of the $[\text{Al}_8\text{Rh}_2]^\delta-$ with the $\text{Sr}^{\delta+}$ occupying the pentagonal prismatic vacancies.

Additionally, to the quantum chemical calculations and resistivity measurements, energy dispersive X-ray spectroscopy (EDX) inside a scanning electron microscope were performed on both the single crystal and bulk material, which are shown in **Figure 3.36** top. The EDX results are in a good agreement with Sr content being 9 at.-%, Al 69/70 at.-% and Rh 22/21 at.-% for SC and bulk sample respectively, compared to the ideal composition of Sr = 9.1 at.-%, Al = 72.7 at.-% and Rh = 18.2 at.-%. Although small deviations from the ideal composition are visible, these can be easily explained by the non-perpendicular orientation of the samples with the electron beam.

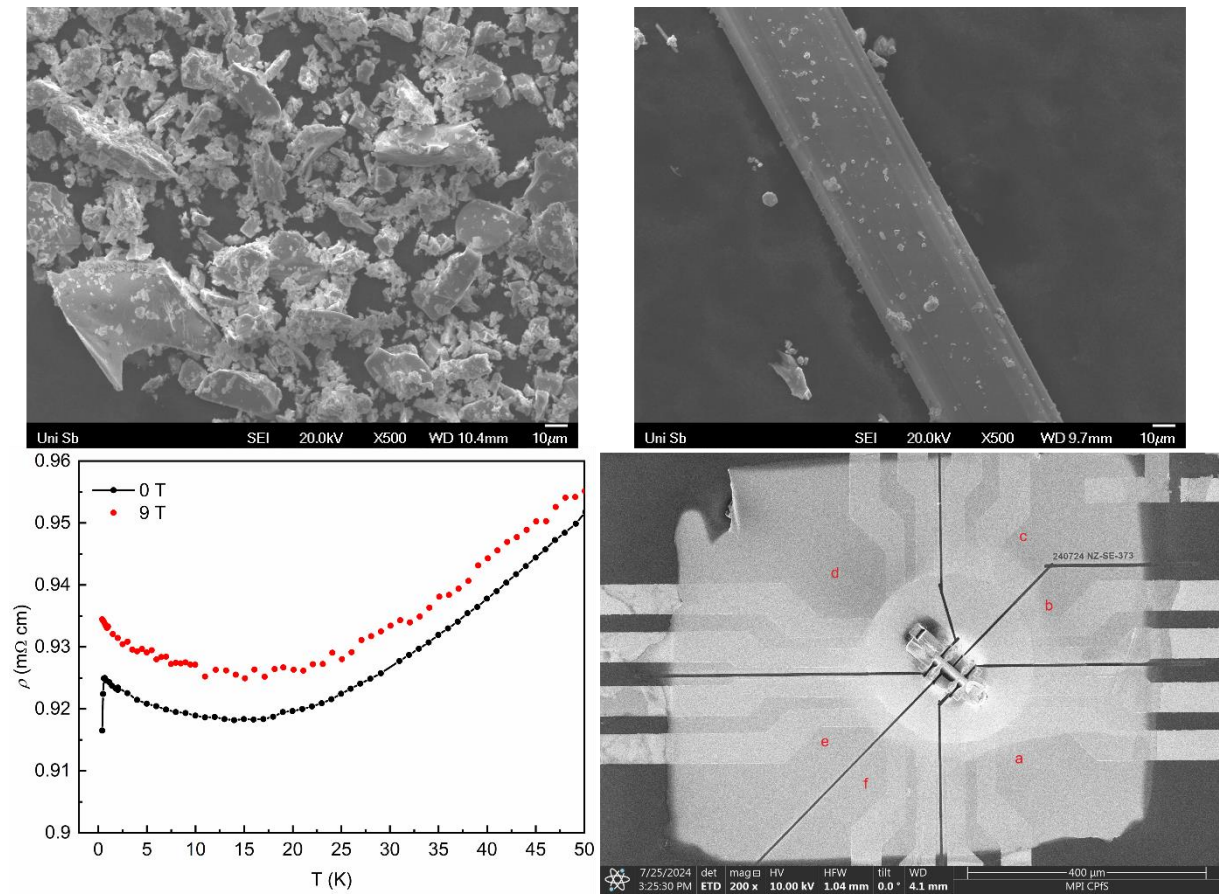


Figure 3.36: Scanning electron microscope image of the powder (top left) and a single crystal of SrAl_3Rh_2 (top right) used for energy dispersive X-ray spectroscopy as well as the anisotropic electrical resistivity measurements (bottom left) alongside the prepared single crystal with the conducting lines (bottom right). The electrical resistance was measured with (red dots) and without (black dots) an applied external magnetic field of 9 T.

Stefan Engel, Judith Bönnighausen, Frank Stegemann, Rachid S. Touzani and Oliver Janka*

SrAl₅Pt₃ and Sr₂Al₁₆Pt₉ – two new strontium aluminum platinides

<https://doi.org/10.1515/znb-2022-0012>

Received February 1, 2022; accepted February 8, 2022;

published online March 11, 2022

Abstract: During attempts to synthesize new platinides in the ternary system Sr–Al–Pt, single crystals of SrAl₅Pt₃ and Sr₂Al₁₆Pt₉ were obtained from a reaction of the elements with the nominal composition Sr₄Al₁₃Pt₉. Both orthorhombic structures were refined based on single crystal x-ray diffraction data (SrAl₅Pt₃: *Pnma*, Wyckoff sequence *c*⁹, *a* = 2065.04(7), *b* = 413.74(1), *c* = 738.98(3) pm, *wR*₂ = 0.0310, 867 *F*² values, 56 variables; Sr₂Al₁₆Pt₉: *Immm*, Wyckoff sequence *l*⁴*j*²*ihga*, *a* = 416.69(2), *b* = 1193.53(6), *c* = 1832.38(9) pm, *wR*₂ = 0.0517, 671 *F*² values, 49 variables); full atomic ordering was observed in both cases. In order to analyze the bonding situation of these new platinides, quantum-chemical calculations were conducted. According to density functional theory both compounds are polar intermetallics with high negative charges on the Pt atoms and covalently bonded [Al₅Pt₃]/[Al₁₆Pt₉] networks showing strong Pt–Al alongside of weak Al–Al and Pt–Pt bonding.

Keywords: aluminum; intermetallics; platinum; quantum chemistry; strontium.

Dedicated to Professor Martin Lerch on the Occasion of his 60th Birthday.

1 Introduction

Within the last years, the knowledge about the crystal chemistry of ternary transition metal aluminum intermetallics of the alkaline earth elements has significantly

*Corresponding author: Oliver Janka, Anorganische Festkörperchemie, Universität des Saarlandes, Campus C4.1, Saarbrücken, 66123, Germany, E-mail: oliver.janka@uni-saarland.de
Stefan Engel, Anorganische Festkörperchemie, Universität des Saarlandes, Campus C4.1, Saarbrücken, 66123, Germany
Judith Bönnighausen and Frank Stegemann, Institut für Anorganische und Analytische Chemie, Universität Münster, Corrensstrasse 30, Münster, 48149, Germany
Rachid S. Touzani, Institut für Werkstoff- und Fügetechnik (IWF), Otto-von-Guericke-Universität Magdeburg, Universitätsplatz 2, Magdeburg, 39106, Germany

increased since these compounds are especially suitable for investigations of the bonding situation in intermetallic compounds. Due to the absent Curie-paramagnetism, e. g. ²⁷Al MAS-NMR investigations are possible [1] which can be combined with x-ray photoelectron spectroscopy and quantum-chemical calculations.

Especially for the late and heavy transition metal Pt, hardly any compounds had been reported before. Ba₃Al₄Pt₄ (*Cmcm*, own structure type [2]), BaAl₂Pt (*Cmcm*, MgCuAl₂ type [3]) and Ba₆Al₄₉Pt₂₂ (*P6₃/mcm*, own structure type [4]) for example, have thus far been the sole examples for barium aluminum platinides. For the lighter homologues Ni and Pd only two compounds, BaAl₉Ni₂ (*P6/mmm*, BaFe₂Al₉ type [5]) and BaAl_{8.5}Pd_{4.5} (*I4/mcm*, coloring variant of the CeNi₉Si₄ type [6]), have been observed.

For calcium as alkaline earth element, a slightly greater number of compounds has been reported. The equiatomic compounds CaAlPd (*Pbcm*, own type [7, 8]) and CaAlPt (*Pnma*, TiNiSi type [9]), but also Ca₂AlPd₂ and Ca₂AlPt₂ (both *C2/c*, Ca₂Ir₂Si type [10]) as well as CaAl₅Pd₃ (*P6/mmm*, CaCu₅ derivative [11]), CaAl₂Pt (*Cmcm*, MgCuAl₂ type [3]) and Ca₂Al₁₅Pt₆ (modulated monoclinic structure, Sc₂Al₁₅Pt₆ type [12]) are well documented. For *T* = Ni finally, CaAl₉Ni (*P6₃/mmc*, own type [13, 14]) and CaAl₈Ni₂ (*Pbam*, CaFe₂Al₈ type [15, 16]) have been reported as ordered compounds.

For strontium, also a very limited number of compounds has been reported to date. SrAl₉Ni₂ (*P6/mmm*, BaFe₂Al₉ type [5]) is the sole Ni representative, while for palladium Sr₂AlPd₂ (*Fdd2*, Ca₂Pd₂Ge type [17]) and Sr₂Al₅Pd₄ (*Pnma*, own type [18]) were included in previous studies. Figure 1 depicts the ternary system Sr–Al–Pt, where the data for the binary compounds were taken from the Pearson database [19]. As ternary representatives, SrAl₂Pt (*Cmcm*, MgCuAl₂ type [3]), SrAl₂Pt₂ (modulated tetragonal structure, own structure type [20]), SrAl₂Pt₃ (*P6/mmm*, CeCo₃B₂ type [17]) and Sr₂Al₈Pt₃ (site occupation variant of the Eu₂Ni₈Si₃ type [21]) are listed.

Here we report on the new strontium aluminum platinides SrAl₅Pt₃ and Sr₂Al₁₆Pt₉. Both crystallize in the orthorhombic crystal system with space groups *Pnma* and *Immm* and have been obtained from a reaction with the nominal composition Sr₄Al₁₃Pt₉. The title compounds are isostructural to CeAl₅Pt₃ and Ce₂Al₁₆Pt₉ – thus far the sole aluminum compounds with these structure types.

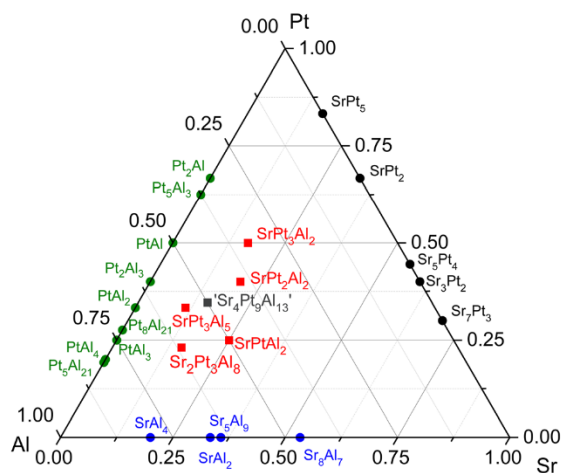


Figure 1: The ternary system Sr–Al–Pt. The data for the depicted compounds has been taken from the Pearson database [18] or the papers cited in the Introduction.

Recently, however, the series of gallium platinides MGa_5Pt_3 ($M = Ca\text{--}Ba, Eu$ [22, 23]) adopting the $CeAl_5Pt_3$ structure type has been completed. As shown by Pöttgen and co-workers [22], $CeAl_5Pt_3$ has to be regarded as a site occupation variant of the YNi_5Si_3 type structure, and the two structures are therefore rather isopointal than isostructural. The Ni positions are occupied by Al/Ga atoms while on the Si sites the Pt atoms are found. In the case of $Sr_2Al_{16}Pt_9$, isotypism with $Ce_2Al_{16}Pt_9$ [24] was observed, the sole representative of this structure type thus far, however, $Th_2Al_{15}Ni_{10}$ has been reported [25] with the same space group and Wyckoff sequence and could therefore also be regarded as a site occupation variant of the $Ce_2Al_{16}Pt_9$ type structure.

2 Experimental

2.1 Synthesis

Initially, a sample with the nominal composition $Sr_4Al_{13}Pt_9$ was prepared from which lath- and block-shaped single crystals were isolated. Single crystal x-ray diffraction experiments led to the refined compositions $SrAl_5Pt_3$ and $Sr_2Al_{16}Pt_9$, respectively. Subsequently, additional synthetic attempts were made using the composition obtained from the refined single crystal diffraction data. Sublimed strontium (Sigma-Aldrich), platinum pieces (Agosi AG) and aluminum turnings (Koch Chemicals), all with stated purities above 99% were used for the reported syntheses. Samples were prepared on a 300 mg scale. The Sr pieces were stored under an argon atmosphere; surface contaminations on the pieces were removed mechanically under sodium dried cyclohexane prior to the reaction. For all reactions, the elements were

arc-welded [26] in tantalum tubes in an argon atmosphere of about 800 mbar. The argon gas was purified over a titanium sponge (873 K), molecular sieves and silica gel prior to the use. The sealed tantalum ampoules were placed in the water-cooled sample chamber of a high-frequency furnace (Hüttinger, TIG 5/300) [27]. Water-cooling was used to prevent reactions of the Ta ampoules. The Ta-container was heated up to ~ 1500 K within 2 min, dwelled at that temperature for 10 min followed by slow cooling to ~ 1000 K. The cooling was achieved by reducing the power output of the generator, leading to a cooling rate of about 15 K min^{-1} . After an annealing step of 4 h at this temperature, the samples were cooled naturally by shutting off the power supply. The temperature was controlled by a pyrometer (Sensortherm, Metis MS09) with a stated accuracy of ± 50 K. The sample with the nominal composition of $Sr_{1.03}Al_5Pt_3$ was additionally annealed at 923 K for 7 d. All samples could easily be separated from the container material and no reactions with the tantalum ampoules could be observed.

2.2 X-ray diffraction

The phase purity of the polycrystalline samples was checked by powder x-ray diffraction (PXRD) patterns using the Guinier method on an Enraf-Nonius FR552 camera, equipped with an imaging plate detector (Fujifilm BAS-1800) and using $CuK\alpha$ radiation. α -Quartz ($a = 491.30$, $c = 540.46$ pm) was utilized as internal standard.

PXRD patterns of the powdered samples were recorded at room temperature on a D8-A25-advance diffractometer (Bruker, Karlsruhe, Germany) in Bragg–Brentano θ – θ -geometry (goniometer radius 280 mm) with $CuK\alpha$ -radiation ($\lambda = 154.0596$ pm). A $12\ \mu\text{m}$ Ni foil working as $K\beta$ filter and a variable divergence slit were mounted at the primary beam side. An LYNXEYE detector with 192 channels was used at the secondary beam side. Experiments were carried out in a 2θ range of 6 to 130° with a step size of 0.013° and a total scan time of 1 h. The recorded data was evaluated using the Bruker TOPAS 5.0 software [28], with the observed reflections being treated via single-line fits.

Lath- and block-shaped crystallites of $SrAl_5Pt_3$ (Figure 2, left) and $Sr_2Al_{16}Pt_9$ (Figure 2, right) were extracted from a crushed sample with a nominal composition of $Sr_4Al_{13}Pt_9$ and investigated at room temperature on a Bruker X8 APEX2, Nonius κ -CCD diffractometer, operating with graphite monochromatized $MoK\alpha$ ($\lambda = 0.71073\ \text{\AA}$) radiation. Numerical absorption corrections using the Bruker SadABS data package [29] was applied to the data set. The structures were solved and refined using SUPERFLIP [30] and JANA2006 [31, 32].

CCDC 2123496 and 2141827 contain the supplementary crystallographic data for this paper. The data can be obtained free of charge from The Cambridge Crystallographic Data Centre via www.ccdc.cam.ac.uk/structures.



Figure 2: Light microscopic image from the crystallites of $SrAl_5Pt_3$ (left, $120 \times 20 \times 20\ \mu\text{m}$) and $Sr_2Al_{16}Pt_9$ (right, $75 \times 40 \times 40\ \mu\text{m}$).

2.3 Quantum-chemical calculations

The first-principles calculation were carried out with Quantum ESPRESSO [33, 34] for the structural relaxation of SrAl_5Pt_3 and $\text{Sr}_2\text{Al}_{16}\text{Pt}_9$ using PAW pseudopotentials [35] from the PSLibrary version 1.0.0 [36]. The kinetic energy cut-off for the plane waves was set to 100 Ry, while the cut-off for the charge density and potential was set to 400 Ry. The structural relaxation stopped when a total energy convergence of 10^{-6} Ry and a force convergence of 10^{-5} Ry/ a_0 was reached. The Marzari–Vanderbilt cold smearing [37] and a Gaussian spreading of 0.01 Ry were chosen to account for the Brillouin-zone integration. The k -mesh was divided by $2 \times 14 \times 8$ in SrAl_5Pt_3 and $14 \times 6 \times 4$ in $\text{Sr}_2\text{Al}_{16}\text{Pt}_9$ using the Monkhorst-Pack algorithm [38]. Exchange and correlation in this density functional theory (DFT) based method were treated with the generalized gradient approximation (GGA) functional as parameterized by Perdew, Burke and Ernzerhof (PBE-GGA) [39]. Quantum ESPRESSO was also used to generate the all-electron and valence electron densities, which were then used to calculate the Bader charges according to the methods described by Henkelman et al. [40–42] and Yu and Trinkle [43] with the *critic2* program [44, 45]. The chemical bonding analysis was carried out using the tight-binding, linear muffin-tin orbitals with the atomic spheres approximation (TB-LMTO-ASA) [46, 47] as implemented in the TB-LMTO 4.7 program [48]. Exchange and correlation were treated with the GGA functional as parameterized by Perdew et al. [49]. The k -mesh was $4 \times 22 \times 12$, which led to 252 k -points in SrAl_5Pt_3 and $22 \times 22 \times 22$, which led to 1530 k -points in $\text{Sr}_2\text{Al}_{16}\text{Pt}_9$ in the irreducible Brillouin zone (IBZ). The radii of the automatically generated *Wigner–Seitz* cells for Sr, Pt and Al were 2.32 Å, 1.48–1.53 Å and 1.39–1.56 Å in SrAl_5Pt_3 and 2.37 Å, 1.50–1.53 Å and 1.42–1.54 Å in $\text{Sr}_2\text{Al}_{16}\text{Pt}_9$. In the LMTO calculations no empty spheres were needed for SrAl_5Pt_3 , but some were included for $\text{Sr}_2\text{Al}_{16}\text{Pt}_9$. The bonding analysis was carried out by calculation of the density-of-states (DOS) and the crystal orbital Hamilton population (COHP) [50] and its integrals (ICOHP). The ICOHP can be seen as a semi-quantitative bonding energy which measures covalent contribution in solids. Because –COHP values are plotted, negative –COHP are antibonding states, positive ones are bonding states and non-bonding states have –COHP values of zero. The Fermi level was set to 0 eV as reference.

3 Results

3.1 Powder x-ray diffraction

Initially, a sample with the nominal composition $\text{Sr}_4\text{Al}_{13}\text{Pt}_9$ was prepared from which single crystals of SrAl_5Pt_3 and $\text{Sr}_2\text{Al}_{16}\text{Pt}_9$ were extracted and investigated via single crystal x-ray diffraction experiments (*vide infra*). A Rietveld refinement of the powder diffraction pattern collected on nominal $\text{Sr}_4\text{Al}_{13}\text{Pt}_9$ revealed the presence of 73(1) at.-% SrAl_5Pt_3 , 7(1) at.-% $\text{Sr}_2\text{Al}_{16}\text{Pt}_9$ along with 12(1) at.-% Al_2Pt and 8(1) at.-% AlPt (Figure 3, top). Subsequently, a sample with the composition SrAl_5Pt_3 was synthesized. Here, 44(1) at.-% SrAl_5Pt_3 , 1(1) at.-% $\text{Sr}_2\text{Al}_{16}\text{Pt}_9$ along with 44(1) at.-% Al_2Pt and 11(1) at.-% AlPt were observed (Figure 3, middle). With an excess of Sr ($\text{Sr}_{1.03}\text{Al}_5\text{Pt}_3$), the formation of the

binary phases could be suppressed and 74(1) at.-% SrAl_5Pt_3 and 26(1) at.-% $\text{Sr}_2\text{Al}_{16}\text{Pt}_9$ were found upon refinement (Figure 3, bottom). Lattice parameters from the refinements are listed in Table 1.

3.2 Single crystal x-ray diffraction and structure refinement

Lath-shaped single crystals (Figure 2, left) were isolated from a sample with a nominal composition of $\text{Sr}_4\text{Al}_{13}\text{Pt}_9$ and mounted onto a Bruker X8 APEX2 single crystal diffractometer. Careful analysis of the obtained data revealed an orthorhombic lattice, and space group $Pnma$ was found to be correct. The structure was solved using the

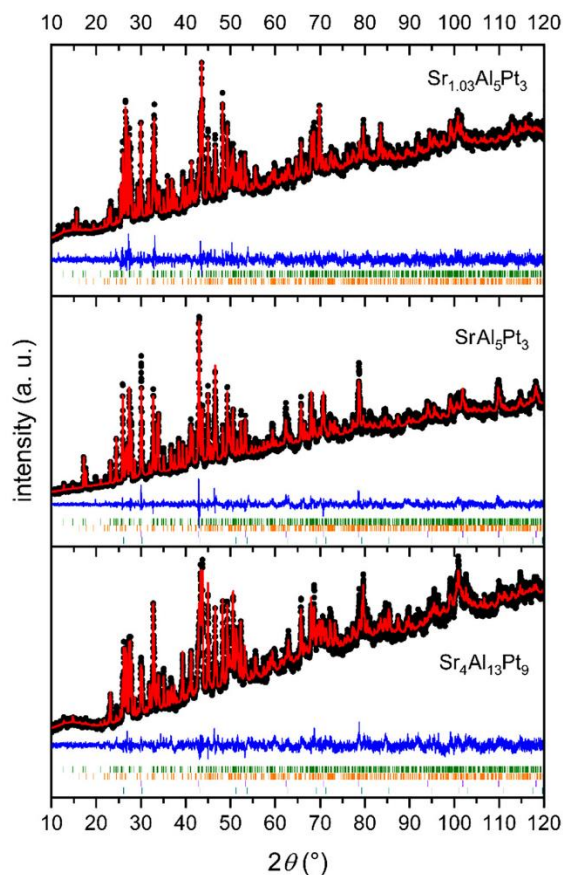


Figure 3: Rietveld refinements of PXRD data obtained from samples with the nominal compositions $\text{Sr}_{1.03}\text{Al}_5\text{Pt}_3$ (top), SrAl_5Pt_3 (middle) and $\text{Sr}_4\text{Al}_{13}\text{Pt}_9$ (bottom). Black dots represent the experimental data, the red line the sum of the calculated data and the blue line the difference between experimental and calculated data. The dashes correspond to the Bragg positions of SrAl_5Pt_3 (green), $\text{Sr}_2\text{Al}_{16}\text{Pt}_9$ (orange), Al_2Pt (purple) and AlPt (blue).

Table 1: Lattice parameters (Guinier powder, single crystal and literature data), and unit cell volumes of SrAl₅Pt₃, Sr₂Al₁₆Pt₉ and selected structurally related compounds.

Compound	<i>a</i> (pm)	<i>b</i> (pm)	<i>c</i> (pm)	<i>V</i> (nm ³)	Ref.
SrAl ₅ Pt ₃ ^{SC}	2065.04(7)	413.74(1)	738.98(3)	0.6314	*
SrAl ₅ Pt ₃ ^{P1}	2067.07(6)	414.16(2)	739.88(3)	0.6334	*
SrAl ₅ Pt ₃ ^{P2}	2067.32(6)	414.27(3)	740.13(4)	0.6339	*
SrAl ₅ Pt ₃ ^{P3}	2067.40(5)	414.30(1)	740.12(2)	0.6340	*
SrAl ₅ Pt ₃ ^{DFT}	2081.49	417.83	746.95	0.6496	*
CaGa ₅ Pt ₃ ^L	2082.5(4)	406.05(8)	739.2(1)	0.6251	[22]
SrGa ₅ Pt ₃ ^L	2092.3(1)	413.16(2)	740.88(3)	0.6404	[23]
BaGa ₅ Pt ₃ ^L	2104.8(2)	420.15(4)	747.7(1)	0.6612	[22]
BaGa ₅ Pt ₃ ^L	2104.3(2)	420.11(5)	747.80(8)	0.6611	[23]
EuGa ₅ Pt ₃ ^L	2085.5(5)	412.75(9)	738.7(1)	0.6359	[22]
Sr ₂ Al ₁₆ Pt ₉ ^{SC}	416.69(2)	1193.53(6)	1832.38(9)	0.9113	*
Sr ₂ Al ₁₆ Pt ₉ ^{P1}	407.49(4)	1200.53(8)	1842.54(11)	0.9009	*
Sr ₂ Al ₁₆ Pt ₉ ^{P2}	417.08(1)	1194.25(5)	1833.08(8)	0.9131	*
Sr ₂ Al ₁₆ Pt ₉ ^{P3}	417.28(3)	1193.73(5)	1833.18(8)	0.9131	*
Sr ₂ Al ₁₆ Pt ₉ ^{DFT}	418.57	1207.65	1854.44	0.9374	*
Ce ₂ Al ₁₆ Pt ₉ ^L	415.97(9)	1191.0(3)	1818.6(4)	0.9010	[24]
Th ₂ Al ₁₅ Ni ₁₀ ^L	399(4)	1118(4)	1734(4)	0.7735	[25]

*this work; ^Lliterature data; ^Ppowder data (^{P1}nominal sample composition SrAl₅Pt₃, ^{P2}nominal sample composition Sr_{1.03}Al₅Pt₃, ^{P3}nominal sample composition Sr₄Al₁₃Pt₉); ^{SC}single crystal data; ^{DFT}quantum-chemical data.

charge flipping algorithm of SUPERFLIP [30], and a least squares refinement on F^2 using the program JANA2006 [31, 32] was carried out. All atomic positions were refined with anisotropic displacement parameters and as a check for correct compositions, the occupancy parameters were refined in a separate series of least-square refinements. All sites were fully occupied within three standard deviations leading to the composition of SrAl₅Pt₃; final difference Fourier syntheses were contourless. From the Pearson database [19], isotypism with CeAl₅Pt₃ [51] was deduced. For the block-shaped crystals (Figure 2, right) found in the same sample, an orthorhombic body-centered cell with space group *Immm* was observed. The structure was again solved and refined using SUPERFLIP [30] and JANA2006 [31, 32]. All atomic positions were refined with anisotropic displacement parameters and all sites are fully occupied within three standard deviations leading to the composition Sr₂Al₁₆Pt₉. Again, final difference Fourier syntheses were contourless. The Pearson database [19] revealed isotypism with Ce₂Al₁₆Pt₉ [24]. Details of the structure determination, atomic parameters and interatomic distances can be found in Tables 2–6.

3.2 Crystal chemistry

SrAl₅Pt₃ crystallizes in the orthorhombic crystal system with space group *Pnma* ($a = 2065.0(2)$, $b = 413.74(4)$,

Table 2: Crystallographic data and structure refinement for SrAl₅Pt₃ (YNi₅Si₃ type, space group *Pnma*, $Z = 4$) and Sr₂Al₁₆Pt₉ (Ce₂Al₁₆Pt₉ type, space group *Immm*, $Z = 2$).

Sum formula	SrAl ₅ Pt ₃	Sr ₂ Al ₁₆ Pt ₉
Formula weight, g mol ⁻¹	807.8	2362.7
Lattice parameters	See Table 1	See Table 1
Calcd. density, g cm ⁻³	8.50	8.61
Crystal size, μm ³	150 × 20 × 20	75 × 40 × 40
Diffractometer	Bruker X8 APEX2	Bruker X8 APEX2
Wavelength; λ, pm	0.71073	0.71073
Absorption correction	Multi-scan Bruker SadABS	Multi-scan Bruker SadABS
	2016 [29]	2016 [29]
Abs. coefficient, mm ⁻¹	75.2	75.3
$F(000)$, e	1348	1972
θ range, deg	1.97–27.99	2.04–27.83
Range <i>hkl</i>	–26, +27; ±5; ±9	–2, +5; –12, +15; ±24
Total no. reflections	10,040	4230
Independent reflections/ R_{int}	867	671
Reflections $I > 3 \sigma(I)/R_\sigma$	815	650
Data/parameters	867/56	671/49
Goodness of fit on F^2	0.960	1.510
$R1/wR2$ for $I > 3 \sigma(I)$	0.0121/0.0310	0.0199/0.0517
$R1/wR2$ (all data)	0.0137/0.0317	0.0215/0.0526
Extinction coefficient	175(7)	121(15)
Extinction scheme	Lorentzian	Lorentzian isotropic
	isotropic [63]	[63]
Larg. diff. peak/hole, e Å ⁻³	+0.72/–0.94	+2.37/–1.41

Table 3: Atomic coordinates and displacement parameters (in pm²) of SrAl₅Pt₃ (YNi₅Si₃ type, space group *Pnma*, all atoms on Wyckoff positions 4c: *x*, 1/4, *z*).

Atom	<i>x</i>	<i>z</i>	<i>U</i> ₁₁	<i>U</i> ₂₂	<i>U</i> ₃₃	<i>U</i> ₁₃	<i>U</i> _{eq} ^a
Sr	0.35981(3)	0.88319(8)	68(3)	76(3)	61(3)	6(2)	68(2)
Pt1	0.07088(1)	0.66813(3)	61(1)	67(1)	45(1)	2(1)	58(1)
Pt2	0.08399(1)	0.07338(4)	60(1)	63(1)	56(1)	−9(1)	60(1)
Pt3	0.26361(1)	0.38829(3)	68(1)	60(1)	59(1)	5(1)	62(1)
Al1	0.00830(9)	0.3697(3)	87(9)	55(9)	65(9)	7(7)	69(5)
Al2	0.19989(9)	0.6943(3)	79(9)	54(9)	49(9)	−17(7)	61(5)
Al3	0.20901(9)	0.0795(3)	70(9)	72(9)	54(9)	13(7)	65(5)
Al4	0.38358(9)	0.3522(3)	84(9)	76(10)	103(10)	−21(7)	88(5)
Al5	0.48200(9)	0.6132(3)	55(9)	73(9)	60(9)	−4(7)	63(5)

^aThe isotropic displacement parameter *U*_{eq} is defined as: *U*_{eq} = 1/3 (*U*₁₁ + *U*₂₂ + *U*₃₃) (pm²); *U*₁₂ = *U*₂₃ = 0. Standard deviations are given in parentheses.

Table 4: Atomic coordinates and displacement parameters (in pm²) of Sr₂Al₁₆Pt₉ (Ce₂Al₁₆Pt₉ type, space group *Immm*).

Atom	<i>x</i>	<i>y</i>	<i>z</i>	<i>U</i> ₁₁	<i>U</i> ₂₂	<i>U</i> ₃₃	<i>U</i> ₂₃	<i>U</i> _{eq} ^a
Sr	0	0	0.22870(8)	63(6)	21(6)	32(7)	0	39(4)
Pt1	0	0.31032(3)	0.34237(2)	36(2)	6(2)	12(2)	3(14)	18(1)
Pt2	1/2	0	0.37870(3)	26(2)	7(3)	19(3)	0	15(2)
Pt3	0	0.25284(3)	1/2	63(3)	47(3)	11(3)	0	40(2)
Pt4	0	0	0	133(4)	78(4)	24(4)	0	78(2)
Al1	0	0.1175(3)	0.3931(2)	37(13)	11(14)	33(16)	−13(12)	27(8)
Al2	0	0.1704(3)	0.0796(2)	41(14)	36(15)	40(16)	14(12)	39(9)
Al3	0	0.3064(3)	0.2053(2)	49(13)	24(15)	21(15)	−5(12)	31(8)
Al4	1/2	0	0.0866(3)	50(20)	60(20)	60(20)	0	56(13)
Al5	0	0.3844(4)	0	53(19)	20(20)	20(20)	0	31(12)

^aThe isotropic displacement parameter *U*_{eq} is defined as: *U*_{eq} = 1/3 (*U*₁₁ + *U*₂₂ + *U*₃₃) (pm²); *U*₁₂ = *U*₁₃ = 0. Standard deviations are given in parentheses.

c = 738.98(8) pm, *oP*36, *c*⁹) and is isostructural with the thus far sole aluminum representative CeAl₅Pt₃ [51]. Both aluminum compounds as well as the reported gallium compounds *M*Ga₅Pt₃ (*M* = Ca–Ba, Eu) cannot be considered isostructural but rather isopointal to the prototypic YNi₅Si₃ structure, especially since the [Ni₅Si₃]^{6−} polyanion exhibits a variation of the site occupation compared to the respective platinides.

The crystal structure of SrAl₅Pt₃ is depicted in a projection along the *b* axis in Figure 4. The Sr atoms are surrounded by six Pt and six Al atoms in the shape of a slightly distorted hexagonal prism with an alternating arrangement of the atoms within the hexagon but congruent arrangement of top and bottom face (Figure 5). These Sr@Al₆Pt₆ prisms are connected over the hexagonal faces to form strands along [010]. Within the prism, the interatomic Sr–Al distances range between 322 and 342 pm, while the Sr–Pt distances are between 328 and 330 pm.

Sr₂Al₁₆Pt₉ also crystallizes in the orthorhombic crystal system, however, with the body-centered space group

Immm (*a* = 416.69(7), *b* = 1193.53(1), *c* = 1832.38(3) pm, *oI*54, *I*⁴₂*hga*), isostructural to Ce₂Al₁₆Pt₉ [24]. The crystal structure projected along the *a* axis is depicted in Figure 6. Like in SrAl₅Pt₃, the Sr atoms are surrounded in the shape of a hexagonal prism by six Pt and six Al atoms (Figure 7). Here, these Sr@Pt₆Al₆ prisms form strands along [100]. Within the prism, the interatomic Sr–Al distances are in the range between 332 and 341 pm, the Sr–Pt distances are 334 and 345 pm long. In both compounds, both distances are in line with the ones found in binary intermetallics e. g. SrAl₂ (KHg₂ type, 327–360 pm [52, 53]), SrAl₄ (BaAl₄ type, 342 pm [54]), SrPt₂ (MgCu₂ type, 274 pm [55]) or SrPt₅ (CaCu₅ type, 312 & 347 pm [55]) as well as with the sum of the covalent radii (Sr + Al = 192 + 125 = 317 pm; Sr + Pt = 192 + 129 = 321 pm [56]). The known ternary compounds in this system, SrAl₂Pt (Sr–Al: 340–343 pm; Sr–Pt: 308–336 pm) [3], Sr₂Al₈Pt₃ (Sr–Al: 314–343 pm; Sr–Pt: 335–352 pm) [21], SrAl₂Pt₂ (Sr–Al: 335–338 pm; Sr–Pt: 330–334 pm) [20] or SrAl₂Pt₃ (Sr–Al: 327 pm; Sr–Pt: 344 pm) [17], also exhibit similar distances.

Table 5: Interatomic distances (pm) in of SrAl₅Pt₃ (YNi₅Si₃ type, space group *Pnma*). All distances of the first coordination spheres are listed. Standard deviations are equal or smaller than 0.2 pm.

Sr	1	Al5	321.7	Al1	1	Pt1	255.6			
	2	Pt1	328.1		2	Pt1	265.2			
	2	Pt3	328.2		1	Pt2	268.9			
	2	Pt2	329.7		2	Al5	281.3			
	2	Al2	332.9		2	Al1	284.7			
	2	Al3	336.6		1	Al4	305.3			
	2	Al1	342.2		Al2	1	Pt3	261.6		
	1	Al3	343.6			2	Pt3	262.7		
	1	Al4	350.1			1	Pt1	267.1		
	1	Al1	357.0			1	Al3	285.4		
	1	Al2	358.5			2	Al3	292.3		
	Pt1	1	Al5			244.5	2	Al4	293.5	
		1	Al1			255.6	Al3	1	Pt3	254.6
		2	Al4			264.8		2	Pt3	256.8
		2	Al1			265.2		1	Pt2	258.3
1		Al2	267.1	1		Al2		285.4		
1	Pt2	300.7	2	Al2		292.3				
Pt2	2	Al5	249.5	2		Al4	328.0			
	1	Al5	251.7	Al4		1	Pt3	249.2		
	1	Al3	258.3			2	Pt1	264.8		
	1	Al1	268.9			2	Pt2	272.1		
	2	Al4	272.1		1	Al5	280.2			
1	Pt1	300.7	2		Al2	293.5				
Pt3	1	Al4	249.2	1	Al1	305.3				
	1	Al3	254.6	2	Al3	328.0				
	2	Al3	256.8	Al5	1	Pt1	244.5			
	1	Al2	261.6		2	Pt2	249.5			
	2	Al2	262.7		1	Pt2	251.7			
1	Al4	280.2	2		Al5	276.3				
			2		Al1	281.3				

Table 6: Interatomic distances (pm) in of Sr₂Al₁₆Pt₉ (Ce₂Al₁₆Pt₉ type, space group *Immm*). All distances of the first coordination spheres are listed. Standard deviations are equal or smaller than 0.2 pm.

Sr	2	Al1	332.3	Al2	1	Pt4	250.3		
	2	Al4	333.5		2	Pt1	253.8		
	4	Al3	333.8		2	Pt3	270.3		
	4	Pt1	334.2		1	Al3	281.8		
	2	Al2	340.6		2	Al4	291.4		
	2	Pt2	344.9		1	Al2	291.7		
	Pt1	4	Al1		248.1	Al3	1	Al5	294.1
		1	Al3		251.2		1	Pt1	251.2
		2	Al2		253.8		2	Pt1	265.4
		2	Al4		261.2		2	Pt2	277.7
		2	Al3		265.4		2	Al2	281.8
	Pt2	1	Pt3		296.6	Al4	2	Al1	290.2
		4	Al1		252.5		2	Al3	297.2
		2	Al5		261.6		2	Pt1	261.2
		2	Al3		277.7		2	Pt4	261.9
2		Al1	253.8	4	Al2		291.4		
Pt3	2	Al5	265.0	Al5	2	Pt2	261.6		
	4	Al2	270.3		2	Pt3	265.0		
	2	Pt1	296.9		1	Al5	275.9		
	4	Al2	250.3		4	Al1	286.0		
	4	Al4	261.9		2	Al2	294.1		
Pt4	1	Pt1	248.1						
	2	Pt2	252.5						
	1	Pt3	253.8						
	1	Al1	280.5						
	2	Al5	286.0						
	2	Al3	290.2						

Within the [Al₅Pt₃]^{δ-} polyanion, three platinum and five aluminum sites are observed (Figure 5) while the [Al₁₆Pt₉]^{δ-} polyanion has four platinum and five aluminum sites (Figure 7). In both networks, hexagonal cavities are observed in which the Sr cations are located. In SrAl₅Pt₃, the Pt atoms exhibit a coordination number of seven, with highly asymmetrical coordination spheres and interatomic distances between 245 and 272 pm. In Sr₂Al₁₆Pt₉, Pt1 exhibits a sevenfold coordination environment, while Pt2 to Pt4 exhibit coordination numbers of eight with Pt–Al distances in the range from 248 to 278 pm. These distances are in line with those in binary (AlPt: 248–273 pm [57]; Al₂Pt: 256 pm [58]) and ternary intermetallics (SrAl₂Pt: 255–257 pm [3]; Sr₂Al₈Pt₃: 252–279 pm [21]; SrAl₂Pt₂: 249–255 pm [20]; SrAl₂Pt₃: 254 pm [17]) as well as with the sum of the covalent radii (Pt + Al = 129 + 125 = 254 pm [56]). In both compounds, the homoatomic distances (SrAl₅Pt₃: Pt–Pt: 301 pm; Al–Al: 276–347 pm; Sr₂Al₁₆Pt₉: Pt–Pt: 297 pm; Al–Al: 276–317 pm) are significantly longer compared to the sum of the covalent

radii as well as the distances found in elemental Pt (277 pm [59]). The Al–Al distances, however, agree with what is observed in elemental Al (286 pm [60]), therefore suggesting partial bonding contributions.

3.3 Quantum-chemical calculations

The results of the DFT calculations regarding the structural optimization, Bader charges and covalent bonding situation are discussed in this paragraph. The experimental data of the single crystals was used as a starting point for the DFT-GGA-PBE calculations. The optimized lattice parameters for SrAl₅Pt₃ are $a_{\text{theo}} = 2081.49$ pm, $b_{\text{theo}} = 417.83$ pm and $c_{\text{theo}} = 746.95$ pm, and the ones for Sr₂Al₁₆Pt₉ are $a_{\text{theo}} = 418.57$ pm, $b_{\text{theo}} = 1207.65$ pm and $c_{\text{theo}} = 1854.44$ pm. Both sets are in very good agreement with the experimental XRD results (Table 1). The bond lengths after structural relaxation can be found in Tables 7 and 8. In general, the bond lengths are slightly larger than those found in the experiments as often observed with

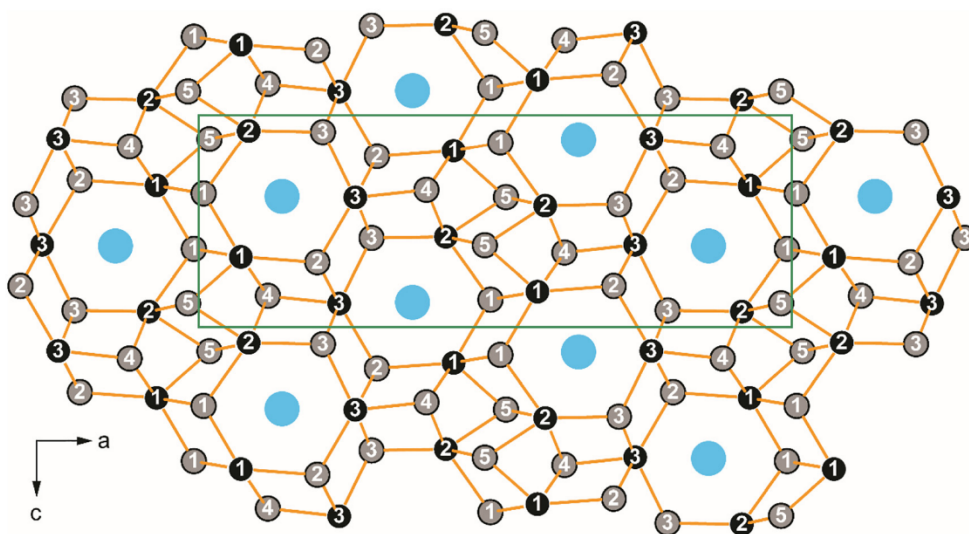


Figure 4: Unit cell of SrAl_5Pt_3 , projected along the b axis. Sr, Pt and Al atoms are shown in blue, black and grey circles. The shortest Pt–Al bonds are emphasized.

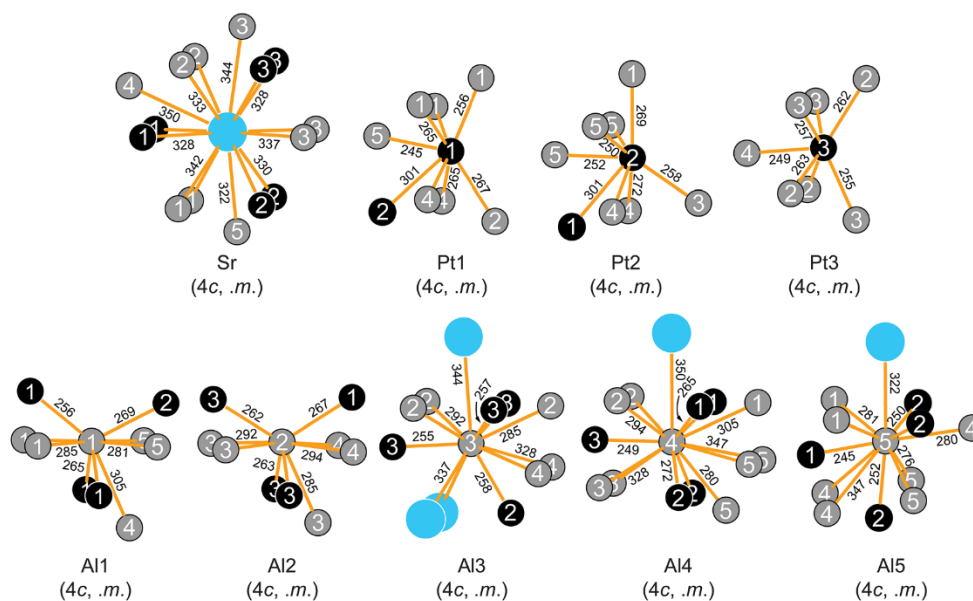


Figure 5: Coordination environments surrounding the Sr, Pt and Al atoms in the structure of SrAl_5Pt_3 . Sr, Pt and Al atoms are shown as blue, black and grey circles. Wyckoff sites, site symmetries and interatomic distances (in pm) are given.

the GGA functional, but still in good agreement. The absolute Pearson electronegativities of Sr, Pt and Al are 2.0, 5.6 and 3.23 eV, respectively, and hence one would expect a relatively high positive charge on Sr to balance the negative charge of the polyanionic $[\text{Al}_5\text{Pt}_3]^{6-}$ and

$[\text{Al}_{16}\text{Pt}_9]^{6-}$ networks. To check this hypothesis, Bader charges were calculated. Bader charges according to the methods of Henkelman et al., and of Yu and Trinkle are +1.33/+1.33, $-3.02/-3.03$ to $-3.35/-3.36$ and +1.52/+1.54 to +1.80/+1.79 for Sr, Pt and Al in SrAl_5Pt_3 and +1.32/

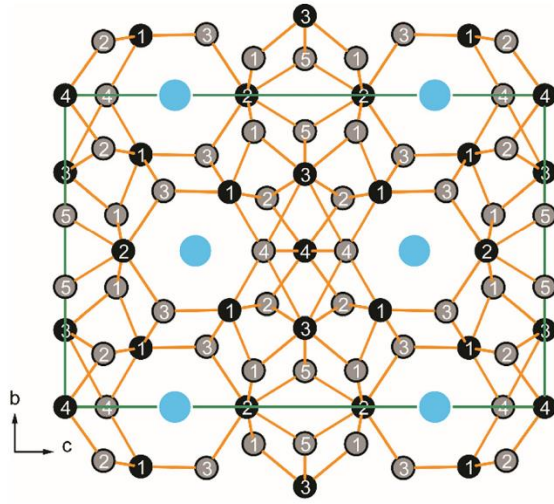


Figure 6: Unit cell of Sr₂Al₁₆Pt₉, projected along the *a* axis. Sr, Pt and Al atoms are shown in blue, black and grey circles. The shortest Pt–Al bonds are emphasized.

+1.31, –2.71/–2.71 to –3.82/–3.78 and +1.53/+1.55 to +1.82/+1.80, respectively in Sr₂Al₁₆Pt₉ (Tables 9 and 10). The Bader charges of Sr and Al in SrAl₅Pt₃ and Sr₂Al₁₆Pt₉ are comparable of those in SrAl₂Pt₃ (Sr: +1.38, Al: +1.73) [17]. The higher charge of Pt in SrAl₅Pt₃ (–3.02 to –3.35) and

Sr₂Al₁₆Pt₉ (–2.71 to –3.82) compared to SrAl₂Pt₃ (–1.64) [17] is simply due to the higher content of Al per formula unit. Interestingly, the negative charge on Pt shows a higher inhomogeneity in Sr₂Al₁₆Pt₉ ($\Delta e = 1.11$) compared with SrAl₅Pt₃ ($\Delta e = 0.33$) and might be due to the different Pt to Sr + Al ratio and the resulting modified bonding situation.

A look onto the DOSs of SrAl₅Pt₃ (Figure 8, left) and Sr₂Al₁₆Pt₉ (Figure 9, left) reveals that both are not purely ionic compounds. SrAl₅Pt₃ and Sr₂Al₁₆Pt₉, similar to SrAl₂Pt₃ [17], are metals because of the presence of states at and near the Fermi level. The presence of pseudo-gaps near and at the Fermi level from –2.5 to +2.5 eV for SrAl₅Pt₃ and from –3 to +1.5 eV for Sr₂Al₁₆Pt₉, with no clear maximum of the DOS at the Fermi level indicates electronically stable compounds with both ionic and covalent interactions [61, 62]. Sr contributes little to the DOS in both compounds, while Al contributes most significantly in the range between –11 to –6 eV and +2 eV and above in SrAl₅Pt₃, and in the area of –11 to about –7 eV in Sr₂Al₁₆Pt₉. The Pt states in SrAl₅Pt₃ dominate the DOS from –6 to –1 eV, while in Sr₂Al₁₆Pt₉, these states dominate from –7 to –0.5 eV. For this reason, Pt is significantly involved in ionic and covalent bonding in both compounds as its states are localized near a certain energy level, while Sr and Al contribute mainly to the metallic bonding in these compounds. Due to the similar shapes of the Pt and Al DOS in the range from –11 to –5 eV and –3 to at least +6 eV in both compounds, a

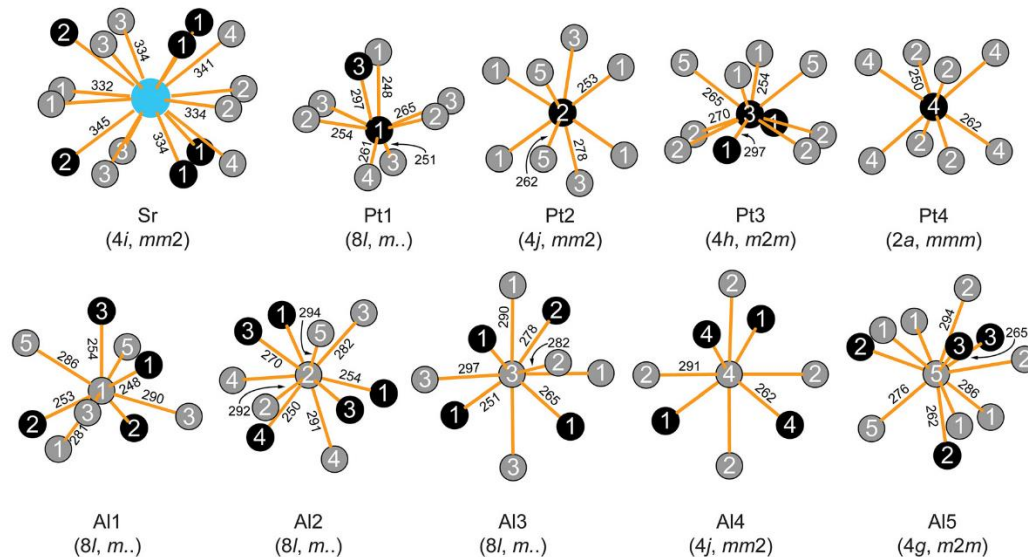


Figure 7: Coordination environments surrounding the Sr, Pt and Al atoms in the structure of Sr₂Al₁₆Pt₉. Sr, Pt and Al atoms are shown as blue, black and grey circles. Wyckoff sites, site symmetries and interatomic distances (in pm) are given.

Table 7: Interactions, counts, their distances after structure relaxation and their corresponding ICOHPs in SrAl₅Pt₃.

Interaction	Count	Distance (pm)	ICOHP (eV)
Sr–Al5	1	325.2	–0.28
Sr–Al2	2	336.5	–0.26
Sr–Al3	2	341.0	–0.29
Sr–Al1	2	345.6	–0.24
Sr–Al3	1	346.2	–0.22
Sr–Al4	1	353.4	–0.24
Sr–Al1	1	358.6	–0.20
Sr–Al2	1	361.5	–0.20
Sr–Pt1	2	329.8	–0.35
Sr–Pt3	2	331.3	–0.29
Sr–Pt2	2	331.7	–0.35
Pt1–Al5	1	247.5	–2.28
Pt1–Al1	1	257.7	–2.09
Pt1–Al4	2	267.1	–1.71
Pt1–Al1	2	267.7	–1.79
Pt1–Al2	1	269.3	–1.74
Pt2–Al5	2	251.9	–2.27
Pt2–Al5	1	254.2	–1.81
Pt2–Al3	1	260.6	–1.82
Pt2–Al1	1	270.5	–1.72
Pt2–Al4	2	276.0	–1.65
Pt3–Al4	1	252.0	–2.27
Pt3–Al3	1	257.5	–1.81
Pt3–Al3	2	259.1	–1.82
Pt3–Al2	1	264.3	–1.72
Pt3–Al2	2	265.1	–1.65
Al1–Al5	2	284.2	–0.99
Al1–Al1	2	287.4	–1.00
Al1–Al4	1	306.5	–0.67
Al2–Al3	1	287.3	–0.82
Al2–Al3	2	294.8	–0.83
Al2–Al4	2	296.7	–0.79
Al3–Al4	2	331.2	–0.25
Al4–Al5	1	283.0	–1.05
Al5–Al5	2	278.5	–0.98
Pt1–Pt2	1	307.4	–0.59

Table 8: Interactions, counts, their distances after structure relaxation and their corresponding ICOHPs in Sr₂Al₁₆Pt₉.

Interaction	Count	Distance (pm)	ICOHP (eV)
Sr–Al1	2	336.4	–0.26
Sr–Al3	4	337.2	–0.31
Sr–Al4	2	337.4	–0.27
Sr–Al2	2	345.9	–0.25
Sr–Al3	2	372.8	–0.17
Sr–Pt1	4	335.9	–0.32
Sr–Pt2	2	347.8	–0.30
Pt1–Al1	1	252.2	–1.89
Pt1–Al3	1	253.6	–2.27
Pt1–Al2	2	257.0	–1.88
Pt1–Al4	1	265.3	–1.64
Pt1–Al3	2	266.7	–1.67
Pt2–Al1	4	254.4	–1.79
Pt2–Al5	2	264.6	–1.44
Pt2–Al3	2	279.9	–1.23
Pt3–Al1	2	253.9	–1.98
Pt3–Al5	2	264.8	–1.70
Pt3–Al2	4	273.1	–1.53
Pt3–Al4	2	342.4	–0.21
Pt4–Al2	4	253.4	–2.15
Pt4–Al4	4	263.1	–1.86
Al1–Al1	1	284.3	–0.80
Al1–Al5	2	288.3	–0.65
Al1–Al3	2	291.6	–0.68
Al1–Al2	2	333.9	–0.11
Al2–Al3	1	284.4	–0.79
Al2–Al2	1	293.4	–0.63
Al2–Al4	2	294.4	–0.75
Al2–Al5	1	297.3	–0.52
Al3–Al3	2	301.1	–0.66
Al4–Al4	1	319.0	–0.48
Al5–Al5	1	277.3	–0.96
Pt1–Pt3	1	303.4	–0.59

strong covalently bonded Pt–Al network is expected, while the interactions of Sr with Pt and Al appear to be rather weak. To investigate this further, the integrated crystal orbital Hamilton population (ICOHP, Table 7 and 8) was calculated. The ICOHPs of these bonds are indeed low ranging between –0.20 and –0.29 eV (Sr–Al) and –0.29 and –0.35 eV (Sr–Pt) in SrAl₅Pt₃, and –0.17 to –0.31 eV (Sr–Al) and –0.30 to –0.32 eV (Sr–Pt) in Sr₂Al₁₆Pt₉. Similar weak covalent interactions of the Sr–Al and Sr–Pt bonds were also found in SrAl₂Pt₃ (–0.33 and –0.40 eV, respectively) [17].

Table 9: Bader effective charges of the atomic species in SrAl₅Pt₃.

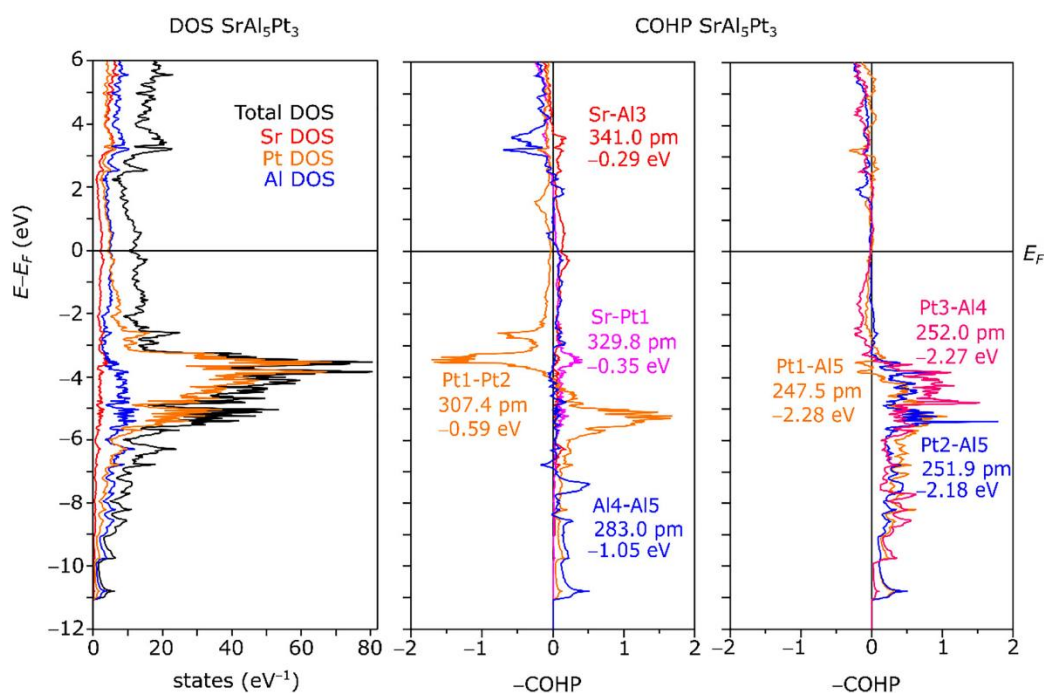
Atom	Henkelman et al. (e)	Yu and Tinkle (e)
Sr	+1.33	+1.33
Pt1	–3.15	–3.16
Pt2	–3.02	–3.03
Pt3	–3.35	–3.36
Al1	+1.65	+1.64
Al2	+1.52	+1.54
Al3	+1.58	+1.60
Al4	+1.65	+1.66
Al5	+1.80	+1.79

Table 10: Bader effective charges of the atomic species in Sr₂Al₁₆Pt₉.

Atom	Henkelman et al. (e)	Yu and Tinkle (e)
Sr	+1.32	+1.31
Pt1	-3.29	-3.30
Pt2	-3.82	-3.78
Pt3	-2.71	-2.71
Pt4	-3.43	-3.44
Al1	+1.82	+1.80
Al2	+1.74	+1.74
Al3	+1.53	+1.55
Al4	+1.60	+1.59
Al5	+1.71	+1.70

Akin to SrAl₂Pt₃, there are Pt–Pt bonds in SrAl₅Pt₃ and Sr₂Al₁₆Pt₉. The covalent interactions of the Pt1–Pt2 (SrAl₅Pt₃) and Pt1–Pt3 (Sr₂Al₁₆Pt₉) bonds, however, are quite weak as the ICOHPs are only -0.59 and -0.73 eV, respectively, as compared to the Pt–Pt bonds in SrAl₂Pt₃ (286.1 pm, -1.39 eV) [17]. The COHP plots of the Pt–Pt bonds (Figure 8, center and Figure 9, center) reveal that there are

strong antibonding interactions below the Fermi level which weaken this bond. In contrast to SrAl₂Pt₃, Al–Al bonds can be observed in SrAl₅Pt₃ and Sr₂Al₁₆Pt₉. The ICOHPs of these bonds have a range of -0.25 to -1.05 eV in SrAl₅Pt₃ and of -0.11 to -0.96 eV in Sr₂Al₁₆Pt₉ and indicate that the covalent bonding between the Al atoms is weak in both compounds. Far stronger covalent bonds in SrAl₅Pt₃ and Sr₂Al₁₆Pt₉ can be found between the Pt and Al atoms. The ICOHPs of the Pt–Al bonds are in the range from -1.60 to -2.28 eV in SrAl₅Pt₃ and from -1.23 to -2.27 eV in Sr₂Al₁₆Pt₉, suggesting strong covalent interactions validating the picture of a Pt–Al network in both intermetallic compounds. The $-$ COHP-plots of the strongest Pt–Al covalent bonds are shown in Figure 8, right and Figure 9, right. Although there are only weak antibonding interactions below the Fermi level found for the Pt1–Al5 and Pt3–Al4 bonds in SrAl₅Pt₃, all but one Pt–Al bond types show non-bonding states at the Fermi level and its vicinity, which is an indicator of a very stable covalent bond. In the case of the Pt4–Al2 bond present in Sr₂Al₁₆Pt₉, the $-$ COHP-plot shows a small maximum at the Fermi level, possibly a minor hint for an electronic instability.

**Figure 8:** (Left) Density of states (DOS) of SrAl₅Pt₃; (middle) $-$ COHP plots for the Sr–Al3, Sr–Pt1, Al4–Al5 and Pt1–Pt2 bonds; (right) $-$ COHP plots of the Pt1–Al5, Pt2–Al5 and Pt3–Al4 bonds.

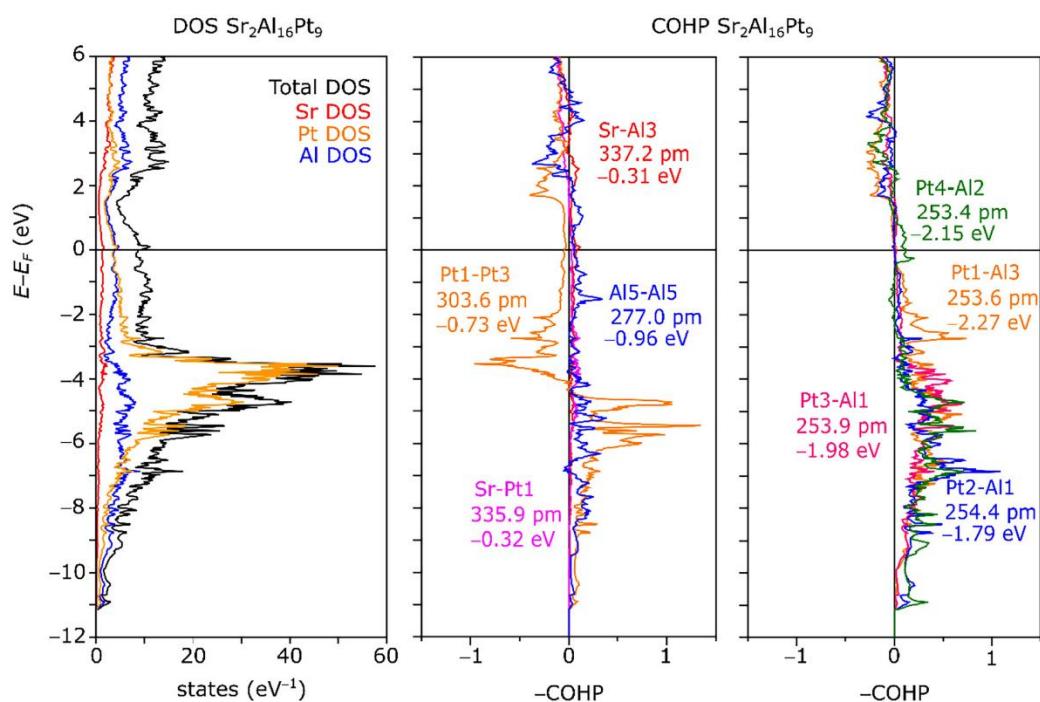


Figure 9: (Left) Density of states (DOS) of Sr₂Al₁₆Pt₉; (middle) -COHP plots for the Sr-Al3, Sr-Pt1, Al5-Al5 and Pt1-Pt3 bonds; (right) -COHP plots of the Pt1-Al3, Pt2-Al1, Pt3-Al1 and Pt4-Al2 bonds.

4 Conclusions

SrAl₅Pt₃ and Sr₂Al₁₆Pt₉ are two new representatives within the Sr-Pt-Al system and crystallize isostructural to CeAl₅Pt₃ and Ce₂Al₁₆Pt₉, respectively. They have been synthesized alongside of each other from the elements in metal ampoules. SrAl₅Pt₃ can be considered as a site occupation variant of the YNi₅Si₃ type structure. Both structures have been determined based on single crystal x-ray diffraction studies. Attempts to synthesize phase pure samples were not successful yet. Quantum-chemical calculations have shown that the structures are based on negatively charged Pt and positively charged Sr and Al atoms. Between Pt and Al, significant covalent interactions are observed, leading to polyanionic [Al₅Pt₃]^{δ-} and [Al₁₆Pt₉]^{δ-} networks with Sr^{δ+} cations located in their cavities. Interestingly, in both cases a weak Pt-Pt interaction can be observed along with Al-Al interactions owing to the Al rich compositions.

Acknowledgments: We thank Dr. Bernd Morgenstern for the collection of the single crystal intensity data. Instrumentation and technical assistance for this work were

provided by the Service Center X-ray Diffraction, with financial support from Saarland University and German Science Foundation (Project Nos. INST 256/349-1 and INST 256/506-1). RT thanks the Universitätsrechenzentrum of the Otto von Guericke University for calculation power and time.

Author contribution: All authors have accepted responsibility for the entire content of this submitted manuscript and approved the submission.

Research funding: Funding has been provided by the Deutsche Forschungsgemeinschaft DFG (JA 1891-10-1).

Conflict of interest statement: The authors declare no conflicts of interest regarding this article.

References

1. Benndorf C., Eckert H., Janka O. *Acc. Chem. Res.* 2017, 50, 1459–1467.
2. Stegemann F., Benndorf C., Bartsch T., Touzani R. S., Bartsch M., Zacharias H., Fokwa B. P. T., Eckert H., Janka O. *Inorg. Chem.* 2015, 54, 10785–10793.
3. Stegemann F., Block T., Klenner S., Zhang Y., Fokwa B. P. T., Timmer A., Mönig H., Doerenkamp C., Eckert H., Janka O. *Chem. Eur J.* 2019, 25, 10735–10747.

4. Stegemann F., Touzani R. S., Janka O. *Dalton Trans.* 2019, 48, 14103–14114.
5. Turban K., Schäfer H. J. *Less Common. Met.* 1975, 40, 91–96.
6. Stotsky V., Pukas S. Y., Akselrud L., Gladyshevskii R. E. *Abstr. 13th Int. Conf. Crystal Chem. Intermet. Compd.* 2016, Vol. 96.
7. Cordier G., Friedrich T. Z. *Kristallogr.* 1993, 205, 135–136.
8. Cordier G., Friedrich T., Henseleit R., Grauel A., Tegel U., Schank C., Geibel C. J. *Alloys Compd.* 1993, 201, 197–201.
9. Kenfack Tsobnang P., Fotio D., Ponou S., Fon Abi C. *Acta Crystallogr.* 2011, E67, i55.
10. Doverbratt I., Ponou S., Zhang Y., Lidin S., Miller G. J. *Chem. Mater.* 2015, 27, 304–315.
11. Cordier G., Dörsam G., Friedrich T., Henseleit R., Röhr C. J. *Alloys Compd.* 1993, 190, 201–207.
12. Radzieowski M., Stegemann F., Hoffmann R.-D., Janka O. *Z. Kristallogr.* 2017, 232, 675–687.
13. Manyako M. B., Yanson T. I., Zarechnyuk O. S. *Sov. Phys. Crystallogr.* 1987, 32, 816–817.
14. Manyako M. B., Zarechnyuk O. S., Yanson T. I. *Kristallografiya* 1987, 32, 1389–1391.
15. Manyako M. B., Yanson T. I., Zarechnyuk O. S. *Russ. Metall.* 1988, 3, 185–188.
16. Gießelmann E., Touzani R. S., Morgenstern B., Janka O. *Z. Naturforsch.* 2021, 76, 659–668.
17. Stegemann F., Benndorf C., Touzani R. S., Fokwa B. P. T., Janka O. *J. Solid State Chem.* 2016, 242, 143–150.
18. Stegemann F., Benndorf C., Touzani R. S., Fokwa B. P. T., Janka O. *Eur. J. Inorg. Chem.* 2016, 1108–1114, <https://doi.org/10.1002/ejic.201501455>.
19. Villars P., Cenzual K. (Eds.) *Pearson's Crystal Data: Crystal Structure Database for Inorganic Compounds*, ASM International®: Materials Park, Ohio (USA), 2021. (release 2020/21).
20. Hoffmann R.-D., Stegemann F., Janka O. Z. *Kristallogr.* 2016, 231, 127–142.
21. Stegemann F., Block T., Klenner S., Zhang Y., Fokwa B. P. T., Doerenkamp C., Eckert H., Janka O. *Eur. J. Inorg. Chem.* 2021, 2021, 3832–3845.
22. Bönnighausen J., Seidel S., Klenner S., Pöttgen R. Z. *Kristallogr.* 2021, 236, 293–300.
23. Langen D. *Dissertation, Ternäre Strontium- und Bariumverbindungen des Galliums mit Platin, Palladium und Iridium*; Universität zu Köln: Köln, 1997.
24. Tursina A. I., Murashova E. V., Noël H., Bukhan'ko N. G., Seropegin Y. D. *Intermetallics* 2009, 17, 780–783.
25. Yaniv G., Meshi L. J. *Alloys Compd.* 2016, 660, 496–502.
26. Pöttgen R., Gulden T., Simon A. *GIT Labor-Fachz* 1999, 43, 133–136.
27. Pöttgen R., Lang A., Hoffmann R.-D., Künnen B., Kotzyba G., Müllmann R., Mosel B. D., Rosenhahn C. Z. *Kristallogr.* 1999, 214, 143–150.
28. Topas (Version 5). *General Profile and Structure Analysis Software for Powder Diffraction Data*; Bruker AXS Inc.: Karlsruhe (Germany), 2014.
29. Saint+ (Version 6.02; includes XPREP and SADABS). *Area Detector Control and Integration Software*; Bruker AXS Inc.: Madison, WI (USA), 1999.
30. Palatinus L., Chapuis G. J. *Appl. Crystallogr.* 2007, 40, 786–790.
31. Petříček V., Dušek M., Palatinus L. *Jana 2006. The Crystallographic Computing System*; Institute of Physics: Praha (Czech Republic), 2006.
32. Petříček V., Dušek M., Palatinus L. Z. *Kristallogr.* 2014, 229, 345–352.
33. Giannozzi P., Baroni S., Bonini N., Calandra M., Car R., Cavazzoni C., Ceresoli D., Chiarotti G. L., Cococcioni M., Dabo I., Dal Corso A., de Gironcoli S., Fabris S., Fratesi G., Gebauer R., Gerstmann U., Gougousis C., Kokalj A., Lazzeri M., Martin-Samos L., Marzari N., Mauri F., Mazzarello R., Paolini S., Pasquarello A., Paulatto L., Sbraccia C., Scandolo S., Sclauzero G., Seitsonen A. P., Smogunov A., Umari P., Wentzcovitch R. M. *J. Phys. Condens. Matter* 2009, 21, 395502.
34. Giannozzi P., Andreussi O., Brumme T., Bunau O., Buongiorno Nardelli M., Calandra M., Car R., Cavazzoni C., Ceresoli D., Cococcioni M., Colonna N., Carnimeo I., Dal Corso A., de Gironcoli S., Delugas P., DiStasio R. A., Ferretti A., Floris A., Fratesi G., Fugallo G., Gebauer R., Gerstmann U., Giustino F., Gorni T., Jia J., Kawamura M., Ko H. Y., Kokalj A., Küçükbenli E., Lazzeri M., Marsili M., Marzari N., Mauri F., Nguyen N. L., Nguyen H. V., Otero-de-la-Roza A., Paulatto L., Poncé S., Rocca D., Sabatini R., Santra B., Schlipf M., Seitsonen A. P., Smogunov A., Timrov I., Thonhauser T., Umari P., Vast N., Wu X., Baroni S. *J. Phys. Condens. Matter* 2017, 29, 465901.
35. Blöchl P. E. *Phys. Rev. B* 1994, 50, 17953–17979.
36. Dal Corso A. *Comput. Mater. Sci.* 2014, 95, 337–350.
37. Marzari N., Vanderbilt D., De Vita A., Payne M. C. *Phys. Rev. Lett.* 1999, 82, 3296–3299.
38. Monkhorst H. J., Pack J. D. *Phys. Rev. B* 1976, 13, 5188–5192.
39. Perdew J. P., Burke K., Ernzerhof M. *Phys. Rev. Lett.* 1996, 77, 3865–3868.
40. Tang W., Sanville E., Henkelman G. J. *J. Phys. Condens. Matter* 2009, 21, 084204.
41. Sanville E., Kenny S. D., Smith R., Henkelman G. J. *Comput. Chem.* 2007, 28, 899–908.
42. Henkelman G., Arnaldsson A., Jónsson H. *Comput. Mater. Sci.* 2006, 36, 354–360.
43. Yu M., Trinkle D. R. *J. Chem. Phys.* 2011, 134, 064111.
44. Otero-de-la-Roza A., Blanco M. A., Pendás A. M., Luaña V. *Comput. Phys. Commun.* 2009, 180, 157–166.
45. Otero-de-la-Roza A., Johnson E. R., Luaña V. *Comput. Phys. Commun.* 2014, 185, 1007–1018.
46. Andersen O. K., Skriver H., Nohl H., Johansson B. *Pure Appl. Chem.* 1980, 52, 93–118.
47. Andersen O. K., Jepsen O. *Phys. Rev. Lett.* 1984, 53, 2571–2574.
48. Jepsen O., Andersen O. K. TB-LMTO-ASA (version 47), Max-Planck-Institut für Festkörperforschung Stuttgart. Germany, 2000. <http://www2.fkf.mpg.de/andersen/LMTODOC/LMTODOC.html> (accessed August, 2021).
49. Perdew J. P., Chevary J. A., Vosko S. H., Jackson K. A., Pederson M. R., Singh D. J., Fiolhais C. *Phys. Rev. B* 1992, 46, 6671.
50. Dronskowski R., Blöchl P. E. J. *Phys. Chem.* 1993, 97, 8617–8624.
51. Tursina A. I., Bukhan'ko N. G., Gribanov A. V., Shchelkunov V. A., Nelyubina Y. V. *Acta Crystallogr.* 2005, E61, i285–i286.
52. Cordier G., Czech E., Schäfer H. Z. *Naturforsch* 1982, 37b, 1442–1445.
53. Nagorsen G., Posch H., Schäfer H., Weiss A. Z. *Naturforsch* 1969, 24b, 1191.
54. Nowotny H., Wesenberg H. Z. *Metallkd.* 1939, 31, 363–364.
55. Heumann T., Kniepmeyer M. Z. *Anorg. Allg. Chem.* 1957, 290, 191–204.
56. Emsley J. *The Elements*; Clarendon Press, Oxford University Press: Oxford, New York, 1998.

57. Schubert K., Burkhardt W., Esslinger P., Günzel E., Meissner H. G., Schütt W., Wegst J., Wilkens M. *Naturwissenschaften* 1956, 43, 248–249.
58. Zintl E., Harder A., Haucke W. *Z. Phys. Chem. B* 1937, 35, 354–362.
59. Hull A. W. *Trans. Am. Inst. Electro. Eng.* 1919, 38, 1445–1466.
60. Hull A. W. *Phys. Rev.* 1917, 10, 661–696.
61. Ravindran P., Asokamani R. *Bull. Mater. Sci.* 1997, 20, 613–622.
62. Dshemuchadse J., Jung D. Y., Steurer W. *Acta Crystallogr.* 2011, B67, 269–292.
63. Becker P. J., Coppens P. *Acta Crystallogr.* 1974, A30, 129–147.

DOI: 10.1002/zaac.202400094

Nominal CaAl_2Pt_2 and $\text{Ca}_2\text{Al}_3\text{Pt}$ – two new Intermetallic Compounds in the Ternary System Ca–Al–Pt

Stefan Engel,^[a] Marcus Koch,^[b] and Oliver Janka^{*[a]}Dedicated to Professor Michael Veith on the Occasion of his 80th Birthday

Single crystals of CaAl_2Pt_2 , $\text{Ca}_2\text{Al}_3\text{Pt}$ and Ca_2AlPt_2 were initially observed in an attempt to synthesize $\text{Ca}_3\text{Al}_4\text{Pt}_4$. Their structures were determined using single-crystal X-ray diffraction experiments. While nominal CaAl_2Pt_2 (CaBe_2Ge_2 type, $P4/nmm$, $a = 426.79(2)$, $c = 988.79(6)$ pm, $wR_2 = 0.0679$, 246 F^2 values and 18 variables) and $\text{Ca}_2\text{Al}_3\text{Pt}$ ($\text{Mg}_2\text{Cu}_3\text{Si}$ type, $P6_3/mmc$, $a = 561.46(5)$, $c = 876.94(8)$ pm, $wR_2 = 0.0664$, 214 F^2 values and 13 variables) exhibit Al/Pt mixing, for Ca_2AlPt_2 ($\text{Ca}_2\text{Ir}_2\text{Si}$ type, $C2/c$, $a = 981.03(2)$, $b = 573.74(1)$, $c = 772.95(2)$ pm, $\beta = 101.862(1)^\circ$, $wR_2 = 0.0307$, 2246 F^2 values and 25 variables) no mixing was

observed. Subsequently, the nominal compositions were targeted with synthetic attempts from the elements using arc-melting and annealing techniques. For CaAl_2Pt_2 and $\text{Ca}_2\text{Al}_3\text{Pt}$ always multi-phase mixtures were observed while Ca_2AlPt_2 could be obtained as almost X-ray pure material. Quantum-chemical calculations were used to investigate the charge transfer in these compounds rendering them polar intermetallics with a designated $[\text{Al}_i\text{Pt}_j]^{b-}$ polyanion and Ca^{b+} cations in the cavities of the polyanions.

1. Introduction

Ternary intermetallic compounds containing an alkaline earth element along with an electronegative transition metal (e.g. Ir, Pt, Au) and aluminum have been studied quite vigorously in the last decade. In contrast to most of their rare-earth containing counterparts (exceptions are Sc, Y, La and Lu), they exhibit no localized unpaired f -electrons which enables for example NMR spectroscopic studies^[1,2] and simplifies quantum-chemical calculations for bonding and charge distribution analysis. A drawback, however, are the significantly different sizes of the Ca, Sr or Ba atoms (174, 192, 198 pm) or cations (106, 127, 143 pm)^[3] which dramatically influence the existence of certain compositions and their respective crystal chemistry. Only a few isostructural series are known in the ternary AE–Al–Pt system, e.g. the orthorhombic MgCuAl_2 type compounds AEAl_2Pt with $\text{AE} = \text{Ca}$, Sr and Ba^[4] while the majority of compounds reported in the Pearson database^[5] are singular (structural) entries. Examples are monoclinic Ca_2AlPt_2 ($\text{Ca}_2\text{Ir}_2\text{Si}$

type, $C2/c$),^[6] hexagonal SrAl_2Pt_3 (CeCo_3B_2 type, $P6/mmm$)^[7] and $\text{Ba}_6\text{Al}_3\text{Pt}_{22}$ (own type, $P6_3/mcm$),^[8] tetragonal $\text{Sr}_2\text{Al}_8\text{Pt}_3$ (anti- $\text{Eu}_2\text{Ni}_8\text{Si}_3$ type, $P4_2/nmc$),^[9] modulated SrAl_2Pt_2 ^[10] and $\text{Ca}_2\text{Al}_{15}\text{Pt}_6$ ^[11] or orthorhombic CaAlPt (TiNiSi type, $Pnma$),^[12,13] $\text{Ca}_2\text{Al}_9\text{Pt}_3$ ($\text{Y}_2\text{Co}_3\text{Ga}_9$ type, $Cmcm$),^[14] CaAl_3Pt_3 (YNi_5Si_3 type, $Pnma$),^[15] SrAl_5Pt_3 (YNi_5Si_3 type, $Pnma$),^[16] $\text{Ca}_2\text{Al}_{16}\text{Pt}_9$ ($\text{Ce}_2\text{Al}_{16}\text{Pt}_9$ type, $Immm$),^[17] $\text{Sr}_2\text{Al}_{16}\text{Pt}_9$ ($\text{Ce}_2\text{Al}_{16}\text{Pt}_9$ type, $Immm$)^[16] and finally $\text{Ba}_3\text{Al}_4\text{Pt}_4$ (own type, $Cmcm$).^[18]

Synthesizing isostructural compounds of the different alkaline earth elements is, as mentioned before, challenging due to the different atomic sizes. Easier, however, is the preparation of the Ca/Yb and Sr/Eu pairs. Here, for example, EuAl_2Pt ^[4] and YbAl_2Pt ^[19] in analogy to SrAl_2Pt and CaAl_2Pt could be obtained and EuAl_5Pt_3 ^[20] as well as $\text{Eu}_2\text{Al}_{16}\text{Pt}_9$ ^[17] were reported besides the Sr compounds. Furthermore, it was shown that $\text{Yb}_2\text{Al}_{15}\text{Pt}_6$ ^[21] is isostructural to the Ca representative; interestingly, also the europium compound is known^[22] while the strontium representative has not been reported thus far.

During attempts to synthesize $\text{Ca}_3\text{Al}_4\text{Pt}_4$ in analogy to $\text{Ba}_3\text{Al}_4\text{Pt}_4$, two new compounds were observed and characterized by means of single crystal X-ray diffraction experiments. CaAl_2Pt_2 , which adopts the tetragonal CaBe_2Ge_2 type structure ($P4/nmm$) and $\text{Ca}_2\text{Al}_3\text{Pt}$, which crystallizes in the hexagonal $\text{Mg}_2\text{Cu}_3\text{Si}$ type ($P6_3/mmc$). Furthermore, the initial reaction mixture contained single crystals of the already reported Ca_2AlPt_2 ($\text{Ca}_2\text{Ir}_2\text{Si}$ type, $C2/c$). We report on the structural investigations on these three compounds, on the attempts to obtain phase pure bulk samples and the analysis of the charge transfer using quantum-chemical calculations.

[a] S. Engel, O. Janka
Saarlandes University, Solid State Inorganic Chemistry, Campus C4
1, 66123 Saarbrücken, Germany
E-mail: oliver.janka@uni-saarland.de

[b] M. Koch
INM-Leibniz Institute for New Materials, Campus D2 2, 66123,
Saarbrücken, Germany

Supporting information for this article is available on the WWW under <https://doi.org/10.1002/zaac.202400094>

© 2024 The Author(s). Zeitschrift für anorganische und allgemeine Chemie published by Wiley-VCH GmbH. This is an open access article under the terms of the Creative Commons Attribution Non-Commercial NoDerivs License, which permits use and distribution in any medium, provided the original work is properly cited, the use is non-commercial and no modifications or adaptations are made.

Experimental

Synthesis

Initially, $\text{Ca}_3\text{Al}_4\text{Pt}_4$ was prepared in analogy to $\text{Ba}_3\text{Al}_4\text{Pt}_4$,^[18] subsequent syntheses were conducted on stoichiometry for Ca_2AlPt_2 , CaAl_2Pt_2 and $\text{Ca}_2\text{Al}_3\text{Pt}$. All samples were prepared from the elements using calcium pieces (Onyxmet), platinum pieces (Agosi AG) and aluminum turnings (Onyxmet), all with stated purities above 99%. Samples were prepared on a 300 mg scale. The Ca pieces were stored in an argon filled drybox; surface contaminations on the pieces were removed mechanically prior to the reaction. For the reaction, the elements were arc-welded^[23] in tantalum tubes in an argon atmosphere of about 800 mbar with the different molar ratios given above. The argon gas was purified over a titanium sponge (873 K), molecular sieves and silica gel prior to the use. The sealed tantalum ampoules were placed in the water-cooled sample chamber of an induction furnace (Trumpf Hüttinger, TruHeat HF 5010).^[24] Water-cooling was used to prevent reactions of the Ta ampoules with the sample chamber. The Ta containers were heated to ~1500 K within 2 minutes, dwelled at that temperature for 10 min followed by slow cooling to ~1000 K. The cooling was achieved by reducing the power output of the generator, leading to a cooling rate of about 100 Kmin⁻¹. After an annealing step of 4 h at this temperature, the samples were cooled naturally by shutting off the power supply. All samples could easily be separated from the container material afterwards and no reactions with the tantalum ampoules could be observed. The samples were metallic, ground powders are grey.

Powder and Single Crystal X-ray Diffraction

The polycrystalline samples were analyzed by powder X-ray diffraction (PXRD) experiments. The PXRD patterns of the pulverized samples were recorded at room temperature on a D8-A25 Advance diffractometer (Bruker, Karlsruhe, Germany) in Bragg-Brentano θ - θ geometry (goniometer radius 280 mm) with non-monochromatized $\text{CuK}\alpha$ radiation ($\lambda = 154.0596$ pm). A 12 μm Ni foil working as $K\beta$ filter and a variable divergence slit were mounted at the primary beam side. A LYNXEYE detector with 192 channels was used at the secondary beam side. Experiments were carried out in a 2θ range of 6 to 130° with a step size of 0.013° and a total scanning time of 1 h. The recorded data was evaluated using the Bruker TOPAS 5.0 software,^[25] using the fundamental parameter approach and the Rietveld method.^[26,27]

From the annealed crushed samples, single crystals of nominal Ca_2AlPt_2 , CaAl_2Pt_2 and $\text{Ca}_2\text{Al}_3\text{Pt}$ were isolated and investigated at room temperature on a Bruker X8 APEX2, Nonius κ -CCD diffractometer, operating with graphite monochromated $\text{MoK}\alpha$ ($\lambda = 0.71073$ Å) radiation. Multi-scan absorption corrections using the Bruker SadABS data package^[28] were applied to the data sets. The data were solved and refined using SUPERFLIP^[29] and JANA2006.^[30–32] Details on the structure refinement, atomic coordinates as well as interatomic distances are compiled in Tables 1–4. Structural drawing were generated with Diamond 4^[33] and edited with Adobe Illustrator CS6.

CSDs 2331503–2331505 contain the supplementary crystallographic data for this paper. The data can be obtained free of charge from The Cambridge Crystallographic Data Centre via www.ccdc.cam.ac.uk/structures.

Energy-Dispersive X-ray Spectroscopy (EDX)

The single crystals of nominal Ca_2AlPt_2 , CaAl_2Pt_2 and $\text{Ca}_2\text{Al}_3\text{Pt}$, investigated on the diffractometer, were semiquantitatively analyzed on an SEM FEI Quanta 400 (FEI, Hillsboro, United States) scanning electron microscope equipped with an EDAX Genesis V6.04 EDX detector (EDAX, Unterschleissheim, Germany) using CaO, Pt and Al_2O_3 as standards. The point measurements on the surfaces of all three crystals clearly showed that all three elements are present, and no tantalum (container material) could be observed. However, the deviations from the weighed and refined compositions are quite significant which can be explained by the irregular crystallite faces, the not perfect perpendicular orientation of the crystal towards the beam and coverage of beeswax on the crystal surface. This leads to a significantly decreased amount of Al in the EDX spectra measured.

Quantum-Chemical Calculations

Electronic structure calculations of nominal Ca_2AlPt_2 , CaAl_2Pt_2 and $\text{Ca}_2\text{Al}_3\text{Pt}$ were performed using the projector augmented wave method (PAW) of Blöchl^[34,35] coded in the Vienna ab initio simulation package (VASP).^[36,37] VASP calculations employed the potentials PAW_PBE Ca_sv 06Sep2000, PAW_PBE Pt_pv 12Dec2005 and PAW_PBE Al 04Jan2001. The cutoff energy for the plane wave calculations was set to 800 eV and the Brillouin zone integration was carried out using a k -point mesh with a spacing of ≈ 0.02 for all compounds.

Table 1. Lattice parameters and unit cell volumes of Ca_2AlPt_2 ($C2/c$, $Z=4$, $\text{Ca}_2\text{Ir}_2\text{Si}$ type), CaAl_2Pt_2 ($P4/nmm$, $Z=2$, CaBe_2Ge_2 type) and $\text{Ca}_2\text{Al}_3\text{Pt}$ ($P6_3/mmc$, $Z=2$, $\text{Mg}_2\text{Cu}_3\text{Si}$ type) determined by powder X-ray diffraction and single crystal diffraction.

Compound	<i>a</i> (pm)	<i>b</i> (pm)	<i>c</i> (pm)	β (°)	<i>V</i> (nm ³)	
Ca_2AlPt_2	Single crystal	981.03(2)	573.74(1)	772.95(2)	101.862(1)	0.4258
	Powder	981.0(1)	573.8(1)	772.9(1)	101.847(1)	0.4258
	DFT	977.9	568.7	770.2	102.11	0.4183
CaAl_2Pt_2	Single crystal	426.79(2)	<i>a</i>	988.79(6)	90	0.1801
	Powder	423.6(1)	<i>a</i>	963.5(1)	90	0.1729
	DFT	412.2	<i>a</i>	1074.3	90	0.1825
$\text{Ca}_2\text{Al}_3\text{Pt}$	Single crystal	561.46(5)	<i>a</i>	876.94(8)	90	0.2394
	Powder	561.7(1)	<i>a</i>	876.8(1)	90	0.2396
	DFT	556.6	<i>a</i>	869.3	90	0.2332

Table 2. Crystallographic data and structure refinement for nominal Ca_2AlPt_2 ($C2/c$, $Z=4$, $\text{Ca}_2\text{Ir}_2\text{Si}$ type), CaAl_2Pt_2 ($P4/nmm$, $Z=2$, CaBe_2Ge_2 type) and nominal $\text{Ca}_2\text{Al}_3\text{Pt}$ ($P6_3/mmc$, $Z=2$, $\text{Mg}_2\text{Cu}_3\text{Si}$ type).

Nominal composition	Ca_2AlPt_2	CaAl_2Pt_2	$\text{Ca}_2\text{Al}_3\text{Pt}$
Refined composition	Ca_2AlPt_2	$\text{CaAl}_{2.24(1)}\text{Pt}_{1.76(1)}$	$\text{Ca}_2\text{Al}_{3.09(1)}\text{Pt}_{0.91(1)}$
CCDC number	2331504	2331503	2331505
Lattice parameters	see Table 1		
Molar mass, g mol^{-1}	497.3	443.9	341.1
Density calc., g cm^{-3}	7.76	8.18	4.73
Crystal size, μm	$55 \times 45 \times 30$	$40 \times 25 \times 20$	$45 \times 35 \times 30$
Detector distance, mm	40	40	40
Exposure time, s	20	20	20
Range in hkl	$-21, +20; \pm 12; \pm 16$	$\pm 6; +6, -5; +15, -10$	$\pm 8; \pm 8; \pm 13$
$\theta_{\text{min}}, \theta_{\text{max}}$, deg	4.14-50.09	4.12-33.15	4.19-33.74
Linear absorption coeff., mm^{-1}	68.0	70.0	29.2
No. of reflections	27558	2449	4761
$R_{\text{int}}/R_{\sigma}$	0.0368/0.0157	0.0431/0.0257	0.0315/0.0113
No. of independent reflections	2246	246	214
Reflections used [$ I \geq 3\sigma(I)$]	2198	222	206
$F(000)$, e	836	378	303
R_1/wR_2 for $I \geq 3\sigma(I)$	0.0164/0.0304	0.0274/0.0671	0.0193/0.0659
R_1/wR_2 for all data	0.0170/0.0307	0.0313/0.0679	0.0204/0.0664
Data/parameters	2246/25	246/18	214/13
Goodness-of-fit on F^2	2.07	1.85	2.59
Extinction coefficient	340(20)	21(16)	430(70)
Diff. Fourier residues/ $\text{e}^{-\text{\AA}^{-3}}$	+3.38/-1.71	+3.10/-2.97	+2.61/-0.66

Table 3. Atom positions and equivalent isotropic displacement parameters (pm^2) for Ca_2AlPt_2 ($C2/c$, $Z=4$, $\text{Ca}_2\text{Ir}_2\text{Si}$ type), nominal CaAl_2Pt_2 ($P4/nmm$, $Z=2$, CaBe_2Ge_2 type) and nominal $\text{Ca}_2\text{Al}_3\text{Pt}$ ($P6_3/mmc$, $Z=2$, $\text{Mg}_2\text{Cu}_3\text{Si}$ type). U_{eq} is defined as one third of the trace of the orthogonalized U_{ij} tensor.

Atom	Wyckoff Position	x	y	z	U_{eq} (pm^2)	site occ.
Ca_2AlPt_2						
Ca	8f	0.64998(5)	0.63116(7)	0.14872(7)	71(1)	1
Pt	8f	0.87101(1)	0.63388(1)	0.49584(1)	47(1)	1
Al	4e	0	0.3927(2)	3/4	60(2)	1
$\text{CaAl}_{2.24(1)}\text{Pt}_{1.76(1)}$						
Ca	2c	1/4	1/4	0.7562(3)	142(7)	1
Pt1	2a	3/4	1/4	0	120(2)	0.80(1)
Al1'	2a	3/4	1/4	0	120(2)	0.20(1)
Pt2	2c	1/4	1/4	0.3560(14)	101(9)	0.69(5)
Pt2'	2c	1/4	1/4	0.3814(10)	101(9)	0.31(5)
Al1	2b	3/4	1/4	1/2	125(11)	1
Al2	2c	1/4	1/4	0.1109(10)	170(20)	1
$\text{Ca}_2\text{Al}_{3.09(1)}\text{Pt}_{0.91(1)}$						
Ca	4f	2/3	1/3	0.0571(1)	80(4)	1
Pt1	2a	0	0	0	66(2)	0.90(1)
Al1	2a	0	0	0	66(2)	0.10(1)
Pt2	6h	0.1629(1)	2x	1/4	75(6)	0.01(1)
Al2	6h	0.1629(1)	2x	1/4	75(6)	0.99(1)

The calculations are done starting from the experimental crystal data and the whole cell undergoes unconstrained geometry relaxing of the structure parameters and coordinates. At high precision integration of the Brillouin-zone (BZ) (Ca_2AlPt_2 : $9 \times 15 \times 11$; CaAl_2Pt_2 : $15 \times 15 \times 9$; $\text{Ca}_2\text{Al}_3\text{Pt}$: $13 \times 13 \times 9$) the charge density issued from the accurate calculations was analyzed using the AIM (atoms in molecules theory) approach^[38] developed by Bader who devised an intuitive way of splitting molecules into atoms as based purely on the electronic charge density. The charge density reaches a

minimum between atoms defining thus a region separating atoms from each other. In the case of a family of compounds such an analysis can be useful to establish trends. Core electrons are included for an accurate account of the charge density. The analysis is done using a fast algorithm operating on a charge density grid. The obtained charges are listed in Table 5.

Table 4. Interatomic distances (pm) for Ca_2AlPt_2 ($C2/c$, $Z=4$, $\text{Ca}_2\text{Ir}_2\text{Si}$ type), nominal CaAl_2Pt_2 ($P4/nmm$, $Z=2$, CaBe_2Ge_2 type) and nominal $\text{Ca}_2\text{Al}_3\text{Pt}$ ($P6_3/mmc$, $Z=2$, $\text{Mg}_2\text{Cu}_3\text{Si}$ type). All distances of the first coordination spheres are listed. All standard uncertainties were less than 0.2 pm.

Ca_2AlPt_2												
Ca	1	Pt	305.6	Al	2	Pt	249.5	Pt	1	Al	249.5	
	1	Pt	306.2		2	Pt	252.1		1	Al	252.0	
	1	Pt	307.6					1	Pt	273.5		
	2	Pt	308.4					1	Pt	295.0		
	1	Pt	310.5									
	1	Al	327.3									
	1	Al	336.4									
	1	Al	347.1									
CaAl_2Pt_2												
Ca	4	Pt2	321.5	Al1	4	Pt2'	243.5	Pt1/Al1'	4	Al2	239.9	
	4	Pt1/Al1'	321.9		4	Pt2	256.5		4	Pt1/Al1'	301.8	
	4	Al2	329.2		4	Al1	301.8					
	4	Pt2'	331.1					Pt2	1	Pt2'	25.1	
	4	Al1	331.3	Al2	4	Pt1/Al1	239.9		1	Al2	242.2	
					1	Pt2'	267.5		4	Al1	256.5	
					1	Pt2	242.4					
								Pt2'	1	Pt2	25.1	
									4	Al1	256.5	
									1	Al2	242.2	
	$\text{Ca}_2\text{Al}_3\text{Pt}$											
	Ca	3	Al2/Pt2	316.3	Pt1/Al1	6	Pt2/Al2	270.5	Pt2/Al2	2	Pt1/Al1	270.5
6		Al2/Pt2	327.8	2								
3		Pt1/Al1	328.0					2	Pt2/Al2	287.1		
1		Ca	338.3									
3		Ca	339.3									

Table 5. Bader charges considering valence states.

	Ca	Al	Pt	Ref.
Ca_2AlPt_2	+1.30	+1.30	-1.95	*
Ca_2AlPt_2	+1.10	+0.62	-1.42	[6]
CaAl_2Pt_2	+1.36	+1.76/+1.74	-3.08/-1.76	*
$\text{Ca}_2\text{Al}_3\text{Pt}$	+1.20	+0.30	-3.30	*

* this work.

2. Results

2.1. Ternary System Ca–Al–Pt

The known phases in the ternary system Ca–Al–Pt are shown in Figure 1. A number of binary phases have been reported in the three systems Ca–Al, Ca–Pt and Al–Pt. A rule of thumb states, that in ternary systems where numerous binary phases are known, also numerous ternary phases should exist. Thus far, the equiatomic CaAlPt , CaAl_2Pt , Ca_2AlPt_2 and the Al-rich $\text{Ca}_2\text{Al}_9\text{Pt}_3$ have been reported. CaAlPt crystallizes in the orthorhombic TiNiSi type structure ($Pnma$),^[12,13] while CaAl_2Pt adopts the also orthorhombic MgCuAl_2 type structure ($Cmcm$)^[4] and $\text{Ca}_2\text{Al}_9\text{Pt}_3$ crystallizes in the $\text{Y}_2\text{Co}_3\text{Ga}_9$ type ($Cmcm$).^[14] Finally, monoclinic Ca_2AlPt_2 ($C2/c$, $\text{Ca}_2\text{Ir}_2\text{Si}$ type) has also been reported.^[6] During attempts to synthesize $\text{Ca}_3\text{Al}_4\text{Pt}_4$, tetragonal CaAl_2Pt_2 ($P4/nmm$, CaBe_2Ge_2 type) and hexagonal $\text{Ca}_2\text{Al}_3\text{Pt}$ ($P6_3/mmc$, $\text{Mg}_2\text{Cu}_3\text{Si}$

type) were discovered. In addition, Ca_2AlPt_2 was observed and subsequently resynthesized.

2.2. Powder X-ray Diffraction

A sample with a nominal starting composition of $\text{Ca}_3\text{Al}_4\text{Pt}_4$ was prepared, in analogy to $\text{Ba}_3\text{Al}_4\text{Pt}_4$,^[18] from which single crystals of monoclinic Ca_2AlPt_2 , tetragonal CaAl_2Pt_2 and hexagonal $\text{Ca}_2\text{Al}_3\text{Pt}$ were extracted and investigated via single crystal X-ray diffraction experiments (*vide infra*). The powder X-ray diffraction pattern indicates the formation of a multi-phase mixture. Ca_2AlPt_2 , CaAl_2Pt_2 , $\text{Ca}_2\text{Al}_3\text{Pt}$ as well as CaAl_2Pt and in addition, at least one yet unidentified side phase, are present in the sample. Subsequently, new samples with the respective nominal compositions Ca_2AlPt_2 , CaAl_2Pt_2 and $\text{Ca}_2\text{Al}_3\text{Pt}$ were prepared. Ca_2AlPt_2 was obtained as nearly phase pure sample. The Rietveld refinement of the powder X-ray data is shown in Figure 2. The desired phase Ca_2AlPt_2 was obtained with 99(1) wt.-%, with an additional 1(1) wt.-% of cubic AlPt ($P2_3$, FeSi type^[39]). For CaAl_2Pt_2 and $\text{Ca}_2\text{Al}_3\text{Pt}$, no phase pure samples could be obtained. For the first, in addition to the targeted compound, also AlPt_3 and $\text{Al}_{21}\text{Pt}_8$ as well as a yet unidentified phase could be observed in the powder diffraction patterns. The samples of nominal $\text{Ca}_2\text{Al}_3\text{Pt}$ indicate the formation of the desired phase as well as CaAl_2Pt and an unknown compound. Attempts to identify the two unknown compounds in the

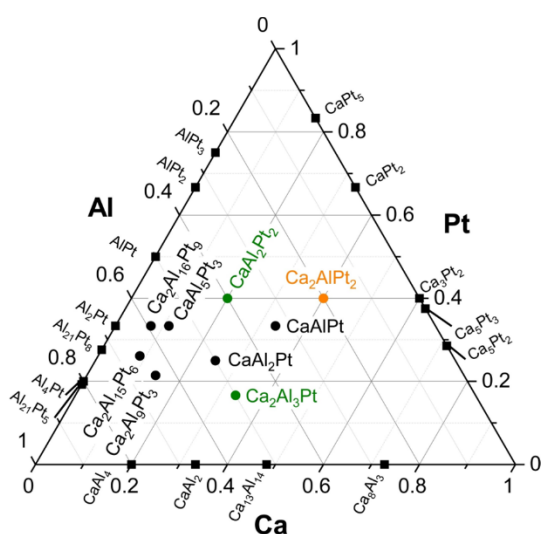


Figure 1. Overview of the binary and ternary phases known in the system Ca–Al–Pt. Data are taken from the Pearson database^[5] and the references cited in the introduction. New reported phases are shown in green, the resynthesized phase in orange.

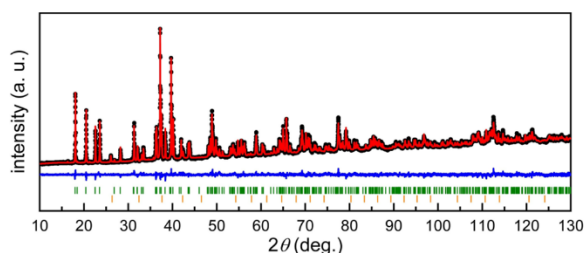


Figure 2. Rietveld refinement of the powder X-ray diffraction pattern of Ca_2AlPt_2 . Collected data are shown as black dots, the refinement as red, the difference as blue line. Green ticks indicate the Bragg positions of Ca_2AlPt_2 , orange ticks the ones of AlPt .

samples of nominal CaAl_2Pt_2 and $\text{Ca}_2\text{Al}_3\text{Pt}$ via single-crystal X-ray diffraction experiments have not been successful thus far.

2.3. Single Crystal X-ray Diffraction and Structure Refinement

From the sample with the nominal composition $\text{Ca}_3\text{Al}_4\text{Pt}_4$, numerous single crystals were selected and analyzed. Careful analysis of the data of the first single crystal X-ray diffraction experiment revealed a C-centered monoclinic lattice and space group $C2/c$ was found to be correct for Ca_2AlPt_2 . The $\text{Ca}_2\text{Ir}_2\text{Si}$ type structure could be assigned, in accordance to the report in literature.^[6] For what turned out to be $\text{CaAl}_{2.24(1)}\text{Pt}_{1.76(1)}$, a tetragonal metric was observed and space group $P4/nmm$ along with the CaBe_2Ge_2 type structure was deduced. Finally,

$\text{Ca}_2\text{Al}_{3.09(1)}\text{Pt}_{0.91(1)}$ crystallizes in the hexagonal crystal system with space group $P6_3/mmc$ and adopts the $\text{Mg}_2\text{Cu}_3\text{Si}$ type structure, a coloring variant of the hexagonal Laves phase MgZn_2 .

All structures were solved using the charge flipping algorithm of SUPERFLIP^[29] and least squares refinements on F^2 using the program JANA2006^[30,31] were carried out. All atomic positions were refined with anisotropic displacement parameters and as a check for correct compositions, the occupancy parameters were refined in a separate series of least-square refinements.

While for Ca_2AlPt_2 no mixed occupancies were observed, nominal $\text{Ca}_2\text{Al}_3\text{Pt}$ shows mixing of Pt and Al on the 2a and 6h site leading to a refined composition of $\text{Ca}_2\text{Al}_{3.09(1)}\text{Pt}_{0.91(1)}$. It has to be noted, that the mixing on the 6h site refines to 0.99(1) Al and 0.01(1) Pt, however, when refining solely as Al, this position refines to a site occupancy of 1.04(1), clearly indicating a mixing with Pt. Due to the significant differences in electron density between Al and Pt only around 1% Pt is refined on this site. Also, the R-values show that a mixing is appropriate since they decrease from 0.0213/0.0714 to 0.0204/0.0664 for R_1/wR_2 for all data.

Nominal CaAl_2Pt_2 exhibits Pt and Al mixing on the 2a site. In addition, significant residual electron density near the Pt2 position (2c) can be observed with a distance of ~ 66 pm. Therefore, this site has been refined as a split site with a constrained overall occupation of 1 and constrained displacement parameters but the possibility to freely refine the z parameter. This leads to a composition of $\text{CaAl}_{2.24(1)}\text{Pt}_{1.76(1)}$. The final difference Fourier syntheses for all three structures were contour less. Details of the structure determination, atomic parameters and interatomic distances can be found in Tables 1–4. CSDs 2331503–2331505 contains the supplementary crystallographic data for this paper. These data can be obtained free of charge from The Cambridge Crystallographic Data Centre via www.ccdc.cam.ac.uk/data_request/cif.

2.4. Crystal Chemistry

In the following paragraph, the three structure types will be briefly introduced, a detailed structure description, however, can be found in the respective original papers. The unit cells are depicted in Figure 3. We will begin with nominal CaAl_2Pt_2 which crystallizes in the tetragonal crystal system with space group $P4/nmm$, isostructural to CaBe_2Ge_2 .^[40] The structure can be derived from BaAl_4 via a *klassengleiche* transition of index 2 leading to a split of the two crystallographically independent Al sites in BaAl_4 .^[41–43] Therefore, five crystallographic atom positions (2a, 2b and $3 \times 2c$) can be found in the CaBe_2Ge_2 type.^[40] The Ca position is also occupied by Ca atoms in nominal CaAl_2Pt_2 , while the Al1 and Al2 atoms occupy the Be positions of the prototype. The Ge atoms of the prototype are finally replaced by Pt atoms. The refinement, however, indicates that Pt1 position in nominal CaAl_2Pt_2 is not fully occupied by Pt. A freely refined occupancy factor led to a reduced site occupation. Therefore, a mixed occupied site with Al was introduced (Figure 3, segmented black/white spheres) as this has been

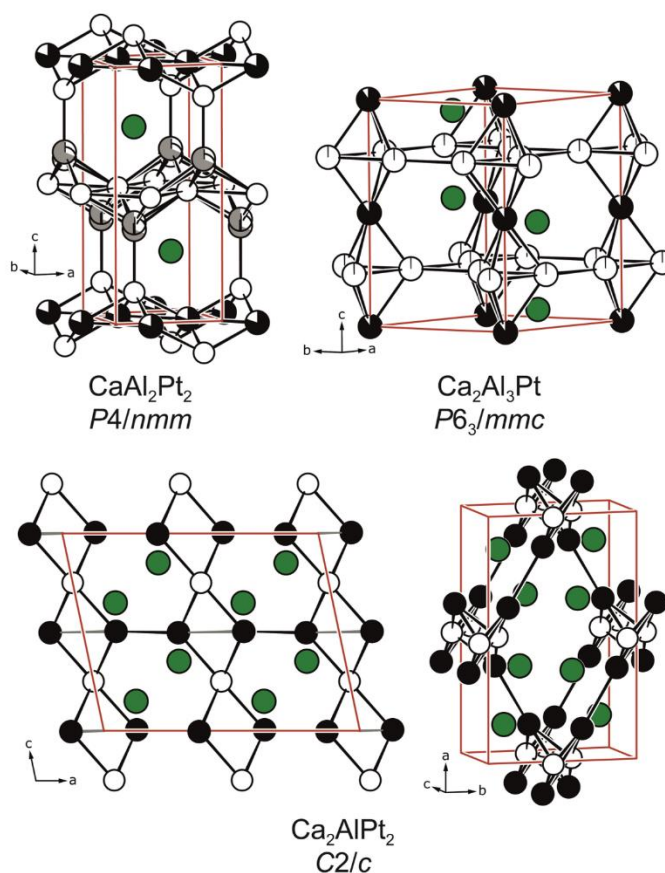


Figure 3. Unit cells of (top left) CaAl_2Pt_2 (CaBe_2Ge_2 type, $P4/nmm$) depicted roughly along the b axis; (top right) $\text{Ca}_2\text{Al}_3\text{Pt}$ ($\text{Mg}_2\text{Cu}_3\text{Si}$ type, $P6_3/mmc$) and (bottom) Ca_2AlPt_2 along the b and roughly along the c axis. Ca, Al and Pt atoms are shown in green, white and black circles. Partially occupied sites are shown as segmented or grey circles (see text).

observed in BaAl_4 related compounds.^[44] The Pt2 position exhibits a significantly enhanced anisotropic displacement parameter as well as residual electron density nearby ($d \sim 60$ pm). A refinement of the occupancy parameter of the Pt2 site led to a significant improve in the R -values, however, the additional electron density did not vanish. Therefore, the Pt2 site was refined as a split position with both the ADPs and the overall composition fixed (Figure 3, grey spheres). This leads to a refined composition of $\text{CaAl}_{2.24(1)}\text{Pt}_{1.76(1)}$. It is interesting to note that SrAl_2Pt_2 also exists and crystallizes in a (3+2)D incommensurately modulated structure^[10] related to the CaBe_2Ge_2 type. However, even upon close inspection, no superstructure reflections are visible for CaAl_2Pt_2 . And also, the defects observed in modulated $\text{SrPt}_{1.833}\square_{0.167}\text{Sn}_2$ are not applicable here.^[45] The interatomic distances in $\text{CaAl}_{2.24(1)}\text{Pt}_{1.76(1)}$ ($d(\text{Ca}-\text{Pt}) = 322\text{--}331$ pm; $d(\text{Ca}-\text{Al}) = 329\text{--}351$ pm; $d(\text{Al}-\text{Pt}) = 240\text{--}268$ pm; $d(\text{Pt}-\text{Pt}) = 302$ pm; $d(\text{Al}-\text{Al}) = 302$ pm) are in agreement with other binaries like Al_2Pt (CaF_2 type, $d(\text{Al}-\text{Pt}) = 256$ pm; $d(\text{Al}-\text{Al}) = 296$ pm),^[46] CaAl_2 (MgCu_2 type, $d(\text{Al}-\text{Al}) = 284$ pm; $d(\text{Ca}-\text{Al}) = 333$ pm)^[47] or CaPt_2 (MgCu_2 type, $d(\text{Pt}-\text{Pt}) = 270$ pm; $d(\text{Ca}-\text{Pt}) =$

316 pm)^[48] or ternaries like CaAlPt ($d(\text{Ca}-\text{Pt}) = 294\text{--}305$ pm; $d(\text{Ca}-\text{Al}) = 308\text{--}336$ pm; $d(\text{Al}-\text{Pt}) = 261\text{--}275$ pm; $d(\text{Al}-\text{Al}) = 311$ pm),^[12,13] $\text{Ca}_2\text{Al}_3\text{Pt}_3$ ($d(\text{Ca}-\text{Pt}) = 343\text{--}347$ pm; $d(\text{Ca}-\text{Al}) = 303\text{--}318$ pm; $d(\text{Al}-\text{Pt}) = 257\text{--}264$ pm; $d(\text{Al}-\text{Al}) = 269\text{--}293$ pm)^[4] or CaAl_3Pt ($d(\text{Ca}-\text{Pt}) = 284\text{--}314$ pm; $d(\text{Ca}-\text{Al}) = 323\text{--}342$ pm; $d(\text{Al}-\text{Pt}) = 255\text{--}258$ pm; $d(\text{Al}-\text{Al}) = 276\text{--}290$ pm).^[4] The relatively short Al–Pt distances point towards bonding interactions.

Nominal $\text{Ca}_2\text{Al}_3\text{Pt}$ (Figure 3, top right) crystallizes in the hexagonal $\text{Mg}_2\text{Cu}_3\text{Si}$ type, an ordering variant of the hexagonal Laves phase MgZn_2 . Two structural reviews on Laves phases addressing the ordering variants have been published recently.^[49,50] It is interesting to note, that the Al phases usually exhibit a $M_2\text{Al}_3T$ composition ($M = \text{Sc}, \text{Y}, \text{La-Nd}, \text{Sm}, \text{Gd-Lu}; T = \text{Ru}, \text{Rh}, \text{Ir}$)^[51,52] while the isostructural gallides have a $M_2\text{Ga}_3$ stoichiometry ($M = \text{Y}, \text{La-Nd}, \text{Sm}, \text{Gd-Er}; T = \text{Rh}$).^[53] With the early transition metal Ti, the $M_2\text{Al}_3\text{Ti}$ series ($M = \text{Y}, \text{Gd-Tm}, \text{Lu}$) adopts the rhombohedral $\text{Mg}_2\text{Ni}_3\text{Si}$ type structure.^[54] Since the $\text{Mg}_2\text{Ni}_3\text{Si}$ type is a coloring variant of MgZn_2 , the structure description is straightforward. The Zn1 site (6 h) is occupied by Al atoms while the Pt atoms reside on the Zn2 site (2a). The Ca atoms can be

finally found on the Mg position (4f) of the prototype. As for the rare-earth compounds RE_2Al_3T with $RE=Sc, Y, La-Nd, Sm, Gd-Lu$ and $T=Ru, Rh, Ir$,^[51] mixing of the Al and the transition metal atoms can take place. In nominal Ca_2Al_3Pt , nearly 10% Al can be found on the Pt site (2a) while 1% Pt can be observed on the Al site (6h). This leads to a refined composition of $Ca_2Al_{3.09(1)}Pt_{0.91(1)}$. The interatomic distances in $Ca_2Al_{3.09(1)}Pt_{0.91(1)}$ ($d(Ca-Pt)=328$ pm; $d(Ca-Al)=316$ & 328 pm; $d(Al-Pt)=270$ pm; $d(Al-Al)=274$ & 287 pm) are in agreement with the compounds named before. And again, the relatively short Al-Al and Al-Pt distances point towards bonding interactions.

Ca_2AlPt_2 (Figure 3, bottom) finally crystallizes in the monoclinic crystal system and adopts the Ca_2Ir_2Si type structure. In the crystal structure, the Pt atoms form chains with alternating distances ($d(Pt-Pt)=274$ & 295 pm) running within the ab plane. The Pt chains are found on $z=0$ and $1/2$ with an angle of 61° to each other. The Al atoms connect these Pt chains forming cavities for the Ca atoms. The atomic arrangement is similar to the one observed in the Ca_2Pd_2Ge type structure,^[6] however, the distinct difference are the alternating Pt-Pt distances in the chains. In contrast to the two structures mentioned before, no mixing of Al and Pt was observed. The interatomic distances in Ca_2AlPt_2 ($d(Ca-Pt)=306-311$ pm; $d(Ca-Al)=327-351$ pm; $d(Al-Pt)=249-252$ pm; $d(Pt-Pt)=274$ & 295 pm) are again in agreement with the compounds named in the discussion about nominal $CaAl_2Pt_2$. In contrast to the two structure types named before, no Al-Al bonding was observed.

2.5. Quantum-Chemical Calculations

Quantum-mechanical calculations were performed on the DFT level using the experimental lattice parameters and atomic positions as starting points. The idealized structures, with respect to mixed occupancies, were used. In the cases of Ca_2AlPt_2 and Ca_2Al_3Pt the unit cell parameters after structural relaxation are in good agreement with the experimentally observed lattice parameters. For $CaAl_2Pt_2$, however, significant deviations are observed. This can be probably related to the fact that the starting lattice parameters of ideal $CaAl_2Pt_2$ are in fact the ones of $CaAl_{2.24(1)}Pt_{1.76(1)}$ which exhibits severe mixing of Al and Pt, which was removed for the quantum-chemical calculations. After structural relaxation (Table 1), self-consistent runs were conducted and subsequent high precision integrations of the Brillouin-zone (BZ) (Ca_2AlPt_2 : $9 \times 15 \times 11$; $CaAl_2Pt_2$: $15 \times 15 \times 9$; Ca_2Al_3Pt : $13 \times 13 \times 9$) were used for the calculation of the Bader charges [21], the obtained Bader charges are listed in Table 5. It should be noted, that Doverbratt and coworkers already calculated Bader charges for Ca_2AlPt_2 ^[6] which differ to the values reported in this work, most likely due to the use of different functionals. However, the overall trend is the same. When looking at the trends of the Bader charges, the Ca and Al atoms exhibit positive charges while the Pt atoms are formally anionic. This is in line with the Pauling electronegativities ($\chi(Ca)=1.00$; $\chi(Al)=1.61$; $\chi(Pt)=2.28$) of the constituent elements. When going from Ca_2AlPt_2 (40 at.-% Ca; 40 at.-% Pt) over $CaAl_2Pt_2$ (20 at.-% Ca; 40 at.-% Pt) to Ca_2Al_3Pt (33.3 at.-%

Ca; 16.7 at.-% Pt) the absolute values of the overall charge of the Pt atoms increases significantly from -1.42 to -3.30 . This can also be easily explained by the fact that the Pt content decreases, hence the ratio of electronegative Pt to the less electronegative Ca and Al shifts, leading to an increased charge transfer. Overall, all three compounds should therefore be regarded as polar intermetallic compounds with Ca cations compensated by $[Al_xPt_y]^{3-}$ polyanions.

3. Conclusion

With tetragonal $CaAl_2Pt_2$ ($CaBe_2Ge_2$ type) and hexagonal Ca_2Al_3Pt ($MgZn_2/Mg_2Cu_3Si$ type), two new intermetallic compounds have been found in the ternary system Ca-Al-Pt upon attempts to synthesize $Ca_3Al_4Pt_4$, in analogy to $Ba_3Al_4Pt_4$. In addition, the already reported monoclinic Ca_2AlPt_2 (Ca_2Ir_2Si type) was observed. Single crystal X-ray diffraction experiments showed that the latter compound has a defined composition, while nominal $CaAl_2Pt_2$ and Ca_2Al_3Pt exhibit significant Al/Pt mixing. The refined compositions of the investigated single crystals are $CaAl_{2.24(1)}Pt_{1.76(1)}$ and $Ca_2Al_{3.09(1)}Pt_{0.91(1)}$. Attempts to synthesize bulk samples of Ca_2AlPt_2 were successful, however, all syntheses of $CaAl_2Pt_2$ and Ca_2Al_3Pt led to the formation of multi-phase mixtures. Quantum-chemical calculations indicate that all three compounds are polar intermetallics with a designated charge transfer from the Ca/Al onto the Pt atoms while at the same time, distinct Al-Pt and homoatomic Al-Al/Pt-Pt bonding takes place. Therefore, the structures can be understood as $[Al_xPt_y]^{3-}$ polyanions with the Ca cations residing in cavities of the respective networks.

Author Contribution

All authors have accepted responsibility for the entire content of this submitted manuscript and approved the submission.

Acknowledgements

Instrumentation and technical assistance for this work were provided by the Service Center X-ray Diffraction, with financial support from Saarland University and German Research Foundation (project numbers INST 256/506-1 and INST 256/349-1). Funding was provided by the Deutsche Forschungsgemeinschaft DFG (JA 1891-10-1). Open Access funding enabled and organized by Projekt DEAL.

Conflict of Interest

The authors declare no conflicts of interest regarding this article.

Data Availability Statement

The data that supports the findings of this study are available from the corresponding author upon reasonable request.

Keywords: intermetallics · single-crystal · quantum-chemical calculations

- [1] C. Benndorf, H. Eckert, O. Janka, *Acc. Chem. Res.* **2017**, *50*, 1459–1467.
- [2] H. Eckert, R. Pöttgen, *Z. Anorg. Allg. Chem.* **2010**, *636*, 2232–2243.
- [3] J. Emsley, *The Elements*, Clarendon Press, Oxford University Press, Oxford, New York, **1998**.
- [4] F. Stegemann, T. Block, S. Klenner, Y. Zhang, B. P. T. Fokwa, A. Timmer, H. Mönig, C. Doerenkamp, H. Eckert, O. Janka, *Chem. Eur. J.* **2019**, *25*, 10735–10747.
- [5] P. Villars, K. Cenzual, Pearson's Crystal Data: Crystal Structure Database for Inorganic Compounds, ASM International®, Materials Park, Ohio, USA **2023**.
- [6] I. Doverbratt, S. Ponou, Y. Zhang, S. Lidin, G. J. Miller, *Chem. Mater.* **2015**, *27*, 304–315.
- [7] F. Stegemann, C. Benndorf, R. S. Touzani, B. P. T. Fokwa, O. Janka, *J. Solid State Chem.* **2016**, *242*, 143–150.
- [8] F. Stegemann, R. S. Touzani, O. Janka, *Dalton Trans.* **2019**, *48*, 14103–14114.
- [9] F. Stegemann, T. Block, S. Klenner, Y. Zhang, B. P. T. Fokwa, C. Doerenkamp, H. Eckert, O. Janka, *Eur. J. Inorg. Chem.* **2021**, 3832–3845.
- [10] R.-D. Hoffmann, F. Stegemann, O. Janka, *Z. Kristallogr.* **2016**, *231*, 127–142.
- [11] M. Radzieowski, F. Stegemann, R.-D. Hoffmann, O. Janka, *Z. Kristallogr.* **2017**, *232*, 675–687.
- [12] P. Kenfack Tsobnang, D. Fotio, S. Ponou, C. Fon Abi, *Acta Crystallogr.* **2011**, *E67*, i55.
- [13] F. Hulliger, *J. Alloys Compd.* **1993**, *196*, 225–228.
- [14] F. Stegemann, Y. Zhang, B. P. T. Fokwa, O. Janka, *Dalton Trans.* **2020**, *49*, 6398–6406.
- [15] S. Engel, E. C. J. Giebelmann, L. Schumacher, Y. Zhang, F. Müller, O. Janka, *Dalton Trans.* **2024**, in review.
- [16] S. Engel, J. Bönnighausen, F. Stegemann, R. S. Touzani, O. Janka, *Z. Naturforsch.* **2022**, *77*, 367–379.
- [17] S. Engel, O. Janka, *Z. Naturforsch.* **2024**, *79b*, accepted. DOI: 10.1515/znb-2024-0022.
- [18] F. Stegemann, C. Benndorf, T. Bartsch, R. S. Touzani, M. Bartsch, H. Zacharias, B. P. T. Fokwa, H. Eckert, O. Janka, *Inorg. Chem.* **2015**, *54*, 10785–10793.
- [19] M. Radzieowski, F. Stegemann, C. Doerenkamp, S. F. Matar, H. Eckert, C. Dosche, G. Wittstock, O. Janka, *Inorg. Chem.* **2019**, *58*, 7010–7025.
- [20] T. Koizumi, F. Honda, Y. J. Sato, D. Li, D. Aoki, Y. Haga, J. Gouchi, S. Nagasaki, Y. Uwatoko, Y. Kaneko, Y. Ōnuki, *J. Phys. Soc. Jpn.* **2022**, *91*, 043704 (043705 pages).
- [21] M. Radzieowski, F. Stegemann, O. Janka, *Eur. J. Inorg. Chem.* **2020**, *2020*, 1199–1210.
- [22] M. Radzieowski, F. Stegemann, T. Block, J. Stahl, D. Johrendt, O. Janka, *J. Am. Chem. Soc.* **2018**, *140*, 8950–8957.
- [23] R. Pöttgen, T. Gulden, A. Simon, *GIT Labor-Fachz.* **1999**, *43*, 133–136.
- [24] R. Pöttgen, A. Lang, R.-D. Hoffmann, B. Künnen, G. Kotzyba, R. Müllmann, B. D. Mosel, C. Rosenhahn, *Z. Kristallogr.* **1999**, *214*, 143–150.
- [25] Bruker AXS Inc., Topas, Version 5, Karlsruhe (Germany) **2014**.
- [26] H. M. Rietveld, *Acta Crystallogr.* **1967**, *22*, 151–152.
- [27] H. M. Rietveld, *J. Appl. Crystallogr.* **1969**, *2*, 65–71.
- [28] Bruker AXS Inc., Saint +, Madison, WI (USA) **1999**.
- [29] L. Palatinus, G. Chapuis, *J. Appl. Crystallogr.* **2007**, *40*, 786–790.
- [30] V. Petříček, M. Dušek, L. Palatinus, Jana2006. The crystallographic computing system, Institute of Physics, Praha (Czech Republic) **2006**.
- [31] V. Petříček, M. Dušek, L. Palatinus, *Z. Kristallogr.* **2014**, *229*, 345–352.
- [32] V. Petříček, L. Palatinus, J. Plášil, M. Dušek, *Z. Kristallogr.* **2023**, *238*, 271–282.
- [33] K. Brandenburg, Crystal Impact, Diamond, Bonn (Germany) **2022**.
- [34] P. E. Blöchl, *Phys. Rev. B* **1994**, *50*, 17953–17979.
- [35] G. Kresse, D. Joubert, *Phys. Rev. B* **1999**, *59*, 1758–1775.
- [36] G. Kresse, J. Furthmüller, *Phys. Rev. B* **1996**, *54*, 11169–11186.
- [37] G. Kresse, J. Furthmüller, *Comput. Mater. Sci.* **1996**, *6*, 15–50.
- [38] R. F. W. Bader, *Chem. Rev.* **1991**, *91*, 893–928.
- [39] K. Schubert, W. Burkhardt, P. Esslinger, E. Günzel, H. G. Meissner, W. Schütt, J. Wegst, M. Wilkens, *Naturwissenschaften* **1956**, *43*, 248–249.
- [40] B. Eisenmann, N. May, W. Müller, H. Schäfer, *Z. Naturforsch.* **1972**, *27b*, 1155–1157.
- [41] R. Pöttgen, *Z. Anorg. Allg. Chem.* **2014**, *640*, 869–891.
- [42] D. Kußmann, R. Pöttgen, U. C. Rodewald, C. Rosenhahn, B. D. Mosel, G. Kotzyba, B. Künnen, *Z. Naturforsch.* **1999**, *54b*, 1155–1164.
- [43] E. Parthé, L. M. Gelato, B. Chabot, M. Penzo, K. Cenzual, E. I. Gladyshevskii, *TYPIX-Standardized Data and Crystal Chemical Characterization of Inorganic Structure Types*, in: *Gmelin Handbook of Inorganic and Organometallic Chemistry*, Springer, Germany, Berlin, **1993**.
- [44] D. Johrendt, H. Hosono, R.-D. Hoffmann, R. Pöttgen, *Z. Kristallogr.* **2011**, *226*, 435–446.
- [45] C. Schwickert, R.-D. Hoffmann, F. Winter, R. Pöttgen, *Z. Kristallogr.* **2014**, *229*, 525–535.
- [46] E. Zintl, A. Harder, W. Hauke, *Z. Phys. Chem. B* **1937**, *35*, 354–362.
- [47] H. Nowotny, E. Wormnes, A. Mohrheim, *Z. Metallkd.* **1940**, *32*, 39–42.
- [48] E. A. Wood, V. B. Compton, *Acta Crystallogr.* **1958**, *11*, 429–433.
- [49] E. C. J. Giebelmann, R. Pöttgen, O. Janka, *Z. Anorg. Allg. Chem.* **2023**, *649*, e202300109.
- [50] O. Janka, R. Pöttgen, *Z. Naturforsch.* **2024**, *79b*, 63–70.
- [51] F. Eustermann, F. Stegemann, S. Gausebeck, O. Janka, *Z. Naturforsch.* **2018**, *73b*, 819–830.
- [52] T. Mishra, R.-D. Hoffmann, C. Schwickert, R. Pöttgen, *Z. Naturforsch.* **2011**, *66b*, 771–776.
- [53] S. Seidel, O. Janka, C. Benndorf, B. Mausolf, F. Haarmann, H. Eckert, L. Heletta, R. Pöttgen, *Z. Naturforsch.* **2017**, *72b*, 289–303.
- [54] E. C. J. Giebelmann, S. Engel, I. El Saudi, L. Schumacher, M. Radzieowski, J. M. Gerdes, O. Janka, *Solids* **2023**, *4*, 160–180.

Manuscript received: June 3, 2024
 Revised manuscript received: June 24, 2024
 Accepted manuscript online: June 24, 2024



Stefan Engel, Maximilian K. Reimann, Eteri Svanidze, Mitja Krnel, Nazar Zaremba, Markus König and Oliver Janka*

SrAl₈Rh₂ – the first phase in the Sr/Al/Rh system and new representative of the CeAl₈Fe₂ type structure

<https://doi.org/10.1515/zkri-2024-0115>

Received November 20, 2024; accepted November 22, 2024;

published online January 31, 2025

Abstract: Large lath-shaped single crystals of SrAl₈Rh₂ were grown during attempts to synthesize SrAl₄Rh₂ in analogy to SrAl₄Ir₂. Single crystal experiments determined the structure to be isostructural to the CeAl₈Fe₂ type crystallizing in the orthorhombic crystal system with space group *Pbam* ($a = 1269.74(4)$, $b = 1475.43(5)$, $c = 412.55(1)$ pm, $wR2 = 0.0398$, $2088 F^2$ values and 70 variables). SrAl₈Rh₂ is the first reported compound in the ternary system Sr–Al–Rh. No mixing on any atomic position was observed. Attempts to synthesize SrAl₈Rh₂ in bulk led to a multiphase mixture according to powder X-ray diffraction experiments. However, here also growth of large single crystals was possible. Subsequently, electrical resistivity measured on a single crystal of SrAl₈Rh₂ revealed an onset of superconductivity around $T_c = 0.8$ K. Finally, quantum-chemical calculations gave an insight into the chemical bonding and the charge distribution, showing that the compound consists of a [Al₈Rh₂]⁶⁻ polyanion with the Sr^{δ+} residing in the pentagonal cavities.

Keywords: strontium; rhodium; aluminum; intermetallics; physical properties; single crystal

1 Introduction

Ternary intermetallic compounds with an element of low electronegativity, e.g. an alkaline earth metal ($AE = Ca–Ba$), a

highly electronegative electron-rich transition metal ($T = Rh, Ir, Pd, Pt, Ag, Au$) and aluminum are only poorly investigated with only 81 entries in the Pearson's Crystal Data database¹ when compared to the overwhelming number of compounds observed in the $RE–Al–T$ ($RE = Sc, Y, La–Nd, Sm–Lu; T = Rh, Ir, Pd, Pt, Ag, Au$) systems with close to 800 entries in Pearson's database. The lack of interest in alkaline earth compounds might come from the fact that these compounds typically do not show pronounced magnetic behavior like magnetic order due to the closed f -shell. This, however, is not necessarily a downside but can also be an advantage. For example, specific analytic techniques like ²⁷Al NMR can be performed on these dia- or Pauli-paramagnetic compounds, giving insight into the coordination environment of magnetically independent Al positions as well as their respective distortions.^{2–11} Also, quantum chemical calculations become vastly easier due the absence of f -electrons.

In the case of the Sr–Al– T system with $T = Co, Rh, Ir, Ni, Pd, Pt$ only nine compounds plus the newly found SrAl₈Rh₂ exist with SrAl₉Co₂ and SrAl₉Ni₂ being the only two compounds with the same structure type (BaAl₉Fe₂ type, *P6/mmm*).¹² The other six compounds are Sr₂Al₉Ir₃ (Y₂Ga₉Co₃ type, *Cmcm*),¹³ Sr₂Al₅Pd₄ (own type, *Pnma*),¹⁴ Sr₂AlPd₂ (Ca₂GePd₂ type, *Fdd2*),¹⁵ Sr₂Al₈Pt₃ (Eu₂Si₃Ni₃ type, *P4₂/nmc*),¹⁶ SrAl₂Pt (MgAl₂Cu, *Cmcm*)¹⁷ and SrAl₂Pt₃ (CeB₂Co₃, *P6/mmm*).¹⁵ Figure 1 shows all existing phases in the ternary system Sr–Al– T . It is interesting to note, that all known compounds are located in the middle and the Al-rich corner, with no compounds with high Sr or T content reported so far.

SrAl₈Rh₂ is the first compound in the Sr–Al–Rh system adopting the orthorhombic CeAl₈Fe₂ type structure (*Pbam*, *oP44*, h^5g^5da).¹⁸ The isotypic Eu compound EuAl₈Rh₂ was reported in 2023 by He et al.¹⁹ Besides these compounds the isostructural series only exhibits compounds with the 3d elements iron and cobalt namely $REAl_8Fe_2$ ($RE = La–Pr, Eu$),^{18,20,21} MAl_8Co_2 ($M = Ca, La–Nd, Sm, Yb$)^{22–27} and the sole representative with nickel being CaAl₈Ni₂.^{28,29} In case of Ga and In, more compounds are known to literature, with all MX_8T_2 compounds forming in the CeAl₈Fe₂ type structure summarized in Table 1. Additionally, CeAl₈Pd₂ was reported – it crystallizes in its own structure type in the monoclinic crystal system, space group *C2/m*.³⁰

*Corresponding author: Oliver Janka, Inorganic Solid State Chemistry, Saarland University, Campus C4 1, 66123, Saarbrücken, Germany, E-mail: oliver.janka@uni-saarland.de

Stefan Engel, Inorganic Solid State Chemistry, Saarland University, Campus C4 1, 66123, Saarbrücken, Germany, E-mail: stefan.engel@uni-saarland.de

Maximilian K. Reimann, Institut für Anorganische und Analytische Chemie, Universität Münster, Corrensstrasse 28/30, 48149, Münster, Germany, E-mail: maximilian.reimann@uni-muenster.de

Eteri Svanidze, Mitja Krnel, Nazar Zaremba and Markus König, Max Planck Institute for Chemical Physics of Solids, Nöthnitzer Straße 40, 01187, Dresden, Germany, E-mail: eteri.svanidze@cpfs.mpg.de (E. Svanidze), mitja.krnel@cpfs.mpg.de (M. Krnel), nazar.zaremba@cpfs.mpg.de (N. Zaremba), markus.koenig@cpfs.mpg.de (M. König)

Open Access. © 2024 the author(s), published by De Gruyter. This work is licensed under the Creative Commons Attribution 4.0 International License.

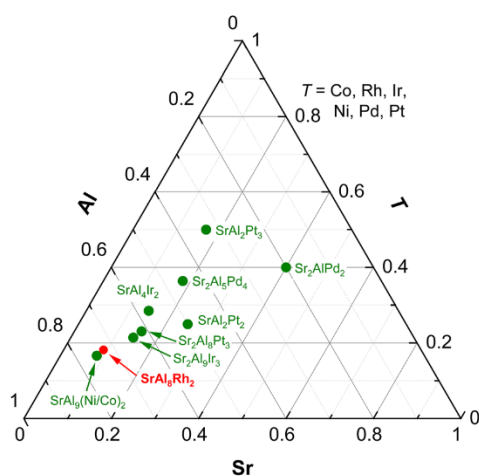


Figure 1: Overview of the ternary phases known in the Sr–Al–*T* system (*T* = Co, Rh, Ir, Ni, Pd, Pt). Data is taken from the Pearson's crystal database.¹ References are cited above in the introduction. Since ternary phases of six transition metals are plotted, the binary compounds are omitted for clarity.

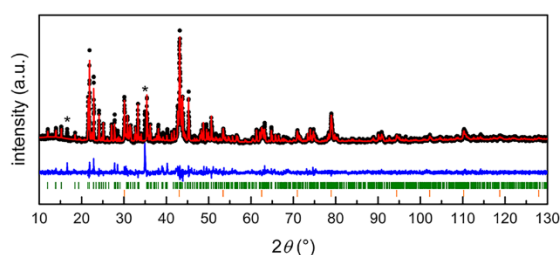


Figure 2: Powder X-ray diffraction pattern of the attempt to synthesize SrAl₈Rh₂. Experimental data is shown as black dots, simulated diffraction pattern from refinement as red line, the difference is shown as continuous blue line, the Bragg positions for SrAl₈Rh₂ and AlRh are shown as green and orange ticks. The unidentified side phase is marked with asterisks.

The synthesis of isostructural *AE* compounds is rather difficult due to the significantly different sizes of the alkaline earth metals, but in the case of the rare earth to *AE* metals distinctive isostructural atom pairs are known. Due to their similar ionic sizes³¹ of Sr²⁺ ($r_{\text{ionic}} = 126$ pm) and Eu²⁺ ($r_{\text{ionic}} = 125$ pm) as well as Ca²⁺ ($r_{\text{ionic}} = 112$ pm) and Yb²⁺ ($r_{\text{ionic}} = 114$ pm), in many cases isostructural compounds exist – for example, SrAl₅Pt₃ and EuAl₅Pt₃ (YNi₅Si₃ type, *Pnma*),^{32,33} SrAl₄Ir₂ and EuAl₄Ir₂ (own type, *P4/ncc*),³⁴ SrAl₂Pt and EuAl₂Pt, CaAl₂Pt and YbAl₂Pt^{6,17} as well as Ca₂Al₁₅Pt₆ and Yb₂Al₁₅Pt₆ (Sc₂Al₁₅Pt₆ type, *P2₁/m*).^{35,36}

During the attempts to synthesize SrAl₄Rh₂ (which could, in principle be analogous to SrAl₄Ir₂³⁴), lath-shaped crystals were observed. A new compound SrAl₈Rh₂ (*Pbam*) crystallizing in the CeAl₈Fe₂ type structure, as characterized by

Table 1: Lattice parameters (powder, single crystal, DFT and literature data), and unit cell volumes of compounds with the CeAl₈Fe₂ type structure (space group *Pbam*, *Z* = 4).

Compound	<i>a</i> (pm)	<i>b</i> (pm)	<i>c</i> (pm)	<i>V</i> (nm ³)	Ref.
SrAl ₈ Rh ₂ ^P	1270.96(2)	1477.56(2)	412.95(1)	0.7755	^a
SrAl ₈ Rh ₂ ^{SC}	1269.74(4)	1475.43(5)	412.55(1)	0.7729	^a
SrAl ₈ Rh ₂ ^{DFT}	1265.82	1472.85	411.10	0.7656	^a
CaAl ₈ Co ₂	1246.6	1441.1	402.8	0.7236	²⁹
CaAl ₈ Ni ₂	1253.2	1450.0	397.5	0.7223	²⁹
LaAl ₈ Fe ₂	1265	1436	427	0.7757	¹⁸
LaAl ₈ Co ₂	1298	1432	417	0.7751	²⁴
CeAl ₈ Fe ₂	1251	1448	407	0.7373	¹⁸
CeAl ₈ Co ₂	1241	1430	412	0.7312	²²
PrAl ₈ Co ₂	1237	1443	401	0.7158	²⁶
PrAl ₈ Fe ₂	1252.16	1445.45	404.4	0.7319	²¹
NdAl ₈ Co ₂	1245.17	1436.21	400.55	0.7163	²⁵
SmAl ₈ Co ₂	1231	1444	397	0.7057	²⁶
EuAl ₈ Rh ₂	1469.5	1263.3	411.4	0.7636	¹⁹
EuAl ₈ Fe ₂	1253.0	1450.3	403.6	0.7334	²⁰
YbAl ₈ Co ₂	1238.30	1440.04	396.08	0.7063	²⁷
LaGa ₈ Fe ₂	1247	1412	410.2	0.7223	³⁹
LaGa ₈ Ru ₂	1264.7	1473.3	411.7	0.7671	⁴⁰
CeGa ₈ Fe ₂	1241	1439	407.5	0.7277	³⁹
CeGa ₈ Ru ₂	1260.3	1470.7	409.7	0.7594	⁴⁰
CeGa ₈ Co ₂	1240.0	1433.1	405.9	0.7213	⁴¹
PrGa ₈ Fe ₂	1247.0	1429.0	408.0	0.7270	⁴¹
PrGa ₈ Ru ₂	1260.7	1471.1	408.0	0.7567	⁴⁰
PrGa ₈ Co ₂	1239.2	1429.9	405.5	0.7185	⁴¹
NdGa ₈ Fe ₂	1242.2	1427.0	407.9	0.7231	⁴¹
NdGa ₈ Ru ₂	1258.1	1469.8	407.1	0.7528	⁴⁰
SmGa ₈ Fe ₂	1229.0	1425.3	407.9	0.7145	⁴¹
EuGa ₈ Co ₂	1237.8	1441	404.7	0.7219	⁴¹
EuGa ₈ Rh ₂	1465.77	1256.77	410.73	0.7566	⁴²
EuGa ₈ Ir ₂	1262.37	1469.78	414.86	0.7697	⁴³
YbGa ₈ Co ₂	1240.2	1442.2	398.45	0.7127	⁴⁴
SrIn ₈ Rh ₂	1387.4	1617.0	438.26	0.9832	⁴⁵
SrIn ₈ Ir ₂	1384.7	1611.3	439.62	0.9809	⁴⁶
EuIn ₈ Rh ₂	1381.7	1611.8	436.44	0.9720	⁴⁷
EuIn ₈ Ir ₂	1384.68	1611.77	438.85	0.9794	⁴²

^athis work; ^L literature data; ^P powder data; ^{SC} single crystal data; ^{DFT} after structural optimization.

single crystal X-ray diffraction experiments, was thus discovered. In addition, quantum-chemical calculations were performed in order to examine the bonding situation. Electrical resistivity measurements on a single crystal specimen reveal onset of superconductivity around $T_C = 0.8$ K.

2 Experimental

2.1 Synthesis

The samples of nominal SrAl₄Rh₂ and SrAl₈Rh₂ both were prepared from the elements using strontium pieces

(Onyxmet), rhodium pieces (Agosi AG) and aluminum pieces (Onyxmet), all with stated purities above 99.5%. Samples were prepared on a 100–150 mg scale. Strontium was stored under argon atmosphere in a dry box (MBraun, Garching, Germany). In all cases, the starting materials were transferred into an Ta ampoule, which was subsequently sealed in a custom-build arc-melting apparatus³⁷ under 800 mbar argon pressure using the ideal ratios of Sr:Al:Rh (1:4:2 or 1:8:2). The argon gas was purified over a titanium sponge (873 K), molecular sieves, activated carbon, and silica gel prior to use. To react the starting materials, the Ta ampoule was enclosed in silica glass and placed into a muffle furnace at 1273 K for 96 h; no reaction with the Ta container was observed. All samples are metallic, ground powders (particle size >100 μm) are grey and stable in air over a period of several months.

2.2 X-ray diffraction

The pulverized samples of nominal SrAl₈Rh₂ and SrAl₄Rh₂ were investigated at room temperature on a D8-A25-Advance diffractometer (Bruker, Karlsruhe, Germany) in Bragg-Brentano θ - θ -geometry (goniometer radius 280 mm) with non-monochromatic Cu K α -radiation ($\lambda = 154.0596$ pm). Diffraction patterns were recorded between 6 and 130° 2 θ with a step size of 0.013° and a total scan time of 1 h. A 12 μm Ni foil working as K β filter and a variable divergence slit were mounted at the primary beam side. A LYNXEYE detector with 192 channels was used at the secondary beam side. The recorded data was evaluated using the Bruker TOPAS 5.0 software,³⁸ with the observed reflections being treated via single-line fits. The refined lattice parameters are given in Table 1.

Lath-shaped crystals of SrAl₈Rh₂ were obtained from both attempts, nominal SrAl₄Rh₂ and SrAl₈Rh₂. The crystals were glued to silica fibers using beeswax. An intensity data set of a suitable crystal was collected at room temperature using a Bruker × 8 APEX2 diffractometer (Bruker, Karlsruhe, Germany). A multi-scan absorption correction using SadABS⁴⁸ was applied to the data set. All relevant crystallographic data, deposition and details of the data collection and evaluation are listed in Tables 2–4.

CSD 2343482 contains the supplementary crystallographic data for this paper. The data can be obtained free of charge from The Cambridge Crystallographic Data Centre via www.ccdc.cam.ac.uk/structures.

2.3 Scanning electron microscopy

The powdered bulk sample and single crystals of an on-stoichiometry synthesis of SrAl₈Rh₂ were attached to a

Table 2: Crystallographic data and structure refinement for SrAl₈Rh₂ (CeAl₈Fe₂ type structure, space group *Pbam*, *Z* = 4).

Sum formula	SrAl ₈ Rh ₂
Formula weight, g mol ⁻¹	509.3
Lattice parameters	Table 1
Calcd. Density, g cm ⁻³	4.38
Crystal size, μm ³	200 × 30 × 30
Diffractometer	Bruker × 8 APEX2
Wavelength; λ, pm	71.073
Absorption correction	Multi-scan Bruker SADABS
Abs. coefficient, mm ⁻¹	78.7
<i>F</i> (000), <i>e</i>	2222
θ range, deg	2.12–36.36
Range <i>hkl</i>	± 21; ± 24; ± 6
Total no. reflections	20824
Independent reflections/ <i>R</i> _{int}	2088/0.0289
Reflections <i>I</i> > 3 σ (<i>I</i>)/ <i>R</i> _{σ}	1937/0.0133
Data/parameters	2088/70
Goodness of fit on <i>F</i> ²	1.29
<i>R</i> ₁ / <i>wR</i> ₂ for <i>I</i> > 3 σ (<i>I</i>)	0.0159/0.0391
<i>R</i> ₁ / <i>wR</i> ₂ (all data)	0.0179/0.0398
Extinction coefficient	7680(110)
Extinction scheme	Lorentzian isotropic ⁴⁹
Larg. diff. peak/hole, e Å ⁻³	+ 1.58/–1.13

Table 3: Atomic coordinates and displacement parameters (in pm²) of SrAl₈Rh₂ (CeAl₈Fe₂ type structure, space group *Pbam*, *Z* = 4). The isotropic displacement parameter *U*_{eq} is defined as: *U*_{eq} = 1/3(*U*₁₁ + *U*₂₂ + *U*₃₃) (pm²); *U*₁₃ = *U*₂₃ = 0. Standard deviations are given in parentheses.

Atom	Wyckoff position	<i>x</i>	<i>y</i>	<i>z</i>	<i>U</i> _{eq}
Sr	4 <i>g</i>	0.34106(1)	0.31858(1)	0	75(7)
Rh1	4 <i>g</i>	0.03480(1)	0.40459(1)	0	42(5)
Rh2	4 <i>g</i>	0.15220(1)	0.09659(1)	0	45(6)
Al1	2 <i>a</i>	0	0	0	89(3)
Al2	2 <i>d</i>	0	1/2	1/2	74(3)
Al3	4 <i>h</i>	0.23889(4)	0.17287(4)	1/2	82(2)
Al4	4 <i>h</i>	0.45227(4)	0.18157(3)	1/2	73(7)
Al5	4 <i>h</i>	0.16139(4)	0.37977(4)	1/2	79(2)
Al6	4 <i>g</i>	0.33987(4)	0.04388(4)	0	104(2)
Al7	4 <i>g</i>	0.09641(4)	0.25243(3)	0	86(2)
Al8	4 <i>h</i>	0.16933(5)	–0.00973(4)	1/2	78(2)
Al9	4 <i>h</i>	0.02619(4)	0.13239(4)	1/2	68(2)

sticky carbon tape and semi quantitatively analyzed in a JEOL 7000 F (JEOL, Freising, Germany) scanning electron microscope (SEM) equipped with an EDAX Genesis 2000 energy-dispersive X-ray spectroscopy (EDX) detector (EDAX, Unterschleissheim, Germany). The standard deviations are ±2 at.% due to the irregular shape of the powder. The results are listed in Table 5.

Table 4: Interatomic distances (pm) in of SrAl₈Rh₂ (CeAl₈Fe₂ type structure, space group *Pbam*, *Z* = 4). All distances of the first coordination spheres are listed. Standard deviations are equal or smaller than 0.2 pm.

Sr	2	Al5	320.5	Al3	2	Rh2	259.5	Al7	1	Rh1	237.7
	2	Al9	321.0		1	Al4	271.2		1	Rh2	240.6
	2	Al4	321.5		1	Al9	276.6		2	Al9	286.1
	2	Al3	324.9		1	Al8	283.5		2	Al5	291.0
	1	Al7	325.5		2	Al7	298.4		2	Al4	292.5
	2	Al8	327.0		2	Al6	308.6		2	Al3	298.4
	1	Al1	335.2		1	Al5	320.7		1	Sr	325.5
Rh1	1	Al7	340.8	Al4	2	Sr	324.9	Al8	1	Sr	340.8
	1	Al7	237.7		2	Rh1	264.0		2	Rh2	260.0
	2	Al2	253.6		1	Al3	271.2		1	Al5	269.8
	1	Al6	258.9		1	Al2	274.7		1	Al9	277.5
	1	Al6	259.9		1	Al5	280.5		1	Al3	283.5
	2	Al4	264.0		1	Al9	290.1		2	Al1	298.3
	2	Al5	264.1		2	Al7	292.5		1	Al9	307.2
Rh2	1	Rh1	295.0	Al5	2	Sr	321.5	Al9	2	Al6	309.3
	1	Al1	240.2		2	Al6	322.8		2	Sr	327.0
	1	Al7	240.6		2	Rh1	264.1		2	Rh2	266.3
	1	Al6	250.7		1	Al8	269.8		1	Al3	276.6
	2	Al3	259.5		1	Al2	271.0		1	Al8	277.5
	2	Al8	260.0		1	Al4	280.5		2	Al1	286.0
	2	Al9	266.3		2	Al7	291.0		2	Al7	286.1
Al1	2	Rh2	240.2	Al6	2	Al6	318.1	Al9	1	Al4	290.1
	4	Al9	286.0		2	Sr	320.5		1	Al8	307.2
	4	Al8	298.3		1	Al3	320.7		2	Sr	321.0
	2	Sr	335.2		1	Rh2	250.7				
Al2	4	Rh1	253.6	Al6	1	Rh1	258.9	Al9			
	2	Al5	271.0		1	Rh1	259.9				
	2	Al4	274.7		2	Al2	296.8				
	4	Al6	296.8		2	Al3	308.6				
				2	Al8	309.3					
				2	Al5	318.1					
				2	Al4	322.8					

2.4 Electrical resistivity measurements

The *ac* electrical resistivity measurements in a temperature range from $T = 0.4$ K to $T = 300$ K were carried out using a Quantum Design Physical Property Measurement System for magnetic fields up to $\mu_0 H = 9$ T. Given the microscopic size of the crystals, electrical contacts were created with the help of focused-ion-beam patterning. The current was applied along the *c*-axis of the single crystal, given the fixed position of the crystal with respect to voltage and current pairs. An example of the micro-scale device is shown in the inset of Figure 6a.

2.5 Quantum-chemical calculations

Electronic structure calculations of SrAl₈Rh₂ were performed using the projector augmented wave method (PAW) of Blöchl^{50,51} coded in the Vienna *ab initio* simulation

Table 5: SEM-EDX data of SrAl₈Rh₂, measured on powder and single crystals. The maximum deviations are ± 2 at. %.

Sample	Sr (at.%)	Al (at.%)	Rh (at.%)
Ideal composition	9.1	72.7	18.2
Powder	9	69	22
Single crystal	9	70	21

package (VASP).^{52,53} VASP calculations employed the potentials PAW_PBE Sr_sv 07Sep2000, PAW_PBE Al 04Jan2001 and PAW_PBE Rh_pv 25Jan2005. The cutoff energy for the plane wave calculations was set to 800 eV and the Brillouin zone integration was carried out using a *k*-point mesh with a spacing of ≈ 0.02 ($5 \times 5 \times 15$) using the Monkhorst Pack algorithm.⁵⁴ The exchange-correlation effects were accounted for within the generalized gradient approximation GGA according to Perdew, Burke and Ernzerhof.⁵⁵

The calculations were conducted starting from the experimental single crystal data and the whole cell underwent unconstrained geometry relaxation of the structural parameters.

Based on the optimized structure, the electronic structure of SrAl₈Rh₂ was projected from the plane-wave base onto a local orbital basis set using the LOBSTER (Local Orbital Basis Suite Towards Electronic-Structure Reconstruction) program package.^{56–60} Based on these projections, the local density-of-states-matrices can be accessed enabling the calculation of Löwdin-related gross populations as well as atomic charges.⁶¹ In addition, the recently introduced crystal-orbital-bond-index (COBI) can be derived.⁶² The COBI can be rationalized as the solid-state pendant to the molecular bond index as introduced by Wiberg and Mayer.^{63,64} When integrating the COBI values (then called ICOBI) they correspond to the covalent bond orders within the context of solid-state materials.

3 Results

3.1 Powder X-ray diffraction

Powder X-ray diffraction measurements of the initial attempts to synthesize SrAl₄Rh₂ yielded the title compound in low amounts alongside numerous side phases. Attempts to target SrAl₈Rh₂ with a stoichiometric starting composition led to the title compound being the main product (80.7 mass %) alongside AlRh (19.3 mass%) and at least one unidentified side product (Figure 2).

3.2 Single crystal X-ray diffraction and structure refinement

Careful analysis of the obtained single crystal X-ray diffraction data on needle shaped crystals (Figure 3) obtained from attempts to synthesize SrAl₄Rh₂ revealed an orthorhombic lattice with space group *Pbam*. The structure was solved using the charge flipping algorithm of SUPERFLIP⁶⁵ and a least squares refinement on F^2 using the program JANA 2006^{66,67} was carried out. All atomic positions were refined with anisotropic displacement parameters and as a check for correct compositions, the occupancy parameters were refined in a separate series of least-square refinements. All sites were fully occupied within three standard deviations leading to a refined composition of SrAl₈Rh₂ in contrast to the targeted composition. Final difference Fourier syntheses were contour less. From the Pearson database,¹ isotypism with CeAl₈Fe₂⁶⁸ was deduced.

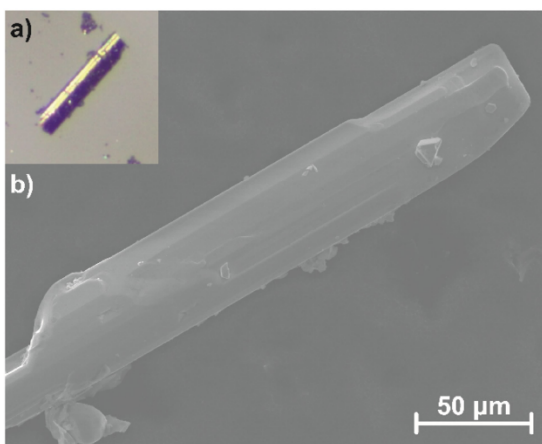


Figure 3: Images of a SrAl₈Rh₂ single crystal taken by a) light microscope and b) electron microscope.

Details of the structure determination, atomic parameters and interatomic distances can be found in Tables 2–4.

CSD2343482 contains the supplementary crystallographic data for this paper. These data can be obtained free of charge from The Cambridge Crystallographic Data Centre via www.ccdc.cam.ac.uk/data_request/cif.

3.3 Crystal chemistry

SrAl₈Rh₂ crystallizes in the CeAl₈Fe₂ type structure in the orthorhombic crystal system with space group *Pbam* (*oP44*, h^5g^5da). Similar to MAl_5Pt_3 ¹¹ and $M_2Al_{16}Pt_9$ ⁶⁹ ($M = Ca, Sr, Y, La-Nd, Sm-Er$), it forms a polyanionic network with separated cavities hosting the Sr atoms. In contrast to the aforementioned compounds, the cavities in the case of SrAl₈Rh₂ are pentagonal (not hexagonal) prisms and are formed only from Al atoms (Sr@Al₁₀; Figure 4, green highlight). The atomic positions alongside their interatomic distances are shown in Figure 5. Both crystallographically independent Rh atoms are surrounded by nine Al atoms in the shape of a threefold capped trigonal prism (Rh@Al₉; Figure 4, light and dark blue regions). Furthermore, Rh1 has another Rh1 in its coordination environment with a distance of 295 pm. In addition to the one Sr and two Rh positions, the structure exhibits nine independent Al positions. Al1 and Al7 (Figure 4, light and medium orange highlights) exhibit similar coordination environments consisting of two Sr, two Rh and eight Al atoms, which form a fourfold capped distorted cube. Al2 is surrounded by eight Al atoms, forming a distorted square prism capped on four sides with Rh atoms. Al6 (Figure 4, yellow color) possesses a coordination number

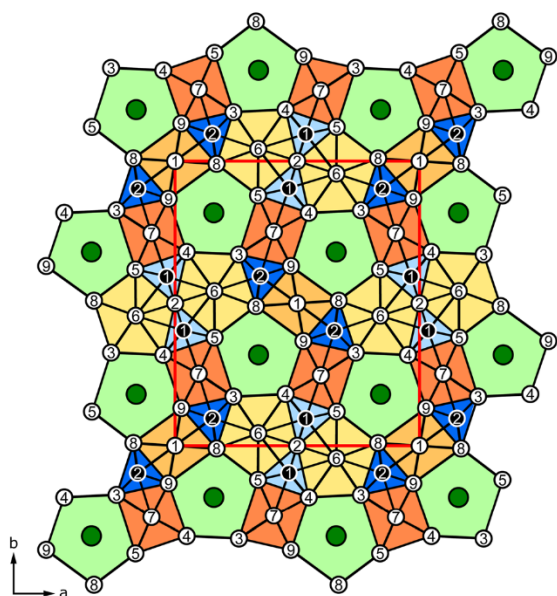


Figure 4: Unit cell of SrAl₈Rh₂ as projection along [001]. Sr, Al and Rh atoms are shown in green, white and black circles, respectively. The coordination environments are highlighted, see text for explanation.

of 13, consisting of 10 Al atoms forming a pentagonal prism which is threefold capped with rhodium. Al3 to Al5 and Al8 all have a coordination number of 12 and a coordination environment of two Rh, two Sr and eight Al forming highly distorted cuboctahedra. The interatomic distances in SrAl₈Rh₂ are $d(\text{Sr}-\text{Al}) = 320\text{--}341$ pm, $d(\text{Al}-\text{Al}) = 270\text{--}329$ pm,

$d(\text{Rh}-\text{Al}) = 238\text{--}266$ pm and $d(\text{Rh}-\text{Rh}) = 295$ pm. No Sr–Sr and Sr–Rh distances below 350 pm are observed. A comparison with selected reference compounds is given in Table 6.

3.4 Scanning electron microscopy

Powdered parts of the sample with the nominal composition SrAl₈Rh₂ and single crystals of the same sample were investigated by SEM-EDX. The average of three point measurements are given in Table 5 and are in good agreement with the ideal composition (9.1 at.-% Sr, 18.2 at.-% Al, 72.7 at.-% Rh). The deviations can be explained by the irregular sample surface and the imperfect orientation of the powder towards the beam. No impurity elements heavier than sodium (detection limit of the instrument) were detected in the single crystal measurements.

3.5 Electrical resistivity measurements

The results of the temperature dependent measurements of the electrical resistivity of a single crystal specimen of SrAl₈Rh₂ are shown in Figure 6. In zero magnetic field, the sample shows a linear decrease of the resistivity with decreasing temperature in the range between 15 and 300 K (black curve). This is indicative of a normal metallic behavior. Below around 15 K, the resistivity shows an upturn, which is likely indicating a small amount of magnetic impurity (on a ppm level) also known as impurity

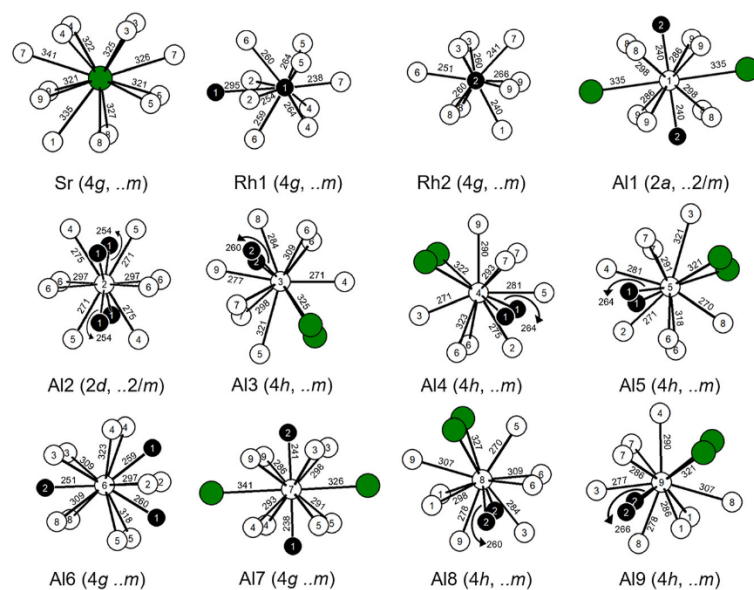


Figure 5: Coordination environments surrounding the Sr, Al and Rh atoms in the crystal structure of SrAl₈Rh₂. Sr, Al and Rh atoms are shown as green, black and white circles, respectively. Wyckoff positions, site symmetries and interatomic distances (in pm) are given.

Table 6: Interatomic distances in SrAl₈Rh₂ and selected reference compounds.

Interaction	Distance in SrAl ₈ Rh ₂ (pm)	Reference compound	Distance in reference (pm)
Sr–Al	320–341	SrAl ₄ (BaAl ₄ type, <i>I4/mmm</i>)	341 ⁷⁰
		Sr ₅ Al ₉ (own type, <i>R$\bar{3}m$</i>)	330–346 ⁷¹
		Sr ₈ Al ₇ (Ba ₈ Ga ₇ type, <i>P2₁3</i>)	334–342 ⁷²
		Sr ₂ Al ₅ Pd ₄ (own type, <i>Pnma</i>)	337–347 ¹⁴
		Sr ₂ Al ₉ Ir ₃ (Y ₂ Ga ₉ Co ₃ type, <i>Cmcm</i>)	309–314 ⁷³
		Sr ₂ AlPd ₂ (Ca ₂ GePd ₂ type, <i>Fdd2</i>)	345–369 ¹⁵
Rh–Rh	295	Al ₁₃ Rh ₄	306–332 ⁷⁴
		AlRh (CsCl type, <i>Pm$\bar{3}m$</i>)	299 ⁷⁵
		Al ₅ Rh ₂ (Al ₅ Co ₂ type, <i>P6₃/mmc</i>)	284 ⁷⁶
Rh–Al	238–266	Al ₉ Rh ₂ (Al ₉ Co ₂ type, <i>P2₁/c</i>)	245–260 ⁷⁷
		Al ₁₃ Rh ₄ (Al ₁₃ Fe ₄ type, <i>C2/m</i>)	253–335 ⁷⁴
		Al ₅ Rh ₂ (Al ₅ Co ₂ type, <i>P6₃/mmc</i>)	239–277 ⁷⁶
		AlRh (CsCl type, <i>Pm$\bar{3}m$</i>)	259 ⁷⁵
		Ca ₃ Al ₁₂ Rh ₄ (Gd ₃ Al ₁₂ Ru ₄ type, <i>P6₃/mmc</i>)	238–270 ⁷³
		Eu ₃ Al ₁₂ Rh ₄ (Gd ₃ Al ₁₂ Ru ₄ type, <i>P6₃/mmc</i>)	240–270 ⁷³
Al–Al	270–329	SrAl ₄ (BaAl ₄ type, <i>I4/mmm</i>)	265–315 ⁷⁰
		Sr ₅ Al ₉ (own type, <i>R$\bar{3}m$</i>)	271–346 ⁷¹
		Sr ₈ Al ₇ (Ba ₈ Ga ₇ type, <i>P2₁3</i>)	263–270 ⁷²
		Al ₉ Rh ₂ (Al ₉ Co ₂ type, <i>P2₁/c</i>)	273–347 ⁷⁷
		Al ₁₃ Rh ₄ (Al ₁₃ Fe ₄ type, <i>C2/m</i>)	254–349 ⁷⁴
		Al ₅ Rh ₂ (Al ₅ Co ₂ type, <i>P6₃/mmc</i>)	272–325 ⁷⁶
		AlRh (CsCl type, <i>Pm$\bar{3}m$</i>)	299 ⁷⁵
		Ca ₃ Al ₁₂ Rh ₄ (Gd ₃ Al ₁₂ Ru ₄ type, <i>P6₃/mmc</i>)	274–326 ⁷³
		Eu ₃ Al ₁₂ Rh ₄ (Gd ₃ Al ₁₂ Ru ₄ type, <i>P6₃/mmc</i>)	275–331 ⁷³
		Sr ₂ Al ₉ Ir ₃ (Y ₂ Ga ₉ Co ₃ type, <i>Cmcm</i>)	278–349 ⁷³
		Sr ₂ Al ₅ Pd ₄ (own type, <i>Pnma</i>)	270–311 ¹⁴
		SrAl ₅ Co ₂ (BaAl ₅ Fe ₂ type, <i>P6/mmm</i>)	285–290 ¹²

Kondo screening.⁷⁸ In zero magnetic field, the resistance drops sharply below 0.8 K, possibly suggesting an onset of superconductivity in SrAl₈Rh₂. With an applied magnetic field of 9 T, the drop disappears (red curve), while the upturn is slightly shifted vertically.

3.6 Quantum-chemical calculations

Quantum-chemical calculations were performed on the DFT level using the experimentally determined crystal structure as the starting point. The unit cell parameters after structural relaxation change only slightly ($\Delta x = -0.31\%$, $\Delta y = -0.18\%$, $\Delta z = -0.35\%$) and are therefore in fair agreement with the experimentally observed ones (Table 1). Based on the recently introduced approaches to calculate Löwdin charges and bond indices using the LOBSTER tool, the transfer of valence electrons as well as chemical bonding via ICOBI can be rationalized rather easily. Before going into more detail, the three scenarios that can occur should be briefly noted. For strong covalent bonds, ICOBI values can reach values up to one while contrasting, values near zero

will indicate no (for large distances) or rather ionic interactions (for appropriate distances).^{62,79} For metallic materials, that exhibit a delocalization of their bonding,⁸⁰ multi-center bonding is observed. This is rationalized by effectively existent ICOBI values somewhere in between 0 and 1. For MgAl₂Cu (own type, space group *Cmcm*), an appropriate example when analyzing and comparing the bonding in SrAl₈Rh₂, a rather high positive Löwdin charge can be observed for the Mg atoms (+1.37), being the ones with the lowest EN and therefore an electron donor. In contrast to the electronegativities, however, Cu also possesses a positive charge (+0.67) while Al is the anion (−1.02).⁸¹ The ICOBI values indicate rather ionic interactions between Cu and Mg (ICOBI = 0.03–0.01) while the Cu–Al interactions are stronger (ICOBI = 0.18–0.16), in line with what is expected for metallic bonding. The Al–Al interactions, however, are significantly stronger with ICOBI values between 0.57–0.53 and 0.57–0.39 depending on the respective Al–Al interaction.⁸¹

Due to the complex nature of the SrAl₈Rh₂ structure, not every individual contact will be discussed in detail, but an overall impression of the Löwdin charges and the bonding situation should be given. Figure 7 depicts the Löwdin

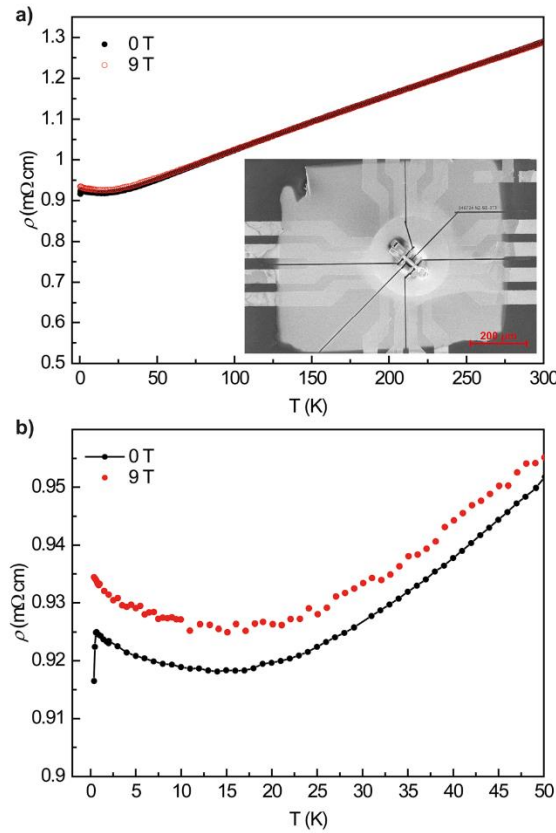


Figure 6: Temperature dependence of the electrical resistivity of a single crystal of SrAl₈Rh₂. Electrical resistivity ρ , measured with (red) and without (black) applied magnetic field of 9 T. a) Temperature range from 300 to 0.4 K. Picture of the prepared micro-scale device is shown in the inset. b) Low temperature regime between 50 and 0.4 K.

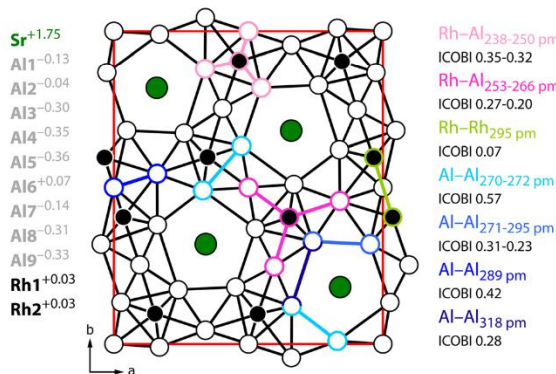


Figure 7: Crystal structure of SrAl₈Rh₂ alongside the Löwdin charges for the individual atomic positions as well as interatomic contacts (color coded) that are discussed in the text. The respective distances and their ICObI values are given.

charges for all crystallographically independent positions. The first interesting aspect is that the Sr atoms show an Löwdin charge of +1.75, indicating an almost full transfer of their valence electrons in line with what has been reported in the literature for other s-element containing metals.^{82,83} The second aspect is, that the Rh atoms almost show no charge transfer based on their Löwdin charges (Rh1 and Rh2 both +0.03). This, however, is in line with what has been observed in e.g. ScRhSi₂ (Rh: –0.02) or Zr₅Rh₂In₄ (Rh: +0.08).⁸¹ The Al atoms finally also show some interesting effects: (I) Al2 (–0.04) and Al6 (+0.07) show Löwdin charges close to zero while (II) Al1 (–0.13) and Al7 (–0.14) show significantly lower values compared to the remaining Al atoms Al3–Al5, Al8 and Al9 with Löwdin charges > –0.30.

When looking at the crystal chemical environments, a rationale for these observed charges can be constructed. Al2 and Al6, which show Löwdin charges close to zero, are only coordinated by Al and Rh atoms with no Sr–Al contacts below 350 pm. It seems, that therefore no distinct charge transfer takes place. Al1 and Al7 show almost similar coordination environments (*vide supra*) in the shape of a fourfold capped distorted cube according to Al@Al₈Rh₂Sr₂. In both cases, the Al–Rh distances are significantly shorter compared to the other Al–Rh interactions in SrAl₈Rh₂ while the Sr–Al distances are amongst the longest when considering distances <350 pm. It seems that therefore a charge transfer onto Al1 and Al7 is hampered significantly, resulting in intermediate Löwdin charges of –0.13 for Al1 and –0.14 for Al7. The remaining Al atoms (Al3–Al5, Al8 and Al9) all exhibit two Sr–Al contacts that are rather “short” (~325 pm) and two Al–Rh contacts that are on the opposite side of the coordination environment. In addition, seven or eight Al–Al contacts are observed. In all cases, the Löwdin charges are between –0.30 and –0.36.

When addressing the bonding situation by analyzing the ICObI values also several interesting things can be observed. First of all, no Sr–Rh interactions below 400 pm can be observed, clearly indicative of no interactions between the two atoms. The Sr–Al distances are between 320 and 339 pm with ICObI values smaller than 0.05. This clearly shows that these interactions are of ionic nature.^{62,79} The Rh–Rh interaction (295 pm) also shows a low ICObI values of 0.07, however, here no bonding interaction has to be attributed due both atoms being the same element. For the Al–Rh interactions stronger (ICObI 0.35–0.32) and weaker ones (ICObI 0.27–0.20) are observed. The stronger ones can be assigned to the short Al–Rh interactions in the Rh coordination environments while the weaker ones stem from the longer bond distances. Finally, for the homoatomic Al–Al interactions, ICObI values of up to 0.57 can be observed for the shortest Al–Al interactions present in the structure.

Similar ICOBI values were reported for Al–Al interactions in BaAl₄, La₃Al₁₁ or MgCuAl₂.⁸¹ The longer Al–Al interactions exhibit smaller ICOBI values between 0.31 and 0.23, which may be indicative of multicenter bonding. One of the longest Al–Al interactions that still shows bonding contributions is around 320 pm yet exhibits an ICOBI value of 0.28. Finally, one of the distances in the Al₆ coordination environment should be discussed. When looking at the coordination environment, all Al–Al distances but the Al₆–Al₂ ones are above 300 pm (Figure 5). The latter is rather long (297 pm from single crystal, 289 pm from DFT), however, the ICOBI value is 0.42 and, therefore, the second strongest interaction is Al–Al.

Overall, Löwdin charges and ICOBI values clearly show, that the structure of SrAl₈Rh₂ can be explained by Sr^{δ+} cations which show ionic interactions with the Al atoms of the [Al₈Rh₂]^{δ-} polyanionic network. Within this network, Al–Al bonding with significant covalent character can be observed. The Al–Rh interaction shows lower covalency which might be attributed to multicenter bonding, in line with the metallic nature of SrAl₈Rh₂.

4 Conclusions

SrAl₈Rh₂ is a new representative with the orthorhombic CeAl₈Fe₂ structure type (space group *Pbma*). It is the first intermetallic compound in the system Sr–Al–Rh. The structure was determined using single crystal diffraction. Attempts to synthesize bulk samples were not yet successful, with the most prominent side products being AlRh alongside at least one more unidentified phase. The measured electrical resistivity shows metallic behavior down to low temperatures and an onset of a superconductivity around 0.8 K. Quantum-chemical calculations show interactions between Al and Rh to be dominant, leading to the assumption that an [Al₈Rh₂]^{δ-} polyanionic network is present. It possesses pentagonal prismatic cavities in which the Sr^{δ+} resides.

Acknowledgments: Instrumentation and technical assistance for this work were provided by the Service Center X-ray Diffraction, with financial support from Saarland University and German Research Foundation (project numbers INST 256/506-1 and INST 256/349-1) and German Research Foundation DFG (project number INST 256/384-1). Funding was provided by the Deutsche Forschungsgemeinschaft DFG (JA 1891-10-1).

Research ethics: Not applicable.

Informed consent: Not applicable.

Author contributions: The authors have accepted responsibility for the entire content of this manuscript and approved its submission.

Use of Large Language Models, AI and Machine Learning

Tools: None declared.

Conflict of interests: The authors state no conflict of interest.

Research funding: Funding is provided by the Deutsche Forschungsgemeinschaft DFG, INST 256/506-1, INST 256/349-1, INST 256/384-1, JA 1891-10-1.

Data availability: The raw data can be obtained on request from the corresponding author.

References

- Villars, P.; Cenzual, K. *Pearson's Crystal Data: Crystal Structure Database For Inorganic Compounds, Release 2023/24*; ASM International®: Materials Park, Ohio, USA, 2023.
- Stegemann, F.; Benndorf, C.; Bartsch, T.; Touzani, R. S.; Bartsch, M.; Zacharias, H.; Fokwa, B. P. T.; Eckert, H.; Janka, O. Ba₃Pt₄Al₄ – Structure, Properties, and Theoretical and NMR Spectroscopic Investigations of a Complex Platinide Featuring Heterocubane [Pt₄Al₄] Units. *Inorg. Chem.* **2015**, *54*, 10785–10793.
- Benndorf, C.; Stegemann, F.; Eckert, H.; Janka, O. New Transition Metal-Rich Rare-Earth Palladium/platinum Aluminides with RET₃Al₂ Composition: Structure, Magnetism and ²⁷Al NMR Spectroscopy. *Z. Naturforsch.* **2015**, *70b*, 101–110.
- Benndorf, C.; Niehaus, O.; Eckert, H.; Janka, O. ²⁷Al and ⁴⁵Sc NMR Spectroscopy on ScT₂Al and Sc(T_{0.5}T'_{0.5})₂Al (T = T' = Ni, Pd, Pt, Cu, Ag, Au) Heusler Phases and Superconductivity in Sc(Pd_{0.5}Au_{0.5})₂Al. *Z. Anorg. Allg. Chem.* **2015**, 168–175.
- Benndorf, C.; Eckert, H.; Janka, O. Structural Characterization of Intermetallic Compounds by ²⁷Al Solid State NMR Spectroscopy. *Acc. Chem. Res.* **2017**, *50*, 1459–1467.
- Radziejewski, M.; Stegemann, F.; Doerenkamp, C.; Matar, S. F.; Eckert, H.; Dosche, C.; Wittstock, G.; Janka, O. Correlations of Crystal and Electronic Structure via NMR and XPS Spectroscopy in the RETMAl₂ (RE = Sc, Y, La–Nd, Sm, Gd–Tm, Lu; TM = Ni, Pd, Pt) Series. *Inorg. Chem.* **2019**, *58*, 7010–7025.
- Engel, S.; Giebelmann, E. C. J.; Schank, L. E.; Heymann, G.; Brix, K.; Kautenburger, R.; Beck, H. P.; Janka, O. Theoretical and ²⁷Al NMR Spectroscopic Investigations of Binary Intermetallic Alkaline-Earth Aluminides. *Inorg. Chem.* **2023**, *62*, 4260–4271.
- Giebelmann, E. C. J.; Engel, S.; Kostusiak, W.; Zhang, Y.; Herbeck-Engel, P.; Kickelbick, G.; Janka, O. Raman and NMR Spectroscopic and Theoretical Investigations of the Cubic Laves-Phases REAl₂ (RE = Sc, Y, La, Yb, Lu). *Dalton Trans.* **2023**, *52*, 3391–3402.
- Giebelmann, E. C. J.; Radziejewski, M.; Matar, S. F.; Janka, O. Formation of the Sub-oxide Sc₄Au₂O_{1-x} and the Drastically Negative ²⁷Al NMR Shift in Sc₂Al. *Inorg. Chem.* **2023**, *62*, 9602–9617.
- Giebelmann, E. C. J.; Engel, S.; Baldauf, J.; Kösters, J.; Matar, S. F.; Kickelbick, G.; Janka, O. Searching for Laves Phase Superstructures: Structural and ²⁷Al NMR Spectroscopic Investigations in the Hf–V–Al System. *Inorg. Chem.* **2024**, *63*, 8180–8193.
- Engel, S.; Giebelmann, E. C. J.; Schumacher, L.; Zhang, Y.; Müller, F.; Janka, O. Synthesis, Magnetic and NMR Spectroscopic Properties of the MA₅Pt₃ Series (M = Ca, Y, La–Nd, Sm–Er). *Dalton Trans.* **2024**, *53*, 12176–12188.

12. Turban, K.; Schäfer, H. Zur Kenntnis des BaFe₂Al₉-Strukturtyps: Ternäre Aluminiume AT₂Al₉ mit A = Ba, Sr und T = Fe, Co, Ni. *J. Less-Common Met.* **1975**, *40*, 91–96.
13. Stegemann, F.; Stahl, J.; Bartsch, M.; Zacharias, H.; Johrendt, D.; Janka, O. Temperature Induced Valence Phase Transition in Intermediate-Valent YbPd₂Al₃. *Chem. Sci.* **2019**, *10*, 11086–11094.
14. Stegemann, F.; Benndorf, C.; Touzani, R. S.; Fokwa, B. P. T.; Janka, O. Sr₂Pd₄Al₅: Synthesis, Crystal and Electronic Structures, and Chemical Bonding of a Polar Intermetallic Compound. *Eur. J. Inorg. Chem.* **2016**, 1108–1114.
15. Stegemann, F.; Benndorf, C.; Touzani, R. S.; Fokwa, B. P. T.; Janka, O. Experimental and Theoretical Investigations of the Polar Intermetallics SrPt₃Al₂ and Sr₂Pd₂Al. *J. Solid State Chem.* **2016**, *242*, 143–150.
16. Stegemann, F.; Block, T.; Klenner, S.; Zhang, Y.; Fokwa, B. P. T.; Doerenkamp, C.; Eckert, H.; Janka, O. Structural, Physical Theoretical and Spectroscopic Investigations of Mixed-Valent Eu₂Ni₈Si₃ and its Structural Anti-type Sr₂Pt₃Al₈. *Eur. J. Inorg. Chem.* **2021**, 3832–3845.
17. Stegemann, F.; Block, T.; Klenner, S.; Zhang, Y.; Fokwa, B. P. T.; Timmer, A.; Mönig, H.; Doerenkamp, C.; Eckert, H.; Janka, O. From 3D to 2D: Structural, Spectroscopic and Theoretical Investigations of the Dimensionality Reduction in the [PtAl₂]²⁻ Polyanions of the Isotypic MPTAl₂ Series (M = Ca–Ba, Eu). *Chem. Eur. J.* **2019**, *25*, 10735–10747.
18. Yarmolyuk, Y. P.; Pykhal, R. M.; Zarechnyuk, O. S. Crystal Structures of the Compounds CeFe₂Al₈ and LaCoAl₄. *Tezisy Dokl. Vses. Konf. Kristalloghim. Intermet. Soeden* **1974**, *2*, 39–40.
19. He, M.; Xu, X.; Wu, Z.; Dong, C.; Liu, Y.; Hou, Q.; Zhou, S.; Han, Y.; Wang, J.; Qu, Z. Magnetic and Electrical Properties of a Heavy-Fermion Compound EuRh₂Al₈. *Phys. Rev. Mater.* **2023**, *7*, 033401.
20. Manyako, M. B.; Stets', I. N.; Kavich, I. V.; Zarechnyuk, O. S.; Yanson, T. I. Crystal Structure of EuFe₂Al₈. *Dopov. Akad. Nauk Ukr. RSR, Ser. B* **1983**, *7*, 39–41.
21. Klesnar, H.; Rogl, P. The Ternary System: Aluminum–Iron–Praseodymium. *J. Mater. Res.* **1991**, *6*, 53–56.
22. Zarechnyuk, O. S.; Rykhal', R. M.; Korin', V. V. X-Ray Study of the Cerium–Cobalt Aluminium Ternary System Alloys in the Range of 0–33.3 at.% of Cerium. *Dopov. Akad. Nauk Ukr. RSR, Ser. A* **1980**, *1*, 84–85.
23. Watkins-Curry, P.; Burnett, J. V.; Samanta, T.; Young, D. P.; Stadler, S.; Chan, J. Y. Strategic Crystal Growth and Physical Properties of Single-Crystalline LnCo₂Al₈ (Ln = La–Nd, Sm, Yb). *Cryst. Growth Des.* **2015**, *15*, 3293–3298.
24. Ghosh, S.; Strydom, A. M. Strongly Correlated Electron Behaviour in CeT₂Al₈ (T = Fe, Co). *Acta Phys. Pol., A* **2012**, *121*, 1082–1084.
25. He, W.; Zhong, H.; Liu, H.; Zhang, J.; Zeng, L. Crystal Structure and Electrical Resistivity of NdCo₂Al₈. *J. Alloys Compd.* **2009**, *467*, 6–9.
26. Rykhal', R. M.; Zarechnyuk, O. S.; Protasov, V. S. Isothermal Sections at 873 K of Ternary (Praseodymium,samarium)-cobalt-aluminium Systems within the Ranges of 0–0.333 Atomic Parts of the Rare Earth. *Dopov. Akad. Nauk Ukr. RSR, Ser. A* **1985**, *12*, 72–75.
27. Manyako, M. B.; Yanson, T. I.; Bodak, O. I.; Cerny, R.; Yvon, K. Crystal Structure of Ytterbium Cobalt Aluminium, YbCo₂Al₈. *Z. Kristallogr.* **1996**, *211*, 216.
28. Giebelmann, E.; Touzani, R. S.; Morgenstern, B.; Janka, O. Synthesis, Crystal and Electronic Structure of CaNi₂Al₈. *Z. Naturforsch.* **2021**, *76b*, 659–668.
29. Manyako, M. B.; Yanson, T. I.; Zarechnyuk, O. S. Phase Equilibria in the Ca-Co(Ni)-Al Systems at 700 K. *Russ. Metall.* **1988**, *3*, 185–188.
30. Ogunbunmi, M. O. Electronic and Magnetic Properties of the Quasi-Skutterudite RT₂X₈ Intermetallic Compounds. *Prog. Solid State Chem.* **2020**, *58*, 100275.
31. Shannon, R. D. Revised Effective Ionic Radii and Systematic Studies of Interatomic Distances in Halides and Chalcogenides. *Acta Crystallogr.* **1976**, *A32*, 751–767.
32. Engel, S.; Bönnighausen, J.; Stegemann, F.; Touzani, R. S.; Janka, O. SrAl₅Pt₃ and Sr₂Al₁₆Pt₉ – Two New Strontium Aluminum Platinides. *Z. Naturforsch.* **2022**, *77b*, 367–379.
33. Koizumi, T.; Honda, F.; Sato, Y. J.; Li, D.; Aoki, D.; Haga, Y.; Gouchi, J.; Nagasaki, S.; Uwatoko, Y.; Kaneko, Y.; Önuki, Y. Abrupt Change in Electronic States under Pressure in New Compound EuPt₃Al₅. *J. Phys. Soc. Jpn.* **2022**, *91*, 043704.
34. Zaremba, N.; Pavlyuk, V.; Stegemann, F.; Hlukhyy, V.; Engel, S.; Klenner, S.; Pöttgen, R.; Janka, O. MAI₂Ir₂ (M = Ca, Sr, Eu) – Superstructures of the KA₄In₂ Type. *Monatsh. Chem.* **2022**, *154*, 43–52.
35. Radziejowski, M.; Stegemann, F.; Janka, O. Magnetic Properties of the RE₂Pt₆X₁₅ (RE = Y, La–Nd, Sm, Gd–Lu; X = Al, Ga) Series. *Eur. J. Inorg. Chem.* **2020**, 1199–1210.
36. Prots, Y. M.; Deppe, M.; Cardoso Gil, R. H.; Cervellino, A.; Ormeci, A.; Geibel, C.; Grin, Y. Yb₂Al₁₅Pt₆ – the Most Ordered Variety of the Sc_{1,2}Fe₄Si_{9,8} Aristotype. *Chem. Met. Alloys* **2014**, *7*, 85–99.
37. Pöttgen, R.; Gulden, T.; Simon, A. Miniaturisierte Lichtbogenapparat für den Laborbedarf. *GIT Labor-Fachz.* **1999**, *43*, 133–136.
38. Bruker AXS Inc. Topas, Version 5; Karlsruhe (Germany), **2014**.
39. Lapunova, R. V.; Grin, Y.; Yarmolyuk, Y. P. The Li-Ga-Fe and Ce-Ga-Fe Systems. *Sov. Non-Ferrous Met. Res.* **1983**, *11*, 169–172.
40. Schlüter, M.; Jeitschko, W. Ternary Lanthanoid Ruthenium Gallides with a High Gallium Content: Ln₂Ru₃Ga₁₀ (Ln = Yb, Lu) with a New Structure Type and LnRu₂Ga₈ (Ln = La–Nd) with CaCo₂Al₈-type Structure. *Inorg. Chem.* **2001**, *40*, 6362–6368.
41. Sichevich, O. M.; Lapunova, R. V.; Grin, Y.; Yarmolyuk, Y. P. Intermetallic Compounds RGe₂Fe₂ and RGe₂Co₂ (R = La, Ce, Pr, Nd, Sm, Eu). *Russ. Metall.* **1985**, *6*, 109–110.
42. Fritsch, V.; Bobev, S.; Moreno, N. O.; Fisk, Z.; Thompson, J. D.; Sarrao, J. L. Antiferromagnetic Order in EuRh₂(Ga,In)₈. *Phys. Rev. B* **2004**, *70*, 052410.
43. Sichevych, O.; Kohout, M.; Schnelle, W.; Borrmann, H.; Cardoso-Gil, R.; Schmidt, M.; Burkhardt, U.; Grin, Y. EuTM₂Ga₈ (TM = Co, Rh, Ir) – A Contribution to the Chemistry of the CeFe₂Al₈-type Compounds. *Inorg. Chem.* **2009**, *48*, 6261–6270.
44. Gladyshevskii, R. E.; Yarmolyuk, Y. P.; Grin, Y. Crystal Structure of YbGa₈Co₂. *Sov. Phys. Crystallogr.* **1983**, *28*, 641–643.
45. Muts, I. R.; Zaremba, V. I.; Pöttgen, R. Centered Indium Cubes as Structural Motifs in SrRh₂In₈ and SrIrIn₄. *Z. Anorg. Allg. Chem.* **2007**, *633*, 2234–2237.
46. Caltà, N. P.; Bud'ko, S. L.; Rodriguez, A. P.; Han, F.; Chung, D. Y.; Kanatzidis, M. G. Synthesis, Structure, and Complex Magnetism of MTr₂In₈ (M = Eu, Sr). *Inorg. Chem.* **2016**, *55*, 3128–3135.
47. Pöttgen, R.; Kußmann, D. New Indium-Rich Compounds EuRhIn₂ and EuRh₂In₈. *Z. Anorg. Allg. Chem.* **2001**, *627*, 55–60.
48. Sheldrick, G. M. SADABS; University of Göttingen: Germany, 1996.
49. Becker, P. J.; Coppens, P. Extinction within the Limit of Validity of the Darwin Transfer Equations. I. General Formalism for Primary and Secondary Extinction and Their Applications to Spherical Crystals. *Acta Crystallogr.* **1974**, *A30*, 129–147.
50. Blöchl, P. E. Projector Augmented-Wave Method. *Phys. Rev. B* **1994**, *50*, 17953–17979.

51. Kresse, G.; Joubert, D. From Ultrasoft Pseudopotentials to the Projector Augmented-Wave Method. *Phys. Rev. B* **1999**, *59*, 1758–1775.
52. Kresse, G.; Furthmüller, J. Efficient Iterative Schemes for Ab Initio Total-Energy Calculations Using a Plane-Wave Basis Set. *Phys. Rev. B* **1996**, *54*, 11169–11186.
53. Kresse, G.; Furthmüller, J. Efficiency of Ab-Initio Total Energy Calculations for Metals and Semiconductors Using a Plane-Wave Basis Set. *Comput. Mater. Sci.* **1996**, *6*, 15–50.
54. Monkhorst, H. J.; Pack, J. D. Special Points for Brillouin-Zone Integrations. *Phys. Rev. B* **1976**, *13*, 5188–5192.
55. Perdew, J. P.; Burke, K.; Ernzerhof, M. Generalized Gradient Approximation Made Simple. *Phys. Rev. Lett.* **1996**, *77*, 3865–3868.
56. Dronskowski, R.; Blöchl, P. E. Crystal Orbital Hamilton Populations (COHP): Energy-Resolved Visualization of Chemical Bonding in Solids Based on Density-Functional Calculations. *J. Phys. Chem.* **1993**, *97*, 8617–8624.
57. Nelson, R.; Ertural, C.; George, J.; Deringer, V. L.; Hautier, G.; Dronskowski, R. LOBSTER: Local Orbital Projections, Atomic Charges, and Chemical-Bonding Analysis from Projector-Augmented-Wave-Based Density-Functional Theory. *J. Comput. Chem.* **2020**, *41*, 1931–1940.
58. Maintz, S.; Deringer, V. L.; Tchougréeff, A. L.; Dronskowski, R. LOBSTER: A Tool to Extract Chemical Bonding from Plane-Wave Based DFT. *J. Comput. Chem.* **2016**, *37*, 1030–1035.
59. Maintz, S.; Deringer, V. L.; Tchougréeff, A. L.; Dronskowski, R. Analytic Projection from Plane-Wave and PAW Wavefunctions and Application to Chemical-Bonding Analysis in Solids. *J. Comput. Chem.* **2013**, *34*, 2557–2567.
60. Deringer, V. L.; Tchougréeff, A. L.; Dronskowski, R. Crystal Orbital Hamilton Population (COHP) Analysis as Projected from Plane-Wave Basis Sets. *J. Phys. Chem. A* **2011**, *115*, 5461–5466.
61. Ertural, C.; Steinberg, S.; Dronskowski, R. Development of a Robust Tool to Extract Mulliken and Löwdin Charges from Plane Waves and its Application to Solid-State Materials. *RSC Adv.* **2019**, *9*, 29821–29830.
62. Müller, P. C.; Ertural, C.; Hempelmann, J.; Dronskowski, R. Crystal Orbital Bond Index: Covalent Bond Orders in Solids. *J. Phys. Chem. C* **2021**, *125*, 7959–7970.
63. Mayer, I. Charge, Bond Order and Valence in the Ab Initio SCF Theory. *Chem. Phys. Lett.* **1983**, *97*, 270–274.
64. Wiberg, K. B. Application of the Pople-Santry-Segal CNDO Method to the Cyclopropylcarbinyl and Cyclobutyl Cation and to Bicyclobutane. *Tetrahedron* **1968**, *24*, 1083–1096.
65. Palatinus, L.; Chapuis, G. SUPERFLIP – a Computer Program for the Solution of Crystal Structures by Charge Flipping in Arbitrary Dimensions. *J. Appl. Crystallogr.* **2007**, *40*, 786–790.
66. Petříček, V.; Dušek, M.; Palatinus, L. J. The Crystallographic Computing System; Institute of Physics: Praha (Czech Republic), 2006.
67. Petříček, V.; Dušek, M.; Palatinus, L. Crystallographic Computing System JANA2006: General Features. *Z. Kristallogr.* **2014**, *229*, 345–352.
68. Tursina, A. I.; Bukhan'ko, N. G.; Gribanov, A. V.; Shchelkunov, V. A.; Nelyubina, Y. V. A New Ternary Aluminide, CePt₃Al₅. *Acta Crystallogr.* **2005**, *E61*, i285–i286.
69. Engel, S.; Janka, O. New Alkaline Earth and Rare Earth Representatives Adopting the Ce₂Al₁₆Pt₉ Type Structure. *Z. Naturforsch.* **2024**, *79b*, accepted; <https://doi.org/10.1515/znb-2024-0022>.
70. Nowotny, H.; Wesenberg, H. Untersuchungen im System Aluminium-Strontium. *Z. Metallkd.* **1939**, *31*, 363–364.
71. Manyako, M. B.; Zarechnyuk, O. S.; Yanson, T. I. Crystal Structure of Sr₅Al₉. *Sov. Phys. Crystallogr.* **1987**, *32*, 196–198.
72. Bruzzone, G.; Merlo, F. The Strontium-Aluminium and Barium-Aluminium Systems. *J. Less-Common Met.* **1975**, *39*, 1–6.
73. Stegemann, F.; Zhang, Y.; Fokwa, B. P. T.; Janka, O. On the Formation of the Gd₃Ru₄Al₁₂ versus the Y₂Co₃Ga₉ Type Structure – M₃Rh₄Al₁₂ (M = Ca, Eu) versus M₂T₃Al₉ (M = Ca, Sr, Eu, Yb; T = Ir, Pt). *Dalton Trans.* **2020**, *49*, 6398–6406.
74. Chaudhury, Z. A.; Suryanarayana, C. Al₁₃X₄-type Phases in Aluminium-Group VIII Metal Systems. *J. Less-Common Met.* **1983**, *91*, 181–187.
75. Schubert, K.; Breimer, H.; Burkhardt, W.; Günzel, E.; Haufler, R.; Lukas, H. L.; Vetter, H.; Wegst, J.; Wilkens, M. Einige Strukturelle Ergebnisse an Metallischen Phasen II. *Naturwissenschaften* **1957**, *44*, 229–230.
76. Ferro, R.; Rambaldi, G.; Capelli, R.; Bonino, G. B. Ricerche sulle leghe dei metalli nobili con gli elementi più elettropositivi. VIII. Esame micrografico e coi raggi X delle leghe alluminio/rodio. *Atti Accad. Naz. Lincei, Cl. Sci. Fis., Mat. Nat., Rend.* **1964**, *36*, 491–497.
77. Edshammar, L.-E.; Johansson, G.; Sandberg, F.; Norin, T. The Crystal Structure of Rh₂Al₉ and Ir₂Al₉. *Acta Chem. Scand.* **1968**, *22*, 2822–2826.
78. Barua, S.; Hatnean, M. C.; Lees, M. R.; Balakrishnan, G. Signatures of the Kondo Effect in VSe₂. *Sci. Rep.* **2017**, *7*, 10964.
79. Simons, J.; Hempelmann, J.; Fries, K. S.; Müller, P. C.; Dronskowski, R.; Steinberg, S. Bonding Diversity in Rock Salt-type Tellurides: Examining the Interdependence between Chemical Bonding and Materials Properties. *RSC Adv.* **2021**, *11*, 20679–20686.
80. Steinberg, S.; Dronskowski, R. The Crystal Orbital Hamilton Population (COHP) Method as a Tool to Visualize and Analyze Chemical Bonding in Intermetallic Compounds. *Crystals* **2018**, *8*, 225.
81. Reitz, L. S.; Hempelmann, J.; Müller, P. C.; Dronskowski, R.; Steinberg, S. Bonding Analyses in the Broad Realm of Intermetallics: Understanding the Role of Chemical Bonding in the Design of Novel Materials. *Chem. Mater.* **2024**, *36*, 6791–6804.
82. Lin, Q.; Miller, G. J. Electron-poor Polar Intermetallics: Complex Structures, Novel Clusters, and Intriguing Bonding with Pronounced Electron Delocalization. *Acc. Chem. Res.* **2018**, *51*, 49–58.
83. Corbett, J. D. Exploratory Synthesis: The Fascinating and Diverse Chemistry of Polar Intermetallic Phases. *Inorg. Chem.* **2010**, *49*, 13–28.

Supplementary Material: This article contains supplementary material (<https://doi.org/10.1515/zkri-2024-0115>).

IV. Investigations of New Ternary Intermetallic Compounds $M_xAl_zT_y$ containing Divalent Species with $M = \text{Eu}$

1. Introduction

Intermetallic europium compounds exhibit in many cases isotypic structures to the Sr containing compounds, which is caused by the similar ionic radii of both elements with $r_{\text{ionic}}(\text{Eu}^{2+}) = 125 \text{ pm}$ and $r_{\text{ionic}}(\text{Sr}^{2+}) = 126 \text{ pm}$.⁷⁹ Known isotypic pairs are, e.g. EuAl_9Co_2 ²²¹ and SrAl_9Co_2 (BaAl₉Fe₂ type, *P6/mmm*),⁵⁴ Eu_2AlPd_2 ⁸⁷ and Sr_2AlPd_2 (Ca₂GePd₂ type, *Fdd2*),⁶⁵ EuAl_2Pt and SrAl_2Pt (MgAl₂Cu type, *Cmcm*),⁶³ $\text{Eu}_2\text{Al}_9\text{Ir}_3$ ⁸⁶ and $\text{Sr}_2\text{Al}_9\text{Ir}_3$ (Y₂Ga₉Co₃ type, *Cmcm*),⁶¹ but also isotypic structures are known, which only exist with Eu and Ca, where no Sr compound is known like $\text{Eu}_3\text{Al}_{12}\text{Rh}_4$ and $\text{Ca}_3\text{Al}_{12}\text{Rh}_4$ (Gd₃Al₁₂Ru₄ type, *P6₃/mmc*),⁶¹ $\text{Eu}_2\text{Al}_{15}\text{Pt}_6$ ⁹² and $\text{Ca}_2\text{Al}_{15}\text{Pt}_6$ (average *RE_{0.67}Al₅Pt₂* type, average structure *P6₃/mmc*).⁷¹ A reason for the existence of Ca and Eu compound can be, that ionic size of trivalent europium ($r_{\text{ionic}} = 107 \text{ pm}$) is smaller than the divalent and closer to the size of Ca ions ($r_{\text{ionic}} = 112 \text{ pm}$).⁷⁹

In the next section, a new divalent europium compound will be described as well as the quaternary (pseudo-ternary) solid solutions $\text{Eu}_2\text{Al}_{15}\text{Pt}_{6-x}\text{T}_x$ with $T = \text{Pd, Ir and Au}$.

$\text{Eu}_4\text{Al}_{13}\text{Pt}_9$ was discovered during investigation in the ternary system Eu–Al–Pt. The compound crystallizes in the orthorhombic Ho₄Ge₉Ir₁₃ type structure with space group *Pmmn* and exhibits isotypism with the existing cerium compound.²²² Quantum chemical calculations on $\text{Eu}_4\text{Al}_{13}\text{Pt}_9$ led to the classification of the structure as polar intermetallic material, which exhibits like the alkaline earth compounds in the chapter before, a polyanionic network consisting of the Al and Pt atoms, whereas the Eu atoms reside in hexagonal prismatic cavities.

The $\text{Eu}_2\text{Al}_{15}\text{Pt}_6$ was reported to exhibit a temperature dependent valence change at low temperatures (45 K), in which the valence of the europium atoms changes from divalent to trivalent and vice versa.²²³ A recent study also showed that the transition temperature can be tuned by partially substituting the Al atoms with Ga atoms. The solid solution $\text{Eu}_2(\text{Al}_{1-x}\text{Ga}_x)_{15}\text{Pt}_6$ with $x = 0, 0.05, 0.1, 0.2, 0.3$ and 1 showed that small amounts of substitution ($x = 0.1$) suppress the valence change completely, even though the valence electron count does not differ.²²⁴ In that regard a study was performed by us in which not the Al positions are substituted but the Pt positions. The substitution led to the X-ray pure solid solution $\text{Eu}_2\text{Al}_{15}(\text{Pt}_{1-x}\text{Pd}_x)_6$, $\text{Eu}_2\text{Al}_{15}(\text{Pt}_{1-x}\text{Ir}_x)_6$ and $\text{Eu}_2\text{Al}_{15}(\text{Pt}_{1-x}\text{Au}_x)_6$ with $x = 1/6$, the powder X-ray diffraction showed that only 1/6 of the Pt atoms could be substituted. The magnetic measurements of the X-ray pure samples (by PXRD and SEM/EDX analysis) resulted in a change of the transition temperature. The Pd substituted solid solution exhibits a slightly lower

transition temperature of 42 K (compared to 45 K), whereas in the case of the Ir substitution the transition temperature could be increased to 52 K, an overview of the change of the transition temperature depending on the substitution element is shown in **Figure 3.37**. As for the Au containing solid solution, due to the increased valence electron count, the valence transition was suppressed.

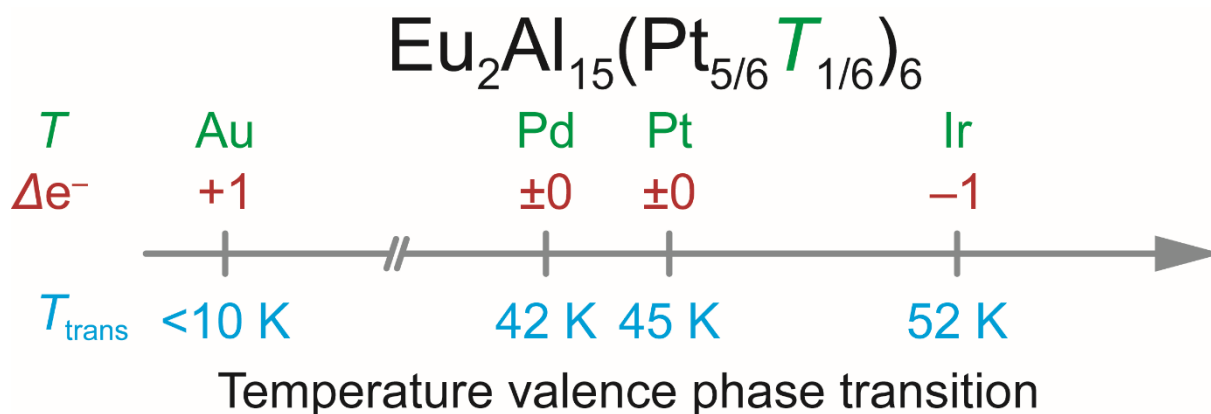


Figure 3.37: Overview of the substitution element of the solid solution of $\text{Eu}_2\text{Al}_{15}(\text{Pt}_{5/6}\text{T}_{1/6})_6$ alongside their electron difference and change of the transition temperature.

2. $\text{Eu}_4\text{Al}_{13}\text{Pt}_9$ – a coloring variant of the $\text{Ho}_4\text{Ir}_{13}\text{Ge}_9$ type structure

Collaborations to disclose: In this chapter the work with the same title as the headline is summarized. The results have already been published in *Z. Naturforsch.* **2023**, 78b, 147. Dr. N. Zaremba provided bulk samples of $\text{Eu}_4\text{Al}_{13}\text{Pt}_9$, Dr. R. S. Touzani performed the quantum chemical calculations, Dr. Y. Prots and PD Dr. O. Janka along with the aforementioned worked on the manuscript.

Explorative investigations in the Eu–Al–Pt system led to the discovery of the new phase $\text{Eu}_4\text{Al}_{13}\text{Pt}_9$, during the attempt to synthesize EuAl_4Pt_2 in analogy to the existing phase EuAl_4Ir_2 (own type, *P4/ncc*).²¹² Needle shaped single crystals (**Figure 3.38**) were isolated from the nominal EuAl_4Pt_2 sample. Single crystal X-ray diffraction measurements resulted in the discovery of the $\text{Eu}_4\text{Al}_{13}\text{Pt}_9$ phase, crystallizing in the orthorhombic crystal system with space group *Pmmn* in the $\text{Ho}_4\text{Ge}_9\text{Ir}_{13}$ type structure. The refinement parameters are listed in the publication (*Z. Naturforsch.* **2023**, 78b, 147). The structure is shown and described in the beginning of **Chapter 3.a** in **Figure 3.11-3.12**. To semi-quantify the element composition of the $\text{Eu}_4\text{Al}_{13}\text{Pt}_9$ single crystal, energy dispersive X-ray spectroscopy measurement were performed, the results are summarized in **Table 3.7**, which show a good agreement with the europium content, but the Al content is too high whereas the Pt content is too low, which can be explained by the orientation of the single crystal being not perpendicular to the electron beam (**Fig. 3.a.38**).

$\text{Eu}_4\text{Al}_{13}\text{Pt}_9$ exhibits like the isotypic cerium compound $\text{Ce}_4\text{Al}_{13}\text{Pt}_9$ three RE, six Pt and eight Al positions. The compound exhibits Eu–Al distances of 326-360 pm, Eu–Pt of 322-332 pm, Al–Al of 277-284 pm, Al–Pt of 247-265 pm and Pt–Pt distances of 282-285 pm.

The Eu–Al distances are in line with the binary and ternary compounds EuAl_2 (MgCu_2 type, *Fd $\bar{3}m$*) $d(\text{Eu–Al}) = 337$ pm,²⁰⁴ EuAl_4 (BaAl_4 type, *I4/mmm*) $d(\text{Eu–Al}) = 347$ pm,²²⁵ EuAl_5Pt_3 (YNi_5Si_3 type, *Pnma*) $d(\text{Eu–Al}) = 327-342, 320-350$ pm,^{91, 172} $\text{Eu}_2\text{Al}_{16}\text{Pt}_9$ ($\text{Ce}_2\text{Al}_{16}\text{Pt}_9$ type, *Immm*) $d(\text{Eu–Al}) = 330-338$ pm¹⁷⁴ and EuAl_2Pt (MgAl_2Cu type, *Cmcm*) $d(\text{Eu–Al}) = 335-337$ pm.⁶³ The Eu–Pt distances in the structure are shorter than the ones found in EuPt_2 (MgCu_2 type, *Fd $\bar{3}m$*) with $d(\text{Eu–Pt}) = 337$ pm²⁰⁶ and are in line with the ternary compounds EuAl_5Pt_3 , $\text{Eu}_2\text{Al}_{16}\text{Pt}_9$ and EuAl_2Pt with: $d(\text{Eu–Pt}) = 320-325, 320-328$ pm, 332-342 pm and 302-330 pm, respectively. In the case of the polyanionic network consisting of the Al and Pt atoms, the Al–Al distances are shorter than in elemental Al (Cu type, *Fm $\bar{3}m$* , 286 pm)²⁰⁸ and AlPt (CsCl type,

$Pm\bar{3}m$)²⁰⁰ with 302 pm, but in line with the ternary compounds EuAl_5Pt_3 $d(\text{Al}-\text{Al}) = 261\text{-}328$ pm,^{91, 172} $\text{Eu}_2\text{Al}_{16}\text{Pt}_9$ $d(\text{Al}-\text{Al}) = 275\text{-}331$ pm¹⁷⁴ and EuAl_2Pt $d(\text{Al}-\text{Al}) = 279\text{-}285$ pm.⁶³

The Pt–Pt distances are longer than in elemental Pt (Cu type, $Fm\bar{3}m$, 274 pm)²⁰⁹ and shorter compared to the ones in EuAl_5Pt_3 (308, 302 pm),^{91, 172} $\text{Eu}_2\text{Al}_{16}\text{Pt}_9$ (296 pm)¹⁷⁴ and AlPt (FeSi type, $P2_13$, 299 pm).²⁰⁰ The Al–Pt are in line with the following compounds EuAl_5Pt_3 $d(\text{Al}-\text{Pt}) = 235\text{-}276$, $246\text{-}272$ pm,^{91, 172} $\text{Eu}_2\text{Al}_{16}\text{Pt}_9$ $d(\text{Al}-\text{Pt}) = 258\text{-}333$ pm,¹⁷⁴ AlPt $d(\text{Al}-\text{Pt}) = 248\text{-}273$ pm²⁰⁰ and EuAl_2Pt $d(\text{Al}-\text{Pt}) = 254\text{-}258$ pm.⁶³

To investigate the bonding characteristics of this compound, quantum chemical calculations were performed by creating a non-magnetic and a ferromagnetic model for the structure. DFT calculations were performed with the single crystal data as starting point, optimizing the structure to $a = 415.46$, $b = 1155.37$, $c = 2010.79$ pm for the non-magnetic and $a = 416.34$, $b = 1155.20$, $c = 2005.88$ pm for the ferromagnetic model with both models being near the experimental unit cell parameters. From the DFT data Bader charges were calculated according to the Henkelman et al. and the Yu and Trinkle methods showing values of +1.36 to +1.38/+1.35 to 1.37 for Eu, –2.51 to –3.46/–2.52 to –3.48 for Pt and +1.24 to +1.71/+1.27 to +1.72 for Al. Additionally, DOS and ICOHPs were calculated, the –COHP-plots of selected Eu–Al, Eu–Pt, Al–Al, Al–Pt and Pt–Pt are shown in **Figure 3.a.39**. The –COHP-plot of the Al–Pt bonds show a small number of antibonding states above the Fermi level, at the Fermi level non-bonding and slightly bonding states are present with the stronger bonding states being below the Fermi level, hinting to a covalent bonding character between the Pt and Al atoms exhibiting ICOHP values of –0.98 to –2.02 eV. In the case of the homoatomic bonds for Al–Al and Pt–Pt express ICOHP values of –0.11 to –0.76 eV and –0.67 to –0.74 eV, respectively, indicating rather weak covalent bonding. When looking at the corresponding –COHP-plots the Pt–Pt bonds exhibit strong antibonding states below the Fermi level leading to a destabilization of the bonding, whereas the Al–Al bonds do not show any strong bonding or antibonding states. As for the Eu–Al and Eu–Pt bonds, these possess ICOHP values ranging from –0.08 to –0.39 eV and –0.36 to –0.58 eV, these values are expected taken the atomic distances into account. The –COHP-plots show no antibonding states for Eu–Al and a few antibonding states for Eu–Pt below the Fermi level. Due to the strong bonding between the Al and Pt atoms, a formation of the $[\text{Al}_{13}\text{Pt}_9]^{8-}$ polyanion is indicated.

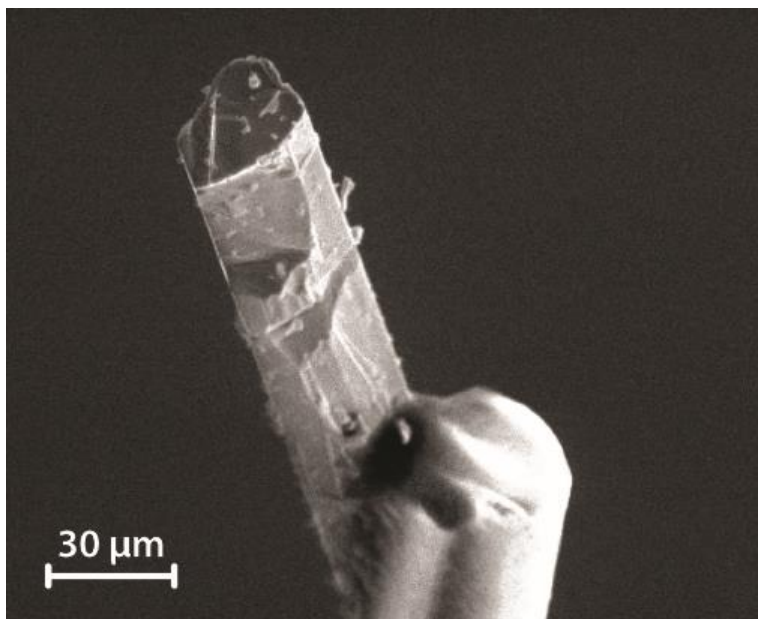


Figure 3.38: Single crystal of $\text{Eu}_4\text{Al}_{13}\text{Pt}_9$ glued on a glass fiber for SCXRD and EDX measurements.

Table 3.7: Energy dispersive X-ray spectroscopy data of the $\text{Eu}_4\text{Al}_{13}\text{Pt}_9$ single crystal. Standard deviations are ± 2 at.-%.

Compound	Eu	Al	Pt
Ideal composition	15.4	50.0	34.6
$\text{Eu}_4\text{Al}_{13}\text{Pt}_9$	14	56	30

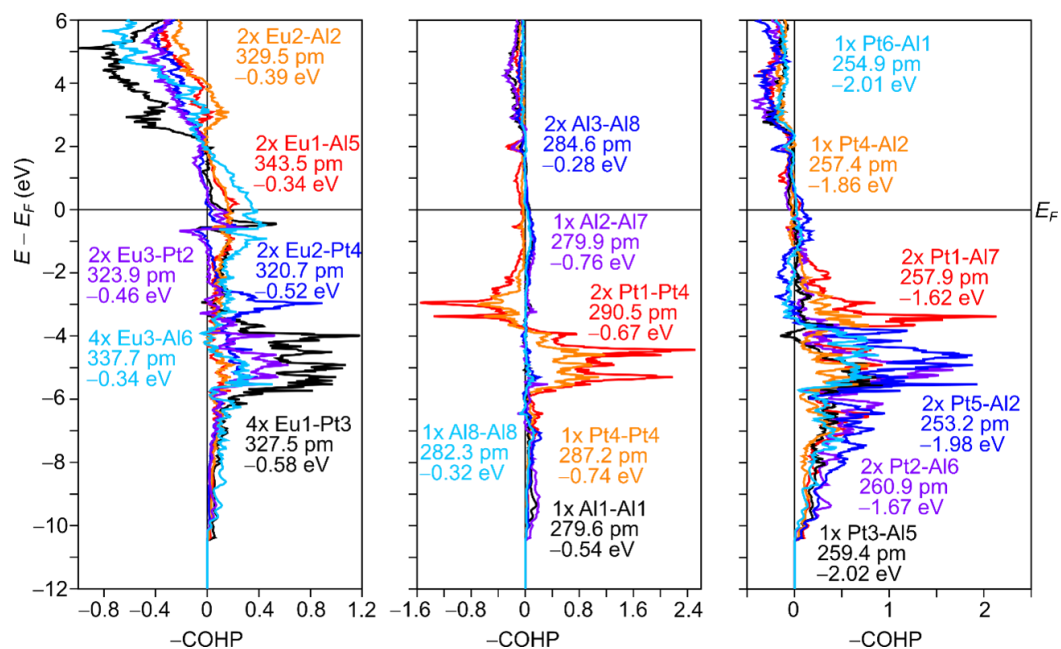


Figure 3.39: -COHP-plots of the spin-polarized ferromagnetic model of $\text{Eu}_4\text{Al}_{13}\text{Pt}_9$, for selected Eu-Pt, Eu-Al (left), Al-Al/Pt-Pt (middle), and Pt-Al bonds (right).

Overall, it can be said that the europium containing compounds are similar to the alkaline earth phases, especially to the Sr compounds a high resemblance is present. When taking the structural motifs into account, the newly found Sr and Eu compounds MA_5Pt_3 , $M_2Al_{16}Pt_9$ and $Eu_4Al_{13}Pt_9$ show the formation of a polyanionic network consisting of the Al and Pt atoms, which form exclusive or condensed hexagonal prismatic cavities in which the Sr or Eu in form of the cationic species reside. In these structures, strong covalent Al–Pt and Al–Al bonds are present, whereas the bonding interactions of the Sr or the Eu with the network is rather of ionic character. Even though the electron count is so different, the Sr and Eu compounds exhibit the same structure, indicating that the main factor for the formation of the structure is the size of the cation, which would also be the reason why no barium compounds exist with this structure motif, due to the significant larger size of Ba compared to Sr and Eu. Although Ce does not exhibit the same oxidation state, many structures were first discovered with the cerium compound, for example the $Ce_2Al_{16}Pt_9$, $CeAl_5Pt_3$ and $Ce_4Al_{13}Pt_9$, which is caused by the excessive research done on cerium compounds in the past. So, to find new phases, compositions with existing cerium can be used as a starting point, due to the size of cerium ions with $r_{\text{ionic}}(\text{Ce}^{3+}) = 114 \text{ pm}$ being between that of divalent and trivalent Eu ions $r_{\text{ionic}}(\text{Eu}^{2+}) = 125 \text{ pm}$ and $r_{\text{ionic}}(\text{Eu}^{3+}) = 107 \text{ pm}$.⁷⁹

Stefan Engel, Nazar Zaremba, Yurii Prots, Rachid S. Touzani and Oliver Janka*

Eu₄Al₁₃Pt₉ – a coloring variant of the Ho₄Ir₁₃Ge₉ type structure

<https://doi.org/10.1515/znb-2023-0300>

Received January 6, 2023; accepted January 9, 2023;

published online March 8, 2023

Abstract: Investigations in the ternary system Eu–Al–Pt led to the discovery of Eu₄Al₁₃Pt₉, a new representative exhibiting a coloring variant of the Ho₄Ir₁₃Ge₉ type structure. The orthorhombic structure was refined based on single crystal X-ray diffraction data (*Pmmn*, Wyckoff sequence $e^9b^3a^5$, $a = 415.38(1)$, $b = 1149.73(2)$, $c = 1994.73(5)$ pm, $wR2 = 0.0622$, 1901 F^2 values, 88 variables) and full atomic ordering was observed for all atoms. The structure features a complex [Al₁₃Pt₉]^{δ-} network with the Eu atoms occupying hexagonal prismatic cavities. The bonding situation of this new platinumide was investigated via quantum-chemical calculations. According to Density Functional Theory (DFT) the title compound has to be described as a polar intermetallic material with a covalently bonded [Al₁₃Pt₉]^{δ-} polyanion showing strong Pt–Al alongside weak Al–Al and Pt–Pt bonding and Eu cations in the cavities.

Keywords: aluminum; europium; intermetallics; platinum; quantum chemistry.

Dedicated to Professor Gerhard Müller on the occasion of his 70th birthday.

1 Introduction

Europium intermetallics are a fascinating class of compounds from various points of view. First, the Eu atoms in intermetallic compounds exhibit, in contrast to ionic compounds,

*Corresponding author: Oliver Janka, Anorganische Festkörperchemie, Universität des Saarlandes, Campus C4.1, 66123 Saarbrücken, Germany, E-mail: oliver.janka@uni-saarland.de

Stefan Engel, Anorganische Festkörperchemie, Universität des Saarlandes, Campus C4.1, 66123 Saarbrücken, Germany, E-mail: stefan.engel@uni-saarland.de

Nazar Zaremba and Yurii Prots, Chemische Metallkunde, Max-Planck-Institut für Chemische Physik fester Stoffe, Nöthnitzer Straße 40, 01187 Dresden, Germany, E-mail: nazar.zaremba@gmail.com (N. Zaremba), prots@cpfs.mpg.de (Y. Prots)

Rachid S. Touzani, Otto-von-Guericke-Universität Magdeburg, Institut für Werkstoff- und Füge-technik (IWF), Universitätsplatz 2, 39106 Magdeburg, Germany, E-mail: rachid.touzani@ovgu.de

usually a divalent oxidation state with a half-filled 4f shell. The structure makes this valence state quite stable which is isoelectronic with Gd³⁺. Therefore, the Eu²⁺ cations exhibit an effective magnetic moment of $\mu_{\text{eff}} = 7.94 \mu_B$, which is prone to ferro- or antiferromagnetic ordering phenomena. EuAl₂Pt for example shows ferromagnetic ordering below $T_C = 54.0(1)$ K [1], the isostructural indium representative orders at $T_C = 32.5(1)$ K [2], while e.g. Eu₂Ga₁₅Pt₆ [3] and Eu₅In₉Pt₇ [4] order antiferromagnetically at $T_N = 13.1(1)$ and 11.6(5) K, respectively. However, due to the second possible oxidation state, which is Eu³⁺, purely trivalent europium intermetallics can be observed, too. The occurrence of these, however, is rather rare. For the binary compounds these are EuRh₂ [5], EuIr₂ [5], EuNi₅ [5], Eu₂Ni₁₇ [5], EuPd₃ [5] and EuPt₅ [5]. As for the ternary intermetallics, EuRu₄B₄ [6], EuRuB₄ [6], EuCo₂Si₂ [7–10], EuRu₂Si₂ [8], Eu₂Co₁₂P₇ [11] and finally Eu₂Al₉Ir₃ [12] have been reported.

An even rarer phenomenon is a so-called valence phase transition that can occur in these materials. Here, the valence changes from Eu²⁺ to Eu³⁺, due to external stimuli such as temperature or pressure. Intermetallic EuPd₂Si₂ ($T_{\text{trans}} \sim 200$ K) [13] and Eu₂Al₁₅Pt₆ ($T_{\text{trans}} \sim 45$ K) [3] exhibit temperature dependent valence phase transitions, while EuCo₂As₂ [14, 15] exhibits a pressure dependent shift of its Eu valence. Finally, in EuPtP two new pressure induced valence ordered structures were observed [16]. Besides europium, also cerium (Ce³⁺: [Xe] 4f¹; Ce⁴⁺: [Xe] 4f⁰) and ytterbium (Yb³⁺: [Xe] 4f¹³; Yb²⁺: [Xe] 4f¹⁴) can exhibit these kinds of phenomena. YbAl₃ [17] and YbAl₃Pd₂ [18] as well as the solid solutions CeNi_{1-x}Co_xSn ($x = 0.4$; $T_{\text{trans}} \sim 95$ K) [19] and Yb_xIn_{1-x}Cu₂ ($x = 0.6$; $T_{\text{trans}} \sim 55$ K) [20–22] show temperature induced valence phase transitions.

Here, we report on a new Eu intermetallic in the Eu–Al–Pt system (Figure 1), Eu₄Al₁₃Pt₉. Its crystal structure has been determined by single crystal X-ray diffraction. Quantum-chemical calculations indicate that the title compound is a platinumide with polar Pt–Al bonding.

2 Experimental

2.1 Synthesis

Eu₄Al₁₃Pt₉ was prepared from the elements using europium ingots (Onyxmet), platinum pieces (Agosi AG) and aluminum turnings (Koch

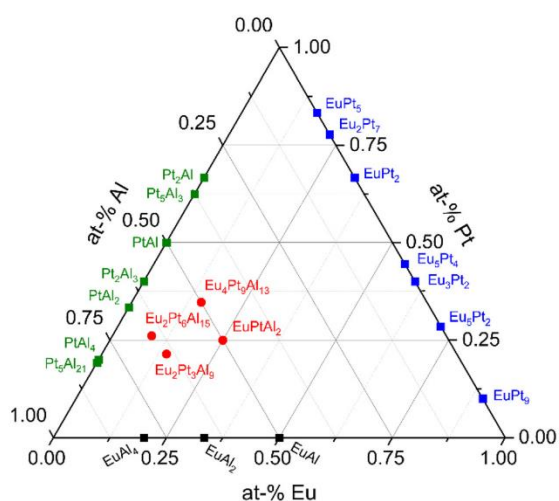


Figure 1: The ternary system Eu–Pt–Al. The data for the depicted compounds has been taken from the Pearson database [23] or the papers cited in the Introduction.

Chemicals), all with stated purities above 99%. Samples were prepared on a 300 mg scale. The Eu pieces were stored under an argon atmosphere; surface contaminations on the pieces were removed mechanically under sodium dried cyclohexane prior to the reaction. For the reaction, the elements were arc-welded [24] in tantalum tubes in an argon atmosphere of about 800 mbar in a ratio of 1:4:2 (Eu:Al:Pt). The argon gas was purified over a titanium sponge (873 K), molecular sieves and silica gel prior to use. The sealed tantalum ampoules were placed in the water-cooled sample chamber of a high-frequency furnace (Hüttinger, TIG 5/300) [25]. The water-cooling was used to prevent reactions of the Ta ampoules with the sample chamber. The Ta-container was heated up to ~1500 K within 2 min, kept at that temperature for 10 min followed by slow cooling to ~1000 K. The cooling was achieved by reducing the power output of the generator, leading to a cooling rate of about 15 K min^{-1} . After an annealing step of 4 h at this temperature, the samples were cooled by shutting off the power supply. The temperature was controlled by a pyrometer (Sensortherm, Metis MS09) with a stated accuracy of $\pm 50 \text{ K}$. All samples could easily be separated from the container material and no reactions with the tantalum ampoules could be observed.

2.2 X-ray diffraction

The phase purity of the polycrystalline sample was checked by powder X-ray diffraction patterns using the Guinier method on an Enraf-Nonius FR552 camera, equipped with an imaging plate detector (Fujifilm BAS-1800) and $\text{CuK}\alpha_1$ radiation. α -Quartz ($a = 491.30$, $c = 540.46 \text{ pm}$) was utilized as internal standard.

Needle-shaped crystals (Figure 2) were glued to quartz fibers using beeswax and their quality for intensity data collection was checked by Laue photographs on a Buerger camera (white molybdenum radiation, image plate technique, Fujifilm, BAS-1800). The data set was collected on a Stoe IPDS-II diffractometer (graphite monochromatized MoKa

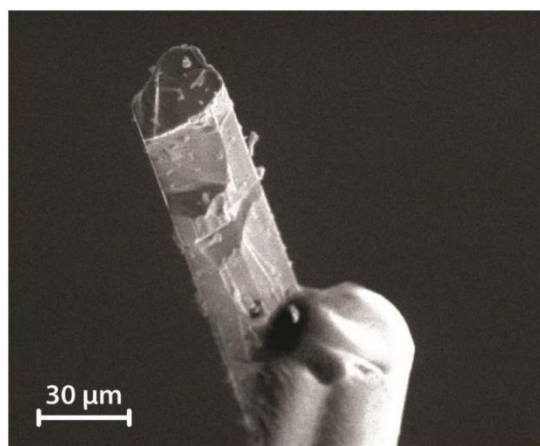


Figure 2: Electron microscopic image from the crystallite of $\text{Eu}_4\text{Al}_{13}\text{Pt}_9$ attached to a glass fiber used for the single crystal structure determination.

radiation; oscillation mode). A numerical absorption correction [26] was applied to the data set. The data was solved and refined using SUPERFLIP [27] and JANA2006 [28, 29]. All relevant crystallographic data and details of the data collection and evaluation are listed in Tables 1–4.

CCDC 2202108 contains the supplementary crystallographic data for this paper. The data can be obtained free of charge from The Cambridge Crystallographic Data Centre via www.ccdc.cam.ac.uk/structures.

2.3 Energy-dispersive X-ray spectroscopy (EDX)

The single crystal of $\text{Eu}_4\text{Al}_{13}\text{Pt}_9$, investigated on the diffractometer, was semiquantitatively analyzed by EDX in a Zeiss EVO[®] MA10 scanning electron microscope (variable pressure mode (60 Pa) and W cathode) using EuF_3 , Pt and Al_2O_3 as standards. The average of three point measurements on the crystal surfaces resulted in $14 \pm 2 \text{ at.-% Eu}$, $56 \pm 2 \text{ at.-% Al}$, and $30 \pm 2 \text{ at.-% Pt}$, which is in fair agreement with the ideal composition (15.4 at.-% Eu, 50.0 at.-% Al, 34.6 at.-% Pt) refined from the single crystal X-ray data. The deviations can be explained by the irregular crystallite faces and the not perfect perpendicular orientation of the crystal towards the beam. No impurity elements heavier than sodium (detection limit of the instrument) were detected.

Table 1: Lattice parameters (single crystal, DFT and literature data), and unit cell volumes of $\text{Eu}_4\text{Al}_{13}\text{Pt}_9$ and $\text{Ce}_4\text{Al}_{13}\text{Pt}_9$.

Compound	a (pm)	b (pm)	c (pm)	V (nm^3)	Ref.
$\text{Eu}_4\text{Al}_{13}\text{Pt}_9^{\text{SC}}$	415.38(1)	1149.73(2)	1994.73(5)	0.9526	^a
NM- $\text{Eu}_4\text{Al}_{13}\text{Pt}_9^{\text{DFT}}$	415.46	1155.37	2010.79	0.9652	^a
FM- $\text{Eu}_4\text{Al}_{13}\text{Pt}_9^{\text{DFT}}$	416.34	1155.20	2005.88	0.9647	^a
$\text{Ce}_4\text{Al}_{13}\text{Pt}_9^{\text{L}}$	418.26(1)	1144.24(3)	1984.75(5)	0.9499	[52]

^aThis work; ^Lliterature data; ^{SC}single crystal data; ^{DFT}quantum chemical data.

Table 2: Crystallographic data and structure refinement for $\text{Eu}_4\text{Al}_{13}\text{Pt}_9$ ($\text{Ho}_4\text{Ir}_{13}\text{Ge}_9$ type, space group $Pm\bar{m}n$, $Z = 2$).

CSD number	2202108
Molar mass/g mol ⁻¹	2714.3
Unit cell dimensions/pm single crystal data	$a = 415.38(1)$ $b = 1149.73(2)$ $c = 1994.73(5)$
Volume/nm ³	$V = 0.9526$
Calculated density/g cm ⁻³	9.46
Linear absorption coeff./mm ⁻¹	79.3
Transm. ratio (min/max)	0.007/0.103
$F(000)$	2246
Crystal size/ μm^3	$200 \times 30 \times 20$
Diffractometer	Stoe IPDS-II
Wavelength	MoK α (71.073 pm)
Detector distance/mm	80
Exposure time/s	240
Integr. param./A, B, EMS	12.1/1.4/0.013
θ Range/ $^\circ$	2.0–31.9
Range in hkl	–6, +5; –17, +17; –29, +29
Total no. reflections	66423
Independent reflections	1901 ($R_{\text{int}} = 0.0714$)
Reflections with $I \geq 3\sigma(I)$	1774 ($R_o = 0.0034$)
Data/parameters	1901/88
Goodness-of-fit	2.36
Final R indices [$I \geq 3\sigma(I)$]	$R = 0.0269/wR = 0.0613$
R Indices for all data	$R = 0.0301/wR = 0.0622$
Extinction scheme	Lorentzian isotropic [55]
Extinction coefficient	3580(130)
Largest diff. peak and hole/e Å^{-3}	4.23 –3.42

2.4 Quantum-chemical calculations

The first-principles calculations were carried out with Quantum ESPRESSO [30, 31] for the structural relaxation of $\text{Eu}_4\text{Al}_{13}\text{Pt}_9$ using PAW pseudopotentials [32] from the PSLibrary version 1.0.0 [33] for Al, Pt and in the case of the non-magnetic (NM) model for Eu. For the ferromagnetic (FM) model the PAW pseudopotential of Eu created by the method of Wentzcovitch et al. [34] was used with the aforementioned pseudopotentials for Pt and Al from the PSLibrary. The kinetic energy cut-off for the plane waves was set to 100 Ry, while the cut-off for the charge density and potential was set to 400 Ry. The structural relaxation stopped when a total energy convergence of 10^{-6} Ry and a force convergence Ry a_0^{-1} was reached. The Marzari-Vanderbilt cold smearing [35] and a Gaussian spreading of 0.01 Ry were chosen to account for the Brillouin-zone integration. The k-mesh was divided by $14 \times 4 \times 2$ using the Monkhorst-Pack algorithm [36]. Exchange and correlation in this density functional theory (DFT) based method were treated with the generalized gradient approximation (GGA) functional as parameterized by Perdew, Burke and Ernzerhof (PBE-GGA) [37]. Quantum ESPRESSO was also used to generate the all-electron and valence electron densities, which were then used to calculate the Bader charges according to the methods described by Henkelman et al. [38–40] and Yu and Trinkler [41] with the critic2 program [42, 43]. The chemical bonding analysis was carried out using the tight-binding, linear muffin-tin orbitals with the atomic spheres approximation (TB-LMTO-ASA) [44, 45] as implemented in the TB-LMTO 4.7 program [46]. Exchange and correlation were treated with the GGA functional as parameterized by Perdew et al. [47]. The k-mesh was $22 \times 8 \times 4$, which leads to 180 k-points in the irreducible Brillouin zone (IBZ). The radii of the automatically generated Wigner-Seitz cells for Eu, Pt and Al were 2.07–2.15 Å, 1.47–1.55 Å and 1.40–1.47 Å, respectively. Empty spheres were needed for the LMTO calculations. The bonding analysis was done by calculation of the density-of-states

Table 3: Atomic coordinates and displacement parameters (in pm²) of $\text{Eu}_4\text{Al}_{13}\text{Pt}_9$ ($\text{Ho}_4\text{Ir}_{13}\text{Ge}_9$ type, space group $Pm\bar{m}n$).

Atom	Wyck.	x	y	z	U_{11}	U_{22}	U_{33}	U_{23}	U_{eq}^a
Eu1	2a	1/4	1/4	0.02129(3)	60(2)	110(2)	115(2)	0	95(1)
Eu2	4e	1/4	0.55618(3)	0.71013(2)	68(2)	121(2)	116(2)	–4(1)	101(1)
Eu3	2b	1/4	3/4	0.51587(3)	68(2)	126(2)	119(2)	0	104(1)
Al1	4e	1/4	0.6292(2)	0.35622(13)	71(1)	115(10)	123(10)	–1(8)	103(6)
Al2	4e	1/4	0.0656(2)	0.16261(13)	55(1)	119(10)	110(10)	1(7)	95(6)
Al3	2a	1/4	1/4	0.73178(17)	50(14)	155(14)	97(13)	0	101(8)
Al4	2a	1/4	1/4	0.35628(19)	186(19)	122(14)	128(14)	0	145(9)
Al5	2b	1/4	3/4	0.84250(18)	86(16)	114(13)	117(13)	0	106(8)
Al6	4e	1/4	0.0487(2)	0.54825(13)	83(11)	136(10)	131(10)	6(8)	117(6)
Al7	4e	1/4	0.5539(2)	0.04109(13)	68(11)	115(10)	106(10)	8(8)	96(6)
Al8	4e	1/4	0.1276(2)	0.85542(13)	55(10)	105(10)	132(10)	12(8)	97(6)
Pt1	2b	1/4	3/4	0.10310(2)	62(2)	109(2)	94(2)	0	88(1)
Pt2	2a	1/4	1/4	0.60811(2)	52(2)	122(2)	99(2)	0	91(1)
Pt3	4e	1/4	0.56180(2)	0.91371(1)	51(1)	105(1)	99(1)	–5(1)	91(8)
Pt4	4e	1/4	0.62755(2)	0.22702(1)	62(1)	104(1)	106(1)	5(1)	91(7)
Pt5	2a	1/4	1/4	0.23090(2)	73(2)	100(2)	102(2)	0	92(1)
Pt6	4e	1/4	0.06177(2)	0.41976(1)	74(2)	109(1)	110(1)	–4(1)	98(8)

^aThe isotropic displacement parameter U_{eq} is defined as: $U_{\text{eq}} = 1/3 (U_{11} + U_{22} + U_{33})$ (pm²); $U_{12} = U_{13} = 0$. Standard deviations are given in parentheses.

Table 4: Interatomic distances (pm) in $\text{Eu}_4\text{Al}_{13}\text{Pt}_9$ ($\text{Ho}_4\text{Ir}_{13}\text{Ge}_9$ type, space group $Pmmn$). All distances of the first coordination spheres are listed. Standard deviations are equal or smaller than 0.2 pm.

Eu1	2	Pt1	323.6	Pt4	1	Al2	256.6	Al4	1	Pt5	250.1
	4	Pt3	326.7		1	Al1	257.6		2	Pt6	250.7
	4	Al7	330.8		2	Al3	264.0		2	Eu3	328.9
	2	Al5	341.9		2	Al8	264.9		4	Eu2	332.2
	2	Al7	351.6		1	Pt4	281.5	Al5	2	Pt5	254.1
	2	Al2	352.7		1	Pt1	284.5		2	Pt3	258.8
	2	Al8	359.6		2	Eu2	321.6		4	Al2	296.9
Eu2	2	Pt4	321.6	Pt5	1	Al4	250.1		2	Eu1	341.9
	2	Al1	325.7		2	Al2	252.0		2	Eu2	345.5
	2	Pt5	326.6		2	Al5	254.1	Al6	2	Pt6	251.7
	2	Al2	328.2		4	Eu2	326.6		1	Pt6	256.8
	2	Pt6	332.1	Pt6	1	Al4	250.7		1	Pt2	260.4
	1	Al3	354.6		2	Al6	251.7		2	Al1	296.6
	2	Al4	332.2		1	Al1	253.5		2	Al6	304.6
	1	Al6	344.7		1	Al6	256.8		2	Eu3	336.3
	1	Al5	345.5		2	Eu3	326.3		1	Eu2	344.7
	1	Al8	358.6		2	Eu2	332.1		1	Eu3	349.5
Eu3	2	Pt2	322.9	Al1	1	Pt6	253.5	Al7	1	Pt3	254.2
	4	Pt6	326.3		1	Pt4	257.6		1	Pt1	257.2
	2	Al4	328.9		1	Pt2	259.8		2	Pt3	262.6
	4	Al6	336.3		1	Al1	277.8		1	Al2	278.7
	2	Al1	347.5		2	Al6	296.6		2	Al7	292.1
	2	Al6	349.5		2	Al3	305.3		2	Al8	304.9
Pt1	2	Al7	257.2		2	Eu2	325.7		2	Eu1	330.8
	4	Al8	264.2		1	Eu3	347.5		1	Eu1	351.6
	2	Pt4	284.5	Al2	1	Pt5	252.0	Al8	1	Pt3	246.9
	2	Eu1	323.6		1	Pt4	256.6		2	Pt1	264.2
Pt2	1	Al3	246.7		2	Pt3	257.5		2	Pt4	264.9
	4	Al1	259.8		1	Al7	278.7		1	Al8	281.4
	2	Al6	260.4		2	Al5	296.9		1	Al3	283.9
	2	Eu3	322.9		2	Al8	306.2		2	Al7	304.9
Pt3	1	Al8	246.9		2	Eu2	328.2		2	Al2	306.2
	1	Al7	254.2		1	Eu1	352.7		1	Eu2	358.6
	2	Al2	257.5	Al3	1	Pt2	246.7		1	Eu1	356.9
	1	Al5	258.8		4	Pt4	264.0				
	2	Al7	262.6		2	Al8	283.9				
	1	Eu1	326.7		4	Al1	305.3				
					2	Eu2	354.6				

(DOS) and the crystal orbital Hamilton population (COHP) [48] and its integrals (ICOHP). The ICOHP can be seen as a semi-quantitative bonding energy which measures covalent contribution in solids. Because $-\text{COHP}$ values are plotted, negative $-\text{COHP}$ are antibonding states, positive ones are bonding states and non-bonding states have $-\text{COHP}$ values of zero. The Fermi level was set to 0 eV as reference.

3 Results

3.1 Powder X-ray diffraction

A sample with a nominal starting composition of EuAl_4Pt_2 was prepared, in analogy to EuAl_4Ir_2 [49], from which single crystals (Figure 2) with the composition $\text{Eu}_4\text{Al}_{13}\text{Pt}_9$ were

extracted and investigated via single crystal X-ray diffraction experiments (*vide infra*). The powder X-ray diffraction pattern clearly indicates the formation of binary AlPt (cubic CsCl type, $Pm\bar{3}m$) [50] and ternary $\text{Eu}_2\text{Al}_9\text{Pt}_3$ (orthorhombic $\text{Y}_2\text{Co}_3\text{Ga}_9$ type, $Cmcm$) [51] besides the title compound. In addition, at least one, yet unidentified side phase, is present in the sample.

3.2 Single crystal X-ray diffraction and structure refinement

Careful analysis of the obtained single crystal X-ray diffraction data revealed an orthorhombic lattice, and space group

$Pmmn$ was found to be correct. The structure was solved using the charge flipping algorithm of SUPERFLIP [27] and a least squares refinement on F^2 using the program JANA2006 [28, 29] was carried out. All atomic positions were refined with anisotropic displacement parameters and as a check for the correct composition, the occupancy parameters were refined in a separate series of least-square refinements. All sites were fully occupied within three standard deviations. The final difference Fourier syntheses were contour less. From the Pearson database [23], isotypism with $\text{Ce}_4\text{Al}_{13}\text{Pt}_9$ [52] was deduced.

3.3 Crystal chemistry

$\text{Eu}_4\text{Al}_{13}\text{Pt}_9$ crystallizes in the orthorhombic crystal system with space group $Pmmn$ ($a = 415.38(1)$, $b = 1149.73(2)$, $c = 1994.73(5)$ pm, $oP52$, $e^9b^3a^5$) and is isostructural with the thus far sole aluminum representative $\text{Ce}_4\text{Al}_{13}\text{Pt}_9$ [52]. However, the structure can be regarded as a coloring or site exchange variant of the $\text{Ho}_4\text{Ir}_{13}\text{Ge}_9$ type structure [53].

One way to describe the crystal structure of $\text{Eu}_4\text{Al}_{13}\text{Pt}_9$ (Figure 3, left) is based on the coordination polyhedra surrounding the Eu atoms. All three independent crystallographic Eu positions are surrounded by six Al and six Pt atoms in the shape of a (slightly distorted) hexagonal prism (Figure 4). The six-membered rings are alternately occupied by Al and Pt, and the two opposing rings exhibit the same orientation, meaning Al on top of Al and Pt on top of Pt. All prisms form strands running along the a axis via condensation over the common hexagonal faces. While the Eu1 prisms are isolated within the $[\text{Al}_{13}\text{Pt}_9]^{6-}$ polyanion, two

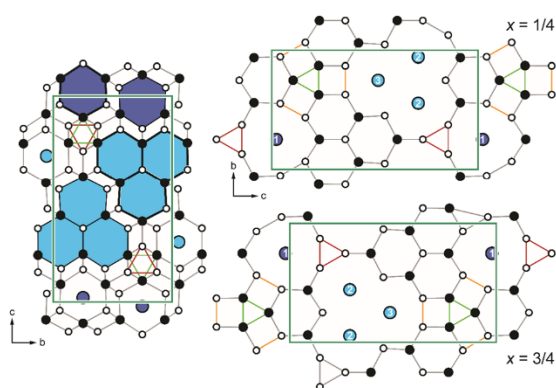


Figure 3: Unit cell of $\text{Eu}_4\text{Al}_{13}\text{Pt}_9$ depicted along the a axis (left). Layers located on $x = 1/4$ (right top) and $x = 3/4$ (right bottom). The Al_3 triangles are highlighted in red, the Pt_3 triangles in green, the Al_2 dumbbells in orange. Eu, Pt and Al atoms are shown in blue, black and white circles.

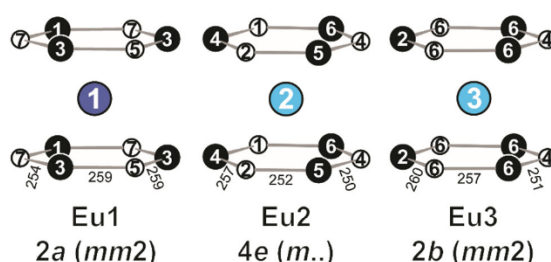


Figure 4: Coordination environments surrounding the Eu atoms in the structure of $\text{Eu}_4\text{Al}_{13}\text{Pt}_9$. Eu, Pt and Al atoms are shown in blue, black and white circles, Wyckoff sites, site symmetries and interatomic distances (in pm) are given.

Eu2 and one Eu3 prism are condensed via rectangular faces to form trimeric units that also form strands along [100] by condensation via the respective hexagonal faces. Within the unit cell, these units are shifted by $x = 1/2$ with respect to each other as highlighted in Figure 3 (left) by the thick and thin polyhedron borders. These alternately occupied hexagonal prismatic arrangements are rather common in aluminum-rich intermetallics and can be found e.g. in the recently reported strontium aluminum platinides SrAl_5Pt_3 and $\text{Sr}_2\text{Al}_{16}\text{Pt}_9$ [54] or the rare-earth aluminum platinides of the REAl_3Pt_2 ($\text{RE} = \text{Y}, \text{Dy-Tm}$) or $\text{RE}_2\text{Al}_4\text{Pt}_3$ ($\text{RE} = \text{Tm}, \text{Lu}$) series [55]. In all three prisms, the interatomic Eu–Pt (322–332 pm) and Eu–Al distances (326–360 pm) are in line with the ones found in binary intermetallics e.g. EuAl_2 (MgCu_2 type, 337 pm [56]), EuAl_4 (BaAl_4 type, 347 pm [57]) or EuPt_2 (MgCu_2 type, 321 pm [58]), but slightly longer than the sum of the covalent radii ($\text{Eu}+\text{Al} = 185+125 = 310$ pm; $\text{Eu}+\text{Pt} = 185+129 = 314$ pm [59]). The known ternary compounds in this system, EuAl_2Pt (Eu–Al: 335–355 pm; Eu–Pt: 302–330 pm) [1], $\text{Eu}_2\text{Al}_9\text{Pt}_3$ (Eu–Al: 306–313 pm; Eu–Pt: 347–348 pm) [51], or $\text{Eu}_2\text{Al}_{15}\text{Pt}_6$ (Eu–Al: 304–340 pm; Eu–Pt: 343 pm) [12], exhibit similar distances.

The complex $[\text{Al}_{13}\text{Pt}_9]^{6-}$ polyanion is formed by six platinum and eight aluminum atoms (Figure 3). Both atom types are either found on $x = 1/4$ or $3/4$, due to the symmetry of the space group. Cutouts of the respective layers are shown in Figure 3 (right). The faces forming the hexagonal prisms can be easily recognized. Al_2 dumbbells and Al_3 and Pt_3 triangles that exhibit homoatomic bonding are embedded within both layers. The Al–Al distances within the dumbbell are 277–279 pm and 282–284 pm within the triangular units, while the Pt–Pt distances range between 282 and 285 pm. The homoatomic Al–Al distances are slightly larger compared to the ones found in other intermetallic compounds that exhibit Al_3 triangles ($\text{Eu}_2\text{Al}_{15}\text{Pt}_6$: 263–268 pm [3]; $\text{Eu}_2\text{Al}_9\text{Ir}_3$: 273–275 pm [12]). In comparison with molecular Al_3 triangles, e.g. in the tetra(supersilyl)cyclotriallyl $(t\text{Bu}_3\text{Si})_4\text{Al}_3^+$ radical [60] and in

$\text{Na}_2[(\text{Ar}''\text{Al})_3]$ [61], the distances are quite similar ($(t\text{Bu}_3\text{Si})_4\text{Al}_3$: 270–276 pm). The Pt_3 triangles exhibit distances between 282 and 285 pm, in line with the Pt–Pt distances of 277 pm found in the REAl_3Pt_6 ($\text{RE} = \text{Ce-Nd, Sm, Gd, Tb}$) series [62] or the two molecular examples, namely $[(\text{Mes}^{\text{NHP}}\text{PtBr})_3]$ [63] and $[(\text{Pt}(\text{PMe}_3))_3\{\mu\text{-SiPh}_2\}_3]$ [64], which exhibit interatomic Pt–Pt distances of 269–270 and 270–272 pm. Furthermore, the distances within the Al_2 dumbbells and the Al_3 and Pt_3 triangles are well in line with the distances found in the elements (Pt: 277 pm [65]; Al: 286 pm [66]). Finally, the heteroatomic Pt–Al distances range between 247 and 265 pm. These distances are in line with those in the binary aluminum platinides AlPt (248–273 pm [67]) and Al_2Pt (256 pm [68]) and in ternary intermetallics like EuAl_2Pt (254–258 pm [1]), and as also close to the sum of the covalent radii ($\text{Pt}+\text{Al} = 129+125 = 254$ pm [59]).

3.4 Quantum-chemical calculations

To check for possible magnetic interactions of the Eu atoms two models were constructed: a non-magnetic (NM) and a ferromagnetic (FM) one. The experimental single crystal diffraction data was used as a starting point for the DFT-GGA-PBE calculations of both models. The optimized lattice parameters for the NM model are $a_{\text{theo}} = 415.46$, $b_{\text{theo}} = 1155.37$, $c_{\text{theo}} = 2010.79$ pm, while for the FM model $a_{\text{theo}} = 416.34$, $b_{\text{theo}} = 1155.20$, $c_{\text{theo}} = 2005.88$ pm are found. The lattice parameters of both models are in good agreement with the experimental ones: $a = 415.38(1)$, $b = 1149.73(2)$, $c = 1994.73(5)$ pm. The formation enthalpy per formula unit of the NM and FM model are 2599 and 2609 kJ mol^{-1} , respectively, hence slightly favoring the FM model. Therefore, the further discussion will focus on the FM model only.

Table 5: Interactions and their counts and distances after structure relaxation, and the corresponding ICOHPs in $\text{Eu}_4\text{Al}_{13}\text{Pt}_9$ ($\text{Ho}_4\text{Ir}_{13}\text{Ge}_9$ type, space group $Pmmn$).

Interaction	Count	Distance (pm)	ICOHP (eV)	Interaction	Count	Distance (pm)	ICOHP (eV)
Eu1–Pt1	2	322.8	–0.46	Pt1–Al7	2	257.9	–1.62
Eu1–Pt3	4	327.5	–0.58	Pt1–Al8	4	265.9	–1.00
Eu1–Al7	4	332.2	–0.31	Pt2–Al3	1	249.9	–1.01
Eu1–Al5	2	343.5	–0.34	Pt2–Al6	2	260.9	–1.67
Eu1–Al7	2	353.0	–0.22	Pt2–Al1	4	261.1	–1.35
Eu1–Al2	2	355.2	–0.25	Pt3–Al8	1	250.0	–1.48
Eu1–Al8	2	361.7	–0.08	Pt3–Al7	1	255.0	–1.87
Eu2–Pt4	2	320.7	–0.52	Pt3–Al2	2	259.0	–1.79
Eu2–Pt5	2	327.5	–0.47	Pt3–Al5	1	259.4	–2.02
Eu2–Pt6	2	333.0	–0.45	Pt3–Al7	2	263.2	–1.47
Eu2–Al1	2	327.4	–0.34	Pt4–Al2	1	257.4	–1.86
Eu2–Al2	2	329.5	–0.39	Pt4–Al1	1	258.0	–1.66
Eu2–Al4	2	333.0	–0.23	Pt4–Al3	2	265.5	–0.98
Eu2–Al6	1	347.7	–0.18	Pt4–Al8	2	266.4	–1.05
Eu2–Al5	1	347.9	–0.24	Pt5–Al4	1	249.9	–1.72
Eu2–Al3	1	356.4	–0.09	Pt5–Al2	2	253.2	–1.98
Eu2–Al8	1	359.7	–0.11	Pt5–Al5	2	255.8	–1.71
Eu3–Pt2	2	323.9	–0.46	Pt6–Al4	1	250.9	–1.70
Eu3–Pt6	4	326.3	–0.36	Pt6–Al6	2	253.8	–1.79
Eu3–Al4	2	329.9	–0.22	Pt6–Al1	1	254.9	–2.01
Eu3–Al6	4	337.7	–0.34	Pt6–Al6	1	258.3	–1.67
Eu3–Al1	2	350.1	–0.27				
Eu3–Al6	2	350.9	–0.16				
Pt1–Pt4	2	290.5	–0.67				
Pt4–Pt4	1	287.2	–0.74				
Al1–Al1	1	279.6	–0.54				
Al1–Al6	2	297.6	–0.53				
Al1–Al3	2	307.0	–0.11				
Al2–Al7	1	279.9	–0.76				
Al2–Al5	2	297.8	–0.61				
Al2–Al8	2	307.6	–0.28				
Al3–Al8	2	284.6	–0.28				
Al6–Al6	2	304.7	–0.35				
Al7–Al7	2	293.1	–0.52				
Al7–Al8	2	307.0	–0.20				
Al8–Al8	1	282.3	–0.32				

The bond lengths of the FM model after structural relaxation can be found in Table 5. The bond lengths are slightly larger than those found in the experiment, a common feature observed when using the GGA functional. The absolute Pearson electronegativities [69] of Pt and Al are 5.6 and 3.23 eV, respectively. For Eu no Pearson electronegativity is reported, but the Pearson electronegativity of the chemically similar element La is 3.1 eV [69]. Therefore, the title compound clearly can be described as a platinide with polar covalent bonding between Pt and Al forming a $[\text{Al}_{13}\text{Pt}_9]^{6-}$ polyanion. This interpretation was underlined by Bader charge calculations. The Bader charges for Eu, Pt and Al according to the Henkelman et al. and the Yu and Trinkle methods are +1.36 to +1.38/+1.35 to +1.37, -2.51 to $-3.46/-2.52$ to -3.48 and +1.24 to +1.71/+1.27 to +1.72, respectively (Table 6). Similar charges for Eu were found in EuAl_2Pt (Eu: +1.39 [1]), but the Pt atoms carry lower negative charges and the Al atoms higher positive charges in the title compound (EuAl_2Pt : Pt: -3.67 , Al: +1.14 [1]). This is most likely caused by a higher Pt and Al to Eu and lower Al to Pt ratio for $\text{Eu}_4\text{Al}_{13}\text{Pt}_9$ compared with EuAl_2Pt .

The spin-polarized DOS of the FM model of $\text{Eu}_4\text{Al}_{13}\text{Pt}_9$ is shown in Figure 5. As the FM model is spin-polarized, two densities-of-states can be plotted. Both types of DOSs are similar in shape from -10 to -1 eV and above the Fermi level. The total DOS of the majority electrons with α -spin features a large peak at around -0.5 eV, which is absent in the DOS of the minority electrons. This peak originates from the f -electrons of Eu. This is the only contribution of the Eu f -electrons to the DOS indicating a high magnetic moment on Eu. Indeed, according to the Quantum ESPRESSO and LMTO

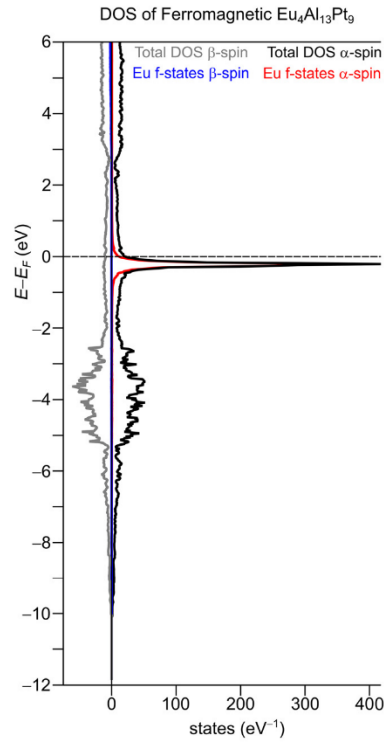


Figure 5: Density-of-states (DOS) of the spin-polarized ferromagnetic model of $\text{Eu}_4\text{Al}_{13}\text{Pt}_9$. Shown in black is the total DOS of the majority electrons (α -spin), while the DOS of the minority electrons (β -spin) is shown in grey. The DOS of the α -spin f -electrons of Eu is shown in red, while the DOS of the β -spin f -electrons of Eu is shown in blue.

Table 6: Bader Effective Charges of the atomic species in $\text{Eu}_4\text{Al}_{13}\text{Pt}_9$ ($\text{Ho}_4\text{Ir}_{13}\text{Ge}_9$ type, space group $Pm\bar{3}n$).

Atom	Henkelman et al. (e)	Yu and Tinkle (e)
Eu1	+1.24	+1.24
Eu2	+1.22	+1.22
Eu3	+1.22	+1.22
Al1	+1.66	+1.67
Al2	+1.70	+1.70
Al3	+1.70	+1.72
Al4	+1.30	+1.30
Al5	+1.66	+1.66
Al6	+1.64	+1.66
Al7	+1.66	+1.67
Al8	+1.69	+1.70
Pt1	-2.51	-2.51
Pt2	-3.36	-3.36
Pt3	-3.41	-3.42
Pt4	-2.50	-2.49
Pt5	-2.88	-2.91
Pt6	-2.88	-2.90

calculations the magnetic moment on Eu is $\mu_{\text{calc}} = 6.62 \mu_B$ and 6.83 – $6.89 \mu_B$, respectively. As the magnetic moment is not an integer, one can assume an itinerant magnetism present in this compound. However, the peak of the DOS of the f -electrons just below the Fermi level E_F is quite narrow, which indicates somewhat localized moments due to the ionic interactions which are present in $\text{Eu}_4\text{Al}_{13}\text{Pt}_9$. The remaining DOS originates from Pt and Al states as expected. The DOS of Pt and Al (not shown here) are shaped similarly in the area -10 to -5 eV and from 0 eV to at least $+6$ eV. This points to covalent bonding between Pt and Al. To discuss the chemical bonding, the COHP technique comes in handy. First the Pt–Al bonds will be discussed. The ICOHPs of these bonds are in the range of -0.98 to -2.02 eV, which, again, indicates covalent bonding between Pt and Al similar to the Pt–Al bonds in EuAl_2Pt (ICOHP of Pt–Al: -1.82 to -1.95 eV [1]). In Figure 6 (right), the $-\text{COHP}$ -plots of selected Pt–Al bonds are shown. Only little anti-bonding states below the Fermi level and non-bonding or slightly bonding states are

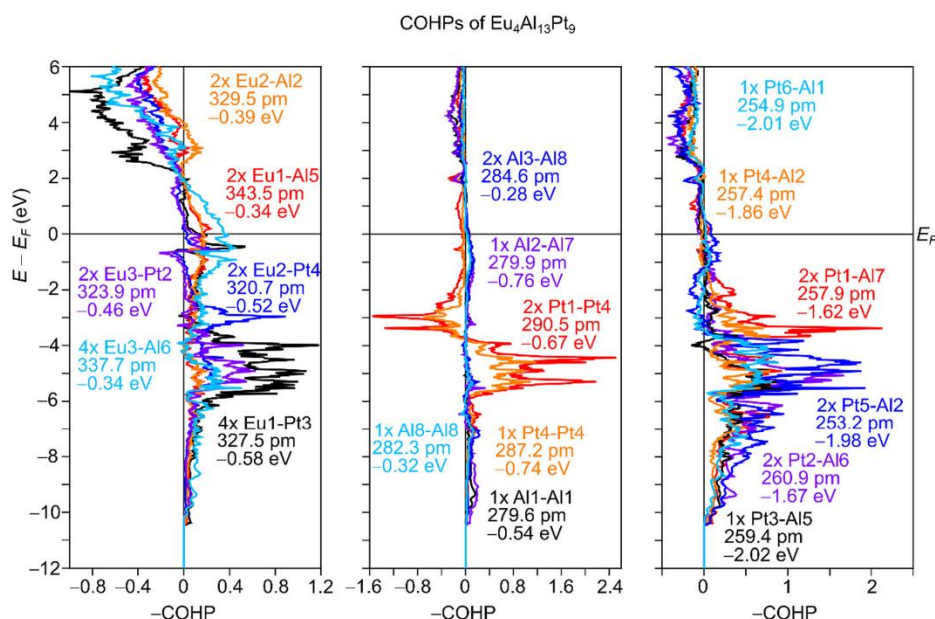


Figure 6: –COHP-plots of the spin-polarized ferromagnetic model of $\text{Eu}_4\text{Al}_{13}\text{Pt}_9$. –COHP-plots for selected Eu–X (X = Pt, Al), Al–Al/Pt–Pt, and Pt–Al bonds are shown on the left, center and right side of the Figure, respectively.

occupied at E_F , which points to a stable covalent bond type. Next, the Eu–Pt and Eu–Al bonds are discussed. As expected, based on the bond lengths (see Table 5) the ICOHPs are -0.36 to -0.58 eV and -0.08 to -0.39 eV for the Eu–Pt and Eu–Al bonds, respectively. For EuAl_2Pt the ICOHPs of the Eu–Al bonds are comparable with the ICOHPs of the Eu–Al bonds of the title compound (-0.03 to -0.29 eV [1]). Similar weak covalent bonding can be found between the homoa-tomic Pt–Pt and Al–Al bonds with ICOHPs -0.67 to -0.74 eV and -0.11 to -0.76 eV, respectively. The Al–Al bonds within the aforementioned Al_2 dumbbells are rather strong with ICOHPs of -0.76 and -0.54 eV compared with the other Al–Al bonds in this compound. The Al–Al interactions within the Al_3 triangles, however, are rather weak (-0.28 and -0.32 eV) compared with other Al–Al bonds with similar bond lengths. The ICOHPs of the Al–Al bonds in EuAl_2Pt are slightly higher (-0.19 to -1.11 eV [1]), which might be caused by the lower positive charge of the Al atoms and the absence of Al_3 triangles in EuAl_2Pt . Similar to the Ni–Ni bonds in CaNi_2Al_8 [70] and the Pt–Pt bonds in SrAl_5Pt_3 and $\text{Sr}_2\text{Al}_{16}\text{Pt}_9$ [54], the unexpectedly weak Pt–Pt bonds within the Pt_3 triangle originate from a destabilizing bonding situation, which becomes obvious in Figure 6 (center). From -4 eV to the Fermi level the anti-bonding states are occupied in both Pt–Pt bond types. The Eu–X (X = Pt, Al) bonds in Figure 6 (left) and Al–Al bonds in Figure 6 (center) show no or only very few occupied antibonding states.

Acknowledgements: We thank Ute Ch. Rodewald for the collection of the single crystal intensity data. Instrumentation and technical assistance for this work were also provided by the Service Center X-ray Diffraction, with financial support from Saarland University and German Science Foundation (project number INST 256/349-1 and INST 256/506-1). RT thanks the Universitätsrechenzentrum of the Otto von Guericke University for calculation power and time.

Author contributions: All authors have accepted responsibility for the entire content of this submitted manuscript and approved the submission.

Research funding: Funding is provided by the Deutsche Forschungsgemeinschaft DFG (JA 1891-10-1, INST 256/349-1 and INST 256/506-1).

Conflict of interest statement: The authors declare no conflicts of interest regarding this article.

References

1. Stegemann F., Block T., Klenner S., Zhang Y., Fokwa B. P. T., Timmer A., Mönig H., Doerenkamp C., Eckert H., Janka O. *Chem. Eur. J.* 2019, 25, 10735–10747.
2. Klenner S., Heletta L., Pöttgen R. *Dalton Trans.* 2019, 48, 3648–3657.
3. Radziejowski M., Stegemann F., Block T., Stahl J., Johrendt D., Janka O. *J. Am. Chem. Soc.* 2018, 140, 8950–8957.

4. Heying B., Kösters J., Heletta L., Klenner S., Pöttgen R. *Monatsh. Chem.* 2019, 150, 1163–1173.
5. De Vries J. W. C., Thiel R. C., Buschow K. H. J. *Phys. B+C* 1984, 124, 291–298.
6. Harmening T., Pöttgen R. *Z. Naturforsch.* 2009, 65b, 90–94.
7. Seiro S., Kummer K., Vyalikh D., Caroca-Canales N., Geibel C. *Phys. Status Solidi* 2013, 250, 621–625.
8. Felner I., Nowik I. *J. Phys. Chem. Solid.* 1984, 45, 419–426.
9. Mayer I., Felner I. *J. Phys. Chem. Solid.* 1977, 38, 1031–1034.
10. Maślankiewicz P., Szade J. *J. Alloys Compd.* 2006, 423, 69–73.
11. Mörsen E., Mosel B. D., Müller-Warmuth W., Reehuis M., Jeitschko W. *J. Phys. C Solid State Phys.* 1988, 21, 3133–3140.
12. Stegemann F., Block T., Klenner S., Janka O. *Chem. Eur. J.* 2019, 25, 3505–3509.
13. Sampathkumar E. V., Gupta L. C., Vijayaraghavan R., Gopalakrishnan K. V., Pillay R. G., Devare H. G. *J. Phys. C Solid State Phys.* 1981, 14, L237–L242.
14. Menushenkov A. P., Yaroslavtsev A. A., Geondzhian A. Y., Chernikov R. V., Nataf L., Tan X., Shatrak M. *J. Supercond. Nov. Magnetism* 2017, 30, 75–78.
15. Tan X., Fabbris G., Haskel D., Yaroslavtsev A. A., Cao H., Thompson C. M., Kovnir K., Menushenkov A. P., Chernikov R. V., Garlea V. O., Shatrak M. *J. Am. Chem. Soc.* 2016, 138, 2724–2731.
16. Akihiro M., Shigeki M., Masafumi U., Hirofumi W., Kazuyuki M., Yoshiya U., Masaichiro M., Naomi K., Kiyofumi N., Naohisa H., Yasuo O., Naoki I. *J. Phys.: Condens. Matter* 2018, 30, 105603.
17. Kumar R. S., Svane A., Vaitheeswaran G., Kanchana V., Bauer E. D., Hu M., Nicol M. F., Cornelius A. L. *Phys. Rev. B* 2008, 78, 075117.
18. Stegemann F., Stahl J., Bartsch M., Zacharias H., Johrendt D., Janka O. *Chem. Sci.* 2019, 10, 11086–11094.
19. Adroja D. T., Rainford B. D., de Teresa J. M., del Moral A., Ibarra M. R., Knight K. S. *Phys. Rev. B* 1995, 52, 12790–12797.
20. Felner I., Nowik I. *Phys. Rev. B* 1986, 33, 617–619.
21. Felner I., Nowik I., Vaknin D., Potzel U., Moser J., Kalvius G. M., Wortmann G., Schmiester G., Hilscher G., Gratz E., Schmitzer C., Pillmayr N., Prasad K. G., de Waard H., Pinto H. *Phys. Rev. B* 1987, 35, 6956–6963.
22. Müller H., Bauer E., Gratz E., Yoshimura K., Nitta T., Mekata M. *J. Magn. Magn. Mater.* 1988, 76, 159–160.
23. Villars P., Cenzual K. *Pearson's Crystal Data: Crystal Structure Database for Inorganic Compounds*; ASM International®: Materials Park, Ohio (USA), 2023.
24. Pöttgen R., Gulden T., Simon A. *GIT Labor-Fachz.* 1999, 43, 133–136.
25. Pöttgen R., Lang A., Hoffmann R.-D., Künnen B., Kotzyba G., Müllmann R., Mosel B. D., Rosenhahn C. *Z. Kristallogr.* 1999, 214, 143–150.
26. *X-Area (Version 1.70)*; Stoe & Cie GmbH, 2014.
27. Palatinus L., Chapuis G. *J. Appl. Crystallogr.* 2007, 40, 786–790.
28. Petříček V., Dušek M., Palatinus L. *Jana2006. The Crystallographic Computing System*; Institute of Physics: Praha (Czech Republic), 2006.
29. Petříček V., Dušek M., Palatinus L. *Z. Kristallogr.* 2014, 229, 345–352.
30. Giannozzi P., Baroni S., Bonini N., Calandra M., Car R., Cavazzoni C., Ceresoli D., Chiarotti G. L., Cococcioni M., Dabo I., Dal Corso A., de Gironcoli S., Fabris S., Fratesi G., Gebauer R., Gerstmann U., Gougousis C., Kokalj A., Lazzeri M., Martin-Samos L., Marzari N., Mauri F., Mazzarello R., Paolini S., Pasquarello A., Paulatto L., Sbraccia C., Scandolo S., Sclauzero G., Seitsonen A. P., Smogunov A., Umari P., Wentzcovitch R. M. *J. Phys.: Condens. Matter* 2009, 21, 395502.
31. Giannozzi P., Andreussi O., Brumme T., Bunau O., Buongiorno Nardelli M., Calandra M., Car R., Cavazzoni C., Ceresoli D., Cococcioni M., Colonna N., Carnimeo I., Dal Corso A., de Gironcoli S., Delugas P., DiStasio R. A., Ferretti A., Floris A., Fratesi G., Fugallo G., Gebauer R., Gerstmann U., Giustino F., Gorni T., Jia J., Kawamura M., Ko H. Y., Kokalj A., Küçükbenli E., Lazzeri M., Marsili M., Marzari N., Mauri F., Nguyen N. L., Nguyen H. V., Otero-de-la-Roza A., Paulatto L., Poncé S., Rocca D., Sabatini R., Santra B., Schlipf M., Seitsonen A. P., Smogunov A., Timrov I., Thonhauser T., Umari P., Vast N., Wu X., Baroni S. *J. Phys.: Condens. Matter* 2017, 29, 465901.
32. Blöchl P. E. *Phys. Rev. B* 1994, 50, 17953–17979.
33. Dal Corso A. *Comput. Mater. Sci.* 2014, 95, 337–350.
34. Topsakal M., Wentzcovitch R. M. *Comput. Mater. Sci.* 2014, 95, 263–270.
35. Marzari N., Vanderbilt D., De Vita A., Payne M. C. *Phys. Rev. Lett.* 1999, 82, 3296–3299.
36. Monkhorst H. J., Pack J. D. *Phys. Rev. B* 1976, 13, 5188–5192.
37. Perdew J. P., Burke K., Ernzerhof M. *Phys. Rev. Lett.* 1996, 77, 3865–3868.
38. Tang W., Sanville E., Henkelman G. *J. Phys.: Condens. Matter* 2009, 21, 084204.
39. Sanville E., Kenny S. D., Smith R., Henkelman G. *J. Comput. Chem.* 2007, 28, 899–908.
40. Henkelman G., Arnaldsson A., Jónsson H. *Comput. Mater. Sci.* 2006, 36, 354–360.
41. Yu M., Trinkle D. R. *J. Chem. Phys.* 2011, 134, 064111.
42. Otero-de-la-Roza A., Blanco M. A., Pendás A. M., Luaña V. *Comput. Phys. Commun.* 2009, 180, 157–166.
43. Otero-de-la-Roza A., Johnson E. R., Luaña V. *Comput. Phys. Commun.* 2014, 185, 1007–1018.
44. Andersen O. K., Skriver H., Nohl H., Johansson B. *Pure Appl. Chem.* 1980, 52, 93–118.
45. Andersen O. K., Jepsen O. *Phys. Rev. Lett.* 1984, 53, 2571–2574.
46. TB-LMTO-ASA, Jepsen O., Andersen O. K. Max-Planck-Institut für Festkörperforschung Stuttgart (Germany), 2000.
47. Perdew J. P., Chevary J. A., Vosko S. H., Jackson K. A., Pederson M. R., Singh D. J., Fiolhais C. *Phys. Rev. B* 1992, 46, 6671–6687.
48. Dronskowski R., Blöchl P. E. *J. Phys. Chem.* 1993, 97, 8617–8624.
49. Zaremba N., Pavlyuk V., Stegemann F., Hlukhyy V., Engel S., Klenner S., Pöttgen R., Janka O. *Monatsh. Chem.* 2022; <https://doi.org/10.1007/s00706-00022-03005-00708>.
50. Bhan S., Kudielka H. *Int. J. Mater. Res.* 1978, 69, 333–336.
51. Stegemann F., Zhang Y., Fokwa B. P. T., Janka O. *Dalton Trans.* 2020, 49, 6398–6406.
52. Morozova Y., Gribanov A., Murashova E., Dunaev S., Grytsiv A., Rogl P., Giester G., Kaczorowski D. *J. Alloys Compd.* 2018, 767, 496–503.
53. Sologub O. L., Prots Y. M., Salamakha P. S., Pecharskii V. K., Bodak O. I. *J. Alloys Compd.* 1993, 202, 13–15.
54. Engel S., Bönnighausen J., Stegemann F., Touzani R. S., Janka O. *Z. Naturforsch.* 2022, 77b, 367–379.
55. Eustermann F., Gausebeck S., Dosche C., Haensch M., Wittstock G., Janka O. *Crystals* 2018, 8, 169.
56. Harris I. R., Mansey R. C., Raynor G. V. *J. Less-Common Met.* 1965, 9, 270–280.
57. Krypyakevych P. I., Zalutskii I. I. *Vopr. Teor. Primen. Redkozem. Met., Mater. Soveshch.* 1964, 144–145.
58. Elliott R. P. *Proc. Conf. Rare Earth Res., 4th*, Phoenix, 1965; pp. 215–245.
59. Emsley J. *The Elements*; Clarendon Press, Oxford University Press: Oxford, New York, 1998.
60. Wiberg N., Blank T., Kaim W., Schwederski B., Linti G. *Eur. J. Inorg. Chem.* 2000, 2000, 1475–1481.
61. Wright R. J., Brynda M., Power P. P. *Angew. Chem. Int. Ed.* 2006, 45, 5953–5956.

62. Eustermann F., Stegemann F., Renner K., Janka O. *Z. Anorg. Allg. Chem.* 2017, *643*, 1836–1843.
63. Nickolaus J., Imbrich D. A., Schlindwein S. H., Geyer A. H., Nieger M., Gudat D. *Inorg. Chem.* 2017, *56*, 3071–3080.
64. Tanaka K., Kamono M., Tanabe M., Osakada K. *Organometallics* 2015, *34*, 2985–2990.
65. Hull A. W. *Trans. Am. Inst. Electro. Eng.* 1919, *38*, 1445–1466.
66. Hull A. W. *Phys. Rev.* 1917, *10*, 661–696.
67. Schubert K., Burkhardt W., Esslinger P., Günzel E., Meissner H. G., Schütt W., Wegst J., Wilkens M. *Naturwissenschaften* 1956, *43*, 248–249.
68. Zintl E., Harder A., Haucke W. *Z. Phys. Chem. B* 1937, *35*, 354–362.
69. Pearson R. G. *Inorg. Chem.* 1988, *27*, 734–740.
70. Gießelmann E., Touzani R. S., Morgenstern B., Janka O. *Z. Naturforsch.* 2021, *76b*, 659–668.

3. Modifying the valence phase transition in $\text{Eu}_2\text{Al}_{15}\text{Pt}_6$ via the solid solutions $\text{Eu}_2\text{Al}_{15}(\text{Pt}_{1-x}\text{T}_x)_6$ ($T = \text{Pd, Ir, Au; } x = 1/6$)

Collaborations to disclose: In this chapter the work from the publication with the same title as the headline is summarized (*Z. Naturforsch. B* **2024**, 79b, 21). L. Schumacher, M.Sc provided the magnetic measurements of the three phases and PD Dr. O. Janka along with the aforementioned worked on the manuscript.

The compound $\text{Eu}_2\text{Al}_{15}\text{Pt}_6$ crystallizes in a (3+2)D modulated structure adopting a monoclinic superstructure with space group $P2_1/m$, which originates from the hexagonal $\text{Sc}_{0.6}\text{Fe}_2\text{Si}_{4.9}$ type structure (own type, $P6_3/mmc$).²²⁶ Besides the modulated structure, the compound also exhibits a temperature induced valence transition at $T_{\text{Trans}} = 45$ K, at which the valence of the europium atoms in the structure changes from the di- (high temperature) to trivalent state (low temperature) or vice versa.⁹² Oyama et al. reported that the transition temperature can be influenced by substitution of the Al atoms with Ga. By substituting over 10 at.-% of the aluminum with gallium the divalent state of europium atoms stabilizes, also an antiferromagnetic ordering occurs,²²⁴ which was already found in the pure Ga compound.⁹² Due the substituent elements being isovalent, the overall valence electron count and valence electron concentration does not change. To research the influence of different electron counts, different strategies can be employed: substitution of Al by an element from a neighboring group or by substitution on the transition metal site. During attempts to achieve the latter, it was observed that only 1/6 of the Pt atoms could be substituted by Ir, Pd or Au atoms. The compounds were synthesized in the arc furnace by using the elements. Additionally, a heat treatment step in a muffle furnace was added to improve the phase purity. The samples were annealed at 1123 K for 96 h and cooled slowly to RT with a cooling rate of 2 K h⁻¹. The products were analyzed via powder X-ray diffraction and the resulting Rietveld refinement showed nearly phase pure products for the Pd and Ir (**Fig. 3.40**) samples (<2 wt.-% binary side phases Al_3Pd_2 (Al_3Ni_2 type, $P\bar{3}m1$, $a = 428.1(3)$, $c = 504.3(4)$ pm)²²⁷ and <1 wt.-% IrAl (CsCl type, $Pm\bar{3}m$, $a = 297.96(3)$ pm)),²²⁸ for the gold substituted compound higher amounts (5 wt.-%) of Al_2Au (CaF_2 type, $Fm\bar{3}m$, $a = 596.38(3)$ pm)²⁰⁷ and traces of an unknown europium containing side phase was observed.

The lattice parameters resulting from the Rietveld-refinement are summarized in **Table 3.8**.

The average structure of $\text{Eu}_2\text{Al}_{15}\text{PdPt}_5$ exhibits one Eu, three Al and one T position, the T position is occupied by 16.7% Pd and 83.3% Pt atoms. The interatomic distances found in the

compound are $d(\text{Eu}-T) = 344\text{-}345$ pm, $d(\text{Eu}-\text{Al}) = 313\text{-}343$ pm, $d(\text{Al}-\text{Al}) = 179\text{-}295$ pm, $d(\text{Al}-T) = 251\text{-}269$ pm. When compared to binary Eu-Pd or Eu-Pt compounds like EuPd_3 (Cu_3Au type, $Pm\bar{3}m$): $d(\text{Eu}-\text{Pd}) = 290$ pm,²²⁹ or EuPd_2 (MgCu_2 type, $Fd\bar{3}m$): $d(\text{Eu}-\text{Pd}) = 322$ pm,²³⁰ the found distance in this ternary structure is significantly longer, whereas the Al-Al and Al-Pd distances are in line with the following binary and ternary compounds $\text{Al}_{21}\text{Pd}_8$ ($\text{Al}_{21}\text{Pt}_8$ type, $I4_1/a$): $d(\text{Al}-\text{Al}) = 267\text{-}348$ pm, $d(\text{Al}-\text{Pd}) = 225\text{-}307$ pm,²³¹ Al_3Pd_2 (Al_3Ni_2 type, $P\bar{3}m1$): $d(\text{Al}-\text{Al}) = 287\text{-}304$ pm, $d(\text{Al}-\text{Pd}) = 255\text{-}265$ pm,²²⁷ AlPd (own type, $R\bar{3}$): $d(\text{Al}-\text{Al}) = 292\text{-}303$ pm, $d(\text{Al}-\text{Pd}) = 258\text{-}263$ pm,²³² AlPd_2 (Co_2Si type, $Pnma$): $d(\text{Al}-\text{Al}) = 345\text{-}347$ pm, $d(\text{Al}-\text{Pd}) = 253\text{-}288$ pm,²¹³ Al_2Pd (CaF_2 type, $Fm\bar{3}m$): $d(\text{Al}-\text{Al}) = 290$ pm, $d(\text{Al}-\text{Pd}) = 251$ pm,²³³ EuAl_9Co_2 (BaAl_9Fe_2 type, $P6/mmm$): $d(\text{Eu}-\text{Al}) = 353\text{-}394$ pm, $d(\text{Al}-\text{Al}) = 278\text{-}294$ pm,²²¹ $\text{Eu}_2\text{Al}_9\text{Ir}_3$ ($\text{Y}_2\text{Ga}_9\text{Co}_3$ type, $Cmcm$): $d(\text{Eu}-\text{Al}) = 306\text{-}315$ pm, $d(\text{Al}-\text{Al}) = 273\text{-}337$ pm⁸⁶ and EuAl_2Pt (MgAl_2Cu type, $Cmcm$): $d(\text{Eu}-\text{Al}) = 335\text{-}337$ pm, $d(\text{Eu}-\text{Pt}) = 302\text{-}330$ pm, $d(\text{Al}-\text{Al}) = 279\text{-}285$ pm, $d(\text{Al}-\text{Pt}) = 254\text{-}258$ pm.⁶³ The found Al-Al and Al-T distances indicate interaction between the Al and T atoms suggesting forming a polyanionic network.

With no europium containing side phases in the substituted $\text{Eu}_2\text{Al}_{15}(\text{Pt}_{1-x}\text{T}_x)_6$ samples present and an unknown europium containing side phase present, magnetic measurements could be performed to investigate the valence transition behavior of the substituted compounds. **Figure 3.a.41** shows the magnetic susceptibility and magnetization isotherm from the three compounds. Notable is that the transition temperature decreases to 42 K when Pd is substituted into the structure and when Ir is used, which possesses an electron less than Pt, the transition shifts to 52 K. When a valence electron is added by substituting gold, no valence transition is observable in the high and low field susceptibility measurements, but the 4 K magnetization isotherm gives a hint that a valence phase transition is occurring at a lower temperature, due to a bend curve that is being lower than the 10 K isotherm at high fields. Additionally, the 4 K isotherm exhibits a steep increase at low field, which together with the observable small bent in the high- and low-field measurements at 10 K indicates a ferromagnetic transition originating from the europium containing side phase. By calculating the effective magnetic moment for all three compounds, values of $7.77 \mu_B$ for the Pd, $7.80 \mu_B$ for the Ir and $7.43 \mu_B$ for the Au substituted $\text{Eu}_2\text{Al}_{15}\text{Pt}_{1-x}\text{T}_x)_6$ result, which compared to the magnetic moment of free Eu^{2+} ions with $7.94 \mu_B$ point to divalent states of the Eu atoms in these compounds at high temperatures. To analyze the purity of the prepared bulk samples, energy dispersive X-ray spectroscopy measurements were taken, the results are summarized in **Table 3.9** alongside the corresponding scanning electron image of the samples (**Fig. 3.42**). All three compounds are in a good

agreement with the ideal composition in regard to the Eu and Al values, but when looked at the Pt and T value, which are apart further especially the Au value is too high, whereas the amount of Pd and Ir are too low, leading to the assumption that the gold substituted compounds possess a higher amount of Au or that the binary side phase was measured alongside the main phase during the EDX measurement. Also, small deviations can be explained by the sample preparation of sprinkling crystallites on the sticky tape leading to a non-perpendicular alignment of the surface to the electron beam.

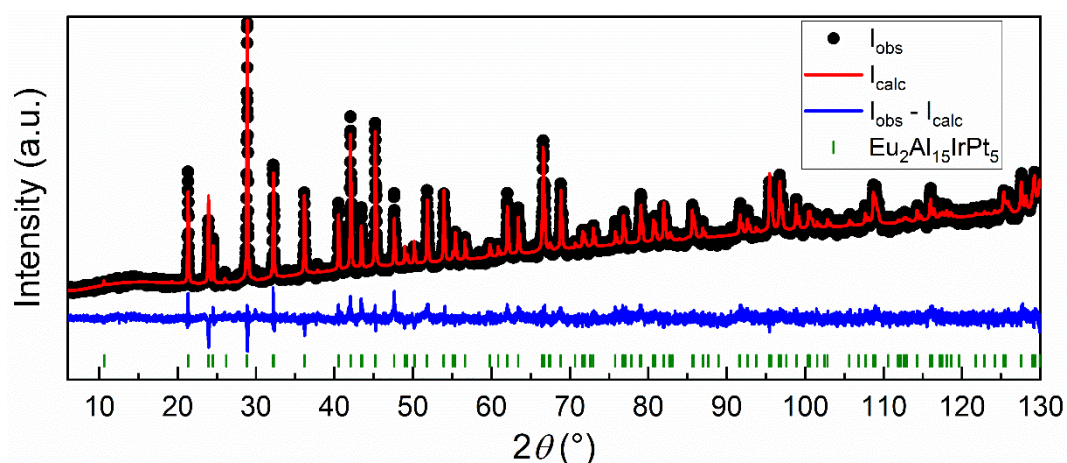


Figure 3.40: Rietveld refinement of the powder X-ray diffraction pattern of $\text{Eu}_2\text{Al}_{15}\text{IrPt}_5$. Collected data are shown in black dots, the refinement as red and the difference as blue line. Olive ticks indicate the Bragg positions of $\text{Eu}_2\text{Al}_{15}\text{IrPt}_5$ using the average hexagonal structure ($\text{Sc}_{0.6}\text{Fe}_2\text{Si}_{4.9}$ type, $P6_3/mmc$).

Table 3.8: Lattice parameters and cell volumes of $\text{Eu}_2\text{Al}_{15}(\text{Pt}_{1-x}\text{T}_x)_6$ ($T = \text{Pd}, \text{Ir}, \text{Au}, x = 1/6$) using the average hexagonal structure ($\text{Sc}_{0.6}\text{Fe}_2\text{Si}_{4.9}$, $P6_3/mmc$)

Compound	a (pm)	c (pm)	V (nm^3)
$\text{Eu}_2\text{Al}_{15}\text{Pt}_6^{\text{L}}$	429.47	1666.7	0.2652
$\text{Eu}_2\text{Al}_{15}\text{IrPt}_5^{\text{P*}}$	429.38	1666.2	0.2660
$\text{Eu}_2\text{Al}_{15}\text{PdPt}_5^{\text{P*}}$	429.55	1665.9	0.2662
$\text{Eu}_2\text{Al}_{15}\text{AuPt}_5^{\text{P*}}$	430.32	1665.8	0.2671

^L literature, ^P powder, ^{*} own work

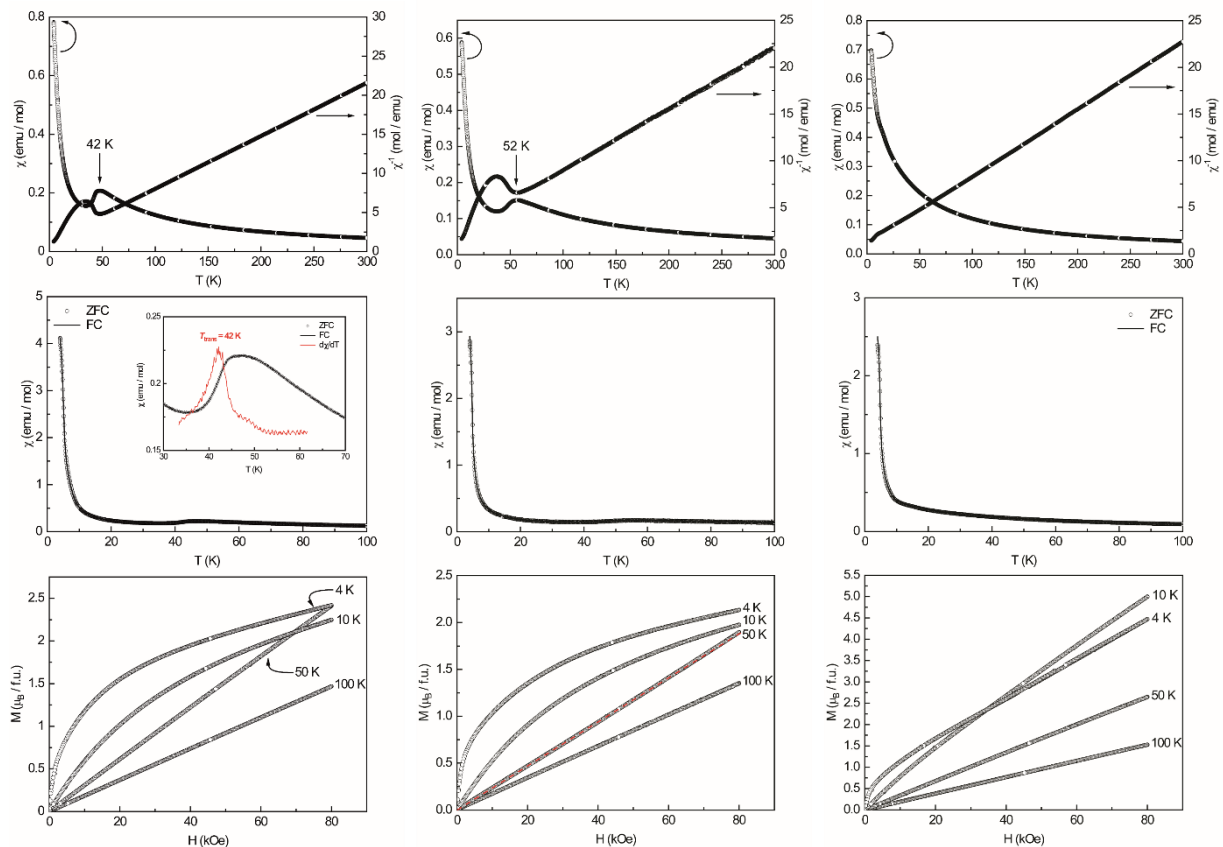


Figure 3.41: Magnetic properties of $\text{Eu}_2\text{Al}_{15}\text{Pt}_5T$ ($T = \text{Pd}$ (left), Ir (center), Au (right)). Top row shows the magnetic and inverse magnetic susceptibility measured at 10 kOe in zero-field-cooled mode (ZFC), middle row depicts the magnetic susceptibility in ZFC/FC (zero-field-cooled/field-cooled) mode at 100 Oe and bottom row shows the magnetization isotherm recorded at $T = 4, 10, 50$ and 100 K.

Table 3.9: EDX data of $\text{Eu}_2\text{Al}_{15}\text{Pt}_5T$ ($T = \text{Pd}, \text{Ir}, \text{Au}$) with standard deviations of ± 2 at.-%.

Compound	Ideal	P1	P2	P3	mean
$\text{Eu}_2\text{Al}_{15}\text{Pt}_5\text{Pd}$	Eu: 8.7	8	8	11	9
	Al: 65.2	65	67	65	65
	Pd: 4.35	2	2	1	2
	Pt: 21.7	25	23	23	24
$\text{Eu}_2\text{Al}_{15}\text{Pt}_5\text{Ir}$	Eu: 8.7	8	8	9	8
	Al: 65.2	64	67	65	66
	Ir: 4.35	3	2	2	2
	Pt: 21.7	25	23	24	24
$\text{Eu}_2\text{Al}_{15}\text{Pt}_5\text{Au}$	Eu: 8.7	8	7	7	7
	Al: 65.2	62	68	67	66
	Au: 4.35	7	8	7	7
	Pt: 21.7	23	17	19	20

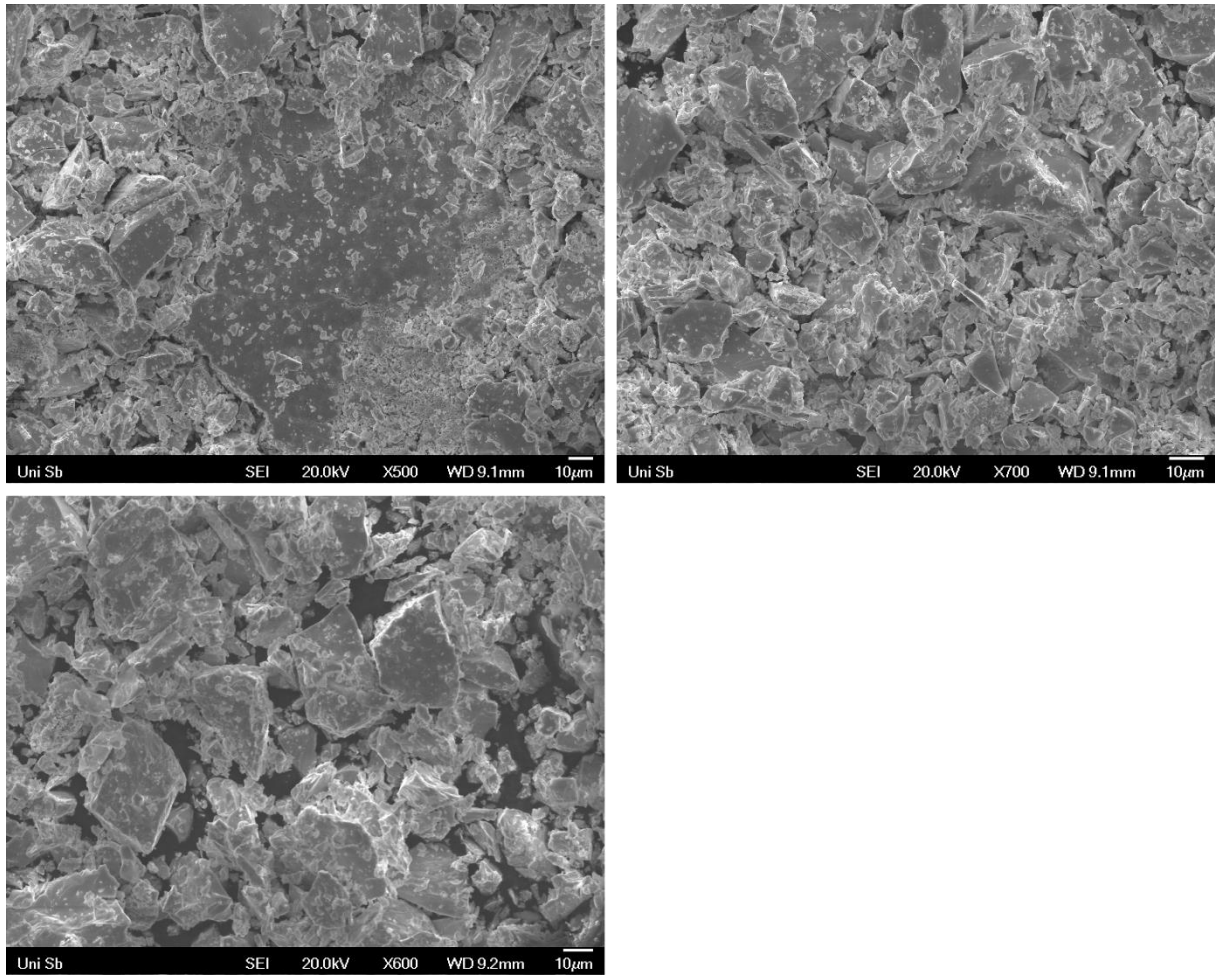


Figure 3.42: SEM image of $\text{Eu}_2\text{Al}_{15}\text{PdPt}_5$ (top left), $\text{Eu}_2\text{Al}_{15}\text{IrPt}_5$ (top right) and $\text{Eu}_2\text{Al}_{15}\text{Pt}_5\text{Au}$ (bottom left).

Stefan Engel, Lars Schumacher and Oliver Janka*

Modifying the valence phase transition in $\text{Eu}_2\text{Al}_{15}\text{Pt}_6$ by the solid solutions $\text{Eu}_2\text{Al}_{15}(\text{Pt}_{1-x}\text{T}_x)_6$ ($\text{T} = \text{Pd}, \text{Ir}, \text{Au}; x = 1/6$)

<https://doi.org/10.1515/znb-2023-0072>

Received September 5, 2023; accepted September 30, 2023

Abstract: The solid solutions $\text{Eu}_2\text{Al}_{15}(\text{Pt}_{1-x}\text{T}_x)_6$ with $\text{T} = \text{Pd}, \text{Ir}, \text{Au}$ and $x = 1/6$ were prepared by arc-melting the stoichiometric mixture of the elements, and subsequent annealing. For $x = 1/6$, all three solid solutions adopt the same structure type as $\text{Eu}_2\text{Al}_{15}\text{Pt}_6$ according to powder X-ray diffraction data. Since the platinumide $\text{Eu}_2\text{Al}_{15}\text{Pt}_6$ exhibits a (3 + 1)D modulated structure (approximant in space group $P12_1/m1$), only the averaged hexagonal unit cell ($P6_3/mmc$, $\text{Sc}_{0.6}\text{Fe}_2\text{Si}_{4.9}$ type) was refined by the Rietveld method. Scanning electron microscopy in combination with energy-dispersive X-ray spectroscopy (SEM/EDX) showed that the degree of substitution is in line with the weighed amounts. For values of $x > 1/6$, no phase-pure samples could be obtained. The results of the magnetic susceptibility measurements indicate that the isoelectronic substitution of Pd for Pt lowers the temperature of the first-order valence phase transition from $T_{\text{trans}} = 45$ K in $\text{Eu}_2\text{Al}_{15}\text{Pt}_6$ to $T_{\text{trans}} = 42$ K in $\text{Eu}_2\text{Al}_{15}(\text{Pt}_{5/6}\text{Pd}_{1/6})_6$. For $\text{Eu}_2\text{Al}_{15}(\text{Pt}_{5/6}\text{Ir}_{1/6})_6$ and $\text{Eu}_2\text{Al}_{15}(\text{Pt}_{5/6}\text{Au}_{1/6})_6$ a change in the electronic situation occurs since the Ir substituted compound exhibits one electron less compared to the pristine Pt compound, while $\text{Eu}_2\text{Al}_{15}(\text{Pt}_{5/6}\text{Au}_{1/6})_6$ has one additional electron. As a consequence, $\text{Eu}_2\text{Al}_{15}(\text{Pt}_{5/6}\text{Ir}_{1/6})_6$ shows a higher valence phase transition temperature of $T_{\text{trans}} = 52$ K while for $\text{Eu}_2\text{Al}_{15}(\text{Pt}_{5/6}\text{Au}_{1/6})_6$ no such transition is obvious.

Keywords: europium; aluminum; intermetallics; magnetism; valence change

Dedicated to Professor Wolfgang Bensch on the occasion of his 70th birthday.

*Corresponding author: **Oliver Janka**, Anorganische Festkörperchemie, Universität des Saarlandes, Campus C4.1, 66123 Saarbrücken, Germany, E-mail: oliver.janka@uni-saarland.de

Stefan Engel, Anorganische Festkörperchemie, Universität des Saarlandes, Campus C4.1, 66123 Saarbrücken, Germany

Lars Schumacher, Institut für Anorganische und Analytische Chemie, Universität Münster, Corrensstrasse 28/30, 48149 Münster, Germany

1 Introduction

Europium compounds are fascinating from different points of view. In the oxide EuO as well as in some halides EuX_2 ($X = \text{F} - \text{I}$) the Eu cations exhibit a formal +2 oxidation state [1–3]. In intermetallic compounds the divalent oxidation state is also observed quite frequently. The stability of this oxidation state is based on the half-filled $4f^7$ shell making the Eu^{2+} ion isoelectronic with Gd^{3+} . Therefore, the Eu^{2+} cations exhibit an effective magnetic moment of $\mu_{\text{eff}} = 7.94 \mu_B$ [4], which is prone to ferro- or antiferromagnetic ordering phenomena. $\text{Eu}_5\text{In}_9\text{Pt}_7$ [5] for example orders antiferromagnetically at $T_N = 11.6(5)$ K while EuAl_2Pt and EuIn_2Pt show ferromagnetic ordering below $T_C = 54.0(1)$ [6] and $32.5(1)$ K [7].

The second possible oxidation state (Eu^{3+} , electron configuration $4f^6$) is quite common in ionic compounds (Eu_2O_3 [8, 9], EuX_3 ($X = \text{F}, \text{Cl}, \text{Br}$) [10–12]), however, rarely observed in intermetallics. For the binary compounds EuRh_2 [13], EuIr_2 [13], EuNi_5 [13], $\text{Eu}_2\text{Ni}_{17}$ [13], EuPd_3 [13], and EuPt_5 [13] the presence of trivalent europium has been confirmed as well as for the ternary intermetallics, EuCo_2Si_2 [14–17], $\text{Eu}_2\text{Co}_{12}\text{P}_7$ [18], EuRuB_4 [19], EuRu_4B_4 [19], EuRu_2Si_2 [15], $\text{Eu}_2\text{Ru}_3\text{Si}_5$ [20], and $\text{Eu}_2\text{Al}_9\text{Ir}_3$ [21]. A recent review summarizes the relevant information on trivalent europium intermetallics [22].

A rather rare phenomenon is the so-called valence phase transition. Here, the valence changes reversibly from $\text{Eu}^{2+/3+}$ to $\text{Eu}^{3+/2+}$ upon external stimuli such as temperature or pressure. This phenomenon is not only known for Eu intermetallics but also Ce and Yb compounds can exhibit these valence phase transition. Metallic cerium for example transforms from α -Ce to γ -Ce [23] upon electron localization. The intermetallic solid solutions $\text{CeNi}_{1-x}\text{Co}_x\text{Sn}$ [24] and $\text{Yb}_{1-x}\text{In}_x\text{Cu}_2$ [25–27] as well as YbPd_2Al_3 [28] exhibit at least a partial temperature-dependent valence phase transition. As for the Eu compounds, EuCo_2As_2 [29, 30] and EuAl_5Pt_3 [31] for example exhibit pressure-dependent shifts of their Eu valence, while e.g. EuPd_2Si_2 ($T_{\text{trans}} \sim 200$ K) [32] and $\text{Eu}_2\text{Al}_{15}\text{Pt}_6$ ($T_{\text{trans}} \sim 45$ K) [33] exhibit temperature-dependent valence phase transitions. The solid solution $\text{Eu}(\text{Ir}_{1-x}\text{Pd}_x)_2\text{Si}_2$ with $x = 0.75, 0.81$ and 0.94 shows a continuous valence phase transition [34], while $\text{Eu}(\text{Pd}_{1-x}\text{Au}_x)_2\text{Si}_2$ with $x = 0.15$ exhibits a

step-wise transition [35]. Recently, the solid solution $\text{Eu}_2(\text{Al}_{1-x}\text{Ga}_x)_{15}\text{Pt}_6$ has been studied for $x = 0, 0.05, 0.1, 0.2, 0.3$, and 1 [36]. Already small amounts of Ga ($x = 0.1$) have been shown to shift the Eu valence towards a stable divalent oxidation state and an antiferromagnetic ordering of $\text{Eu}_2\text{Ga}_{15}\text{Pt}_6$ is established. This is interesting because the valence electron concentration does not change due to the isovalent substitution of Al by Ga.

In this article, we show the influence of substitutions on the Pt positions in $\text{Eu}_2\text{Al}_{15}\text{Pt}_6$. In most cases only small amounts of a component can be substituted without the formation of side phases, but $\text{Eu}_2\text{Al}_{15}(\text{Pt}_{5/6}\text{Pd}_{1/6})_6$, $\text{Eu}_2\text{Al}_{15}(\text{Pt}_{5/6}\text{Ir}_{1/6})_6$, and $\text{Eu}_2\text{Al}_{15}(\text{Pt}_{5/6}\text{Au}_{1/6})_6$ could be synthesized and characterized by means of powder X-ray diffraction (PXRD), scanning electron microscopy paired with energy-dispersive X-ray spectroscopy (SEM/EDX) and magnetic susceptibility measurements.

2 Experimental

2.1 Synthesis

$\text{Eu}_2\text{Al}_{15}(\text{Pt}_{5/6}\text{T}_{1/6})_6$ samples were prepared from the elements using europium ingots (Onyxmet, Olsztyn, Poland), platinum pieces (Agosi AG, Pforzheim, Germany), gold foil (Agosi AG, Pforzheim, Germany) or gold shots (abcr, Karlsruhe, Germany), iridium granules (Chempur, Karlsruhe, Germany), palladium sponge (Chempur, Karlsruhe, Germany), aluminum pieces (Onyxmet, Olsztyn, Poland) and aluminum foil (Alujet, Mammendorf, Germany), all with stated purities above 99.9 %. Samples were prepared on a 200 mg scale. The Eu pieces were stored under an argon atmosphere; surface contaminations on the pieces were removed mechanically prior to the reaction, which was carried out in a custom-built arc furnace [37]. The elements were weighed in an atomic ratio of 2:15:5:1 (Eu:Al:Pt:T) and transferred under argon to a water-cooled copper hearth and arc melted under dried argon at 800 mbar. The argon gas was purified over a titanium sponge ($T = 873\text{ K}$), molecular sieves, activated carbon, and silica gel prior to use. To prevent the evaporation of Eu during the heating, the starting materials were wrapped in aluminum foil. The resulting bead obtained after arc-melting was turned over several times and remelted to increase its homogeneity. The weight loss in all cases was <1 %. As-cast samples are silver metallic, while ground powders are grey and stable in air over months. An additional heat treatment was performed. The ground samples were pressed to pellets, enclosed in evacuated torch-sealed silica ampoules, and annealed at $T = 1123\text{ K}$ for 96 h in a Nabertherm box furnace (N 11/HR P300, Lilienthal, Germany) followed by cooling to RT with a cooling rate of 2 K h^{-1} .

2.2 X-ray diffraction

The annealed polycrystalline samples were analyzed by powder X-ray diffraction (PXRD) experiments. The PXRD pattern of the pulverized samples were recorded at room temperature on a D8-A25 Advance diffractometer (Bruker, Karlsruhe, Germany) in Bragg-Brentano θ - θ

geometry (goniometer radius 280 mm) with non-monochromatized $\text{CuK}\alpha$ radiation ($\lambda = 154.0596\text{ pm}$). A $12\text{ }\mu\text{m}$ Ni foil working as $K\beta$ filter and a variable divergence slit were mounted at the primary beam side. A LYNXEYE detector with 192 channels was used at the secondary beam side. Experiments were carried out in a 2θ range of 6 – 130° with a step size of 0.013° and a total scanning time of 1 h. The recorded data was evaluated using the Bruker TOPAS 5 software [38], with the observed reflections being treated via single-line fits.

2.3 Scanning electron microscopy/energy-dispersive X-ray spectroscopy (SEM/EDX)

Semiquantitative EDX analyses of the bulk samples were conducted on a JEOL 7000F (JEOL, Freising, Germany) scanning electron microscope equipped with an EDAX Genesis 2000 EDX detector (EDAX, Unterschleissheim, Germany). The samples were sprinkled on conductive carbon tape and two area scans as well as five independent data points were measured.

2.4 Magnetic susceptibility measurements

The polycrystalline samples of $\text{Eu}_2\text{Al}_{15}(\text{Pt}_{5/6}\text{Pd}_{1/6})_6$, $\text{Eu}_2\text{Al}_{15}(\text{Pt}_{5/6}\text{Ir}_{1/6})_6$, and $\text{Eu}_2\text{Al}_{15}(\text{Pt}_{5/6}\text{Au}_{1/6})_6$ were investigated by temperature dependent magnetic susceptibility measurements at external fields up to 80 kOe ($1\text{ kOe} = 7.96 \times 10^4\text{ A m}^{-1}$). The samples were ground to a fine powder, filled into a polypropylene capsule and attached to the sample holder rod of a Vibrating Sample Magnetometer (VSM) option of a Physical Property Measurement System (PPMS) by Quantum Design. The magnetization data $M(T, H)$ of the samples was investigated in the temperature range between 4 and 300 K.

3 Results

3.1 Crystal chemistry

The $\text{RE}_2\text{X}_{15}\text{Pt}_6$ ($\text{RE} = \text{Sc, Y, La-Nd, Sm-Lu}$; $\text{X} = \text{Al, Ga}$) compounds [33, 39, 40] have been reported to adopt a monoclinic superstructure (space group $P2_1/m$) of the hexagonal $\text{Sc}_{0.6}\text{Fe}_2\text{Si}_{4.9}$ -type structure (space group $P6_3/mmc$; please note that the composition is given according to the electronegativities of the constituent elements and reversed with respect to the aluminum compounds) [41]. For all compounds that were previously characterized by single-crystal X-ray diffraction, the hexagonal subcell was readily observed. However, additional reflections in the $hk0$ planes could be found in all cases. These were treated as satellite reflections and the diffraction data was consequently integrated as an orthorhombic (3 + 1)D data set with a q vector of $(2/3\text{ }a^*, 0, 0)$, which led to concise structure solutions for $\text{Sc}_2\text{Al}_{15}\text{Pt}_6$ [40], $\text{Eu}_2\text{Al}_{15}\text{Pt}_6$ [33], and $\text{Ho}_2\text{Al}_{15}\text{Pt}_6$ [39].

As the crystal structure of the $\text{RE}_2\text{Al}_{15}\text{Pt}_6$ series has been described in detail before [40], only a brief review of the important structural features is given here. Two distinct

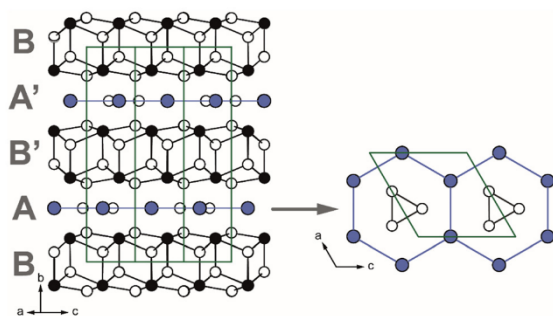


Figure 1: (left) Unit cell of the monoclinic approximant of the $\text{RE}_2\text{Al}_{15}\text{Pt}_6$ ($\text{RE} = \text{Sc}, \text{Y}, \text{La-Nd}, \text{Sm-Lu}$) series [33, 39, 40]. Bonding contacts between the layers have been omitted for clarity; (right) cut-out of the layer formed by a honeycomb arrangement of RE atoms and Al_3 triangles; RE atoms are depicted in blue, Al atoms as open circles and Pt atoms in black, respectively.

building blocks can be observed. Honeycomb arrangements of the RE atoms that are centered by Al_3 triangles (block A) and $[\text{Pt}_3\text{Al}_6]$ slabs (block B). These units are alternately stacked along the crystallographic b axis (monoclinic setting) in a ...ABA'B'... sequence. The Pt-Al and Al-Al distances in all structurally characterized compounds are in the ranges 244–271 and 263–268 pm, respectively, indicating bonding interactions [33, 39, 40]. Between the layers bonding interactions are also observed, however, the contacts have been omitted in the structural drawing in Figure 1. Additional details regarding the structure description can be found in the literature [40].

3.2 Powder X-ray diffraction

The annealed samples were investigated by powder X-ray diffraction experiments. For the Rietveld refinements, the hexagonal averaged structure of the $\text{RE}_{0.67}\text{Al}_5\text{Pt}_2$ series [39, 42–48] was used with the lattice parameters of $\text{Eu}_{0.67}\text{Al}_5\text{Pt}_2$ (space group $P6_3/mmc$, $\text{Sc}_{0.6}\text{Fe}_2\text{Si}_{4.9}$ type, $a = 429.47(2)$, $c = 1666.7(2)$ pm) [33] as starting point. The refined unit cell parameters of $\text{Eu}_2\text{Al}_{15}(\text{Pt}_{5/6}\text{Pd}_{1/6})_6$, $\text{Eu}_2\text{Al}_{15}(\text{Pt}_{5/6}\text{Ir}_{1/6})_6$, and $\text{Eu}_2\text{Al}_{15}(\text{Pt}_{5/6}\text{Au}_{1/6})_6$ (Table 1) exhibit comparable values, in line with the similar covalent radii of Pt (129 pm), Pd (128 pm), Ir (126 pm), and Au (134 pm) [2]. For the refinement, the occupancies of Pt and T were fixed to the ideal ratios. Figure 2 exemplarily shows the Rietveld refinement of $\text{Eu}_2\text{Al}_{15}(\text{Pt}_{5/6}\text{Pd}_{1/6})_6$. The positional parameters are given in Table 2. Substitutions within the solid solution $\text{Eu}_2\text{Al}_{15}(\text{Pt}_{1-x}\text{T}_x)_6$ for $x > 1/6$ and $T = \text{Pd}, \text{Ir},$ and Au always resulted in non-phase-pure samples according to powder X-ray diffraction experiments.

Table 1: Lattice parameters and unit cell volumes of $\text{Eu}_2\text{Al}_{15}\text{Pt}_6$, $\text{Eu}_2\text{Al}_{15}(\text{Pt}_{5/6}\text{Pd}_{1/6})_6$, $\text{Eu}_2\text{Al}_{15}(\text{Pt}_{5/6}\text{Ir}_{1/6})_6$, and $\text{Eu}_2\text{Al}_{15}(\text{Pt}_{5/6}\text{Au}_{1/6})_6$ determined by powder X-ray diffraction. The lattice parameters of the average hexagonal structure ($\text{Sc}_{0.6}\text{Fe}_2\text{Si}_{4.9}$ type, space group $P6_3/mmc$ [41]) are given.

Compound	a (pm)	c (pm)	V (nm^3)	Ref.
$\text{Eu}_2\text{Al}_{15}\text{Pt}_6$	429.47(2)	1666.7(2)	0.2652	[33]
$\text{Eu}_2\text{Al}_{15}(\text{Pt}_{5/6}\text{Pd}_{1/6})_6$	429.55(1)	1665.9(2)	0.2662	*
$\text{Eu}_2\text{Al}_{15}(\text{Pt}_{5/6}\text{Ir}_{1/6})_6$	429.38(1)	1666.2(2)	0.2660	*
$\text{Eu}_2\text{Al}_{15}(\text{Pt}_{5/6}\text{Au}_{1/6})_6$	430.32(1)	1665.8(3)	0.2671	*

*This work.

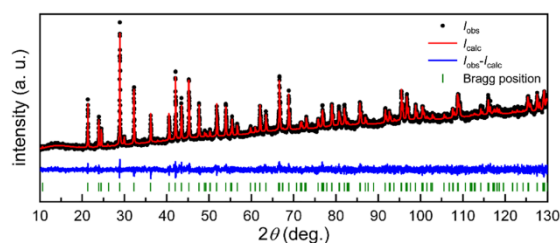


Figure 2: Powder X-ray diffraction data and Rietveld refinement of $\text{Eu}_2\text{Al}_{15}(\text{Pt}_{5/6}\text{Pd}_{1/6})_6$. The black dots represent the experimental data, the red line the respective fit while the blue line indicates the difference between experimental and theoretical data. The green bars show the Bragg positions of $\text{Eu}_2\text{Al}_{15}(\text{Pt}_{5/6}\text{Pd}_{1/6})_6$ using the average hexagonal structure ($\text{Sc}_{0.6}\text{Fe}_2\text{Si}_{4.9}$ type, space group $P6_3/mmc$ [41]).

3.3 SEM/EDX investigations

The prepared samples were investigated by SEM/EDX. The experimentally determined averaged element ratios were obtained from two area and five spot measurements and are, within the instrumental error, in good agreement with the weighed ones (Table 3), confirming the successful substitution of Pt by Pd , Ir and Au in the respective solid solutions. The deviations are ± 2 at.% due to the use of powdered samples sprinkled onto conductive carbon tape and their therefore not perfectly perpendicular alignment towards the beam and the semi-quantitative nature of the EDX measurements. No impurity elements heavier than sodium (detection limit of the instrument) were observed.

3.4 Magnetic measurements

$\text{Eu}_2\text{Al}_{15}\text{Pt}_6$ exhibits a temperature dependent valence phase transition at $T_{\text{trans}} = 45$ K at which the Eu^{2+} cations are oxidized to Eu^{3+} cations delivering one electron for delocalization into the conduction band. This valence phase transition has been characterized in detail by magnetic,

Table 2: Positional parameters of $\text{Eu}_2\text{Al}_{15}(\text{Pt}_{5/6}\text{Pd}_{1/6})_6$, $\text{Eu}_2\text{Al}_{15}(\text{Pt}_{5/6}\text{Ir}_{1/6})_6$, and $\text{Eu}_2\text{Al}_{15}(\text{Pt}_{5/6}\text{Au}_{1/6})_6$ obtained from Rietveld refinements.

Compound	Wyckoff position	x	y	z	Site occupation	
$\text{Eu}_2\text{Al}_{15}(\text{Pt}_{5/6}\text{Pd}_{1/6})_6$	Eu	2c	1/3	2/3	1/2	0.667
	Pt/Pd	4f	1/3	2/3	0.60653(7)	0.833/0.167
	Al1	4f	0	0	0.1290(4)	1
	Al2	4e	1/3	2/3	0.0444(4)	1
	Al3	6h	0.5278(4)	2x	1/4	0.333
$\text{Eu}_2\text{Al}_{15}(\text{Pt}_{5/6}\text{Ir}_{1/6})_6$	Eu	2c	1/3	2/3	1/2	0.667
	Pt/Ir	4f	1/3	2/3	0.60712(5)	0.833/0.167
	Al1	4f	0	0	0.1300(4)	1
	Al2	4e	1/3	2/3	0.0461(3)	1
	Al3	6h	0.5313(4)	2x	1/4	0.333
$\text{Eu}_2\text{Al}_{15}(\text{Pt}_{5/6}\text{Au}_{1/6})_6$	Eu	2c	1/3	2/3	1/2	0.667
	Pt/Au	4f	1/3	2/3	0.60658(8)	0.833/0.167
	Al1	4f	0	0	0.1270(4)	1
	Al2	4e	1/3	2/3	0.04340(5)	1
	Al3	6h	0.5427(5)	2x	1/4	0.333

Table 3: Chemical composition determined by SEM/EDX. The standard deviations are ± 2 at. %.

Compound	Eu (at.%)	Al (at.%)	Pt (at.%)	T (at.%)
Ideal composition	8.7	65.2	21.7	4.3
$\text{Eu}_2\text{Al}_{15}(\text{Pt}_{5/6}\text{Pd}_{1/6})_6$	10	63	24	3
$\text{Eu}_2\text{Al}_{15}(\text{Pt}_{5/6}\text{Ir}_{1/6})_6$	9	64	24	3
$\text{Eu}_2\text{Al}_{15}(\text{Pt}_{5/6}\text{Au}_{1/6})_6$	9	63	23	5

resistivity and heat capacity measurements [33]. The unambiguous proof has been obtained by ^{151}Eu Mössbauer spectroscopic investigations. An isovalent Ga substitution in the solid solution $\text{Eu}_2(\text{Al}_{1-x}\text{Ga}_x)_{15}\text{Pt}_6$ showed that the first order valence phase transition is shifted towards lower temperatures for $x = 0.05$. For $x = 0.1$ the valence phase transition is already suppressed and traces of the antiferromagnetic transition reported for $\text{Eu}_2\text{Ga}_{15}\text{Pt}_6$ already emerge [36].

Three different solid solutions were investigated to modify the prototypic $\text{Eu}_2\text{Al}_{15}\text{Pt}_6$. In contrast to $\text{Eu}_2(\text{Al}_{1-x}\text{Ga}_x)_{15}\text{Pt}_6$, the substitution happens there on the Pt position. By the formal isovalent substitution of Pt by Pd, a similar situation as shown for $\text{Eu}_2(\text{Al}_{0.95}\text{Ga}_{0.05})_{15}\text{Pt}_6$ is obtained. The magnetic data of $\text{Eu}_2\text{Al}_{15}(\text{Pt}_{5/6}\text{Pd}_{1/6})_6$ is shown in Figure 3. As for the Ga-substituted compound, the valence phase transition is shifted to lower temperatures ($T_{\text{trans}} = 42$ K) for $\text{Eu}_2\text{Al}_{15}(\text{Pt}_{5/6}\text{Pd}_{1/6})_6$. The shift of the first order valence phase transition is subtle but clearly visible in the first derivative of the magnetic

susceptibility χ measured at 10 kOe in ZFC (zero-field-cooled) mode (Figure 3, top and inset middle). Also, the low field measurement recorded at 100 Oe shows the characteristic “bump” (Figure 3, middle). Finally, the magnetization isotherms recorded at 50 and 100 K are linear, in line with a paramagnetic system, while the ones at 4 and 10 K are curved (Figure 3, bottom) as an effect originating from Eu^{3+} , as observed for $\text{Eu}_2\text{Al}_{15}\text{Pt}_6$ [33]. The effective magnetic moment obtained from a Curie-Weiss fit between 100 and 300 K results in $\mu_{\text{eff}} = 7.77(1) \mu_{\text{B}}$, in line with Eu^{2+} ($\mu_{\text{calc}} = 7.94 \mu_{\text{B}}$) [4].

To the contrary, the magnetic data of $\text{Eu}_2\text{Al}_{15}(\text{Pt}_{5/6}\text{Ir}_{1/6})_6$ shows a different behavior (Figure 4). In this case the temperature of the valence phase transition is shifted to higher values of $T_{\text{trans}} = 52$ K as observed from the magnetic susceptibility data χ at 10 kOe (ZFC) (Figure 4, top). Regarding the electronic situation, $\text{Eu}_2\text{Al}_{15}(\text{Pt}_{5/6}\text{Ir}_{1/6})_6$ has one electron less compared to the pure platinum compound. This electron deficiency seems to be a possible reason for the shift of the valence phase transition temperatures. Low field measurements in ZFC/FC mode (100 Oe) also confirm the shift in temperature (Figure 4, middle) and the absence of magnetic ordering at low temperatures. Only the magnetization isotherm recorded at 100 K shows a clear linear trace. The ones at 4 and 10 K are visibly curved while the 50 K isotherm only shows a slight deviation from linearity (Figure 4, bottom). The effective magnetic moment is $\mu_{\text{eff}} = 7.80(1) \mu_{\text{B}}$, again in line with Eu^{2+} ($\mu_{\text{calc}} = 7.94 \mu_{\text{B}}$) at high temperatures.

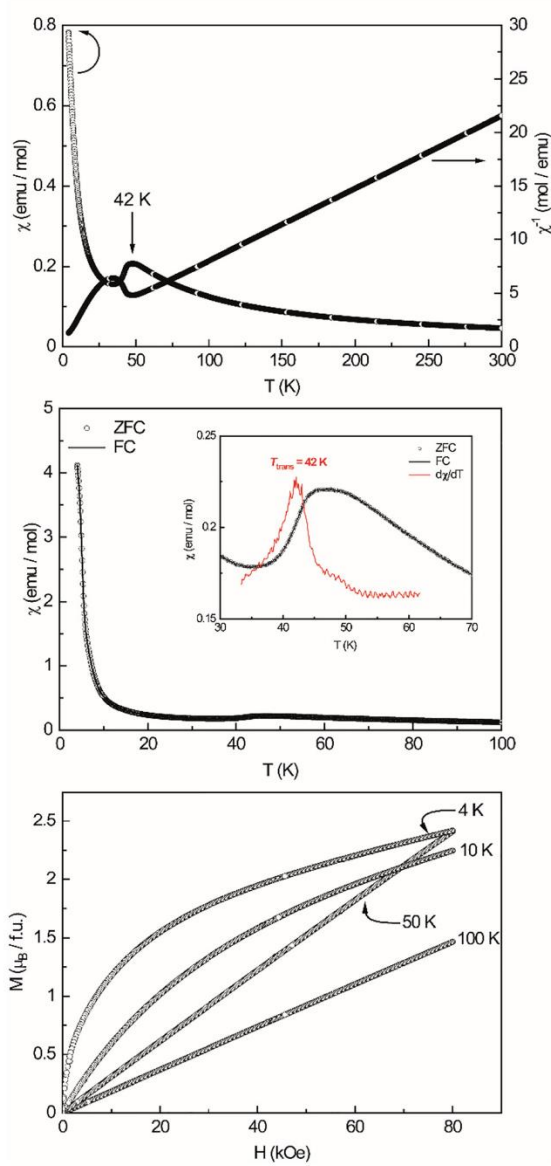


Figure 3: Magnetic properties of $\text{Eu}_2\text{Al}_{15}(\text{Pt}_{5/6}\text{Pd}_{1/6})_6$: (top) magnetic and inverse magnetic susceptibility measured at 10 kOe in ZFC (zero-field-cooled) mode, (middle) magnetic susceptibility measured in ZFC/FC (zero-field-cooled/field-cooled) mode at 100 Oe, (inset) zoom and first derivative, (bottom) magnetization isotherms recorded at $T = 4, 10, 50$ and 100 K.

The magnetic data of $\text{Eu}_2\text{Al}_{15}(\text{Pt}_{5/6}\text{Au}_{1/6})_6$ is shown in Figure 5. No obvious valence phase transition can be detected both in the magnetic susceptibility data χ at 10 kOe (ZFC) (Figure 5, top) and in the low field measurements in ZFC/FC mode (100 Oe) (Figure 5, middle). Only in the

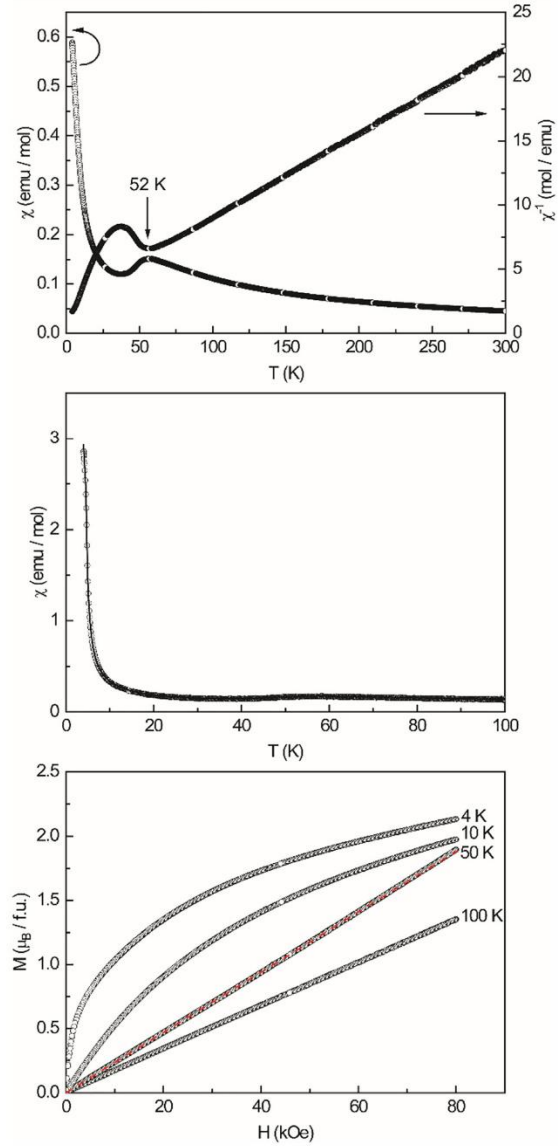


Figure 4: Magnetic properties of $\text{Eu}_2\text{Al}_{15}(\text{Pt}_{5/6}\text{Ir}_{1/6})_6$: (top) magnetic and inverse magnetic susceptibility measured at 10 kOe in ZFC (zero-field-cooled) mode, (middle) magnetic susceptibility measured in ZFC/FC (zero-field-cooled/field-cooled) mode at 100 Oe, (bottom) magnetization isotherms recorded at $T = 4, 10, 50$ and 100 K.

magnetization isotherm a curvature is visible in the 4 K isotherm with the values at 80 kOe being smaller compared to the 10 K isotherm (Figure 5, bottom) giving a hint for a valence phase transition at significantly lower temperatures. In addition, the high- and low-field measurements show a small bent around 10 K and the 4 K magnetization isotherm exhibits a steep increase at low fields. Both facts

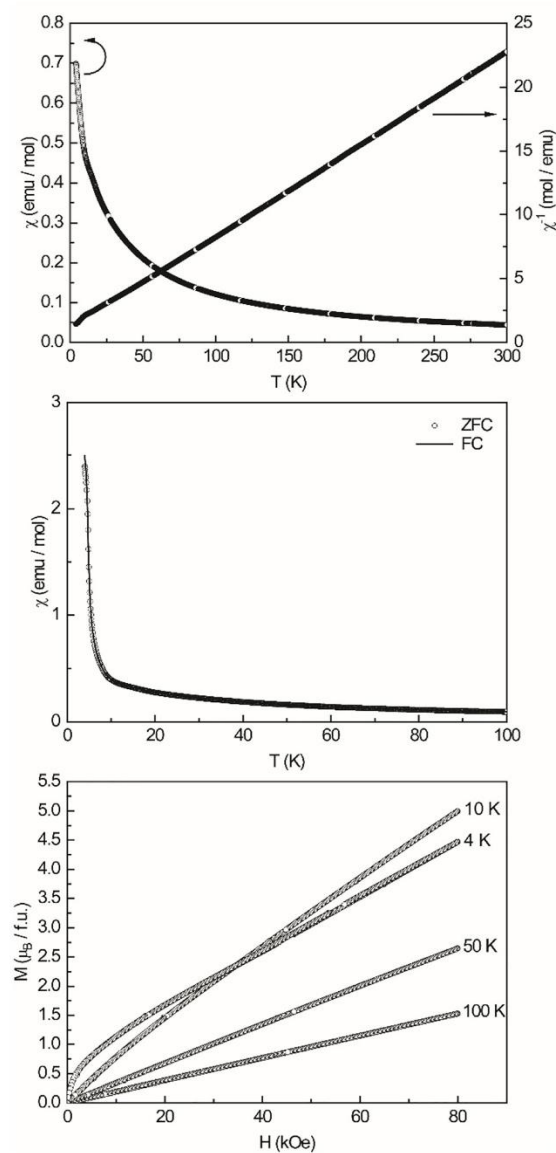


Figure 5: Magnetic properties of $\text{Eu}_2\text{Al}_{15}(\text{Pt}_{5/6}\text{Au}_{1/6})_6$: (top) magnetic and inverse magnetic susceptibility measured at 10 kOe in ZFC (zero-field-cooled) mode, (middle) magnetic susceptibility measured in ZFC/FC (zero-field-cooled/field-cooled) mode at 100 Oe, (bottom) magnetization isotherms recorded at $T = 4, 10, 50$ and 100 K.

point to a ferromagnetic transition which is probably originating from an impurity due to its weakness. $\text{Eu}_2\text{Al}_{15}(\text{Pt}_{5/6}\text{Au}_{1/6})_6$ has one electron more than $\text{Eu}_2\text{Al}_{15}\text{Pt}_6$ and two electrons more than $\text{Eu}_2\text{Al}_{15}(\text{Pt}_{5/6}\text{Ir}_{1/6})_6$. This additional electron seems to suppress/hamper the valence phase transition as it possibly fills states that are needed for the delocalization of the electron when Eu^{2+} turns into

Eu^{3+} . Again, the effective magnetic moment ($\mu_{\text{eff}} = 7.43(1) \mu_{\text{B}}$) points towards Eu^{2+} ($\mu_{\text{calc}} = 7.94 \mu_{\text{B}}$) at high temperatures.

4 Conclusions

The solid solutions $\text{Eu}_2\text{Al}_{15}(\text{Pt}_{1-x}\text{T}_x)_6$ with $T = \text{Pd, Ir and Au}$ have been synthesized from the elements via arc-melting. For $x = 1/6$, phase-pure samples have been obtained as characterized by powder X-ray diffraction as well as scanning electron microscopy coupled with energy-dispersive X-ray spectroscopy. Magnetic susceptibility measurements clearly indicate that for $T = \text{Pd and Ir}$ the expected valence phase transition can be observed, however, with respect to $\text{Eu}_2\text{Al}_{15}\text{Pt}_6$ ($T_{\text{trans}} = 45$ K) shifted to a lower temperature in the case of $\text{Eu}_2\text{Al}_{15}(\text{Pt}_{5/6}\text{Pd}_{1/6})_6$ ($T_{\text{trans}} = 42$ K). $\text{Eu}_2\text{Al}_{15}(\text{Pt}_{5/6}\text{Ir}_{1/6})_6$ in contrast shows a valence phase transition temperature of $T_{\text{trans}} = 52$ K. $\text{Eu}_2\text{Al}_{15}(\text{Pt}_{5/6}\text{Au}_{1/6})_6$ finally exhibits no clearly visible transition temperature. The observed changes in the transition temperatures T_{trans} can be explained by the changes in the (electronic) structure as the valence electron concentration changes for $T = \text{Ir and Au}$ with respect to the prototype $\text{Eu}_2\text{Al}_{15}\text{Pt}_6$. For $T = \text{Pd}$ only structural distortions take place, however these observations are in line with literature data as $\text{Eu}_2(\text{Al}_{1-x}\text{Ga}_x)_{15}\text{Pt}_6$ shows a similar behavior for small values of x .

Acknowledgments: Instrumentation and technical assistance for this work were provided by the Service Center X-ray Diffraction, with financial support from Saarland University and German Science Foundation (project number INST 256/349-1 and INST 256/506-1). The magnetometer was funded by German Science Foundation through INST 211/1034-1. Funding was provided by the Deutsche Forschungsgemeinschaft DFG (JA 1891-10-1).

Research ethics: Not applicable.

Author contributions: The authors have accepted responsibility for the entire content of this manuscript and approved its submission.

Competing interests: The authors state no conflict of interest.

Research funding: Funding is provided by the Deutsche Forschungsgemeinschaft DFG (JA 1891-10-1, INST 256/349-1, INST 256/506-1 and INST 211/1034-1).

Data availability: Not applicable.

References

1. Szytuła A., Leciejewicz J., Eds. *Handbook of Crystal Structures and Magnetic Properties of Rare Earth Intermetallics*; CRC Press: Boca Raton, 1994.

2. Emsley J. *The Elements*; Clarendon Press, Oxford University Press: Oxford, New York, 1998.
3. Cotton S. *Lanthanides & Actinides*; Macmillan Education: Basingstoke, 1991.
4. Lueken H. *Magnetochemie*; B. G. Teubner: Stuttgart, Leipzig, 1999.
5. Heying B., Kösters J., Heletta L., Klenner S., Pöttgen R. *Monatsh. Chem.* 2019, *150*, 1163–1173.
6. Stegemann F., Block T., Klenner S., Zhang Y., Fokwa B. P. T., Timmer A., Mönig H., Doerenkamp C., Eckert H., Janka O. *Chem. Eur. J.* 2019, *25*, 10735–10747.
7. Klenner S., Heletta L., Pöttgen R. *Dalton Trans.* 2019, *48*, 3648–3657.
8. Zachariasen W. H. *Nor. Geol. Tidsskr.* 1927, *9*, 310–316.
9. Zacharias W. H. *Skr. Nor. Vidensk.-Akad.* 1928, *4*, 1–166.
10. Zalkin A., Templeton D. H. *J. Am. Chem. Soc.* 1953, *75*, 2453–2458.
11. Templeton D. H., Dauben C. H. *J. Am. Chem. Soc.* 1954, *76*, 5237–5239.
12. Lyle S. J., Westall W. A. *J. Less-Common Met.* 1985, *106*, 109–116.
13. De Vries J. W. C., Thiel R. C., Buschow K. H. J. *Physica B+C* 1984, *124*, 291–298.
14. Seiro S., Kummer K., Vyalikh D., Caroca-Canales N., Geibel C. *Phys. Status Solidi B* 2013, *250*, 621–625.
15. Felner I., Nowik I. *J. Phys. Chem. Solids* 1984, *45*, 419–426.
16. Mayer I., Felner I. *J. Phys. Chem. Solids* 1977, *38*, 1031–1034.
17. Maślankiewicz P., Szade J. *J. Alloys Compd.* 2006, *423*, 69–73.
18. Mörsen E., Mosel B. D., Müller-Warmuth W., Reehuis M., Jeitschko W. *J. Phys. C: Solid State Phys.* 1988, *21*, 3133–3140.
19. Harmening T., Pöttgen R. *Z. Naturforsch.* 2009, *65b*, 90–94.
20. Seidel S., Harmening T., Kösters J., Koldemir A., Pröbsting W., Engelbert S., Pöttgen R. *Z. Naturforsch.* 2023, *78b*, 293–300.
21. Stegemann F., Block T., Klenner S., Janka O. *Chem. Eur. J.* 2019, *25*, 3505–3509.
22. Engel S., Gießelmann E. C. J., Pöttgen R., Janka O. *Rev. Inorg. Chem.* 2023, *43*, 571–582.
23. Koskenmaki D. C., Gschneidner Jr. K. A. Cerium. In *Handbook on the Physics and Chemistry of Rare Earths*, Vol. 1; Gschneidner Jr. K. A., Eyring L., Eds. North Holland: Amsterdam, 1978, chapter 4; pp. 337–377.
24. Adroja D. T., Rainford B. D., de Teresa J. M., del Moral A., Ibarra M. R., Knight K. S. *Phys. Rev. B* 1995, *52*, 12790–12797.
25. Felner I., Nowik I. *Phys. Rev. B* 1986, *33*, 617–619.
26. Felner I., Nowik I., Vaknin D., Potzel U., Moser J., Kalvius G. M., Wortmann G., Schmiester G., Hilscher G., Gratz E., Schmitzer C., Pillmayr N., Prasad K. G., de Waard H., Pinto H. *Phys. Rev. B* 1987, *35*, 6956–6963.
27. Müller H., Bauer E., Gratz E., Yoshimura K., Nitta T., Mekata M. *J. Magn. Magn. Mater.* 1988, *76*, 159–160.
28. Stegemann F., Stahl J., Bartsch M., Zacharias H., Johrendt D., Janka O. *Chem. Sci.* 2019, *10*, 11086–11094.
29. Menushenkov A. P., Yaroslavtsev A. A., Geondzhian A. Y., Chernikov R. V., Nataf L., Tan X., Shatruk M. *J. Supercond. Novel Magn.* 2017, *30*, 75–78.
30. Tan X., Fabbri G., Haskel D., Yaroslavtsev A. A., Cao H., Thompson C. M., Kovnir K., Menushenkov A. P., Chernikov R. V., Garlea V. O., Shatruk M. *J. Am. Chem. Soc.* 2016, *138*, 2724–2731.
31. Koizumi T., Honda F., Sato Y. J., Li D., Aoki D., Haga Y., Gouchi J., Nagasaki S., Uwatoko Y., Kaneko Y., Ōnuki Y. *J. Phys. Soc. Jpn.* 2022, *91*, 043704 (5 pages).
32. Sampathkumaran E. V., Gupta L. C., Vijayaraghavan R., Gopalakrishnan K. V., Pillay R. G., Devare H. G. *J. Phys. C: Solid State Phys.* 1981, *14*, L237–L241.
33. Radziejewski M., Stegemann F., Block T., Stahl J., Johrendt D., Janka O. *J. Am. Chem. Soc.* 2018, *140*, 8950–8957.
34. Fournes L., Chevalier B., Lloret B., Etourneau J. *Z. Phys. B: Condens. Matter* 1989, *75*, 501–505.
35. Segre C. U., Croft M., Hodges J. A., Murgai V., Gupta L. C., Parks R. D. *Phys. Rev. Lett.* 1982, *49*, 1947–1950.
36. Oyama K., Mitsuda A., Wada H., Narumi Y., Hagiwara M., Takahashi R., Wadati H., Setoyama H., Kindo K. *J. Phys. Soc. Jpn.* 2020, *89*, 114713 (7 pages).
37. Pöttgen R., Gulden T., Simon A. *GIT Labor-Fachz.* 1999, *43*, 133–136.
38. TOPAS (version 5). *General Profile and Structure Analysis Software for Powder Diffraction Data*; Bruker AXS Inc.: Karlsruhe (Germany), 2014.
39. Radziejewski M., Stegemann F., Janka O. *Eur. J. Inorg. Chem.* 2020, *2020*, 1199–1210.
40. Radziejewski M., Stegemann F., Hoffmann R.-D., Janka O. *Z. Kristallogr.* 2017, *232*, 675–687.
41. Kotur B. Y., Bruvo M. *Sov. Phys. Crystallogr.* 1991, *36*, 787–789.
42. Lattner S. E., Kanatzidis M. G. *Inorg. Chem.* 2002, *41*, 5479–5486.
43. Niermann J., Jeitschko W. *Z. Anorg. Allg. Chem.* 2004, *630*, 361–368.
44. Murashova E. V., Tursina A. I., Bukhan'ko N. G., Gribanov A. V., Chernyshev I. V., Seropegin Y. D. *J. Alloys Compd.* 2005, *398*, 100–105.
45. Lutsyshyn Y., Tokaychuk Y., Gladyshevskii R. E. *Chem. Met. Alloys* 2012, *5*, 98–102.
46. Lutsyshyn Y., Tokaychuk Y., Gladyshevskii R. *Chem. Met. Alloys* 2009, *2*, 75–82.
47. Lutsyshyn Y., Tokaychuk Y., Davydov V., Gladyshevskii R. *Chem. Met. Alloys* 2008, *1*, 303–316.
48. Kwei G. H., Lawson A. C., Larson A. C., Morosin B., Larson E. M., Canfield P. C. *Acta Crystallogr.* 1996, *B52*, 580–585.

V. New Intermetallic Aluminum Compounds with a Trivalent Cationic Species

1. Introduction

Besides the alkaline earth and europium containing MA_5Pt_3 and $M_2Al_{16}Pt_9$ compounds also the respective cerium compounds exist. Due to the difference in electron count and the ionic radii of the cerium compared to the europium and strontium, it led to the investigation on which rare earth elements also form these two structures alongside their magnetic properties.

The investigations led to the extension of the MA_5Pt_3 series with $M = Y, La-Nd$ and $Sm, Gd-Er$, whereas the $M_2Al_{16}Pt_9$ series only exists for $M = La-Nd$ and Sm, Gd . The MA_5Pt_3 representatives structures crystallize isotypic to the Sr, Ce and Eu phases in the YNi_5Si_3 type structure with space group $Pnma$. The compounds with Y, Pr and Gd could be obtained X-ray pure, whereas the samples with La formed large amounts of $La_2Al_{16}Pt_9$, the remaining samples exhibit small quantities of Al_3Pt_2 present in the powder X-ray diffraction patterns. Semiquantitative analysis of $NdAl_5Pt_3, GdAl_5Pt_3$ and $ErAl_5Pt_3$ were performed via energy dispersive X-ray spectroscopy showing good agreement of the composition with the stoichiometric values. On the phases containing $Y, Ce-Nd$ and $Gd-Ho$ magnetic measurements were conducted, YAl_5Pt_3 shows the expected Pauli-paramagnetic behavior, whereas the other compounds with trivalent RE species exhibit Curie paramagnetism. An antiferromagnetic transition was observable for the $Nd, Gd-Ho$ containing compounds. The structure exhibits five Al sites, which could be confirmed with ^{27}Al NMR measurements on YAl_5Pt_3 . Also, XPS measurements of the yttrium compound were recorded, but due to the surface oxidation, no useful information could be gained. Lastly a bonding analysis via quantum chemical calculations was performed showing, as in the alkaline earth phases, the charge transfer of the Y atoms to the Pt atoms, in which also the Al atoms exhibit a positive charge.

As for the $M_2Al_{16}Pt_9$ series, all samples formed the corresponding MA_5Pt_3 as well as the Al_3Pt_2 as side products. Due to the side phases, no magnetic properties could be measured. Single crystal studies of the La and Eu containing compounds were conducted, showing isotypism with $Ce_2Al_{16}Pt_9$. Additionally, the lanthanum compounds experienced mixed occupancy on the Al_5 position by 3% with Pt atoms, leading to a refined sum formula of $La_2Al_{15.95(1)}Pt_{9.05(1)}$. Heat treatment experiments on the La sample showed that $La_2Al_{16}Pt_9$ peritectically decomposes into $LaAl_5Pt_3$ and Al_3Pt_2

2. Trivalent Compounds in the MA_5Pt_3 Series

Collaborations to disclose: In this chapter the trivalent compounds from the paper “Synthesis, magnetic and NMR spectroscopic properties of the MA_5Pt_3 series ($M = Ca, Y, La-Nd, Sm-Er$)” are summarized (*Dalton Trans.* **2024**, 53, 12176-12188). E. C. J. Gießelmann measured and interpreted the ^{27}Al NMR spectra, L. Schumacher provided the magnetic property measurements, Prof. Dr. Y. Zhang performed the bonding analysis via the quantum chemical calculations and PD Dr. F. Müller performed the XPS analysis. PD Dr. O. Janka along with the aforementioned people worked on the manuscript.

After the recent report of the existence of $EuAl_5Pt_3$ ⁹¹ and the discovery of the Sr containing compounds¹⁷⁵ in the scope of this thesis alongside the literature known cerium compound $CeAl_5Pt_3$,¹⁹⁶ an investigation was performed, which *RE* compounds in the MA_5Pt_3 series exist. **Figure 3.43** shows the melting bead of $LaAl_5Pt_3$ with prominent needle shaped crystals. The series could be extended from Ce and Eu to Y, La-Nd, Sm and Gd-Er in which the Y, Pr, Gd can be obtained X-ray pure. Lattice parameters of all structures are summarized in **Table 3.10**. In the cases of the La and Sm compounds, both form the corresponding $M_2Al_{16}Pt_9$ phase during the reaction, whereas the remaining samples formed trace amounts of Al_3Pt_2 (Al_3Ni_2 type, $P\bar{3}m1$).¹⁹⁹ When looking at the lattice parameters and cell volumes, the lanthanide contraction becomes visible, which causes a decrease in cell volume due to the smaller ionic radii of the *RE* element with La possessing the largest radius decreasing continuously to Er, as long as all the rare earth elements are trivalent. In the case of the europium compound (discussed in **Chapter 3.a.I**), the unit cell volume is significantly enlarged and similar to the strontium compound, suggesting that the europium is divalent. To affirm the structure being isotypic to $CeAl_5Pt_3$, single crystal studies on $ErAl_5Pt_3$ were performed, resulting in an orthorhombic structure with space group *Pnma* and confirmed the isotypism with $CeAl_5Pt_3$ and isopointalism to the YNi_5Si_3 type structure. $ErAl_5Pt_3$ exhibits one Er, three Pt and five Al positions with interatomic ranging from $d(Er-Al) = 318-349$ pm, $d(Er-Pt) = 316-317$ pm, $d(Al-Al) = 272-343$ pm, $d(Al-Pt) = 247-270$ pm and $d(Pt-Pt) = 308$ pm. The found distances are in line with the ones found in the ternary compounds $Er_{0.67}Al_5Pt_2$ ($Sc_{0.6}Fe_2Si_{4.9}$ type, $P6_3/mmc$): $d(Er-Al) = 154-334$ pm, $d(Er-Pt) = 339$ pm, $d(Al-Al) = 267-289$ pm, $d(Al-Pt) = 249-267$ pm,¹⁸³ $ErAlPt$ ($TiNiSi$ type, *Pnma*): $d(Er-Al) = 286-303$ pm, $d(Er-Pt) = 304-330$ pm, $d(Al-Pt) = 257-268$ pm, $d(Pt-Pt) = 306$ pm,²³⁴ $EuAl_2Pt$ ($MgAl_2Cu$ type, *Cmcm*): $d(Er-Al) = 307-332$ pm, $d(Er-Pt) =$

297-298 pm, $d(\text{Al-Al}) = 267\text{-}311$ pm, $d(\text{Al-Pt}) = 251\text{-}262$ pm,²³⁵ ErAl_3Pt_2 (YAl_3Pt_2 type, $Cmmm$): $d(\text{Er-Al}) = 328\text{-}347$ pm, $d(\text{Er-Pt}) = 300\text{-}316$ pm, $d(\text{Al-Al}) = 274\text{-}279$ pm, $d(\text{Al-Pt}) = 253\text{-}343$ pm, $d(\text{Pt-Pt}) = 300$ pm,²³⁶ ErAl_2Pt_5 (ZrAl_5Ni_2 type, $I4/mmm$): $d(\text{Er-Pt}) = 287\text{-}301$ pm, $d(\text{Al-Al}) = 290$ pm, $d(\text{Al-Pt}) = 243\text{-}264$ pm, $d(\text{Pt-Pt}) = 243\text{-}302$ pm,²³⁷ $\text{Er}_4\text{Al}_{24}\text{Pt}_9$ (own type, $P\bar{1}$): $d(\text{Er-Al}) = 304\text{-}319$ pm, $d(\text{Er-Pt}) = 326\text{-}350$ pm, $d(\text{Al-Al}) = 264\text{-}335$ pm, $d(\text{Al-Pt}) = 250\text{-}275$ pm²³⁸ and Er_4AlPt (Gd_4InRh type, $F\bar{4}3m$): $d(\text{Er-Al}) = 319\text{-}342$ pm, $d(\text{Er-Pt}) = 277\text{-}341$ pm, $d(\text{Al-Al}) = 309$ pm²³⁹ as well as for the binary compounds ErAl_2 (MgCu_2 type, $Fd\bar{3}m$): $d(\text{Er-Al}) = 323$ pm, $d(\text{Al-Al}) = 276$ pm,²⁴⁰ ErAl_3 (Cu_3Au type, $Pm\bar{3}m$): $d(\text{Er-Al}) = 298$ pm, $d(\text{Al-Al}) = 298$ pm,²⁴¹ ErAl (DyAl type, $Pbcm$): $d(\text{Er-Al}) = 302\text{-}350$ pm, $d(\text{Al-Al}) = 265\text{-}279$ pm,²⁴² Er_2Al (Co_2Si type, $Pnma$): $d(\text{Er-Al}) = 304\text{-}347$ pm,²⁴³ Er_3Al_2 (Zr_3Al_2 type, $P4_2/mnm$): $d(\text{Er-Al}) = 293\text{-}323$ pm, $d(\text{Al-Al}) = 287\text{-}314$ pm,²⁴⁴ ErPt_2 (MgCu_2 type, $Fd\bar{3}m$): $d(\text{Er-Pt}) = 314$ pm, $d(\text{Pt-Pt}) = 268$ pm,²⁴⁵ ErPt_3 (Cu_3Au type, $Pm\bar{3}m$): $d(\text{Er-Pt}) = 286$ pm, $d(\text{Pt-Pt}) = 286$ pm,²⁴⁵ ErAl_5 (CaCu_5 type, $P6/mmm$): $d(\text{Er-Pt}) = 304\text{-}344$ pm, $d(\text{Pt-Pt}) = 263\text{-}304$ pm²⁴⁶ and ErPt (FeB type, $Pnma$): $d(\text{Er-Pt}) = 278\text{-}305$ pm, $d(\text{Pt-Pt}) = 258$ pm.²⁴⁷ Due to the similarity of the Al–Pt distances with the alkaline earth containing compounds of the series, so the same structural bonding behavior and structural motifs can be assumed. To validate the structure of the series, a ²⁷Al MAS NMR spectrum of the yttrium containing compound was recorded, showing exactly five different signals corresponding to the number of independent Al positions present in the structure. To investigate the bonding, quantum chemical calculations were performed. The resulting DOS of YAl_5Pt_3 is shown in **Figure 3.45** and indicates a metallic character of the compounds, due to the high number of states at the fermi level, which is in line with the metallic silvery appearance of the sample. The ICOHP values alongside the Bader charges show that the majority of COHP values originate from the Al–Pt interaction followed by the homoatomic Al–Al interactions which supports the assumption of the polyanionic network inside the structure.

Energy dispersive X-ray spectroscopy measurements were performed on NdAl_5Pt_3 , GdAl_5Pt_3 and ErAl_5Pt_3 , the overall results show a good agreement with the ideal composition (**Table 3.11**).

The powder X-ray diffraction pattern of NdAl_5Pt_3 (YNi_5Si_3 type, $Pnma$, $a = 2059.92(1)$, $b = 412.054(3)$, $c = 729.261(5)$ pm) showed only a small amount of Al_3Pt_2 (Al_3Ni_2 type, $P\bar{3}m1$, $a = 421.56(3)$, $c = 515.12(7)$ pm)²⁴⁸ as side phase, the binary compound does not exhibit a magnetic moment, so that the magnetic moment of YAl_5Pt_3 could be investigated by Lars Schumacher at the University of Münster. The field-cooled and zero-field-cooled measurements show an antiferromagnetic ordering at $T_N = 5.1$ K for the neodymium compound, the yttrium compound

is Pauli-paramagnetic. The effective magnetic moment of Nd is $3.82 \mu_B$, which is in line with the magnetic moment of free Nd^{3+} ion with $3.62 \mu_B$ (**Fig. 3.44**).

Table 3.10: Lattice parameters and unit cell volumes of $REAl_5Pt_3$ ($RE = Y, La-Nd, Sm, Gd-Er$) with the YNi_5Si_3 type structure, $Pnma$, $Z = 4$.

Compound	a (pm)	b (pm)	c (pm)	V (nm ³)
YAl ₅ Pt ₃ ^P	2052.8(1)	406.7(1)	728.7(1)	0.6084
LaAl ₅ Pt ₃ ^P	2068.7(1)	415.5(1)	732.2(1)	0.6293
CeAl ₅ Pt ₃ ^P	2063.9(1)	414.0(1)	730.1(1)	0.6239
CeAl ₅ Pt ₃ ¹⁹⁶	2065.1(4)	413.81(8)	728.42(15)	0.6225
PrAl ₅ Pt ₃ ^P	2061.4(2)	413.0(1)	729.6(1)	0.6212
NdAl ₅ Pt ₃ ^P	2059.9(1)	412.1(1)	729.3(1)	0.6191
SmAl ₅ Pt ₃ ^P	2057.0(1)	410.2(1)	728.5(1)	0.6148
GdAl ₅ Pt ₃ ^P	2055.3(2)	408.7(1)	728.3(2)	0.6117
TbAl ₅ Pt ₃ ^P	2052.9(1)	407.7(1)	728.2(1)	0.6095
DyAl ₅ Pt ₃ ^P	2051.5(1)	406.7(1)	728.5(1)	0.6079
HoAl ₅ Pt ₃ ^P	2050.4(1)	405.9(1)	729.1(1)	0.6067
ErAl ₅ Pt ₃ ^P	2048.4(1)	405.1(1)	729.3(1)	0.6052
ErAl ₅ Pt ₃ ^{SC}	2045.82(6)	404.40(1)	728.45(2)	0.6027

^{SC} single crystal, ^P powder

Table 3. 11: EDX data of trivalent members of the $REAl_5Pt_3$ series ($RE = Nd, Gd, Er$) with standard deviations of ± 2 at.-%.

Compound	Ideal	P1	P2	P3	mean
NdAl ₅ Pt ₃	Nd: 11.1	10	11	9	10
	Al: 55.6	56	54	57	56
	Pt: 33.3	33	35	34	34
GdAl ₅ Pt ₃	Gd: 11.1	10	12	10	11
	Al: 55.6	59	51	53	54
	Pt: 33.3	31	37	37	35
ErAl ₅ Pt ₃	Er: 11.1	10	10	11	11
	Al: 55.6	59	57	56	57
	Pt: 33.3	31	33	33	32

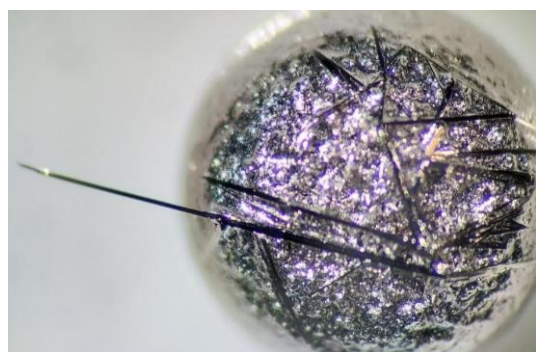


Figure 3.43: Melting bead of $LaAl_5Pt_3$ with prominent single crystal growth.

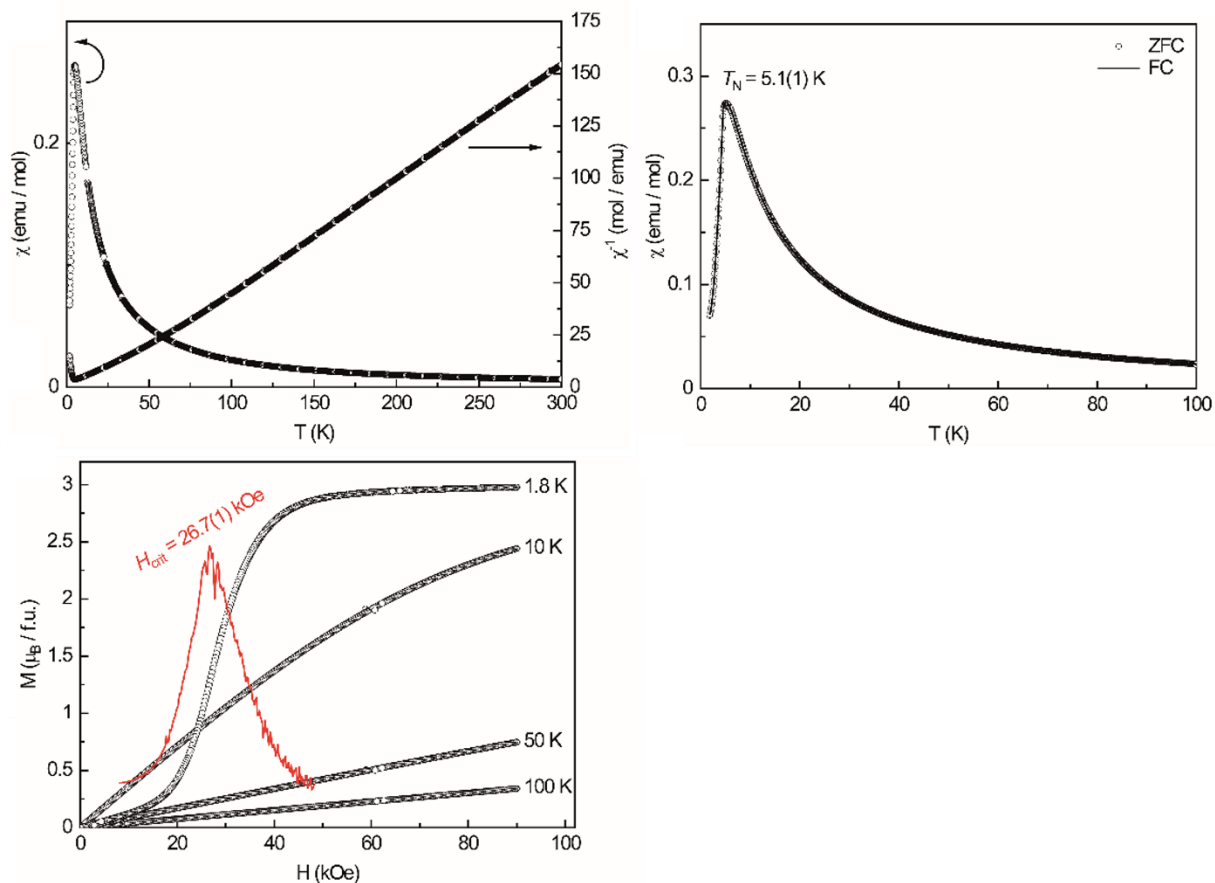


Figure 3.44: Magnetic data of NdAl_5Pt_3 . Temperature dependence of the magnetic and inverse magnetic susceptibility (χ and χ^{-1} data) measured with an applied external field of 10 kOe (top left), zero-field-cooled/field-cooled (ZFC/FC) measurements with an applied field of 100 Oe (top right), magnetization isotherm measurements at 1.8, 10, 50 and 100 K, inflection point determined by the first derivative of dM/dH shown in red.

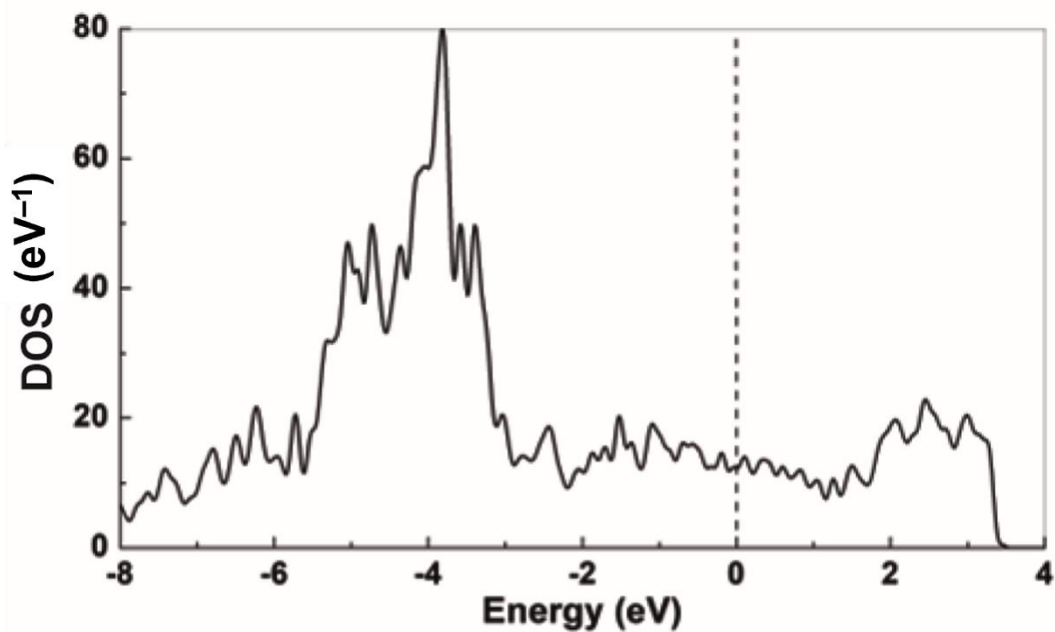


Figure 3.45: Density of states (DOS) of YAl_5Pt_3 , data from non-polarized DFT calculations, Fermi level indicated with dotted line.



Cite this: *Dalton Trans.*, 2024, 53, 12176

Synthesis, magnetic and NMR spectroscopic properties of the MAl_5Pt_3 series ($\text{M} = \text{Ca}, \text{Y}, \text{La-Nd}, \text{Sm-Er}$)[†]

Stefan Engel,^a Elias C. J. Giebelmann,^a Lars Schumacher,^b Yuemei Zhang,^c Frank Müller^d and Oliver Janka^{*a}

Following recent investigation in the ternary system Sr–Al–Pt led to the discovery of SrAl_5Pt_3 which crystallizes in the orthorhombic YNi_5Si_3 type (*Pnma*) structure. Interestingly, only two more aluminum representatives, CeAl_5Pt_3 and EuAl_5Pt_3 , have been reported to adopt this structure type. Therefore, we decided to investigate the existence range of compounds adopting the YNi_5Si_3 type structure. Besides the already known Sr, Ce and Eu members, the series could be extended to Ca, Y and La–Nd as well as Sm–Er. All compounds were synthesized from the elements and characterized by powder X-ray diffraction. While for CaAl_5Pt_3 and LaAl_5Pt_3 also the respective $\text{M}_2\text{Al}_6\text{Pt}_9$ members were observed, the other compounds could be obtained either as X-ray pure materials or with small amounts of Al_3Pt_2 as a side phase. The structure of ErAl_5Pt_3 could be refined from single crystal data, verifying that also the small rare-earth elements adopt the YNi_5Si_3 type structure. Selected members of the series were furthermore characterized by magnetization and susceptibility measurements. Since YAl_5Pt_3 could be obtained as a phase pure material and exhibits no paramagnetic behaviour it was investigated by ^{27}Al MAS NMR investigations. Also, XPS measurements were conducted on this compound to gain an insight into the charge distribution. Finally, quantum-chemical calculations supported the NMR measurements and gave an insight into the chemical bonding and the charge distribution.

Received 2nd May 2024,
Accepted 17th June 2024
DOI: 10.1039/d4dt01296h
rsc.li/dalton

1 Introduction

Cerium, europium and ytterbium intermetallics often exhibit interesting physical properties due to their two possible oxidation states. For cerium Ce^{3+} ($[\text{Xe}] 4f^1$) and Ce^{4+} ($[\text{Xe}] 4f^0$) are known while europium exhibits Eu^{3+} ($[\text{Xe}] 4f^6$) and Eu^{2+} ($[\text{Xe}] 4f^7$) and ytterbium Yb^{3+} ($[\text{Xe}] 4f^{13}$) and Yb^{2+} ($[\text{Xe}] 4f^{14}$). Of these, Ce^{4+} and Yb^{2+} are diamagnetic due to their empty and full 4f shell, respectively.^{1,2} Eu^{2+} has a half-filled 4f shell ($S = 7/2$, isoelectronic to Gd^{3+}) and therefore exhibits a high magnetic moment of $\mu_{\text{theo}} = 7.94\mu_{\text{B}}$. For Eu^{3+} ($S = 3$, $L = 3$) in total seven states of the multiplet 7F_7 exist with the ground state being 7F_0 . The ground state is diamagnetic due to spin–orbit coupling.

However, the lowest state is only solely considered when the separation of the multiplet components is sufficiently large compared to $k_{\text{B}}T$. Therefore, the contributions of the different components of the multiplet have to be taken into account for higher temperatures. The paramagnetic susceptibility can be expressed with the help of the Van Vleck theory.³ The availability of a second oxidation state, however, can result in numerous interesting physical phenomena. Static mixed valence states can be found (Eu_3O_4 ,^{4–6} Eu_3S_4 ,⁷ or EuPPt ⁸) as well as intermetallic valence fluctuation materials (e.g. CeAl_3 ,^{9,10} $\text{Yb}_4\text{Ga}_{24}\text{Pt}_9$,¹¹ $\text{CeMo}_2\text{Si}_2\text{C}$,¹² $\text{CeAlRu}_{1-x}\text{Ni}_x$,¹³ $\text{Ce}_2\text{Sn}_5\text{Rh}_3$,¹⁴ CeCu_2Si_2 ,¹⁵ EuCu_2Si_2 ,^{15,16} YbCu_2Si_2 ¹⁵). A rather rare feature is a temperature or pressure dependent valence phase transition. Well known transitions of this type are e.g. the ones from metallic $\alpha\text{-Ce}$ to $\gamma\text{-Ce}$,¹⁷ where electron localization takes place, accompanied by a drastic volume effect. In EuPPt ,¹⁸ EuCo_2As_2 and YbAl_3 pressure dependent shifts of the Eu/Yb valence are observed.^{19,20} Finally, $\text{CeNi}_{1-x}\text{Co}_x\text{Sn}$,²¹ and $\text{Yb}_{1-x}\text{In}_x\text{Cu}_2$ ^{22–24} exhibit at least partial temperature dependent valence phase transitions. EuSi_2Pd_2 ,^{25,26} $\text{EuSi}_2(\text{Ir}_{1-x}\text{Pd}_x)_2$,²⁷ $\text{EuSi}_2(\text{Pd}_{1-x}\text{Au}_x)_2$,²⁸ $\text{Eu}_2\text{Al}_{15}\text{Pt}_6$ ²⁹ and YbAl_3Pd_2 ³⁰ all show valence phase transitions in different expressions. Some review articles summarize at least some aspects of intermetallic cerium,^{31–36} europium³⁷ and ytterbium³⁸ intermetallics.

^aInorganic Solid State Chemistry, Saarland University, Campus C4 1, 66123 Saarbrücken, Germany. E-mail: oliver.janka@uni-saarland.de

^bInstitut für Anorganische und Analytische Chemie, Universität Münster, Corrensstrasse 28/30, 48149 Münster, Germany

^cDepartment of Chemistry and Physics, Warren Wilson College, Swannanoa, NC, 28778, USA

^dExperimental Physics and Center for Biophysics, Saarland University, Campus E2 9, 66123 Saarbrücken, Germany

[†]Electronic supplementary information (ESI) available. CCDC 2349082. For ESI and crystallographic data in CIF or other electronic format see DOI: <https://doi.org/10.1039/d4dt01296h>



Recently, we reported on a new compound in the ternary system Sr–Al–Pt, SrAl₅Pt₃,³⁹ which adopts the orthorhombic YNi₅Si₃ type structure (*Pnma*).⁴⁰ It is furthermore isostructural to CeAl₅Pt₃ and EuAl₅Pt₃. The europium compound shows antiferromagnetic ordering and an interesting change in electronic states under pressure.⁴¹ Since three compounds are known to crystallize in the same structure type, the question arose if other rare-earth or alkaline-earth members can be synthesized. Here we report that the series could be extended to Ca, Y and La–Nd as well as Sm–Er. All compounds were synthesized from the elements and characterized by powder X-ray diffraction. The structure of ErAl₅Pt₃ was refined from single crystal data, YAl₅Pt₃ was investigated by ²⁷Al MAS NMR measurements. Furthermore, XPS measurements were conducted on YAl₅Pt₃ and Al₃Pt₂ and quantum-chemical calculations supported the NMR measurements and gave an insight into the chemical bonding and the charge distribution.

2 Experimental

2.1 Synthesis

All members of the MAl₅Pt₃ series were prepared from the elements using calcium pieces (Onyxmet), rare earth ingots (Onyxmet), platinum (Agosi AG) and aluminum pieces (Onyxmet), all with stated purities above 99.5%. Samples were prepared on a 100 to 150 mg scale. The early rare earth elements were stored under an argon atmosphere in a dry box (MBraun, Garching, Germany). In all cases, the starting materials were arc-melted⁴² in a custom build arc-melting apparatus in a water-cooled copper hearth under 800 mbar argon pressure using the ideal ratios of M : Al : Pt (1 : 5 : 3). To achieve homogeneous samples, the arc-melting was repeated three times and the buttons were turned over in between. For calcium and europium, the pieces were wrapped in aluminum foil (Alujet, Mammendorf, Germany). In all cases, no significant evaporation was observed, as determined by weighing the arc-melted beads after the reaction. The argon gas was purified over a titanium sponge (873 K), molecular sieves, activated carbon and silica gel prior to the use. Subsequently, the samples were enclosed in evacuated silica tubes and annealed in muffle furnaces. They were heated to 973 K within two hours and then kept at this temperature for 14 days. Afterwards they were cooled to room temperature with 2 K h⁻¹. All samples are metallic, ground powders (particle size >100 μm) are grey and insensitive to air over months.

2.2 X-ray diffraction

The pulverized samples were investigated at room temperature on a D8-A25-Advance diffractometer (Bruker, Karlsruhe, Germany) in Bragg–Brentano θ – θ -geometry (goniometer radius 280 mm) with Cu K α -radiation ($\lambda = 154.0596$ pm). Diffraction patterns were recorded between 6 and 130° 2 θ with a step size of 0.013° and a total scan time of 1 h. A 12 μm Ni foil working as K β filter and a variable divergence slit were mounted at the primary beam side. A LYNXEYE detector with 192 channels

was used at the secondary beam side. The recorded data was evaluated using the Bruker TOPAS 5.0 software,⁴³ with the observed reflections being treated *via* single-line fits. The refined lattice parameters are given in Table 1. Powder patterns of all samples are depicted in Fig. S1–S12.†

Lath shaped crystal fragments of ErAl₅Pt₃ were obtained from the as-cast buttons. The crystals were glued to glass fibers using beeswax. An intensity data set of a suitable crystal was collected at room temperature using a Bruker X8 APEX2 diffractometer (Bruker, Karlsruhe, Germany). A multi-scan absorption correction using SadABS⁴⁶ was applied to the data set. All relevant crystallographic data, deposition and details of the data collection and evaluation are listed in Tables 2–4.

CSD 2349082 contains the supplementary crystallographic data for this paper.†

2.3 Scanning electron microscopy

The powdered bulk samples of NdAl₅Pt₃, GdAl₅Pt₃ and ErAl₅Pt₃ were attached to a sticky carbon tape and semiquantitatively analyzed in a JEOL 7000F (Jeol, Freising, Germany) scanning electron microscope (SEM) equipped with an EDAX Genesis 2000 energy-dispersive X-ray spectroscopy (EDX) detector (EDAX, Unterschleissheim, Germany). Results are listed in Table 5.

2.4 Magnetic measurements

Annealed pieces or powder of the respective X-ray pure REAl₅Pt₃ (RE = Y, Ce–Nd, Gd–Ho) samples were attached to the sample holder rod of a Vibrating Sample Magnetometer (VSM) using Kapton-foil or PE capsules for measuring the magnetization $M(H, T)$ in a Quantum Design Physical Property

Table 1 Lattice parameters (powder, single crystal and literature data), and unit cell volumes of the members of the MAl₅Pt₃ series as well as selected structurally related compounds

Compound	<i>a</i> (pm)	<i>b</i> (pm)	<i>c</i> (pm)	<i>V</i> (nm ³)	Ref.
CaAl ₅ Pt ₃	2050.3(1)	409.0(1)	736.4(1)	0.6175	^a
SrAl ₅ Pt ₃ ^{L,SC}	2065.04(7)	413.74(1)	738.98(3)	0.6314	39
SrAl ₅ Pt ₃ ^{L,P}	2067.07(6)	414.16(2)	739.88(3)	0.6334	39
YAl ₅ Pt ₃ ^P	2052.8(1)	406.7(1)	728.7(1)	0.6084	^a
LaAl ₅ Pt ₃ ^P	2068.7(1)	415.5(1)	732.2(1)	0.6293	^a
CeAl ₅ Pt ₃ ^L	2065.1(4)	413.81(8)	728.42(15)	0.6225	40
CeAl ₅ Pt ₃ ^P	2063.9(1)	414.0(1)	730.1(1)	0.6239	^a
PrAl ₅ Pt ₃ ^P	2061.4(2)	413.0(1)	729.6(1)	0.6212	^a
NdAl ₅ Pt ₃ ^P	2059.9(1)	412.1(1)	729.3(1)	0.6190	^a
SmAl ₅ Pt ₃ ^P	2057.0(1)	410.2(1)	728.5(1)	0.6148	^a
EuAl ₅ Pt ₃ ^L	2066.2(3)	412.58(6)	738.16(11)	0.6293	41
GdAl ₅ Pt ₃ ^P	2055.3(2)	408.7(1)	728.3(2)	0.6117	^a
TbAl ₅ Pt ₃ ^P	2052.9(1)	407.7(1)	728.2(1)	0.6095	^a
DyAl ₅ Pt ₃ ^P	2051.5(1)	406.7(1)	728.5(1)	0.6079	^a
HoAl ₅ Pt ₃ ^P	2050.4(1)	405.9(1)	729.1(1)	0.6067	^a
ErAl ₅ Pt ₃ ^P	2048.4(1)	405.1(1)	729.3(1)	0.6052	^a
ErAl ₅ Pt ₃ ^{SC}	2045.82(6)	404.40(1)	728.45(2)	0.6027	^a
CaGa ₅ Pt ₃ ^L	2082.5(4)	406.05(8)	739.2(1)	0.6251	44
SrGa ₅ Pt ₃ ^L	2092.3(1)	413.16(2)	740.88(3)	0.6404	45
BaGa ₅ Pt ₃ ^L	2104.8(2)	420.15(4)	747.7(1)	0.6612	44
BaGa ₅ Pt ₃ ^L	2104.3(2)	420.11(5)	747.80(8)	0.6611	45
EuGa ₅ Pt ₃ ^L	2085.5(5)	412.75(9)	738.7(1)	0.6359	44

^a This work; ^L literature data; ^P powder data; ^{SC} single crystal data.



Table 2 Crystallographic data and structure refinement for ErAl₅Pt₃ (YNi₅Si₃ type, space group *Pnma*, *Z* = 4)

CSD number	2349082
Sum formula	ErAl ₅ Pt ₃
Formula weight, g mol ⁻¹	887.4
Lattice parameters	see Table 1
Calcd density, g cm ⁻³	9.78
Crystal size, μm ³	120 × 40 × 30
Diffractometer	Bruker X8 APEX2
Wavelength; λ, pm	0.71073
Absorption correction	Multi-scan
	Bruker SadABS
Abs. coefficient, mm ⁻¹	83.8
<i>F</i> (000), <i>e</i>	1468
<i>θ</i> range, °	2.97–33.15
Range <i>hkl</i>	–31, +21; ±6; –10, +11
Total no. reflections	8867
Independent reflections/ <i>R</i> _{int}	1279/0.0636
Reflections <i>I</i> > 3σ(<i>I</i>)/ <i>R</i> _σ	950/0.0494
Data/parameters	1279/56
Goodness of fit on <i>F</i> ²	1.09
<i>R</i> ₁ / <i>wR</i> ₂ for <i>I</i> > 3σ(<i>I</i>)	0.0291/0.0594
<i>R</i> ₁ / <i>wR</i> ₂ (all data)	0.0457/0.0650
Extinction coefficient	31(7)
Extinction scheme	Lorentzian isotropic ⁴⁷
Larg. diff. peak/hole, e Å ⁻³	+3.64/–2.64

Measurement System (PPMS2) or a Quantum Design PPMS DynaCool system. All samples were investigated in the temperature range of 3–300 K or 1.9–300 K with applied external magnetic fields of up to 80/90 kOe. The results of the magnetic measurements are given in Table 6.

2.5 ²⁷Al solid-state NMR spectroscopy

The ²⁷Al MAS-NMR spectra of YAl₅Pt₃ were recorded at 104.31 MHz on an Avance III 400 WB spectrometer (Bruker, Billerica, US; 9.4 T) using magic-angle spinning (MAS) conditions. The sample was ground to a fine powder and mixed with an appropriate amount of NaCl (sample : NaCl = 1 : 9), to reduce the density and the electrical conductivity of the sample. The diluted sample was loaded into a cylindrical ZrO₂ rotor with a diameter of 4 mm and spun at the magic angle with a frequency of 10/13 kHz. A single-pulse experiment with a typical pulse length of 0.83 μs and a relaxation delay of 1 s

Table 4 Interatomic distances (pm) in of ErAl₅Pt₃ (YNi₅Si₃ type, space group *Pnma*). All distances of the first coordination spheres are listed. Standard deviations are equal or smaller than 0.2 pm

Er	2	Pt3	315.5	Al1	1	Pt1	251.4
	2	Pt1	316.2		1	Pt2	263.4
	2	Pt2	317.2		2	Pt1	264.1
	1	Al5	318.0		2	Al5	274.3
	2	Al2	321.4		2	Al1	278.6
	1	Al3	337.8		1	Al4	306.9
	2	Al1	337.8	Al2	1	Pt3	252.1
	2	Al3	338.2		1	Pt1	258.9
	1	Al4	348.9		2	Pt3	260.0
	1	Al1	352.4		1	Al3	280.4
	1	Al2	357.3		2	Al3	287.1
Pt1	1	Al5	246.9		2	Al4	293.3
	1	Al1	251.4	Al3	1	Pt3	247.2
	1	Al2	258.9		1	Pt2	251.9
	2	Al4	263.6		2	Pt3	255.0
	2	Al1	264.1		1	Al2	280.4
	1	Pt2	308.4		2	Al2	287.1
Pt2	2	Al5	248.4		2	Al4	310.7
	1	Al3	251.9	Al4	1	Pt3	251.3
	1	Al5	252.2		2	Pt1	263.6
	1	Al1	263.4		2	Pt2	269.9
	2	Al4	269.9		1	Al5	284.4
	1	Pt1	308.4		2	Al2	293.3
Pt3	1	Al3	247.2		1	Al1	306.9
	1	Al4	251.3		2	Al3	310.7
	1	Al2	252.1		2	Al5	342.7
	2	Al3	255.0	Al5	1	Pt1	246.9
	2	Al2	260.0		2	Pt2	248.4
					1	Pt2	252.2
					2	Al5	272.1
					2	Al1	274.3
					1	Al4	284.4

Table 5 SEM-EDX data of selected members of the REAl₅Pt₃ series. Standard deviations are ±2 at%

Compound	RE (at%)	Al (at%)	Pt (at%)
Ideal composition	11.1	55.6	33.3
NdAl ₅ Pt ₃	10	55	35
GdAl ₅ Pt ₃	11	53	36
ErAl ₅ Pt ₃	11	55	34

Table 3 Atomic coordinates and displacement parameters (in pm²) of ErAl₅Pt₃ (YNi₅Si₃ type, space group *Pnma*, all atoms on Wyckoff positions 4c: *x*, 1/4, *z*)

Atom	<i>x</i>	<i>z</i>	<i>U</i> ₁₁	<i>U</i> ₂₂	<i>U</i> ₃₃	<i>U</i> ₁₃	<i>U</i> _{eq} ^a
Er	0.36014(3)	0.87991(8)	81(3)	74(3)	101(3)	7(2)	85(3)
Al1	0.0076(2)	0.3702(5)	57(2)	67(2)	71(3)	–1(2)	65(2)
Al2	0.2011(2)	0.6766(5)	54(2)	60(2)	82(2)	1(2)	65(2)
Al3	0.2081(2)	0.0610(5)	70(2)	50(2)	69(2)	1(2)	63(2)
Al4	0.3809(2)	0.3553(5)	55(17)	54(18)	68(18)	–5(13)	59(18)
Al5	0.4842(2)	0.6168(5)	70(17)	79(19)	47(18)	–6(13)	65(18)
Pt1	0.07482(2)	0.65917(7)	73(17)	36(18)	78(19)	16(14)	62(18)
Pt2	0.08523(2)	0.08160(7)	24(16)	18(16)	76(18)	5(13)	39(17)
Pt3	0.25819(2)	0.36976(7)	57(17)	69(18)	87(19)	–1(14)	71(18)

^aThe isotropic displacement parameter *U*_{eq} is defined as: *U*_{eq} = 1/3 (*U*₁₁ + *U*₂₂ + *U*₃₃) (pm²); *U*₁₂ = *U*₂₃ = 0. Standard deviations are given in parentheses.



Table 6 Physical properties of the REAl₅Pt₃ (RE = Y, Ce–Nd, Gd–Ho) series: T_N , Néel temperature; μ_{eff} , effective magnetic moment; μ_{theo} , theoretical magnetic moment; θ_p , paramagnetic Curie temperature; H_{crit} , critical field for meta-magnetic transition; μ_{sat} , experimental saturation magnetization; $g_J \times J$, theoretical saturation magnetization

Compound	T_N (K)	μ_{eff} (μ_B)	μ_{theo} (μ_B)	θ_p (K)	H_{crit} (kOe)	μ_{sat} (μ_B/RE^{3+})	$g_J \times J$ (μ_B/RE^{3+})
YAl ₅ Pt ₃	Pauli-paramagnetic, non-superconducting, $\chi(300 \text{ K}) = +8.63(1) \times 10^{-5} \text{ emu mol}^{-1}$						
CeAl ₅ Pt ₃	—	2.76(1)	2.54	−41(1)	—	0.99(1) ^a	2.14
PrAl ₅ Pt ₃	—	3.69(1)	3.58	−13(1)	4.4(1)	2.28(1) ^b	3.20
NdAl ₅ Pt ₃	5.1(1)	3.82(1)	3.62	+18(1)	26.7(1)	2.98(1) ^a	3.27
GdAl ₅ Pt ₃	8.7(1)	7.99(1)	7.94	−7(1)	—	2.98(1) ^a	7
TbAl ₅ Pt ₃	15.3(1)	9.49(1)	9.72	+16(1)	33.2(1)	5.36(1) ^a	9
DyAl ₅ Pt ₃	5.8(1)	10.83(1)	10.65	+9(1)	9.8(1)	7.85(1) ^b	10
HoAl ₅ Pt ₃	2.4(1)	10.95(1)	10.61	+19(1)	5.1(1)	8.78(1) ^a	10

^a 1.8 K, 90 kOe. ^b 3 K, 80 kOe.

Table 7 Summary of the NMR observables of YAl₅Pt₃, extracted from the DMFit simulation of the ²⁷Al MAS-NMR spectra with δ being the resonance (in ppm), C_Q the quadrupolar parameter (in kHz), η_Q the asymmetry parameter and G/L the Gaussian to Lorentz ratio. Theoretically calculated values from DFT are given with the subscript calc

Site	δ	FWHM	$C_{Q,\text{calc}}$	$\eta_{Q,\text{theo}}$
Signal 1	693	31	—	—
Signal 2	642	24	—	—
Signal 3	602	13	—	—
Signal 4	567	17	—	—
Signal 5	510	14	—	—
Al1 (4c)	—	—	−2484	0.771
Al2 (4c)	—	—	−1642	0.523
Al3 (4c)	—	—	−2302	0.425
Al4 (4c)	—	—	+3819	0.519
Al5 (4c)	—	—	+5487	0.690

was conducted. Resonance shifts were referenced to aqueous 1 molar AlCl₃ solutions. The NMR-spectra were recorded using the Bruker TOPSPIN software,⁴⁸ the analysis was performed with the help of the DMFIT program package.⁴⁹ The extracted data is compiled in Table 7.

2.6 X-ray photoelectron spectroscopy (XPS)

For XPS experiments an ESCALab Mk II spectrometer by *Vacuum Generators* with non-monochromatic Al-K α radiation ($h\nu = 1486.6 \text{ eV}$) was used. The original 150°-type hemispherical analyzer with a three channeltron detector system was replaced by a 180°-type *PreVac* EA 15 analyzer with a multichannelplate detector. All spectra were recorded in normal emission mode (polar angle $\theta = 0^\circ$) at a pass energy of 50 eV for survey spectra and 20 eV for detail spectra. The step widths in binding energy were 1.0 eV for survey spectra and 100 meV for detail spectra.

Powders of Al₃Pt₂ and YAl₅Pt₃ were pressed to pellets (diameter approx. 4 mm) and glued by a conductive carbon tape

on an Al sample holder (diameter slightly lower than 4 mm to avoid spectral features from the sample holder and the tape). Due to the strong charging of the Al₃Pt₂ and YAl₅Pt₃ samples the C 1s peak was used for calibration of the binding energy E_B , i.e. all spectra were shifted in binding energy by $\Delta = E_B(\text{C } 1s) - E_B(\text{C } 1s_{\text{HOPG}})$ with $E_B(\text{C } 1s_{\text{HOPG}}) = 284.3 \text{ eV}$ as probed on an *in situ* cleaved HOPG sample (Highly Oriented Pyrolytic Graphite). Pt 4f and Al 2s reference spectra were recorded on a sample from a Pt foil (cleaned by Ar ion etching) and an Al sheet (with the oxide only partially removed by Ar ion etching), respectively.

2.7 Quantum-chemical calculations

Density functional theory (DFT) calculations of YAl₅Pt₃ were performed using the projector augmented wave method (PAW) of Blöchl^{50,51} coded in the Vienna *ab initio* simulation package (VASP).^{52,53} All VASP calculations employed the generalized gradient approximation (GGA) with exchange and correlation treated by Perdew-Burke-Enzerhof (PBE).⁵⁴ The cut-off energy for the plane wave calculations was set to 500 eV and the Brillouin zone integration was carried out using $3 \times 15 \times 9$ k -point meshes. NMR parameters were evaluated through the field gradient tensor calculations in VASP with the nuclear quadrupole moment of 146.6 mb for ²⁷Al. The Bader charge analysis was based on VASP calculations with subsequent calculations using the Bader program developed by the Henkelman group.^{55–57} Results of the Bader charge calculations are listed in Table 8. Chemical bonding was assessed *via* crystal orbital Hamiltonian population (COHP) analysis using the Stuttgart version of the tight-binding, linear muffin-tin orbital (TB-LMTO) method with the atomic spheres approximation.⁵⁸ Within TB-LMTO, exchange and correlation were treated using the von Barth-Hedin local density approximation (LDA). All relativistic effects except for spin-orbit coupling were taken into account using a scalar relativistic

Table 8 Bader charges in YAl₅Pt₃ from non-spin-polarized DFT calculations

YAl ₅ Pt ₃	Y	Al1	Al2	Al3	Al4	Al5	Pt1	Pt2	Pt3
Charge	+1.25	+0.76	+0.79	+0.91	+0.93	+0.93	−1.80	−1.80	−1.98



approximation.⁵⁹ The basis sets were 5s/(5p)/4d/(4f) for Y, 6s/6p/5d/(5f) for Pt, and 3s/3p/(3d) for Al, with orbitals in parentheses down-folded.⁶⁰ The Brillouin zone was sampled by 280 *k*-points. Results of bonding analysis are summarized in Table 9.

3 Results

3.1 Powder X-ray diffraction

All samples were prepared with the nominal composition of MAl_5Pt_3 ($M = Ca, Y, La-Nd, Sm-Er$) in analogy to $SrAl_5Pt_3$,³⁹ $EuAl_5Pt_3$,⁴¹ and $CeAl_5Pt_3$.⁴⁰ The powder X-ray diffraction patterns clearly indicate the formation of the title compounds as well as them being isostructural to their Sr/Eu/Ce analogues. Most of the compounds could be obtained as X-ray pure

Table 9 Atomic interactions/distances and their corresponding integrated COHPs (ICOHPs) in eV per bond and eV per f.u. of YAl_5Pt_3 (YNi_5Si_3 type, space group $Pnma$, $Z = 4$). All interactions/distances of the first coordination spheres are listed

Interaction	Counts	Distance	ICOHP/bond	ICOHP/f.u.
Y–Pt1	2	318.1	−0.65	−1.30
Y–Pt2	2	319.2	−0.65	−1.30
Y–Pt3	2	318.2	−0.62	−1.23
Y–Al1	2	339.3	−0.40	−0.81
	1	353.3	−0.30	−0.30
Y–Al2	2	322.5	−0.51	−1.02
	1	358.5	−0.29	−0.29
Y–Al3	2	336.4	−0.48	−0.95
	1	339.8	−0.37	−0.37
Y–Al4	1	347.6	−0.36	−0.36
Y–Al5	1	319.0	−0.46	−0.46
Sum				−8.40 (14.3%)
Pt1–Al1	1	251.9	−2.19	−2.19
	2	264.8	−1.74	−3.48
Pt1–Al2	1	259.3	−1.96	−1.96
Pt1–Al4	2	263.7	−1.91	−3.81
Pt1–Al5	1	246.2	−2.25	−2.25
Pt2–Al1	1	264.0	−1.80	−1.80
Pt2–Al3	1	252.5	−2.36	−2.36
Pt2–Al4	2	270.8	−1.73	−3.47
Pt2–Al5	2	249.1	−2.17	−4.35
Pt3–Al2	1	252.1	−2.05	−2.05
	2	252.9	−2.07	−4.07
	2	261.2	−1.81	−3.63
Pt3–Al3	1	247.7	−2.21	−2.21
	2	255.8	−1.98	−3.97
Pt3–Al4	1	250.2	−2.32	−2.32
Sum				−39.6 (67.4%)
Pt1–Pt2	1	306.5	−0.65	−0.65
Sum				−0.65 (1.10%)
Al1–Al1	2	279.5	−1.09	−2.19
Al1–Al4	1	306.8	−0.63	−0.63
Al1–Al5	2	275.2	−1.14	−2.29
Al2–Al3	1	282.4	−0.84	−0.84
	2	288.7	−0.84	−1.68
Al2–Al4	2	292.5	−0.80	−1.61
Al3–Al4	2	314.0	−0.41	−0.82
Al4–Al5	2	284.8	−0.98	−1.95
	1	344.0	−0.07	−0.07
Al5–Al5	2	272.9	−0.11	−0.22
Sum				−10.1 (17.2%)
Overall ICOHP				−58.8

materials crystallizing in the orthorhombic YNi_5Si_3 type structure ($Pnma$).⁶¹ But especially for lanthanum and calcium, orthorhombic $M_2Al_{16}Pt_9$ ($Immm$, $Ce_2Al_{16}Pt_9$ type)⁶² could be identified as a side phase. In some cases, also trigonal Al_3Pt_2 ($P\bar{3}m1$, Al_3Ni_2 type)^{63,64} was observed as binary by-product. In many cases, annealing led to X-ray pure samples or a drastic reduction of the Al_3Pt_2 amounts to <2 mass%. Fig. 1 depicts the trend of the unit cell volumes plotted versus the ionic radius of the respective metal ions. Most of the rare earth cations exhibit a trivalent oxidation state, however, europium and the alkaline earth metals are divalent in these compounds as can be seen from the significantly larger unit cell volumes. Also, the isostructural MGa_5Pt_3 ($M = Ca, Sr, Eu, Ba$)^{44,45} exhibit slightly larger unit cells as shown in Table 1 and Fig. 1.

3.2 Single crystal X-ray diffraction and structure refinement

Analysis of the obtained single crystal X-ray diffraction data of $ErAl_5Pt_3$ revealed an orthorhombic lattice and space group $Pnma$ was found to be correct. The structure was solved using the charge flipping algorithm of Superflip⁶⁵ and a least squares refinement on F^2 using the program Jana2006^{66,67} was carried out. All atomic positions were refined with anisotropic displacement parameters and as a check for correct compositions, the occupancy parameters were refined in a separate series of least-square refinements. All sites were fully occupied within three standard deviations leading to the targeted compositions. Final difference Fourier syntheses were contour less. From the Pearson database,⁶⁸ isotypism with $CeAl_5Pt_3$ ⁴⁰ adopting the YNi_5Si_3 type⁶¹ was deduced. In contrast to UFe_5As_3 and related compounds no twinning was observed.⁶⁹ Details of the structure determination, atomic parameters and interatomic distances can be found in Tables 2–4. When looking at the refined anisotropic displacement parameters (ADP) of the atoms, Er exhibits a value of 85 pm², which is larger than the

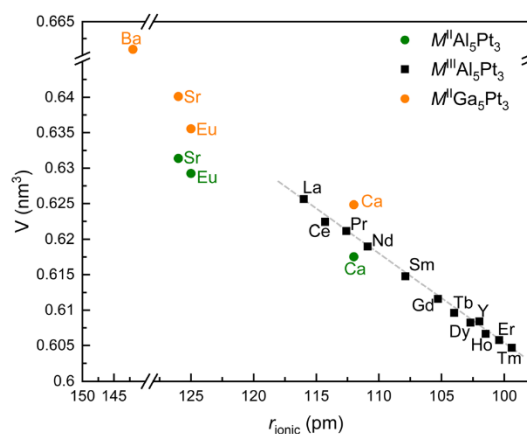


Fig. 1 Plot of the unit cell volumes (in nm³) for the MAl_5Pt_3 series ($M = Ca, Sr, Y, La-Nd, Sm-Er$) versus the M^{n+} radius (in pm). Formally divalent metal atoms are depicted in green, trivalent ones in black, the members of the gallium series are shown in orange.



one of Pt and Al. This might be explained by the fact that ErAl_5Pt_3 is the last compound of this series, leading to the assumption that the Er atoms rattle inside the cavities of the polyanionic framework, leading to an increased ADP.

CSD 2349082 contains the supplementary crystallographic data for this paper.†

3.3 Crystal chemistry

All members of the MAl_5Pt_3 series crystallize in the orthorhombic crystal system with space group $Pnma$ ($oP36$, c^9) and are isostructural with the aluminum representatives CeAl_5Pt_3 , EuAl_5Pt_3 and SrAl_5Pt_3 .^{39–41} Besides the aluminum compounds also several gallium compounds MGa_5Pt_3 ($M = \text{Ca–Ba, Eu}$)^{44,45} have been reported, having the corresponding composition. These compounds, however, should not be considered isostructural to the prototypic YNi_5Si_3 structure,⁶¹ but rather isopointal. Especially since the $[\text{Ni}_5\text{Si}_3]^{6-}$ polyanion exhibits a different transition metal to main group element ratio, compared to the respective platinides of aluminum and gallium.

Fig. 2a exemplarily depicts the crystal structure of YAl_5Pt_3 as projection along $[010]$. The Y atoms exhibit a slightly distorted hexagonal prismatic coordination environment with an alternating arrangement of the Al and Pt atoms within the hexagon, but a congruent arrangement of top and bottom face is observed (Fig. 3). The $\text{Y@Al}_6\text{Pt}_6$ form strands along $[010]$ via condensation of their hexagonal faces. Within the prism, the interatomic Y–Al distances range between 322 and 342 pm, while the Y–Pt distances are between 328 and 330 pm. Both, the Y–Al and Y–Pt distances are in line with the ones found in binary intermetallics e.g. YAl_2 (MgCu₂ type, 325–340 pm⁷⁰), YAl_3 (Mg₃Cd type, 302–310 pm⁷¹), YPt_2 (MgCu₂ type, 314–328 pm⁷⁰) or YPt_3 (Cu₃Au type, 288 pm⁷²) as well as with the sum of the covalent radii ($\text{Y} + \text{Al} = 162 + 125 =$

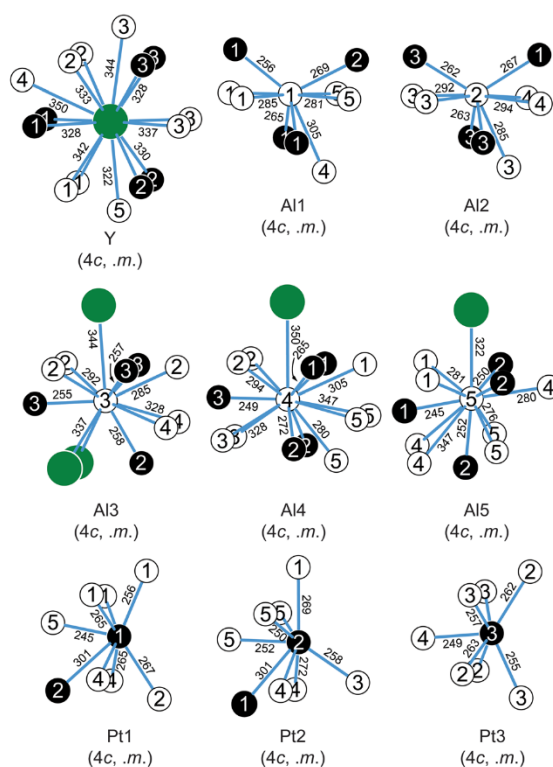


Fig. 3 Coordination environments surrounding the Y, Pt and Al atoms in the structure of YAl_5Pt_3 . Sr, Pt and Al atoms are shown as green, white and black circles, respectively. Wyckoff sites, site symmetries and interatomic distances (in pm) are given.

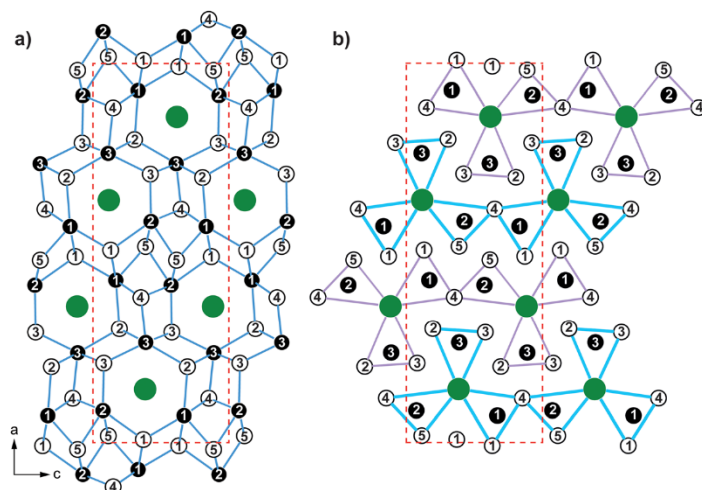


Fig. 2 Unit cell of YAl_5Pt_3 as projection along $[010]$ (a) highlighting the polyanionic $[\text{Al}_5\text{Pt}_3]^{6-}$ framework (the shortest Al–Pt interactions are emphasized in blue) and (b) using $\text{X@M}_2\text{T}_4$ prisms to illustrate the structure (the interactions forming the prisms are highlighted in blue and purple). Y, Al and Pt atoms are shown in green, white and black circles, respectively.



287 pm; Y + Pt = 162 + 129 = 291 pm⁷³). Similar distances can be observed in ternary compounds of the Y–Al–Pt system like YAlPt (TiNiSi type, Y–Al: 308–336 pm; Y–Pt: 257–267 pm),⁷⁴ YAl₂Pt (MgAl₂Cu type, Y–Al: 287–305 pm; Y–Pt: 287–308 pm),⁷⁵ Y₄Al₂₄Pt₉ (own type, Y–Al: 304–321 pm; Y–Pt: 328–336 pm),⁷⁶ YAl₃Pt₂ (own type, Y–Al: 329–348 pm; Y–Pt: 301–316 pm),⁷⁷ YAl₂Pt₅ (ZrAl₃Ni₂ type, Y–Al: no contacts; Y–Pt: 288–302 pm),⁷⁸ Y₄AlPt (Gd₄InRh type, Y–Al: 324–348 pm; Y–Pt: 281–347 pm)⁷⁹ or Y₁₀Al₃Pt (Y₁₀Cd₃Ru type, Y–Al: 324–348 pm; Y–Pt: 275 & 349 pm).⁸⁰

The [Al₅Pt₃]⁶⁻ polyanion is formed by five crystallographically independent aluminum and three platinum sites (Fig. 2). All Pt sites exhibit a coordination number of seven with a highly asymmetrical coordination environment and interatomic Al–Pt distances between 247 and 270 pm. These agree well with those in binary (AlPt: 248–273 pm;^{81,82} Al₂Pt: 256 pm;⁸³ Al₃Pt₂: 255–286 pm^{63,64}) and ternary intermetallics (YAlPt: Al–Pt 308–336 pm,⁷⁴ YAl₂Pt: Al–Pt 287–305 pm,⁷⁵ YAl₃Pt₂: Al–Pt: 329–348 pm⁷⁷) as well as with the sum of the covalent radii (Pt + Al = 129 + 125 = 254 pm⁷³). The respective homoatomic distances (YAl₅Pt₃: Pt–Pt: 306 pm; Al–Al: 273–293 pm) agree with what is observed in elemental Al (286 pm⁸⁴), therefore suggesting partial bonding contributions while the Pt–Pt distances are significantly longer compared to the distances found in the elemental Pt (277 pm⁸⁵) or the sum of the covalent radii (Al: 250 pm; Pt: 258 pm).⁷³ Another possibility to describe the YNi₅Si₃ type structure, especially when compared to other structure types of the same stoichiometry MT₅X₃ such as the UFe₅As₃, the LaCo₅P₃, the UCo₅Si₃ or the YCo₅P₃ type structures, is to use trigonal prisms surrounding the As, P or Si atoms. These X@M₂T₄ prisms condense *via* common M₂ or T₂ edges to form “shamrock” like structures that are further condensed. One possibility is to form chains are linear in the case of the YNi₅Si₃ type structure (Fig. 2b). A more detailed description can be found in a recent publication.⁶⁹

3.4 Scanning electron microscopy

Powders of NdAl₅Pt₃, GdAl₅Pt₃ and ErAl₅Pt₃ were investigated by SEM-EDX. The average of three point measurements are given in Table 5 and are in good agreement with the ideal composition (11.1 at% M, 55.6 at% Al, 33.3 at% Pt). The slight deviations can be explained by the irregular sample surface and the not perfect perpendicular orientation of the powder towards the beam. No impurity elements heavier than sodium (detection limit of the instrument) were detected.

3.5 Magnetic measurements

YAl₅Pt₃ is, as expected, a Pauli-paramagnetic material with a positive susceptibility since the Pauli contribution originating from the conduction electrons overcompensates the intrinsic diamagnetism. No superconductivity was observed at 20 K down to 2.5 K.

All other X-ray pure members of the REAl₅Pt₃ series (RE = Y, Ce–Nd, Gd–Ho) exhibit an open-shell 4f electron configuration leading to paramagnetic behavior. Their effective magnetic

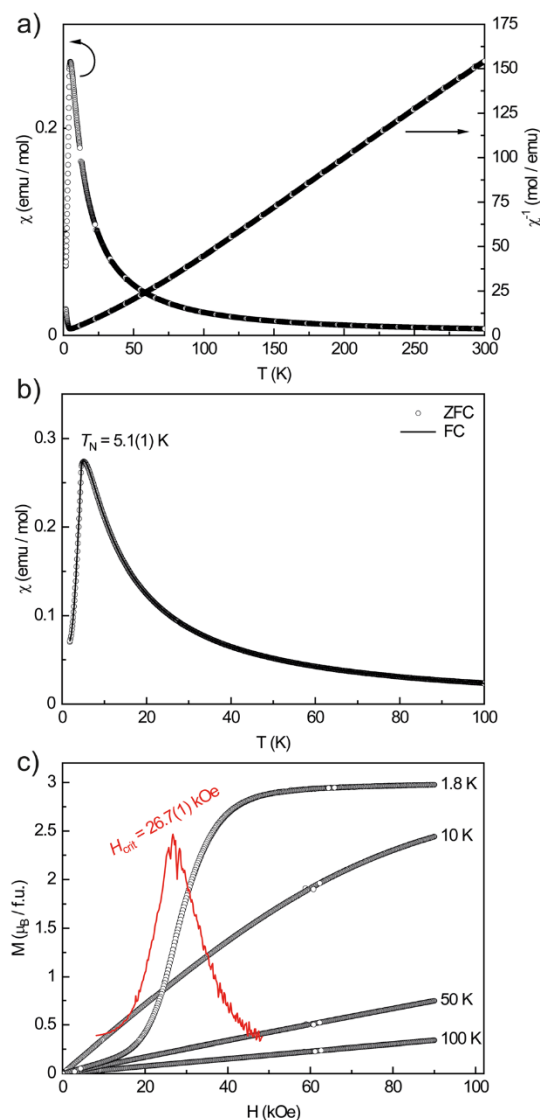


Fig. 4 Magnetic data of NdAl₅Pt₃. (a) Temperature dependence of the magnetic and inverse magnetic susceptibility (χ and χ^{-1} data) measured with an applied external field of 10 kOe; (b) zero-field-cooled/field-cooled (ZFC/FC) measurements measured with an applied external field of 100 Oe; (c) magnetization isotherms recorded at 1.8, 10, 50 and 100 K, the inflection point is determined by the first derivative of dM/dH , shown in red.

moments calculated from modified Curie–Weiss fits indicate a stable trivalent oxidation state in all cases in good agreement with the expected moments for the free RE³⁺ cations (Table 6). Fig. 4 exemplarily depicts the magnetic behavior of NdAl₅Pt₃. The magnetic susceptibility data recorded between 1.8 and 300 K in zero-field-cooled mode (ZFC) at 10 kOe already shows a maximum at low temperatures indicating an antiferro-



magnetic transition (Fig. 4a). From the inverse susceptibility, the experimental magnetic moment was calculated to be $\mu_{\text{exp}} = 3.82(1)\mu_{\text{B}}$, in line with Nd^{3+} ($\mu_{\text{eff}} = 3.62\mu_{\text{B}}$). The positive Weiss constant of $\theta_{\text{p}} = 18(1)$ K points towards ferromagnetic interactions in the paramagnetic temperature regime and could be a sign of so called A-type antiferromagnetism in which each layer orders ferromagnetically but antiparallel to adjacent layers.⁸⁶ The low field data (100 Oe) was recorded in zero-field-cooled and field-cooled (ZFC/FC) mode between 1.8 and 100 K (Fig. 4b). At $T_{\text{N}} = 5.1(1)$ K a clear maximum can be observed, originating from the antiferromagnetic ordering which causes the magnetic susceptibility to drop below the Néel temperature. Since the ZFC and FC curves are on top of each other, ferromagnetic impurities can be excluded. The magnetization isotherms are finally shown in Fig. 4c. The isotherms recorded at 50 and 100 K are linear up to 90 kOe, indicating Curie paramagnetism at these temperatures. The 10 K isotherm is slightly curved due to the proximity of the magnetic phase transition. The 1.8 K isotherm finally shows a pronounced S-shape indicating a meta-magnetic step. While at low magnetic fields the antiparallel orientation of the spins persists, a spontaneous reorientation is observed at a critical field of $H_{\text{crit}} = 26.7(1)$ kOe. The inflection point is determined by the first derivative dM/dH . The saturation magnetization at 1.8 K and 90 kOe reaches $\mu_{\text{sat}} = 2.98(1)\mu_{\text{B}}$ which is close to the theoretical saturation magnetization according to $g_{\text{J}} \times J$ of $3.27\mu_{\text{B}}$ and in line with the almost horizontal trace.

Since the interatomic M–M distances in the whole MAl_5Pt_3 series are rather large (>550 pm), RKKY (Ruderman-Kittel-Kasuya-Yosida) interactions between the rare-earth atoms are expected. In this case, the magnetic ordering temperatures, in this case the Néel temperatures, should scale with the de Gennes factor G [$(g_{\text{J}} - 1)^2 J(J + 1)$]. Fig. 5 shows the obtained correlation between T_{N} and G , clearly indicating a deviation from the expected behavior. This points towards crystal field

influences in the REAl_5Pt_3 series. Similar results have been observed for example in the RE_2InT_2 (RE = La–Nd, Sm, Gd–Lu; T = Ni, Cu, Pd) series.^{87–89}

Finally, for some of the other samples, the determined saturation magnetizations (Table 6) are significantly different to the values according to $g_{\text{J}} \times J$ which can either be explained by crystal field effects (see de Gennes scaling) or the polycrystalline nature of the samples.

3.6 ^{27}Al solid-state NMR spectroscopy

Solid-state MAS NMR spectroscopy is a powerful tool to support crystallography. Besides a plain confirmation of the crystal structure (number of sites equals number of signals) also structural distortions or the presence of solid solutions can be probed based on the shape of the *e.g.* ^{27}Al NMR signal.^{78,90–93}

Fig. 6 depicts the results of the ^{27}Al MAS-NMR spectroscopic investigations on YAl_5Pt_3 . Consistent with its crystal structure, the spectrum confirms the presence of five crystallographically independent Al sites. However, only the intense central line originating from the $|+1/2\rangle \leftrightarrow |-1/2\rangle$ transitions of the five Al sites can be modelled with a Gauss-Lorentz fit. Since no significant broadening is observed, one can conclude that the electric quadrupolar couplings C_{Q} are rather small (in a range <5 MHz) and second order quadrupole effects (SOQE) are not dominant, in line with the results from the quantum-chemical calculations (Table 7). The resonances of these five signals are significantly shifted compared to the standard of an aqueous solution of Al^{3+} (AlCl_3), however, they are in line with the reported shifts for intermetallic aluminum compounds. The drastic shift, typically in the range of 200–1200 ppm,⁹⁰ is caused by the s-electron spin density at the Fermi level as probed by the ^{27}Al nuclei and dominated by the Knight shift contribution.⁹⁰ Under magic angle spinning (MAS) conditions one can potentially observe a wide spinning sideband pattern originating from the outer satellite transitions, $|\pm 1/2\rangle \leftrightarrow |\pm 3/2\rangle$ and $|\pm 3/2\rangle \leftrightarrow |\pm 5/2\rangle$, however, this is not the case here.

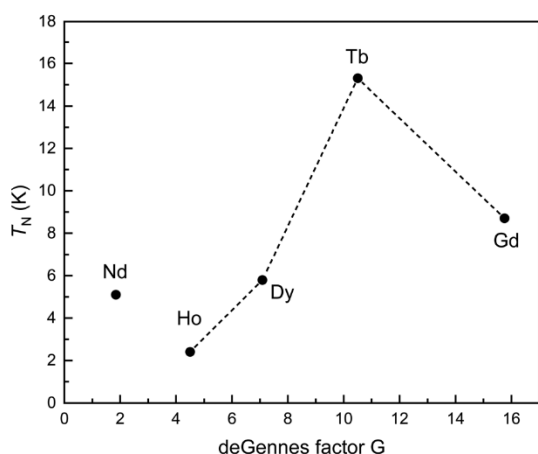


Fig. 5 Plots of the ordering temperatures versus the de Gennes factor $(g_{\text{J}} - 1)^2 J(J + 1)$ for the REAl_5Pt_3 series.

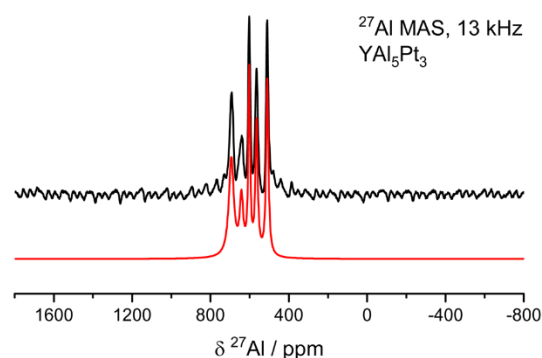


Fig. 6 ^{27}Al MAS-NMR spectra (black) of YAl_5Pt_3 (YNi_5Si_3 type) along with the fit of the central transitions (red).

3.7 XPS

X-ray photoelectron spectra have been recorded to investigate the electronic properties in the synthesized compounds from an experimental point of view. The 4f core levels of, *e.g.*, Pt are very sensitive towards the electronic structure at the respective atom, allowing a spectroscopic approach to analyze the charge transfer in these intermetallic compounds. For intermetallic alkaline earth or rare-earth aluminum compounds with late transition metals, especially with 5d elements, an electron transfer from the AE/RE and Al atoms to the platinum atoms can be observed. This has been shown for quite some instances, *e.g.*, $\text{Ba}_3\text{Al}_4\text{Pt}_4$ ⁹⁴ and the REAl_3Pt_2 (RE = Y, Dy–Tm) series.⁷⁷ Since the most electronegative elements acquire additional electron density, shifts of the binding energies of the Pt 4f lines towards lower binding energies can be observed in the respective XPS measurements.^{94–97} In general, the Pt 4f states can be chosen as a reference as they are intense and sharp enabling the detection of already small shifts. However, it has to be mentioned that the Pt 4f and Al 2p levels have almost the same binding energy.⁹⁸

Fig. 7a depicts the XPS spectra of the Pt 4f lines of elemental Pt (black), YAl_5Pt_3 (red) and Al_3Pt_2 (blue). For the Pt reference (Pt foil) a binding energy of $\text{BE}(\text{Pt}) = 71.0(1)$ eV was observed, in line with the literature.⁹⁸ For YAl_5Pt_3 and Al_3Pt_2 shifts of +0.23 and +0.76 eV were obtained ($\text{BE}(\text{YAl}_5\text{Pt}_3) = 71.23$ eV; $\text{BE}(\text{Al}_3\text{Pt}_2) = 71.76$ eV). In contrast to what is intuitively expected and described before, the shift of the Pt lines to higher binding energies indicates a formal formation of cationic Pt species in both compounds. Given the drastic electronegativity differences ($\chi(\text{Pt}) = 2.28$ and $\chi(\text{Al}) = 1.61$ ⁷³), a shift towards lower binding energies, in line with an anionic character, is expected. However, a recent HAXPES study has shown, that, although a charge transfer towards an anionic Pt species is expected based on quantum-chemical data, shifts towards formal cationic Pt are visible in binary aluminum platinides.⁹⁹ The authors could show, that the QTAIM charges on the Pt atoms correlate with the positive shifts of the Pt 4f binding energies. This was attributed to changes in the Pt 5d orbital occupancies preventing an easy interpretation only based on the shifts of the Pt 4f binding energies in this binary system. Therefore the question arises if this is also applicable in the system reported here.

When looking at the intensities of the $4f_{7/2}$ and $4f_{5/2}$ peaks, however, only the elemental Pt reference shows the expected 4 : 3 ratio.⁹⁸ For YAl_5Pt_3 and Al_3Pt_2 , the $4f_{5/2}$ peaks seem to be equally high if not higher compared to the $4f_{7/2}$ peak. This is probably either due to at least a second set of Pt 4f levels. For Al, a shift towards higher binding energies, corresponding to a cationic character, is expected. Fig. 7b shows the XPS spectra of the Al 2s lines of elemental Al (black), YAl_5Pt_3 (red) and Al_3Pt_2 (blue). Here, the expected shift can be observed, however, the main peak corresponds to the one of trivalent Al as in Al_2O_3 . Subsequently, XPS spectra of the oxygen 1s lines were conducted (Fig. 7c). Here, a signal corresponding to the expected value of Al_2O_3 can be observed for Al_3Pt_2 , for YAl_5Pt_3 ,

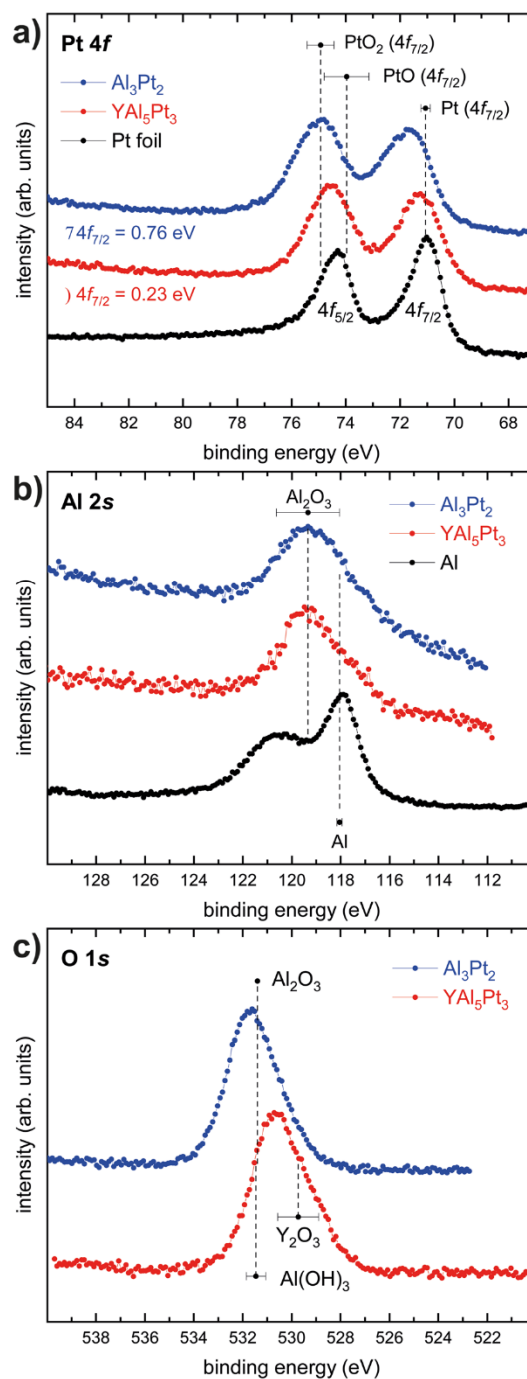


Fig. 7 (a) Pt 4f spectra of YAl_5Pt_3 (red) and Al_3Pt_2 (blue) and Pt (black); (b) Al 2s spectra of YAl_5Pt_3 (red) and Al_3Pt_2 (blue) and Al (black); (c) O 1s spectra of YAl_5Pt_3 (red) and Al_3Pt_2 (blue). Mean values of binding energies and standard deviations are obtained by averaging over all entries in the NIST XPS database for the compounds specified in (a)–(c).¹⁰¹



two overlapping lines can be observed that originate from Al_2O_3 and Y_2O_3 . This suggests that the surface of the powder particles used for the XPS investigations is oxidized. This leads to the conclusion, that although these XPS investigations show an effect similar to what has been observed and reported for the binary Al–Pt system in literature, here a fully oxidized surface is present. Therefore, the shifts to higher binding energies in line with the literature are probably a mere coincidence. In the investigated samples, Pt atoms in an Al_2O_3 matrix rather than in the intermetallic compounds YAl_5Pt_3 and Al_3Pt_2 were probed in the XPS-accessible subsurface range. Studies on Al containing metallic glasses have shown a similar effect. Here, Al was oxidized throughout the material while all other metals were only oxidized within the first 5 nm below the surface.¹⁰⁰

3.8 Quantum-chemical calculations

The chemical bonding within YAl_5Pt_3 was investigated through crystal orbital Hamiltonian population (COHP) analysis. The integrated COHP (ICOHP) values, as listed in Table 9, highlights the predominant role of Al–Pt bonds, contributing over 65% to the total ICOHP value. Following these, the interactions of Al–Al are notable, while those involving Y–Al, Y–Pt, and Pt–Pt are relatively weaker. Particularly, the differences in the strengths between Al–Pt (−1.73 to −2.36 eV) and Al–Al interactions (−0.07 to −1.14 eV), in contrast to the Y–Pt (−0.62 to −0.65 eV) and Y–Al (−0.29 to −0.51 eV) ones, suggest the presence of a polyanionic $[\text{Al}_5\text{Pt}_3]^{6-}$ network, with Y^{3+} cations occupying the resulting cavities.

The electronic structure of YAl_5Pt_3 was analyzed using density functional theory (DFT) calculations. The electron density of states (DOS) curves for YAl_5Pt_3 are depicted in Fig. 8. Notably, there exists a significant density of states at the Fermi level, indicative of metallic behavior, consistent with the observed silver to grey metallic appearance. The calculated Bader effective charges for YAl_5Pt_3 are detailed in Table 8. Each of the five crystallographically independent Al atoms exhibits positive charges. Moreover, the deviation of all Al atom charges from +3 (with values from +0.76 to +0.93) suggests that the Al–Pt interactions possess a predominantly

covalent character than ionic. This observation aligns with the large negative Al–Pt ICOHP values and supporting the presence of a polyanionic $[\text{Al}_5\text{Pt}_3]^{6-}$ network. Conversely, all Pt atoms demonstrate negative charges. Yttrium (Y) is observed to possess a positive charge of +1.25, which is notably less than a trivalent oxidation state. This suggests significant electron delocalization and robust Y–Pt and Y–Al covalent/metallic interactions, consistent with the noteworthy negative ICOHP values. These findings support the metallic character of YAl_5Pt_3 .

4 Conclusion

The MAl_5Pt_3 series with $M = \text{Sr}, \text{Ce}, \text{Eu}$ could be significantly extended to $M = \text{Ca}, \text{Y}$ and La–Nd as well as Sm–Er . All compounds were synthesized from the elements using arc-melting and subsequent annealing and were characterized by powder X-ray diffraction. For CaAl_5Pt_3 and LaAl_5Pt_3 also the respective $\text{M}_2\text{Al}_{16}\text{Pt}_9$ members were observed, however, the other compounds could be obtained either as X-ray pure materials or with small amounts of Al_3Pt_2 as side phase. Single-crystal X-ray diffraction studies on ErAl_5Pt_3 verified that also the small rare-earth elements adopt the YNi_5Si_3 type structure. For selected members of the series ($M = \text{Y}, \text{Ce–Nd}, \text{Gd–Ho}$) magnetization and susceptibility measurements were conducted. YAl_5Pt_3 is Pauli-paramagnetic while all other compounds are Curie paramagnets with the RE atoms in the trivalent oxidation state. For $M = \text{Nd}, \text{Gd–Ho}$, antiferromagnetic ordering was observed. Since YAl_5Pt_3 was obtained as phase pure material ^{27}Al MAS NMR investigations were conducted. Five signals were observed, in line with the five crystallographic Al positions in the structure. Also, XPS measurements were conducted on this compound to gain an insight into the charge distribution. However, XPS cannot come up with this task due to the oxidation of the surface and the subsurface bulk. Finally, quantum-chemical calculations supported the NMR measurements and gave an insight into the chemical bonding and the expected charge distribution with the Pt atoms being the formal anions while the Y and Al atoms are cationic in nature.

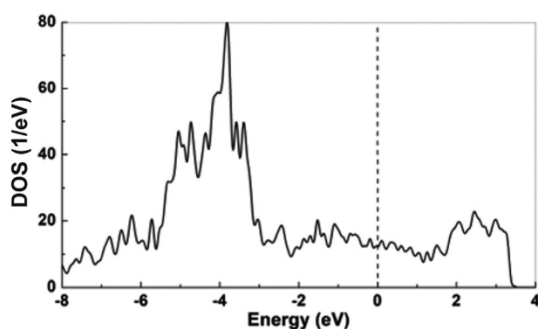


Fig. 8 Total density of states of YAl_5Pt_3 from non-spin-polarized DFT calculation, dotted line indicates the Fermi level.

Author contributions

All authors have accepted responsibility for the entire content of this submitted manuscript and approved the submission.

Data availability

The data supporting this article have been included as part of the ESI.† Crystallographic data for ErAl_5Pt_3 has been deposited at The Cambridge Crystallographic Data Centre (CCDC) under 2349082.†



Conflicts of interest

The authors declare no conflicts of interest regarding this article.

Acknowledgements

Instrumentation and technical assistance for this work were provided by the Service Center X-ray Diffraction, with financial support from Saarland University and German Research Foundation (project numbers INST 256/506-1 and INST 256/349-1) and by the Service Center NMR with financial support from Saarland University and German Research Foundation DFG (project number INST 256/384-1). The magnetometer was funded by the German Science Foundation DFG through INST 211/1034-1. Funding is provided by the Deutsche Forschungsgemeinschaft DFG (JA 1891-10-1, INST 211/1034-1, INST 256/349-1 and INST 256/506-1) and partially by the Collaborative Research Center CRC/SFB 1027. All DFT calculations used Expanse at SDSC through allocation CHE210062 from the Advanced Cyberinfrastructure Coordination Ecosystem: Services & Support (ACCESS) program, which is supported by National Science Foundation grants #2138259, #2138286, #2138307, #2137603, and #2138296.

References

- J. Jensen and A. R. Mackintosh, *Rare earth magnetism: Structures and excitations*, Clarendon Press, Oxford, 1991.
- H. Lueken, *Magnetochemie*, B. G. Teubner, Stuttgart, Leipzig, 1999.
- J. H. van Vleck, *The Theory Of Electric And Magnetic Susceptibilities*, Oxford At The Clarendon Press, 1932.
- H. Bärnighausen and G. Brauer, *Acta Crystallogr.*, 1962, **15**, 1059.
- R. Rau, *Acta Crystallogr.*, 1966, **20**, 716–723.
- F. F. Y. Wang, *Phys. Status Solidi*, 1966, **14**, 189–192.
- F. L. Carter, *J. Solid State Chem.*, 1972, **5**, 300–313.
- N. Lossau, H. Kierspel, J. Langen, W. Schlabbitz, D. Wohlleben, A. Mewis and C. Sauer, *Z. Phys. B: Condens. Matter*, 1989, **74**, 227–232.
- K. H. J. Buschow and H. J. Vandall, *Solid State Commun.*, 1970, **8**, 363–365.
- K. H. Mader and W. M. Swift, *J. Phys. Chem. Solids*, 1968, **29**, 1759–1764.
- O. Sichevych, Y. Prots, Y. Utsumi, L. Akselrud, M. Schmidt, U. Burkhardt, M. Coduri, W. Schnelle, M. Bobnar, Y.-T. Wang, Y.-H. Wu, K.-D. Tsuei, L. H. Tjeng and Y. Grin, *Inorg. Chem.*, 2017, **56**, 9343–9352.
- U. B. Paramanik, Anupam, U. Burkhardt, R. Prasad, C. Geibel and Z. Hossain, *J. Alloys Compd.*, 2013, **580**, 435–441.
- O. Niehaus, U. C. Rodewald, P. M. Abdala, R. S. Touzani, B. P. T. Fokwa and O. Janka, *Inorg. Chem.*, 2014, **53**, 2471–2480.
- M. B. Gamza, R. Gumeniuk, U. Burkhardt, W. Schnelle, H. Rosner, A. Leithe-Jasper and A. Ślebarski, *Phys. Rev. B*, 2017, **95**, 165142.
- B. C. Sales and R. Viswanathan, *J. Low Temp. Phys.*, 1976, **23**, 449–467.
- E. R. Bauminger, D. Froindlich, I. Nowik, S. Ofer, I. Felner and I. Mayer, *Phys. Rev. Lett.*, 1973, **30**, 1053–1056.
- D. C. Koskenmaki and K. A. Gschneidner, *Handbook on the Physics and Chemistry of Rare Earths*, 1978, vol. 1, pp. 337–377.
- M. Akihiro, M. Shigeki, U. Masafumi, W. Hirofumi, M. Kazuyuki, U. Yoshiya, M. Masaichiro, K. Naomi, N. Kiyofumi, H. Naohisa, O. Yasuo and I. Naoki, *J. Phys.: Condens. Matter*, 2018, **30**, 105603.
- R. S. Kumar, A. Svane, G. Vaitheeswaran, V. Kanchana, E. D. Bauer, M. Hu, M. F. Nicol and A. L. Cornelius, *Phys. Rev. B: Condens. Matter Mater. Phys.*, 2008, **78**, 075117.
- X. Tan, G. Fabbri, D. Haskel, A. A. Yaroslavlsev, H. Cao, C. M. Thompson, K. Kovnir, A. P. Menushenkov, R. V. Chernikov, V. O. Garlea and M. Shatruk, *J. Am. Chem. Soc.*, 2016, **138**, 2724–2731.
- D. T. Adroja, B. D. Rainford, J. M. de Teresa, A. del Moral, M. R. Ibarra and K. S. Knight, *Phys. Rev. B: Condens. Matter Mater. Phys.*, 1995, **52**, 12790–12797.
- I. Felner and I. Nowik, *Phys. Rev. B: Condens. Matter Mater. Phys.*, 1986, **33**, 617–619.
- I. Felner, I. Nowik, D. Vaknin, U. Potzel, J. Moser, G. M. Kalvius, G. Wortmann, G. Schmiester, G. Hilscher, E. Gratz, C. Schmitzer, N. Pillmayr, K. G. Prasad, H. de Waard and H. Pinto, *Phys. Rev. B: Condens. Matter Mater. Phys.*, 1987, **35**, 6956–6963.
- H. Müller, E. Bauer, E. Gratz, K. Yoshimura, T. Nitta and M. Mekata, *J. Magn. Magn. Mater.*, 1988, **76**, 159–160.
- E. V. Sampathkumaran, L. C. Gupta, R. Vijayaraghavan, K. V. Gopalakrishnan, R. G. Pillay and H. G. Devare, *J. Phys. C: Solid State Phys.*, 1981, **14**, L237.
- M. Croft, J. A. Hodges, E. Kemly, A. Krishnan, V. Murgai and L. C. Gupta, *Phys. Rev. Lett.*, 1982, **48**, 826–829.
- L. Fournes, B. Chevalier, B. Lloret and J. Etourneau, *Z. Phys. B: Condens. Matter*, 1989, **75**, 501–505.
- C. U. Segre, M. Croft, J. A. Hodges, V. Murgai, L. C. Gupta and R. D. Parks, *Phys. Rev. Lett.*, 1982, **49**, 1947–1950.
- M. Radzieowski, F. Stegemann, T. Block, J. Stahl, D. Johrendt and O. Janka, *J. Am. Chem. Soc.*, 2018, **140**, 8950–8957.
- F. Stegemann, J. Stahl, M. Bartsch, H. Zacharias, D. Johrendt and O. Janka, *Chem. Sci.*, 2019, **10**, 11086–11094.
- O. Janka, O. Niehaus, R. Pöttgen and B. Chevalier, *Z. Naturforsch.*, 2016, **71b**, 737–764.
- R. Pöttgen and B. Chevalier, *Z. Naturforsch.*, 2015, **70b**, 289–304.



- 33 R. Pöttgen and B. Chevalier, *Z. Naturforsch.*, 2015, **70b**, 695–704.
- 34 R. Pöttgen, O. Janka and B. Chevalier, *Z. Naturforsch.*, 2016, **71b**, 165–191.
- 35 S. F. Matar, *Prog. Solid State Chem.*, 2013, **41**, 55–85.
- 36 S. Gupta and K. G. Suresh, *J. Alloys Compd.*, 2015, **618**, 562–606.
- 37 S. Engel, E. C. J. Giebelmann, R. Pöttgen and O. Janka, *Rev. Inorg. Chem.*, 2023, **43**, 571–582.
- 38 S. Engel, E. C. J. Giebelmann, M. K. Reimann, R. Pöttgen and O. Janka, *ACS Org. Inorg. Au*, 2024, **4**, 188–222.
- 39 S. Engel, J. Bönnighausen, F. Stegemann, R. S. Touzani and O. Janka, *Z. Naturforsch.*, 2022, **77**, 367–379.
- 40 A. I. Tursina, N. G. Bukhan'ko, A. V. Gribov, V. A. Shchelkunov and Y. V. Nelyubina, *Acta Crystallogr., Sect. E: Struct. Rep. Online*, 2005, **E61**, i285–i286.
- 41 T. Koizumi, F. Honda, Y. J. Sato, D. Li, D. Aoki, Y. Haga, J. Gouchi, S. Nagasaki, Y. Uwatoko, Y. Kaneko and Y. Ōnuki, *J. Phys. Soc. Jpn.*, 2022, **91**, 043704.
- 42 R. Pöttgen, T. Gulden and A. Simon, *GIT Labor-Fachz.*, 1999, **43**, 133–136.
- 43 *Topas, Version 5 Version 5*, Bruker AXS Inc., Karlsruhe (Germany), 2014.
- 44 J. Bönnighausen, S. Seidel, S. Klenner and R. Pöttgen, *Z. Kristallogr.*, 2021, **236**, 293–300.
- 45 D. Langen, Dissertation, Universität zu Köln, 1997.
- 46 G. M. Sheldrick, SADABS University of Göttingen, Germany, 1996.
- 47 P. J. Becker and P. Coppens, *Acta Crystallogr., Sect. A: Cryst. Phys., Diffr., Theor. Gen. Crystallogr.*, 1974, **30**, 129–147.
- 48 *Topspin Version 2.1*, Bruker Corp., Karlsruhe, 2008.
- 49 D. Massiot, F. Fayon, M. Capron, I. King, S. Le Calvé, B. Alonso, J.-O. Durand, B. Bujoli, Z. Gan and G. Hoatson, *Magn. Reson. Chem.*, 2002, **40**, 70–76.
- 50 P. E. Blöchl, *Phys. Rev. B: Condens. Matter Mater. Phys.*, 1994, **50**, 17953–17979.
- 51 G. Kresse and D. Joubert, *Phys. Rev. B: Condens. Matter Mater. Phys.*, 1999, **59**, 1758–1775.
- 52 G. Kresse and J. Furthmüller, *Phys. Rev. B: Condens. Matter Mater. Phys.*, 1996, **54**, 11169–11186.
- 53 G. Kresse and J. Furthmüller, *Comput. Mater. Sci.*, 1996, **6**, 15–50.
- 54 J. P. Perdew, K. Burke and M. Ernzerhof, *Phys. Rev. Lett.*, 1996, **77**, 3865–3868.
- 55 E. Sanville, S. D. Kenny, R. Smith and G. Henkelman, *J. Comput. Chem.*, 2007, **28**, 899–908.
- 56 G. Henkelman, A. Arnaldsson and H. Jónsson, *Comput. Mater. Sci.*, 2006, **36**, 354–360.
- 57 W. Tang, E. Sanville and G. Henkelman, *J. Phys.: Condens. Matter*, 2009, **21**, 084204.
- 58 O. K. Andersen, R. W. Tank and O. Jepsen, *TB-LMTO-ASA version 4.7*, Max-Planck-Institut für Festkörperforschung, Stuttgart (Germany), 1998.
- 59 D. D. Koelling and B. N. Harmon, *J. Phys. C: Solid State Phys.*, 1977, **10**, 3107.
- 60 W. R. L. Lambrecht and O. K. Andersen, *Phys. Rev. B: Condens. Matter Mater. Phys.*, 1986, **34**, 2439–2449.
- 61 L. G. Akselrud, V. I. Yarovets, O. I. Bodak, Y. P. Yarmolyuk and E. I. Gladyshevskii, *Kristallografiya*, 1976, **21**, 383–386.
- 62 A. I. Tursina, E. V. Murashova, H. Noël, N. G. Bukhan'ko and Y. D. Seropegin, *Intermetallics*, 2009, **17**, 780–783.
- 63 J. Comer, *Acta Crystallogr.*, 1964, **17**, 444–445.
- 64 M. Ellner, U. Kattner and B. Predel, *J. Less-Common Met.*, 1982, **87**, 305–325.
- 65 L. Palatinus and G. Chapuis, *J. Appl. Crystallogr.*, 2007, **40**, 786–790.
- 66 V. Petříček, M. Dušek and L. Palatinus, *Jana2006. The crystallographic computing system Institute of Physics, Praha (Czech Republic)*, 2006.
- 67 V. Petříček, M. Dušek and L. Palatinus, *Z. Kristallogr.*, 2014, **229**, 345–352.
- 68 P. Villars and K. Cenzual, *Pearson's Crystal Data: Crystal Structure Database for Inorganic Compounds release 2023/24*, ASM International®, Materials Park, Ohio, USA, 2023.
- 69 N. Zaremba, M. Krnel, Y. Prots, M. König, L. Akselrud, Y. Grin and E. Svanidze, *Inorg. Chem.*, 2024, **63**, 4566–4573.
- 70 V. B. Compton and B. T. Matthias, *Acta Crystallogr.*, 1959, **12**, 651–654.
- 71 T. M. Gumenyuk, Y. B. Kuz'ma and B. M. Stel'makhovich, *J. Alloys Compd.*, 2000, **299**, 213–216.
- 72 B. Erdmann and C. Keller, *J. Solid State Chem.*, 1973, **7**, 40–48.
- 73 J. Emsley, *The Elements*, Clarendon Press, Oxford University Press, Oxford, New York, 1998.
- 74 A. E. Dwight, *J. Less-Common Met.*, 1984, **102**, L9–L13.
- 75 M. Radzieowski, F. Stegemann, C. Doerenkamp, S. F. Matar, H. Eckert, C. Dosche, G. Wittstock and O. Janka, *Inorg. Chem.*, 2019, **58**, 7010–7025.
- 76 V. M. T. Thiede, B. Fehrmann and W. Jeitschko, *Z. Anorg. Allg. Chem.*, 1999, **625**, 1417–1425.
- 77 F. Eusermann, S. Gausebeck, C. Dosche, M. Haensch, G. Wittstock and O. Janka, *Crystals*, 2018, **8**, 169.
- 78 C. Benndorf, F. Stegemann, H. Eckert and O. Janka, *Z. Naturforsch.*, 2015, **70b**, 101–110.
- 79 S. Engelbert and O. Janka, *Intermetallics*, 2018, **96**, 84–89.
- 80 C. Benndorf, H. Eckert and O. Janka, *Dalton Trans.*, 2017, **46**, 1083–1092.
- 81 K. Schubert, W. Burkhardt, P. Esslinger, E. Günzel, H. G. Meissner, W. Schütt, J. Wegst and M. Wilkens, *Naturwissenschaften*, 1956, **43**, 248–249.
- 82 K. Schubert, H. Breimer, W. Burkhardt, E. Günzel, R. Haufler, H. L. Lukas, H. Vetter, J. Wegst and M. Wilkens, *Naturwissenschaften*, 1957, **44**, 229–230.
- 83 E. Zintl, A. Harder and W. Haucke, *Z. Phys. Chem., Abt. B*, 1937, **35**, 354–362.
- 84 A. W. Hull, *Phys. Rev.*, 1917, **10**, 661–696.
- 85 A. W. Hull, *Trans. Am. Inst. Electr. Eng.*, 1919, **38**, 1445–1466.



- 86 E. O. Wollan and W. C. Koehler, *Phys. Rev.*, 1955, **100**, 545–563.
- 87 M. Giovannini, H. Michor, E. Bauer, G. Hilscher, P. Rogl and R. Ferro, *J. Alloys Compd.*, 1998, **280**, 26–38.
- 88 I. R. Fisher, Z. Islam and P. C. Canfield, *J. Magn. Magn. Mater.*, 1999, **202**, 1–10.
- 89 Y. Tyvanchuk, S. Baran, T. Jaworska-Gołąb, R. Duraj, Y. M. Kalychak and A. Szytuła, *Acta Phys. Pol., A*, 2012, **121**, 678–681.
- 90 C. Benndorf, H. Eckert and O. Janka, *Acc. Chem. Res.*, 2017, **50**, 1459–1467.
- 91 C. Benndorf, O. Niehaus, H. Eckert and O. Janka, *Z. Anorg. Allg. Chem.*, 2015, **641**, 168–175.
- 92 S. Engel, E. C. J. Gieselmann, L. E. Schank, G. Heymann, K. Brix, R. Kautenburger, H. P. Beck and O. Janka, *Inorg. Chem.*, 2023, **62**, 4260–4271.
- 93 E. C. J. Gieselmann, S. Engel, J. Baldauf, J. Kösters, S. F. Matar, G. Kickelbick and O. Janka, *Inorg. Chem.*, 2024, **63**, 8180–8193.
- 94 F. Stegemann, C. Benndorf, T. Bartsch, R. S. Touzani, M. Bartsch, H. Zacharias, B. P. T. Fokwa, H. Eckert and O. Janka, *Inorg. Chem.*, 2015, **54**, 10785–10793.
- 95 F. Stegemann, C. Benndorf, Y. Zhang, M. Bartsch, H. Zacharias, B. P. T. Fokwa, H. Eckert and O. Janka, *Inorg. Chem.*, 2017, **56**, 1919–1931.
- 96 F. Stegemann, C. Benndorf, Y. Zhang, M. Bartsch, H. Zacharias, B. P. T. Fokwa, H. Eckert and O. Janka, *Z. Anorg. Allg. Chem.*, 2017, **643**, 1379–1390.
- 97 C. Benndorf, F. Stegemann, S. Seidel, L. Schubert, M. Bartsch, H. Zacharias, B. Mausolf, F. Haarmann, H. Eckert, R. Pöttgen and O. Janka, *Chem. – Eur. J.*, 2017, **23**, 4187–4196.
- 98 J. F. Moulder, W. F. Stickle, P. E. Sobol and K. D. Bomben, *Handbook of X-Ray Photoelectron Spectroscopy*, Physical Electronics, Minnesota, 1995.
- 99 I. Antonyshyn, O. Sichevych, U. Burkhardt, A. M. Barrios Jiménez, A. Melendez-Sans, Y.-F. Liao, K.-D. Tsuei, D. Kasinathan, D. Takegami and A. Ormeci, *Phys. Chem. Chem. Phys.*, 2023, **25**, 31137–31145.
- 100 J. Heinrich, R. Busch, F. Müller, S. Grandthyll and S. Hüfner, *Appl. Phys. Lett.*, 2012, **100**, 071909.
- 101 *NIST X-ray Photoelectron Spectroscopy Database, NIST Standard Reference Database Number 20*, National Institute of Standards and Technology, Gaithersburg MD, 20899, 2000, (retrieved Dec. 17th 2023), DOI: [10.18434/T4T88K](https://doi.org/10.18434/T4T88K).



3. Trivalent members of the $RE_2Al_{16}Pt_9$ series adopting the $Ce_2Al_{16}Pt_9$ type structure

Collaborations to disclose: In this chapter the trivalent compound of the paper “New alkaline earth and rare earth representatives adopting the $Ce_2Al_{16}Pt_9$ type structure” are summarized (*Z. Naturforsch.* **2024**, *79b*, 12, 595-603). PD Dr. O. Janka is a coworker on the manuscript.

The trivalent compounds crystallize in analogy to the divalent phases in the $Ce_2Al_{16}Pt_9$ type structure in the orthorhombic crystal system with space group *Immm*. The lattice parameters are summarized in **Table 3.12**. When the unit cell volume vs ionic radii of the *RE* element is plotted, the trend of smaller unit cell volumes the later the *RE* element is observable. Bulk samples were prepared by using the elements in the arc furnace, the resulting samples were analyzed by PXRD measurements with exemplary the Rietveld-refinement of $La_2Al_{16}Pt_9$, as shown in **Figure 3.46**.

The synthesis resulted in no X-ray pure samples, but in a mixture of $La_2Al_{16}Pt_9$ ($Ce_2Al_{16}Pt_9$ type, *Immm*, $a = 416.919(9)$, $b = 1190.69(2)$, $c = 1825.10(3)$ pm)¹⁷⁴ as main phase with the corresponding $LaAl_5Pt_3$ (YNi_5Si_3 type, *Pnma*, $a = 2069.5(5)$, $b = 415.96(9)$, $c = 731.1(2)$ pm)¹⁷² phase and Al_3Pt_2 (Al_3Ni_2 type, $P\bar{3}m1$, $a = 420.93(7)$, $c = 517.0(1)$ pm)¹⁹⁹ as side phases. To improve the phase purity heat treatments were performed, resulting in an increase in the amount of the side phases suggesting that the $La_2Al_{16}Pt_9$ phase is decomposing peritectically into $LaAl_5Pt_3$ and Al_3Pt_2 . **Table 3.13** shows the composition change of $LaAl_5Pt_3$ and $La_2Al_{16}Pt_9$ before and after the annealing step. Single crystal studies of the La compound were conducted, resulting in an isotopic variant of $Ce_2Al_{16}Pt_9$ with a mixture of the Al5 position with 0.05% Pt, so that the structure was determined to be $La_2Al_{15.95(1)}Pt_{9.05(1)}$. Additionally, to the PXRD measurements, SEM/EDX analysis were performed the results are summarized in **Table 3.14**. The EDX data shows a good agreement of the *RE* values of ~ 7 to the ideal 7.4, but in case of the other elements, a difference in the measured amount compared to the ideal values are observable. In all cases the Al amount is lower, whereas the platinum value is increased. This could be caused by the rough surface and non-optimal orientation of the crystallites to the electron beam, or that the Pt reabsorbs the X-ray radiation from the Al. SEM images of the measured samples are shown in **Figure 3.47**.

The structure is shown above using the isotopic Sr compound in **Figure 3.9** and **3.10** and exhibits five crystallographically independent Al positions, which should have different NMR shifts depending on the coordination environment. Due to the side phases with equally many

Al positions no ^{27}Al NMR spectra were measured as well as no magnetic measurements were conducted.

The similar atomic distances of the Al–Al, Al–Pt and Pt–Pt in all compounds compared to the Sr compound, suggest the existence of the $[\text{Al}_{16}\text{Pt}_9]^{6-}$ polyanionic network in which the cationic RE atoms reside. When comparing the Al–Al, Al–Pt and Pt–Pt distances inside the series of compounds, two structures exhibit different distances, for the powdered samples of La–Nd, Sm, Gd the interatomic distances are in good agreement. When looking at the Al–Al distances of the Al2–Al2 the La and Gd compounds exhibit larger distances compared to the other phases in the series, which can be explained by the fact that the Al2 atoms in the La containing compound is neighboring the mixed occupied Al5/Pt5 position leading to a shift in the atomic coordinates. After reevaluating the occupancy of the Al positions in the Gd structure, an occupancy value of 1.6 was observed, concluding that the Al5 position is like in the case of the La compound mixed occupied with Pt. The refinement led to an occupancy of Al:Pt 90:10.

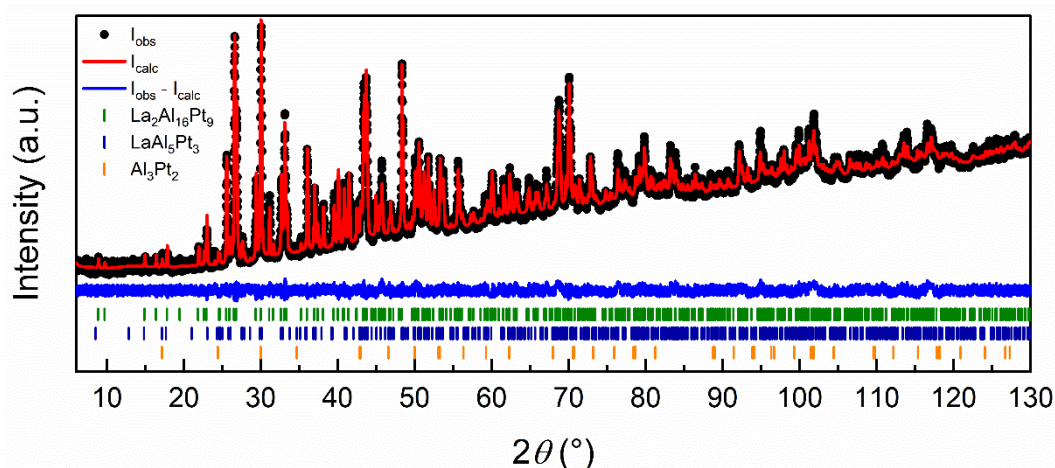


Figure 3.46: Rietveld refinement of the powder X-ray diffraction pattern of $\text{La}_2\text{Al}_{16}\text{Pt}_9$. Collected data are shown in black dots, refinement as red and the difference as blue line. Olive ticks indicate the Bragg positions of $\text{La}_2\text{Al}_{16}\text{Pt}_9$ ($\text{Ce}_2\text{Al}_{16}\text{Pt}_9$ type, $Immm$), royal blue of LaAl_5Pt_3 (YNi_5Si_3 type, $Pnma$) and orange ticks the Bragg positions of Al_3Pt_2 (Al_3Ni_2 type, $P\bar{3}m1$) respectively.

Table 3.12: Lattice parameters of the trivalent members of the $RE_2Al_{16}Pt_9$ series ($RE = La-Nd, Sm, Gd, Ce_2Al_{16}Pt_9$ type, $Immm, Z = 2$)

Compound	a (pm)	b (pm)	c (pm)	V (nm ³)
$La_2Al_{16}Pt_9^{P,*}$	416.92(1)	1190.68(1)	1825.09(2)	0.9060
$La_{2.05}Al_{16}Pt_9^{P,*}$	416.99(1)	1190.72(2)	1825.27(2)	0.9063
$La_2Al_{15.95(1)}Pt_{9.05(1)}^{SC,*}$	416.35(1)	1190.49(10)	1820.72(18)	0.9025
$Ce_2Al_{16}Pt_9^{P,*}$	416.10(1)	1189.26(1)	1821.41(2)	0.9013
$Ce_2Al_{16}Pt_9^{L,173}$	415.97	1191.0	1818.6	0.9010
$Pr_2Al_{16}Pt_9^{P,*}$	415.52(1)	1190.18(3)	1818.45(4)	0.8992
$Nd_2Al_{16}Pt_9^{P,*}$	414.84(1)	1186.53(3)	1820.72(4)	0.8962
$Sm_2Al_{16}Pt_9^{P,*}$	413.84(1)	1187.99(2)	1816.10(3)	0.8929
$Gd_2Al_{16}Pt_9^{P,*}$	412.80(1)	1186.15(2)	1816.85(3)	0.8896

^L: Literature, *: own work, ^P: powder data, ^{SC}: single crystal data

Table 3.13: Phase composition change of the $La_2Al_{16}Pt_9$ and $LaAl_5Pt_3$ phases before and after the 12 d at 1123 K annealing step. Only the changes of $La_2Al_{16}Pt_9$ and $LaAl_5Pt_3$ are shown.

Phase	$La_2Al_{16}Pt_9$ arc-melted	$La_2Al_{16}Pt_9$ annealed	$LaAl_5Pt_3$ arc-melted	$LaAl_5Pt_3$ annealed
$LaAl_5Pt_3$	5.6	9.9	65.1	70.1
$La_2Al_{16}Pt_9$	94.4	90.1	34.9	29.9

Table 3.14: EDX data of trivalent members of the $RE_2Al_{16}Pt_9$ series ($RE = La, Ce, Pr, Nd, Sm, Gd$) with standard deviations of ± 2 at.-%.

Compound	Ideal	P1	P2	P3	mean
$La_2Al_{16}Pt_9$	La: 7.4	7	7	8	7
	Al: 59.3	49	59	55	54
	Pt: 33.3	44	34	38	39
$Ce_2Al_{16}Pt_9$	Ce: 7.4	7	7	7	7
	Al: 59.3	57	61	56	58
	Pt: 33.3	36	32	37	35
$Pr_2Al_{16}Pt_9$	Pr: 7.4	8	7	8	7
	Al: 59.3	52	54	52	53
	Pt: 33.3	40	39	40	40
$Nd_2Al_{16}Pt_9$	Nd: 7.4	8	7	8	8
	Al: 59.3	54	61	54	56
	Pt: 33.3	38	32	38	36
$Sm_2Al_{16}Pt_9$	Sm: 7.4	8	9	8	8
	Al: 59.3	54	56	54	55
	Pt: 33.3	38	35	38	37
$Gd_2Al_{16}Pt_9$	Gd: 7.4	7	7	6	7
	Al: 59.3	56	59	59	56
	Pt: 33.3	37	34	35	35

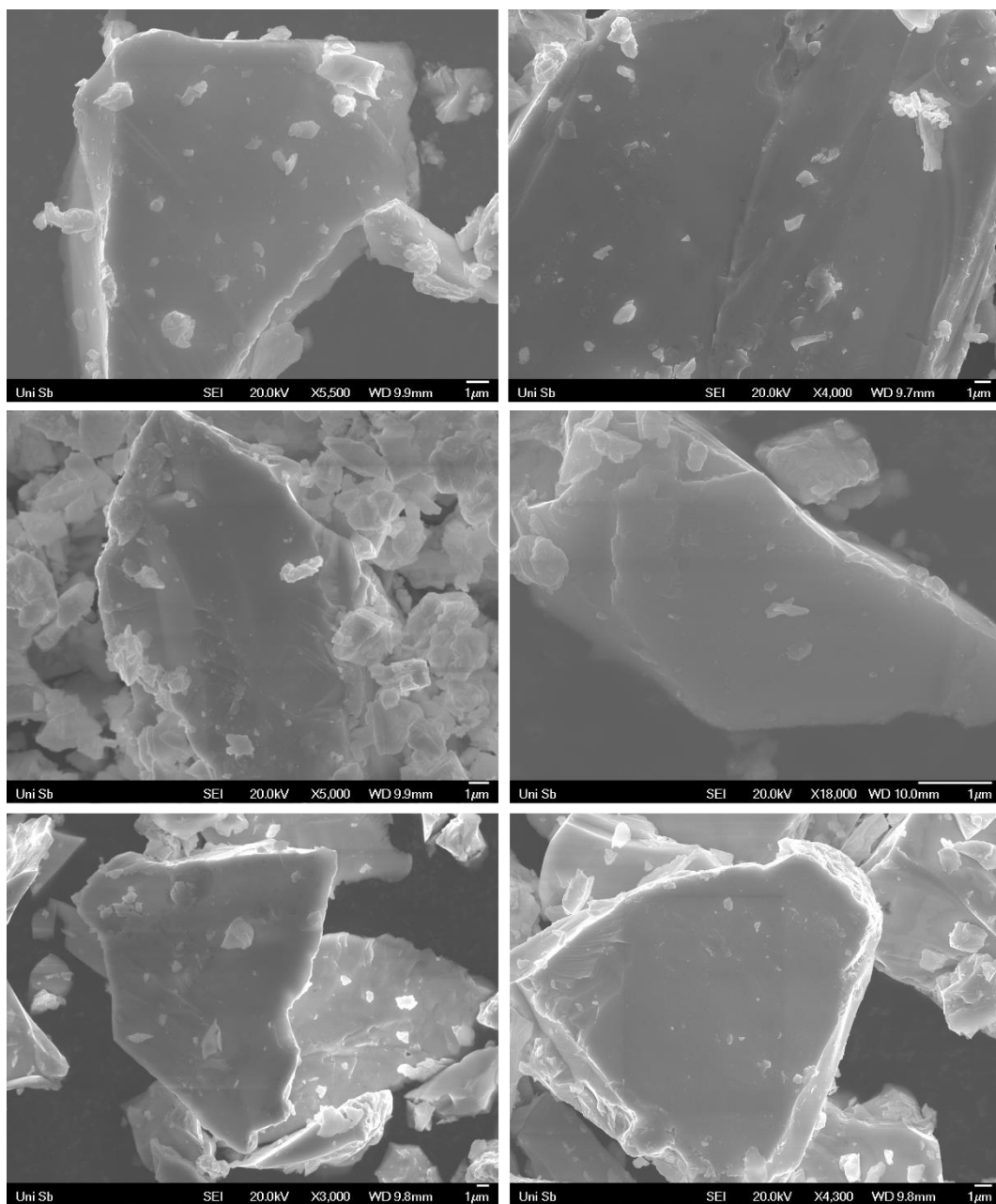


Figure 3.47: Scanning electron microscopy images of the trivalent member of the $RE_2Al_{16}Pt_9$ series ($RE = La$ (top left), Ce (top right), Pr (middle left), Nd (middle right), Sm (bottom left), Gd (bottom right)).

Stefan Engel and Oliver Janka*

New alkaline earth and rare earth representatives adopting the $\text{Ce}_2\text{Al}_{16}\text{Pt}_9$ -type structure

<https://doi.org/10.1515/znb-2024-0022>

Received March 28, 2024; accepted May 10, 2024

Abstract: The $M_2\text{Al}_{16}\text{Pt}_9$ series with $M = \text{Ca}, \text{La-Nd}$ and Sm-Gd was synthesized from the elements in analogy to the literature known compounds $\text{Ce}_2\text{Al}_{16}\text{Pt}_9$ and $\text{Sr}_2\text{Al}_{16}\text{Pt}_9$. All compounds crystallize in the orthorhombic crystal system with space group $Immm$ and have been characterized by powder X-ray diffraction. For $\text{La}_2\text{Al}_{16}\text{Pt}_9$ and $\text{Eu}_2\text{Al}_{16}\text{Pt}_9$ also single-crystal investigations have been conducted. In all cases, Al_3Pt_2 as well as the members of the $RE\text{Al}_5\text{Pt}_3$ series (YNi_5Si_3 type, space group $Pnma$) have been observed as side phases. Annealing led in all cases to an increase of the side phases, suggesting that the title compounds decompose peritectically. In the crystal structures, polyanionic $[\text{Al}_y\text{Pt}_z]^{6-}$ networks can be found with large fourfold capped hexagonal prismatic cavities ($M@[\text{Al}_6\text{Pt}_6\text{Al}_4]$), which host the respective M atoms. As seen from the unit cell volumes, the $\text{La-Nd}, \text{Sm}$ and Gd compounds exhibit a formally trivalent oxidation state while the Ca and Eu atoms in $\text{Ca}_2\text{Al}_{16}\text{Pt}_9$ and $\text{Eu}_2\text{Al}_{16}\text{Pt}_9$ are divalent.

Keywords: rare earth elements; platinum; aluminum; intermetallics

1 Introduction

Ternary compounds of the noble metals, aluminum and an element with a low electronegativity such as alkali, alkaline earth or rare earth elements exhibit a wide plethora of different chemical compositions and structures. Within the last decade, we have reported on numerous new compounds and interestingly, especially the heavy noble metals Ir, Au and Pt seem to form a manifold of different structures. Though magnetically rather uninteresting, compounds of

the alkaline earth elements as well as $\text{Sc}, \text{Y}, \text{La}$ and Lu (M) allow for solid-state MAS-NMR spectroscopic investigations on the ^{27}Al nucleus¹ and are quantum-chemically easier to address due to the closed valence shells of the constituent elements. This enables studies of the electron transfer in these compounds, both from an experimental and a theoretical point of view. In pretty much all cases, where the sum of transition metal T plus aluminum is larger than the M element, polyanionic $[\text{Al}_y\text{T}_z]^{6-}$ networks are formed which exhibit cavities that host the M atoms. The degree of charge transfer in these compounds depends on the electronegativity/electron affinity of M and T .

The first investigations that were conducted by our group focused on the $RE\text{Al}_2\text{T}_5$ members (ZrAl_5Ni_2 type, space group $I4/mmm$) with $RE = \text{Y}$ and Lu and $T = \text{Pd}$ and Pt .² Later, the significantly larger $RE_{10}\text{Al}_3\text{T}$ ($\text{Y}_{10}\text{Cd}_3\text{Ru}$ type, $RE = \text{Y}, \text{Ho}, \text{Tm}, \text{Lu}$; $T = \text{Fe}, \text{Co}, \text{Ni}, \text{Ru}, \text{Rh}, \text{Pd}, \text{Os}, \text{Ir}, \text{Pt}$, space group $P6/mmm$) series allowed a deeper insight via ^{27}Al NMR spectroscopy.³ Amongst the alkaline earth members, however, in numerous cases only singular compounds were observed, e.g. CaAl_3Pd_2 (YAl_3Ni_2 type, space group $P6/mmm$),⁴ $\text{Sr}_2\text{Al}_5\text{Pd}_4$ (own type, space group $Pnma$)⁵ or SrAl_2Pt_3 (CeCo_3B_2 type, space group $P6/mmm$) and Sr_2AlPd_2 (Ca_2GePd_2 type, space group $Fdd2$),⁶ $\text{Ba}_6\text{Al}_{53}\text{Pt}_{22}$ (own type, space group $P6_3/mcm$)⁷ and $\text{Ba}_3\text{Al}_4\text{Pt}_4$ (own type, space group $Cmcm$).⁸ A small series was finally found for the orthorhombic MgCuAl_2 type compounds of the MAl_2Pt series with $M = \text{Ca}, \text{Sr}, \text{Ba}$ and Eu .⁹ This series interestingly significantly extends to the rare earth elements and other transition metals.¹⁰

Recently, we reported on SrAl_5Pt_3 and $\text{Sr}_2\text{Al}_{16}\text{Pt}_9$,¹¹ which are isostructural to CeAl_5Pt_3 (YNi_5Si_3 type, space group $Pnma$)¹² and $\text{Ce}_2\text{Al}_{16}\text{Pt}_9$ (own type, space group $Immm$).¹³ In 2022, Ōnuki already reported on EuAl_5Pt_3 , which shows abrupt changes in its electronic states under pressure¹⁴ and in late 2023, further members of the $RE\text{Al}_5\text{Pt}_3$ series ($RE = \text{La-Nd}, \text{Eu-Tm}$) were reported and investigated with respect to their physical properties.¹⁵ Therefore, the question arose if other members of the potential $RE_2\text{Al}_{16}\text{Pt}_9$ series might exist. Since Sr is formally divalent and the cerium compound is also known, it should be possible to synthesize and investigate at least the members with the early (and therefore large) rare earth elements. In this paper we report on the synthesis and crystal structure of the $M_2\text{Al}_{16}\text{Pt}_9$ series which could be established for $M = \text{Ca}, \text{La-Nd}$ and Sm-Gd .

Dedicated to Professor Hubert Schmidbaur on the Occasion of his 90th Birthday.

*Corresponding author: **Oliver Janka**, Inorganic Solid State Chemistry, Saarland University, Campus C4.1, 66123 Saarbrücken, Germany, E-mail: oliver.janka@uni-saarland.de

Stefan Engel, Inorganic Solid State Chemistry, Saarland University, Campus C4.1, 66123 Saarbrücken, Germany, E-mail: stefan.engel@uni-saarland.de

2 Experimental

2.1 Synthesis

Ingots of the rare earth elements or calcium (Onyxmet), platinum pieces (Agosi AG) and aluminum pieces (Onyxmet), all with stated purities above 99.5 % were used for the reported syntheses. Samples were prepared on a 150–200 mg scale. The rare earth pieces of La–Nd, Sm and Eu as well as Ca were stored under an argon atmosphere; surface contaminations on the pieces were removed mechanically in a dry box prior to the reaction. For all reactions, the elements were

arc-melted under an argon atmosphere of about 800 mbar.¹⁶ The argon gas was purified over a titanium sponge ($T = 873$ K), molecular sieves and silica gel prior to the use. For the synthesis of $\text{Ca}_2\text{Al}_{16}\text{Pt}_9$ and $\text{Eu}_2\text{Al}_{16}\text{Pt}_9$, a slight excess of Ca and Eu was used (nominal composition $M_{2.1}\text{Al}_{16}\text{Pt}_9$). The samples were heated to 873 K within 1 h and kept at the temperature for 31 d. Afterwards they were cooled to room temperature within 6 h. All samples possess a metallic luster while ground powders are grey and all samples are insensitive to air over a month.

2.2 X-ray diffraction

Powder X-ray diffraction (PXRD) patterns of the powdered samples were recorded at room temperature on a D8-A25-Advance diffractometer (Bruker, Karlsruhe, Germany) in Bragg-Brentano θ - θ geometry (goniometer radius 280 mm) with CuK_α radiation ($\lambda = 154.0596$ pm). A 12 μm Ni foil working as K_β filter and a variable divergence slit were mounted at the primary beam side. A LYNXEYE detector with 192 channels was used at the secondary beam side. Experiments were carried out in a 2θ range of 6–130° with a step size of 0.013° and a total scan time of 1 h. The recorded data was evaluated using the Bruker TOPAS 5.0 software¹⁷ using the fundamental parameter approach and the Rietveld method.^{18,19} Details of the refinements are listed in Tables 1–3.

Block-shaped crystallites of $\text{La}_2\text{Al}_{16}\text{Pt}_9$ and $\text{Eu}_2\text{Al}_{16}\text{Pt}_9$ were extracted from a crushed sample and investigated at room temperature on a Bruker X8 APEX2, Nonius κ -CCD diffractometer, operating with graphite-monochromatized MoK_α ($\lambda = 0.71073$ Å) radiation. Numerical absorption

Table 1: Compositions of the samples with a nominal composition of $M_2\text{Al}_{16}\text{Pt}_9$, refined from powder X-ray data using the Rietveld method. Both compositions of the as-cast as well as the annealed samples are given.

RE	Treatment	wt% ($RE_2\text{Al}_{16}\text{Pt}_9$)	wt% ($RE\text{Al}_5\text{Pt}_3$)	wt% (Al_3Pt_2)
Ca	As-cast	10.7(5)	74.1(5)	15.2(5)
La	As-cast	92.9(5)	4.6(5)	2.5(5)
	Annealed	88.5(5)	3.8(5)	7.7(5)
Ce	As-cast	94.3(5)	1.3(5)	4.4(5)
	Annealed	89.9(5)	4.2(5)	5.9(5)
Pr	As-cast	92.5(5)	2.9(5)	4.6(5)
	Annealed	87.9(5)	2.3(5)	9.8(5)
Nd	As-cast	85.9(5)	6.0(5)	8.1(5)
	Annealed	80.0(5)	9.9(5)	10.1(5)
Sm	As-cast	82.6(5)	10.6(5)	6.8(5)
	Annealed	81.2(5)	9.9(5)	8.9(5)
Eu	As-cast	88.3(5)	5.6(5)	6.1(5)
	Annealed	87.5(5)	2.6(5)	9.9(5)
Gd	As-cast	79.0(5)	10.1(5)	10.9(5)
	Annealed	77.2(5)	9.6(5)	13.2(5)

Table 2: Lattice parameters (X-ray powder, X-ray single-crystal and literature data), and unit cell volumes of $M_2\text{Al}_{16}\text{Pt}_9$ and selected structurally related compounds³.

Compound	CSD	a (pm)	b (pm)	c (pm)	V (nm ³)	Ref.
$\text{Ca}_2\text{Al}_{16}\text{Pt}_9^{\text{P}}$	2356797	414.02(1)	1181.6(2)	1830.4(3)	0.8954	*
$\text{Sr}_2\text{Al}_{16}\text{Pt}_9^{\text{SC}}$	2141827	416.69(2)	1193.53(6)	1832.38(9)	0.9113	11
$\text{Sr}_2\text{Al}_{16}\text{Pt}_9^{\text{P}}$	–	417.08(1)	1194.25(5)	1833.08(8)	0.9131	11
$\text{La}_2\text{Al}_{16}\text{Pt}_9^{\text{P}}$	2355075	416.92(1)	1190.68(1)	1825.09(2)	0.9060	*
$\text{La}_{2.05}\text{Al}_{16}\text{Pt}_9^{\text{P}}$	–	416.99(1)	1190.72(2)	1825.27(2)	0.9063	*
$\text{La}_2\text{Al}_{15.95(1)}\text{Pt}_{9.05(1)}^{\text{SC}}$	2343765	416.35(1)	1190.49(10)	1820.72(18)	0.9025	*
$\text{Ce}_2\text{Al}_{16}\text{Pt}_9^{\text{P}}$	2355903	416.10(1)	1189.26(1)	1821.41(2)	0.9013	*
$\text{Ce}_2\text{Al}_{16}\text{Pt}_9^{\text{SC}}$	–	415.97(9)	1191.0(3)	1818.6(4)	0.9010	13
$\text{Pr}_2\text{Al}_{16}\text{Pt}_9^{\text{P}}$	2355902	415.52(1)	1190.18(3)	1818.45(4)	0.8992	*
$\text{Nd}_2\text{Al}_{16}\text{Pt}_9^{\text{P}}$	2355901	414.84(1)	1186.53(3)	1820.72(4)	0.8962	*
$\text{Sm}_2\text{Al}_{16}\text{Pt}_9^{\text{P}}$	2355900	413.84(1)	1187.99(2)	1816.10(3)	0.8929	*
$\text{Eu}_2\text{Al}_{16}\text{Pt}_9^{\text{P}}$	2355898	416.67(1)	1189.76(1)	1827.87(2)	0.9061	*
$\text{Eu}_2\text{Al}_{16}\text{Pt}_9^{\text{SC}}$	2343483	416.08(2)	1187.98(5)	1823.92(8)	0.9016	*
$\text{Gd}_2\text{Al}_{16}\text{Pt}_9^{\text{P}}$	2355899	412.80(1)	1186.15(2)	1816.85(3)	0.8896	*

^aAbbreviations: *this work; ^Ppowder data; ^{SC}single-crystal data.

Table 3: Atomic coordinates of the $M_2Al_{16}Pt_9$ series ($M = Ca, La-Nd, Sm-Gd$; $Ce_2Al_{16}Pt_9$ type, space group $Im\bar{m}m$) refined from powder X-ray diffraction data.

Atom	x	y	z	Atom	x	y	z
$Ca_2Al_{16}Pt_9$				$La_2Al_{16}Pt_9$			
Ca	0	0	0.3237(2)	La	0	0	0.2285(2)
Pt1	0	0.3167(1)	0.3416(1)	Pt1	0	0.3123(1)	0.34063(8)
Pt2	1/2	0	0.3884(1)	Pt2	1/2	0	0.3755(1)
Pt3	0	0.2529(2)	1/2	Pt3	0	0.2508(2)	1/2
Pt4	0	0	0	Pt4	0	0	0
Al1	0	0.1115(6)	0.4059(7)	Al1	0	0.1117(8)	0.3960(7)
Al2	0	0.1856(8)	0.0674(6)	Al2	0	0.1651(9)	0.0755(6)
Al3	0	0.2982(6)	0.1751(4)	Al3	0	0.3115(9)	0.2076(5)
Al4	1/2	0	0.0194(7)	Al4	1/2	0	0.0890(8)
Al5	0	0.3534(11)	0	Al5	0	0.3759(12)	0
$Ce_2Al_{16}Pt_9$				$Pr_2Al_{16}Pt_9$			
Ce	0	0	0.2289(1)	Pr	0	0	0.2299(2)
Pt1	0	0.3124(1)	0.34130(7)	Pt1	0	0.3134(2)	0.34138(9)
Pt2	1/2	0	0.3747(1)	Pt2	1/2	0	0.3740(1)
Pt3	0	0.2529(2)	1/2	Pt3	0	0.2520(2)	1/2
Pt4	0	0	0	Pt4	0	0	0
Al1	0	0.1180(7)	0.3915(6)	Al1	0	0.1200(9)	0.3910(7)
Al2	0	0.1730(9)	0.0788(5)	Al2	0	0.1735(11)	0.0818(6)
Al3	0	0.3153(9)	0.2023(5)	Al3	0	0.3040(11)	0.2040(6)
Al4	1/2	0	0.0912(7)	Al4	1/2	0	0.0870(10)
Al5	0	0.3970(11)	0	Al5	0	0.3885(14)	0
$Nd_2Al_{16}Pt_9$				$Sm_2Al_{16}Pt_9$			
Nd	0	0	0.2296(2)	Sm	0	0	0.2277(2)
Pt1	0	0.3135(2)	0.34147(9)	Pt1	0	0.3134(2)	0.3401(1)
Pt2	1/2	0	0.3743(1)	Pt2	1/2	0	0.3741(1)
Pt3	0	0.2519(2)	1/2	Pt3	0	0.2523(2)	1/2
Pt4	0	0	0	Pt4	0	0	0
Al1	0	0.1208(9)	0.3930(7)	Al1	0	0.1284(10)	0.3846(7)
Al2	0	0.1721(11)	0.0817(6)	Al2	0	0.1686(13)	0.0834(7)
Al3	0	0.3035(11)	0.2032(5)	Al3	0	0.3145(13)	0.2067(6)
Al4	1/2	0	0.0875(9)	Al4	1/2	0	0.0954(10)
Al5	0	0.3869(14)	0	Al5	0	0.3995(17)	0
$Eu_2Al_{16}Pt_9$				$Gd_2Al_{16}Pt_9$			
Eu	0	0	0.2280(2)	Gd	0	0	0.2307(2)
Pt1	0	0.3087(2)	0.3417(9)	Pt1	0	0.3146(2)	0.3416(1)
Pt2	1/2	0	0.3768(1)	Pt2	1/2	0	0.3744(2)
Pt3	0	0.2537(2)	1/2	Pt3	0	0.2512(3)	1/2
Pt4	0	0	0	Pt4	0	0	0
Al1	0	0.1248(9)	0.3958(7)	Al1	0	0.1250(11)	0.3902(8)
Al2	0	0.1776(11)	0.0770(7)	Al2	0	0.1686(14)	0.0825(7)
Al3	0	0.3060(11)	0.2043(6)	Al3	0	0.3070(14)	0.2030(7)
Al4	1/2	0	0.0814(10)	Al4	1/2	0	0.0921(11)
Al5	0	0.3896(14)	0	Al5	0	0.3827(19)	0

corrections using the program SADABS²⁰ were applied to the data sets. The structures were solved and refined using SUPERFLIP²¹ and JANA2006.^{22–24} Tables 4–6 contain the refinement details.

Table 4: Crystallographic data and structure refinement for nominal La₂Al₁₆Pt₉ and Eu₂Al₁₆Pt₉ (Ce₂Al₁₆Pt₉ type, space group *Immm*, *Z* = 2).

Nominal composition	La ₂ Al ₁₆ Pt ₉	Eu ₂ Al ₁₆ Pt ₉
Refined sum formula	La ₂ Al _{15.95(1)} Pt _{9.05(1)}	Eu ₂ Al ₁₆ Pt ₉
Formula weight, g mol ⁻¹	2465.2	2491.4
Lattice parameters	See Table 2	See Table 2
Calcd. density, g cm ⁻³	9.07	9.18
Crystal size, μm ³	55 × 40 × 20	50 × 35 × 20
Diffractometer	Bruker X8 APEX2	Bruker X8 APEX2
Wavelength λ, pm	0.71073	0.71073
Absorption correction	Multi-scan, Bruker SADABS 2016 ²⁰	
Abs. Coefficient, mm ⁻¹	74.8	77.1
<i>F</i> (000), <i>e</i>	2056	2072
<i>θ</i> range, deg	3.77–28.30	2.05–33.22
Range <i>hkl</i>	–5, +4/±13/–23, +24	±6/–15, +18/–28, +27
Total no. reflections	3064	9286
Independent refl./ <i>R</i> _{int}	558/0.0291	1,018/0.0536
Reflections <i>I</i> > 3σ(<i>I</i>)/ <i>R</i> _σ	506/0.0226	846/0.0327
Data/parameters	558/50	1,018/49
Goodness of fit on <i>F</i> ²	1.16	1.25
<i>R</i> ₁ / <i>wR</i> ₂ for <i>I</i> > 3σ(<i>I</i>)	0.0190/0.0407	0.0238/0.0505
<i>R</i> ₁ / <i>wR</i> ₂ (all data)	0.0222/0.0418	0.0329/0.0527
Extinction coefficient	132(10)	139(13)
Extinction scheme	Lorentzian isotropic ³⁷	
Larg. diff. peak/hole, e Å ⁻³	+1.59/–1.68	+2.46/–2.71

Table 5: Atomic coordinates of nominal La₂Al₁₆Pt₉ and Eu₂Al₁₆Pt₉ (Ce₂Al₁₆Pt₉ type, space group *Immm*) refined from single-crystal X-ray data. *U*_{eq} is defined as one third of the trace of the orthogonalized *U*_{*ij*} tensor.

Atom	<i>x</i>	<i>y</i>	<i>z</i>	<i>U</i> _{eq}
La	0	0	0.22816(4)	54(1)
Pt1	0	0.31203(4)	0.34140(2)	46(1)
Pt2	1/2	0	0.37583(3)	52(1)
Pt3	0	0.25260(6)	1/2	88(1)
Pt4	0	0	0	113(1)
Al1	0	0.1171(3)	0.3940(2)	69(11)
Al2	0	0.1717(3)	0.0791(2)	83(12)
Al3	0	0.3071(3)	0.2046(2)	59(11)
Al4	1/2	0	0.0863(2)	89(17)
Al5/Pt5 ^a	0	0.3820(4)	0	77(14)
Eu	0	0	0.22896(4)	76(2)
Pt1	0	0.31098(3)	0.34189(2)	52(1)
Pt2	1/2	0	0.37794(3)	50(1)
Pt3	0	0.25332(4)	1/2	75(1)
Pt4	0	0	0	122(2)
Al1	0	0.1175(2)	0.3929(2)	62(7)
Al2	0	0.1703(2)	0.0804(2)	70(8)
Al3	0	0.3077(2)	0.2054(2)	71(8)
Al4	1/2	0	0.0870(2)	83(11)
Al5	0	0.3844(3)	0	67(11)

^aMixed occupancy: Al5/Pt5: 0.97(1)/0.03(1).**Table 6:** Interatomic distances (pm) in nominal La₂Al₁₆Pt₉ and Eu₂Al₁₆Pt₉ (Ce₂Al₁₆Pt₉ type, space group *Immm*). All distances of the first coordination spheres are listed. Standard deviations are equal or smaller than 0.2 pm.

Atom	Coordination	Distance (pm)	Atom	Coordination	Distance (pm)						
La	4 Pt1	330.8	Eu	2 Al1	330.0						
	2 Al4	331.7		4 Al3	331.4						
	2 Al1	332.5		2 Al4	332.1						
	4 Al3	333.3		4 Pt1	332.3						
	2 Al2	339.7		2 Al2	338.1						
	2 Pt2	340.0		2 Pt2	342.2						
	Pt1	1 Al3		249.1	Pt1	1 Al1	248.0				
		1 Al1		251.0		1 Al3	249.0				
		2 Al2		254.3		2 Al2	252.7				
		1 Al4		259.6		1 Al4	259.3				
		2 Al3		265.5		2 Al3	265.7				
		2 Pt1		297.3		2 Pt1	296.4				
Pt2		4 Al1	252.7	Pt2		4 Al1	252.0				
		2 Al5/Pt5	266.2			2 Al5	261.6				
		2 Al3	272.4			2 Al3	274.4				
		Pt3	2 Al1			251.6	Pt3	2 Al1	253.4		
			2 Al5/Pt5			262.7		2 Al5	264.7		
			4 Al2			268.7		4 Al2	270.2		
	2 Pt1		297.3		2 Pt1	296.4					
	Pt4		4 Al2		250.1	Pt4		4 Al2	249.8		
			4 Al4		260.8			4 Al4	261.6		
			Al1		1 Pt1			251.0	Al1	1 Pt1	247.9
					1 Pt3			251.6		2 Pt2	252.0
					2 Pt2			252.7		1 Pt3	253.4
1 Al1				278.8	1 Al1			279.2			
2 Al5/Pt5				283.9	2 Al5			285.4			
2 Al3				289.3	2 Al3			288.6			
Al2		1 Pt4		250.1	Al2		1 Pt4	249.9			
		2 Pt1		254.3			2 Pt1	252.7			
		2 Pt3		268.7			2 Pt3	270.2			
		1 Al3		279.6			1 Al3	280.4			
	2 Al2	288.1		2 Al4		290.4					
	1 Al5/Pt5	288.8		1 Al2		293.2					
	2 Al4	292.0	1 Al5	293.6							
	Al3	1 Pt1	249.1	Al3		1 Pt1	249.1				
		2 Pt1	265.5			2 Pt1	265.7				
		1 Pt2	272.4			2 Pt2	274.4				
		1 Al2	279.6			2 Al2	280.4				
		2 Al1	289.3			2 Al1	288.6				
2 Al3		298.6	2 Al3		297.6						
Al4		2 Pt1	259.6		Al4	2 Pt1	259.2				
		2 Pt4	260.8			2 Pt4	261.7				
		4 Al2	292.0			4 Al2	290.4				
		Al5/Pt5	2 Pt3			262.7	Al5	2 Pt2	261.6		
			2 Pt2			266.2		2 Pt3	264.7		
			1 Al5/Pt5			281.0		1 Al5	274.6		
	4 Al1		283.9	4 Al1		285.4					
	2 Al2		288.8	2 Al2		293.6					

CSDs 2343483 and 2343765 contain the supplementary crystallographic data for this paper. The data can be obtained free of charge from The Cambridge Crystallographic Data Centre via www.ccdc.cam.ac.uk/structures.

2.3 SEM/EDX

Semiquantitative EDX analyses of the bulk samples were conducted on a JEOL 7000F (JEOL, Freising, Germany) scanning electron microscope equipped with an EDAX Genesis 2000 EDX detector (EDAX, Unterschleissheim, Germany). The samples were sprinkled on conductive carbon tape and one area scans as well as three independent data points were measured. The results of the SEM/EDX investigations are listed in Table 7.

3 Results

3.1 Powder X-ray diffraction

All samples of the $M_2Al_{16}Pt_9$ series ($RE = Ca, La-Nd, Sm-Gd$) were investigated by powder X-ray diffraction measurements. The powder patterns clearly indicate that all compounds of the series are isostructural with orthorhombic $Ce_2Al_{16}Pt_9$ ¹³ and $Sr_2Al_{16}Pt_9$ ¹¹ (space group $Immm$). Figure 1 exemplarily depicts the powder patterns of $La_2Al_{16}Pt_9$ and $Gd_2Al_{16}Pt_9$. Rietveld refinements of the data indicate that in all cases the as-cast samples are not phase pure but contain traces of Al_3Pt_2 (Al_3Ni_2 type, space group $P\bar{3}m1$)²⁵ and $REAl_5Pt_3$ (YNi_5Si_3 type, space group $Pnma$).^{12,14,15} Table 1 summarizes the refined phase compositions of all prepared samples. Annealing of $La_2Al_{16}Pt_9$ and all other samples of the series leads to a decomposition of the title compounds along with an increase of the Al_3Pt_2 and $REAl_5Pt_3$ fractions. No phase-pure samples could be obtained for any of the reported compounds, leading to the suggestion that the $RE_2Al_{16}Pt_9$ compounds decompose peritectically during annealing.

Figure 2 depicts the lattice parameters and unit cell volumes of the presented series, clearly underlining the

Table 7: Chemical compositions of the samples with a nominal composition of $RE_2Al_{16}Pt_9$, obtained by SEM-EDX measurements. All values are the average of four area scans. Standard deviations are 2 at%.

RE	at% RE	at% Al	at% Pt
Nominal	7.4	59.3	33.3
La	8	58	34
Ce	7	57	36
Pr	7	56	37
Nd	8	55	37
Sm	8	54	38
Eu	7	57	36
Gd	8	56	36

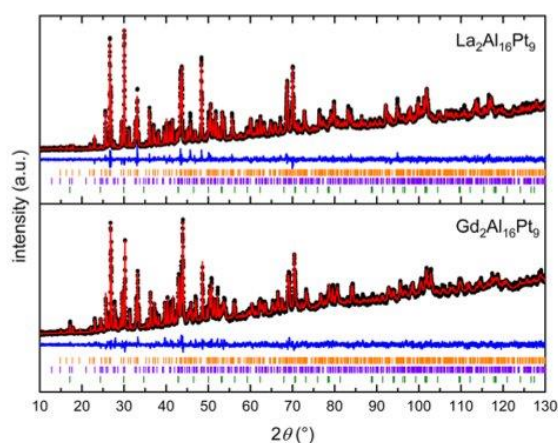


Figure 1: Rietveld refinements of the powder X-ray diffraction data of $La_2Al_{16}Pt_9$ (top) and $Gd_2Al_{16}Pt_9$ (bottom). Black dots represent the experimental data, the red line the sum of the calculated data and the blue line the difference between experimental and calculated data. The dashes correspond to the Bragg positions of $RE_2Al_{16}Pt_9$ (orange), $REAl_5Pt_3$ (purple), and Al_3Pt_2 (green).

trivalent oxidation state of the RE elements $La-Nd, Sm$ and Gd (in comparison to $Sr_2Al_{16}Pt_9$) and their decrease due to the lanthanide contraction. $Ca_2Al_{16}Pt_9$ and $Eu_2Al_{16}Pt_9$, however, clearly have larger lattice parameters and an increased unit cell volume compared to the aforementioned compounds, indicating divalent oxidation states for the Ca and Eu atoms.

3.2 SEM/EDX

The samples of the $M_2Al_{16}Pt_9$ series ($M = La-Nd, Sm-Gd$) were additionally analyzed by SEM/EDX measurements. Area scans on four different regions of the attached powdered samples were collected. Figure 3 shows one example per rare earth element where an area scan was conducted. The determined sample compositions (Table 7) are in good agreement with the nominal compositions, keeping in mind that the measurements were conducted on non-polished samples with conchoidal fractures.

3.3 Single-crystal X-ray diffraction and structure refinement

Block-shaped single crystals were isolated from samples of $La_2Al_{16}Pt_9$ and $Eu_2Al_{16}Pt_9$ and mounted onto a Bruker X8 APEX2 single-crystal diffractometer. Careful analysis of the obtained data revealed an orthorhombic lattice, and space

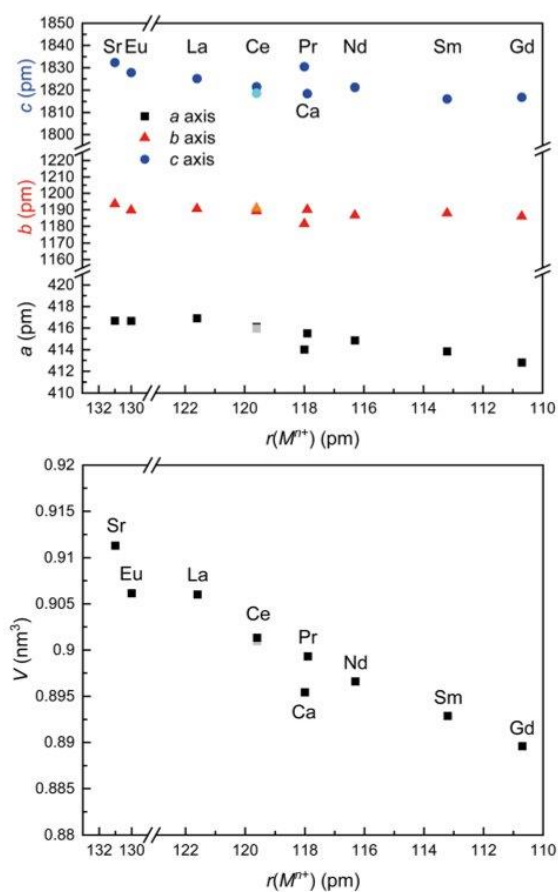


Figure 2: (Top) Lattice parameters a , b and c of the $M_2\text{Al}_{16}\text{Pt}_9$ series with $M = \text{Ca}, \text{Sr}, \text{La-Nd}, \text{Sm}$ and Gd obtained from powder X-ray diffraction data. For $\text{Ce}_2\text{Al}_{16}\text{Pt}_9$, the unit cell parameters from the literature are given in slightly varied colors. (bottom) Unit cell volumes of the $M_2\text{Al}_{16}\text{Pt}_9$ series with $M = \text{Ca}, \text{Sr}, \text{La-Nd},$ and Sm-Gd .

group $Immm$ was found to be correct. The structures were solved using the charge flipping algorithm of SUPERFLIP,²¹ and a least-squares refinement on F^2 using the program JANA2006^{22–24} was carried out. All atomic positions were refined with anisotropic displacement parameters and as a check for the correct compositions, the occupancy parameters were refined in separate series of least-squares refinements. While for $\text{Eu}_2\text{Al}_{16}\text{Pt}_9$ all sites were fully occupied within three standard deviations leading to the targeted composition, for nominal $\text{La}_2\text{Al}_{16}\text{Pt}_9$ a small mixing of Al and Pt was observed on one crystallographic site. In both cases, the final difference Fourier syntheses were contourless. From the powder diffraction data and in comparison with the Pearson database,²⁶ isotypism with $\text{Ce}_2\text{Al}_{16}\text{Pt}_9$ ¹³ and $\text{Sr}_2\text{Al}_{16}\text{Pt}_9$ ¹¹ was deduced. Details of the structure

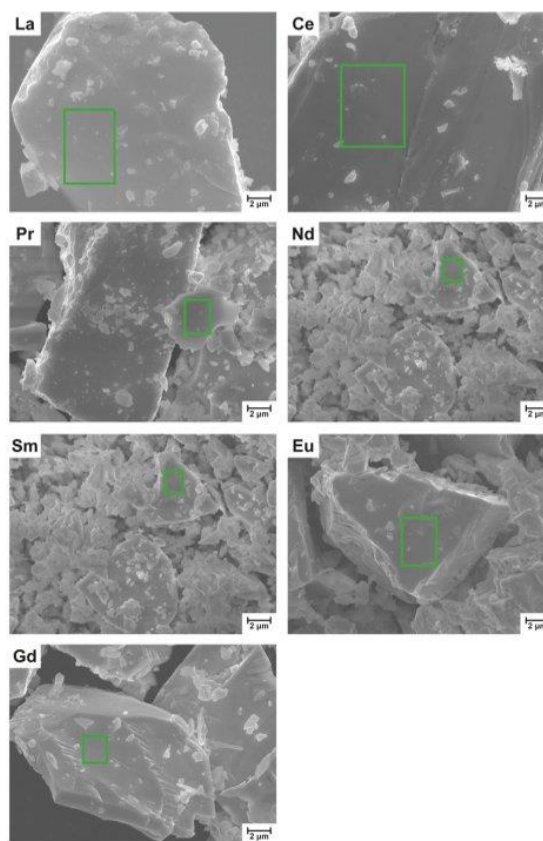


Figure 3: Scanning electron microscopy images of the members of the $M_2\text{Al}_{16}\text{Pt}_9$ series ($M = \text{La-Nd}, \text{Sm-Gd}$). The green rectangles illustrate the by EDX analyzed areas.

determination, atomic parameters and interatomic distances can be found in Tables 2–6.

3.4 Crystal chemistry

All members of the $M_2\text{Al}_{16}\text{Pt}_9$ series ($RE = \text{Ca}, \text{La-Nd}, \text{Sm-Gd}$) crystallize in the orthorhombic crystal system with space group $Immm$ (Pearson code $oF54$, Wyckoff sequence $I_1^2 thga$) and are isostructural with $\text{Ce}_2\text{Al}_{16}\text{Pt}_9$ ¹³ and $\text{Sr}_2\text{Al}_{16}\text{Pt}_9$.¹¹ The crystal structure will be exemplarily discussed based on the single-crystal data of $\text{Eu}_2\text{Al}_{16}\text{Pt}_9$. The unit cell is depicted in a projection along the a axis in Figure 4. The Eu atoms are surrounded by six Pt and six Al atoms in the shape of a hexagonal prism (Figure 5). These $\text{Eu@Pt}_6\text{Al}_6$ prisms form strands along $[100]$ with interatomic Eu–Al distances ranging from 330 to 332 pm while the Eu–Pt distances are 332 and 342 pm. Both distances are in line with the ones found in

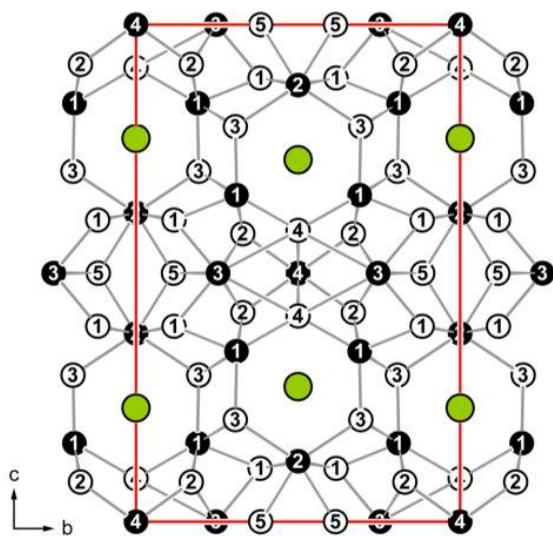


Figure 4: Unit cell of $Eu_2Al_{16}Pt_9$, projected along the a axis. Eu, Pt and Al atoms are shown in green, black and white circles. The shortest Pt–Al contacts are emphasized.

binary intermetallics e. g. $EuAl_2$ (MgCu₂ type, 337 pm²⁷) or $EuAl_4$ (BaAl₄ type, 339 + 356 pm²⁸) as well as $EuPt_2$ (MgCu₂ type, 320 pm²⁹). The sums of the covalent radii of Eu + Al = 185 + 125 = 310 pm and Eu + Pt = 185 + 129 = 314 pm³⁰ agree with the observed distances, so do the distances in the known ternary compounds $Eu_4Al_{13}Pt_9$ (Eu–Al: 326–360 pm; Eu–Pt: 322–332 pm),³¹ $Eu_2Al_9Pt_3$ (Eu–Al: 306–313 pm; Eu–Pt: 347–348 pm),³² $EuAl_2Pt$ (Eu–Al: 335–355 pm; Eu–Pt: 302–330 pm).⁹

Within the $[Al_{16}Pt_9]^{6-}$ polyanion four platinum and five aluminum sites are observed (Figure 5) forming hexagonal cavities in which the Eu cations reside. Within the network, Pt1 exhibits a sevenfold coordination environment, while Pt2 to Pt4 exhibit coordination numbers of eight with Pt–Al

distances ranging from 247 to 274 pm. These distances are again in line with those in binary (AlPt: 248–273 pm;³³ Al₂Pt: 256 pm³⁴) and ternary intermetallics ($Eu_4Al_{13}Pt_9$ (247–265 pm),³¹ $Eu_2Al_9Pt_3$ (256–264 pm),³² $EuAl_2Pt$ (254–258 pm)⁹) as well as with the sum of the covalent radii (Pt + Al = 129 + 125 = 254 pm³⁰). Furthermore, homoatomic Pt–Pt (296 pm) and Al–Al (275–297 pm) distances can be found. While the platinum distances are significantly longer compared to the sum of the covalent radii as well as the distances found in elemental fcc Pt (12×277 pm³⁵), the aluminum distances, agree with the ones in elemental fcc Al (12×286 pm³⁶), therefore suggesting partial bonding contributions.

4 Conclusions

The $M_2Al_{16}Pt_9$ series was extended from the thus far known metals $M = Sr$ and Ce to additional members with the rare earth elements $RE = La-Nd$ and $Sm-Gd$ as well as calcium. All samples were prepared via arc-melting of the elements. The as-cast samples were characterized by powder X-ray diffraction and SEM-EDX. In all cases, the compounds could not be obtained as phase pure samples, Al_3Pt_2 and MA_5Pt_3 were always observed as byproducts. Annealing led to an increase of the impurities, rendering the $M_2Al_{16}Pt_9$ phases as peritectially decomposing compounds. The isostructural nature of the series to $Ce_2Al_{16}Pt_9$ was furthermore shown by single-crystal investigations on $La_2Al_{16}Pt_9$ and $Eu_2Al_{16}Pt_9$. While the latter exhibits the nominal composition, the crystal from the lanthanum sample shows a small mixing of Pt and Al on one crystallographic site leading to a refined composition of $La_2Al_{15.95(1)}Pt_{9.05(1)}$. Within the $M_2Al_{16}Pt_9$ series, the unit cell volumes decrease from $RE = La$ to Gd as expected from the lanthanide contraction, $Ca_2Al_{16}Pt_9$ and $Eu_2Al_{16}Pt_9$, however, exhibits a significantly increased unit

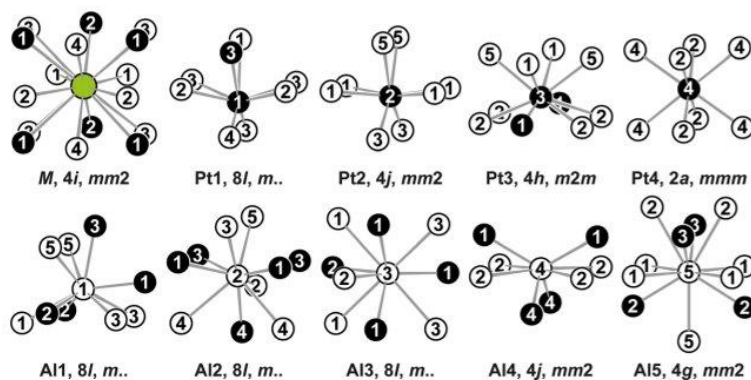


Figure 5: Coordination environments surrounding the M , Pt and Al atoms in the structures of the $M_2Al_{16}Pt_9$ series. M , Pt and Al atoms are shown as green, black and white circles. Atom labels, Wyckoff sites, site symmetries are given.

cell volume which leads to the conclusion that the Eu cations are divalent in contrast to the other rare earth elements being trivalent.

Acknowledgements: The authors thank Dr. Bernd Morgenstern for the help with the interpretation of the single-crystal X-ray data. Instrumentation and technical assistance for this work were provided by the Service Center X-ray Diffraction.

Research ethics: Not applicable.

Author contributions: The authors have accepted responsibility for the entire content of this manuscript and approved its submission.

Competing interests: The authors state no conflict of interest.

Research funding: Financial support from Saarland University and German Science Foundation (project number INST 256/349-1 and INST 256/506-1). Funding was furthermore provided by the Deutsche Forschungsgemeinschaft DFG for project JA 1891-10-1.

Data availability: The raw data can be obtained on request from the corresponding author.

References

- Benndorf, C.; Eckert, H.; Janka, O. Structural Characterization of Intermetallic Compounds by ²⁷Al Solid State NMR Spectroscopy. *Acc. Chem. Res.* **2017**, *50*, 1459–1467.
- Benndorf, C.; Stegemann, F.; Eckert, H.; Janka, O. New Transition Metal-Rich Rare-Earth Palladium/Platinum Aluminides with RET₅Al₂ Composition: Structure, Magnetism and ²⁷Al NMR Spectroscopy. *Z. Naturforsch.* **2015**, *70b*, 101–110.
- Benndorf, C.; Eckert, H.; Janka, O. Ternary Rare-Earth Aluminium Intermetallics RE₁₀TAl₃ (RE = Y, Ho, Tm, Lu; T = Fe, Co, Ni, Ru, Rh, Pd, Os, Ir, Pt) with an Ordered Anti-Co₂Al₅ Structure. *Dalton Trans.* **2017**, *46*, 1083–1092.
- Stegemann, F.; Stahl, J.; Bartsch, M.; Zacharias, H.; Johrendt, D.; Janka, O. Temperature Induced Valence Phase Transition in Intermediate-Valent YbPd₂Al₃. *Chem. Sci.* **2019**, *10*, 11086–11094.
- Stegemann, F.; Benndorf, C.; Touzani, R. S.; Fokwa, B. P. T.; Janka, O. Sr₂Pd₄Al₅: Synthesis, Crystal and Electronic Structures, and Chemical Bonding of a Polar Intermetallic Compound. *Eur. J. Inorg. Chem.* **2016**, *2016*, 1108–1114.
- Stegemann, F.; Benndorf, C.; Touzani, R. S.; Fokwa, B. P. T.; Janka, O. Experimental and Theoretical Investigations of the Polar Intermetallics SrPt₃Al₂ and Sr₂Pd₂Al₃. *J. Solid State Chem.* **2016**, *242*, 143–150.
- Stegemann, F.; Touzani, R. S.; Janka, O. Unusually Strong Heteroatomic Bonding in the Complex Polyanion of Intermetallic Ba₆Pt₂₂Al₅₃. *Dalton Trans.* **2019**, *48*, 14103–14114.
- Stegemann, F.; Benndorf, C.; Bartsch, T.; Touzani, R. S.; Bartsch, M.; Zacharias, H.; Fokwa, B. P. T.; Eckert, H.; Janka, O. Ba₃Pt₄Al₄ – Structure, Properties, and Theoretical and NMR Spectroscopic Investigations of a Complex Platinide Featuring Heterocubane [Pt₄Al₄] Units. *Inorg. Chem.* **2015**, *54*, 10785–10793.
- Stegemann, F.; Block, T.; Klenner, S.; Zhang, Y.; Fokwa, B. P. T.; Timmer, A.; Mönig, H.; Doerenkamp, C.; Eckert, H.; Janka, O. From 3D to 2D: Structural, Spectroscopic and Theoretical Investigations of the Dimensionality Reduction in the [PtAl₂]⁶⁻ Polyanions of the Isotypic MPTAl₂ Series (M = Ca–Ba, Eu). *Chem. Eur. J.* **2019**, *25*, 10735–10747.
- Radziejowski, M.; Stegemann, F.; Doerenkamp, C.; Matar, S. F.; Eckert, H.; Dosche, C.; Wittstock, G.; Janka, O. Correlations of Crystal and Electronic Structure via NMR and XPS Spectroscopy in the RETMAL₂ (RE = Sc, Y, La–Nd, Sm, Gd–Tm, Lu; TM = Ni, Pd, Pt) Series. *Inorg. Chem.* **2019**, *58*, 7010–7025.
- Engel, S.; Bönnighausen, J.; Stegemann, F.; Touzani, R. S.; Janka, O. SrAl₅Pt₃ and Sr₂Al₁₆Pt₉ – Two New Strontium Aluminium Platinides. *Z. Naturforsch.* **2022**, *77b*, 367–379.
- Tursina, A. I.; Bukhan'ko, N. G.; Gribov, A. V.; Shchelkunov, V. A.; Nelyubina, Y. V. A New Ternary Aluminide, CePt₃Al₅. *Acta Crystallogr.* **2005**, *E61*, i285–i286.
- Tursina, A. I.; Murashova, E. V.; Noël, H.; Bukhan'ko, N. G.; Seropegin, Y. D. Crystal Structure and Magnetic Properties of the New Intermetallic Ce₂Pt₉Al₁₆. *Intermetallics* **2009**, *17*, 780–783.
- Koizumi, T.; Honda, F.; Sato, Y. J.; Li, D.; Aoki, D.; Haga, Y.; Gouchi, J.; Nagasaki, S.; Uwatoko, Y.; Kaneko, Y.; Ōnuki, Y. Abrupt Change in Electronic States under Pressure in New Compound EuPt₃Al₅. *J. Phys. Soc. Jpn.* **2022**, *91*, 043704 (5 pages).
- Fukuda, H.; Koizumi, T.; Sato, Y. J.; Shimizu, Y.; Nakamura, A.; Li, D.; Homma, Y.; Miyake, A.; Aoki, D.; Tokunaga, M.; Kato, R.; Shiga, M.; Kawae, T.; Honda, F. Physical Properties of a New Ternary Compound RPt₃Al₅ (R = Rare Earth). *New Phys.: Sae Mulli* **2023**, *73*, 1135–1139.
- Pöttgen, R.; Gulden, T.; Simon, A. Miniaturisierte Lichtbogenapparat für den Laborbedarf. *GIT Labor-Fachz.* **1999**, *43*, 133–136.
- Topas (version 5). *General Profile and Structure Analysis Software for Powder Diffraction Data*; Bruker AXS Inc.: Karlsruhe (Germany), 2014.
- Rietveld, H. M. Line Profiles of Neutron Powder-Diffraction Peaks for Structure Refinement. *Acta Crystallogr.* **1967**, *22*, 151–152.
- Rietveld, H. M. A Profile Refinement Method for Nuclear and Magnetic Structures. *J. Appl. Crystallogr.* **1969**, *2*, 65–71.
- Sheldrick, G. M. S_{AD}ABS (Version 2016); Bruker AXS Inc.: Madison, Wisconsin (USA), 2016.
- Palatinus, L.; Chapuis, G. SUPERFLIP – A Computer Program for the Solution of Crystal Structures by Charge Flipping in Arbitrary Dimensions. *J. Appl. Crystallogr.* **2007**, *40*, 786–790.
- Petríček, V.; Dušek, M.; Palatinus, L. JANA 2006, *The Crystallographic Computing System*; Institute of Physics, Academy of Sciences of the Czech Republic: Prague (Czech Republic), 2006.
- Petríček, V.; Dušek, M.; Palatinus, L. Crystallographic Computing System JANA2006: General Features. *Z. Kristallogr.* **2014**, *229*, 345–352.
- Petríček, V.; Palatinus, L.; Plášil, J.; Dušek, M. Jana2020 – A New Version of the Crystallographic Computing System Jana. *Z. Kristallogr.* **2023**, *238*, 271–282.
- Ferro, R.; Capelli, R.; Rambaldi, G.; Bonino, G. B. Ricerche sulle leghe dei metalli nobili con gli elementi più elettropositivi. VI. Esame micrografico e roentgenografico di alcune leghe del sistema alluminio-platino. *Atti Accad. Naz. Lincei, Cl. Sci. Fis., Mat. Nat., Rend.* **1963**, *34*, 45–47.
- Villars, P.; Cenzual, K., Eds. *Pearson's Crystal Data: Crystal Structure Database for Inorganic Compounds* (Release 2023/24); ASM International[®]: Materials Park, Ohio (USA), 2023.
- Haszko, S. E. Intermediate Phases with the MgCu₂ Structure. *Trans. Metall. Soc. AIME* **1960**, *218*, 958.
- Van Vucht, J. H. N.; Buschow, K. H. J. On the Binary Aluminium-Rich Compounds of the Rare-Earth Elements. *Philips Res. Rep.* **1964**, *19*, 319–322.
- Harris, I. R. The Constitution of Some R.E.Pt₃ Alloys. *J. Less-Common Met.* **1968**, *14*, 459–462.
- Emsley, J. *The Elements*; Clarendon Press, Oxford University Press: Oxford, New York, 1998.

31. Engel, S.; Zaremba, N.; Prots, Y.; Touzani, R. S.; Janka, O. $Eu_4Al_{13}Pt_9$ – A Coloring Variant of the $Ho_4Ir_{13}Ge_9$ Type Structure. *Z. Naturforsch.* **2023**, *78b*, 147–156.
32. Stegemann, F.; Zhang, Y.; Fokwa, B. P. T.; Janka, O. On the Formation of the $Gd_3Ru_4Al_{12}$ versus the $Y_2Co_3Ga_9$ Type Structure – $M_3Rh_4Al_{12}$ ($M = Ca, Eu$) versus $M_2T_3Al_9$ ($M = Ca, Sr, Eu, Yb; T = Ir, Pt$). *Dalton Trans.* **2020**, *49*, 6398–6406.
33. Schubert, K.; Burkhardt, W.; Esslinger, P.; Günzel, E.; Meissner, H. G.; Schütt, W.; Wegst, J.; Wilkens, M. Einige Strukturelle Ergebnisse an Metallischen Phasen. *Naturwissenschaften* **1956**, *43*, 248–249.
34. Zintl, E.; Harder, A.; Haucke, W. Legierungsphasen mit Fluoritstruktur (22. Mitteilung über Metalle und Legierungen). *Z. Phys. Chem. B* **1937**, *35*, 354–362.
35. Hull, A. W. The Positions of Atoms in Metals. *Trans. Am. Inst. Electro. Eng.* **1919**, *38*, 1445–1466.
36. Hull, A. W. A New Method of X-Ray Crystal Analysis. *Phys. Rev.* **1917**, *10*, 661–696.
37. Becker, P. J.; Coppens, P. Extinction within the Limit of Validity of the Darwin Transfer Equations. I. General Formalism for Primary and Secondary Extinction and Their Applications to Spherical Crystals. *Acta Crystallogr.* **1974**, *A30*, 129–147.

b. Unpublished Results from Own Work

1. Introduction

The following chapter contains preliminary results, which are not as advanced as it needed to be publishable. For a publication, more research on these systems has to be done e.g. better single crystals have to be measured or phase pure samples are necessary. The order of the corresponding element combinations is analogue to the published section of the work, starting with a new compound of in the system Ca–Al–Ni, which is followed by a new ternary europium phase and new compounds with rare earth elements including a continuation of the $RE_4Al_{13}Pt_9$ series based on the already found Ce and Eu compounds. In the last part of the chapter, literature known $YbAlT$ phases with $T = Ru, Co, Rh$ and Ni–Au were synthesized to investigate the ^{27}Al NMR shift. None of the compounds could be synthesized X-ray pure, all samples had at least Yb_2O_3 as side phase.

Investigation in the Ca–Al–Ni system resulted in the observation of $CaAl_5Ni_2$, which crystallizes in the $PrAl_5Ni_2$ type structure with space group $Immm$. Syntheses via various routes resulted in non-X-ray pure samples, in which the target compound is present to a maximum of 10 wt.-%, besides $CaAl_2$ as main phase and Al_3Ni_2 as another side phase. Due to the low amount of the desired phase, no single crystal of this compound could be found, yet. To advance the research, synthesis in closed metal ampoules should be performed, preventing the loss of calcium during the reaction, of which single crystals should be picked and measured to confirm the structure of $CaAl_5Ni_2$.

Due to the existence of $Eu_4Al_{13}Pt_9$ and the similar covalent size of the Pt and Pd atoms, an experiment was performed to test, if the Pd variant $Eu_4Al_{13}Pd_9$ can be synthesized. As the powder X-ray diffraction pattern could not be refined with the data of the Pt compound, single crystal of the sample were picked, resulting in $Eu_5Al_{0.70(1)}Pd_{2.30(1)}$, a structure which crystallizes in the Mo_5SiB_2 type with space group $I4/mcm$. Bulk samples of this composition did not lead to X-ray pure samples, rather a mixture of various phases. The structure can be described by a checkerboard pattern of $Eu@Eu_8$ cubes in one layer and $Al/Pd@Al_8$ square antiprisms in the neighboring layer. To publish the results, a better single crystal has to be measured, due to the high residual electron density. Also, further investigations with other element combinations could be made, looking for isotopic compounds with aluminum, as well as the synthesis of an X-ray pure sample or the growth of a large single crystal to investigate the physical properties.

Similar to the discovery of the nominal Eu_5AlPd_2 compound, also an investigation in the *RE*–Al–Pt system with the composition $\text{RE}_4\text{Al}_{13}\text{Pt}_9$ was conducted, due to the discovery of the europium containing phase and the literature known cerium and praseodymium compound. The series could be extended to La–Nd and Sm–Gd. Single crystal X-ray diffraction data was recorded of the Nd compound, confirming the isotypism to the Ce and Pr compound. The synthesis of bulk samples was successful for the Dy and Nd containing samples, whereas the other samples contained Al_3Pt_2 or other side phases. Semiquantitative analysis via SEM/EDX showed a good agreement of measured composition with stoichiometric values.

As next step to publication would be to measure the physical properties of the X-ray pure samples. Additionally, new synthetic attempts for X-ray pure samples should be considered, or a heat treatment step for the bulk samples to possibly reduce the amount of side phases. Also, single crystals of the later *RE* samples can be picked and measured to validate the crystal structure.

2. On the Existence of CaAl_5Ni_2

In the attempt to synthesize CaAl_9Ni (own type, $P6_3/mmc$)²⁴⁹ for characterization with ^{27}Al NMR spectroscopy, the product resulted in a mixture of unreacted aluminum, the intended CaAl_9Ni (own type, $P6_3/mmc$, $a = 760.02$, $c = 794.57$ pm),²⁴⁹ CaAl_8Ni_2 (CeAl_8Fe_2 type, $Pbam$, $a = 1253.2/1252.30$, $b = 1450.0/1443.73$, $c = 397.5/395.78$ pm)^{55, 58} and at least two unknown phases according to the PXRD pattern. By using the indexing function of the Topas program,⁹⁵ one unknown phase could be determined to be isostructural to PrAl_5Ni_2 (own type, $Immm$)²⁵⁰ and subsequently an attempt to synthesize CaAl_5Ni_2 was conducted, resulting in another mixture of mainly the cubic Laves phase CaAl_2 (MgCu_2 type, $Fd\bar{3}m$, $a = 803.3$ pm, 51 wt.-%)¹⁸⁵ and Al_3Ni_2 (own type, $P\bar{3}m1$, $a = 402.82$, $c = 489.06$ pm, 36 wt.-%)²⁴⁸ with the targeted CaAl_5Ni_2 phase (PrAl_5Ni_2 type, $Immm$, $a = 404.17(2)$, $b = 737.7(3)$, $c = 938.8(3)$ pm) as side phase with around 10 wt.-% along with CaO (NaCl type, $Fm\bar{3}m$, $a = 476.8$ pm, 3 wt.-%)²⁵¹ and an unknown phase, shown in **Figure 3.48**. The CaO originated from impure argon, which was used directly without prior purification and the reaction in an open alumina crucible. By calculating the overall element composition of the formed phases, a ratio of $\text{Ca}:\text{Al}:\text{Ni}$ of 1.8:5:1.2 respectively, due to the excess of Ca found in the sample indicates that the unknown phase should contain aluminum and nickel. Multiple reactions with different Ca surplus of 0.05 to 0.5, heating and cooling rates from 100 K/min to 1000 K/min were performed to obtain phase pure CaAl_5Ni_2 , but all failed, due to the high likelihood of the formation of CaAl_2 , also no single crystals of this phase could be obtained.

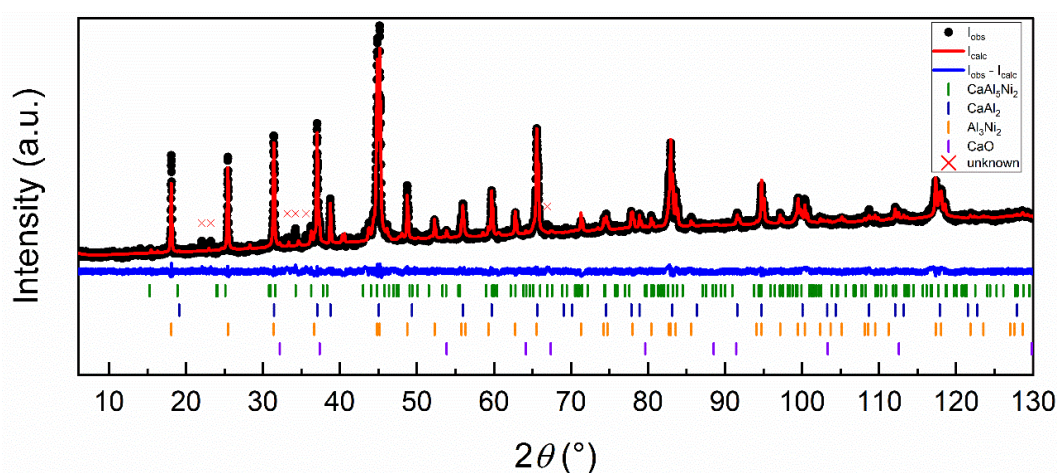


Figure 3.48: Rietveld refinement of the powder X-ray diffraction pattern of CaAl_5Ni_2 . Collected data are shown in black dots, the refinement as red and the difference as blue line. Olive ticks indicate the Bragg positions CaAl_5Ni_2 (PrAl_5Ni_2 type, $Immm$), royal blue CaAl_2 (MgCu_2 type, $Fd\bar{3}m$), orange Al_3Ni_2 (own type, $P\bar{3}m1$), violet ticks CaO (NaCl type, $Fm\bar{3}m$) and red crosses the undefined reflections respectively.

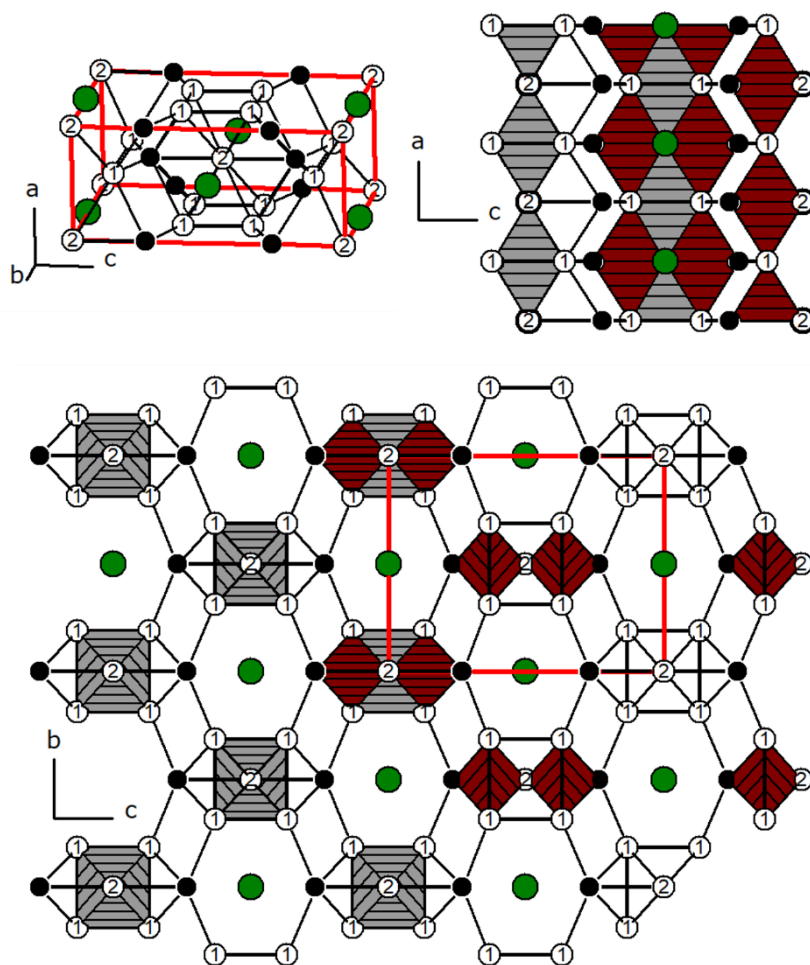


Figure 3.49: Unit cell of CaAl_5Ni_2 (top left), Al octahedra (grey) and Al–Pt tetrahedra (red) projected along $[010]$ (top right) and $[100]$ (bottom), Ca, Al, Ni atoms are shown in green, white and black circles, respectively.

CaAl_5Ni_2 crystallizes in the orthorhombic crystal system with space group $Immm$ in the PrAl_5Ni_2 type structure with the following lattice parameters $a = 404.2(1)$, $b = 737.9(3)$ and $c = 938.7(3)$ pm and is the first compound of this structure with an alkaline earth metal. The other known phases with this prototype contain La–Nd.^{252, 253, 250, 254} By comparing the lattice parameters with the *RE* variants, a significant increase of about 18 pm in the b and a decrease of about 22 pm in the c parameter are present, whereas the lattice parameter a is similar with a slight increase of 5 pm compared to the other compounds, resulting in an overall slightly higher unit cell volume of 0.2740 nm^3 compared to 0.2737 , 0.2670 , 0.2725 and 0.2685 nm^3 for La, Ce, Pr and Nd respectively.^{252, 253, 250, 254} By considering the ionic radii of the elements with $r_{\text{ionic}}(\text{Ca}) = 112 \text{ pm}$, $r_{\text{ionic}}(\text{La}) = 116 \text{ pm}$, $r_{\text{ionic}}(\text{Ce}) = 114 \text{ pm}$, $r_{\text{ionic}}(\text{Pr}) = 113 \text{ pm}$ and $r_{\text{ionic}}(\text{Nd}) = 111 \text{ pm}$,⁷⁹ the lattice parameters and the cell volume should be between Pr and Nd. Another noticeable irregularity is the significantly lower cell volume for the cerium compounds, which normally lies perfectly between the lanthanum and praseodymium samples but is smaller than even the neodymium compound.

CeAl₅Ni₂ is one of the most investigated compounds due to the exhibition of the Kondo effect, the phase was analyzed e.g. via XPS, ²⁷Al NMR spectroscopy,²⁵⁵ physical properties alongside magnetism, X-ray diffraction, neutron diffraction²⁵³ and even quantum chemical calculations were done, but no one explains the small cell volume in comparison with the other *RE* compounds. One possible explanation could be that the Ce atoms are not fully trivalent but a mixture of Ce³⁺ and Ce⁴⁺, which would be a rare case of tetravalence, but the effective magnetic moment of the Ce in the compound is 2.66 μ_B (theoretical magnetic moment of free Ce³⁺ ions: 1.73 μ_B) and also the XPS results indicate fully trivalent cerium.^{256, 257} The COHP calculation shows a significant interaction between the Ce and Ni atoms as well as optimized Al–Al and Al–Ni bonding interactions, which could lead to the shrinking of the unit cell volume.²⁵⁸

The lattice parameters and unit cell volumes of the *MAl₅T₂* representatives are summarized in **Table 3.15**.

The structure exhibits two aluminum positions and one position each for calcium and nickel respectively. The unit cell is shown in **Figure 3.49** alongside the corner-shared empty Al₆ octahedra strands (grey) along [100]. On the level of the corner-sharing Al atoms, nickel atoms reside on the left and right side, forming Al₃Ni tetrahedra (red), which are face-sharing to the octahedra strands. These tetrahedra are alternately corner and edge-shared along [100]. The strands are placed in a checkerboard-like pattern, as shown in **Figure 3.49** bottom left. The resulting cavities, alias the other color in the checkerboard, is filled with Ca atoms, which are occupying hexagonal cavities formed from four Al and two Ni atoms. When looked along [010] and [001], the shift of [0,0,1/2] of the polyhedral strands is visible, which occurs in the neighboring strands diagonally, but all strands are connected to their neighbor. So that the Al and Ni atoms form the polyanionic structure with the calcium atoms as cationic species.

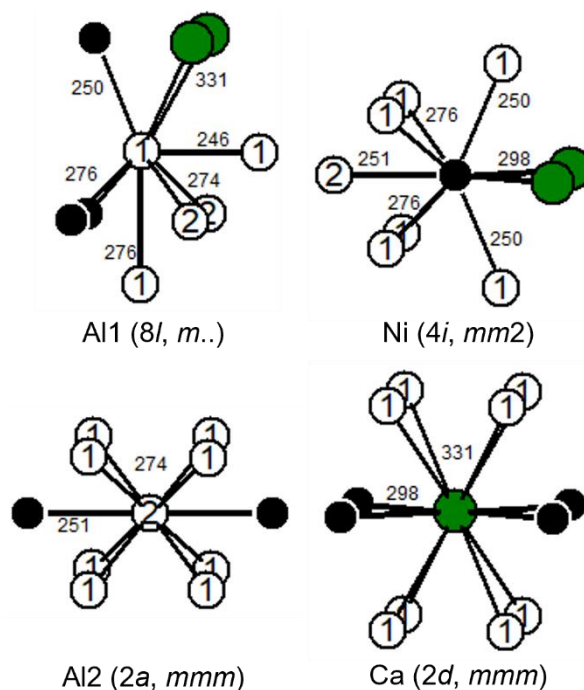


Figure 3.50: Coordination environments surrounding the Al1 (top left), Al2 (bottom left), Ni (top right) and Ca (bottom right) atoms in CaAl_5Ni_2 . Ca, Al, Ni atoms are shown in green, white and black circles, respectively. Wyckoff positions, site symmetries and interatomic distances (in pm) are given.

The coordination environment of the crystallographically independent atom positions alongside the corresponding interatomic distances are shown in **Figure 3.50**. Whereas the Al2 and Ca sites are highly symmetrical coordinated, by a twofold capped cube ($\text{Al2@Al}_8\text{Ni}_2$) and a fourfold capped square prism ($\text{Ca@Al}_8\text{Ni}_4$). The Al1 and Ni in comparison are rather asymmetrically surrounded by two Al1, two Al2, three Ni and two Ca and six Al1, one Al2 and two calcium atoms respectively.

Due to the low amount of CaAl_5Ni_2 in the investigated powder diffraction pattern, the standard deviations of the interatomic distances are rather large (± 2 pm) compared to single crystal data. The Al–Al distances range from 246, 274 to 276 pm, Al–Ni from 250 to 276 pm, Ca–Ni distance is 298 pm and Ca–Al distances of 331 pm were observed. No homoatomic Ca–Ca, Ni–Ni distances under 350 pm are present within the structure. The Al–Al distances of CaAl_5Ni_2 of 246 to 276 pm are in range with the sum of the covalent radii of 250 pm⁴ or the bond length found in elemental aluminum (*fcc*, Cu type, $Fm\bar{3}m$) of 286 pm.²⁰⁸ When compared to the following ternary compounds, the Al–Al distances are also in good agreement. The remaining REAl_5Ni_2 compounds exhibit Al–Al distances ranging from 267–297 pm (La), 264–309 pm (Ce), 267–294 pm (Pr), 265–304 pm (Nd), the existing ternary Ca–Al–Ni compounds CaAl_9Ni (own type, $P6_3/mmc$),²⁴⁹ CaAl_8Ni_2 (CeAl_8Fe_2 type, $Pbam$)⁵⁵ and $\text{CaAl}_{1.8}\text{Ni}_{0.2}$ (MgCu_2 type, $Fd\bar{3}m$)⁶⁰ exhibit Al–Al distances from 275–328 pm, 265–314 pm and 284 pm, respectively. The Al–Al distances of 246 are shorter than the other ternary compounds, the ones found in

elemental Al and also in the binary compounds CaAl_4 (BaAl_4 type, $I4/mmm$)¹⁸⁵ with 261-308 pm, 284 pm in CaAl_2 (MgCu_2 type, $Fd\bar{3}m$), 275-290 pm in Al_3Ni_2 (own type, $P\bar{3}m1$)²⁴⁸ and 288 pm in AlNi (CsCl type, $Pm\bar{3}m$).⁶⁰ These distances indicate different degrees of Al–Al bonding interactions in the compound. The Al–Ni distances range from 250-276 pm and are longer than the sum of the covalent radii ($\text{Al} + \text{Ni} : 125 + 115 = 240 \text{ pm}$)⁴. In the ternary Ca–Al–Ni compounds Al–Ni distances from 234-261 pm in CaAl_8Ni_2 ,⁵⁵ 249 pm in CaAl_9Ni ²⁴⁹ and in the $RE\text{Al}_5\text{Ni}_2$ series, the Al–Ni distances range from 234-259 pm in La,²⁵⁴ 223-249 pm in Ce,²⁵⁴ 229-251 pm in Nd²⁵² to 231-257 pm in Pr.²⁵⁰ The binary aluminum nickelide compounds exhibit Al–Ni distances of 249 pm in AlNi (CsCl type, $Pm\bar{3}m$)²⁵⁹ and are ranging from 244-253 pm in Al_3Ni_2 (own type, $P\bar{3}m1$).²⁴⁸ In comparison to $\text{CaAl}_{1.8}\text{Ni}_{0.2}$ ⁶⁰ with a distance of 284 pm is significantly longer than found in CaAl_5Ni_2 . Bonding interactions of Al and Ni like forming a polyanionic network is expected, which forms distorted hexagonal prismatic cavities in which the calcium atoms reside. The Ca–Ni distances are 298 pm, which is quite well in range with the sum of the covalent radii ($\text{Ca} + \text{Ni} : 174 + 115 = 289 \text{ pm}$)⁴ and the binary compounds CaNi_2 (MgCu_2 type, $Fd\bar{3}m$): 300 pm,²⁶⁰ CaNi_3 (PuNi_3 type, $R\bar{3}mh$): 289-322 pm,²⁶⁰ CaNi_5 (CaCu_5 type, $P6/mmm$): 286-316 pm,¹⁶⁶ and Ca_2Ni_7 (Gd_2Co_7 type, $R\bar{3}mh$): 285-322 pm.²⁶⁰ In comparison, $\text{CaAl}_{1.8}\text{Ni}_{0.2}$ ⁶⁰ exhibits a Ca–Ni distance of 330 pm, which is longer than CaAl_5Ni_2 , whereas the CaAl_9Ni ²⁴⁹ and CaAl_8Ni_2 ⁵⁵ compounds do not report a meaningful Ca–Ni interaction below 350 pm. Ca–Al distances of 331 pm found in CaAl_5Ni_2 are in line with ternary compounds CaAl_8Ni_2 $d(\text{Ca–Al}) = 267\text{-}337 \text{ pm}$,⁵⁵ CaAl_9Ni $d(\text{Ca–Al}) = 332\text{-}346 \text{ pm}$,²⁴⁹ $\text{CaAl}_{1.8}\text{Ni}_{0.2}$ $d(\text{Ca–Al}) = 330 \text{ pm}$ ⁶⁰ and also with the binary Ca–Al compounds CaAl_2 (MgCu_2 type, $Fd\bar{3}m$) $d(\text{Ca–Al}) = 333 \text{ pm}$ ¹⁸⁵ and CaAl_4 (BaAl_4 type, $I4/mmm$) $d(\text{Ca–Al}) = 335 \text{ pm}$.¹⁸⁵ Besides the *RE* variants (La, Ce, Pr, Nd) of the CaAl_5Ni_2 , other compounds with the general composition of $M\text{Al}_5\text{Ni}_2$ ($M = \text{Zr, Hf}$; ZrAl_5Ni_2 type, $I4/mmm$)^{261, 262} are literature known, interestingly there are also compounds known with have an inverse Al : *T* ratio, these phases possess the general composition of $RE\text{Al}_2T_5$ ($RE = \text{Y, Ce, Nd, Gd-Lu}$, $T = \text{Pd, Pt}$, ZrAl_5Ni_2 type, $I4/mmm$)^{237, 263-268} and like the Zr and Hf phase exhibit a completely different crystal structure.

Table 3.15: Lattice parameters of the MAl_5Ni_2 ($M = Ca, La-Nd, PrAl_5Ni_2$ type, space group $Immm, Z = 2$) and the series.

Compound	a (pm)	b (pm)	c (pm)	V (nm ³)
CaAl ₅ Ni ₂	404.33(4)	722.1(2)	938.6(2)	0.2740
LaAl ₅ Ni ₂ ²⁵⁴	402.1	703.3	967.7	0.2737
CeAl ₅ Ni ₂ ²⁵³	397.7	701.8	956.6	0.2670
PrAl ₅ Ni ₂ ²⁵⁰	401.2	707.5	960.0	0.2725
NdAl ₅ Ni ₂ ²⁵²	397.9	705.1	956.9	0.2685

3. The First Europium Rich Aluminum Palladinide Eu_5AlPd_2

In analogy to $\text{Eu}_4\text{Al}_{13}\text{Pt}_9$ and other existing compounds with the general composition $M_4\text{Al}_{13}T_9$ the synthesis of $\text{Eu}_4\text{Al}_{13}\text{Pd}_9$ was attempted due to the similar covalent radii of Pt and Pd with 129 and 128 pm,⁴ which should potentially lead to the same composition and crystal structure. The reaction was performed in a Nb ampoule in the induction furnace, one half of the product was used for the powder X-ray diffraction experiment, showing a mixture of phases with EuAl_3Pd_2 (YAl_3Ni_2 type, $P6/mmm$, $a = 947.012(8)$, $c = 426.920(7)$ pm)⁸⁷ as main phase, EuAl_2Pd_2 (defect $\text{Sr}_2\text{Al}_5\text{Pd}_4$ type, $Pnma$, $a = 1833.9(3)$, $b = 429.9(2)$, $c = 1091.95(8)$ pm), Eu_3Pd_2 (Er_3Ni_2 type, $R\bar{3}$, $a = 918.4(1)$, $c = 1780.6(5)$ pm)²⁶⁹ and at least one unknown phase. The Rietveld refinement is shown in **Figure 3.51**. The structure of $\text{Sr}_2\text{Al}_5\text{Pd}_4$ (own type, $Pnma$) found by Stegemann et al.⁷² was used as starting point for the refinement of the EuAl_2Pd_2 phase, the refinement looked fine at first glance, but when drawing the unit cell, the Al2 and Al5 position only had a distance of less than 100 pm. Therefore, the occupancy of Al2 and Al5 was refined, leading to an occupancy ratio of the Al2 / Al5 position of round 61 / 39. This resulted in a sum formula of EuAl_2Pd_2 (defect $\text{Sr}_2\text{Al}_5\text{Pd}_4$ type, $Pnma$, $a = 1833.9(3)$, $b = 429.8(2)$, $c = 1091.94(8)$ pm, S.O.F. Al2 = 0.6067, Al5 = 0.3933) due to the same $4c$ Wyckoff position of all atoms in the structure. Single crystals studies of the remaining half of the sample were performed by isolating and measuring the single crystals, resulting in a new europium rich phase, $\text{Eu}_5\text{Al}_{0.70(1)}\text{Pd}_{2.30(1)}$. The refinement parameters are summarized with the atom parameters and interatomic distances in **Tables 3.16-3.19**. **Table 3.16** contains the lattice parameters alongside literature known compounds, whereas **Tables 3.17-3.19** are summarized data from the singly crystal diffraction experiment. The structure is shown in **Figure 3.52**. with the coordination sphere of the atoms in **Figure 3.53**. The residual electron density after refinement is still high, however, to solve and roughly refine the structure the single crystal is good enough. However, a better crystal has to be picked and measured for a publication.

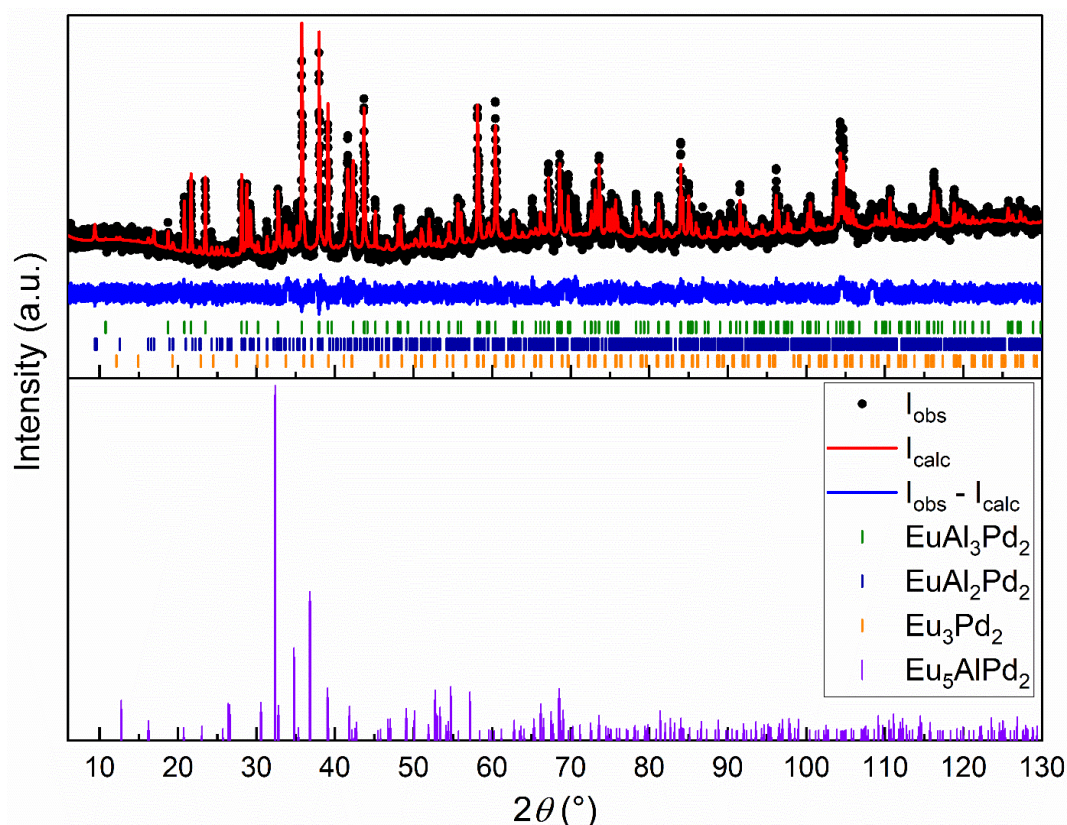


Figure 3.51: Rietveld refinement of the powder X-ray diffraction pattern of nominal $\text{Eu}_4\text{Al}_{13}\text{Pd}_9$. Collected data are shown in black dots, the refinement as red and the difference as blue line. Olive ticks indicate the Bragg positions of EuAl_3Pd_2 (YAl_3Ni_2 type, $P6/mmm$), royal blue of EuAl_2Pd_2 (defect $\text{Sr}_2\text{Al}_3\text{Pd}_4$ type, $Pnma$) and orange ticks the Bragg positions of Eu_3Pd_2 (Er_3Ni_2 type, $R\bar{3}$). Violet lines in the bottom half indicate the calculated diffraction pattern of the $\text{Eu}_5\text{Al}_{0.70(1)}\text{Pd}_{2.30(1)}$ phase (Mo_5SiB_2 type, $I4/mcm$), respectively.

Table 3.16: Lattice parameters and unit cell volumes of selected compounds with the general composition of $\text{RE}_5\text{T}_{3-x}\text{X}_x$ ($\text{RE} = \text{Y, La-Nd, Sm-Lu}$; $\text{T} = \text{Fe-Cu, Ru-Ag, Ir-Au}$; $\text{X} = \text{Al, Si, Ga, Ge, In, Sn}$), sorted after X , then RE element. Structure types are Mo_5SiB_2 ($I4/mcm$), Mn_5Si_3 ($P6_3/mcm$), Y_2HfS_5 ($Pnma$), Ba_5Si_3 ($P4/ncc$), Ce_5NiGe_2 ($P4/ncc$), and W_5Si_3 ($I4/mcm$).

Compound	Structure type	a (pm)	b (pm)	c (pm)	V (nm^3)
$\text{Eu}_5\text{Al}_{0.70(1)}\text{Pd}_{2.30(1)}$	Mo_5SiB_2 ($I4/mcm$)	771.64(3)	a	1383.13(5)	0.8236
$\text{Gd}_5\text{Ga}_{1.8}\text{Ni}_{1.2}$ ²⁷⁰	Mo_5SiB_2 ($I4/mcm$)	771.4	a	1354.93	0.8063
$\text{Tb}_5\text{Ga}_{2.6}\text{Co}_{0.4}$ ²⁷¹	Mo_5SiB_2 ($I4/mcm$)	765.98	a	1384.93	0.8126
$\text{Ho}_5\text{Ga}_{2.9}\text{Co}_{0.1}$ ²⁷²	Mn_5Si_3 ($P6_3/mcm$)	853.39	a	640.86	0.4667
$\text{Ho}_5\text{Ga}_{2.6}\text{Co}_{0.4}$ ²⁷²	Mo_5SiB_2 ($I4/mcm$)	759.71	a	1388.2	0.8012
$\text{Er}_5\text{Ga}_{2.6}\text{Fe}_{0.4}$ ²⁷²	Mo_5SiB_2 ($I4/mcm$)	753	a	1383.4	0.7844
$\text{Er}_5\text{Ga}_{2.6}\text{Co}_{0.4}$ ²⁷²	Mo_5SiB_2 ($I4/mcm$)	753.4	a	1377	0.7816
$\text{Er}_5\text{Ga}_{2.4}\text{Cu}_{0.6}$ ²⁷³	Ba_5Si_3 ($P4/ncc$)	751.5	a	1396	0.7884
$\text{Y}_{4.69}\text{In}_{1.31}\text{Pd}_2$ ²⁷⁴	Mo_5SiB_2 ($I4/mcm$)	779.8	a	1359.8	0.8269
Dy_5InPd_2 ²⁷⁴	Mo_5SiB_2 ($I4/mcm$)	784.9	a	1349.2	0.8312
Er_5InNi_2 ²⁷⁵	Mo_5SiB_2 ($I4/mcm$)	754.6	a	1323.3	0.7535
$\text{La}_5\text{Co}_{0.3}\text{Si}_2$ ²⁷⁶	Mo_5SiB_2 ($I4/mcm$)	793.1	a	1418.1	0.8920
$\text{La}_5\text{Ni}_{0.129}\text{Si}_2$ ²⁷⁶	Mo_5SiB_2 ($I4/mcm$)	792.3	a	1419.8	0.8913
$\text{La}_5\text{Ni}_{0.265}\text{Si}_2$ ²⁷⁶	Mo_5SiB_2 ($I4/mcm$)	792.1	a	1422.4	0.8924
$\text{Ce}_5\text{Ni}_{0.355}\text{Si}_2$ ²⁷⁶	Mo_5SiB_2 ($I4/mcm$)	782.2	a	1378.8	0.8436
$\text{Ce}_5\text{Ni}_{0.72}\text{Si}_2$ ²⁷⁷	Mo_5SiB_2 ($I4/mcm$)	785	a	1470	0.9059

Compound	Structure type	<i>a</i> (pm)	<i>b</i> (pm)	<i>c</i> (pm)	<i>V</i> (nm ³)
Ce ₅ Si _{2.32} Ru _{0.68} ²⁷⁸	Mo ₅ SiB ₂ (<i>I4/mcm</i>)	784.66	<i>a</i>	1362.2	0.8387
Ce ₅ Si _{2.54} Rh _{0.46} ²⁷⁸	Mo ₅ SiB ₂ (<i>I4/mcm</i>)	787.3	<i>a</i>	1379.6	0.8551
Ce ₅ Si _{2.1} Rh _{0.9} ²⁷⁸	Mo ₅ SiB ₂ (<i>I4/mcm</i>)	785.92	<i>a</i>	1365.7	0.8436
Ce ₅ Si _{2.58} Pd _{0.42} ²⁷⁹	Mo ₅ SiB ₂ (<i>I4/mcm</i>)	785.63	<i>a</i>	1382.5	0.8533
Ce ₅ Si _{2.5} Ir _{0.5} ²⁸⁰	Mo ₅ SiB ₂ (<i>I4/mcm</i>)	787.27	<i>a</i>	1379.35	0.8549
Ce ₅ Si _{2.1} Pt _{0.9} ²⁸¹	Mo ₅ SiB ₂ (<i>I4/mcm</i>)	785.5	<i>a</i>	138.5	0.0855
Pr ₅ Ag _{0.32} Si _{2.68} ²⁸²	Mo ₅ SiB ₂ (<i>I4/mcm</i>)	782	<i>a</i>	1383	0.8457
Nd ₅ Co _{0.31} Si _{2.69} ²⁷⁶	Mo ₅ SiB ₂ (<i>I4/mcm</i>)	794.9	<i>a</i>	1418.1	0.8960
Nd ₅ CoSi ₂ ²⁸³	Mo ₅ SiB ₂ (<i>I4/mcm</i>)	772.8	<i>a</i>	1352.85	0.8079
Nd ₅ CoSi ₂ ²⁸³	Mo ₅ SiB ₂ (<i>I4/mcm</i>)	774.72	<i>a</i>	1359.81	0.8161
Nd ₅ Ni _{0.633} Si _{2.367} ²⁷⁶	Mo ₅ SiB ₂ (<i>I4/mcm</i>)	769.5	<i>a</i>	1390.2	0.8232
Nd ₅ Si _{2.25} Ru _{0.75} ²⁸⁴	Mo ₅ SiB ₂ (<i>I4/mcm</i>)	774	<i>a</i>	1361	0.8153
Gd ₅ CoSi ₂ ²⁸⁵	Mo ₅ SiB ₂ (<i>I4/mcm</i>)	757.99	<i>a</i>	1350.91	0.7762
Lu ₅ Ag _{0.3} Si _{2.7} ²⁸⁶	Mn ₅ Si ₃ (<i>P6₃/mcm</i>)	818.98	<i>a</i>	615	0.4125
Y ₅ Fe _{0.4} Ge _{2.6} ²⁸⁷	Mn ₅ Si ₃ (<i>P6₃/mcm</i>)	846.2	<i>a</i>	637.8	0.4567
Ce ₅ CoGe ₂ ²⁸⁸	Y ₂ HfS ₅ (<i>Pnma</i>)	1224.5	885.7	789.1	0.8558
Ce ₅ CoGe ₂ ²⁸⁹	Y ₂ HfS ₅ (<i>Pnma</i>)	1227	885.7	795.8	0.8648
Ce ₅ CoGe ₂ ²⁸⁸	Mn ₅ Si ₃ (<i>P6₃/mcm</i>)	886.7	<i>a</i>	664.8	0.5227
Ce ₅ NiGe ₂ ²⁸⁸	Mn ₅ Si ₃ (<i>P6₃/mcm</i>)	886.4	<i>a</i>	665	0.5225
Ce ₅ NiGe ₂ ²⁸⁸	Mo ₅ SiB ₂ (<i>I4/mcm</i>)	786.1	<i>a</i>	1385.8	0.8564
Ce ₅ NiGe ₂ ²⁹⁰	Ce ₅ NiGe ₂ (<i>P4/ncc</i>)	1176	<i>a</i>	642.9	0.8891
Ce ₅ Ge ₂ Ru ²⁸⁸	Y ₂ HfS ₅ (<i>Pnma</i>)	1222.8	890.2	799.6	0.8704
Ce ₅ Ge ₂ Ru ²⁹¹	Y ₂ HfS ₅ (<i>Pnma</i>)	1225.5	889.8	800.8	0.8732
Ce ₅ Ge ₂ Rh ²⁹²	Y ₂ HfS ₅ (<i>Pnma</i>)	1230.05	888.5	796.49	0.8705
Ce ₅ Ge ₂ Rh ²⁸⁸	Y ₂ HfS ₅ (<i>Pnma</i>)	1234.2	893.2	798.5	0.8803
Ce ₅ Ge ₂ Rh ²⁹²	Mn ₅ Si ₃ (<i>P6₃/mcm</i>)	883.98	<i>a</i>	654.99	0.5118
Ce ₅ Ge ₂ Pd ²⁸⁸	Mn ₅ Si ₃ (<i>P6₃/mcm</i>)	889.1	<i>a</i>	669.1	0.5289
Ce ₅ Ge ₂ Pd ²⁸⁸	Mo ₅ SiB ₂ (<i>I4/mcm</i>)	793.5	<i>a</i>	1378.4	0.8679
Ce ₅ AgGe ₂ ²⁹³	Mn ₅ Si ₃ (<i>P6₃/mcm</i>)	887.8	<i>a</i>	658.03	0.5187
Ce ₅ Ge ₂ Ir ²⁸⁸	Y ₂ HfS ₅ (<i>Pnma</i>)	1237.7	893	800.2	0.8844
Pr ₅ Co _{0.6} Ge _{2.4} ²⁹⁴	Mn ₅ Si ₃ (<i>P6₃/mcm</i>)	882	<i>a</i>	661	0.5142
Sm ₅ Co _{1.4} Ge _{1.6} ²⁹⁵	Mn ₅ Si ₃ (<i>P6₃/mcm</i>)	860	<i>a</i>	651.1	0.4816
Sm ₅ GeRu ₂ ²⁹⁶	Mo ₅ SiB ₂ (<i>I4/mcm</i>)	773.6	<i>a</i>	1342.6	0.8035
Tb ₅ Ni _{0.3} Ge _{2.7} ²⁹⁷	Mn ₅ Si ₃ (<i>P6₃/mcm</i>)	847.2	<i>a</i>	634.8	0.4556
Er ₅ Cu _{0.8} Ge _{2.2} ²⁹⁸	Mn ₅ Si ₃ (<i>P6₃/mcm</i>)	829.8	<i>a</i>	621.66	0.4281
Tm ₅ Co _{0.24} Ge _{2.76} ²⁹⁹	Mn ₅ Si ₃ (<i>P6₃/mcm</i>)	831.6	<i>a</i>	621.6	0.4299
Tm ₅ Ni _{0.64} Ge _{2.36} ³⁰⁰	Mn ₅ Si ₃ (<i>P6₃/mcm</i>)	832	<i>a</i>	622	0.4306
Lu ₅ Ag _{0.3} Ge _{2.6} ³⁰¹	Mn ₅ Si ₃ (<i>P6₃/mcm</i>)	826.2	<i>a</i>	620.1	0.4233
La ₅ Ag _{0.72} Sn _{2.28} ³⁰²	W ₅ Si ₃ (<i>I4/mcm</i>)	1276.1	<i>a</i>	634.7	1.0336
Ce ₅ Ni _{1.41} Sn _{1.59} ³⁰³	Mo ₅ SiB ₂ (<i>I4/mcm</i>)	797.5	<i>a</i>	1359	0.8643
Nd ₅ Ni _{1.4} Sn _{1.6} ³⁰⁴	Mo ₅ SiB ₂ (<i>I4/mcm</i>)	792.4	<i>a</i>	1367	0.8583
Sm ₅ Ni _{1.5} Sn _{1.5} ³⁰⁵	Mo ₅ SiB ₂ (<i>I4/mcm</i>)	790.5	<i>a</i>	1363	0.8517
Gd ₅ SnIr ₂ ³⁰⁶	Mo ₅ SiB ₂ (<i>I4/mcm</i>)	774.4	<i>a</i>	1367.3	0.8200
Tb ₅ SnIr ₂ ³⁰⁶	Mo ₅ SiB ₂ (<i>I4/mcm</i>)	775.9	<i>a</i>	1363.9	0.8211

The lattice parameters of Eu₅Al_{0.70(1)}Pd_{2.30(1)} fit to the literature known compounds with the general composition of RE₅T_{3-x}X_x where the majority of reported compounds containing tetrel

elements, but a small amount of triel elements with seven gallium and three indium containing compounds are known. No metalides with aluminum were reported except the newly found $\text{Eu}_5\text{Al}_{0.70(1)}\text{Pd}_{2.30(1)}$.

By comparing the size of the elements using the covalent radii of the anionic elements in the compounds and the ionic radii in the cationic elements, Y ($r_{\text{ionic}} = 102 \text{ pm}$),⁷⁹ Dy ($r_{\text{ionic}} = 103 \text{ pm}$)⁷⁹ and In ($r_{\text{cov}} = 150 \text{ pm}$)⁴ in $\text{Y}_{4.69}\text{In}_{1.31}\text{Pd}_2$, Dy_5InPd_2 and Eu ($r_{\text{ionic}}(\text{Eu}^{2+}) = 125 \text{ pm}$, $r_{\text{ionic}}(\text{Eu}^{3+}) = 107 \text{ pm}$),⁷⁹ Al ($r_{\text{cov}} = 125 \text{ pm}$)⁴ in $\text{Eu}_5\text{Al}_{0.703}\text{Pd}_{2.297}$ with the corresponding cell volumes of 0.8269, 0.8312 and 0.8236 nm³, only a slight decrease in the aluminum compound is apparent despite the significant bigger size of the indium compared to aluminum, leading to the assumption that the europium is divalent in the compound.

Table 3.17: Crystallographic data and structure refinement for $\text{Eu}_5\text{Al}_{0.70(1)}\text{Pd}_{2.30(1)}$ (Mo_5SiB_2 type, space group $I4/mcm$, $Z = 4$).

Sum formula	$\text{Eu}_5\text{Al}_{0.70(1)}\text{Pd}_{2.30(1)}$
Formula weight, g mol ⁻¹	1023.2
Lattice parameters	see Table 3.16
Calcd. density, g cm ⁻³	8.25
Crystal size, μm^3	$35 \times 40 \times 40$
Diffractionmeter	Bruker X8 APEX2
Wavelength; λ , pm	71.073
Absorption correction	multi-scan Bruker SadABS
Abs. coefficient, mm ⁻¹	42.3
$F(000)$, e	1719
θ range, deg	2.95-30.45
Range hkl	-10, +9; -8, +10; ± 19
Total no. reflections	4748
Independent reflections / R_{int}	363 / 0.0523
Reflections $I > 3 \sigma(I)$ / R_{σ}	326 / 0.0224
Data/ parameters	363 / 18
Goodness of fit on F^2	1.88
$R1$ / $wR2$ for $I > 3 \sigma(I)$	0.0221 / 0.0660
$R1$ / $wR2$ (all data)	0.0260 / 0.0670
Extinction coefficient	90(20)
Extinction scheme	Lorentzian isotropic ³⁰⁷
Larg. diff. peak / hole, $e \text{ \AA}^{-3}$	+5.23 / -3.82

Table 3.18: Atomic coordinates and displacement parameters (in pm²) of Eu₅Al_{0.70(1)}Pd_{2.30(1)} (Mo₅SiB₂ type, space group *I4/mcm*, *Z* = 4).

Atom	Wyckoff	S.O.F.	<i>x</i>	<i>y</i>	<i>z</i>
Eu1	4 <i>c</i>	1	0	0	0
Eu2	16 <i>l</i>	1	0.33631(5)	0.16369(5)	0.14548(4)
Pd1	8 <i>h</i>	1	0.62511(9)	<i>x</i>	0
Pd2	4 <i>a</i>	0.70(1)	0	0	1/4
All	4 <i>a</i>	0.30(1)	0	0	1/4

Atom	<i>U</i> ₁₁	<i>U</i> ₂₂	<i>U</i> ₃₃	<i>U</i> ₁₂	<i>U</i> _{eq}
Eu1	161(3)	161(3)	223(5)	0	182(4)
Eu2	156(2)	156(2)	113(3)	-12(2)	148(2)
Pd1	113(3)	113(3)	101(5)	13(4)	109(4)
Pd2	112(10)	112(10)	110(15)	0	111(12)
All	112(10)	112(10)	110(15)	0	111(12)

^a The isotropic displacement parameter *U*_{eq} is defined as: *U*_{eq} = 1/3 (*U*₁₁ + *U*₂₂ + *U*₃₃) (pm²); *U*₁₃ and *U*₂₃ for Eu₂ 4(12) and -4(12) respectively, for other atoms 0. Standard deviations are given in parentheses.

Table 3.19: Interatomic distances (pm) in Eu₅Al_{0.70(1)}Pd_{2.30(1)} (Mo₅SiB₂ type, space group *I4/mcm*). All distances of the first coordination spheres are listed. Standard deviations equal or smaller than 0.2 pm.

Eu1	4	Pd1	305.0	Pd1	1	Pd1	273.1
	2	All/Pd2	345.8		4	Eu2	301.7
	8	Eu2	351.8		2	Eu1	305.0
Eu2	2	Pd1	301.7		2	Eu2	306.0
	1	Pd1	305.9	All/Pd2	8	Eu2	322.8
	2	All/Pd2	322.8		2	Eu1	345.8
	1	Eu2	345.1				
	2	Eu1	351.8				
	1	Eu2	357.3				

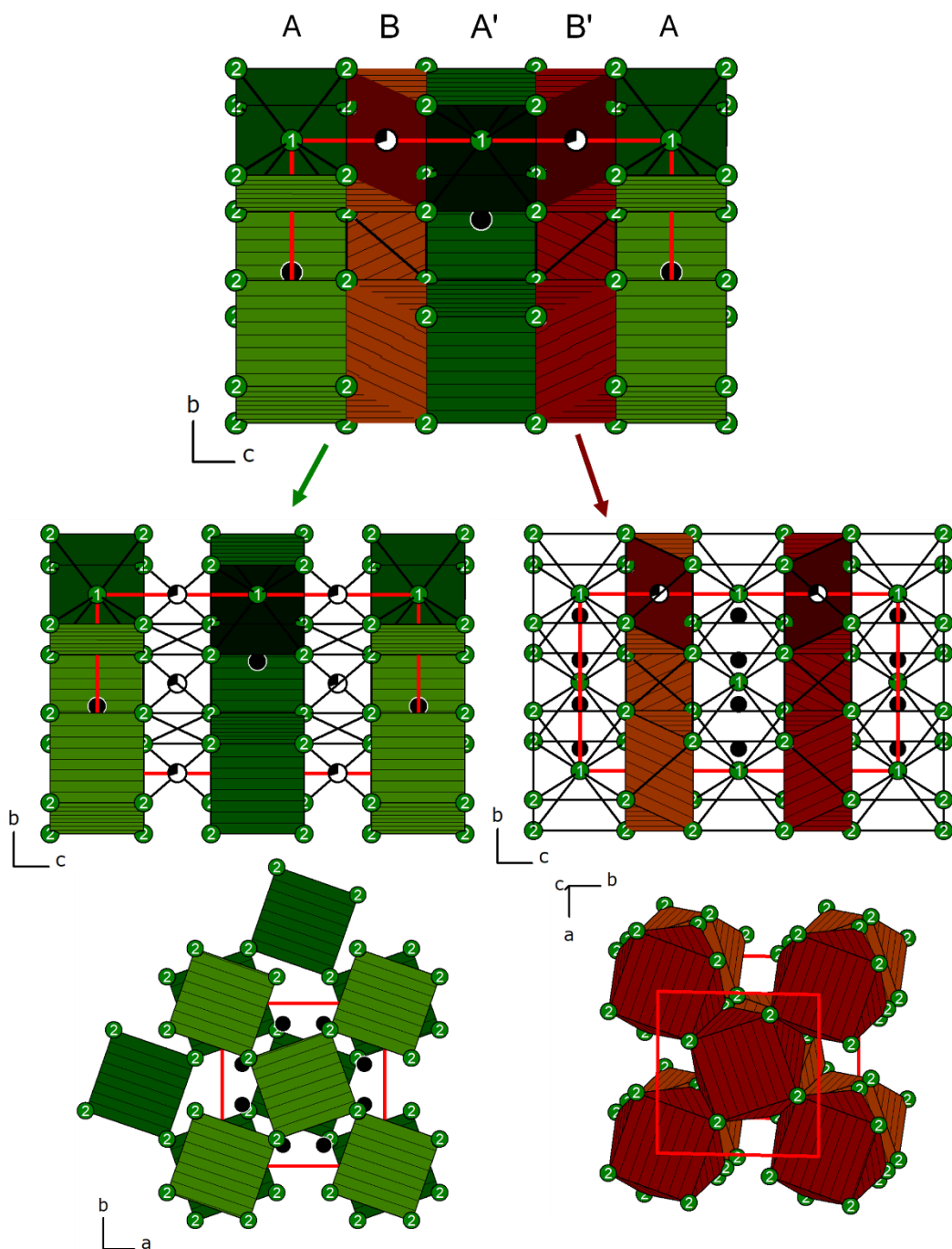


Figure 3.52: Unit cell of $\text{Eu}_5\text{Al}_{0.70(1)}\text{Pd}_{2.30(1)}$ with layer-like cubic and antiprismatic with a ABA'B' stacking (top), edge-shared Eu2 cubic polyhedra layer (middle left), Eu2 antiprismatic polyhedra (middle right) along [100], tilted Eu2 cubes shown along [001] (bottom left) and Eu2 antiprismatic layers (bottom right). Eu, Al, Pd atoms are shown in green, white and black circles, respectively. Mixed occupations are given by segmented circles.

The structure of $\text{Eu}_5\text{Al}_{0.70(1)}\text{Pd}_{2.30(1)}$ can be described as an alternating layer-like structure of edge-shared europium cubes (green polyhedra, $\text{Eu}_1@(\text{Eu}_2)_8$) and europium square antiprisms (red polyhedra, $\text{Al}_1/\text{Pd}_2@(\text{Eu}_2)_8$) with an ABA'B' stacking. The green cubes exhibit two different layers, the bright green layer A and the dark green layer B. When looking along the c -axis the 45° tilt of the cubes of A to B are observable alongside the edge-sharing and the Pd atoms, residing in the vacancies between the cubes inside the layer. The second kind of layer is

formed by the Eu2 atoms surrounding the Al1/Pd2 atoms in the shape of an antiprism. The antiprisms are like the Eu2 cubes edge-shared with each other inside the layer and the layers B and B' are 45° tilted. When looking along the *c*-axis the face-sharing of the antiprisms to the cubes is visible. Also, between the antiprisms inside the layer, no additional atoms are placed in the cavities.

The coordination sphere of Eu1 consists of cubes of eight Eu2 atoms face capped at all sides with four Pd1, top and bottom face capped with Al1/Pd2 atoms. The Eu2 is surrounded by two Eu2 and one Pd1 in a trigonal planar arrangement and additional by a distorted trigonal prism consisting of two Eu1, two Pd1 and two Al1/Pd2 atoms. Pd1 is also coordinated by a trigonal prism, but these contain six Eu2 atoms, the sides are capped with two Eu1 atoms and one Pd1 atom. The last crystallographic position is Al1/Pd2, which resides in a square antiprism of eight Eu2 atoms with the top and bottom capped with two Eu1 atoms.

The Eu–Eu distances range from 345–357 pm and are significantly smaller than the ones found in elemental europium (*W* type, $Im\bar{3}m$) with 399 pm³⁰⁸ and the sum of the covalent radius of europium with $r_{cov} = 185 + 185 = 370$ pm,⁴ but are in line with the binary compounds EuAl₂ (*MgCu*₂ type, $Fd\bar{3}m$, $d(\text{Eu–Eu}) = 352$ pm)²⁰⁴ and EuAl (own type, $Pm\bar{m}n$)³⁰⁹ with $d(\text{Eu–Eu}) = 350$ – 394 pm. When compared to the europium-palladides Eu₃Pd₂ (*Er*₃*Ni*₂ type, $R\bar{3}h$)²⁶⁹, EuPd (*TII* type, $Cmcm$)³¹⁰ and Eu₅Pd₂ (*Mn*₅*C*₂ type, $C2/c$)²⁶⁹ with distances ranging from 362–376 pm, 369–398 pm and 376–393 pm as well as the ternary phases EuGaPd (*TiNiSi* type, $Pnma$)³¹¹, Eu₂InPd₂ (*Ca*₂*Ir*₂*Si* type, $C2/c$)³¹² and Eu₃Al₁₂Rh₄ (*Gd*₃*Al*₁₂*Ru*₄ type, $P6_3/mmc$)⁶¹ with $d(\text{Eu–Eu}) = 362$ – 381 , 379 – 385 pm and 379 pm, respectively, showing a significant shorter distance between the europium atoms. The distances for Eu with Al in the structure of Eu₅Al_{0.70(1)}Pd_{2.30(1)} range from 323 pm to 346 pm, which is in line with the distances found in EuAl₂ (337 pm),²⁰⁴ EuAl (327–373 pm),³⁰⁹ EuAl₃Pd₂ (*YAl*₃*Ni*₂ type, $P6/mmm$, 331–357 pm),⁸⁷ EuAl₆Pd (own type, $Cmmm$, 324–313 pm)⁸⁹ and Eu₄Al₁₃Pt₉ (*Ho*₄*Ge*₉*Ir*₁₃, $Pm\bar{m}n$, 326–359 pm),¹⁷⁶ but slightly longer than Eu₃Al₁₂Rh₄ (*Gd*₃*Al*₁₂*Ru*₄ type, $P6_3/mmc$, 294–321 pm)⁶¹ and Eu₂Al₉Pt₃ (*Y*₂*Ga*₉*Co*₃ type, $Cmcm$, 306–313 pm)⁶¹ and slightly shorter than in EuAl₄ (*BaAl*₄ type, $I4/mmm$)²⁰⁵ with $d(\text{Eu–Al}) = 347$ – 359 pm. The distances of Eu–Pd with 302–346 pm are longer than in EuAl₆Pd⁸⁹ with 369 pm, but are in line with EuPd (*TII* type, $Cmcm$, 287–336 pm),³¹⁰ Eu₅Pd₂ (*Mn*₅*C*₂ type, $C12/c1$, 298–395 pm),²⁶⁹ Eu₃Pd₂ (*Er*₃*Ni*₂ type, $R\bar{3}$, 299–357 pm),²⁶⁹ EuAl₃Pd₂ (302–325 pm),⁸⁷ EuGaPd (311–346 pm),³¹¹ EuGa₃Pd (*SrGa*₃*Pd* type, $Cmcm$, 330–366 pm)³¹³ and Eu₂InPd₂ (315–327 pm).³¹² Also, no homoatomic Al–Al or Al–Pd distances below 350 pm were present in the structure, on the contrary to Pd–Pd distances with 273 pm, which are longer than the sum of the covalent radii with r_{cov} : $128 + 128 = 256$ pm⁴, but in line with the distance found in elemental

palladium with 279 pm.³¹⁴ The distances found in Eu_3Pd_2 ²⁶⁹ with $d(\text{Pd-Pd}) = 279$ pm, Al_3Pd_5 (Rh_5Ge_3 type, $Pbam$)³¹⁵ with 271-325 pm and AlPd_5 (own type, $Pnma$)³¹⁶ 269-307 pm are in line, compared to Eu_2InPd_2 ³¹² with $d(\text{Pd-Pd}) = 276$ -320 pm. The Pd-Pd distances are slightly shorter in comparison to EuPd 327 pm,³¹⁰ EuAl_3Pd_2 302 pm,⁸⁷ EuGaPd 320 pm³¹¹ and EuGa_3Pd with $d(\text{Pd-Pd}) = 357$ pm.³¹³ These atomic distances suggest no bonding interactions between Al-Al and Al-Pd, also the observed distances between Eu-Eu are significantly shorter than in the element and thus have bonding interactions similar to the Eu-Al and Eu-Pd interactions. In the literature other *RE* rich compounds are known, for example RE_4AlPt (Gd_4InRh type, $F\bar{4}3m$)²³⁹ and $\text{RE}_{14}\text{Al}_3\text{Pd}_3$ ($\text{Gd}_{14}\text{In}_{2.7}\text{Co}_3$ type, $P4_2/nmc$) series,³¹⁷ the compounds feature vastly different building blocks than $\text{Eu}_5\text{Al}_{0.7(1)}\text{Pd}_{2.30(1)}$. The RE_4AlPt phases have three crystallographic independent *RE* positions and one each for Pt and Al and exhibits three building blocks, isolated Al_4 tetrahedra, empty RE_6 octahedra and RE_6 trigonal prisms, in which the Pt resides, the octahedra and trigonal prisms form a network using common faces and corners. The interatomic distances here exemplarily given for Ho_4AlPt are $d(\text{Al-Al}) = 293$ pm, $d(\text{Ho-Ho}) = 345$ -403 pm, $d(\text{Ho-Pt}) = 283$ -284 pm.²³⁹ Although the size of trivalent holmium atoms is significant smaller than divalent europium atoms, the *RE-RE* distances are in range, but the Ho-Pt distances are smaller than the Eu-Pd ones, which is then in range if the difference in ionic radii is included with around 24 pm.⁴ In contrast to Ho_4AlPt , $\text{RE}_{14}\text{Al}_3\text{Pd}_3$ series exhibits seven *RE*, two Pd and two crystallographic independent mixed occupied sites with Al/Pd, of which over 85% are occupied with Al. Like in the Ho_4AlPt phase the transition metal resides in a trigonal prism of *RE* atoms, which is additionally capped on three sides with *RE* and Al atoms. Except the *RE3* site, all crystallographic independent *RE* positions can be described as pentagonal prisms of *RE* atoms, of which some are capped with Al and Pd atoms. *RE3* possesses a more distorted coordination environment of three Al, three Pd and eight *RE* atoms. Al1 is surrounded by two Pd atoms and ten *RE* atoms in form of an isolated fourfold *RE* capped RE_6Pd_2 tetragonal prism. Al1 resides in a *RE* capped pentagonal antiprism. Besides the trigonal prisms and pentagonal antiprisms, the structure also contains empty RE_6 octahedra, of which some octahedra form isolated edge-sharing double units, whereas the remaining octahedra form corner-shared strands. The strands and double units are face-shared. Two polyhedra of the Al1 atoms are condensed over a common face and these double units are corner-shared to other double units. The trigonal prisms of the Pd atoms are connected by common edges. When comparing the reported atomic distances for $\text{Y}_{14}\text{Al}_{2.84(1)}\text{Pd}_{3.16(1)}$, the structure exhibits distances of $d(\text{Y-Y}) = 348$ -373 pm, $d(\text{Pd-Pd}) = 299$ -303 pm, $d(\text{Y-Pd}) = 279$ -371 pm and $d(\text{Y-Al}) = 299$ -361 pm,³¹⁷ of which the *RE-RE*, *RE-Pd* and *RE-Al* distances are again in line with the ones

found in the Eu compound, only the homoatomic Pd–Pd distances are significant longer than the ones found in $\text{Eu}_5\text{Al}_{0.70(1)}\text{Pd}_{2.30(1)}$.

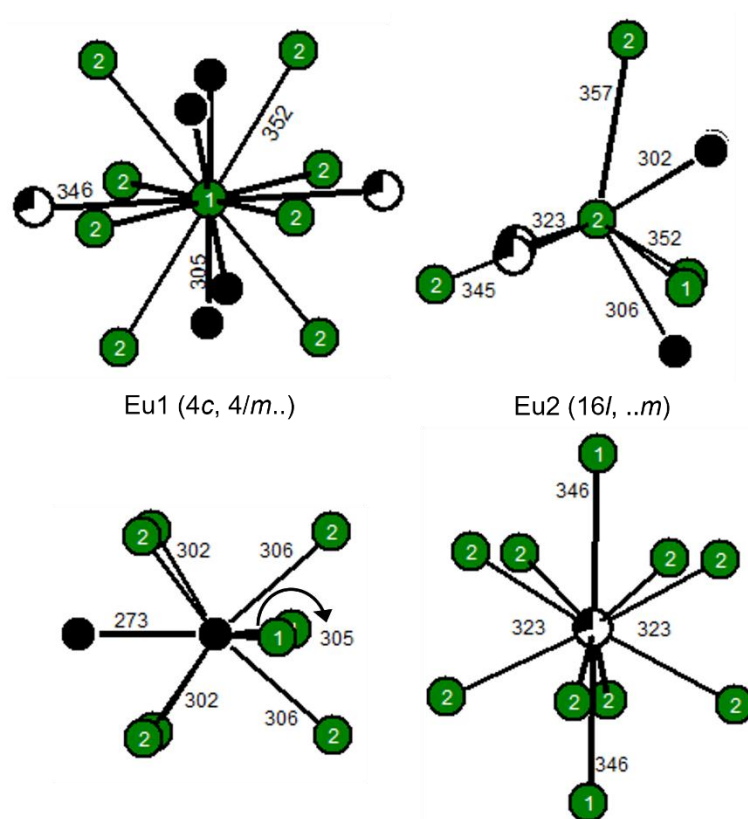


Figure 3.53: Coordination environments surrounding the Eu1 (top left), Eu2 (top right), Pd1 (bottom left) and Al1/Pd2 (bottom right) of $\text{Eu}_5\text{Al}_{0.70(1)}\text{Pd}_{2.30(1)}$. Eu, Al, Pd atoms are shown in green, white and black circles, respectively. Wyckoff positions, site symmetries and interatomic distances (in pm) are given.

4. New Representatives with the $M_4Al_{13}Pt_9$ Structure

Due to the discovery of $Eu_4Al_{13}Pt_9$ and the literature known existence of the cerium compound, an investigation was conducted to evaluate if other rare earth and alkaline earth compounds in the $M_4Al_{13}Pt_9$ system with $M = Sr, Y, La-Nd, Sm-Gd$ can be synthesized. The samples were prepared from the elements in the corresponding ratio in the arc furnace. The resulting melting beads were crushed into pieces, some were stored for single crystal diffraction experiments. The remaining pieces were ground to a fine powder and powder X-ray diffraction measurements were taken, exemplary the Rietveld refinement of $Sm_4Al_{13}Pt_9$ is shown in **Figure 3.54**.

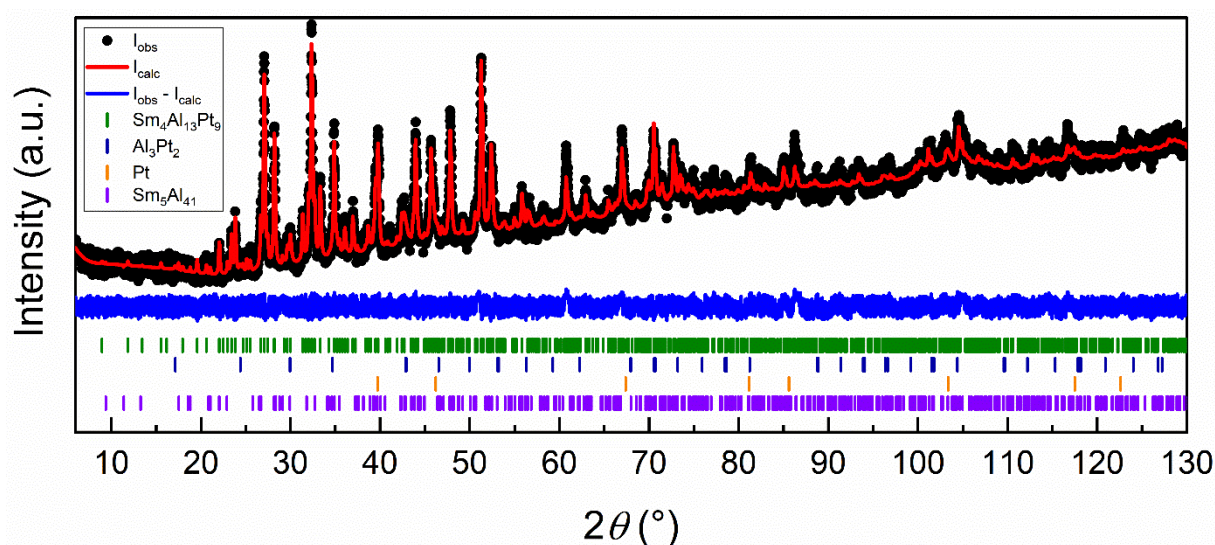


Figure 3.54: Rietveld refinement of the powder X-ray diffraction pattern of $Sm_4Al_{13}Pt_9$. Collected data are shown in black dots, the refinement as red and the difference as blue line. Olive ticks indicate the Bragg positions of $Sm_4Al_{13}Pt_9$ ($Ho_4Ge_9Ir_{13}$ type, $Pm\bar{m}n$), royal blue of Al_3Pt_2 (Al_3Ni_2 type, $P\bar{3}m1$), orange of elemental Pt (Cu type, $Fm\bar{3}m$) and violet ticks the Bragg position of Sm_5Al_{41} (Ce_5Mg_{41} type, $I4/m$) respectively.

The reactions performed in the arc furnace did not lead to a phase pure product. The main phase is the targeted $Sm_4Al_{13}Pt_9$ ($Ho_4Ge_9Ir_{13}$ type, $Pm\bar{m}n$, $a = 411.62(2)$, $b = 1139.64(9)$, $c = 1974.8(1)$ pm) with 94 wt.-% accompanied by the binary compounds Al_3Pt_2 (Al_3Ni_2 type, $P\bar{3}m1$, $a = 521.1(4)$, $c = 516.9(7)$, 1 wt.-%)¹⁹⁹ and Sm_5Al_{41} (Ce_5Mg_{41} type, $I4/m$, $a = 1333.8(2)$, $c = 955.8(6)$ pm, 4 wt.-%)³¹⁸ as well as unreacted platinum (Cu type, $Fm\bar{3}m$, $a = 392.7(2)$ pm)²⁰⁹ with 1 wt.-% leading to an overall composition of $Sm_{3.6(1)}Al_{13}Pt_{7.7(1)}$ indicating the loss of 0.4 eq Sm and 1.3 eq Pt from the ideal composition. The leftover Pt and the appearing side phases indicate that the reaction was not finished and homogeneous during the melting and reaction of the reactants. For the other rare earth elements La, Ce, Pr, Nd and Sm also side phases in the low wt.-% range were observed besides $RE_4Al_{13}Pt_9$ as the main phase, for comparison of the phase composition see **Table 3.20**.

Table 3.20: Phase composition from the PXRD measurements of $RE_4Al_{13}Pt_9$ ($RE = La-Nd, Sm, Gd$), standardized on Al_{13} .

Sample	Main phase (wt.-%)	Side phase (wt.-%)	Overall composition
$La_4Al_{13}Pt_9$	$La_4Al_{13}Pt_9$ (95)	La_3Al_{11} (4), Al_3Pt_2 (1)	$La_{3.9(1)}Al_{13}Pt_{7.9(1)}$
$Ce_4Al_{13}Pt_9$	$Ce_4Al_{13}Pt_9$ (70)	Ce_3Al_{11} (16), Al_3Pt_2 (1), $Ce_{11}O_{20}$ (13)	$Ce_{5.5(1)}Al_{13}Pt_{5.3(1)}O_{3.1(1)}$
$Pr_4Al_{13}Pt_9$	$Pr_4Al_{13}Pt_9$ (97)	PrO_2 (3)	$Pr_{4.5(1)}Al_{13}Pt_{9(1)}O_{1(1)}$
$Nd_4Al_{13}Pt_9$	$Nd_4Al_{13}Pt_9$ (100)	-	$Nd_4Al_{13}Pt_9$
$Sm_4Al_{13}Pt_9$	$Sm_4Al_{13}Pt_9$ (94)	Pt (1), Al_3Pt_2 (1), Sm_5Al_{41} (4)	$Sm_{3.6(1)}Al_{13}Pt_{7.7(1)}$
$Gd_4Al_{13}Pt_9$	$Gd_4Al_{13}Pt_9$ (99)	Al_3Pt_2 (1)	$Gd_{3.9}Al_{13}Pt_9$

In the cases of Sr and Y, no compound formation of the targeted compound was observed, only a mixture of other phases was present, a reason for the failed synthesis could be that Y is too small for the hexagonal prism inside the structure. As for Sr, during the reaction in the arc furnace, too much of the volatile Sr could have been evaporated, so that the reaction is depleted of Sr. Planned are syntheses of the later REs (Tb-Lu) in the arc furnace and also of the Sr and Ca compound in a Ta ampoule to prevent the loss of the AE .

The synthesized $RE_4Al_{13}Pt_9$ compounds are isostructural to the literature known compounds and isopointal to the $Ho_4Ge_9Ir_{13}$ structure type, however, the inversion of occupied sites in the $RE_4T_{13}X_9$ compared to the $RE_4X_{13}T_9$ structure type is observed. **Table 3.21** lists the lattice parameters of the synthesized and literature known compounds.

Table 3.21: Lattice parameters of $M_4X_{13}T_9$ ($Ho_4Ge_9Ir_{13}$ type, $Pmmn$; $M = Sr, Y, La-Nd, Sm-Lu$; $T = Rh, Ir, Pt$; $X = Al, In, Si, Ge$) representatives and $Sr_4In_{13}Au_9$ (own type, $P\bar{6}m2$).

Compound	a (pm)	b (pm)	c (pm)	V (nm ³)
$La_4Al_{13}Pt_9^{P,*}$	419.87(1)	1147.49(5)	1988.63(9)	0.9581
$Ce_4Al_{13}Pt_9^{P,*}$	417.24(2)	1144.26(3)	1982.30(5)	0.9464
$Ce_4Al_{13}Pt_9^{222}$	418.26	1144.24	1984.75	0.9499
$Ce_4Al_{13}Pt_9^{319}$	417.39	1143.73	1981.25	0.9458
$Pr_4Al_{13}Pt_9^{P,*}$	415.80(1)	1142.81(7)	1980.22(12)	0.9409
$Pr_4Al_{13}Pt_9^{319}$	416.15	1141.62	1976.20	0.9389
$Nd_4Al_{13}Pt_9^{P,*}$	414.35(1)	1141.69(7)	1978.34(11)	0.9359
$Nd_4Al_{13}Pt_9^{SC,*}$	413.68(8)	1140.06(2)	1977.18(4)	0.9325
$Sm_4Al_{13}Pt_9^{P,*}$	411.62(2)	1139.64(9)	1974.80(12)	0.9264
$Eu_4Al_{13}Pt_9^{176}$	415.38	1149.73	1994.73	0.9526
$Gd_4Al_{13}Pt_9^{P,*}$	409.40(1)	1138.46(5)	1973.04(7)	0.9196
$Sr_4In_{13}Pt_9^{197}$	439.17	1232.20	2135.30	1.1555
$Sr_4In_{13}Au_9^{320}$	1270.1	a	443.50	0.6196
$Y_4Si_9Ir_{13}^{321}$	392.5	1092.2	1885.6	0.8083
$Sm_4Si_9Ir_{13}^{321}$	395.7	1101.6	1898.3	0.8275
$Gd_4Si_9Ir_{13}^{321}$	394.7	1098.5	1893.9	0.8212
$Tb_4Si_9Ir_{13}^{321}$	393.6	1096.1	1890.8	0.8157

Compound	<i>a</i> (pm)	<i>b</i> (pm)	<i>c</i> (pm)	<i>V</i> (nm ³)
Dy ₄ Si ₉ Ir ₁₃ ³²¹	392.6	1094.3	1887.4	0.8109
Ho ₄ Si ₉ Ir ₁₃ ³²¹	391.7	1090.4	1886.9	0.8059
Er ₄ Si ₉ Ir ₁₃ ³²¹	391.53	1091.8	1884.8	0.8057
Tm ₄ Si ₉ Ir ₁₃ ³²¹	390.8	1090.9	1883.2	0.8029
Yb ₄ Si ₉ Ir ₁₃ ³²¹	390.6	1091.6	1884.9	0.8037
Lu ₄ Si ₉ Ir ₁₃ ³²¹	389.9	1091.2	1880.7	0.8002
Ce ₄ Ge ₉ Rh ₁₃ ³²²	398.9	1125	1944.6	0.8727
La ₄ Ge ₉ Ir ₁₃ ³²³	400.79	1123.4	1944.4	0.8755
Ce ₄ Ge ₉ Ir ₁₃ ³²³	401.08	1124.1	1946.6	0.8776
Pr ₄ Ge ₉ Ir ₁₃ ³²³	401.45	1124.3	1946	0.8783
Nd ₄ Ge ₉ Ir ₁₃ ³²³	400.72	1122.3	1945	0.8747
Sm ₄ Ge ₉ Ir ₁₃ ³²³	399.28	1122.01	1938.29	0.8683
Ho ₄ Ge ₉ Ir ₁₃ ¹⁷⁷	395.4	1118.6	1930.1	0.8537

^P powder data, ^{SC} single crystal data, * own work

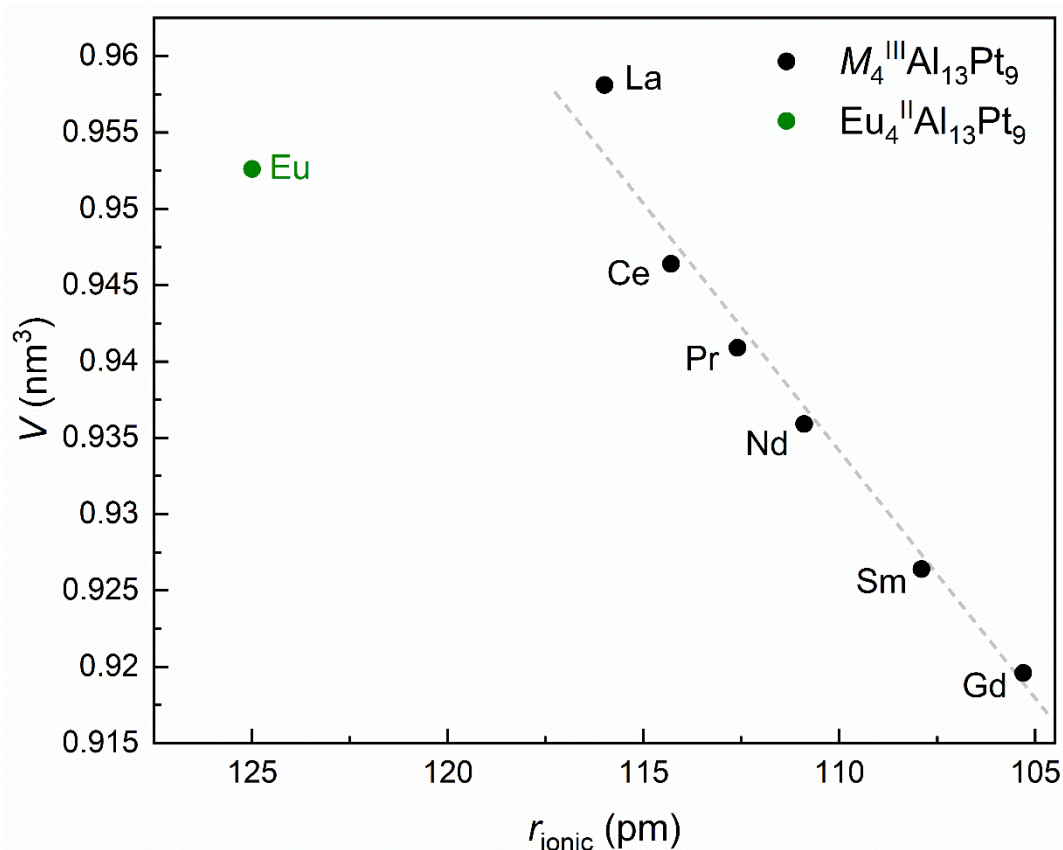


Figure 3.55: Plot of the unit cell volumes (in nm³) for the RE₄Al₁₃Pt₉ series (RE = La-Nd, Sm-Gd) versus the REⁿ⁺ radius (in pm for CN = 8). Formally divalent metal atoms are depicted in olive dots, trivalent ones in black.

As the structure is isostructural with the cerium, praseodymium and europium compound the unit cell and structural description is given in **Chapter 3.a.** already. So here only the lattice parameters and atomic distances will be discussed.

Figure 3.55 shows the unit cell volume plot of the RE₄Al₁₃Pt₉ compounds versus their ionic radii,⁷⁹ showing a linear trend for the early RE metals indicating a trivalent state, except for

europium, which possesses a higher unit cell volume and thus should be not purely trivalent due to the size difference of Eu^{2+} (125 pm) to Eu^{3+} (107 pm).⁷⁹ The compounds in the system $RE/\text{Si}/\text{Ir}$ follow the same trend, starting from samarium with a cell volume of 0.8275 nm^3 with the highest volume decreasing to the lutetium compound with 0.8002 nm^3 .³²¹ Interestingly, the isopointal series of $RE_4\text{Ge}_9\text{Ir}_{13}$ with $RE = \text{Pr}, \text{Nd}$ and Sm ³²³ shows an analogue trend of decreasing unit cell volumes with progressing RE metal, but the La and Ce containing structures possess a lower cell volume with increasing atomic number when going from La over Ce to Pr.³²³

To verify the structure type of the newly found $RE_4\text{Al}_{13}\text{Pt}_9$ compounds, SCXRD measurements of the $\text{Nd}_4\text{Al}_{13}\text{Pt}_9$ sample were conducted by isolating block shaped single crystals from the as-cast melting bead and glueing them on glass fibers using beeswax. The results from the single crystal measurements are summarized in **Tables 3.22-3.24**. As preliminary results the measured single crystal has a relatively high residue electron density, however the data can be used to solve and refine the structure. For a publication, a better single crystal has to be picked and measured.

The structure features three independent rare earth positions residing in channels surrounded by a polyanionic network of Al and Pt, when comparing the motive to similar structures like the $M\text{Al}_5\text{Pt}_3$ (YNi_5Si_3 type, $Pnma$)¹⁷² and the $M_2\text{Al}_{16}\text{Pt}_9$ ($\text{Ce}_2\text{Al}_{16}\text{Pt}_9$ type, $Immm$)¹⁷⁴ series, which only have one crystallographic cation position, the same trend of decrease in unit cell volume along smaller RE ion size emerges with the Eu compound being significant bigger due to the divalent state of the Eu. When looking at the Nd–Al and Nd–Pt distances of the Al and Pt atoms forming the hexagonal prism in the three phases, $d(\text{Nd–Al}) = 323\text{-}344, 324\text{-}333, 324\text{-}341 \text{ pm}$ and $d(\text{Nd–Pt}) = 323\text{-}326, 330\text{-}337, 317\text{-}329 \text{ pm}$ for NdAl_5Pt_3 (YNi_5Si_3 type, $Pnma$),¹⁷² $\text{Nd}_2\text{Al}_{16}\text{Pt}_9$ ($\text{Ce}_2\text{Al}_{16}\text{Pt}_9$ type, $Immm$)¹⁷⁴ and $\text{Nd}_4\text{Al}_{13}\text{Pt}_9$ ($\text{Ho}_4\text{Ge}_9\text{Ir}_{13}$ type, $Pm\bar{m}n$) respectively, all of the observable exhibit atomic distances in the same range, leading to the assumption that the Nd atoms in $\text{Nd}_4\text{Al}_{13}\text{Pt}_9$ are trivalent as in the other two compounds.

Table 3.22: Crystallographic data and structure refinement for Nd₄Al₁₃Pt₉ (Ho₄Ge₉Ir₁₃ type, space group *Pmmn*, *Z* = 2).

Sum formula	Nd ₄ Al ₁₃ Pt ₉
Formula weight, g mol ⁻¹	2683.4
Lattice parameters	See Table 3.21
Calcd. density, g cm ⁻³	9.56
Crystal size, μm ³	50 × 45 × 40
Diffractometer	Bruker X8 APEX2
Wavelength; λ, pm	71.073
Absorption correction	multi-scan Bruker SadABS
Abs. coefficient, mm ⁻¹	78.7
<i>F</i> (000), <i>e</i>	2222
<i>θ</i> range, deg	1.03-37.34
Range <i>hkl</i>	-7, +6; -18, +19; ±33
Total no. reflections	21945
Independent reflections / <i>R</i> _{int}	2771 / 0.0508
Reflections <i>I</i> > 3 <i>σ</i> (<i>I</i>) / <i>R</i> _σ	2171 / 0.0307
Data/ parameters	2771 / 88
Goodness of fit on <i>F</i> ²	1.26
<i>R</i> 1 / w <i>R</i> 2 for <i>I</i> > 3 <i>σ</i> (<i>I</i>)	0.0250 / 0.0571
<i>R</i> 1 / w <i>R</i> 2 (all data)	0.0381 / 0.0613
Extinction coefficient	147(10)
Extinction scheme	Lorentzian isotropic ³⁰⁷
Larg. diff. peak / hole, <i>e</i> Å ⁻³	+3.89 / -3.48

Table 3.23: Atomic coordinates and displacement parameters (in pm²) of Nd₄Al₁₃Pt₉ (Ho₄Ge₉Ir₁₃ type, space group *Pmmn*, *Z* = 2).

Atom	<i>Wyckoff</i>	<i>x</i>	<i>y</i>	<i>z</i>
Nd1	4 <i>e</i>	1/4	0.55457(4)	0.71066(2)
Nd2	2 <i>b</i>	1/4	3/4	0.51584(3)
Nd3	2 <i>a</i>	1/4	1/4	0.02051(3)
Pt1	4 <i>e</i>	1/4	0.06359(3)	0.41890(1)
Pt2	4 <i>e</i>	1/4	0.56329(3)	0.91439(1)
Pt3	4 <i>e</i>	1/4	0.62662(3)	0.22798(1)
Pt4	2 <i>b</i>	1/4	3/4	0.10299(2)
Pt5	2 <i>a</i>	1/4	1/4	0.23177(2)
Pt6	2 <i>a</i>	1/4	1/4	0.60606(2)
Al1	4 <i>e</i>	1/4	0.0481(2)	0.5476(1)
Al2	4 <i>e</i>	1/4	0.0667(2)	0.1626(1)
Al3	4 <i>e</i>	1/4	0.1271(2)	0.8548(1)
Al4	4 <i>e</i>	1/4	0.5533(2)	0.04106(13)
Al5	4 <i>e</i>	1/4	0.6291(2)	0.35773(12)
Al6	2 <i>b</i>	1/4	3/4	0.8425(2)
Al7	2 <i>a</i>	1/4	1/4	0.3560(2)
Al8	2 <i>a</i>	1/4	1/4	0.7309(2)

Atom	<i>U</i> ₁₁	<i>U</i> ₂₂	<i>U</i> ₃₃	<i>U</i> ₂₃	<i>U</i> _{eq}
Nd1	92(2)	58(2)	74(2)	-2(1)	75(2)
Nd2	97(2)	63(2)	72(2)	0	77(2)
Nd3	84(2)	48(2)	78(2)	0	70(2)
Pt1	106(1)	45(1)	70(1)	-1(9)	74(1)
Pt2	74(1)	43(1)	62(1)	-3(1)	60(1)
Pt3	86(1)	41(1)	63(1)	2(9)	63(1)
Pt4	90(2)	42(17)	57(2)	0	63(7)
Pt5	103(2)	41(2)	64(2)	0	69(2)
Pt6	74(2)	59(17)	64(2)	0	66(7)
Al1	132(11)	63(11)	80(1)	-2(9)	92(8)
Al2	83(10)	53(10)	73(10)	4(8)	70(10)
Al3	93(10)	26(10)	79(10)	11(8)	66(10)
Al4	100(1)	53(10)	74(10)	7(8)	76(7)
Al5	119(10)	43(11)	67(9)	9(8)	76(10)
Al6	115(15)	23(14)	106(15)	0	81(15)
Al7	214(18)	44(15)	60(14)	0	106(16)
Al8	116(15)	44(15)	64(13)	0	75(14)

^a The isotropic displacement parameter *U*_{eq} is defined as: *U*_{eq} = 1/3 (*U*₁₁ + *U*₂₂ + *U*₃₃) (pm²); *U*₁₂ and *U*₁₃ = 0. Standard deviations are given in parentheses.

Table 3.24: Interatomic distances (pm) in Nd₄Al₁₃Pt₉ (Ho₄Ge₉Ir₁₃ type, space group *Pmmn*, *Z* = 2). All distances of the first coordination spheres are listed. Standard deviations equal or smaller than 0.2 pm.

Nd1	2	Pt3	316.5	Pt3	1	Al2	255.5	Al3	1	Pt2	246.9
	2	Al5	323.9		1	Al5	256.6		2	Pt4	263.5
	2	Pt5	324.7		2	Al8	263.0		2	Pt3	263.7
	2	Al2	325.3		2	Al3	263.8		1	Al3	280.3
	2	Pt1	329.4		1	Pt3	281.3		1	Al8	282.2
	2	Al7	331.3		1	Pt4	284.4		2	Al4	303.7
	1	Al6	343.0		2	Nd1	316.5		2	Al2	304.6
	1	Al1	343.0	Pt4	2	Al4	255.5		1	Nd1	352.3
	1	Al8	349.5		4	Al3	263.4		1	Nd3	356.4
	1	Al3	352.3		2	Pt3	284.4	Al4	1	Pt2	250.8
Nd2	2	Pt6	317.6		2	Nd3	320.0		1	Pt4	255.4
	4	Pd1	323.5	Pt5	1	Al7	245.6		2	Pt2	261.2
	2	Al7	327.2		2	Al2	249.7		1	Al2	276.5
	4	Al1	333.9		2	Al6	253.7		2	Al4	289.7
	2	Al5	341.6		4	Nd1	324.6		2	Al3	303.7
	2	Al1	345.6	Pt6	1	Al8	246.8		2	Nd3	328.5
Nd3	2	Pt4	320.0		2	Al1	257.7		1	Nd3	348.2
	4	Pt2	323.5		4	Al5	258.7	Al5	1	Pt1	205.8
	4	Al4	328.5		2	Nd2	317.7		1	Pt3	256.6
	2	Al6	340.7	Al1	2	Pt1	251.8		2	Pt6	258.6
	2	Al4	348.2		1	Pt1	254.9		1	Al5	275.6
	2	Al2	350.1		1	Pt6	257.7		2	Al1	293.9
	2	Al3	356.4		2	Al5	294.0		2	Al8	304.1
Pt1	1	Al7	246.3		2	Al1	300.2		2	Nd1	323.9
	1	Al5	250.7		2	Nd2	333.9		1	Nd2	341.7
	2	Al1	251.8		1	Nd1	343.1	Al6	2	Pt5	253.7
	1	Al1	255.0		1	Nd2	345.5		2	Pt2	255.9
	2	Nd2	323.4	Al2	1	Pt5	249.7		4	Al2	294.2
	2	Nd1	329.4		1	Pt3	255.5		2	Nd3	340.7
Pt2	1	Al3	246.9		2	Pt2	256.8		2	Nd1	343.0
	1	Al4	250.8		1	Al4	276.5	Al7	1	Pt5	245.6
	1	Al6	255.9		2	Al6	294.2		2	Pt1	246.3
	2	Al2	256.8		2	Al3	304.6		2	Nd2	327.1
	2	Al4	261.1		2	Nd1	325.3		4	Nd1	331.3
	2	Nd3	323.5		1	Nd3	350.2	Al8	1	Pt6	246.7
									4	Pt3	263.1
									2	Al3	282.3
									4	Al5	304.1
									2	Nd1	349.5

The results from the single crystal X-ray diffraction indicate that the Nd containing compound crystallizes indeed in the Ho₄Ge₉Ir₁₃ type structure. The atomic distances range from 276-306 pm for Al–Al, 324-356 pm for Nd–Al, 246-264 pm for Al–Pt, 317-329 pm and 281-284 pm for Nd–Pt and Pt–Pt distances respectively. The distances of Al–Al and Pt–Pt are longer than the sum of the covalent radii of $r_{\text{cov}}(\text{Al}) = 125 + 125 = 250 \text{ pm}^4$ and $r_{\text{cov}}(\text{Pt}) = 129 + 129 =$

258 pm,⁴ but in range of the distances found in the corresponding elements Al (Cu type, $Fm\bar{3}m$, 286 pm)²⁰⁸ and Pt (Cu type, $Fm\bar{3}m$, 277 pm).²⁰⁹ When comparing the Pt–Pt distances found in $Nd_4Al_{13}Pt_9$ with the binary and ternary compounds NdPt (FeB type, $Pnma$, 325 pm),³²⁴ AlPt (FeSi type, $P2_13$, 300 pm),²²⁸ Al_3Pt_2 (Al_3Ni_2 type, $P\bar{3}m1$, 294 pm), $NdAl_5Pt_3$ (YNi_5Si_3 type, $Pnma$, 300 pm),¹⁷² and $Nd_2Al_{16}Pt_9$ ($Ce_2Al_{16}Pt_9$ type, $Immm$, 300 pm)¹⁷⁴ slightly shorter distances are found. The distances in Al_3Pt_5 (Ge_3Rh_5 type, $Pbam$, 273-336 pm),³²⁵ $NdPt_5$ (CaCu₅ type, $P6/mmm$, 267-346 pm)³²⁶ and $NdAl_3Pt_6$ (own type, $R\bar{3}c$, 274-349 pm)³²⁷ are in better agreement. In case of $NdPt_2$ (MgCu₂ type, $Fd\bar{3}m$)³²⁸ the Pt–Pt distances are 272 pm and slightly shorter than in $Nd_4Al_{13}Pt_9$ but in line with regard to the Nd–Pt distances of 319 pm for $NdPt_2$ (MgCu₂ type, $Fd\bar{3}m$).³²⁸ Other Nd–Pt distances found in the binary compounds range from 279-323 pm in NdPt (TII type, $Cmcm$),³²⁹ 289-300 pm Nd_7Pt_3 (Th_7Fe_3 type, $P6_3mc$)³³⁰ to 309-346 pm for $NdPt_5$ (CaCu₅ type, $P6/mmm$),³²⁶ which are in the same range as the ones found in $Nd_4Al_{13}Pt_9$ and for the ternary compounds $NdAl_5Pt_3$,¹⁷² $Nd_2Al_{16}Pt_9$,¹⁷⁴ $NdAl_3Pt_6$,³²⁷ and $NdAlPt$ ⁶⁷ with 323-326 pm, 330-337 pm, 308-328 pm, 291-317 pm and 340 pm respectively. The Nd–Al distances found in $Nd_4Al_{13}Pt_9$ range from 324 to 356 pm, these are in line with the binary and ternary compounds $NdAl_2$ (MgCu₂ type, $Fd\bar{3}m$, 332 pm),³³¹ Nd_3Al (Mg_3Cd type, $P6_3/mmc$, 337-348 pm),³³² Nd_3Al_{11} (La_3Al_{11} type, $Immm$, 320-333 pm),³³² $NdAl$ (DyAl type, $Pbcm$, 310-346 pm),²⁴² $NdAl_5Pt_3$ (YNi_5Si_3 type, $Pnma$, 323-348 pm),¹⁷² $Nd_2Al_{16}Pt_9$ ($Ce_2Al_{16}Pt_9$ type, $Immm$, 323-333 pm),¹⁷⁴ $NdAlPt$ (TiNiSi type, $Pnma$, 309-334 pm)⁶⁷ and $NdAl_3Pt_6$ (own type, $R\bar{3}c$, 334-338 pm).³²⁷ As already discussed in the **Chapter 3.a** the structure forms a polyanionic network $[Al_{13}Pt_9]^{\delta-}$ in which the RE in this case the $Nd^{\delta+}$ ions reside. Due to the Eu variant being isostructural, the atomic distances of Al–Al and Al–Pt are in the same range to the Eu compound with 277-284 pm and 247-265 pm for $Eu_4Al_{13}Pt_4$ ($Ho_4Ge_9Ir_{13}$ type, $Pmnm$)¹⁷⁶ and 276-306 pm and 246-264 pm for $Nd_4Al_{13}Pt_9$. When compared to binary and ternary phases the aforementioned Al–Al and Pt–Al distances are in range with the ones found in AlPt (FeSi type, $P2_13$, $d(Al-Al)$: 301 pm, $d(Al-Pt)$: 259-262 pm),²²⁸ Al_2Pt (CaF₂ type, $Fm\bar{3}m$, $d(Al-Al)$: 296 pm, $d(Al-Pt)$: 256 pm)²⁰⁷, Al_3Pt_5 ($d(Al-Al)$: 314,345 pm, $d(Al-Pt)$: 253-295 pm),³²⁵ Al_3Pt_2 (Al_3Ni_2 type, $P\bar{3}m1$, $d(Al-Al)$: 278-309 pm, $d(Al-Pt)$: 243-274 pm),¹⁹⁹ $NdAl_2$ (MgCu₂ type, $Fd\bar{3}m$, $d(Al-Al)$: 283 pm),³³¹ Nd_3Al_{11} (La_3Al_{11} type, $Immm$, $d(Al-Al)$: 262-326 pm),³³² $NdAl$ (DyAl type, $Pbcm$, $d(Al-Al)$: 274-286 pm),³³² $NdAl_5Pt_3$ (YNi_5Si_3 type, $Pnma$, $d(Al-Al)$: 270-342 pm, $d(Al-Pt)$: 237-279 pm),¹⁷² $Nd_2Al_{16}Pt_9$ ($Ce_2Al_{16}Pt_9$ type, $Immm$, $d(Al-Al)$: 286-339 pm, $d(Al-Pt)$: 239-336 pm),¹⁷⁴ $NdAlPt$ (TiNiSi type, $Pnma$, $d(Al-Al)$: 320 pm, $d(Al-Pt)$: 260-268 pm),⁶⁷ $NdAl_3Pt_6$ ($d(Al-Al)$: 316-327 pm, $d(Al-Pt)$: 250-286 pm).³²⁷

In addition to the X-ray diffraction experiments, semiquantitative analyses via SEM/EDX were performed on $\text{La}_4\text{Al}_{13}\text{Pt}_9$, $\text{Gd}_4\text{Al}_{13}\text{Pt}_9$ and $\text{Sm}_4\text{Al}_{13}\text{Pt}_9$. The results as well as the scanning electron microscopy images of the compounds are summarized and presented in **Table 3.25** and **Figure 3.56** showing a good agreement with the *RE* element content, the Al and Pt ratio however is far from what would be expected in regard to the ideal composition. The occurring deviations can be partially explained by the rough texture of the samples and the non-perfect orientation of the crystallites to the electron beam, another explanation could be that the platinum is reabsorbing part of the emission spectra of the aluminum leading to a higher amount of Pt and decreased amount of Al. As already discussed with the powder X-ray diffraction, the Sm sample does not contain a compound with a high content of Pt, except for the elemental platinum. If the elemental platinum had been measured, Al and Sm should not have been detected, although if an area measurement was done, different crystallites could have been measured, which still would lead to a significant lower amount of Al and Sm compared to Pt. Although the samples are not phase pure as shown in the Rietveld refinement, the structure could be solved and refined, also the side phases in these samples are less than five wt.-%.

Table 3.25: SEM/EDX data of $\text{La}_4\text{Al}_{13}\text{Pt}_9$, $\text{Sm}_4\text{Al}_{13}\text{Pt}_9$ and $\text{Gd}_4\text{Al}_{13}\text{Pt}_9$ with standard deviations of ± 2 at.-%.

Compound	Ideal	P1	P2	P3	mean
$\text{La}_4\text{Al}_{13}\text{Pt}_9$	La: 15.4	16	17	16	16
	Al: 50.0	40	42	42	41
	Pt: 34.6	44	41	43	43
$\text{Sm}_4\text{Al}_{13}\text{Pt}_9$	Sm: 15.4	15	16	15	15
	Al: 50.0	40	42	50	44
	Pt: 34.6	45	42	35	41
$\text{Gd}_4\text{Al}_{13}\text{Pt}_9$	Gd: 15.4	18	18	19	18
	Al: 50.0	36	41	36	38
	Pt: 34.6	46	41	45	44

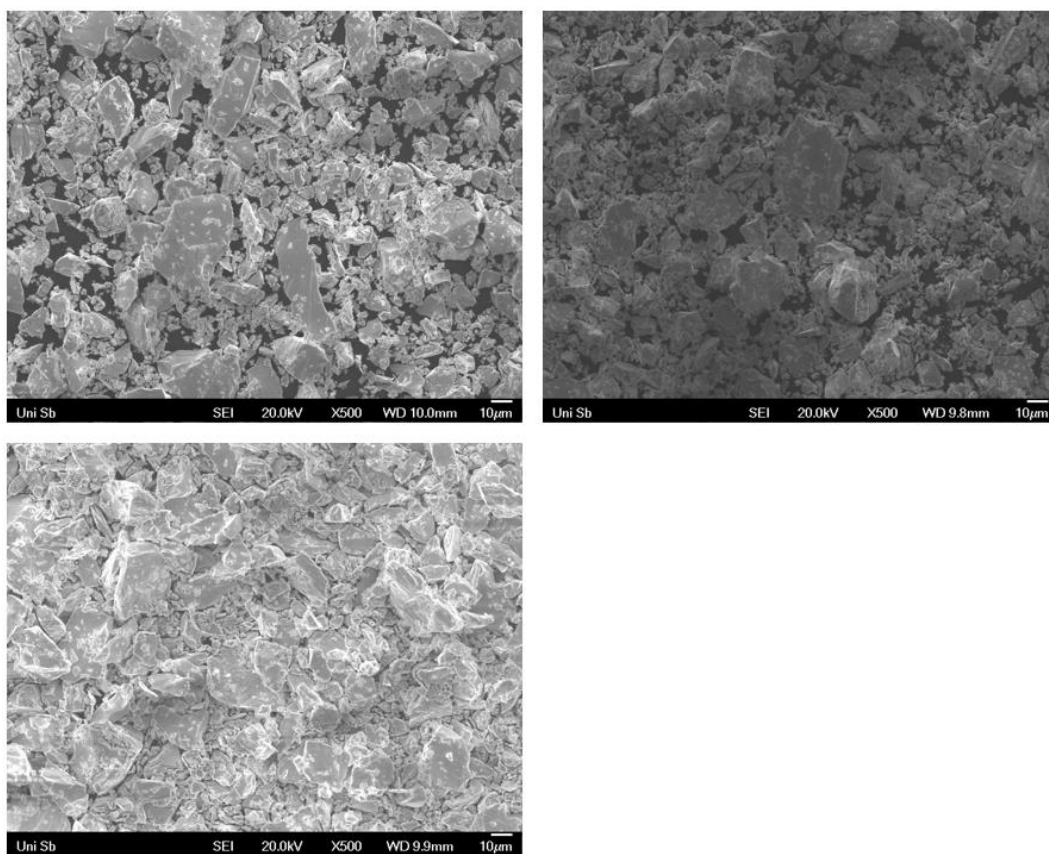


Figure 3.56: Scanning electron microscopy images of $\text{La}_4\text{Al}_{13}\text{Pt}_9$ (top left), $\text{Sm}_4\text{Al}_{13}\text{Pt}_9$ (top right) and $\text{Gd}_4\text{Al}_{13}\text{Pt}_9$ (bottom left).

5. ^{27}Al NMR Investigations in the System Yb–Al– T

The YbAl T series exists with $T = \text{Ru, Co, Rh, Ni, Pd, Pt, Cu, Ag, Au}$ and depending on the transition metal and reaction conditions the MgZn $_2$ type, MgCu $_2$ type, TiNiSi type ($Pnma$) or ZrNiAl type ($P\bar{6}2m$) can form. These structures feature one to two different crystallographic Al positions making them prime candidates for ^{27}Al MAS NMR studies. All compounds are summarized in **Table 3.26** along the structure type and number of independent Al positions.

Table 3.26: YbAl T series with corresponding structure type and number of Al positions.

Compound	Structure types (SG)	Number of Al positions
YbAlRu ³³³	MgZn $_2$ ($P6_3/mmc$)	2 mixed with Ru
YbAlCo ³³⁴	MgZn $_2$ ($P6_3/mmc$)	2 mixed with Co
YbAlRh ³³⁵	TiNiSi ($Pnma$)	1 unmixed
YbAlNi np ³³⁶	ZrNiAl ($P\bar{6}2m$)	1 unmixed
YbAlNi hp ³³⁷	MgZn $_2$ ($P6_3/mmc$)	2 mixed with Ni
YbAlPd ³³⁸	TiNiSi ($Pnma$)	1 unmixed
YbAlPt ⁶⁶	TiNiSi ($Pnma$)	1 unmixed
YbAlCu np ³³⁹	ZrNiAl ($P\bar{6}2m$)	1 unmixed
YbAlCu hp ³³⁷	MgCu $_2$ ($Fd\bar{3}m$)	1 mixed with Cu
YbAlAg ³⁴⁰	MgZn $_2$ ($P6_3/mmc$)	2 mixed with Ag
YbAlAu ³⁴¹	TiNiSi ($Pnma$)	1 unmixed

Due to the low boiling point of the Yb, reactions were performed primarily in the induction furnace in sealed Ta ampoules to prevent Yb from evaporating. The elements were weighted according to the ideal ratio and placed in the Ta ampoule, subsequently the ampoule was sealed with a Ta lid inside the arc furnace and placed inside the induction furnace afterwards. A temperature of 1573 K was applied for 10 min and an additional heat treatment step by reducing the power output to get a temperature of about 1073 K over a period of 5 h followed. Afterwards the induction furnace was shut off. The resulting powder X-ray diffraction pattern for the YbAlPt sample is shown in **Figure 3.57**.

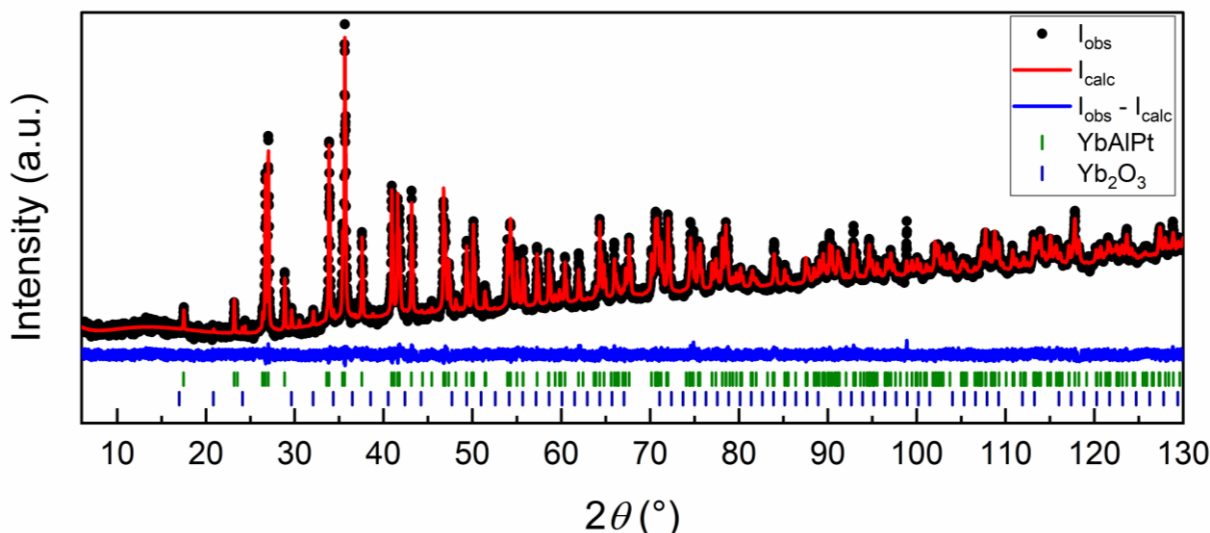


Figure 3.57: Rietveld refinement of the powder X-ray diffraction pattern of YbAlPt. Collected data are shown in black dots, the refinement as red and the difference as blue line. Olive ticks indicate the Bragg positions of YbAlPt (TiNiSi type, $Pnma$) and royal blue ticks of Yb₂O₃ ((Mn_{0.5}Fe_{0.5})₂O₃ type, $Ia\bar{3}$) respectively.

As in the powder X-ray diffraction pattern observable, the sample of YbAlPt (TiNiSi type, $Pnma$, $a = 675.42(1)$, $b = 434.08(1)$, $c = 767.49(1)$ pm),⁶⁶ is not phase pure and contains 1 wt.-% Yb₂O₃ ((Mn_{0.5}Fe_{0.5})₂O₃ type, $Ia\bar{3}$, $a = 1043.6(1)$ pm).³⁴² An attempt to measure the ²⁷Al MAS NMR spectrum resulted in a failure due to the paramagnetism of the sample, originating either from Yb₂O₃ or YbAlPt directly, which exhibits an antiferromagnetic ordering below 5.8 K, an effective magnetic moment of 4.5 μ_B per Yb atom (effective magnetic moment of free Yb³⁺ ions: 4.5 μ_B) and a Curie-Weiss temperature of -60 K (YbAlNi: $T_N = 2.8$ K, $\mu_{\text{eff}} = 4.4$ μ_B per Yb atom, Curie-Weiss temperature: -35 K).³⁴³ The synthesis of the compounds with other transition metal resulted in mixtures of more side phases, e.g. YbAlPd contains 67 wt.-% YbAlPd (TiNiSi type, $Pnma$, $a = 680.86(1)$, $b = 434.83(1)$, $c = 778.95(1)$ pm),⁶⁶ 2 wt.-% Yb₂O₃ ((Mn_{0.5}Fe_{0.5})₂O₃ type, $Ia\bar{3}$, $a = 1043.54(3)$ pm),³⁴² 3 wt.-% Pd (Cu type, $Fm\bar{3}m$, $a = 396.18(1)$ pm),³⁴⁴ 25 wt.-% Al₂₁Pd₈ (Al₂₁Pt₈ type, $I4_1/a$, $a = 1279.1(4)$, $c = 1102.7(2)$ pm)²³¹ and 3 wt.-% AlPd (own type, $R\bar{3}$, $a = 1615.2(9)$, $c = 494.4(4)$ pm).²³² The results of the Rietveld refinement phase analysis are summarized in **Table 3.27**.

In the literature besides reaction using induction, also synthesis in resistance furnaces were used for the syntheses of the YbAlT compounds, e.g. YbAlAu synthesized from the elements in corundum crucible at 1400 K for 2 h,³⁴¹ so for the next step an attempt to replicate the compounds using a resistance furnace is planned.

Table 3.27: Phase compositions of YbAlT samples synthesized inside Ta ampoules.

Compound	Main Phase (wt.-%)	Side phases (wt.-%)
YbAlNi	YbAlNi (69)	Ta (5), Ni (1), Yb ₂ O ₃ (15), YbAlO ₃ (9), Ta _{0.5} Al _{0.5} O ₂ (1)
YbAlPd	YbAlPd (67)	Yb ₂ O ₃ (2), Pd (3), Al ₂₁ Pd ₈ (25), AlPd (3)
YbAlPt	YbAlPt (99)	Yb ₂ O ₃ (1)
YbAlAg	YbAlAg (72)	Yb ₂ O ₃ (1), Al _{2.66} O ₄ (27)
YbAlAu	YbAlAu (97)	Yb ₂ O ₃ (2), AlAu ₄ (1)

c. Cooperation Work

I. Intermetallic Compounds

For the following publications either synthetic work or SEM/EDX measurements were performed for the corresponding cooperation partner.

1. MA_4Ir_2 ($M = Ca, Sr, Eu$): Superstructures of the KAu_4In_2 Type

N. Zaremba, V. Pavlyuk, F. Stegemann, V. Hlukhyy, S. Engel, S. Klenner, R. Pöttgen, O. Janka, *Monatsh. Chem.* **2022**, *154*, 43-52.

Contribution: synthetic work, SCXRD studies of the $SrAl_4Ir_2$ compound.

In cooperation with Dr. Nazar Zaremba (Ivan Franko National University of Lviv, Department of Analytical Chemistry) bulk samples of the $CaAl_4Ir_2$, $SrAl_4Ir_2$ and $EuAl_4Ir_2$ were prepared from the elements, the resulting PXRD showed no phase pure compounds but rather a mixture of the title compounds, equiatomic $AlIr$ (CsCl type, $Pm\bar{3}m$, $a = 298.3$ pm)²²⁸ and ternary $M_2Al_9Ir_3$ ($Y_2Ga_9Co_3$ type, $Cmcm$, Ca compound $a = 1295.50$, $b = 758.34$, $c = 961.75$ pm, Eu phase $a = 1301.75$, $b = 760.21$, $c = 951.29$ pm),^{61, 86} also an unknown phase for the Sr sample.²¹² Single crystal studies of the $SrAl_4Ir_2$ were performed on the Bruker X8 ApexII, resulting in an isotopic structure as found in the Ca and Eu containing compounds. The refinement parameters as well as the atom parameters and interatomic distances are summarized in **Tables 3.28-3.30**.

Table 3.28: Crystallographic data and structure refinement details for SrAl₄Ir₂ (own type, space group *P4/ncc*, *Z* = 4).

Sum formula	SrAl ₄ Ir ₂
Formular weight, g mol ⁻¹	580.0
Lattice parameters, pm	<i>a</i> = 796.13(6) <i>c</i> = 771.57(7)
Cell volume, nm ³	0.4980
Calculated density, g cm ⁻³	7.88
Crystal size, μm ³	36 × 62 × 75
Diffractometer type	Bruker X8 APEX-II
Wavelength; λ, pm	71.073
Detector distance, mm	40
Absorption correction	multi-scan Bruker SadABS
Absorption coefficient, mm ⁻¹	65.7
<i>F</i> (000), <i>e</i>	976
θ range, deg	3.62-31.78
Range <i>hkl</i>	±10; ±11; -1,+11
Total no. reflections	4042
Independent reflections / <i>R</i> _{int}	399 / 0.0304
Reflections <i>I</i> ≥ 3σ(<i>I</i>) / <i>R</i> _σ	341 / 0.0169
Data / parameters	399 / 19
Goodness of fit on <i>F</i> ²	1.23
<i>R</i> 1 / <i>wR</i> 2 for <i>I</i> ≥ 3σ(<i>I</i>)	0.0201 / 0.0155
<i>R</i> 1 / <i>wR</i> 2 for all data	0.0418 / 0.0401
Extinction coefficient	149(13)
Extinction scheme	Lorentzian isotropic ³⁰⁷
Largest diff. peak / hole, e Å ⁻³	+1.40 / -1.20

Table 3.29: Atomic coordinates and displacement parameters (in pm²) for SrAl₄Ir₂ (space group *P4/ncc*, *Z* = 4).

Atom	Wyckoff	<i>x</i>	<i>y</i>	<i>z</i>
Sr	4 <i>c</i>	3/4	3/4	0.14563(9)
Ir	8 <i>f</i>	0.89194(2)	1/2+ <i>x</i>	3/4
Al	16 <i>g</i>	0.4140(2)	0.8838(2)	0.9137(2)

Atom	<i>U</i> ₁₁	<i>U</i> ₂₂	<i>U</i> ₃₃	<i>U</i> ₁₂	<i>U</i> ₂₃	<i>U</i> ₁₃	<i>U</i> _{eq}
Sr	51(2)	<i>U</i> ₁₁	121(4)	0	0	0	74(2)
Ir	41(1)	<i>U</i> ₁₁	32(2)	1(1)	0(1)	0(1)	38(1)
Al	70(6)	53(3)	40(8)	-10(4)	-4(5)	-1(5)	54(4)

The equivalent isotropic displacement parameter *U*_{eq} is defined as *U*_{eq} = 1/3 (*U*₁₁ + *U*₂₂ + *U*₃₃) (pm²). Standard deviations are given in parentheses.

Table 3.30: Interatomic distances (pm) in SrAl₄Ir₂ (own type, space group *P4/ncc*, *Z* = 4). All distances of the first coordination spheres are listed. Standard deviations equal or smaller than 0.2 pm

Sr:	4	Ir	317.0	Al:	1	Ir	253.9
	4	Al	322.7		1	Al	254.9
	4	Al	339.0		1	Ir	260.1
	4	Al	354.5		1	Al	265.9
	2	Sr	385.8		1	Ir	267.7
Ir:	2	Al	253.9		2	Al	273.0
	2	Al	260.1		1	Ir	274.5
	2	Al	267.7		1	Sr	322.7
	2	Al	274.5		1	Sr	339.0
	2	Sr	317.0		1	Sr	354.5

2. Raman and NMR Spectroscopic and Theoretical Investigations of the Cubic Laves-Phases $REAl_2$ ($RE = Sc, Y, La, Yb, Lu$)

E. C. J. Giebelmann, S. Engel, W. Kostusiak, Y. Zhang, P. Herbeck-Engel, G. Kickelbick, O. Janka, *Dalton Trans.* **2023**, 52, 3391-3402.

Contribution: synthetic work

For the work of Elias C. J. Giebelmann, a $YbAl_2$ bulk sample (MgCu₂ type, $Fd\bar{3}m$, $a = 788.419(3)$ pm)²⁰⁴ was prepared from the elements in a closed Nb ampoule by reacting the reactants in the induction furnace at 1273 K for 10 min and subsequent cooling to RT over 5 min. The resulting PXRD pattern indicates a phase pure sample of $YbAl_2$ as shown in **Figure 3.58**. The $REAl_2$ compounds were subsequently analyzed via ²⁷Al NMR and Raman spectroscopy to compare the influence of the ²⁷Al NMR signal shift of from the corresponding along the shift of the vibrational band.

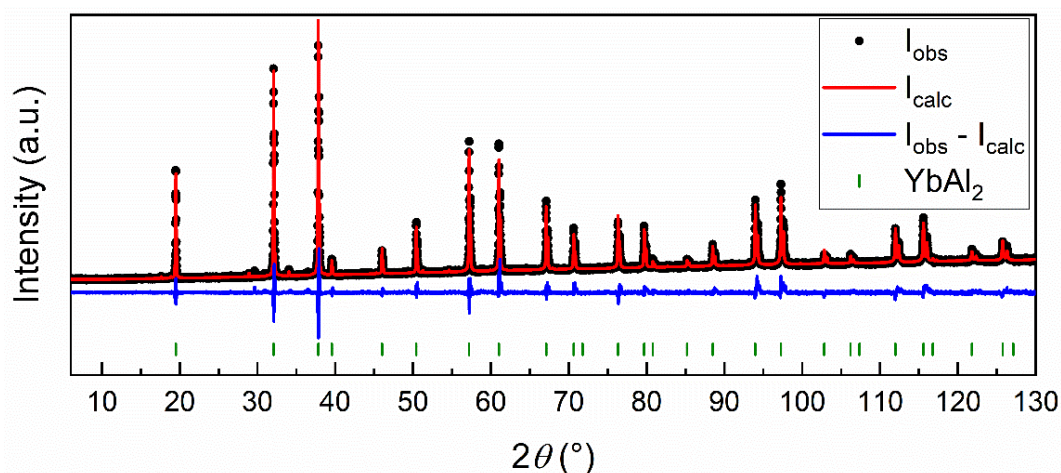


Figure 3.58: Rietveld refinement of the powder X-ray diffraction pattern of $YbAl_2$. Collected data are shown in black dots, the refinement as red and the difference as blue line. Olive ticks indicate the Bragg positions $YbAl_2$ (MgCu₂ type, $Fd\bar{3}m$).

3. On the RE_2TiAl_3 ($RE = Y, Gd-Tm, Lu$) Series – the First Aluminum Representatives of the Rhombohedral Mg_2Ni_3Si Type Structure

E. C. J. Gießelmann, S. Engel, I. El Saudi, L. Schumacher, M. Radzieowski, J. M. Gerdes, O. Janka, *Solids* **2023**, 4, 166-180.

Contribution: SEM/EDX measurements

Bulk samples of Er_2TiAl_3 , Tm_2TiAl_3 and Lu_2TiAl_3 (all Mg_2Ni_3Si type, $R\bar{3}m$),³⁴⁵ prepared by Elias C. J. Gießelmann, were semi-quantitative analyzed using SEM/EDX measurements of five independent points of each sample. The EDX results (**Table 3.31**) are in a good agreement with the ideal composition, deviations originate from the roughness of the samples and the suboptimal orientation of the crystals to the electron beam, SEM images of the measured samples are shown in **Figure 3.59**.

Table 3.31: SEM/EDX data of Er_2TiAl_3 , Tm_2TiAl_3 and Lu_2TiAl_3 with standard deviations of ± 2 at.-%.

Compound	Ideal	P1	P2	P3	P4	P5	mean
Er_2TiAl_3	Er: 33.3	36	38	35	26	32	33
	Ti: 16.7	14	15	15	20	13	15
	Al: 50.0	50	48	50	54	55	51
Tm_2TiAl_3	Tm: 33.3	32	31	32	32	35	33
	Ti: 16.7	17	14	16	15	15	15
	Al: 50.0	51	55	52	53	50	52
Lu_2TiAl_3	Lu: 33.3	33	34	31	38	34	34
	Ti: 16.7	16	14	14	13	16	15
	Al: 50.0	51	52	55	48	50	51

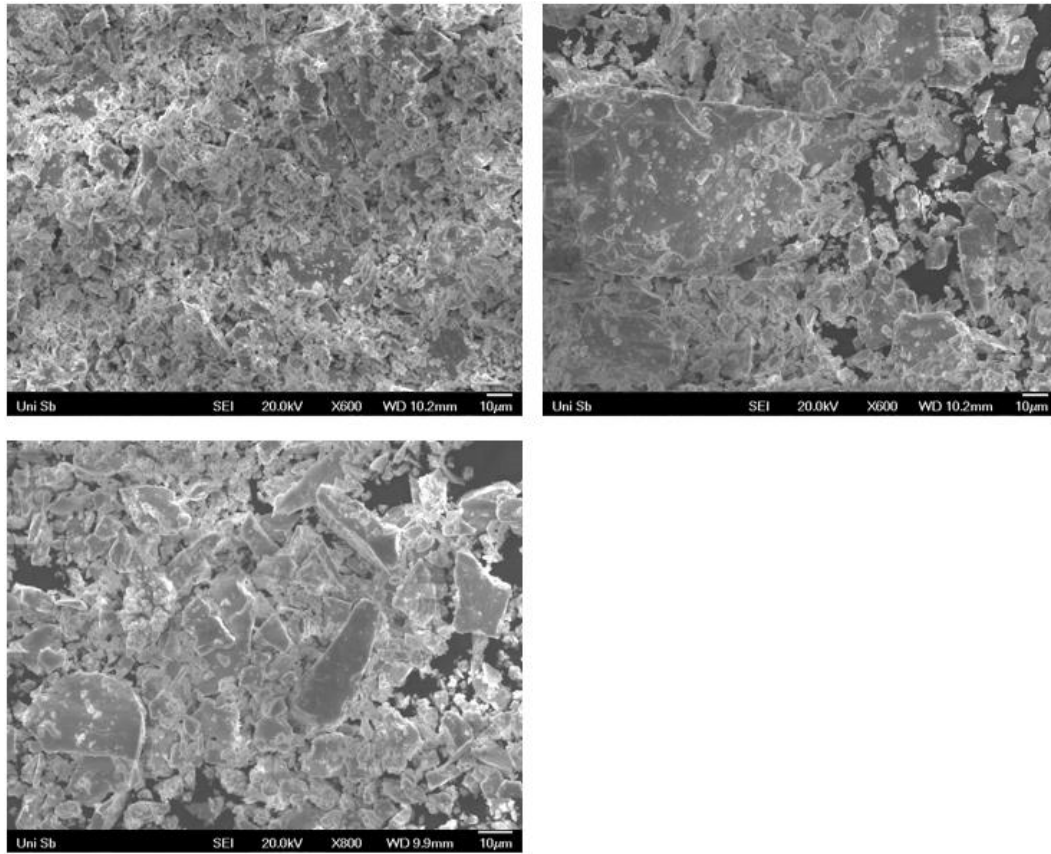


Figure 3.59: Scanning electron microscopy images of Er_2TiAl_3 (top left), Tm_2TiAl_3 (top right) and Lu_2TiAl_3 (bottom).

4. Searching for Laves Phase Superstructures: Structural and ^{27}Al NMR Spectroscopic Investigations in the Hf–V–Al System

E. C. J. Gießelmann, S. Engel, J. Baldauf, J. Kösterns, S. F. Matar, G. Kickelbick, O. Janka, *Inorg. Chem.* **2024**, *63*, 8180-8193.

Contribution: SEM/EDX measurements

SEM/EDX measurements of the X-ray pure bulk samples prepared by Elias C. J. Gießelmann were taken in the electron microscope. The EDX data is summarized in **Table 3.32** and representative SEM images are shown in **Figure 3.60**. The results are in good agreement with the ideal composition, differences originate from the rough surface and the non-optimal orientation of the sample to the electron beam. The compounds from a vanadium content of 0 ($\text{Hf}(\text{V}_0\text{Al}_2)_2$) to 0.8 ($\text{Hf}(\text{V}_{0.8}\text{Al}_{0.2})_2$) all crystallize exclusively in the MgZn_2 type structure ($P6_3/mmc$) with the exception of $\text{Hf}(\text{V}_{0.167}\text{Al}_{0.833})_2$ and $\text{Hf}(\text{V}_{0.125}\text{Al}_{0.875})_2$ these compounds crystallize in a new superstructure first observed Hf_4VAl_7 ($P\bar{3}m1$). With $x = 0.875$ and 0.9 the samples form both the MgZn_2 and the MgCu_2 type ($Fd\bar{3}m$) of the corresponding compounds and by increasing the vanadium content, only the MgCu_2 remains.³⁴⁶

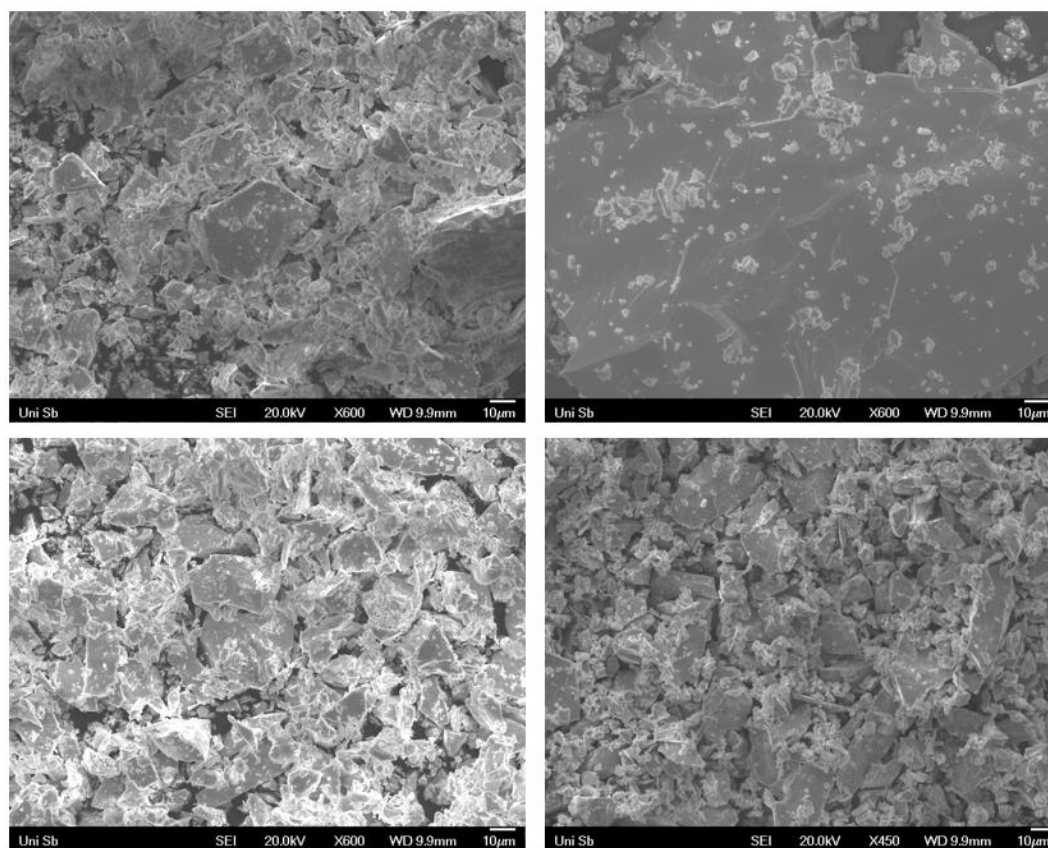


Figure 3.60: Scanning electron microscopy images of $\text{Hf}(\text{V}_{0.05}\text{Al}_{0.95})_2$ (top left), $\text{Hf}(\text{V}_{0.583}\text{Al}_{0.417})_2$ (top right), $\text{Hf}(\text{V}_{0.125}\text{Al}_{0.875})_2$ (bottom left) and HfV_2 (bottom right).

Table 3.32: SEM/EDX data of the Hf–V–Al series, standard deviations of ± 2 at.-%.

Composition	Ideal	P1	P2	P3	mean
HfAl ₂	Hf: 33.3	32	30	39	34
	Al: 66.7	68	70	61	66
Hf(V _{0.05} Al _{0.95}) ₂	Hf: 33.3	34	32	33	33
	V: 3.3	3	3	4	3
	Al: 63.4	63	65	63	64
Hf(V _{0.083} Al _{0.917}) ₂	Hf: 33.3	31	33	33	32
	V: 5.5	6	6	6	6
	Al: 61.2	63	61	61	62
Hf(V _{0.125} Al _{0.875}) ₂	Hf: 33.3	31	36	36	34
	V: 8.3	7	7	8	7
	Al: 58.4	62	57	56	58
Hf(V _{0.167} Al _{0.833}) ₂	Hf: 33.3	36	32	33	34
	V: 11.1	11	11	10	10
	Al: 55.6	53	57	57	56
Hf(V _{0.25} Al _{0.75}) ₂	Hf: 33.3	34	36	35	35
	V: 16.7	15	15	15	15
	Al: 50.0	51	49	50	50
Hf(V _{0.33} Al _{0.67}) ₂	Hf: 33.3	36	32	35	34
	V: 22.2	21	20	21	21
	Al: 44.5	43	48	44	45
Hf(V _{0.417} Al _{0.583}) ₂	Hf: 33.3	39	36	35	37
	V: 27.8	27	26	26	26
	Al: 38.9	34	38	39	37
Hf(V _{0.5} Al _{0.5}) ₂	Hf: 33.3	39	32	33	35
	V: 33.3	30	30	29	30
	Al: 33.4	31	38	38	35
Hf(V _{0.583} Al _{0.417}) ₂	Hf: 33.3	35	35	34	35
	V: 38.9	35	34	35	35
	Al: 27.8	30	30	31	30
Hf(V _{0.67} Al _{0.33}) ₂	Hf: 33.3	37	34	35	35
	V: 44.5	41	40	42	41
	Al: 22.2	22	26	23	24
Hf(V _{0.75} Al _{0.25}) ₂	Hf: 33.3	38	36	35	36
	V: 50.0	47	55	47	50
	Al: 16.7	15	18	18	17
Hf(V _{0.8} Al _{0.2}) ₂	Hf: 33.3	34	35	33	34
	V: 53.3	49	48	54	50
	Al: 13.3	17	17	13	16
Hf(V _{0.875} Al _{0.125}) ₂	Hf: 33.3	35	36	36	35
	V: 58.4	54	54	53	54
	Al: 8.3	11	11	11	11
Hf(V _{0.9} Al _{0.1}) ₂	Hf: 33.3	36	35	37	36
	V: 60.0	55	56	57	56
	Al: 6.7	9	9	6	8
Hf(V _{0.95} Al _{0.05}) ₂	Hf: 33.3	37	37	35	36
	V: 63.4	60	58	60	59
	Al: 6.7	4	5	5	5
HfV ₂	Hf: 33.3	39	35	39	38
	V: 66.7	61	65	61	62

5. Systematic Investigations of the Solid Solution $\text{Zr}(\text{V}_{1-x}\text{Al}_x)_2$ Adopting the Laves Phase Structures

E. C. J. Gießelmann, L. Schumacher, S. F. Matar, S. Engel, G. Kickelbick, O. Janka, *Chem. Eur. J.* **2025**, *31*, e202404248.

Contribution: SEM/EDX measurements

SEM/EDX measurements on samples of the Zr–V–Al system were performed for Elias C. J. Gießelmann. In analogy to the Hf–V–Al system, the bulk samples are X-ray pure. The results are listed below in **Table 3.33** alongside SEM images of a few representatives of the samples in **Figure 3.61**. The EDX data show a higher amount of zirconium in all samples compared to the ideal composition, but the mean value is overall in good agreement with the ideal values, taking the rough surface and non-perfect orientation of the crystals to the electron beam into account.

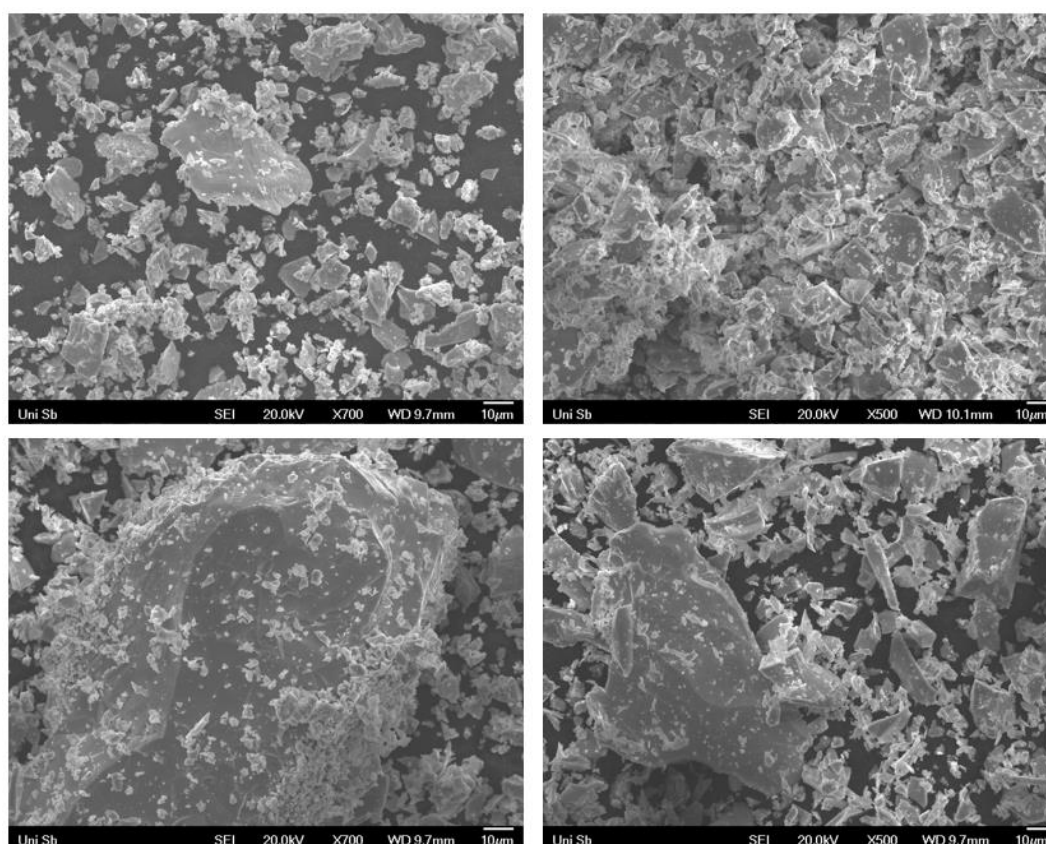


Figure 3.61: Scanning electron microscopy images of ZrV_2 (top left), nominal $\text{Zr}_3\text{V}_2\text{Al}_4$ (top right), nominal $\text{Zr}_2\text{V}_3\text{Al}$ (bottom left) and ZrAl_2 (bottom right).

Table 3.33: SEM/EDX data of the Zr–V–Al series, standard deviations of ± 2 at.-%.

Nominal Composition	Ideal	P1	P2	P3	mean
ZrV ₂	Zr: 33.3	38	36	33	36
	V: 66.7	62	64	67	64
Zr ₄ V ₇ Al	Zr: 33.3	33	35	35	34
	V: 58.3	58	56	58	57
	Al: 8.3	9	8	8	8
Zr ₂ V ₃ Al	Zr: 33.3	34	35	36	35
	V: 50.0	49	48	48	48
	Al: 16.7	16	16	16	16
Zr ₃ V ₄ Al ₂	Zr: 33.3	36	34	36	35
	V: 44.4	42	46	41	43
	Al: 22.2	22	20	23	22
Zr ₄ V ₅ Al ₃	Zr: 33.3	33	34	35	34
	V: 41.7	44	41	41	42
	Al: 25.0	23	24	24	24
Zr ₆ V ₇ Al ₅	Zr: 33.3	34	33	35	34
	V: 38.9	41	39	37	39
	Al: 27.8	25	28	28	27
ZrVAl	Zr: 33.4	33	35	36	35
	V: 33.3	37	35	28	33
	Al: 33.3	30	30	36	32
Zr ₆ V ₅ Al ₇	Zr: 33.3	34	36	36	35
	V: 27.8	30	25	26	27
	Al: 38.9	36	39	38	38
Zr ₃ V ₂ Al ₄	Zr: 33.3	34	36	35	35
	V: 22.2	23	19	24	22
	Al: 44.4	43	45	41	43
Zr ₂ VAl ₃	Zr: 33.3	35	35	35	35
	V: 16.7	16	16	16	16
	Al: 50.0	49	49	49	49
Zr ₄ VAl ₇	Zr: 33.3	35	36	35	35
	V: 8.3	10	8	9	9
	Al: 58.3	55	56	56	56
ZrAl ₂	Zr: 33.3	36	36	36	36
	Al: 66.7	64	64	64	64

6. Structure, Physical and ^{27}Al NMR Spectroscopic Properties of the Missing Members of the Equiatomic REAlRh ($\text{RE} = \text{Sm}, \text{Tb}, \text{Dy}, \text{Er}, \text{and Lu}$) Series

M. Radzieowski, E. C. J. Gießelmann, S. Engel, O. Janka, *Z. Naturforsch.* **2024**, *79b*, 459-467.

Contribution: SEM/EDX measurements

SEM/EDX measurements were conducted for the bulk samples of YAlRh (TiNiSi type, $Pnma$, $a = 686.91(8)$, $b = 418.66(4)$, $c = 794.21(8)$ pm)³⁴⁷ and LuAlRh (TiNiSi type, $Pnma$, $a = 673.31(7)$, $b = 415.92(5)$, $c = 788.22(8)$ pm)³⁴⁸ for the work of Dr. Mathis Radzieowski (Universität of Münster). The EDX data are summarized in **Table 3.34** and images of both samples are shown in **Figure 3.62**. A good agreement of the EDX results with the ideal composition is present, the deviations originate from the rough surface and non-perfect orientation of the crystals with the electron beam.

Table 3.34: SEM/EDX data of YAlRh and LuAlRh , standard deviations of ± 2 at.-%.

Composition	Ideal	P1	P2	P3	mean
YRhAl	Y: 33.3	33	34	35	34
	Rh: 33.4	33	32	31	32
	Al: 33.3	34	34	34	34
LuRhAl	Lu: 33.3	36	33	35	35
	Rh: 33.4	33	35	34	34
	Al: 33.3	31	32	31	31

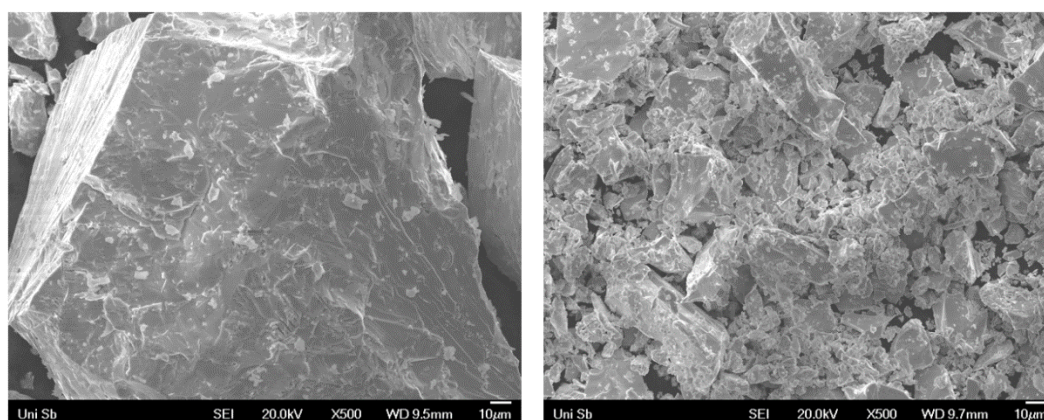


Figure 3.62: Scanning electron microscopy images of YRhAl (left) and LuRhAl (right).

7. Working Title: NMR Spectroscopic Properties of the RE_2AlE_2 Series ($RE = Sc, Y, Lu; E = Si, Ni$)

E. C. J. Gießelmann, S. Engel, O. Janka, manuscript in preparation.

Contribution: SEM/EDX measurements

In cooperation with Elias C. J. Gießelmann, SEM/EDX measurements of the X-ray pure samples Sc_2AlSi_2 (Mo_2FeB_2 type, $P4/mbm$, $a = 659.38(1)$, $c = 399.61(1)$ pm),³⁴⁹ Y_2AlSi_2 (W_2CoB_2 type, $Immm$, $a = 406.68(1)$, $b = 573.96(1)$, $c = 869.38(1)$ pm),³⁵⁰ Lu_2AlSi_2 (W_2CoB_2 type, $Immm$, $a = 398.65(1)$, $b = 569.63(1)$, $c = 839.39(1)$ pm),³⁵⁰ Y_2AlNi_2 (W_2CoB_2 type, $Immm$, $a = 417.63(1)$, $b = 542.77(1)$, $c = 837.76(1)$ pm),³⁵¹ and Lu_2AlNi_2 (W_2CoB_2 type, $Immm$, $a = 411.70(1)$, $b = 532.62(1)$, $c = 816.62(1)$ pm)³⁵¹ were taken. The results are listed in **Table 3.35**. Sc_2AlSi_2 and Y_2AlSi_2 are in a good agreement with the ideal composition, but in case of the lutetium-containing samples, an excess of the rare earth element is present. In Y_2AlNi_2 both Y and Al show a lower amount compared to the ideal composition. Alongside the EDX data SEM images are shown in **Figure 3.63**.

Table 3.35: SEM/EDX data of Sc_2AlSi_2 , Y_2AlSi_2 , Lu_2AlSi_2 , Y_2AlNi_2 , and Lu_2AlNi_2 , standard deviations are ± 2 at.-%.

Composition	Ideal	P1	P2	P3	mean
Sc_2AlSi_2	Sc: 40	38	40	40	40
	Al: 20	21	20	20	20
	Si: 40	41	40	40	40
Y_2AlSi_2	Y: 40	41	40	40	40
	Al: 20	19	20	21	20
	Si: 40	40	40	39	40
Lu_2AlSi_2	Lu: 40	45	44	37	42
	Al: 20	17	22	21	20
	Si: 40	38	34	42	38
Y_2AlNi_2	Y: 40	37	41	38	39
	Al: 20	18	21	18	19
	Ni: 40	45	38	44	42
Lu_2AlNi_2	Lu: 40	42	42	41	42
	Al: 20	18	22	20	20
	Ni: 40	40	36	39	38

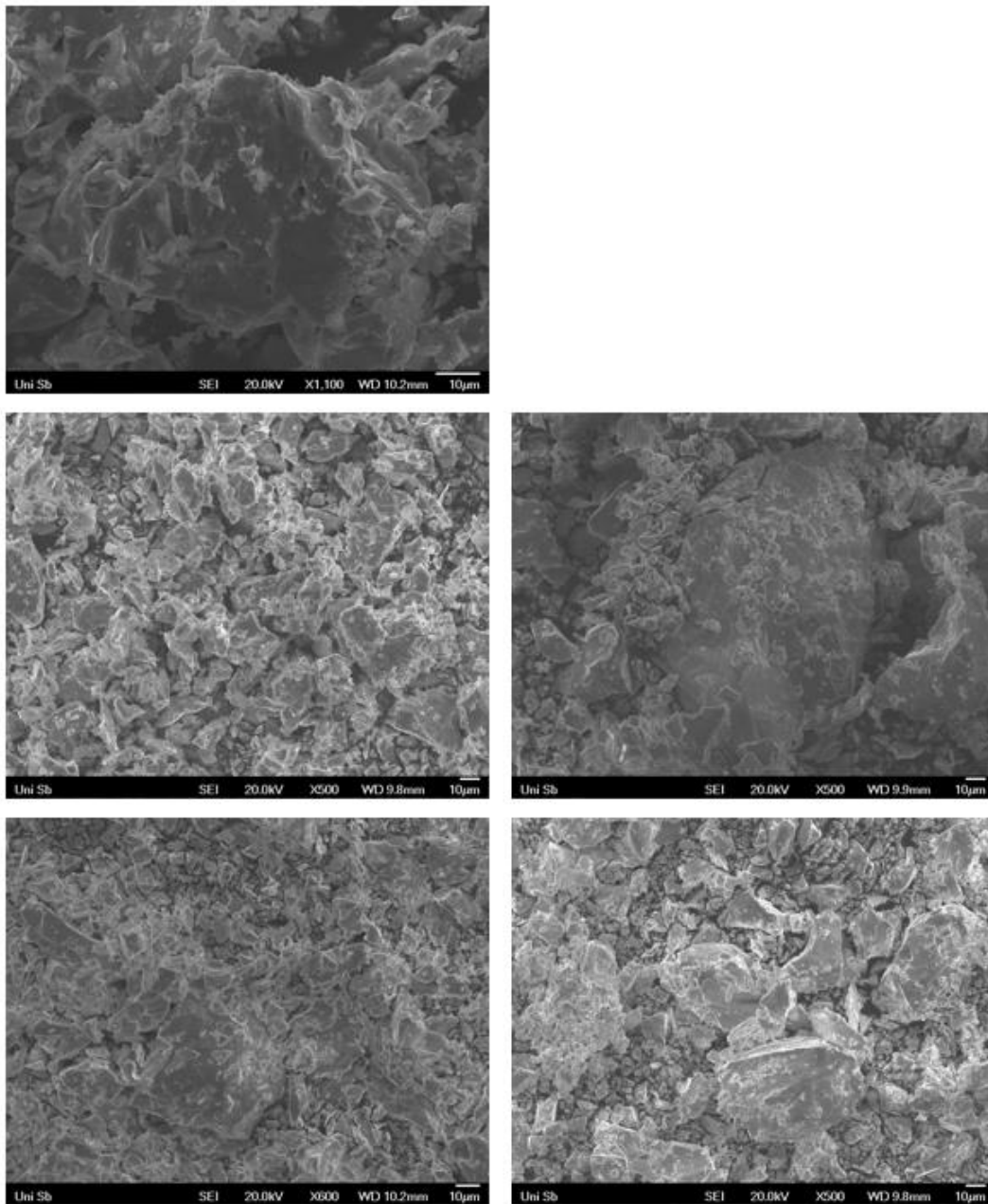


Figure 3.63: Scanning electron microscopy images of Sc₂AlSi₂ (top left), Y₂AlSi₂ (middle left), Lu₂AlSi₂ (bottom left), Y₂AlNi₂ (middle left), and Lu₂AlNi₂ (bottom right).

II. Oxidation of Intermetallic Compounds

1. Mechanistic Studies on the Formation of Ternary Oxides by Thermal Oxidation of the Cubic Laves Phase CaAl_2

E. C. J. Gießelmann, S. Engel, J. G. Volpini, H. Huppertz, G. Kickelbick, O. Janka, *Inorg. Chem. Front.* **2024**, 11, 286-297.

Contribution: synthetic work and SEM/EDX measurements.

For the oxidation studies of Elias C. J. Gießelmann, CaAl_2 was prepared from the elements in the arc furnace, ground to a fine powder and subsequently oxidized repeatedly in a muffle furnace for one minute at 1273 K with a heating and cooling rate of 15 K min^{-1} . The PXRD patterns of CaAl_2 and the second oxidation cycle are shown in **Figure 3.64**. The powder X-ray diffractogram of CaAl_2 shows a mixture of the desired CaAl_2 (MgCu_2 type, $Fd\bar{3}m$, $a = 804.104(4) \text{ pm}$)¹⁸⁵ phase with 97 wt.-% and CaAl_4 (BaAl_4 type, $I4/mmm$, $a = 436.69(5)$, $c = 1124.1(2) \text{ pm}$)¹⁸⁵ with 3 wt.-% due to a slight evaporation of the Ca during the synthesis in the arc furnace. After the first oxidation cycle, a mixture of the mayenite phase $\text{Ca}_{12}\text{Al}_{14}\text{O}_{33}$ (own type, $I\bar{4}3d$, $a = 1203.86(3) \text{ pm}$, 67 wt.-%),³⁵² the anticipated CaAl_2O_4 (own type, $P2_1/c$, $a = 878.1(4)$, $b = 808.3(3)$, $c = 1746.4(9) \text{ pm}$, 3 wt.-%),³⁵³ Al (Cu type, $Fm\bar{3}m$, $a = 405.278(8) \text{ pm}$ 9 wt.-%),³⁵⁴ Al_2O_3 (own type, $R\bar{3}c$, $a = 476.09(2)$, $c = 1299.8(1) \text{ pm}$, 13 wt.-%)³⁵⁵ and CaO (NaCl type, $Fm\bar{3}m$, $a = 481.37(1) \text{ pm}$, 7 wt.-%)³⁵⁶ formed. **Figure 3.65** displays the change of the phase composition after each oxidation cycle, the phase mixture changed during the subsequent oxidation cycles to 62 wt.-%, 15 wt.-%, 2 wt.-%, 18 wt.-% and 3 wt.-% corresponding to the aforementioned phases. Also, a stagnating of the phase change of the mayenite phase and alumina is visible after only a few cycles, compared to the increase of CaAl_2O_4 and decrease of elemental Al and CaO. This indicates that the targeted CaAl_2O_4 originates rather from the reaction of Al, O and CaO during the later cycles and the oxidation of CaAl_2 for one minute is not a viable route for a targeted synthesis of CaAl_2O_4 .

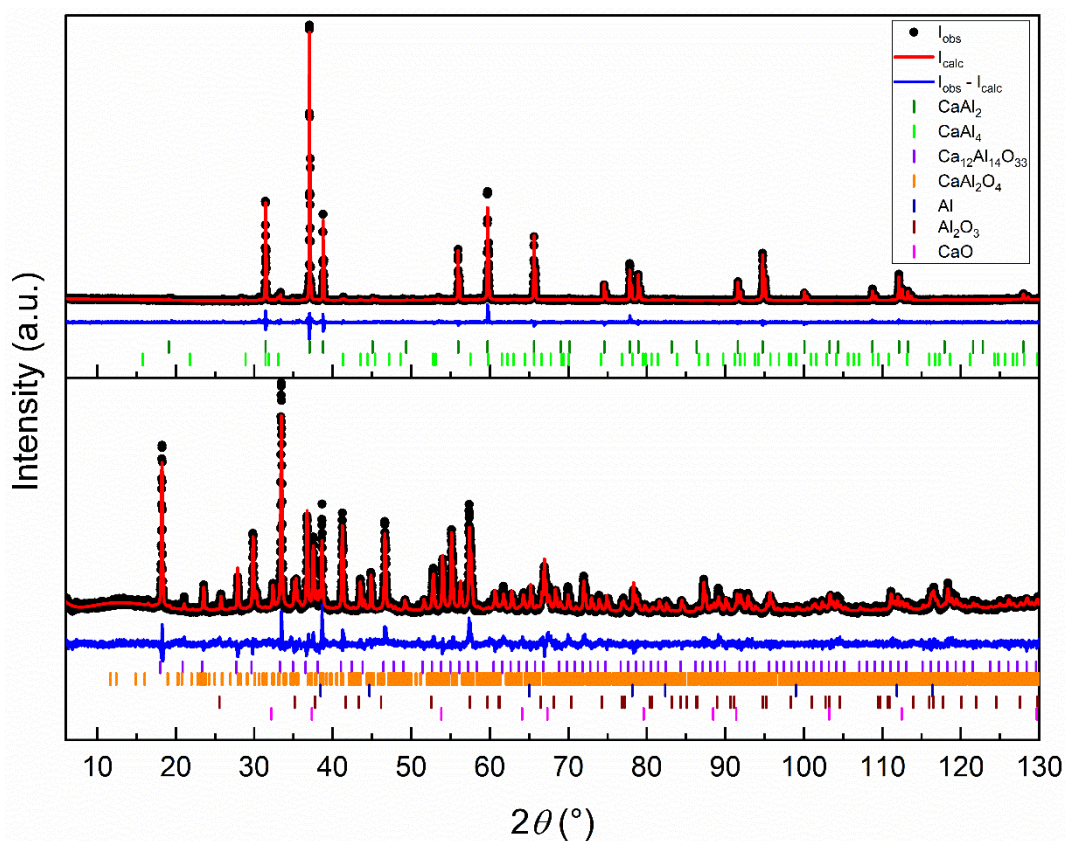


Figure 3.64: Rietveld refinement of the powder X-ray diffraction pattern of CaAl_2 top and various phases from the binary and ternary Ca–Al–O systems at the bottom. Collected data are shown in black dots, the refinement as red and the difference as blue line. Olive ticks indicate the Bragg positions of CaAl_2 (MgCu_2 type, $Fd\bar{3}m$), green ticks of CaAl_4 (BaAl_4 type, $I4/mmm$), violet of $\text{Ca}_{12}\text{Al}_{14}\text{O}_{33}$ (own type, $I\bar{4}3d$), orange of CaAl_2O_4 (own type, $P2_1/c$), royal blue of Al (Cu type, $Fm\bar{3}m$), wine-red of Al_2O_3 (own type, $R\bar{3}c$) and magenta ticks of CaO (NaCl type, $Fm\bar{3}m$) respectively.

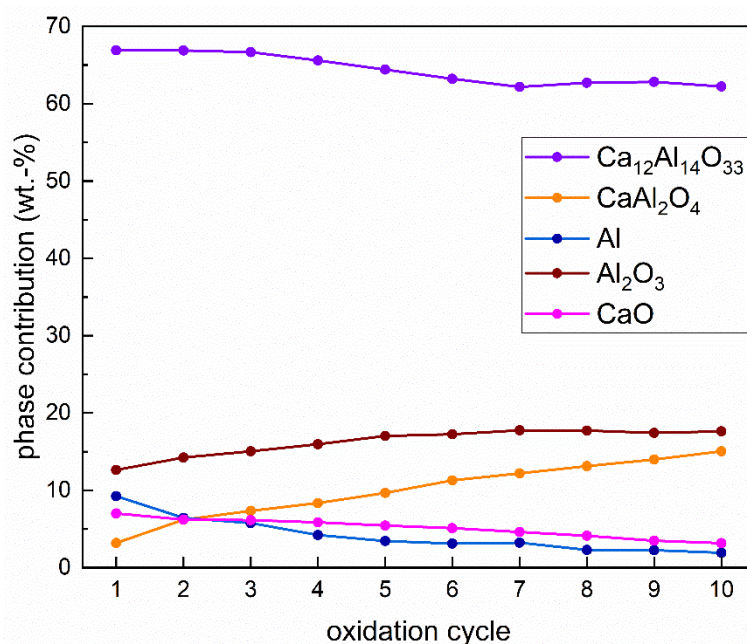


Figure 3.65: Change of phase composition over oxidation cycles. Violet dots indicate $\text{Ca}_{12}\text{Al}_{14}\text{O}_{33}$ (own type, $I\bar{4}3d$), orange CaAl_2O_4 (own type, $P2_1/c$), royal blue Al (Cu type, $Fm\bar{3}m$), wine-red Al_2O_3 (own type, $R\bar{3}c$) and magenta dots as CaO (NaCl type, $Fm\bar{3}m$) respectively.

SEM/EDX analysis were performed additionally to the oxidation cycles and the PXRD measurements. An image of the CaAl_2 and the CaAl_2O_x samples obtained after 97 h of annealing with intermediate grinding and one from the oxidation with pure O_2 over 5 h are given in **Figure 3.66** and in **Table 3.C.9** the results of the EDX measurements are shown. The oxidized sample after 97 h shows the highest amount of CaAl_2O_4 in the PXRD with 90 wt.-%, whereas the second sample possesses a significantly higher amount of the mayenite phase. For the EDX data, oxygen was measured but is not suited for the results based on the intrinsic dependency of electron count for the measurement. So only Ca and Al values are shown in **Table 3.36** with regards to the difference in the ratios of Ca and Al in the CaAl_2O_4 and $\text{Ca}_{12}\text{Al}_{14}\text{O}_{33}$ phases leading to a ratio of 33 : 67 at.-% and 42 : 58 at.-% respectively. The results for CaAl_2 are in a good agreement, the difference between the ideal and measured values originate from the rough surface and the orientation of the sample. The ratio of Ca and Al of the oxidized samples show the expected trend, the 97 h sample exhibit nearly a 1 : 2 ratio, whereas the 5 h sample only 1 : 1.3 due to the higher amount of the mayenite.

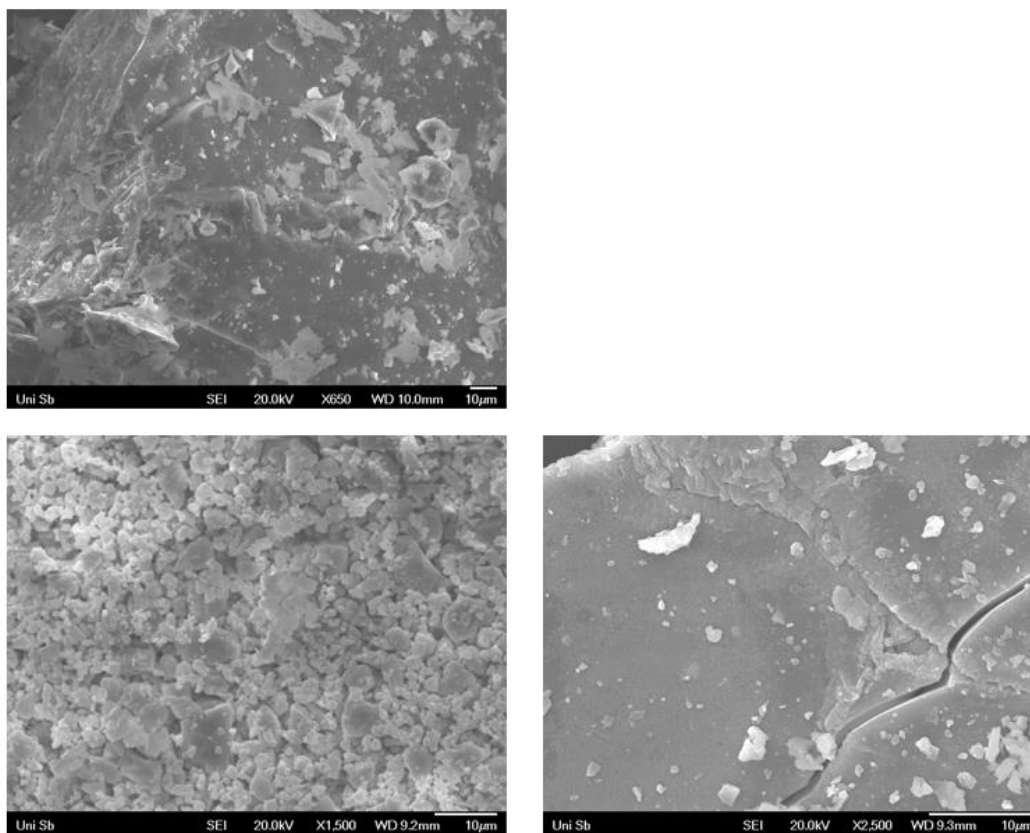


Figure 3.66: Scanning electron microscopy images of CaAl_2 (top), CaAl_2O_x 97 h annealing time (bottom right) and CaAl_2O_x 5h annealing time with pure O_2 (bottom left).

Table 3.36: EDX measurements of CaAl_2 , CaAl_2O_x (97 h) and CaAl_2O_x (5 h), including the ideal values of the elements in the compounds and the mean values of the corresponding three measurement points.

Compound	Ideal	P1	P2	P3	Mean value
CaAl_2	Ca: 33	36	34	36	35
	Al: 67	64	66	64	65
CaAl_2O_x (97h)		21	17	16	18
	Ca: 14	36	31	32	33
CaAl_2O_x (5 h)	Al: 29	33	18	27	26
		32	25	43	33

2. Rapid Synthesis of a Green Emitting Phosphor by Sulfidation of Intermetallic EuAl_2 and Its Use in a Hybrid Material

E. C. J. Giebelmann,[§] S. Engel,[§] S. Pohl, M. Briesenick, L. P. Rütting, C. Kloos, A. Koldemir, L. Schumacher, J. Schmedt auf der Günne, G. Kickelbick, O. Janka, *Chem. Mater.* **2024**, *37*, 97-108.

[§] shared first author.

Contribution: synthetic work and SEM/EDX measurements.

In cooperation with Elias C. J. Giebelmann, EuAl_2S_4 and SrAl_2S_4 were prepared by synthesizing the binary intermetallic aluminum compounds EuAl_2 and SrAl_2 from the elements in the arc furnace and the subsequent sulfidation to the aforementioned sulfides in graphitized fused silica ampoules. The **Figure 3.67** shows the PXRD pattern of EuAl_2 (MgCu_2 type, $Fd\bar{3}m$, $a = 812.25(2) \text{ pm}$)²⁰⁴ and EuAl_2S_4 (EuGa_2S_4 type, $Fddd$, $a = 1211.35(2)$, $b = 2038.85(4)$, $c = 2077.66(4) \text{ pm}$),³⁵⁷ both syntheses resulted in X-ray pure samples.

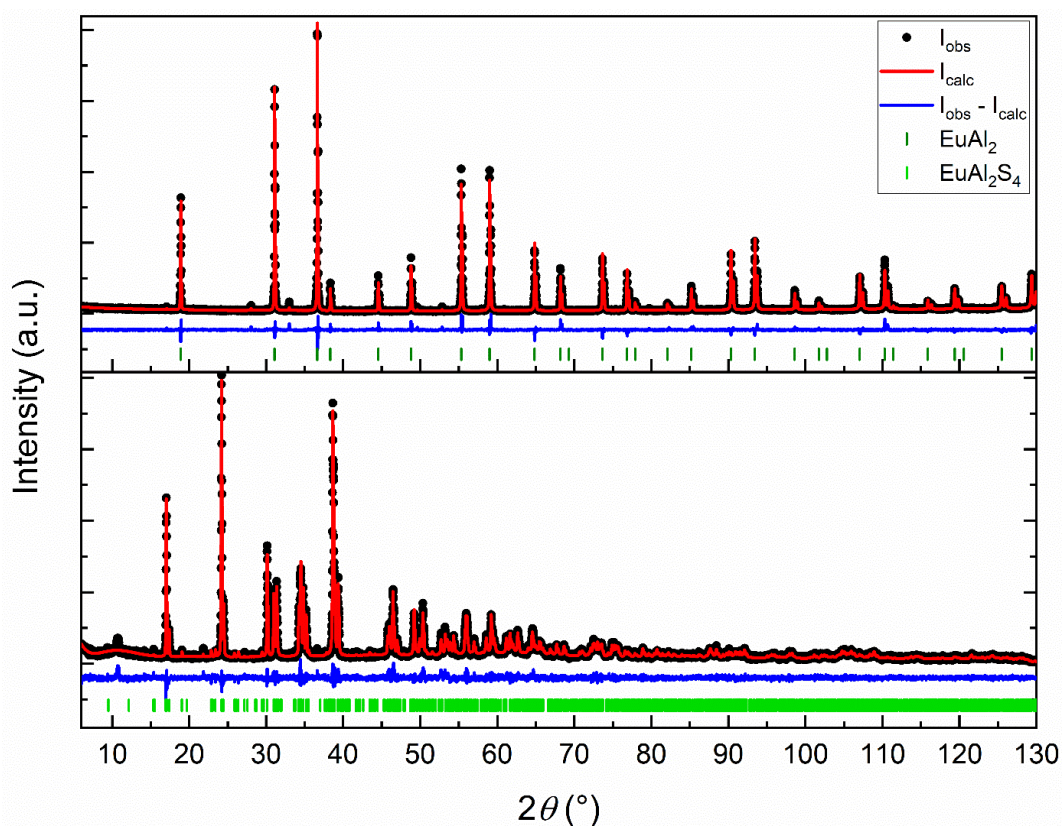


Figure 3.67: Rietveld refinement of the powder X-ray diffraction pattern of EuAl_2 top and EuAl_2S_4 bottom. Collected data are shown in black dots, the refinement as red and the difference as blue line. Olive ticks indicate the Bragg positions EuAl_2 (MgCu_2 type, $Fd\bar{3}m$) and green ticks EuAl_2S_4 (EuGa_2S_4 type, $Fddd$) respectively.

The PXRD pattern of SrAl₂ as well as SrAl₂S₄ are shown in **Figure 3.68**, both display side phases. Whereas the precursor formed the wanted SrAl₂ (KHg₂ type, *Imma*, $a = 479.50(1)$, $b = 789.49(1)$, $c = 796.03(1)$ pm)¹⁸⁶ only to 46 wt.-% and the side phases SrAl₄ (BaAl₄ type, *I4/mmm*, $a = 44.64(1)$, $c = 1121.29(2)$ pm)¹⁹¹ 45 wt.-%, Sr₅Al₉ (own type, *R $\bar{3}m$* , $a = 587.48(2)$, $c = 3566.4(2)$ pm)²¹⁵ 7 wt.-% and SrAl (InCl type, *P2₁3*, $a = 1273.4(3)$ pm)³⁵⁸ with 2 wt.-%, the sulfidation lead to a nearly pure sample of SrAl₂S₄ (EuGa₂S₄ type, *Fddd*, $a = 1212.76(3)$, $b = 2045.98(5)$, $c = 2090.48(6)$ pm)³⁵⁹ with 7 wt.-% S (own type, *P12₁/c1*, $a = 1523.5(5)$, $b = 612.7(1)$, $c = 2070.3(5)$ pm, $\beta = 133.89(2)^\circ$)³⁶⁰ as leftover and no other Sr or Al compounds.

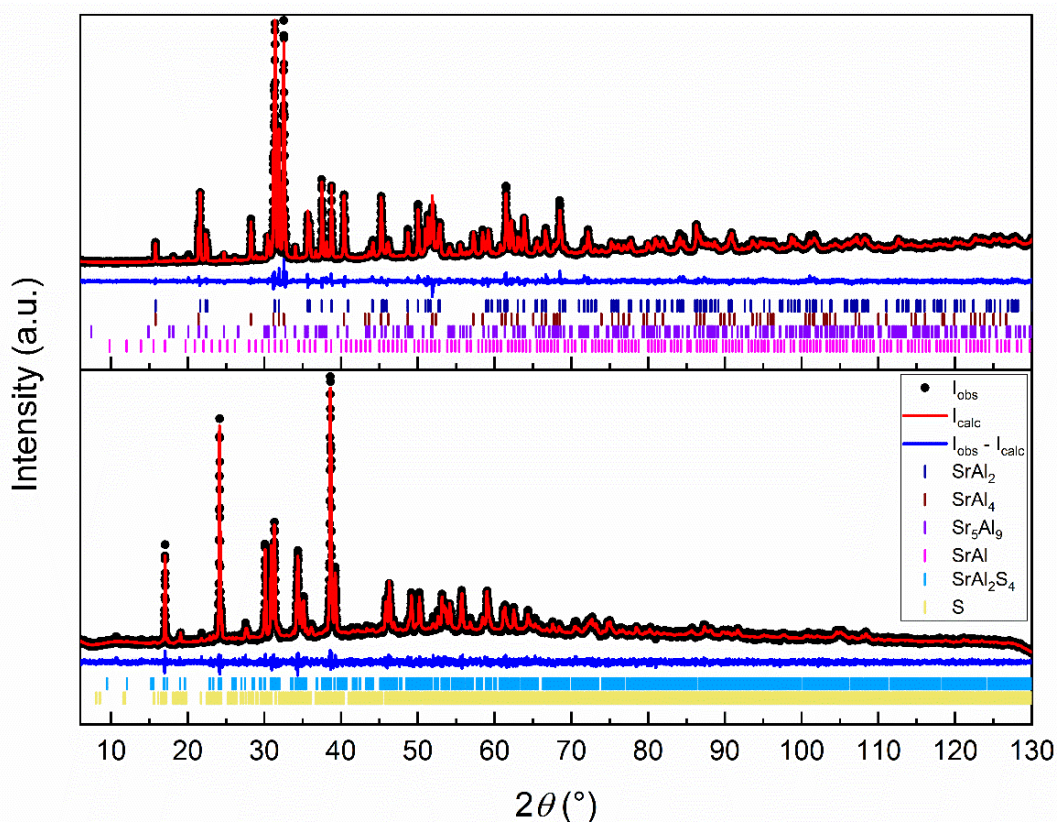


Figure 3.68: Rietveld refinement of the powder X-ray diffraction pattern of SrAl₂ top and SrAl₂S₄ bottom. Collected data are shown in black dots, the refinement as red and the difference as blue line. Royal blue ticks indicate the Bragg positions of SrAl₂ (KHg₂ type, *Imma*), wine-red of SrAl₄ (BaAl₄ type, *I4/mmm*), violet of Sr₅Al₉ (own type, *R $\bar{3}m$*), magenta of SrAl (InCl type, *P2₁3*), bright blue of SrAl₂S₄ (EuGa₂S₄ type, *Fddd*) and yellow ticks for S (own type, *P12₁/c1*) respectively.

Additional SEM/EDX data of the precursors EuAl₂, SrAl₂ and the EuAl₂S₄ sample were collected. The SEM images are shown in **Figure 3.69** and EDX results are given in **Table 3.37**. The EDX results of the binary compounds are in good agreement with the ideal composition. In the case of the sulfidized sample, the measurement values show a significant difference of the element amount, whereas an excess of Eu and Al is present, a deficit of S is observable. The reason for the difference could be a decomposition of the compound in the electron beam,

leading to a loss of sulfur and a higher amount of europium and aluminum in the remaining sample. SrAl_2S_4 could not be measured due to its instability on air.

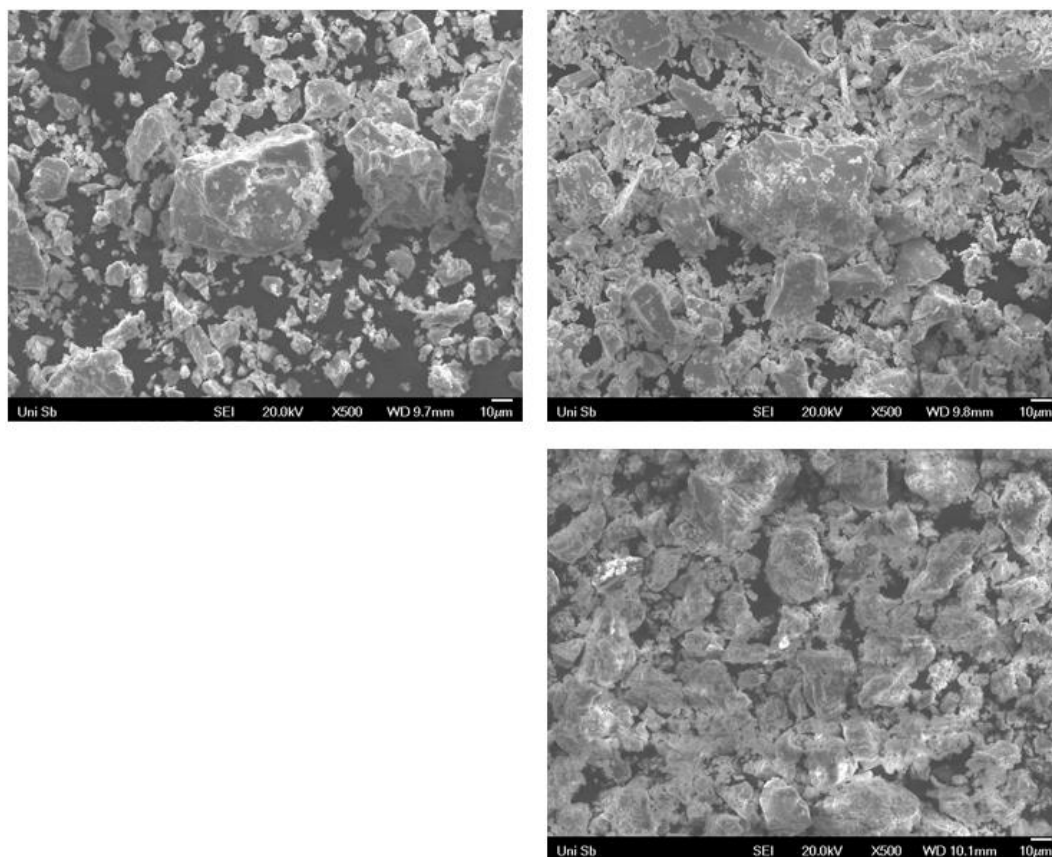


Figure 3.69: Scanning electron microscopy images of SrAl_2 (top left), EuAl_2 (top right) and EuAl_2S_4 (bottom right).

Table 3.37: EDX measurements of SrAl_2 , EuAl_2 and EuAl_2S_4 , including the ideal values of the elements in the compounds and the mean values of the corresponding three measurement points.

Compound	Ideal	P1	P2	P3	Mean value
SrAl_2	Sr: 33	35	35	35	35
	Al: 67	65	65	65	65
EuAl_2	Eu: 33	36	28	36	33
	Al: 67	64	72	64	67
EuAl_2S_4	Eu: 14	19	18	18	18
	Al: 28	34	46	47	42
	S: 57	47	36	35	39

d. Review Articles and Book Chapters

The following review articles and book chapters were additionally published during the PhD phase.

1. Review: On the Ytterbium Valence and the Physical Properties in Selected Intermetallic Phases

The review was written in cooperation with Prof. Dr. Rainer Pöttgen (University of Münster), PD Dr. Oliver Janka, Dr. Maximilian K. Reimann (University of Münster) and Elias C. J. Gießelmann and as the title of the review states, the focus of the work is Yb and its valence states. Due to the overwhelming amount of research on ytterbium compounds, only a small part was used as representative examples. In the review the crystal chemistry, structural (XANES, XPS, NMR) and physical property analyses of intermetallic Yb compounds were summarized.

S. Engel, E. C. J. Gießelmann, M. K. Reimann, R. Pöttgen, O. Janka: **On the Ytterbium Valence and the Physical Properties in Selected Intermetallic Phases**, *ACS Organic & Inorganic Au* **2024**, 4, 188-222.³⁶¹

2. Review: Trivalent Europium – A Scarce Case in Intermetallics

Since the research of ternary intermetallic phases included *RE* elements and in particular europium and synthesizing or substituting the new compounds EuAl_5Pt_3 , $\text{Eu}_2\text{Al}_{16}\text{Pt}_9$, $\text{Eu}_4\text{Al}_{13}\text{Pt}_9$ and $\text{Eu}_2\text{Al}_{15}\text{Pt}_{6-x}\text{T}_x$, a minireview about intermetallic europium compounds with a trivalent oxidation state of Eu was prepared together with Prof. Dr. Rainer Pöttgen (University of Münster), PD Dr. Oliver Janka and Elias C. J. Gießelmann. In this review, ternary Eu compounds were showcased alongside their crystal chemistry, structural and physical property analysis, by e.g. XANES and XPS to show the valency of the europium. Also, examples were stated in which the valence of Eu can be altered through external factors like temperature or pressure.

S. Engel, E. Gießelmann, R. Pöttgen, O. Janka: **Trivalent Europium – A Scarce Case in Intermetallics**, *Rev. Inorg. Chem.* **2023**, 43, 4, 571-582.⁸⁰

3. Book Chapter: “Bulk Metallic Glasses” in Applied Inorganic Chemistry

The book chapter “Bulk Metallic Glasses” in the book “Applied Inorganic Chemistry” was written together with PD Dr. Oliver Janka, which gives a short historical overview of the class of materials alongside their synthesis and properties. The main focus of this work is the applications, which are sorted by the corresponding field, e.g. applications in consumer products or in industrial applications.

S. Engel, O. Janka: „**Bulk Metallic Glasses**“ in *Applied Inorganic Chemistry* DeGruyter, **2022** Chapter 2.11³⁶²

4. Book Chapter: “Shape Memory Alloys” in Applied Inorganic Chemistry

Like the “Bulk Metallic Glasses” chapter, the “Shape Memory Alloys” chapter was also composed for the book “Applied Inorganic Chemistry”, featuring the history of these materials along with the shape memory effect and the accompanying phase transition from martensite to austenite, followed by the different applications of shape memory alloys.

S. Engel, O. Janka: „**Shape Memory Alloy**“ in *Applied Inorganic Chemistry* DeGruyter, **2022** Chapter 2.10³⁹

4. Conclusion

Based on the DFG proposal with the title “Studies concerning the electronic structure and the electron transfer in electron poor intermetallics” (DFG # 441210509) new structures could be synthesized, crystallographically characterized and their properties as well as bonding situation analyzed. The compound series based on CeAl_5Pt_3 and EuAl_5Pt_3 could be extended not only to the rare earth but also to the alkaline earth metals with the compounds crystallizing all isopointal to the YNi_5Si_3 type structure in space group $Pnma$. Of these phases, single crystal data were collected from the Sr and the Er containing compound, validating the isotypism to the cerium compounds and hence the isopointalism to the YNi_5Si_3 type structure. A second compound family which could be extended was the $\text{Ce}_2\text{Al}_{16}\text{Pt}_9$ type structure, of which the Sr, La and Eu containing samples yielded single crystals, which confirmed the isotypism to the $\text{Ce}_2\text{Al}_{16}\text{Pt}_9$ type structure crystallizing in space group $Immm$. The crystal structures of Eu and Sr exhibit full occupancy, whereas in the La compound a mixing on one Al site occurs. Bulk samples of these compounds could be obtained for YAl_5Pt_3 , PrAl_5Pt_3 and GdAl_5Pt_3 , whereas the samples with the elements Nd, Sm, Tb, Dy, Ho and Er formed small quantities of Al_3Pt_2 . CaAl_5Pt_3 , SrAl_5Pt_3 and LaAl_5Pt_3 compounds always formed large amounts of the corresponding $M_2\text{Al}_{16}\text{Pt}_9$ phase along Al_3Pt_2 . All bulk samples of the $M_2\text{Al}_{16}\text{Pt}_9$ phases also resulted in a mixture of the target phase, $M\text{Al}_5\text{Pt}_3$ and Al_3Pt_2 , due to the peritectically decomposition of the $M_2\text{Al}_{16}\text{Pt}_9$ phase into the $M\text{Al}_5\text{Pt}_3$ compound and Al_3Pt_2 , which could be shown by heat treatment experiments on the lanthanum compound. The structure of the $M\text{Al}_5\text{Pt}_3$ could be validated by ^{27}Al NMR spectroscopy on the X-ray pure YAl_5Pt_3 resulting in five signals, corresponding to the five crystallographically independent Al sites in the structure. Besides NMR spectroscopy, also magnetic measurements of YAl_5Pt_3 and the samples containing Ce-Nd and Gd-Ho were recorded, showing the expected Pauli-paramagnetic behavior for the YAl_5Pt_3 , whereas the other compounds exhibit Curie paramagnetism. Additionally, an antiferromagnetic transition was observable for the Nd, Gd-Ho containing compounds.

The third compound family was discovered based on the $\text{Ce}_4\text{Al}_{13}\text{Pt}_9$ and $\text{Pr}_4\text{Al}_{13}\text{Pt}_9$ structures, which crystallize in the $\text{Ho}_4\text{Ge}_9\text{Ir}_{13}$ type structure ($Pmmn$). The family was firstly extended by the europium compound and subsequently for other lanthanides. Of these samples, the Nd containing compound confirmed the isotypism to the $\text{Ce}_4\text{Al}_{13}\text{Pt}_9$ through single crystal X-ray diffraction measurements. X-ray pure samples could be obtained for the Nd and Dy containing phases, whereas the other samples contain side phases like Al_3Pt_2 . The attempt to extend to

family to isostructural Pd containing phases resulted in the formation of $\text{Eu}_5\text{Al}_{0.70(1)}\text{Pd}_{2.30(1)}$, which crystallizes in the Mo_5SiB_2 type structure ($I4/mcm$) and exhibits a thus far unknown composition.

To understand the bonding situation and charge transfer of these structure families, bonding analyses via Bader charge calculations and integrated crystal orbital Hamilton populations for both strontium compounds SrAl_5Pt_3 and $\text{Sr}_2\text{Al}_{16}\text{Pt}_9$, YAl_5Pt_3 and $\text{Eu}_4\text{Al}_{13}\text{Pt}_9$ were conducted in collaboration with researchers at different universities. The Bader charges show positive values for the Sr and lower positive charges for the Al atoms, whereas the Pt atoms exhibit a negative charge, indicating a charge transfer from the Sr to the Pt atoms. The charge transfer is supported by the low ICOHP values of the M -Pt and M -Al pairs, whereas the Al-Al and Al-Pt have a significantly higher value and therefore a stronger bonding interaction, indicating the formation of a polyanionic $[\text{Al}_z\text{T}_y]^{\delta-}$ network. Due to the structural similarity of the motif, all structures can be described by the formation of the polyanionic network, which forms hexagonal prismatic cavities in which the $M^{\delta+}$ resides in, providing the charge transfer to the polyanion.

Additional new compounds were discovered during investigation in the system Ca-Al-Pt, resulting in two new structures the nominal compositions of CaAl_2Pt_2 and $\text{Ca}_2\text{Al}_3\text{Pt}$, which crystallize in the CaBe_2Ge_2 type structure ($P4/nmm$) and $\text{Mg}_2\text{Cu}_3\text{Si}$ type structure ($P6_3/mmc$), respectively. Both compounds exhibit Al/Pt mixing with refined compositions of $\text{CaAl}_{2.24(1)}\text{Pt}_{1.76(1)}$ and $\text{Ca}_2\text{Al}_{3.09(1)}\text{Pt}_{0.91(1)}$. Besides the two structures also the literature known Ca_2AlPt_2 phase (Ca_2SiIr_2 type, $C2/c$) was found, which exhibits a fully ordered structure. No X-ray pure samples of the newly found compounds could be obtained. The bonding analysis of the structures showed a similar trend as in the three structure families, making these phases also polar intermetallic compounds.

Subsequent to the discovery of $\text{CaAl}_{2.24(1)}\text{Pt}_{1.76(1)}$ and $\text{Ca}_2\text{Al}_{3.09(1)}\text{Pt}_{0.91(1)}$, the LOBSTER program package was used to perform bonding analysis based on DFT calculations by calculating the Löwdin charges and ICOBI values of literature known binary and ternary compounds in the Ca-Al-Pt system. The results show similarities to the ICOHP calculations and Bader charges calculated on the three structure families, with a focus on the alkaline earth samples SrAl_5Pt_3 and $\text{Sr}_2\text{Al}_{16}\text{Pt}_9$ compounds. The Ca atoms have a positive Löwdin charge comparable to the Bader charge of the Sr atoms, due to being the less electronegative element, hence transferring the valence electrons to the polyanionic network of Al and Pt. The Löwdin charges of the Pt and Al atoms, as calculated with the parameters now, exhibits positive charges for the Pt and negative charges for the Al atoms, being in contrast to the Bader charges and in regard to the electronegativity. This is currently investigated rendering Löwdin charges maybe

not as the best way to interpret charges in intermetallic compounds. The ICOBI values exhibit significant covalent bonding interactions between the Al–Al and Al–Pt atoms, but have still the highest values with Al–Al being the strongest, followed by the Al–Pt interactions. This is also reported by the new and sole compound SrAl_8Rh_2 (CeAl_8Fe_2 type, *Pbam*). Besides the bonding analysis via LOBSTER also temperature dependent electrical resistivity measurements were performed, showing metallic behavior down to a minimum around 7.5 K. Below the 7.5 K, the resistance rises, due impurity scattering. Additionally, a possible onset of a transition into superconductivity below 0.6 K is observable.

The last new ternary compound discovered is the CaAl_5Ni_2 which crystalizes in the PrAl_5Ni_2 type structure with space group *Immm*, no phase pure bulk samples could be obtained yet, due to evaporation of the Ca as well as the formation of CaAl_2 as main product.

Besides new ternary structures, also experiments on the valence change material $\text{Eu}_2\text{Al}_{15}\text{Pt}_6$ were conducted by partially substituting the Pt sites with Pd, Ir and Au atoms. $\text{Eu}_2\text{Al}_{15}\text{Pt}_6$ exhibits a temperature dependent valence transition at low temperatures (45 K), in which the valence of the europium atoms change from divalent to trivalent. The substitution led to the X-ray pure solid solution $\text{Eu}_2\text{Al}_{15}\text{Pt}_5\text{Pd}$, $\text{Eu}_2\text{Al}_{15}\text{Pt}_5\text{Ir}$ and $\text{Eu}_2\text{Al}_{15}\text{Pt}_5\text{Au}$. The magnetic measurements of the X-ray pure samples resulted in a change of the transition temperature. The Pd substituted solid solution exhibits a lower transition temperature of 42 K, whereas in the case of the Ir substitution the transition temperature could be increased to 52 K. As for the Au containing solid solution, due to the increased valence electron count, the valence transition was suppressed.

Bibliography

1. Behrens R., From Construction Materials to Technical Gases, 2.2 Special Steels and Alloys for Industrial Use. In *Applied Inorganic Chemistry*, R. Pöttgen, T. Jüstel and C. A. Strassert, Eds. De Gruyter: 2023; pp 123-157.
2. Kammer C., *Aluminium Taschenbuch 1, Grundlagen und Werkstoffe*, 16, DIN Media, **2011**.
3. Holleman A. F.; Wiberg E., *Lehrbuch der Anorganischen Chemie, 101. Auflage*, de Gruyter, Berlin, New York, **1995**.
4. Emsley J., *The Elements*, Clarendon Press, Oxford University Press, Oxford, New York, **1998**.
5. Langner B. E., *Volume 1 From Construction Materials to Technical Gases, 2.4 Copper and Copper Alloys*, De Gruyter, **2023**.
6. Reschetilowski W., *Einführung in die Heterogene Katalyse*, 1, Springer Spektrum, Berlin, Heidelberg, **2015**.
7. Faraday M. *Q. J. Sci. Lit. Arts* **1823**, 16, 179.
8. William J. Buehler; Wiley R. C., US3174851A, **1961**.
9. Wang F. E.; Buehler W. J.; Pickart S. J. *J. Appl. Phys.* **1965**, 36, 3232-3239.
10. Buehler W. J.; Gilfrich J. V.; Wiley R. C. *J. Appl. Phys.* **1963**, 34, 1475-1477.
11. Goryczka T.; Morawiec H. *J. Alloys Compd.* **2004**, 367, 137-141.
12. Hara T.; Ohba T.; Okunishi E.; Otsuka K. *Mater. Trans., JIM* **1997**, 38, 11-17.
13. Saburi T.; Nenno S.; Fukuda T. *J. Less-Common Met.* **1986**, 125, 157-166.
14. Fruchart D.; Soubeyroux J. L.; Miraglia S.; Obbade S.; Lorthioir G.; Basile F.; Colin C.; Faudot F.; Ochin P.; Dezellus A. *Z. Phys. Chem.* **1993**, 179, 225-236.
15. Jackson C. M.; Wagner H. J.; Wasilewski R. J., The Alloy With a Memory, 55-Nitinol: Its Physical Metallurgy, Properties, and Applications, Battelle Memorial Institute, **1972**,
16. Duerig T. W. *Mater. Sci. Forum* **1990**, 56-58, 679-691.
17. Jani J. M.; Leary M.; Subic A. *Appl. Mech. Mater.* **2014**, 663, 248-253.
18. Mohd Jani J.; Leary M.; Subic A.; Gibson M. A. *Materials & Design* **2014**, 56, 1078-1113.
19. Epps J. J.; Chopra I. *Smart Mater. Struct.* **2001**, 10, 104-111.
20. Stoeckel D. *Materials & Design* **1990**, 11, 302-307.
21. Alazzawi S.; Filip P. *IOP Conf. Ser.: Mater. Sci. Eng.* **2021**, 1076.
22. Van Humbeeck J. *Mater. Sci. Eng. A* **1999**, 273-275, 134-148.
23. Asai M.; Suzuki Y. *Mater. Sci. Forum* **2000**, 327-328, 17-22.
24. Ming H. Wu; Schetky L. M., Industrial Applications for Shape Memory Alloys, Proceedings of the International Conference on Shape Memory and Superelastic Technologies, Pacific Grove, California, **2000**, p. 171-182.
25. Barth J.; Megnin C.; Kohl M. *J. Microelectromechanical Sys.* **2012**, 21, 76-84.
26. Kohl M., *Shape Memory Microactuators*, 1, Springer Berlin, Heidelberg, Berlin, Heidelberg, **2004**.
27. Fujita H.; Toshiyoshi H. *Microelectron. J.* **1998**, 29, 637-640.
28. Kyu-Jin C.; Hawkes E.; Quinn C.; Wood R. J., Design, Fabrication and Analysis of a Body-Caudal Fin Propulsion System for a Microrobotic Fish, *2008 IEEE International Conference on Robotics and Automation*, **2008**, p. 706-711.
29. Menon C.; Sitti M., Biologically Inspired Adhesion based Surface Climbing Robots, *Proceedings of the 2005 IEEE International Conference on Robotics and Automation*, **2005**, p. 2715-2720.
30. Sun L.; Huang W. M.; Ding Z.; Zhao Y.; Wang C. C.; Purnawali H.; Tang C. *Materials & Design* **2012**, 33, 577-640.
31. Young Pyo L.; Byungkyu K.; Moon Gu L.; Jong-Oh P., Locomotive Mechanism Design and Fabrication of Biomimetic Micro Robot Using Shape Memory Alloy, *IEEE International Conference on Robotics and Automation, 2004. Proceedings. ICRA '04. 2004*, **2004**, p. 5007-5012 Vol.5005.
32. Sugiyama Y.; Hirai S. *Int. J. Robot. Res.* **2006**, 25, 603-620.
33. Cho K.-J.; Rosmarin J.; Asada H., SBC Hand: A Lightweight Robotic Hand with an SMA Actuator Array Implementing C-Segmentation, *Proceedings 2007 IEEE International Conference on Robotics and Automation*, **2007**, p. 921-926.

34. Mantovani D. *JOM* **2000**, 52, 36-44.
35. Miura F.; Mogi M.; Ohura Y.; Hamanaka H. *Am. J. Orthod. Dentofacial. Orthop.* **1986**, 90, 1-10.
36. Moneim M. S.; Firoozbakhsh K.; Mustapha A. A.; Larsen K.; Shahinpoor M. *Clin. Orthop. Relat. Res.* **2002**, 251-259.
37. Petrini L.; Migliavacca F.; Massarotti P.; Schievano S.; Dubini G.; Auricchio F. *J. Biomech. Eng.* **2005**, 127, 716-725.
38. Wolf F.; Thurnher S.; Lammer J. *Rofo* **2001**, 173, 924-930.
39. Engel S.; Janka O., Volume 1 From Construction Materials to Technical Gases, 2.10 Shape Memory Alloys. In *Applied Inorganic Chemistry*, R. Pöttgen, T. Jüstel and C. A. Strassert, Eds. De Gruyter: 2023; pp 255-264.
40. Bajaj P.; Hariharan A.; Kini A.; Kürnsteiner P.; Raabe D.; Jägle E. A. *Mater. Sci. Eng. A* **2020**, 772.
41. Ahmed M. S.; Anwar M. S.; Islam M. S.; Arifuzzaman M. *Results in Materials* **2023**, 20.
42. Willens R. H.; Geballe T. H.; Gossard A. C.; Maita J. P.; Mentha A.; Hull G. W.; Soden R. R. *Solid State Commun.* **1969**, 7, 837-841.
43. Banno N. *Superconductivity* **2023**, 6, 100047.
44. Sampath S.; Ravi V. P.; Sundararajan S. *Crystals* **2023**, 13, 435.
45. Finnis M. W.; Lozovoi A. Y.; Alavi A. *Annual Review of Materials Research* **2005**, 35, 167-207.
46. Djanarthany S.; Viala J. C.; Bouix J. *Mater. Chem. Phys.* **2001**, 72, 301-319.
47. Givord D.; Li H. S.; Moreau J. M. *Solid State Commun.* **1984**, 50, 497-499.
48. Stockert O.; Arndt J.; Faulhaber E.; Geibel C.; Jeevan H. S.; Kirchner S.; Loewenhaupt M.; Schmalzl K.; Schmidt W.; Si Q.; Steglich F. *Nature Physics* **2011**, 7, 119-124.
49. Zhao P.; Xue W.; Zhang Y.; Zhi S.; Ma X.; Qiu J.; Zhang T.; Ye S.; Mu H.; Cheng J.; Wang X.; Hou S.; Zhao L.; Xie G.; Cao F.; Liu X.; Mao J.; Fu Y.; Wang Y.; Zhang Q. *Nature* **2024**, 631, 777-782.
50. Ostermann F., *Anwendungstechnologie Aluminium*, Springer Vieweg, Berlin, Heidelberg, **2014**.
51. Ratvik A. P.; Mollaabbasi R.; Alamdari H. *ChemTexts* **2022**, 8, 10.
52. Survey U. S. G., Mineral Commodity Summaries 2024, U. S. G. Survey (Ed.) Mineral Commodity Summaries, **2024**,
53. Pearson's Crystal Data: Crystal Structure Database for Inorganic Compounds (release 2022/23). Villars P.; Cenzual K.: ASM International®, Materials Park, Ohio, USA 2023.
54. Turban K.; Schäfer H. *J. Less-Common Met.* **1975**, 40, 91-96.
55. Manyako M. B.; Yanson T. I.; Zarechnyuk O. S. *Russ. Metall.* **1988**, 3, 185-188.
56. Ryżyńska Z.; Klimczuk T.; Winiarski M. J. *J. Solid State Chem.* **2020**, 289, 121509.
57. Czech E.; Cordier G.; Schäfer H. *J. Less-Common Met.* **1983**, 95, 205-211.
58. Gießelmann E.; Touzani R. S.; Morgenstern B.; Janka O. *Z. Naturforsch.* **2021**, 76b, 659-668.
59. Zhang Q. A.; Yang W. M.; Hou Q. Y.; Wu H. Y. *Intermetallics* **2005**, 13, 796-799.
60. Zhang Q. A.; Zhao G. P.; Hou Q. Y.; Wu H. Y. *Mater. Sci. Eng. A* **2005**, 397, 113-116.
61. Stegemann F.; Zhang Y.; Fokwa B. P. T.; Janka O. *Dalton Trans.* **2020**, 49, 6398-6406.
62. Bain G. A.; Berry J. F. *J. Chem. Educ.* **2008**, 85, 532.
63. Stegemann F.; Block T.; Klenner S.; Zhang Y.; Fokwa B. P. T.; Timmer A.; Mönig H.; Doerenkamp C.; Eckert H.; Janka O. *Chem. Eur. J.* **2019**, 25, 10735-10747.
64. Doverbratt I.; Ponou S.; Zhang Y.; Lidin S.; Miller G. J. *Chem. Mater.* **2015**, 27, 304-315.
65. Stegemann F.; Benndorf C.; Touzani R. S.; Fokwa B. P. T.; Janka O. *J. Solid State Chem.* **2016**, 242, 143-150.
66. Cordier G.; Friedrich T.; Henseleit R.; Grauel A.; Tegel U.; Schank C.; Geibel C. *J. Alloys Compd.* **1993**, 201, 197-201.
67. Hulliger F. *J. Alloys Compd.* **1993**, 196, 225-228.
68. Kenfack Tsobnang P.; Fotio D.; Ponou S.; Fon Abi C. *Acta Crystallogr.* **2011**, E67, i55.
69. Cordier G.; Dörsam G.; Friedrich T.; Henseleit R.; Röhr C. *J. Alloys Compd.* **1993**, 190, 201-207.
70. Stegemann F.; Stahl J.; Bartsch M.; Zacharias H.; Johrendt D.; Janka O. *Chem. Sci.* **2019**, 10, 11086-11094.
71. Radzieowski M.; Stegemann F.; Hoffmann R.-D.; Janka O. *Z. Kristallogr.* **2017**, 232, 675-687.

72. Stegemann F.; Benndorf C.; Touzani R. S.; Fokwa B. P. T.; Janka O. *Eur. J. Inorg. Chem.* **2016**, 2016, 1108-1114.
73. Havinga E. E.; Damsma H.; Hokkeling P. J. *Less-Common Met.* **1972**, 27, 169-186.
74. Stegemann F.; Block T.; Klenner S.; Zhang Y.; Fokwa B. P. T.; Doerenkamp C.; Eckert H.; Janka O. *Eur. J. Inorg. Chem.* **2021**, 2021, 3832-3845.
75. Hoffmann R.-D.; Stegemann F.; Janka O. *Z. Kristallogr.* **2016**, 231, 127-142.
76. Stotsky V.; Pukas S. Y.; Akselrud L.; Gladyshevskii R. E. *Abstr. 13th Int. Conf. Crystal Chem. Intermet. Compd.* **2016**, 96.
77. Stegemann F.; Benndorf C.; Bartsch T.; Touzani R. S.; Bartsch M.; Zacharias H.; Fokwa B. P. T.; Eckert H.; Janka O. *Inorg. Chem.* **2015**, 54, 10785-10793.
78. Stegemann F.; Touzani R. S.; Janka O. *Dalton Trans.* **2019**, 48, 14103-14114.
79. Shannon R. D. *Acta Crystallogr.* **1976**, A32, 751.
80. Engel S.; Giesselmann E. C. J.; Pöttgen R.; Janka O. *Rev. Inorg. Chem.* **2023**, 43, 571-582.
81. Jensen J.; Mackintosh A. R., *Rare Earth Magnetism*, Clarendon Press, Oxford, **1991**.
82. Lueken H., *Magnetochemie*, B. G. Teubner, Stuttgart, Leipzig, **1999**.
83. Pöttgen R.; Johrendt D. *Chem. Mater.* **2000**, 12, 875-897.
84. Thiede V. M. T.; Jeitschko W. *Z. Kristallogr. - NCS* **1999**, 214, 149-150.
85. He M.; Xu X.; Wu Z.; Dong C.; Liu Y.; Hou Q.; Zhou S.; Han Y.; Wang J.; Qu Z. *Phys. Rev. Mater.* **2023**, 7.
86. Stegemann F.; Block T.; Klenner S.; Janka O. *Chem. Eur. J.* **2019**, 25, 3505-3509.
87. Cordier G.; Dietrich C. *Z. Kristallogr. - NCS* **1997**, 212, 287.
88. Yonehara N.; Nakajima M.; Tenji N.; Yonehara N.; Nakashima M.; Amako Y., Single crystal growth and magnetism of a new rare earth compound EuPdAl₅, Abstracts of the 75th Annual Meeting of the Physical Society of Japan, Physical Society of Japan, Japan, **2020**.
89. Suzuki H.; Nakamura S.; Ohara S., Metamagnetism in a New Material EuPdAl₆, *Proceedings of the 29th International Conference on Low Temperature Physics (LT29)*, **2023**.
90. Ponou S.; Mudring A.-V., Europium-rich ternary phases with noble metals Eu₂M₂X (M = Pd, Pt; X = Al, Ga, Ge, Cd), and their structural relationship to the Laves phase Ca₂Pt₃Al_{1-x}Ag_x, ChemRxiv., **2024**.
91. Koizumi T.; Honda F.; Sato Y. J.; Li D.; Aoki D.; Haga Y.; Gouchi J.; Nagasaki S.; Uwatoko Y.; Kaneko Y.; Ōnuki Y. *J. Phys. Soc. Jpn.* **2022**, 91, 043704.
92. Radziejowski M.; Stegemann F.; Block T.; Stahl J.; Johrendt D.; Janka O. *J. Am. Chem. Soc.* **2018**, 140, 8950-8957.
93. Pöttgen R.; Gulden T.; Simon A. *GIT Labor-Fachz.* **1999**, 43, 133-136.
94. Pöttgen R.; Hoffmann R.-D.; Kußmann D. *Z. Anorg. Allg. Chem.* **1998**, 624, 945-951.
95. Topas (Version 5). *General Profile and Structure Analysis Software for Powder Diffraction Data*, Bruker AXS Inc.: Karlsruhe (Germany) 2014.
96. SADABS, Sheldrick G. M.: University of Göttingen, Germany 1996.
97. Jana2006. The Crystallographic Computing System, Petříček V.; Dušek M.; Palatinus L.: Institute of Physics, Praha (Czech Republic) 2006.
98. Petříček V.; Dušek M.; Palatinus L. *Z. Kristallogr.* **2014**, 229, 345-352.
99. Palatinus L.; Chapuis G. *J. Appl. Crystallogr.* **2007**, 40, 786-790.
100. Massa W., *Kristallstrukturbestimmung*, 5., Vieweg & Teubner, Wiesbaden, Germany, **2007**.
101. Diamond (V 4.6.8). Brandenburg K.: Bonn, Germany 2022.
102. Wollan E. O.; Koehler W. C. *Phys. Rev.* **1955**, 100, 545-563.
103. Ruderman M. A.; Kittel C. *Phys. Rev.* **1954**, 96, 99-102.
104. Kasuya T. *Prog. Theor. Phys.* **1956**, 16, 45-57.
105. Yosida K. *Phys. Rev.* **1957**, 106, 893-898.
106. Kondo J. *Prog. Theor. Phys.* **1964**, 32, 37-49.
107. Hermes W., Diplomarbeit, *Magnetismus und Hydrierungsverhalten äquiatomarer CeTX-Verbindungen*, WWU, **2007**.
108. Stegemann F., PhD Thesis, *Synthese, Strukturchemie, physikalische und spektroskopische Untersuchungen ternärer Aluminium-Übergangsmetallide*, Westfälischen Wilhelms-Universität Münster, **2019**.
109. Benndorf C.; Eckert H.; Janka O. *Acc. Chem. Res.* **2017**, 50, 1459-1467.

110. Kenneth J.D. MacKenzie M. E. S., *Multinuclear Solid-State Nuclear Magnetic Resonance of Inorganic Materials*, 1st, Elsevier, **2002**.
111. Benndorf C., Dissertation, *Multinukleare Festkörper NMR spektroskopische Untersuchungen ausgewählter intermetallischer Verbindungen*, Westfälische Wilhelms-Universität Münster, Münster, **2016**.
112. Stone N. J. *At. Data Nucl. Data Tables* **2016**, 111–112, 1-28.
113. Duer M. J., *Introduction to Solid-State NMR Spectroscopy*, 1, Wiley-Blackwell, Oxford, **2004**.
114. Harris R. K.; Becker E. D.; Cabral de Menezes S. M.; Granger P.; Hoffman R. E.; Zilm K. W. *Pure Appl. Chem.* **2008**, 80, 59-84.
115. Nowak B.; Hayashi S. *Solid State Nucl. Magn. Reson.* **2000**, 18, 59-69.
116. Topspin (Version 2.1). Bruker Corp.: Karlsruhe 2008.
117. Massiot D.; Fayon F.; Capron M.; King I.; Le Calvé S.; Alonso B.; Durand J.-O.; Bujoli B.; Gan Z.; Hoatson G. *Magn. Reson. Chem.* **2002**, 40, 70-76.
118. Güntherodt G.; Jayaraman A.; Batlogg G.; Croft M.; Melczer E. *Phys. Rev. Lett.* **1983**, 51, 2330-2332.
119. Gey M. H., *Instrumentelle Analytik und Bioanalytik*, 4, Springer Spektrum Berlin, Heidelberg, **2021**.
120. Moulder J. F.; Stickle W. F.; Sobol P. E.; Bomben K. D., *Handbook of X-Ray Photoelectron Spectroscopy*, Physical Electronics, Minnesota, **1995**.
121. Hüfner S., *Photoelectron Spectroscopy: Principles and Applications*, Springer, Berlin, **2003**.
122. Mössbauer R. L. *Z. Phys.* **1958**, 151, 124-143.
123. Fluck E.; Kerler W.; Neuwirth W. *Angew. Chem.* **2006**, 75, 461-472.
124. Gütlich P. *Chem. unserer Zeit* **2004**, 4, 133-144.
125. Gütlich P. *Chem. unserer Zeit* **2004**, 5, 131-141.
126. Gütlich P.; Bill E.; Trautwein A. X., *Mössbauer Spectroscopy and Transition Metal Chemistry*, Springer-Verlag, Berlin Heidelberg, **2011**.
127. Stevens J. G. S., V. E., *Mössbauer Effect Data Index*, IFI/Plenum Data Company, New York, USA, **1976**.
128. Long G. J.; Cranshaw T. E.; Longworth G. *Mössbauer Eff. Ref. Data J.* **1983**, 6, 42-49.
129. WinNormos for Igor6, Version for Igor 6.2 or above: 22.02.2017, Brand R. A.: Universität Duisburg, Duisburg (Germany) 2017.
130. Giannozzi P.; Baroni S.; Bonini N.; Calandra M.; Car R.; Cavazzoni C.; Ceresoli D.; Chiarotti G. L.; Cococcioni M.; Dabo I.; Dal Corso A.; de Gironcoli S.; Fabris S.; Fratesi G.; Gebauer R.; Gerstmann U.; Gougoussis C.; Kokalj A.; Lazzeri M.; Martin-Samos L.; Marzari N.; Mauri F.; Mazzarello R.; Paolini S.; Pasquarello A.; Paulatto L.; Sbraccia C.; Scandolo S.; Sclauzero G.; Seitsonen A. P.; Smogunov A.; Umari P.; Wentzcovitch R. M. *J. Phys.: Condens. Matter* **2009**, 21, 395502.
131. Giannozzi P.; Andreussi O.; Brumme T.; Bunau O.; Buongiorno Nardelli M.; Calandra M.; Car R.; Cavazzoni C.; Ceresoli D.; Cococcioni M.; Colonna N.; Carnimeo I.; Dal Corso A.; de Gironcoli S.; Delugas P.; DiStasio R. A.; Ferretti A.; Floris A.; Fratesi G.; Fugallo G.; Gebauer R.; Gerstmann U.; Giustino F.; Gorni T.; Jia J.; Kawamura M.; Ko H. Y.; Kokalj A.; Küçükbenli E.; Lazzeri M.; Marsili M.; Marzari N.; Mauri F.; Nguyen N. L.; Nguyen H. V.; Otero-de-la-Roza A.; Paulatto L.; Poncé S.; Rocca D.; Sabatini R.; Santra B.; Schlipf M.; Seitsonen A. P.; Smogunov A.; Timrov I.; Thonhauser T.; Umari P.; Vast N.; Wu X.; Baroni S. *J. Phys.: Condens. Matter* **2017**, 29, 465901.
132. Blöchl P. E. *Phys. Rev. B* **1994**, 50, 17953-17979.
133. Dal Corso A. *Comput. Mater. Sci.* **2014**, 95, 337-350.
134. Topsakal M.; Wentzcovitch R. M. *Comput. Mater. Sci.* **2014**, 95, 263-270.
135. Marzari N.; Vanderbilt D.; De Vita A.; Payne M. C. *Phys. Rev. Lett.* **1999**, 82, 3296-3299.
136. Monkhorst H. J.; Pack J. D. *Phys. Rev. B* **1976**, 13, 5188-5192.
137. Perdew J. P.; Burke K.; Ernzerhof M. *Phys. Rev. Lett.* **1996**, 77, 3865-3868.
138. Tang W.; Sanville E.; Henkelman G. *J. Phys.: Condens. Matter* **2009**, 21, 084204.
139. Sanville E.; Kenny S. D.; Smith R.; Henkelman G. *J. Comput. Chem.* **2007**, 28, 899-908.
140. Henkelman G.; Arnaldsson A.; Jónsson H. *Comput. Mater. Sci.* **2006**, 36, 354-360.
141. Yu M.; Trinkle D. R. *J. Chem. Phys.* **2011**, 134, 064111.

142. Otero-de-la-Roza A.; Blanco M. A.; Pendás A. M.; Luaña V. *Comput. Phys. Commun.* **2009**, *180*, 157-166.
143. Otero-de-la-Roza A.; Johnson E. R.; Luaña V. *Comput. Phys. Commun.* **2014**, *185*, 1007-1018.
144. TB-LMTO-ASA (version 47). Jepsen O.; Andersen O. K.: Max-Planck-Institut für Festkörperforschung
Stuttgart (Germany) 2000.
<http://www2.fkf.mpg.de/andersen/LMTODOC/LMTODOC.html> (accessed August 2021)
145. Andersen O. K.; Skriver H. L.; Nohl H.; Johansson B. *Pure Appl. Chem.* **1980**, *52*, 93-118.
146. Andersen O. K.; Jepsen O. *Phys. Rev. Lett.* **1984**, *53*, 2571-2574.
147. Perdew J. P.; Wang Y. *Phys. Rev. B* **1992**, *45*, 13244-13249.
148. Dronskowski R.; Blöchl P. E. *J. Phys. Chem.* **1993**, *97*, 8617-8624.
149. Kresse G.; Furthmüller J. *Comput. Mater. Sci.* **1996**, *6*, 15-50.
150. Kresse G.; Furthmüller J. *Phys. Rev. B* **1996**, *54*, 11169-11186.
151. Kresse G.; Joubert D. *Phys. Rev. B* **1999**, *59*, 1758-1775.
152. Bader R. F. W. *Chem. Rev.* **1991**, *91*, 893-928.
153. Savin A.; Nesper R.; Wengert S.; Fässler T. F. *Angew. Chem.* **1997**, *109*, 1892-1918.
154. Silvi B.; Savin A. *Nature* **1994**, *371*, 683-686.
155. Andersen O. K. *Phys. Rev. B* **1975**, *12*, 3060-3083.
156. Andersen O. K.; Pawłowska Z.; Jepsen O. *Phys Rev B Condens Matter* **1986**, *34*, 5253-5269.
157. von Barth U.; Hedin L. *J. Phys. C: Solid State Phys.* **1972**, *5*, 1629.
158. Becke A. D.; Edgecombe K. E. *J. Chem. Phys.* **1990**, *92*, 5397-5403.
159. wxDragon, Eck B.: Aachen, Germany 2013.
160. Maintz S.; Deringer V. L.; Tchougreeff A. L.; Dronskowski R. *J. Comput. Chem.* **2016**, *37*, 1030-1035.
161. Nelson R.; Ertural C.; George J.; Deringer V. L.; Hautier G.; Dronskowski R. *J. Comput. Chem.* **2020**, *41*, 1931-1940.
162. Müller P. C.; Schmit N.; Sann L.; Steinberg S.; Dronskowski R. *Inorg. Chem.* **2024**, *63*, 20161-20172.
163. Müller P. C.; Ertural C.; Hempelmann J.; Dronskowski R. *J. Phys. Chem. C* **2021**, *125*, 7959-7970.
164. Tarschisch L.; Titow A. T.; Garjanow F. K. *Phys. Z. Sowjetunion* **1934**, *5*, 503-510.
165. Friauf J. B. *J. Am. Chem. Soc.* **1927**, *49*, 3107-3114.
166. Nowotny H. N. *Z. Metallkd.* **1942**, *34*, 247-253.
167. Duwell E. J.; Baenziger N. C. *Acta Crystallogr.* **1955**, *8*, 705-710.
168. Andress K. R.; Alberti E. *Z. Metallkd.* **1935**, *27*, 126.
169. Bruzzone G.; Fornasini M. L.; Merlo F. *J. Less-Common Met.* **1989**, *154*, 67-77.
170. Miller G. J.; Li F.; Franzen H. F. *J. Am. Chem. Soc.* **2002**, *115*, 3739-3745.
171. Akselrud L. G.; Yarovets V. I.; Bodak O. I.; Yarmolyuk Y. P.; Gladyshevskii E. I. *Kristallografiya* **1976**, *21*, 383-386.
172. Engel S.; Giesselmann E. C. J.; Schumacher L.; Zhang Y.; Muller F.; Janka O. *Dalton Trans* **2024**.
173. Tursina A. I.; Murashova E. V.; Noël H.; Bukhan'ko N. G.; Seropegin Y. D. *Intermetallics* **2009**, *17*, 780-783.
174. Engel S.; Janka O. *Z. Naturforsch.* **2024**, *79*, 595-603.
175. Engel S.; Bönnighausen J.; Stegemann F.; Touzani R. S.; Janka O. *Z. Naturforsch.* **2022**, *77*, 367-379.
176. Engel S.; Zaremba N.; Prots Y.; Touzani R. S.; Janka O. *Z. Naturforsch.* **2023**, *78*, 147-156.
177. Sologub O. L.; Prots Y. M.; Salamakha P. S.; Pecharsky V. K.; Bodak O. I. *J. Alloys Compd.* **1993**, *202*, 13-15.
178. Schoolaert S.; Jung W. *Z. Anorg. Allg. Chem.* **2002**, *628*, 1806-1810.
179. Eisenmann B.; May N.; Müller W.; Schäfer H. *Z. Naturforsch.* **1972**, *27*, 1155-1157.
180. Pöttgen R. *Z. Anorg. Allg. Chem.* **2014**, *640*, 869-891.
181. H. W. *Z. Angew. Mineral.* **1938**, *1*, 255-268.
182. Yarmolyuk Y. P.; Pykhal R. M.; Zarechnyuk O. S. *Tezisy Dokl. Vses. Konf. Kristalloghim. Intermet. Soeden* **1974**, *2*, 39-40.
183. Niemann J.; Jeitschko W. *Z. Anorg. Allg. Chem.* **2004**, *630*, 361-368.

184. Grin Y.; Gladyshevskii R. E.; Sichevich O. M.; Zavodnik V. E.; Yarmolyuk Y. P.; Rozhdestvenskaya I. V. *Kristallografiya* **1984**, *29*, 893-898.
185. Nowotny H.; Wormnes E.; Mohrheim A. Z. *Metallkd.* **1940**, *32*, 39-42.
186. Nagorsen G.; Posch H.; Schäfer H.; Weiss A. Z. *Naturforsch.* **1969**, *24b*, 1191.
187. Fornasini M. L.; Bruzzone G. *J. Less-Common Met.* **1975**, *40*, 335-340.
188. Cordier G.; Czech E.; Schäfer H. Z. *Naturforsch.* **1982**, *37b*, 1442-1445.
189. Cordier G.; Czech E.; Schäfer H. Z. *Naturforsch.* **1984**, *39b*, 421-423.
190. Kal S.; Stoyanov E.; Belieres J.-P.; Groy T. L.; Norrestam R.; Häussermann U. *J. Solid State Chem.* **2008**, *181*, 3016-3023.
191. Nowotny H.; Wesenberg H. Z. *Metallkd.* **1939**, *31*, 363-364.
192. Miller G. J.; Li F.; Franzen H. F. *J. Am. Chem. Soc.* **1993**, *115*, 3739-3745.
193. Engel S.; Gießelmann E. C. J.; Schank L. E.; Heymann G.; Brix K.; Kautenburger R.; Beck H. P.; Janka O. *Inorg. Chem.* **2023**, *62*, 4260-4271.
194. Engel S.; Koch M.; Janka O. *Z. Anorg. Allg. Chem.* **2024**, *650*.
195. Engel S.; Reimann M. K.; Svanidze E.; Krnel M.; Zaremba N.; König M.; Janka O. *Z. Kristallogr.* **2025**, *240*, 1-11.
196. Tursina A. I.; Bukhan'ko N. G.; Gribov A. V.; Shchelkunov V. A.; Nelyubina Y. V. *Acta Crystallogr.* **2005**, *E61*, i285-i286.
197. Heying B.; Kösters J.; Heletta L.; Klenner S.; Pöttgen R. *Monatsh. Chem.* **2019**, *150*, 1163-1173.
198. Bodak O. I.; Yarovets V. I.; Gladyshevskii E. I., Crystal Structures of Ternary Compounds in the System Y-Ni-Si, *Tezisy Dokl. Vses. Konf. Kristalloghim. Intermet. Soeden*, Lviv, **1974**, p. 32-33.
199. Riccardo Ferro R. C., Gabriella Rambaldi *Atti Accad. Naz. dei Lincei Cl. Sci. Fis. Mat. Nat. Rend. Lincei Mat. Appl.* **1963**, *34*, 45-47.
200. Schubert K.; Burkhardt W.; Esslinger P.; Gnzel E.; Meissner H. G.; Schtt W.; Wegst J.; Wilkens M. *Naturwissenschaften* **1956**, *43*, 248-249.
201. Chattopadhyay T.; Schubert K. *J. Less-Common Met.* **1975**, *41*, 19-32.
202. Rodriguez M. A.; Adams D. P. *Powder Diffr.* **2006**, *21*, 318-319.
203. Heumann T.; Kniepmeyer M. *Z. Anorg. Allg. Chem.* **1957**, *290*, 191-204.
204. Haszko S. E. *Trans. Metall. Soc. AIME* **1960**, *218*, 958.
205. Krypyakevych P. I.; Zalutskii I. I. *Vopr. Teor. Primen. Redkozem. Met., Mater. Soveshch.* **1964**.
206. Elliott R. P. *Proc. Conf. Rare Earth Res., 4th, Phoenix* **1965**, 215-245.
207. Zintl E.; Harder A.; Haucke W. *Z. Phys. Chem. B* **1937**, *35*, 354-362.
208. Hull A. W. *Phys. Rev.* **1917**, *10*, 661-696.
209. Hull A. W. *Trans. Am. Inst. Electro. Eng.* **1919**, *38*, 1445-1466.
210. Edshammar L.-E. *Acta Chem. Scand.* **1966**, *20*, 2683-2688.
211. Wood E. A.; Compton V. B. *Acta Crystallogr.* **1958**, *11*, 429-433.
212. Zaremba N.; Pavlyuk V.; Stegemann F.; Hlukhyy V.; Engel S.; Klenner S.; Pöttgen R.; Janka O. *Monatsh. Chem.* **2022**, *154*, 43-52.
213. Schubert K.; Breimer H.; Burkhardt W.; Günzel E.; Haufner R.; Lukas H. L.; Vetter H.; Wegst J.; Wilkens M. *Naturwissenschaften* **1957**, *44*, 229-230.
214. Jana P. P.; Pankova A. A.; Lidin S. *Inorg. Chem.* **2013**, *52*, 11110-11117.
215. Manyako M.B. Z. O. S., Yanson T.I. *Kristallografiya* **1987**, *32*, 339-342.
216. Bruzzone G.; Merlo F. *J. Less-Common Met.* **1975**, *39*, 1-6.
217. Edshammar L.-E. *Acta Chem. Scand.* **1968**, *22*, 2822-2826.
218. Chaudhury Z. A.; Suryanarayana C. *J. Less-Common Met.* **1983**, *91*, 181-187.
219. Ferro R.; Rambaldi G.; Capelli R.; Bonino G. B. *Atti Accad. Naz. Lincei, Cl. Sci. Fis., Mat. Nat., Rend.* **1964**, *36*, 491-497.
220. Boström M.; Rosner H.; Prots Y.; Burkhardt U.; Grin Y. *Z. Anorg. Allg. Chem.* **2005**, *631*, 534-541.
221. Manjako N. B.; Yanson T. I.; Zarechnyuk O. S.; Stets' I. N. *Visn. Lviv. Derzh. Univ., Ser. Khim.* **1984**, *25*, 13-14.
222. Morozova Y.; Gribov A.; Murashova E.; Dunaev S.; Grytsiv A.; Rogl P.; Giester G.; Kaczorowski D. *J. Alloys Compd.* **2018**, *767*, 496-503.
223. Engel S.; Schumacher L.; Janka O. *Z. Naturforsch.* **2024**, *79*, 21-27.

224. Oyama K.; Mitsuda A.; Wada H.; Narumi Y.; Hagiwara M.; Takahashi R.; Wadati H.; Setoyama H.; Kindo K. *J. Phys. Soc. Jpn.* **2020**, *89*.
225. Van Vucht J. H. N.; Buschow K. H. J. *Philips Res. Rep.* **1964**, *19*, 319-322.
226. Kotur B. Y.; Bruvo M. *Sov. Phys. Crystallogr.* **1991**, *36*, 787-789.
227. Pfisterer H.; Schubert K. *Naturwissenschaften* **1950**, *37*, 112-113.
228. Eßlinger P.; Schubert K. *Int. J. Mater. Res.* **1957**, *48*, 126-134.
229. Harris I. R.; Raynor G. V. *J. Less-Common Met.* **1965**, *9*, 263-269.
230. Harris I. R.; Longworth G. *J. Less-Common Met.* **1971**, *23*, 281-292.
231. Range K.-J.; Christl E. G. *J. Less-Common Met.* **1988**, *136*, 277-285.
232. Matković T.; Schubert K. *J. Less-Common Met.* **1977**, *55*, 45-52.
233. Sastry G. V. S.; Suryanarayana C. *J. Less-Common Met.* **1979**, *63*, P89-P91.
234. Dwight A. E. *J. Less-Common Met.* **1984**, *102*, L9-L13.
235. Radziejowski M.; Stegemann F.; Doerenkamp C.; Matar S. F.; Eckert H.; Dosche C.; Wittstock G.; Janka O. *Inorg. Chem.* **2019**, *58*, 7010-7025.
236. Eustermann F.; Gausebeck S.; Dosche C.; Haensch M.; Wittstock G.; Janka O. *Crystals* **2018**, *8*, 169.
237. Benndorf C.; Stegemann F.; Eckert H.; Janka O. *Z. Naturforsch.* **2015**, *70b*, 101-110.
238. Thiede V. M. T.; Fehrmann B.; Jeitschko W. *Z. Anorg. Allg. Chem.* **1999**, *625*, 1417-1425.
239. Engelbert S.; Janka O. *Intermetallics* **2018**, *96*, 84-89.
240. Gladyshevskii E. I.; Krypyakevych P. I.; Teslyuk M. Y.; Zarechnyuk O. S.; Kuz'ma Y. B. *Sov. Phys. Crystallogr.* **1961**, *6*, 207-208.
241. Krypyakevych P. I.; Zalutskii I. I. *Dopov. Akad. Nauk Ukr. RSR* **1963**, 61-64.
242. Buschow K. H. J. *J. Less-Common Met.* **1965**, *8*, 209-212.
243. Buschow K. H. J.; Van Der Goot A. S. *J. Less-Common Met.* **1971**, *24*, 117-120.
244. Buschow K. H. J.; Vanvucht J. H. *Z. Metallkd.* **1965**, *56*, 9-&.
245. Moriarty J. L., Jr.; Gordon R. O.; Humphreys J. E. *Acta Crystallogr.* **1965**, *19*, 285-286.
246. Kolesnichenko V. E.; Terekhova V. F.; Savitskii E. M. *Diagrammy Sostoyaniya Met. Sist., Mater. Vses. Soveshch.* **1971**, *4th*, 174-176.
247. Dwight A. E.; Conner Jnr R. A.; Downey J. W. *Acta Crystallogr.* **1965**, *18*, 835-839.
248. Bradley A. J.; Taylor A. *Phil. Mag.* **1937**, *23*, 1049-1067.
249. Manyako M. B.; Zarechnyuk O. S.; Yanson T. I. *Kristallografiya* **1987**, *32*, 1389-1391.
250. Rykhal' R. M.; Zarechnyuk O. S. *Tezisy Dokl. Vses. Konf. Kristallokhim. Intermet. Soeden* **1978**, *3rd*, 16.
251. Gerlach W. *Z. Phys.* **1922**, *9*, 184-192.
252. Li D.; Luo K.; He B.; Liang L.; Qin M.; Lu T. *Powder Diffr.* **2018**, *33*, 172-175.
253. Isikawa Y.; Mizushima T.; Sakurai J.; Mori K.; Munoz A.; Givord F.; Boucherle J.-X.; Voiron J.; S. Oliveira I.; Flouquet J. *J. Phys. Soc. Jpn.* **1994**, *63*, 2349-2358.
254. Yarmolyuk Y. P.; Rykhal' R. M.; Akselrud L.; Zarechnyuk O. S. *Dokl. Akad. Nauk. Ukr. SSR* **1981**, *9A*, 86-90.
255. Sarkar R.; Ghoshray K.; Bandyopadhyay B.; Ghoshray A. *Phys. Rev. B* **2005**, *71*.
256. Isikawa Y.; Mizushima T.; Oyabe K.; Mori K.; Sato K.; Kamigaki K. *J. Phys. Soc. Jpn.* **1991**, *60*, 1869-1872.
257. Kashiwakura T.; Okane T.; Suzuki S.; Sato S.; Watanabe M.; Harasawa A.; Kinoshita T.; Kakizaki A.; Ishii T.; Nakai S.-i.; Isikawa Y. *J. Phys. Soc. Jpn.* **2000**, *69*, 3095-3099.
258. Gout D.; Benbow E.; Gourdon O.; Miller G. J. *J. Solid State Chem.* **2003**, *176*, 538-548.
259. Becker K.; Ebert F. *Z. Phys.* **1923**, *16*, 165-169.
260. Buschow K. H. J. *J. Less-Common Met.* **1974**, *38*, 95-98.
261. Markiv V. Y.; Burnashova V. V. *Dopov. Akad. Nauk Ukr. RSR Ser. A: Fiz.-Mat. Tekh. Nauki* **1969**, *5*, 463-464.
262. Markiv V.Y. K. P. I., Belyavina N.N. *Dopov. Akad. Nauk Ukr. RSR* **1982**, *Ser. A*, 76-79.
263. Kundu M.; Mazumdar C.; Ranganathan R.; De Raychaudhury M. *J. Magn. Magn. Mater.* **2019**, *489*.
264. Diviš M.; Čermák P.; Javorský P. *Physica B* **2012**, *407*, 276-279.
265. Onimaru T.; F. Inoue Y.; Shigetoh K.; Umeo K.; Kubo H.; A. Ribeiro R.; Ishida A.; A. Avila M.; Ohoyama K.; Sera M.; Takabatake T. *J. Phys. Soc. Jpn.* **2008**, *77*.

266. Honda F.; Measson M.-A.; Nakano Y.; Yoshitani N.; Yamamoto E.; Haga Y.; Takeuchi T.; Yamagami H.; Shimizu K.; Settai R.; Ōnuki Y. *J. Phys. Soc. Jpn.* **2008**, *77*, 043701.
267. Metoki N.; Yamauchi H.; Kitazawa H.; Suzuki H. S.; Hagihala M.; Frontzek M. D.; Matsuda M.; Fernandez-Baca J. A. *J. Phys. Soc. Jpn.* **2017**, *86*.
268. Zubáč J.; Vlášková K.; Prokleška J.; Proschek P.; Javorský P. *J. Alloys Compd.* **2016**, *675*, 94-98.
269. Iandelli A.; Palenzona A. *J. Less-Common Met.* **1974**, *38*, 1-7.
270. Chen T.; Yao J.; Knotko A. V.; Yapaskurt V. O.; Morozkin A. V. *J. Solid State Chem.* **2022**, *305*.
271. Morozkin A. V.; Garshev A. V.; Knotko A. V.; Yapaskurt V. O.; Yao J. *J. Solid State Chem.* **2019**, *277*, 303-315.
272. Yuan F.; Morozkin A. V.; Mozharivskiy Y. *J. Alloys Compd.* **2015**, *620*, 376-382.
273. Belgacem B.; Pasturel M.; Tougait O.; Nouri S.; Bekkachi H. E.; Péron I.; Hassen R. B.; Noël H. *J. Alloys Compd.* **2012**, *531*, 41-45.
274. Belan B.; Sojka L.; Demchyna M.; Manyako M.; Kalychak Y. *Chem. Met. Alloys* **2016**, *9*, 21-26.
275. Lukachuk M. y.; Kalychak Y. M.; Dzevenko M.; Pöttgen R. *J. Solid State Chem.* **2005**, *178*, 1247-1253.
276. Gout D.; Benbow E.; Miller G. J. *J. Alloys Compd.* **2002**, *338*, 153-164.
277. Bodak O.I. M. k. M. G., Tyvanchuk A.T., Kharchenko O.I., Gladyshevskii E.I. *Inorg. Mater.* **1973**, *777-779*.
278. Sologub O.; Salamakha P.; Bocelli G.; Godart C.; Takabatake T. *J. Alloys Compd.* **2000**, *312*, 172-175.
279. Lipatov A.; Griбанov A.; Grytsiv A.; Rogl P.; Murashova E.; Seropegin Y.; Giester G.; Kalmykov K. *J. Solid State Chem.* **2009**, *182*, 2497-2509.
280. Lipatov A.; Griбанov A.; Dunaev S. *J. Alloys Compd.* **2017**, *696*, 1019-1030.
281. Griбанov A.; Grytsiv A.; Royanian E.; Rogl P.; Bauer E.; Giester G.; Seropegin Y. *J. Solid State Chem.* **2008**, *181*, 2964-2975.
282. Savysyuk I.; Shcherban O.; Semuso N.; Gladyshevskii R.; Gladyshevskii E. *Chem. Met. Alloys* **2012**, *5*, 103-112.
283. Mayer C.; Gaudin E.; Gorsse S.; Porcher F.; Andre G.; Chevalier B. *J. Phys. Condens. Matter* **2012**, *24*, 136001.
284. Salamakha P. S.; Ste,peń-Damm J.; Prots Y.; Bodak O. *J. Alloys Compd.* **1996**, *242*, L3-L4.
285. Mayer C.; Gaudin E.; Gorsse S.; Chevalier B. *J. Solid State Chem.* **2011**, *184*, 325-330.
286. Belan B.; Dzevenko M.; Daszkiewicz M.; Gladyshevskii R. *Phys. Chem. Sol. State* **2021**, *22*, 88-93.
287. Konyk M.; Romaka L.; Stadnyk Y.; Romaka V. V.; Serkiz R. *Visnyk of the Lviv University. Series Chemistry* **2018**, *59*.
288. Sologub O. L.; Salamakha P. S.; Godart C. *J. Alloys Compd.* **2000**, *307*, 31-39.
289. Soudé A.; Tougait O.; Pasturel M.; Kaczorowski D.; Konyk M.; Noël H. *J. Alloys Compd.* **2009**, *488*, 123-128.
290. Belskii V.K. K. M. B., Pecharskii V.K., Bodak O.I. *Sov. Phys. Crystallogr.* **1987**, *139-140*.
291. Gladyshevskii R. E.; Cenzual K.; Zhao J. T.; Parthé E. *Acta Crystallogr. C* **1992**, *48*, 221-225.
292. Skornia P.; Deniszczyk J.; Fijałkowski M.; Ślebarski A. *J. Alloys Compd.* **2019**, *775*, 524-532.
293. Skornia P.; Deniszczyk J.; Fijałkowski M.; Ślebarski A. *J. Alloys Compd.* **2019**, *790*, 1051-1059.
294. Fedyna M.F. B. O. I., Pecharskii V.K. *Inorg. Mater.* **1991**, *918-920*.
295. Bodak O.I. M. O. Y., Pecharskii V.K. *Russ. Metall.* **1993**, *211-214*.
296. Morozkin A. V.; Seropegin Y. D. *J. Alloys Compd.* **2004**, *365*, 168-172.
297. Morozkin A. V.; Yao J.; Mozharivskiy Y.; Isnard O. *J. Magn. Magn. Mater.* **2012**, *324*, 2977-2982.
298. Konyk M.B. H. A. M., Serkiz R.Y. *Visn. Lviv. Derzh. Univ., Ser. Khim.* **2012**, *42-49*.
299. Fedyna M.F. B. O. I., Mokra I.R. *Metally* **1999**, *128 -*
300. Fedyna M. F., Bodak, O.I., & Mokra, I.R. *Metally* **2001**, *118-123*.
301. Belan B.; Manyako M.; Gladyshevskii R. *Chem. Met. Alloys* **2018**, *11*, 1-5.
302. Liang J.; Liao C.; Du Y.; Tang Y.; Han Y.; He Y.; Liu S. *J. Alloys Compd.* **2010**, *493*, 122-127.
303. Skolozdra R.V. K. L. P. *Russ. Metall.* **1988**, *207-212*.

304. Romaka L.; Konyk M.; Romaka V. V.; Melnychenko N.; Rogl P. *J. Alloys Compd.* **2008**, *454*, 136-141.
305. Romaka L.P. D. V. M., Stadnyk Y.V., Phase Equilibria in the Sm-Ni-Sn Ternary System, *Abstr. 10th Int. Conf. Crystal Chem. Intermet. Compd.*, Lviv, **2007**, p. 47.
306. Schäfer K.; Schwickert C.; Niehaus O.; Winter F.; Pöttgen R. *Solid State Sci.* **2014**, *35*, 66-73.
307. Becker P. J.; Coppens P. *Acta Crystallogr.* **1974**, *A30*, 129-147.
308. Herrmann K. W. *Iowa State Coll. J. Sci.* **1955**, *31*, 439-440.
309. Manyako M.B. R. I. V., Zarechnyuk O.S., Yanson T.I. *Sov. Phys. Crystallogr.* **1985** *30*, 280-282.
310. Longworth G.; Harris I. R. *J. Less-Common Met.* **1973**, *33*, 83-90.
311. Dwight A. E. *J. Less-Common Met.* **1987**, *127*, 175-178.
312. Muts I.; Zaremba V. I.; Pöttgen R. *Z. Anorg. Allg. Chem.* **2012**, *638*, 64-67.
313. Seidel S.; Niehaus O.; Matar S. F.; Janka O.; Gerke B.; Rodewald U. C.; Pöttgen R. *Z. Naturforsch.* **2014**, *69b*, 1105-1118.
314. Hull A. W. *Phys. Rev.* **1921**, *17*, 571-588.
315. Schubert K. B. H., Gohle R., Lukas H.L., Meissner H.G., Stolz E. *Naturwissenschaften* **1958**, *45*, 360-361.
316. Wanek C.; Harbrecht B. *Z. Anorg. Allg. Chem.* **2007**, *633*, 1397-1402.
317. Stegemann F.; Janka O. *Monatsh. Chem.* **2019**, *150*, 1175-1185.
318. Ye Z.; Meng F.; Zhang F.; Sun Y.; Yang L.; Zhou S. H.; Napolitano R. E.; Mendeleev M. I.; Ott R. T.; Kramer M. J.; Wang C. Z.; Ho K. M. *Sci Rep* **2019**, *9*, 6692.
319. Nakamura Y.; Matsuoka E.; Sugawara H.; Sakurai T.; Ohta H. *J. Phys.: Conf. Series* **2022**, *2164*.
320. Palasyuk A.; Dai J.-C.; Corbett J. D. *Inorg. Chem.* **2008**, *47*, 3128-3134.
321. Verniere A.; Lejay P.; Bordet P.; Chenavas J.; Tholence J. L.; Boucherle J. X.; Keller N. *J. Alloys Compd.* **1995**, *218*, 197-203.
322. Salamakha P. S.; Sologub O. L. *J. Alloys Compd.* **1999**, *287*, L1-L3.
323. Yarema M.; Zaremba O.; Gladyshevskii R.; Hlukhyy V.; Fässler T. F. *J. Solid State Chem.* **2012**, *196*, 72-78.
324. Palenzona A.; Cirafici S. *Thermochim. Acta* **1978**, *25*, 252-256.
325. Huch R.; Klemm W. *Z. Anorg. Allg. Chem.* **1964**, *329*, 123-135.
326. Dwight A. E. *Trans. Am. Soc. Met.* **1961**, *53*, 479-500.
327. Eustermann F.; Stegemann F.; Renner K.; Janka O. *Z. Anorg. Allg. Chem.* **2017**, *643*, 1836-1843.
328. Compton V. B.; Matthias B. T. *Acta Crystallogr.* **1959**, *12*, 651-654.
329. Le Roy J.; Moreau J. M.; Paccard D.; Parthé E. *Acta Crystallogr.* **1978**, *34*, 9-13.
330. Olcese G. L. *J. Less-Common Met.* **1973**, *33*, 71-81.
331. A. I. *Natl. Phys. Lab. U.K., Symp.* **1958**, 3F-2-3F-11.
332. Buschow K. H. J. *J. Less-Common Met.* **1965**, *9*, 452-456.
333. Eustermann F.; Stegemann F.; Radzieowski M.; Janka O. *Inorg. Chem.* **2019**, *58*, 16211-16226.
334. Oesterreicher H. *J. Less-Common Met.* **1971**, *25*, 228-230.
335. Cardoso Gil R. H.; Trovarelli O.; Geibel C.; Grin Y. Z. *Kristallogr. - NCS* **1999**, *214*, 459.
336. Rossi D.; Mazzone D.; Marazza R.; Ferro R. *Z. Anorg. Allg. Chem.* **1983**, *507*, 235-240.
337. Tsvyashchenko A. V.; Fomicheva L. N. *J. Less-Common Met.* **1987**, *134*, 13-15.
338. Cordier G.; Henseleit R. *Z. Kristallogr.* **1993**, *203*, 144-145.
339. Dwight A. E.; Mueller M. H.; Conner Jr R. A.; Downey J. W.; Knott H. W. *Trans. Metall. Soc. AIME* **1968**, *242*, 2075-2080.
340. Fornasini M. L.; Iandelli A.; Merlo F.; Pani M. *Intermetallics* **2000**, *8*, 239-246.
341. Cordier G.; Henseleit R. *Z. Kristallogr.* **1993**, *203*, 142-143.
342. Zacharias W. H. *Skr. Nor. Vidensk.-Akad.* **1928**, *4*, 1-166.
343. Diehl J.; Davideit H.; Klimm S.; Tegel U.; Geibel C.; Steglich F.; Horn S. *Physica B* **1995**, *206-207*, 344-348.
344. Barth T.; Lunde G. *Z. Phys. Chem.* **1925**, *117U*, 478-490.
345. Giebelmann E. C. J.; Engel S.; El Saudi I. M.; Schumacher L.; Radzieowski M.; Gerdes J. M.; Janka O. *Solids* **2023**, *4*, 166-180.
346. Giesselmann E. C. J.; Engel S.; Baldauf J.; Kosters J.; Matar S. F.; Kickelbick G.; Janka O. *Inorg. Chem.* **2024**, *63*, 8180-8193.
347. Kundaliya D. C.; Malik S. K. *Solid State Commun.* **2004**, *131*, 489-491.

348. Javorský P.; Havela L.; Wastin F.; Boulet P.; Rebizant J. *Phys. Rev. B* **2004**, *69*, 054412.
349. Tyvanchuk A. T., Yanson, T.I., Kotur, B.Ya., Zarechnyuk, O.S., Kharakterova, M.L. *Izvestiya Akademii Nauk SSSR, Metally* **1988**, *4*, 187-188.
350. Kranenberg C.; Mewis A. *Z. Anorg. Allg. Chem.* **2000**, *626*, 1448-1453.
351. Rykhal' R. M., New Members of the Ce₃Co₈Si and Mo₂NiB₂ Structure Types in the Rare-Earth Metal-Nickel-Aluminium Systems, *Tezisy Dokl. Vses. Konf. Kristallokhim. Intermet. Soeden*, **1978**, p. 17.
352. Palacios L.; De La Torre Á. G.; Bruque S.; García-Muñoz J. L.; García-Granda S.; Sheptyakov D.; Aranda M. A. G. *Inorg. Chem.* **2007**, *46*, 4167-4176.
353. Hörkner W.; Müller-Buschbaum H. *J. Inorg. Nucl. Chem.* **1976**, *38*, 983-984.
354. Owen E. A.; Preston G. D. *Proc. Phys. Soc. London* **1922**, *35*, 101-108.
355. Pauling L.; Hendricks S. B. *J. Am. Chem. Soc.* **2002**, *47*, 781-790.
356. Wheeler P. Davey; Hoffman E. O. *Phys. Rev.* **1920**, *15*, 333.
357. Gorochov M. O.; Van T. V.; Huy D. N.; Barthelemy E.; Flahaut J. *Colloq. Int. Centre Natl. Rech. Sci.* **1970**, *2*, 157-168.
358. Fornasini M. L.; Merlo F. *Acta Crystallogr.* **1976**, *B32*, 1864-1867.
359. Eisenmann B. J. M., Klee W., Schafer H. *Rev. Chim. Miner.* **1983**, *20*, 255-263.
360. Steudel R.; Reinhardt R.; Schuster F. *Angew. Chem.* **2006**, *89*, 756-757.
361. Engel S.; Giesselmann E. C. J.; Reimann M. K.; Pöttgen R.; Janka O. *Acs Organic & Inorganic Au* **2024**, *4*, 188-222.
362. Engel S.; Janka O., Volume 1 From Construction Materials to Technical Gases, 2.11 Bulk Metallic Glasses. In R. Pöttgen, T. Jüstel and C. A. Strassert, Eds. De Gruyter: 2023; pp 265-270.

Cooperation Partners

1. Work group intern cooperations and measurements:

- ICP-MS analysis for the $AEAl_2$ and $AEAl_4$ performed by Dr. K. Brix and apl. Prof. Dr. R. Kautenburger
- Quantum chemical calculations for the $AEAl_2$ and $AEAl_4$ compounds performed by Prof. Dr. H. P. Beck
- ^{27}Al MAS NMR analysis performed by E. C. J. Gießelmann
- Synthesis of Melting Gels by S. Pohl and M. F. Briesenick for the incorporation of the $EuAl_2S_4$ in the Melting Gel as well as the fluorescence and UV/Vis spectroscopic measurements
- Synthetic support on many reactions by E. C. J. Gießelmann, L. E. Schank and C. Kloos

2. External cooperations and measurements:

- Synthetic support for the $SrAl_5Pt_3$ and $Sr_2Al_{16}Pt_9$ by Dr. F. Stegemann and J. Bönnighausen from the University of Münster
- Quantum chemical analysis performed on $SrAl_5Pt_3$, $Sr_2Al_{16}Pt_9$ and $Eu_4Al_{13}Pt_9$ by Dr. R. S. Touzani from the Institut für Werkstoff- und Fügetechnik (IWF), Otto-von-Guericke-Universität Magdeburg
- Synthetic support for the $Eu_4Al_{13}Pt_9$ by Dr. N. Zaremba from the MPI CPfS Dresden
- High-pressure synthesis by Dr. G. Heymann from the Institute für Allgemeine, Anorganische und theoretische Chemie, Universität Innsbruck, Austria
- Cooperation partner for the physical property measurements at the University of Münster in the work group of Prof. Dr. R. Pöttgen. Measurements were performed by Dr. M. K. Reimann, L. Schumacher, J. Wiethölter
- Mößbauer spectroscopic measurements performed by A. Koldemir from the University of Münster in the work group of Prof. Dr. R. Pöttgen
- Single crystal SEM/EDX measurements on $CaAl_2Pt_2$, Ca_2Al_3Pt and Ca_2AlPt_2 by Dr. M. Koch from the Leibniz Institute for New Materials
- XPS measurements of YAl_5Pt_3 by Dr. F. Müller from the Department of Experimental Physics and Center for Biophysics at the Saarland University

- Quantum chemical calculations performed by Prof. Dr. Y. Zhang for YAl_5Pt_3 from Department of Chemistry and Physics, Warren Wilson College, Swannanoa, NC, 28778, USA
- Electrical resistivity measurements on the $SrAl_8Rh_2$ single crystal by Eteri Svanidze, Mitja Krnel, Nazar Zaremba, Markus König from the MPI CPfS, Dresden
- NMR measurements on the $CaAl_2S_4$ and $SrAl_2S_4$ by L. P. Rüthing and J. Schmedt auf der Günne from the Department of Chemistry and Biology, Faculty IV: School of Science and Technology, Inorganic Materials Chemistry and Center of Micro- and Nanochemistry and Engineering (Cm), University of Siegen, Germany

Publication List

Own Publications

8. S. Engel, M. K. Reimann, E. Svanidze, M. Krnel, N. Zaremba, M. König, O. Janka:
SrAl₈Rh₂ – the First Phase in the Sr/Al/Rh System and New Representative of the CeAl₈Fe₂ Type Structure
Z. Kristallogr. **2025**, 240, 1-11. [DOI: [10.1515/zkri-2024-0115](https://doi.org/10.1515/zkri-2024-0115)]
7. S. Engel, E. C. J. Gießelmann, L. Schumacher, Y. Zhang, F. Müller, O. Janka:
Synthesis, Magnetic and NMR Spectroscopic Properties of the MA₅Pt₃ Series (M = Ca, Y, La-Nd, Sm-Er)
Dalton Trans. **2024**, 53, 12176-12188. [DOI: [10.1039/d4dt01296h](https://doi.org/10.1039/d4dt01296h)]
6. S. Engel, M. Koch, O. Janka:
Nominal CaAl₂Pt₂ and Ca₂Al₃Pt – Two New Intermetallic Compounds in the Ternary System Ca–Al–Pt
Z. Anorg. Allg. Chem. **2024**, 650, 18, e202400094. [DOI: [10.1002/zaac.202400094](https://doi.org/10.1002/zaac.202400094)]
5. S. Engel, O. Janka:
New rare earth representatives adopting the Ce₂Al₁₆Pt₉ type structure
Z. Naturforsch. **2024**, 79b, 12, 595-603. [DOI: [10.1515/znb-2024-0022](https://doi.org/10.1515/znb-2024-0022)]
4. S. Engel, L. Schumacher, O. Janka:
Modifying the Valence Phase Transition in Eu₂Al₁₅Pt₆ via the Solid Solutions Eu₂Al₁₅(Pt_{1-x}T_x)₆ (T = Pd, Ir, Au; x = 1/6)
Z. Naturforsch. B **2024**, 79b, 21-27. [DOI: [10.1515/znb-2023-0072](https://doi.org/10.1515/znb-2023-0072)]
3. S. Engel, E. Gießelmann, L. E. Schank, G. Heymann, K. Brix, R. Kautenburger, H. P. Beck, O. Janka:
Theoretical and ²⁷Al NMR Spectroscopic Investigations of Binary Intermetallic Alkaline-Earth Aluminides
Inorg. Chem. **2023**, 62, 4260-4271. [DOI: [10.1021/acs.inorgchem.2c04391](https://doi.org/10.1021/acs.inorgchem.2c04391)]
2. S. Engel, N. Zaremba, R. S. Touzani, O. Janka:
Eu₄Al₁₃Pt₉ – A Coloring Variant of the Ho₄Ir₁₃Ge₉ Type Structure
Z. Naturforsch. B **2023**, 78b, 147-15. [DOI: [10.1515/znb-2023-0300](https://doi.org/10.1515/znb-2023-0300)]
1. S. Engel, J. Bönnighausen, F. Stegemann, R. S. Touzani, O. Janka:
SrAl₅Pt₃ and Sr₂Al₁₆Pt₉ – Two New Strontium Aluminum Platinides
Z. Naturforsch. B. **2022**, 77b, 367-379. [DOI: [10.1515/znb-2022-0012](https://doi.org/10.1515/znb-2022-0012)]

Cooperation Publications

8. E. C. J. Gießelmann; L. Schumacher; S. F. Matar; S. Engel; G. Kickelbick; O. Janka:
Systematic Investigations of the Solid Solution Zr(V_{1-x}Al_x)₂ Adopting the Laves Phase Structures
Chem. Eur. J. **2025**, 31, e202404248. [DOI: [10.1002/chem.202404248](https://doi.org/10.1002/chem.202404248)]
7. E. C. J. Gießelmann, S. Engel, S. Pohl, M. Briesenick, L. P. Rütting, C. Kloos, A. Koldemir, L. Schumacher, J. Wiethölter, J. Schmedt auf der Günne, G. Kickelbick, O. Janka:

- Rapid Synthesis of a Green Emitting Phosphor by Sulfidation of Intermetallic EuAl₂ and Its Use in a Hybrid Material**
Chem. Mater. **2024**, *37*, 97-108. [DOI: [10.1021/acs.chemmater.4c02093](https://doi.org/10.1021/acs.chemmater.4c02093)]
6. M. Radzieowski, E. C. J. Giebelmann, S. Engel, O. Janka:
Structure, Physical and ²⁷Al NMR Spectroscopic Properties of the Missing Members of the Equiatomic REAlRh (RE = Sm, Tb, Dy, Er, and Lu) Series
Z. Naturforsch. **2024**, *79b*, 459-467. [DOI: [10.1515/znb-2024-0053](https://doi.org/10.1515/znb-2024-0053)]
 5. E. C. J. Giebelmann, S. Engel, J. Baldauf, J. Köstern, S. F. Matar, G. Kickelbick, O. Janka:
Searching for Laves Phase Superstructures: Structural and ²⁷Al NMR Spectroscopic Investigations in the Hf-V-Al System
Inorg. Chem. **2024**, *63*, 8180-8193. [DOI: [10.1021/acs.inorgchem.4c00391](https://doi.org/10.1021/acs.inorgchem.4c00391)]
 4. E. C. J. Giebelmann, S. Engel, J. G. Volpini, H. Huppertz, G. Kickelbick, O. Janka:
Mechanistic Studies on the Formation of Ternary Oxides by Thermal Oxidation of the Cubic Laves Phase CaAl₂
Inorg. Chem. Front. **2024**, *11*, 286-297. [DOI: [10.1039/d3qi01604h](https://doi.org/10.1039/d3qi01604h)]
 3. E. C. J. Giebelmann, S. Engel, Israa El Saudi, L. Schumacher, M. Radzieowski, J. M. Gerdes, O. Janka:
On the RE₂TiAl₃ (RE = Y, Gd-Tm, Lu) Series – the First Aluminum Representatives of the Rhombohedral Mg₂Ni₃Si Type Structure
Solids **2023**, *4*, 166-180. [DOI: <https://doi.org/10.3390/solids4030011>]
 2. E. C. J. Giebelmann, S. Engel, W. Kostusiak, Y. Zhang, P. Herbeck-Engel, G. Kickelbick, O. Janka:
Raman and NMR Spectroscopic and Theoretical Investigations of the Cubic Laves-Phases REAl₂ (RE = Sc, Y, La, Yb, Lu)
Dalton Trans. **2023**, *52*, 3391-3402. [DOI: [10.1039/D3DT00141E](https://doi.org/10.1039/D3DT00141E)]
 1. N. Zaremba, V. Pavlyuk, F. Stegemann, V. Hlukhyy, S. Engel, S. Klenner, R. Pöttgen, O. Janka:
MA₄Ir₂ (M = Ca, Sr, Eu) – Superstructures of the KAu₄In₂ Type
Monatsh. Chem. **2022**, *154*, 43-52. [DOI: [10.1007/s00706-022-03005-8](https://doi.org/10.1007/s00706-022-03005-8)]

Review articles

2. S. Engel, E. C. J. Giebelmann, M. K. Reimann, R. Pöttgen, O. Janka:
On the Ytterbium Valence and The Physical Properties in Selected Intermetallic Phases
ACS Organic & Inorganic Au **2024**, *4*, 188-222. [DOI: [10.1021/acsorginorgau.3c00054](https://doi.org/10.1021/acsorginorgau.3c00054)]
1. S. Engel, E. C. J. Giebelmann, R. Pöttgen, O. Janka:
Trivalent Europium – A Scarce Case in Intermetallics
Rev. Inorg. Chem. **2023**, *43*, 4, 571-582. [DOI: [10.1515/revic-2023-0003](https://doi.org/10.1515/revic-2023-0003)]

Book Chapters

2. S. Engel, O. Janka:
„Bulk Metallic Glasses“ in *Applied Inorganic Chemistry*
DeGruyter, **2022** Chapter 2.11. [[DOI: 10.1515/9783110733143-018](https://doi.org/10.1515/9783110733143-018)]
1. S. Engel, O. Janka:
„Shape Memory Alloy“ in *Applied Inorganic Chemistry*
DeGruyter, **2022** Chapter 2.10. [[DOI: 10.1515/9783110733143-017](https://doi.org/10.1515/9783110733143-017)]